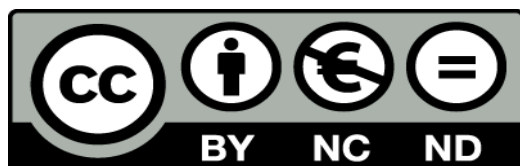




# UNIVERSIDAD DE LA RIOJA

## TESIS DOCTORAL

Título
<b>Diseño y aplicaciones de materiales híbridos fotoactivos</b>
Autor/es
<b>Cintia Ezquerro Parmo</b>
Director/es
Elena Lalinde Peña y Jesús Rubén Berenguer Marín
Facultad
Facultad de Ciencia y Tecnología
Titulación
Departamento
Química
Curso Académico



**Diseño y aplicaciones de materiales híbridos fotoactivos**, tesis doctoral de Cintia Ezquerro Parmo, dirigida por Elena Lalinde Peña y Jesús Rubén Berenguer Marín (publicada por la Universidad de La Rioja), se difunde bajo una Licencia Creative Commons Reconocimiento-NoComercial-SinObraDerivada 3.0 Unported.  
Permisos que vayan más allá de lo cubierto por esta licencia pueden solicitarse a los titulares del copyright.

---

# **DISEÑO Y APLICACIONES DE MATERIALES HÍBRIDOS FOTOACTIVOS**

Memoria presentada en el Departamento de Química de la Universidad de La Rioja  
para optar al título de Doctor por la graduada:

**Cintia Ezquerro Parmo**

Universidad de La Rioja-2019

---



Directores del trabajo de investigación:

Elena Lalinde Peña

Jesús R. Berenguer



**ELENA LALINDE PEÑA**, Catedrática de Química Inorgánica del Departamento de Química de la Universidad de La Rioja.

**JESÚS R. BERENGUER MARÍN**, Profesor Titular de Química Inorgánica del Departamento de Química de la Universidad de La Rioja.

**CERTIFICAN:**

que la presente memoria titulada ***Diseño y aplicaciones de materiales híbridos fotoactivos*** ha sido realizada bajo su supervisión por la graduada en química **CINTIA EZQUERRO PARMO** en el Departamento de Química de la Universidad de La Rioja, y autorizan su presentación para que sea calificada como Tesis Doctoral.

Logroño, junio de 2019

Fdo.: Elena Lalinde Peña

Fdo.: Jesús R. Berenguer Marín



## Agradecimientos

Parece que fue ayer cuando empecé con esta aventura y resulta que ya estoy escribiendo la parte más especial de la tesis, los agradecimientos. Aunque no lo parezca han sido cuatro años muy intensos con muchos altibajos, en los que nunca me ha faltado el apoyo de los míos. Es por ello que quiero dedicarles unas palabras de agradecimiento.

A mis tutores, Elena Lalinde y Jesús R. Berenguer, quienes me han servido de guía y fuente de inspiración a lo largo de todos estos años y de quienes he aprendido infinidad de cosas. Agradecer también su enorme dedicación, implicación en el trabajo y paciencia, en muchas ocasiones. Sinceramente creo que no podría haber tenido mejores jefes.

A mis compañeros de laboratorio: Nora, las monis, Gonzalo, Natalia, David (el gran descubrimiento del año) y, por su puesto, a mi compañera de batallas y protegida, Rebeca Lara. Gracias a ellos, a sus risas y a su buen humor las malas rachas y los momentos de crisis se veían con otros ojos. Un auténtico lujo haber compartido laboratorio y experiencias con todos vosotros.

No quisiera olvidarme de los integrantes del Laboratorio de Nanotecnología Molecular de la Universidad de Alicante y, en especial, de Javier García y Elena Serrano por su implicación en este trabajo, pero, sobre todo, por acogerme y hacerme sentir como en casa durante mi visita express a tierras alicantinas.

Y por supuesto, no podía terminar sin agradecer a mis amigos y familiares, en especial a mi madre y a ti, Eduardo, por vuestro apoyo diario, por hacerme ver los problemas desde otra perspectiva y convencerme de no tirar la toalla en los peores momentos. Gracias por estar ahí.

A todos vosotros ¡GRACIAS!



# Index

<b>Abbreviations and acronyms</b>	<b>9</b>
<b>Presentation</b>	<b>11</b>
<b>Chapter I. Luminescent mesoporous silica materials based on Ir<sup>III</sup> and Pt<sup>II</sup> complexes</b>	<b>17</b>
I.1 PART I: Design of cyclometalated Ir <sup>III</sup> and Pt <sup>II</sup> complexes bearing Si(OEt) <sub>3</sub> groups	33
I.1.1 Synthesis and characterization of complexes <b>1-4</b>	36
I.1.2 Photophysical properties of the Ir <sup>III</sup> and Pt <sup>II</sup> complexes	42
I.1.2.1 Photophysical properties of complexes <b>1-3</b>	42
I.1.2.2 Photophysical properties of complex <b>4</b> and formation of a gel ( <b>4-gel</b> )	49
I.2 PART II: Synthesis of luminescent mesoporous silica-based materials	55
I.2.1 Synthesis of hybrid organometallo-silica materials ( <b>SiO<sub>2</sub>_P</b> , <b>SiO<sub>2</sub>_G</b> )	56
I.2.2 Characterization of the hybrid organometallo-silica materials	57
I.2.2.1 Textural characterization	57
I.2.2.2 Spectroscopy characterization	61
<b>Chapter II. Hybrid white-emitting organometallo-silica nanoparticles</b>	<b>69</b>
II.1 PART I: Desing of blue-to-red phosphorescence cyclometalated Ir <sup>III</sup> complexes	79
II.1.1 Synthesis and characterization of the iridium(III) precursors <b>5-6</b>	81
II.1.2 Photophysical properties of the iridium(III) complexes	83
II.2 PART II: Monochromatic- and white-emitting silica nanoparticles as down-converters for HLEDs	93
II.2.1 Synthesis of organometallo-silica nanoparticles	94
II.2.1.1 Monochromatic-emitting organometallo-silica nanoparticles ([B,G,R]-NP)	94
II.2.1.2 White-emitting organometallo-silica nanoparticles ([W]-NP)	95
II.2.2 Characterization of the organometallo-silica nanoparticles	98
II.2.2.1 Textural characterization	98
II.2.2.2 Spectroscopy characterization	102
II.2.3 Design and study of Hybrid Light Emitting Diodes (HLEDs)	110
II.2.3.1 Monochromatic-emitting HLEDs	110
II.2.3.2 Single component white-emitting HLED	115

<b>Capítulo III. Nanopartículas de sílice mesoporosas como biomarcadores</b>	<b>119</b>
III.1 Síntesis y caracterización de los compuestos <b>7-8</b>	134
III.2 Propiedades fotofísicas	136
III.3 Síntesis de nanopartículas mesoporosas de sílice ( <b>NP<sub>OH</sub>, NP<sub>Me</sub>, NP<sub>APTES</sub></b> )	142
III.4 Caracterización de las nanopartículas	144
III.4.1 Caracterización textural	144
III.4.2 Caracterización espectroscópica	148
III.4.2.1 Espectros de infrarrojo	148
III.4.2.2 Propiedades fotofísicas	149
III.5 Propiedades biológicas	154
III.5.1 Estudio de citotoxicidad	154
III.5.2 Localización celular	155
<b>Chapter IV. Photocatalytic activity of hybrid titania-based materials</b>	<b>161</b>
IV.1 Synthesis and characterization of metal complexes <b>9-10</b>	176
IV.2 Photophysical properties of the complexes	179
IV.3 Synthesis of hybrid titania-based materials ( <b>TiO<sub>2</sub>_IS, TiO<sub>2</sub>_G</b> )	183
IV.4 Characterization of the mesoporous titania-based materials	185
IV.4.1 Textural characterization	185
IV.4.2 Spectroscopy characterization	188
IV.5 Photocatalytic activity of the metal-complex titania-based materials	193
IV.5.1 Estimation of the band-gap energies	193
IV.5.2 Photocatalytic activity of the Ir <sup>III</sup> and Ru <sup>II</sup> titania-based materials	195
IV.5.2.1 Study of the photocatalytic activity under UV and visible light irradiation	196
IV.5.2.2 The role of the carboxylic group on the sensitizer	201
IV.5.3 Evaluation of the stability of the hybrid materials	203
IV.5.4 Photocatalytic mechanisms	205
<b>Summary and conclusions</b>	<b>211</b>
<b>Resumen y conclusiones</b>	<b>227</b>
<b>Experimental Part</b>	<b>243</b>
<b>Bibliography</b>	<b>285</b>
<b>Annexes</b>	<b>309</b>
<b>Research at the Laboratoire de Chimie et des Biomatériaux Supramoléculaires</b>	<b>335</b>

## Abbreviations and acronyms

<b>THF</b>	tetrahydrofuran	<b>CH<sub>2</sub>Cl<sub>2</sub></b>	dichloromethane
<b>DMSO</b>	dimethylsulfoxide	<b>CH<sub>3</sub>CN</b>	acetonitrile
<b>tol</b>	toluene	<b>ppy</b>	2-phenylpyridine
<b>dasipy</b>	4,4'-[CONH(CH <sub>2</sub> ) <sub>3</sub> Si(OCH <sub>2</sub> CH <sub>3</sub> ) <sub>3</sub> ] <sub>2</sub> -bipyridine	<b>dFppy</b>	2-(2,4-difluorophenyl)pyridine
<b>dbbpy</b>	4,4'-[CONH(CH <sub>2</sub> ) <sub>3</sub> CH <sub>3</sub> ] <sub>2</sub> -bipyridine	<b>PPETS</b>	PPh <sub>2</sub> (CH <sub>2</sub> ) <sub>2</sub> Si(OCH <sub>2</sub> CH <sub>3</sub> ) <sub>3</sub>
<b>bpy</b>	bipyridine	<b>bzq</b>	7,8-benzoquinoline
<b>TBOT</b>	titanium tetrabutoxide	<b>CTAB</b>	hexadecyltrimethylammonium bromide
<b>TEOS</b>	tetraethyl orthosilicate	<b>TEA</b>	triethanolamine
<b>DMDES</b>	diethoxydimethylsilane	<b>APTES</b>	(3-aminopropyl)triethoxysilane
<b>ODs</b>	organometallic dots	<b>NPs</b>	nanoparticles
<b>TEM</b>	transmission electron microscopy	<b>FESEM</b>	field emission scanning electron microscopy
<b>DRUV</b>	diffuse reflectance UV-Vis	<b>MALDI</b>	matrix-assisted laser desorption ionization
<b>IR</b>	infrared	<b>NMR</b>	nuclear magnetic resonance
<b>TOCSY</b>	total spectroscopy	<b>COSY</b>	correlation spectroscopy
<b>HSQC</b>	heteronuclear single-quantum correlation	<b>HMBC</b>	heteronuclear multiple bond correlation
<b>CCT</b>	correlated color temperature	<b>CIE</b>	Commision Internationale de l'Eclairage (color coordinates)
<b>CRI</b>	color rendering index	<b>HLED</b>	hybrid light emitting diode
<b>HWLED</b>	hybrid white emitting diode	<b>AIE</b>	aggregation induced emission
<b>s</b>	singlet	<b>d</b>	doublet
<b>t</b>	triplet	<b>c</b>	quadruple
<b>m</b>	multiplet	<b>pst</b>	pseudo triplet

<b>i-</b>	ipso-	<b>o-</b>	ortho-
<b>m-</b>	meta-	<b>p-</b>	para-
<b>vs/ s</b>	very strong/ strong	<b>m</b>	medium
<b>vw/ w</b>	very weak/ weak	<b>sh</b>	shoulder
<b>b</b>	broad	<b>IL</b>	intraligand
<b>LC</b>	ligand centered	<b>CT</b>	charge transfer
<b>MLCT</b>	metal to ligand charge transfer	<b>LLCT</b>	ligand to ligand charge transfer

# ***Presentation***





Nanoscience has caused a great impact in today's society mainly due to the modifications that matter can experience as a consequence of decreasing its size at the nanoscale. At this scale, materials show greater surface areas than in a massive state, modifying the physical, chemical and quantum effects that, in the nanoscale range, can affect their optical, electrical or magnetic properties.<sup>1</sup>

In this context, nanostructured porous materials have gained much interest thanks to their large surface areas, tunable pore size, adjustable framework and surface properties. Many synthetic pathways have been reported for the synthesis of these porous materials, either with a disordered pore system or ordered with various structures, which can meet the demands of the target application. Nevertheless, their use as substrates for the incorporation of light-active phases to obtain new photonic materials has become one of their most common roles. In this regard, some porous nanostructures, such as metal oxides (CdSe, WO<sub>3</sub>, MnO<sub>x</sub>, TiO<sub>2</sub>, etc.), graphene, silica materials or Metal-Organic Frameworks (MOFs), have acquired a remarkably importance.

The photocatalytic activity of some metal oxide has aroused great interest in the last decades and, consequently, the technology of semiconductor-based photocatalysis has progressed rapidly.<sup>2</sup> Among the different materials, titanium dioxide (TiO<sub>2</sub>) has emerged as a potential candidate for this purpose, due to properties such as chemical stability, non-toxicity and good oxidative features.<sup>3</sup> However, crystalline TiO<sub>2</sub> presents a wide band gap, bigger than 3 eV (3.2 eV, for the anatase phase). This means that these materials can only be activated by UV photons (4-5% of the solar spectrum), what greatly limits their efficiencies for solar light applications. Therefore, its modification with active phases able to absorb photons from the visible part (45%) of the solar spectrum is a great challenge.

Graphene has also emerged as the most significant carbon material not only due to its unprecedented physical and chemical properties (high electron conductivity, thermal conductivity and mechanical and chemical stability) but also because of its unique two-dimensional morphology and ultrahigh surface area.<sup>4</sup> Some graphene derivatives (graphene and reduced graphene oxide) also contain oxygen functional groups than can serve as appealing substrates for the binding of different types of photoactive materials (metal nanoparticles, oxides, bimetallic systems, semiconductors, etc.).<sup>5</sup> The ensuing composites have potential applications in chemical sensing,<sup>6</sup> energy storage<sup>7</sup> or photocatalysis.<sup>8</sup> In this last field, graphene have been widely studied due to its capacity to improve the catalytic activity of the incorporated phases.<sup>8-9</sup>

Metal-Organic Frameworks are also of significant interest mainly due to their structural diversity, which allows to explore combining structures with other functional materials (polymers, metal nanoparticles or biomolecules) to form new composites with appealing properties.<sup>10</sup> The resulting materials have demonstrated extraordinary performances in many fields such as catalysis, sensing, gas storage, molecular separation and protection of macromolecules, among others.<sup>10-11</sup>

In a similar way, the incorporation of photoactive centers into porous silica materials have been extensively studied over the last decade. In particular, and thanks to the inertness and the optical transparency in the visible region of silica, the introduction of luminescent metal complexes to obtain luminescent silica-based materials have broaden their versatility; giving rise to new candidates for optical sensing, bioimaging, phototherapy and hydrogen generation.<sup>12</sup>

Considering all these nanostructures, we strongly believe that luminescent silica-based materials offer the most appealing solutions to problems related to lighting, imaging or medical diagnostics, among others. On the other hand, modified titania-based materials are also attractive candidates for photodegradation processes. For these reasons, we decided to focus the research of this thesis in the development of hybrid mesoporous photoactive silica and titania materials. In addition, and thanks to the collaboration that our group maintains with other research groups, the application of some of these materials could also be studied. Thus, the research group of Prof. Javier García Martínez (Molecular Nanotechnology Lab, NANOMOL, Universidad de Alicante) performed the study of the textural properties of all the silica and titania materials described in this work. The group of Dr. Rubén D. Costa (IMDEA Materiales, Madrid) fabricated HLEDs with some of the as-synthetic nanoparticles. Finally, the biological behavior of some of the nanoparticles was also studied by the research groups of Dr. José M. García Pichel (Cáncer de Pulmón y Enfermedades Respiratorias) and Dr. Ignacio Larráyoz (Biomarcadores y Señalización Molecular), from Centro de Investigación Biomédica de La Rioja (CIBIR, Fundación Rioja Salud, Logroño).

To date, this work has given rise to the following publications:

- M. Rico-Santacruz, A.E. Sepúlveda, C. Ezquerro, Serrano, E. Lalinde, J.R Berenguer, J. García-Martínez. Bottom-up construction of highly photoactive dye-sensitized titania using Ru(II) and Ir(III) complexes as building blocks. *Appl. Catal. B: Environmental* **2017**, 200, 93-105.

- C. Ezquerro, A. E. Sepúlveda, A. Grau-Atienza, E. Serrano, E. Lalinde, J. R. Berenguer, J. García-Martínez. Organometallic phosphors as building blocks in sol-gel chemistry: luminescent organometallo-silica materials. *J. Mater. Chem. C* **2017**, *5*, 9721-9732.
- C. Ezquerro, E. Fresta, E. Serrano, E. Lalinde, J. García-Martínez, J. R. Berenguer, R. D. Costa. White-emitting organometallo-silica nanoparticles for sun-like light-emitting diodes. *Mater. Horiz.* **2019**, *6*, 130-136.



# ***Chapter I***

---

***Luminescent mesoporous silica materials based on  
Ir<sup>III</sup> and Pt<sup>II</sup> complexes***

---



## Introduction

As previously commented, in recent decades, the demand imposed by the high level of technological development in which our society is immersed has increased exponentially. This has triggered the necessity of progressing and developing new materials able to meet our specific needs. In this context, nanostructured porous materials, especially mesoporous silica-based materials, have been widely studied in the last 20 years. The inertness, the optical transparency in the visible region and the large surface areas are some of the properties that make them suitable as absorbents<sup>13</sup> or catalysts.<sup>14</sup> Nevertheless, its use as substrates for the incorporation of light-active phases has become one of the most common functions for these porous materials. In particular, the incorporation of luminescent chromophores into mesoporous silicas has allowed the obtaining of new photonic materials.<sup>15</sup> Thus, it is easy to find these luminescent mesoporous silica-based materials in a large number of very important optical, biological or photocatalytic applications such as optical sensing,<sup>16</sup> bioimaging,<sup>12d, 17</sup> phototherapy<sup>12b, 18</sup> or H<sub>2</sub> generation.<sup>12c</sup>

In this regard, the relation between the structure and properties of both the chromophore and the inorganic matrix, as well as the interface between them, are crucial issues for improving and developing more efficient photosystems. Hence, for the design and preparation of luminescent silica materials two critical challenges are generally considered: (i) the choice of the chromophore and (ii) how to combine it with the silica matrix.

### Synthesis of mesoporous silica-based materials

Nowadays, the synthesis of typical mesoporous silica materials is well documented. One of the most common approaches for the synthesis of these materials is the well-known Sol-Gel process, which is based on the generation of a solid framework from a solution through successive condensation reactions. This methodology is very attractive because it requires mild reaction conditions and avoids the typical problems in the synthesis of these materials, such as phase separation or crystallization.<sup>19</sup>

The precursors involved in the formation of the final mesoporous materials are, usually, metallic alkoxides  $M(OR)_n$  ( $M$ : Si, Ti, Zr, Al, etc., R: alkyl group). In particular, for the preparation of silica-based materials, TEOS (tetraethylorthosilicate,  $Si(OEt)_4$ ) is the most common precursor used. The reaction mechanism is summarized in figure 1.1. In detail, once the hydrolysis reaction starts, successive condensation and hydrolysis steps take place. This results in a gradual increase in the viscosity of the solution and in a change of its nature from a *sol* (colloidal suspension formed by small particles with sizes between 1 and 100 nm) to a rigid *gel*.<sup>20</sup>

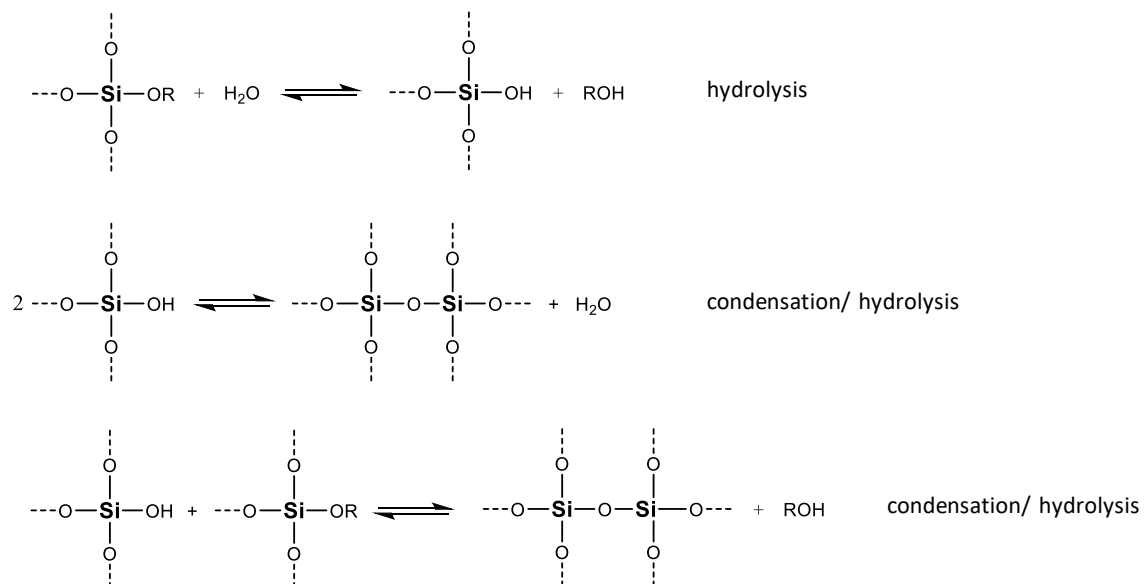


**Figure 1.1.** Reaction mechanism of the formation of a silica-oxides following the Sol-Gel process.

All these hydrolysis steps are highly dependent on the reaction conditions. Therefore, it is worth noting that, minor modifications in the temperature, pH, reactant/catalyst concentrations or reaction time remarkably affect to the properties of the resulting material in terms of morphology, size, etc. For instance, the polymerization reaction is notably pH depending. At acid pH the hydrolysis occurs slowly and, consequently, lineal molecules weakly cross-linked form the

silica framework. Meanwhile, at high pH this process occurs very fast, being the condensation the determining step of the reaction rate. As a result, rather big particles are formed.

Another point to consider is the participation of a catalyst in the formation of the mesoporous material. Thus, the addition of fluorine ions allows to obtain more defined structures, even when the condensation rate is fast.<sup>21</sup> Hence, in the presence of F<sup>-</sup>, the Si-O bonds are activated through nucleophilic catalytic mechanisms, and the poly-condensation of the framework by the formation of Si-O-Si bonds is increased.

Otherwise, when the interests are focused on the obtaining of ordered structured mesoporous materials, the role of surfactants (structure-directing agents, SDA) is crucial. These surfactants are amphiphilic organic molecules, generally formed by a *hydrophilic head* and a *hydrophobic single-tailed*. Depending on their nature, concentration, temperature and the polarity of the solvent in which the molecules are dispersed, they usually organize forming micelles with different geometries (see figure 1.2) that generate supramolecular structures.

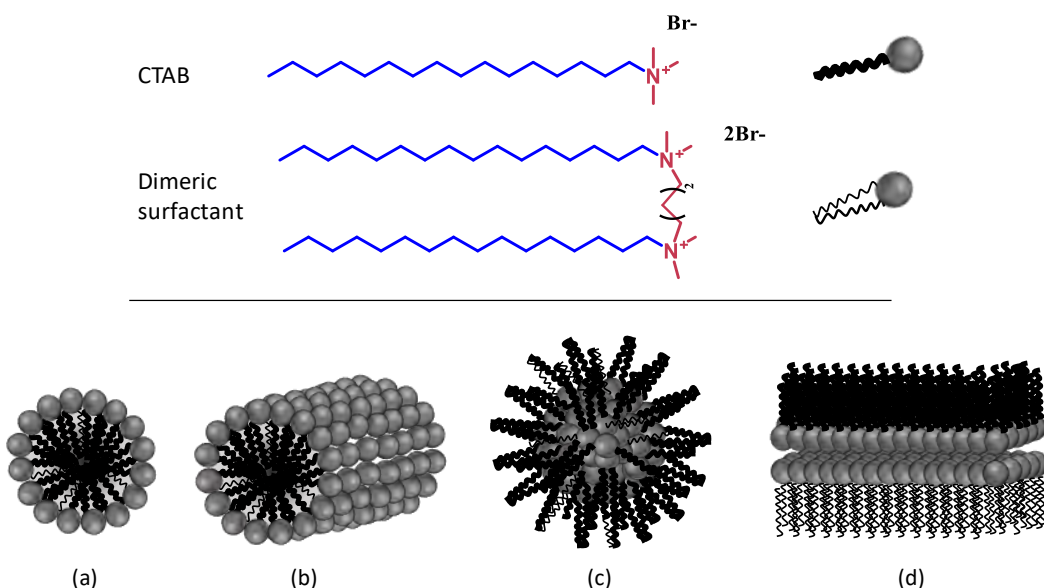


**Figure 1.2.** (Upper part) Examples of surfactants. (Lower part) Schematic representation of micellar aggregates of a surfactant: spherical (a), cylindrical (b), reverse (c) and laminar micelles.

When these molecules are incorporated into the reaction medium, they are able to act as structure-directing agents around which the Sol-Gel process occurs (see figure 1.3). In this way, the inorganic matrix grows forming ordered structured final materials. However, once the Sol-Gel reactions conclude, the pores of the as-synthesized materials are completely blocked by the surfactant molecules. For this reason, they must be removed in order to obtain the porous nature

of the silica. Hence, the elimination of the surfactant can be easily achieved by calcination of the solid or by its extraction with different solvents.

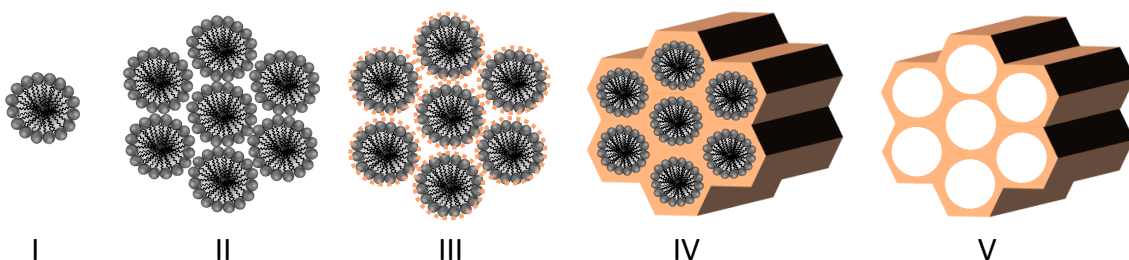


**Figure 1.3.** Schematic model of the templating mechanism in the formation of mesoporous silica-based materials: (I) Micelle formation. (II) Organization of the micelles into aggregates. (III) + TEOS. Silica growth around the surfactant template. (IV) Hydrolysis and condensation reactions. (V) Surfactant removal (*i.e.* calcination or extraction).

### **Functionalization of mesoporous silica-based materials**

In order to prepare effective silicas to be used as potential candidates in the aforementioned applications, they must be functionalized with appropriate active phases. With this aim, different approaches have been developed in the last decades.

#### i. Post-synthetic functionalizations

Traditionally, the functionalization of mesoporous silica materials has been performed by the so-called *post-synthetic* methods, which are based on the surface modification of as-synthesized silicas. The most common strategies consist of non-covalent dye uptake (by impregnation or inclusion)<sup>22</sup> or covalent grafting.<sup>23</sup> Among them, this last approximation is one of the most widely used *post-synthetic* technique.

The grafting process is based on the reaction between molecules with trialkoxysilane terminal groups of the type  $\text{Si}(\text{R}'\text{O})_3\text{R}$  ( $\text{R}$  = organic functional group) and the free silanol groups that still remain on the surface of the silica. This way, the functionality of the organic molecule is linked to the surface of the material by covalent bonds, which become the point of union between both phases (see figure 1.4).

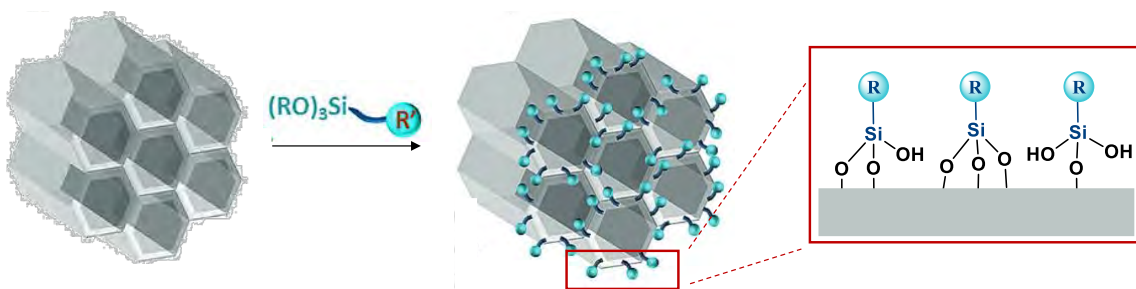


**Figure 1.4.** Grafting functionalization.

In principle, the main advantage of this methodology is that it allows to retain the starting silica phase after the modification of the material. However, depending on the size of the organic moieties and the degree of occupation, the lining of the walls is usually accompanied by a reduction in the porosity of the hybrid. Additional problems are those related to low incorporation yields, poor control over the position of the molecules in the silica material and leaching of the dye in fluid media.

## ii. In-situ functionalizations

### Co-condensation direct synthesis

Alternatively, these mesoporous silicas can also be functionalized following the so-called *in-situ* or co-condensation method.<sup>22f, 24</sup> This synthesis is based on the incorporation of the organic active phase ( $\text{Si}(\text{R}'\text{O})_3\text{R}$ ) during the Sol-Gel process in order to achieve the simultaneous condensation of the chromophore and the silica precursor. Hence, as shown in figure 1.5, the functionality of the molecule is directly incorporated in the network of the silica and becomes part of its matrix.

Following this *in-situ* technique, some of the aforementioned disadvantages can be easily reduced. In this way, the organic units are more homogeneously distributed in the framework of the silica than in the materials synthetized through the grafting route. Moreover, as the organic functionality becomes part of the silica matrix, pore blocking issue is reduced and, therefore, the final material exhibits higher pore volumes and surface areas than those grafted. And, finally, this strategy also allows to minimize leaching problems.

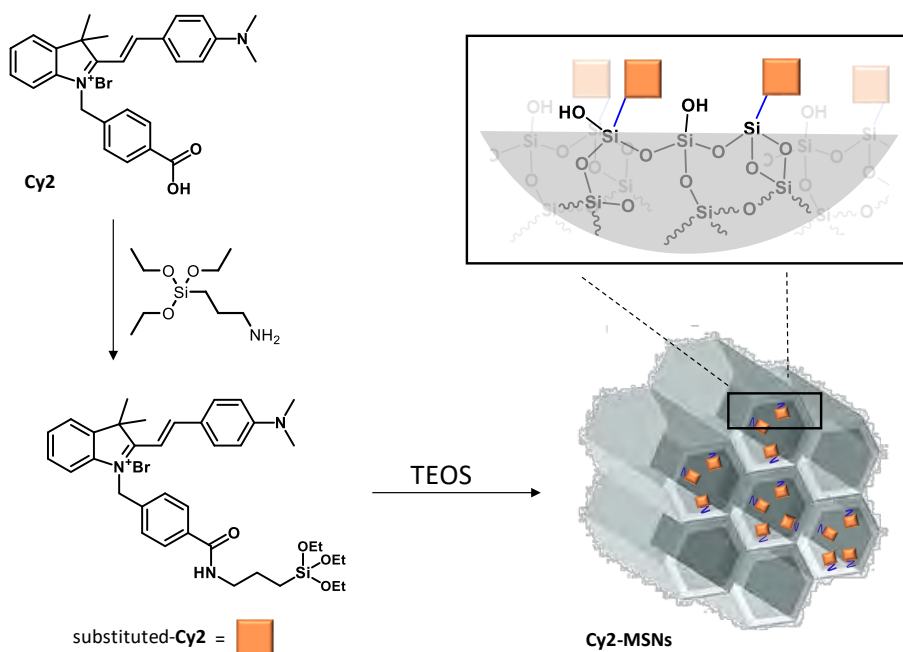


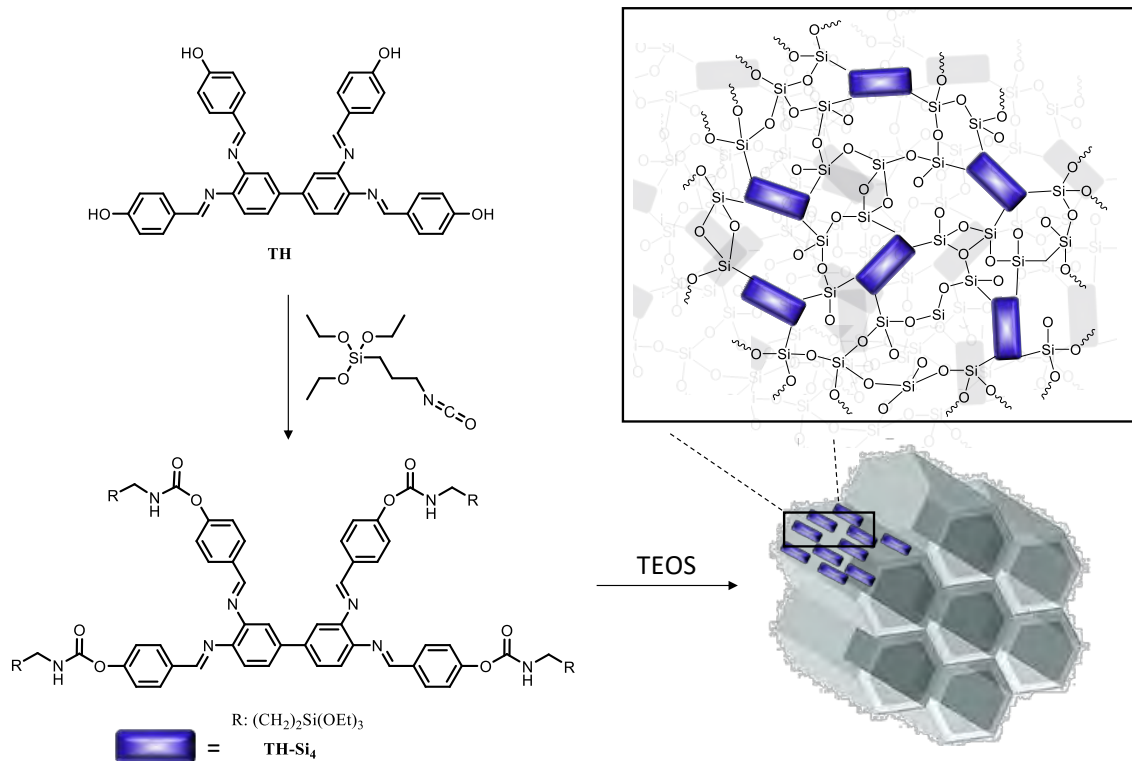
**Figure 1.5.** Co-condensation functionalization. (ACS Appl. Mater. Interfaces 2015, 7, 5462-5470)

Nevertheless, this *in-situ* methodology has also some drawbacks that should be considered. Firstly, in this type of processes, the self-condensation reaction can be a problem.<sup>26</sup> This self-condensation is usually caused by the different rate of hydrolysis and condensation of the structurally different molecules involved in the reaction (the organic functionality and the silica precursor, TEOS). Owing to this fact, a homogenous distribution of the functionality in the silica framework is not always obtained and can lead to the formation of partially or, even, completely disordered porous structures. To reduce this problem, a low proportion of the functionality in the initial reaction mixture and homogenous reaction medium are required.<sup>13</sup> Another point to consider is related to the removal of the surfactant. As previously noted, this is a final step carry out after the synthesis of the hybrid material. Therefore, it is necessary to take into account the stability of the active phase under the harsh conditions (high temperature, aggressive media) employed to remove the molecules of the surfactant.

### Synthesis of PMOs

Since it was firstly reported in 1999,<sup>27</sup> one of the most common *in-situ* approximations studied consists of the preparation of Periodic Mesoporous Organosilicas (PMOs).<sup>28</sup> These systems result from the hydrolysis and condensation reactions of a bridged organosilica precursor of the type  $(R'O)_3Si-R-Si(OR')_3$ , in the presence or absence of a second silica source. In the resulting inorganic-organic hybrid material, the organic molecule is well integrated in the

3-D network of the silica (see figure 1.6) through several Si-C covalent bonds that, unlike Si-O units, are stable against hydrolysis. Consequently, problems related to the stability or the leaching of the chromophore are notably reduced.

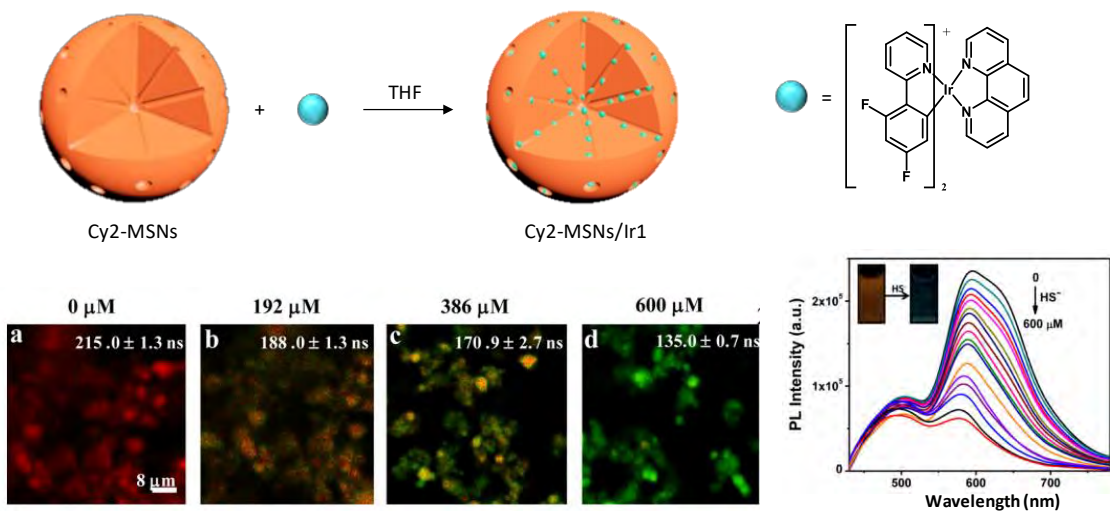


**Figure 1.6.** Schematic representation of a Periodic Mesoporous Organosilica (PMO) prepared using the molecule TH-Si<sub>4</sub> as the organic precursor. (J. Phys. Chem. C 2016, 120, 9299-9307)

In this area, many are the organic chromophores that have been used for the design of new PMOs with tunable optical and/or catalytic properties.<sup>30</sup> In addition, the resulting materials have demonstrated to be very efficient in a wide number of different applications.<sup>28a, 28d, 29-30, 31</sup>

### Functionalization of mesoporous silica-based materials with metal complexes

In a similar way, the incorporation of coordination complexes, mainly organometallic derivatives, into silica materials has also been fairly well explored in the last two decades.<sup>12c, 12e, 15f, 16c, 32</sup> In this sense, the most common strategies used include, once again, non-covalent dye uptake (mainly by impregnation or inclusion) and covalent *post-synthetic* grafting (see figure 1.7).<sup>12e, 15b, 15e, 32b, 32h, 33</sup> Using these methodologies, some luminescent silica-based materials with interesting luminescent properties have been reported in the last years.<sup>12e, 25, 32b, 32h, 33a, 33b, 33d, 34</sup>

NON-COVALENT Ir<sup>III</sup> DYE UPTAKE

## COVALENT GRAFTING

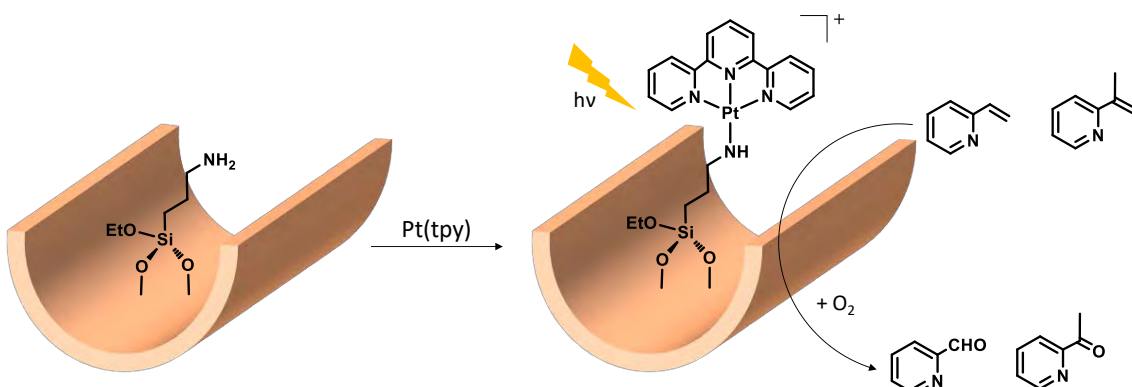


**Figure 1.7.** Functionalization of mesoporous silica nanoparticles by: (Upper part) inclusion of the Ir(III) chromophore in the porous of the material. Photographs of the as-synthesized materials as bioprobes. (*ACS Appl. Mater. Interfaces* 2015, 7, 5462-5470). (Lower part) Post-synthetic grafting with a Pt(II) complex and its used in the photooxidation of styrene derivatives under atmospheric O<sub>2</sub>. (*Chem. Eur. J.* 2016, 22, 11122-11137)

An alternative *in-situ* approach involves the co-condensation of properly functionalized organometallic compounds with terminal trialkoxysilane groups (see some examples in figure 1.8) and the silica precursor (TEOS) during the sol-gel process. This approximation was inspired on the synthesis of the PMOs. Hence, in the final mesoporous material the metal derivative is homogenously incorporated into the network of the silica, becoming part of its structure and, so, avoiding pore blocking. Besides, the extra protection that silica provides to the active phases, compared to grafted complexes, has also been demonstrated.<sup>35</sup>

Following this procedure, some hybrid metal-complex silicas were obtained in the 2000s (figure 1.8).<sup>36</sup> However, in this area, most of the reports were only focused on the synthesis and study of the catalytic properties of the resulting materials. In addition, the synthetic approach of the reported hybrids usually involves harsh thermal treatments, considerable amounts of organic co-solvents and, in many cases, acid or basic media. These synthetic requirements are clearly a problem when selecting organometallic derivatives, since a good number of transition-organometallic complexes are not stable under these reaction conditions.

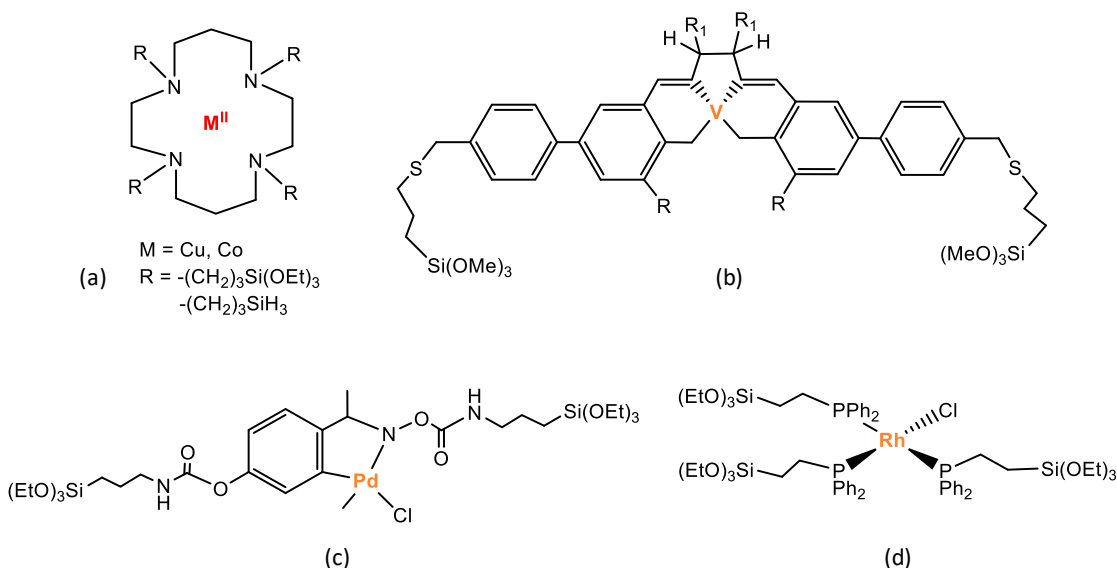


**Figure 1.8.** Examples of well-functionalized organometallic complexes used in the *in-situ* synthesis of hybrid mesoporous silicas.

To overcome some of the above mentioned issues, at the beginning of the 2010s, our group started to study the design of a new versatile approximation that would allow to operate under mild and neutral reaction conditions – the so-called Sol-Gel Coordination Chemistry.<sup>37</sup> This synthetic method led us to prepare efficient hybrid palladium-silica materials in several catalytic reactions.<sup>37</sup> Unlike the previous procedures, this is an environmentally friendly one-pot strategy based on aerobic reaction conditions, reduced amounts of organic co-solvents and the use of the silica source (TEOS) as the reaction medium.

More recently, the use of this *in-situ* approach has been generalized for the preparation of new mesoporous hybrid metal complex-silica materials with catalytic properties<sup>36d, 36f, 38</sup> and, to a smaller extent, for the synthesis of luminescent silica-based materials.<sup>32d, 32g, 35a, 35c, 39</sup>

As far as we know, the first luminescent mesoporous material of this type, prepared using the Sol-Gel Coordination Chemistry, was described by our group in 2012.<sup>35b</sup> In detail, we reported

the synthesis of a highly emissive, but unstable in solution, neutral tetrametallic copper(I) acetylide complex (figure 1.9) bearing four trialkoxysilane terminal groups in a highly symmetric disposition. The co-condensation of this derivative with TEOS in the presence of triton X-100 as a surfactant under mild reaction conditions (room temperature and neutral pH), allowed us to obtain a blue-emitter copper complex-silica material (see figure 1.9). In addition, in contrast to the low stability of the Cu(I) derivative, the resulting hybrid silica featured remarkably stability in suspension in the most common organic solvents, including water. This fact supports the final protection that the metal complex acquires upon its incorporation into the silica framework.

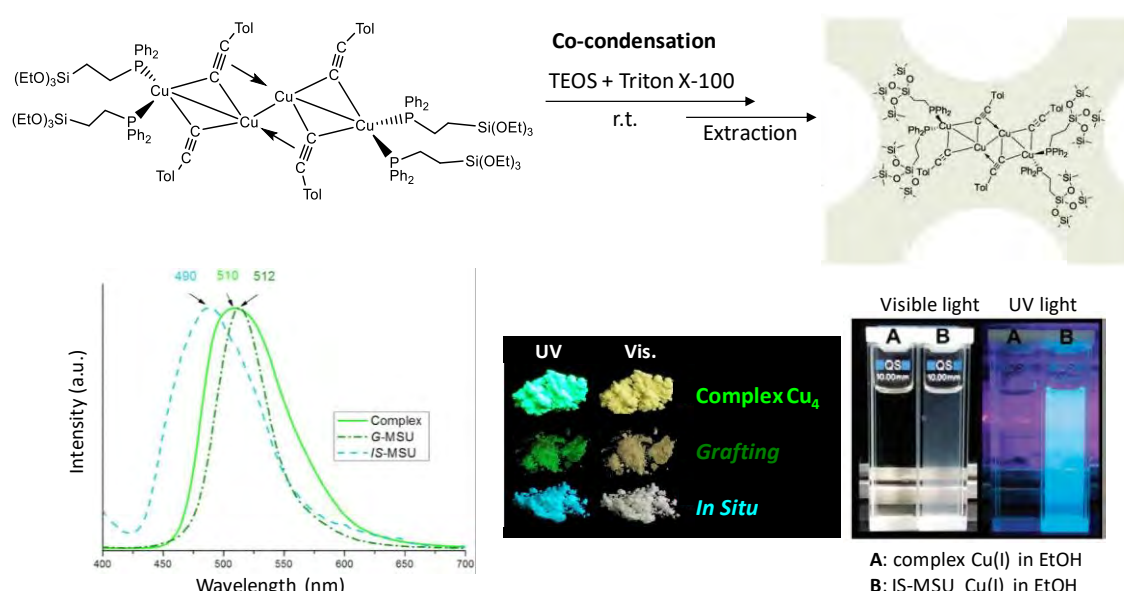


**Figure 1.9.** (Upper part) Schematic representation of the preparation of a luminescent hybrid mesoporous copper-silica material. (Lower part) Emission spectra (left) and photographs under visible and UV light of the solids (middle), solutions and suspensions of the complex and its material, respectively (right). (Chem. Commun. 2012, 48, 8883-8885)

Other materials prepared by this eco-friendly procedure were reported by Prof. Zhao and co-workers, who prepared biological nanoprobes based on two different hybrid mesoporous silica nanoparticles containing neutral or cationic iridium(III) derivatives and an europium(III) complex.<sup>40</sup>

More recently, Prof. Wei Huang and co-workers reported ratiometric oxygen-sensitive nanoprobes with two-channel phosphorescence signals.<sup>32g</sup> They designed a core-shell silica-based nanoparticles with a Ir(III) complex covalently bonded in the solid framework (*in-situ* approach) and an oxygen-sensitive Pt(II) derivative encapsulated in the porous of the silica (non-covalent dye uptake). The resulting luminescent silica-based material featured very interesting

properties and could be used for detecting changes in the intracellular O<sub>2</sub> levels and performing quantitative O<sub>2</sub> measurement *via* ratiometric bioimaging.

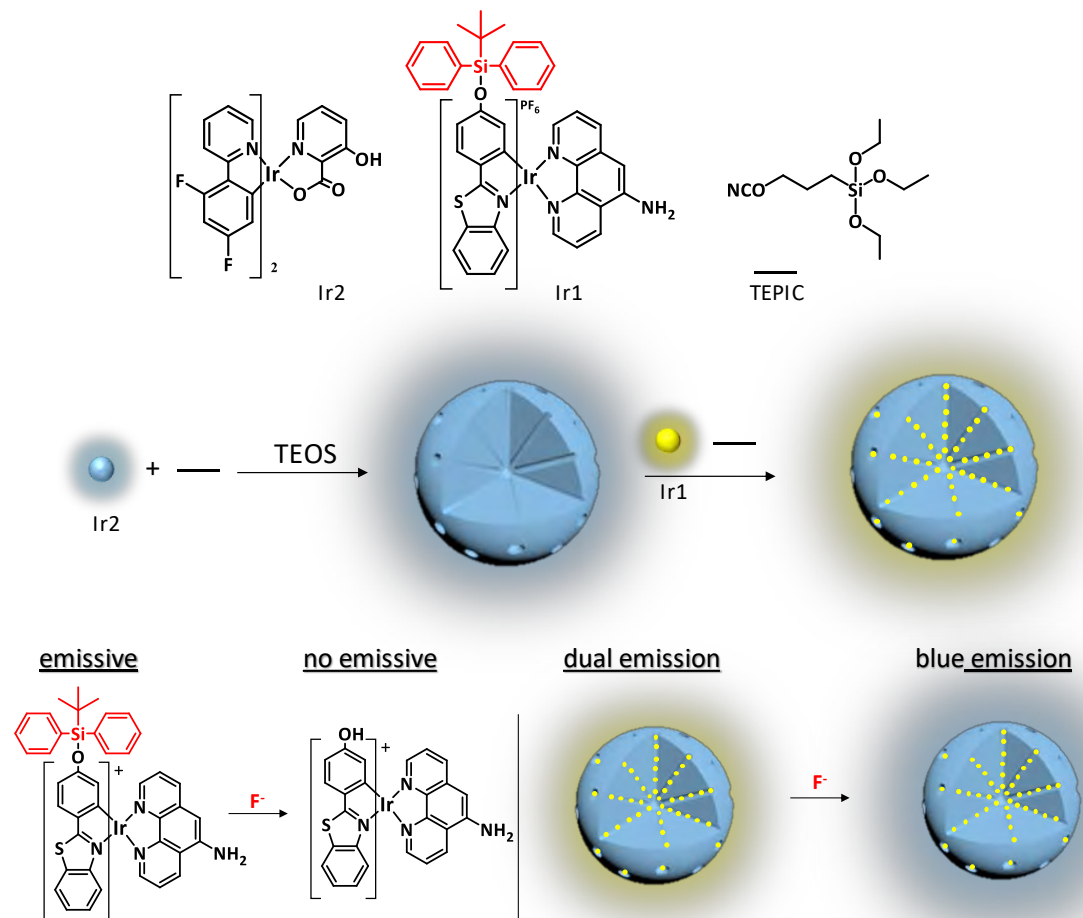


**Figure 1.10.** Schematic representation of the synthesis and operation of the ratiometric fluoride nanosensor. (Chem. Commun. 2015, 51, 12839-12842)

Following the same idea, they also developed a two-channel phosphorescent nanosensor for the detection of fluorine ions in aqueous media and live cells (see figure 1.10).<sup>32f</sup> They selected a blue iridium(III) emitter as the precursor for the preparation of the mesoporous silica nanoparticles and a yellow chromophore, containing the TBDPS (tert-butyldiphenylsilyl) moiety as the specific reaction site for F<sup>-</sup>, grafted on the surface of the material. The resulting material demonstrated promising applications for the sensing of F<sup>-</sup>, since the cleavage of the Si-O bond of the TBDPS produces the loss of the yellow emission, suggesting the presence of fluorine ions.

In this context, considering the potential applications of these hybrid luminescent materials and the advantages of the *in-situ* approximation, we considered of interest to extend it to the incorporation of different emissive complexes. With this aim, and taking into account that

luminescent complexes based on d<sup>6</sup> (Ru<sup>II</sup>, Ir<sup>III</sup>, Os<sup>II</sup>) and d<sup>8</sup> (Pt<sup>II</sup>, Au<sup>III</sup>) ions are nowadays the most widely studied ones due to their excellent photophysical properties, we decided to focus on d<sup>6</sup> Ir(III) and d<sup>8</sup> Pt(II) derivatives.

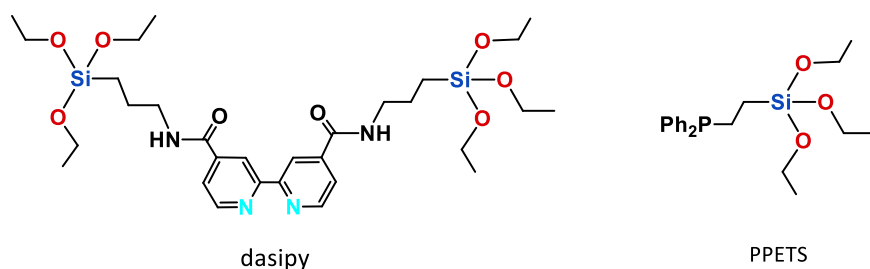
## **OBJECTIVES**

Taking into account the appealing optical properties of the cyclometalated Ir(III) and Pt(II) complexes and the ease tuning of their emission by the modification of the cyclometalated and auxiliary ligands, in this chapter we report:

- i) the design and study of the optical properties of several Ir<sup>III</sup> and Pt<sup>II</sup> cyclometalated complexes bearing Si(OEt)<sub>3</sub> groups (part I), and
- ii) its subsequent use as precursors for the preparation of novel hybrid luminescent organometallo-silica materials (part II).

### **PART I: Design of cyclometalated Ir<sup>III</sup> and Pt<sup>II</sup> complexes bearing Si(OEt)<sub>3</sub> groups**

- In part I, we report the synthesis, characterization and optical properties of several cationic and neutral iridium(III) and platinum(II) complexes: [Ir(ppy)<sub>2</sub>(PPETS)<sub>2</sub>]OTf (**1**), [Pt(bzq)(PPETS)<sub>2</sub>]PF<sub>6</sub> (**2**), [Pt(bzq)(C<sub>6</sub>F<sub>5</sub>)(PPETS)] (**3**) and [Pt(bzq)(dasipy)]PF<sub>6</sub> (**4**). These complexes incorporate two different ancillary ligands bearing trialkoxysilane terminal groups (see scheme 1.1):
  - (i) a monodentate phosphine ligand (PPh<sub>2</sub>(CH<sub>2</sub>)<sub>2</sub>Si(OCH<sub>2</sub>CH<sub>3</sub>)<sub>3</sub>, namely as PPETS), and
  - (ii) a substituted chelate bipyridine (4,4'-[CONH(CH<sub>2</sub>)<sub>3</sub>Si(OCH<sub>2</sub>CH<sub>3</sub>)<sub>3</sub>]<sub>2</sub>-bpy, namely as *dasipy*)



**Scheme 1.1.** Schematic view of the ancillary ligands used in the cyclometalated complexes.

The coordination of these ligands (*dasipy* and PPETS) to the metal center will allow their easy co-condensation with the silica source (TEOS), and the formation of the mesoporous silica-based materials that we present in part II.

**PART II: Synthesis of luminescent mesoporous silica-based materials**

- In this section, we report the preparation, following the Sol-Gel Coordination Chemistry strategy, of luminescent mesoporous organometallo-silica materials using chromophores **1-4** as building blocks.

Based on this approach, we have slightly modified some of the reaction conditions to obtain structurally different hybrid materials. Thus, depending on the molar ratio to form the silica gel, as well as on the reaction conditions for the condensation step (pH, solvent, reaction time, etc.), we obtain powder (**SiO<sub>2</sub>\_P**) or optically transparent gels (**SiO<sub>2</sub>\_G**), which incorporate different amounts of the metal precursor (1 wt% **SiO<sub>2</sub>\_P**, 0.2 wt% for **SiO<sub>2</sub>\_G**).

- This part also includes a detailed study of the textural, spectroscopic and photophysical properties of these new mesoporous organometallo-silicas, and their comparison with those of the precursors.

## I.1 PART I

### Design of cyclometalated Ir<sup>III</sup> and Pt<sup>II</sup> complexes bearing Si(OEt)<sub>3</sub> groups

In contrast to organic luminophores, phosphorescent metal complexes usually display characteristic long emission lifetime, large absorption-emission Stokes shift, and tunable excited states. This fact is attributed to the heavy atom effect that enables a strong spin-orbital coupling (SOC), facilitating fast singlet to triplet intersystem crossing. In the literature, there are numerous reports of the photophysical and photochemical properties of transition metal complexes, which are, particularly, a hot research topic in organic light emitting diodes (OLEDs).

In this field, the properties of cyclometalated d<sup>6</sup> Ir<sup>III</sup> and d<sup>8</sup> Pt<sup>II</sup> complexes have been thoroughly investigated during the last decades. Bis and tris cyclometalated Ir<sup>III</sup> complexes with different auxiliary ligands have been involved in a wide range of applications such as photocatalysis (hydrogenation reactions, water oxidation, etc.)<sup>41</sup> or in organic light emitting devices (OLEDs),<sup>42</sup> including photo-electronic sensors, photochemistry or luminescent chemosensors.<sup>43</sup> These complexes have also been explored as potential biomolecular probes in cellular imaging, and interesting therapeutic properties have been described against different biomolecular targets.<sup>44</sup> In the same line, square planar d<sup>8</sup> Pt<sup>II</sup> derivatives have been commonly used as potential dopants in OLEDs,<sup>44e, 45</sup> biological labelling reagents,<sup>46</sup> solid-state lighting,<sup>47</sup> photocatalysis<sup>48</sup> or photodynamic therapy.<sup>49</sup>

In this context, great efforts have been devoted to the synthesis and study of the photophysical properties of new families of cyclometalated Ir<sup>III</sup> derivatives (figure 1.11). They exhibit outstanding photophysical features including good photo- and thermal-stability, high quantum yields, long lifetimes and an easy adjustment of the emission wavelength by controlling the functionalization of both the cyclometalated and ancillary ligands.<sup>43a, 50</sup> In these complexes, emission properties mainly arise from triplet metal-to-ligand charge transfer (<sup>3</sup>MLCT) or from a mixed <sup>3</sup>MLCT/intraligand <sup>3</sup>LC excited states,<sup>51</sup> depending on the cyclometalated and the auxiliary ligands.

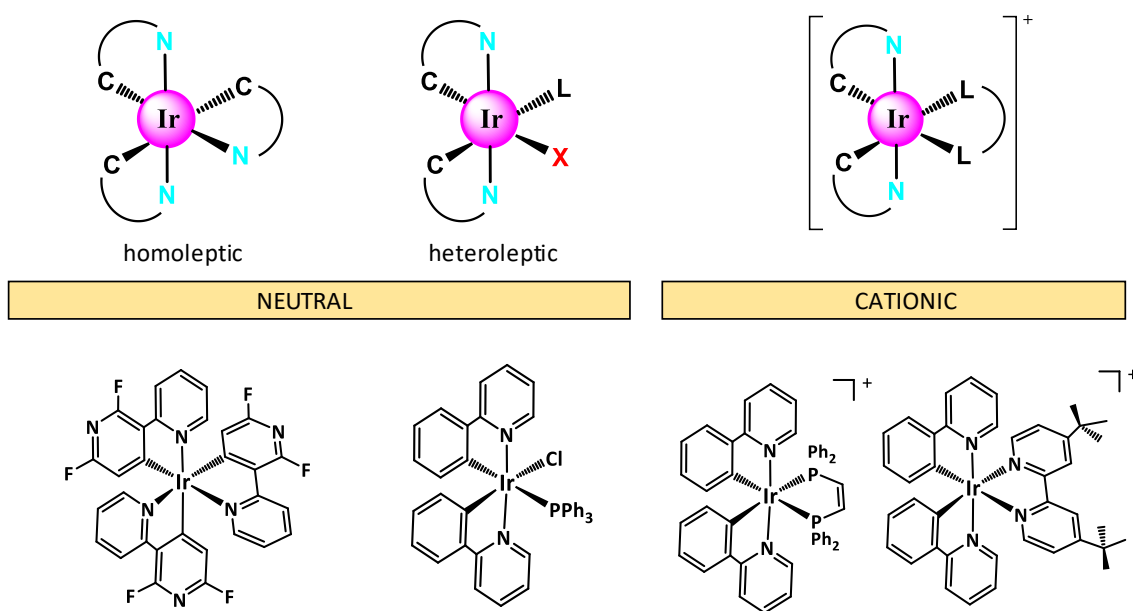


Figure 1.11. Classification of  $\text{Ir}^{\text{III}}$  complexes with bidentate cyclometalated ligands ( $\text{C}^{\text{N}}$ ).

On the other hand, in platinum(II) chemistry, the photophysical properties strongly depend on the nature of the coordinated ligands. Generally, complexes with weak field ligands (amines, phosphines, halides, ...) are no emissive mainly due to the anti-bonding character of the LUMO orbital (metal centered), which favors non-radiative deactivation processes. However,  $\text{Pt}^{\text{II}}$  species with planar aromatic ligands (figure 1.12), such as polypyridyl ( $\text{N}^{\text{A}}\text{N}$ ,  $\text{N}^{\text{A}}\text{N}^{\text{A}}\text{N}$ ) or cyclometalated ( $\text{C}^{\text{N}}$ ,  $\text{C}^{\text{N}}\text{N}^{\text{A}}$ ,  $\text{C}^{\text{N}}\text{N}^{\text{C}}$ ) groups, usually feature interesting photophysical properties.

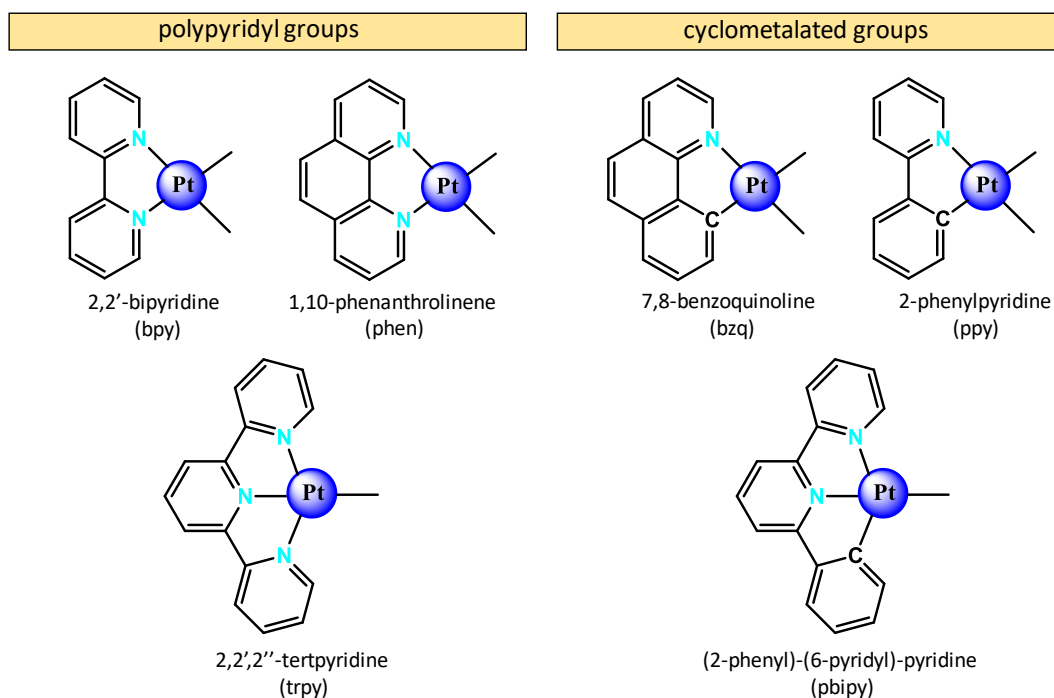
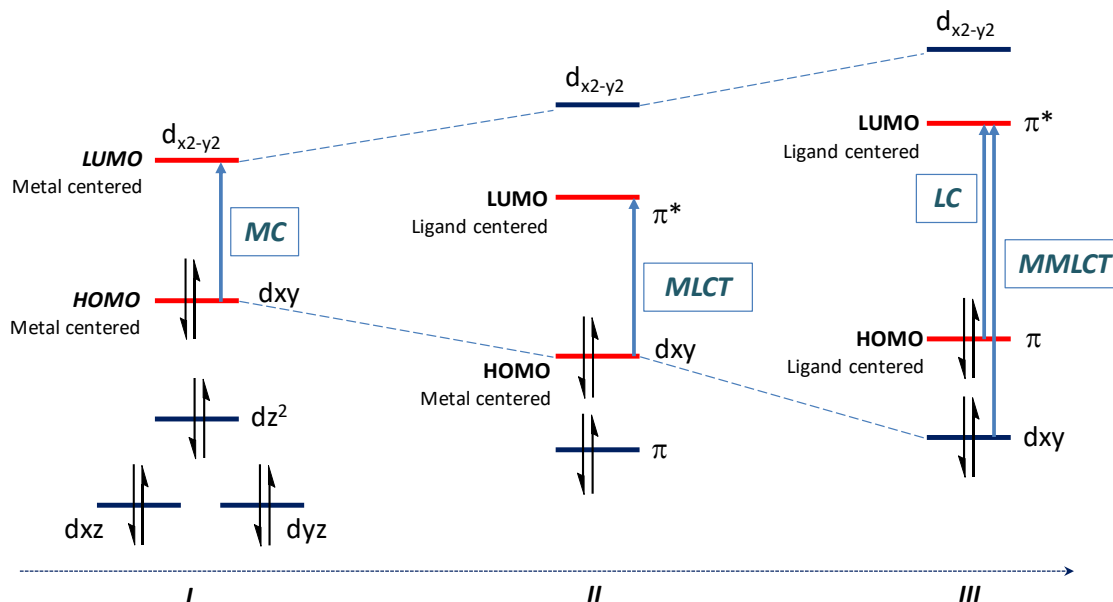


Figure 1.12. Schematic view of  $\text{Pt}^{\text{II}}$  complexes chelated with aromatic ligands.

These ligands produce the destabilization of the unoccupied  $d_{x^2-y^2}$  orbital of the Pt<sup>II</sup> ion, which increases the energies of the  $^3dd$  states to a level high enough to suppress the thermal population. As a consequence, these systems exhibit highly efficient triplet-state phosphorescence, which is commonly attributed to ligand centered ( $^3LC$ ) transitions or admixtures of  $^3LC/^3MLCT$  or  $^3LLCT/^3MLCT$  states (scheme 1.2).<sup>52</sup>



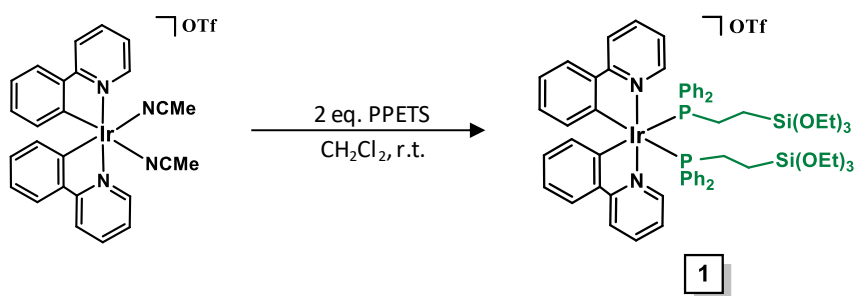
**Scheme 1.2.** Schematic representation of the HOMO-LUMO transition depending on the type of ligand.

In contrast to Ir<sup>III</sup> that has an octahedral coordination geometry, d<sup>8</sup> Pt<sup>II</sup> complexes adopt a square-planar coordination sites with open axial coordination points that favors structural distortion and the presence of intermolecular interactions, which alter the properties of both the ground and the excited states. In occasions, this behavior results on the reduction of color purity and luminescent efficiency, and on a poor stability of the emitters in the devices. However, in other systems, this behavior induces interesting and intriguing photophysical responses. Thus, extremely planar molecules have a great tendency to self-assembly through non-covalent interactions (Pt···Pt or  $\pi$ - $\pi$ ) that are accompanied by characteristic luminescent changes.<sup>53</sup> The assembly-induced luminescence is ascribed to emission from a new low emissive state (metal-metal-to-ligand charge transfer,  $^3MMLCT$ , or  $^3\pi\pi$  excimeric emission), that arises from the aggregation of the molecules through the stacking of the aromatic ligands. As a result, these assembly structures always exhibit lower energy emissions than those of the monomeric molecules,<sup>33d, 46c, 53b, 53e, 54</sup> as well as a strong sensitivity to mechanical<sup>53a, 55</sup> and chemical<sup>53a, 53b, 55a, 55b, 56</sup> stimuli. Notwithstanding, it should be noted that, in solution, the occurrence of intermolecular interactions with solvent molecules and counter ions are also possible, favoring other deactivation process and resulting on reduced luminescence.

Considering the appealing photophysical properties of these systems and the experience of our group in the chemistry of Pt<sup>II</sup> and Ir<sup>III</sup>, our first goal consisted on the preparation of new emissive cyclometalated Ir<sup>III</sup> and Pt<sup>II</sup> species bearing Si(OEt)<sub>3</sub> groups in the auxiliary ligands. It was expected that the incorporation of these organometallic phosphors within the silica network would finally hinder intermolecular interactions and prevent structural distortion, decreasing deactivation processes and enhancing their efficiency.

### I.1.1 Synthesis and characterization of complexes 1-4

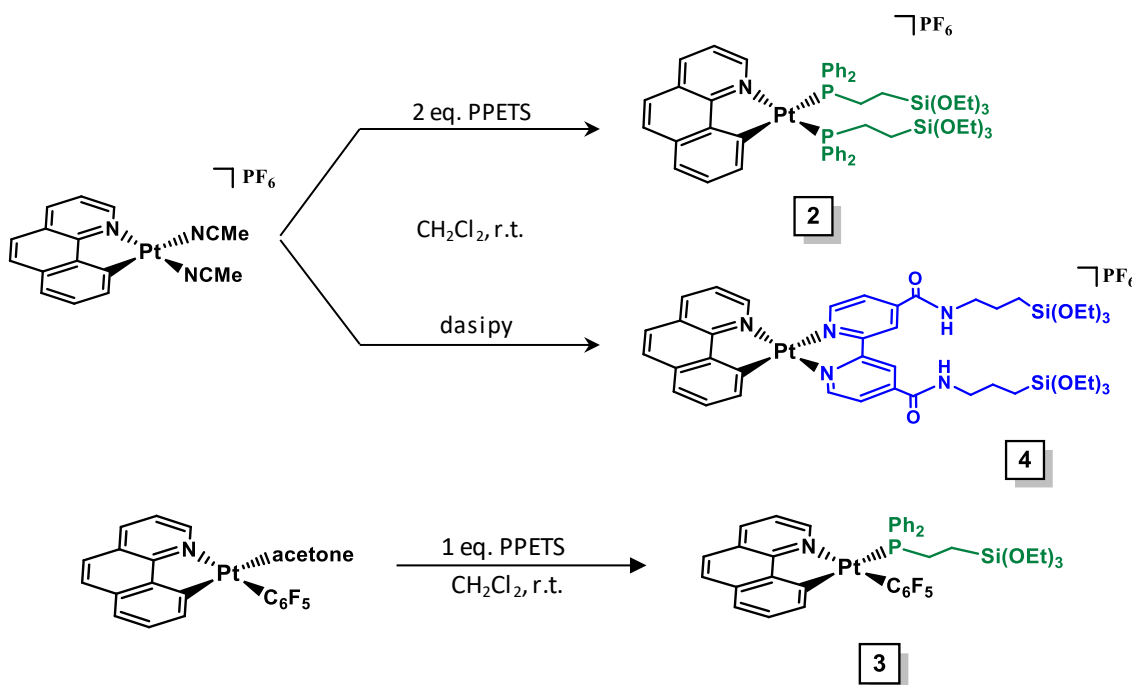
The cationic iridium(III) derivative [Ir(ppy)<sub>2</sub>(PPETS)<sub>2</sub>]OTf (**1**) was obtained by the reaction, under argon atmosphere, between the iridium solvate precursor [Ir(ppy)<sub>2</sub>(MeCN)<sub>2</sub>]OTf<sup>57</sup> and two equivalents of the phosphine PPETS ligand in dichloromethane, see scheme 1.3. After 1.5 hours of reaction and subsequent solvent removal, complex **1** was obtained as a pure yellow solid.



**Scheme 1.3.** Synthetic route of complex [Ir(ppy)<sub>2</sub>(PPETS)<sub>2</sub>]OTf (**1**).

In a similar way, complexes **2-4** were prepared reacting the corresponding solvate precursors ([Pt(bzq)(MeCN)<sub>2</sub>]PF<sub>6</sub> and [Pt(bzq)(C<sub>6</sub>F<sub>5</sub>)(acetone)])<sup>54e, 58</sup> with the stoichiometric amount of the ancillary ligands PPETS (**2** and **3**) or *dasipy* (**4**) (see scheme 1.4). All the reactions were performed at room temperature and using dichloromethane as solvent. Thus, platinum(II) complexes were isolated as yellow (**2** and **3**) and red (**4**) powders.

Compounds **1-3** exhibit high stability under environmental conditions. However, complex **4** needs to be kept completely dry under argon atmosphere because it self-condenses relatively fast in the presence of moisture traces, and tends to form a very insoluble red solid. Therefore, some of the common characterization techniques could not be employed for its characterization.



**Scheme 1.4.** Synthetic route of complexes [Pt(bzq)(PPETS)<sub>2</sub>]PF<sub>6</sub> (**2**), [Pt(bzq)(C<sub>6</sub>F<sub>5</sub>)(PPETS)] (**3**) and [Pt(bzq)(dasipy)]PF<sub>6</sub> (**4**).

The rest of the metal complexes (**1-3**) were fully characterized on the basis of the usual spectroscopic means (IR, UV-vis absorption and multinuclear NMR), elemental analysis and mass spectrometry. The assignment of the signals in the NMR spectra was carried out with the help of correlation experiments such as COSY (<sup>1</sup>H-<sup>1</sup>H correlation), HSQC (single bond <sup>1</sup>H-<sup>13</sup>C correlation), HMBC (multiple bond <sup>1</sup>H-<sup>13</sup>C correlation) and TOCSY (totally correlated spectroscopy).

The IR spectra of all the complexes show the two typical bands related to the stretching of the Si-O-C moieties at *ca.* 1095 cm<sup>-1</sup> and 1074 cm<sup>-1</sup>, assigned to the presence of terminal trialkoxysilyl groups.<sup>59</sup> Additional features are also observed in the high energy region (> 3000 cm<sup>-1</sup>) and in the range between 1600-1400 cm<sup>-1</sup>, which correspond to the  $\nu$ (C-H) and stretching vibrations of the aromatic rings, respectively.<sup>59</sup>

Apart from these common bands, each derivative also exhibits some other characteristic features. Complex **1** ([Ir(ppy)<sub>2</sub>(PPETS)<sub>2</sub>]OTf) shows bands related to the  $\nu$ (P-C) of the phosphine ligand at 1438 cm<sup>-1</sup> and the  $\nu$ (S-O) of the bonds of the triflate anion, at 1418 and 1027 cm<sup>-1</sup>.<sup>60</sup> [Pt(bzq)(C<sub>6</sub>F<sub>5</sub>)(PPETS)] (**3**) displays a single band at 799 cm<sup>-1</sup> that corresponds to the  $\chi$ -sensitive vibration of the C<sub>6</sub>F<sub>5</sub> group. The cationic cycloplatinated derivative **4** ([Pt(bzq)(dasipy)]PF<sub>6</sub>) exhibits the vibration and stretching frequencies of the N-H and N-C moieties at *ca.* 3420 and 3270 cm<sup>-1</sup>, respectively. An intense band at 1657 cm<sup>-1</sup>, due to  $\nu$ (C=O) of the dasipy ligand, and the feature at 833 cm<sup>-1</sup>, associated to  $\nu$ (P-F) in the counter ion PF<sub>6</sub><sup>-</sup>, are also well resolved.

The NMR spectra are also consistent with the structures proposed in schemes 1.3 and 1.4, confirming that the final complexes retain the geometry of their respective solvate precursors.

The  $^1\text{H}$ ,  $^{13}\text{C}\{^1\text{H}\}$  and  $^{31}\text{P}\{^1\text{H}\}$  NMR spectra of the iridium(III) derivative **1** support the mutually *trans* disposition of the pyridinic nitrogen atoms and the presence of only one type of phosphine ligand. Nevertheless, it should be noted that, due to the chiral nature of the metal center, the protons of the Ph rings and those of the aliphatic chain ( $\text{P}-\text{CH}_2\text{CH}_2-\text{Si}$ ) in the phosphine ligand are diastereotopic and, therefore, non-equivalent. This fact is reflected in both the  $^1\text{H}$  (figure 1.13) and the  $^{13}\text{C}\{^1\text{H}\}$  (figure 1.14) NMR spectra, which display five (Ph) and four (aliphatic) distinctive protons and eight distinctive aromatic carbons (2 ipso-C, 2 o-C, 2 m-C and 2 p-C), respectively.

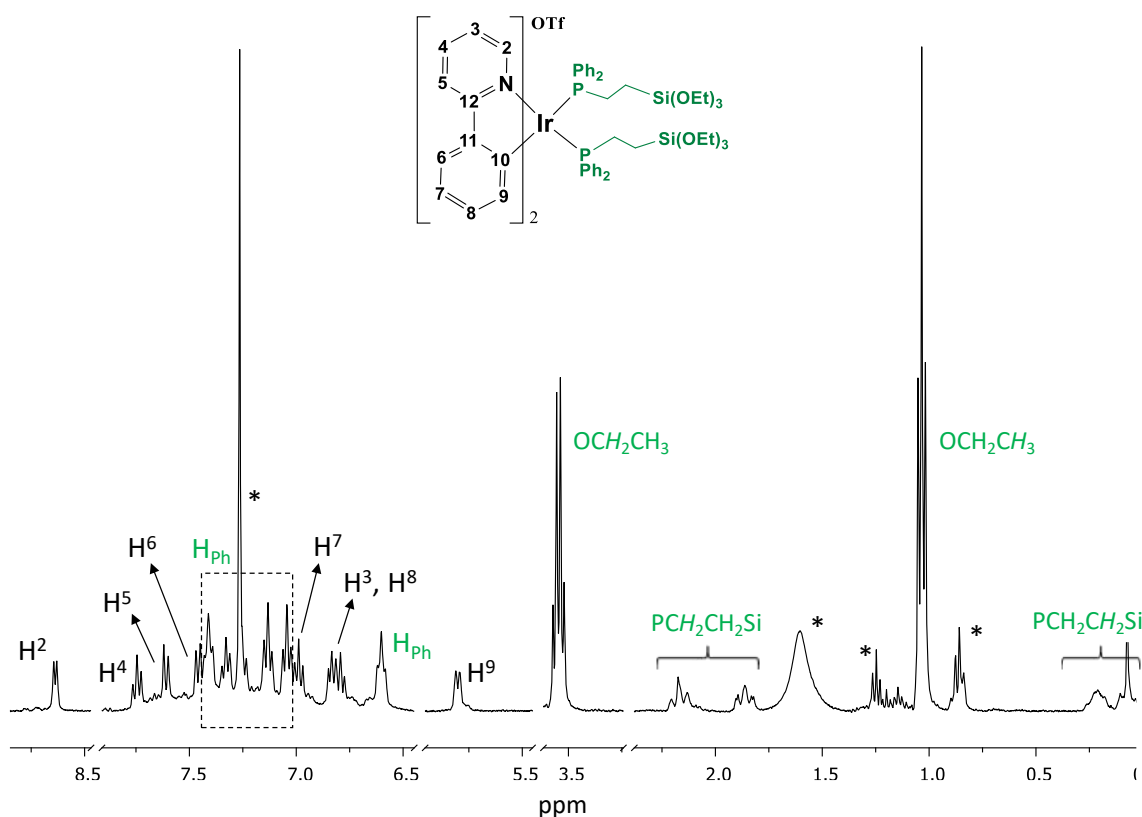


**Figure 1.13.**  $^1\text{H}$  NMR spectrum in  $\text{CDCl}_3$  of complex **1** ( $[\text{Ir}(\text{ppy})_2(\text{PPETS})_2]\text{OTf}$ ). (\*) Deuterium and residual solvents.

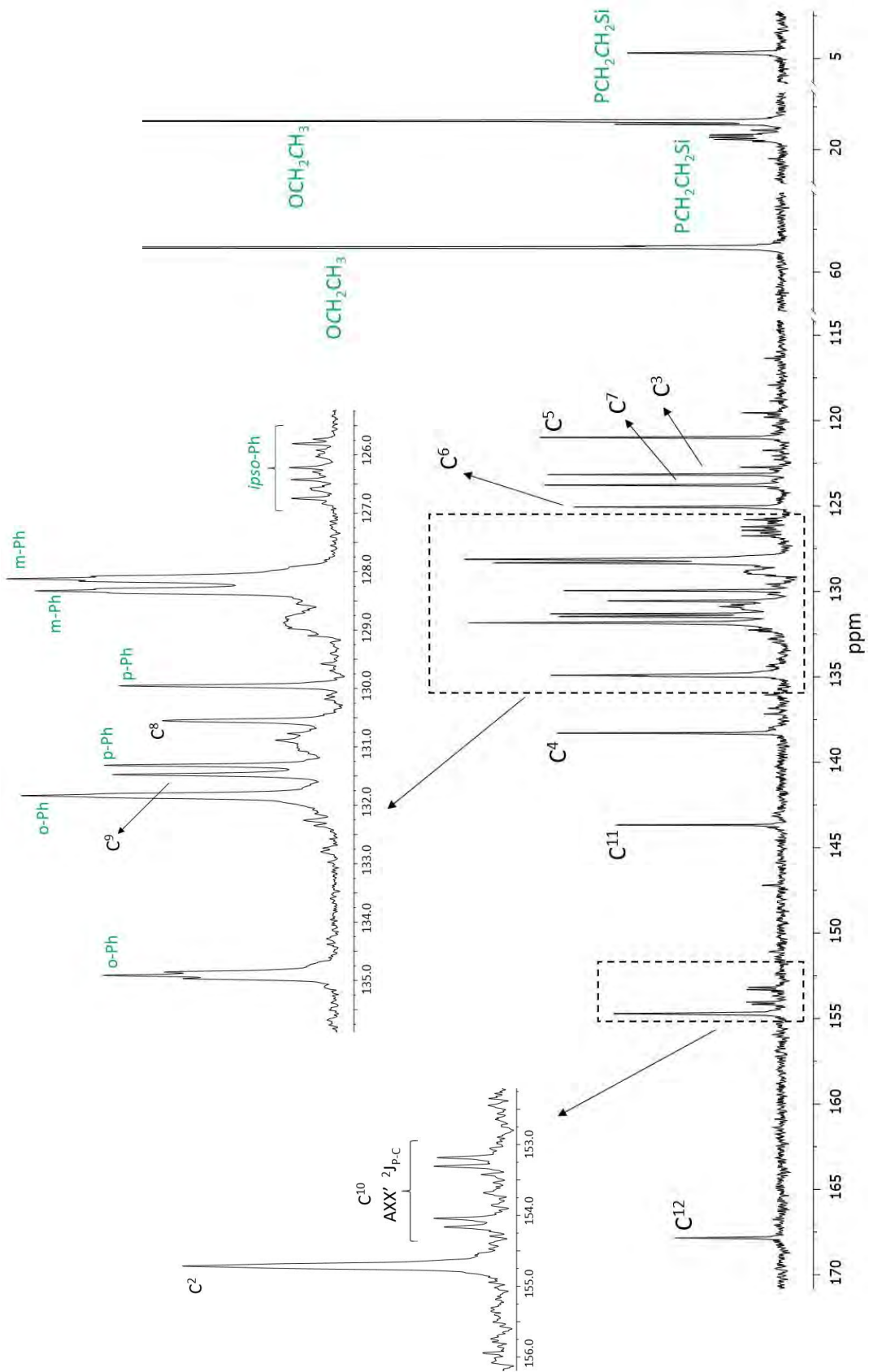


Figure 1.14.  $^{13}\text{C}\{^1\text{H}\}$  NMR spectrum in  $\text{CDCl}_3$  of complex 1 ( $[\text{Ir}(\text{ppy})_2(\text{PPETS})_2]\text{OTf}$ ).

The  $^{31}\text{P}\{\text{H}\}$  NMR spectrum of complex **2** confirms the inequivalence of the phosphine ligands, featuring two doublet signals (*ca.*  $^2\text{J}_{\text{P-P}} = 18 \text{ Hz}$ ) at  $\delta_{\text{P}}$  23.6 (P *trans* to C) and 16.7 (P *trans* to N) flanked by their corresponding  $^{195}\text{Pt}$  satellites ( $^1\text{J}_{\text{Pt-P}} = 1950 \text{ Hz}$  and  $^1\text{J}_{\text{Pt-P}} = 3950 \text{ Hz}$ , respectively) (see figure 1.15).

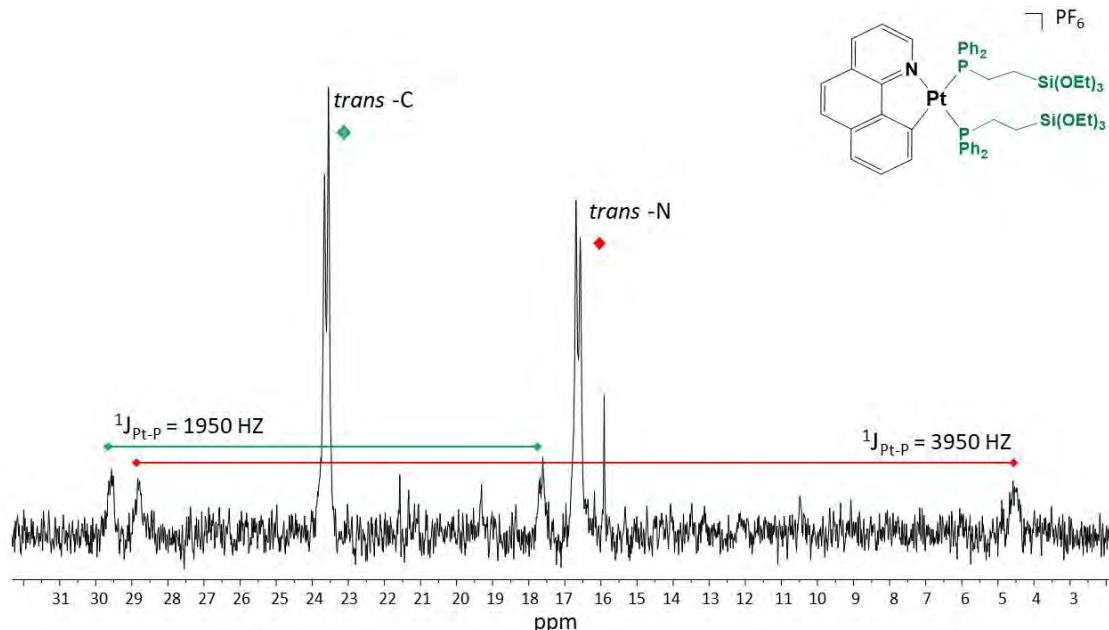


Figure 1.15.  $^{31}\text{P}\{\text{H}\}$  NMR spectrum in  $\text{CDCl}_3$  of complex **2** ( $[\text{Pt}(\text{bzq})(\text{PPETS})_2]\text{PF}_6$ ).

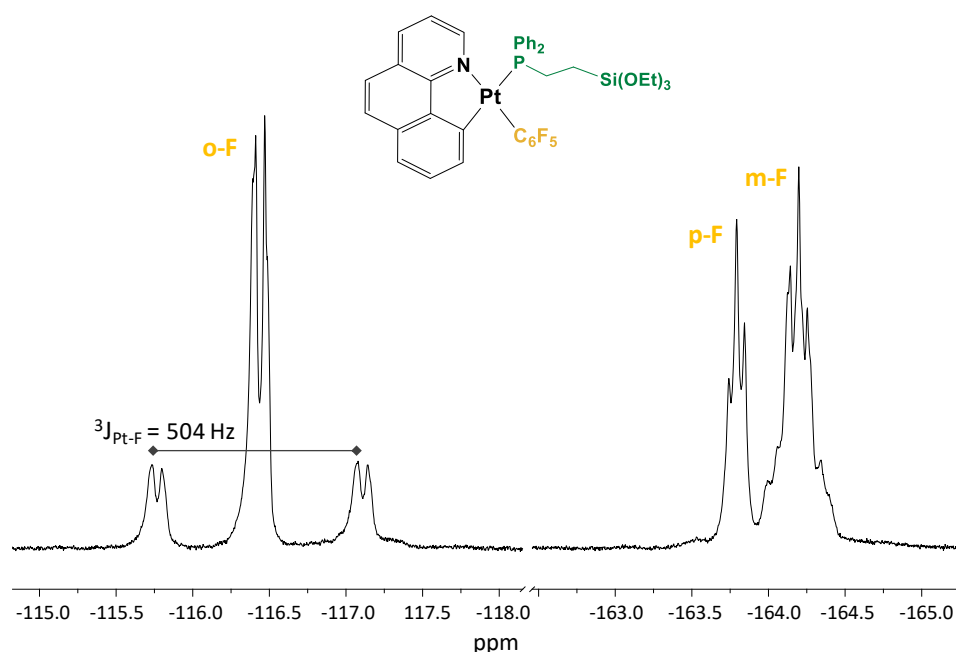
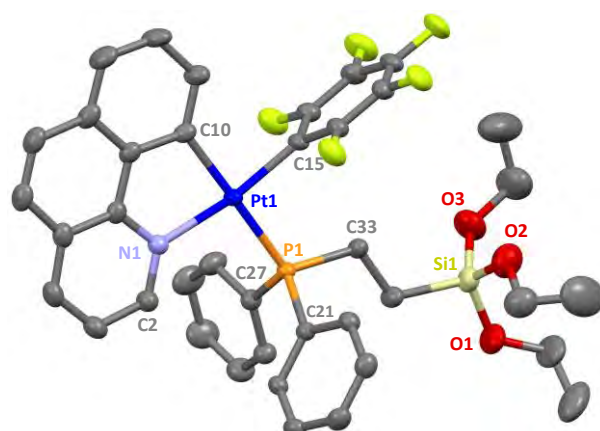


Figure 1.16.  $^{19}\text{F}\{\text{H}\}$  NMR spectrum in  $\text{CDCl}_3$  of complex **3** ( $[\text{Pt}(\text{bzq})(\text{C}_6\text{F}_5)(\text{PPETS})]$ ).

On the other hand, the  $^{19}\text{F}\{\text{H}\}$  NMR spectrum of **3** shows the characteristic AA'XX'M pattern of a free rotating C<sub>6</sub>F<sub>5</sub> ligand ( $\delta_{\text{F}}$  -116.4 (o-F), -163.7 (p-F) and -164.1 (m-F), see figure 1.16). The

large value of the Pt-o-F coupling constant ( $^3J_{\text{Pt}-\text{o-F}} = 504$  Hz) confirms the mutually *trans* disposition between the pentafluorophenyl group and the nitrogen atom of the bzq ligand. Similarly, the  $^{31}\text{P}\{\text{H}\}$  NMR spectrum also supports the coordination of the PPETS *trans* to the metallated carbon ( $\delta_{\text{P}} 22.15$ ,  $J_{\text{Pt-P}} = 1970$  Hz). On the other hand, both the  $^1\text{H}$  and  $^{13}\text{C}\{\text{H}\}$  NMR spectra exhibit the signals of only one type of cyclometalated (bzq) and phosphine (PPETS) ligands (see experimental part).

The structure of complex **3** was also confirmed by X-ray diffraction spectroscopy performed on a yellow monocrystal obtained by slow diffusion of *n*-hexane into a saturated solution of **3** in dichloromethane at room temperature. As shown in figure 1.17, the molecular structure of **3** presents the expected distorted square-planar coordination for the platinum(II) atom, and confirms the mutually *trans* disposition between the nitrogen atom (N1) and the *ipso*-C (C15) of the bzq ligand and the C<sub>6</sub>F<sub>5</sub> group, respectively. Bond distances and angles are comparable to those observed for related cyclometalated derivatives.<sup>54e, 61</sup> In addition, no significant Pt···Pt or  $\pi\cdots\pi$  interactions were observed in the packing likely due to the steric constraints of the C<sub>6</sub>F<sub>5</sub> groups, perpendicular to the bzq-Pt plane, and to the length and branching of the PPETS ligand that avoid the presence of these interactions.



**Figure 1.17.** Molecular structure of  $[\text{Pt}(\text{bzq})(\text{C}_6\text{F}_5)(\text{PPETS})]$  (**3**) with 50% possibility ellipsoids. Selected bond distances and angles: Pt(1)-N(1) 2.105(3), Pt(1)-P(1) 2.3248(8), Pt(1)-C(10) 2.051(3), Pt(1)-C(15) 1.998(3), N(1)-Pt(1)-C(10) 80.3(1) $^\circ$ , C(10)-Pt(1)-C(15) 90.49(9) $^\circ$ , P(1)-Pt(1)-N(1) 99.21(8) $^\circ$ . Find more data in annex I, table A.I.1.

Finally, due to the low stability of  $[\text{Pt}](\text{bzq})(\text{dasipy})\text{PF}_6$  (**4**) and its ability towards the self-condensation, only the  $^1\text{H}$  NMR spectrum could be registered. It confirms the presence of both bzq and dasipy ligands (see experimental part).

## I.1.2 Photophysical properties of the Ir<sup>III</sup> and Pt<sup>II</sup> complexes

### I.1.2.1 Photophysical properties of complexes **1-3**

#### i. Absorption spectra

The absorption spectra of complexes **1-3** were recorded both in the solid state and in THF and CH<sub>2</sub>Cl<sub>2</sub> solutions (5x10<sup>-5</sup> M). All the data are summarized in table 1.1 and figures 1.18-1.21.

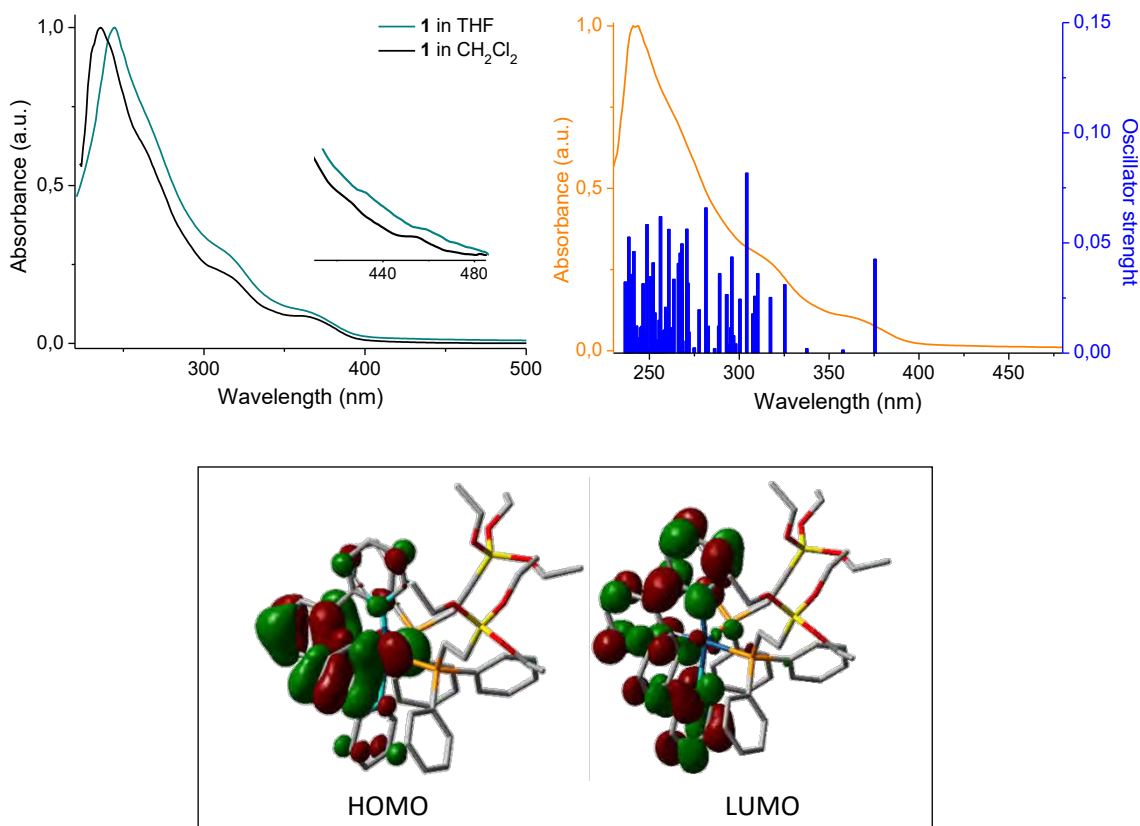


**Figure 1.18.** Absorption spectra in THF and CH<sub>2</sub>Cl<sub>2</sub> solution (5x10<sup>-5</sup> M) of **1** (up, left) compared to the simulated one represented in blue bars (up, right). HOMO and LUMO orbitals of complex **1** (bottom).

As shown in figure 1.18, complex **1** exhibits in solution (THF, CH<sub>2</sub>Cl<sub>2</sub>) an intense band in the high energy region ( $\lambda < 300$  nm), which is assigned, according to TD-DFT calculations on optimized model cation **1**<sup>+</sup>, to spin allowed  $\pi$ - $\pi^*$  transitions of the ligands. At lower energies, the feature at around 320 nm has a mixed of <sup>1</sup>ILCT (ppy)/ <sup>1</sup>L'LCT (PPETS  $\rightarrow$  ppy) configuration. The weaker absorption at 366 nm coincides fairly well with the lower energy singlet transition computed in THF at 375.5 nm, which is principally formed by a HOMO-LUMO transition. In this case, the HOMO orbital is mainly confined on the iridium center and the metallated phenyl groups, whereas the LUMO is localized just on the pyridines of the ppy ligands (see figure 1.18). Thereby,

this transition has a mixed <sup>1</sup>LLCT and <sup>1</sup>MLCT character. Finally, the weakest absorption bands observed at *ca.* 420 and 450 nm are ascribed to spin forbidden transitions (<sup>3</sup>ILCT/<sup>3</sup>MLCT), whose presence is due to the strong spin-orbit coupling (SOC) associated to the iridium center.

**Table 1.1.** Absorption data in solution ( $5 \times 10^{-5}$  M) and in the solid state of complexes **1-3**.

Sample	$\lambda_{\text{abs}}/\text{nm} (\varepsilon/\text{M}^{-1}\text{L}^{-1})$
[Ir(ppy) <sub>2</sub> (PPETS) <sub>2</sub> ]OTf ( <b>1</b> )	242 (22.1), 270 (13.8), 320 (5.5), 366 (2.1), 424 (0.3), 458 (0.02) <b>THF</b> 235 (51.3), 263 (32.6), 318 (10.8), 362 (4.3), 419 (0.2), 452 (0.02) <b>CH<sub>2</sub>Cl<sub>2</sub></b> 221, 248, 267, 321, 366, 420, 452 <b>Solid</b>
[Pt(bzq)(PPETS) <sub>2</sub> ]PF <sub>6</sub> ( <b>2</b> )	239 (18.9), 259 (11.9), 293 (5.9), 386 (1.1), 399 (1.2) <b>THF</b> 232 (48.0), 258 (24.0), 290 (15.6), 387 (1.0), 401 (1.1) <b>CH<sub>2</sub>Cl<sub>2</sub></b> 235, 263, 290, 400 <b>Solid</b>
[Pt(bzq)(C <sub>6</sub> F <sub>5</sub> )(PETS)] ( <b>3</b> )	243 (33.3), 250 (34.7), 302 (17.9), 360 (3.8), 390 (2.6), 405 (2.6) <b>THF</b> 235 (47.1), 250 (37.7), 300 (14.3), 355 (2.7), 388 (1.7), 403 (1.8) <b>CH<sub>2</sub>Cl<sub>2</sub></b> 250, 300, 355, 390, 402 <b>Solid</b>

The cycloplatinated complexes [Pt(bzq)(PPETS)<sub>2</sub>]PF<sub>6</sub> (**2**) and [Pt(bzq)(C<sub>6</sub>F<sub>5</sub>)(PETS)] (**3**) display, in solution, intense high energy bands ( $\lambda < 350$  nm, see figure 1.19), having a ligand center character (<sup>1</sup>LC). According to theoretical calculation in related complexes,<sup>54e, 61b-d, 62</sup> the low energy features (*ca.* 400 nm for **2**; 390 and 400 nm for **3**) are ascribed to a mixed <sup>1</sup>IL (bzq)/<sup>1</sup>MLCT (Pt  $\rightarrow$  bzq) transition with a strong ligand centered character. The slight blue shift observed for the cationic complex **2** might be related to a lower metal contribution in the low energy band than in the neutral derivative (**3**).

Similar spectra were observed by diffuse reflectance spectroscopy in the solid state (table 1.1).

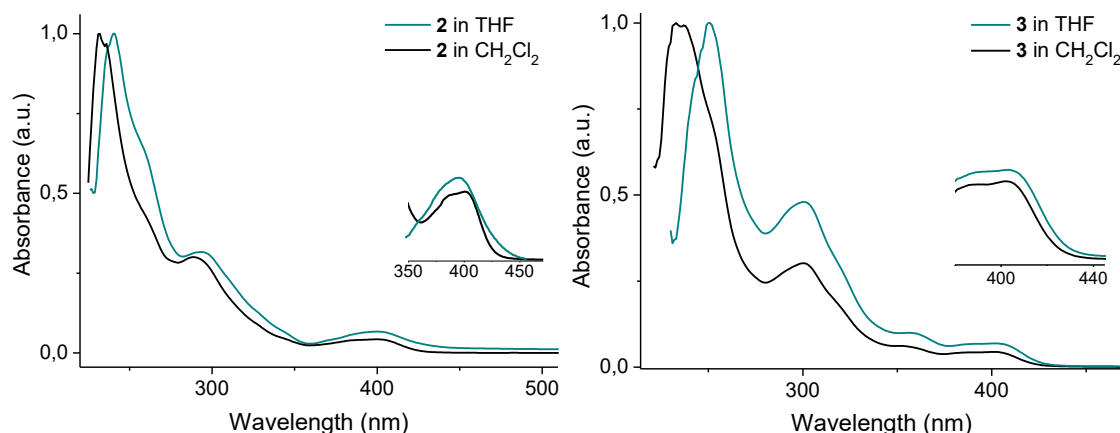


**Figure 1.19.** Normalized absorption spectra in THF and CH<sub>2</sub>Cl<sub>2</sub> solution ( $5 \times 10^{-5}$  M) of complexes **2** (left) and **3** (right).

### *ii. Emission spectra*

The emission spectra of complexes **1-3** were examined in fluid solution, both at room temperature and at 77K, and in rigid media (glass 77K, solid and in PMMA matrix). All data are summarized in tables 1.2-1.3 and figures 1.20-1.25.

Upon photoexcitation ( $\lambda_{\text{ex}}$  365 nm) in degassed THF solution at 298 K, the iridium(III) complex (**1**) exhibits a characteristic long lived and structured emission band at 464 nm ( $\tau$  0.27  $\mu$ s), which is slightly blue-shifted when decreasing the temperature at 77K (see figure 1.20). The emission is comparable to that reported for related phosphine complexes, such as  $[\text{Ir}(\text{ppy})_2(\text{PPh}_2\text{Me})_2]^+$  ( $\lambda$  460, 491 nm;  $\phi$  32% in  $\text{CH}_2\text{Cl}_2$  at room temperature).<sup>63</sup> However, the lower quantum yield measured for **1** in solution ( $\phi$  3.4%) could be associated to the higher flexibility of the PPETS ligands in fluid media that enables new non-radiative deactivation pathways. Based on previous assignments and on our theoretical calculations, this emission is assigned to a triplet excited state of a mixed  $^3\text{ILCT}/^3\text{MLCT}$  contribution.

The SOMO and SOMO-1 orbitals and the spin-density distribution of the lowest optimized triplet state are included in figure 1.21. As observed, the single occupied molecule orbitals SOMO-1 and SOMO are principally centered on one cyclometalated ppy ligand with a low participation of the iridium atom (*ca.* 16%), thus, supporting a remarkable intraligand (ILCT) contribution.

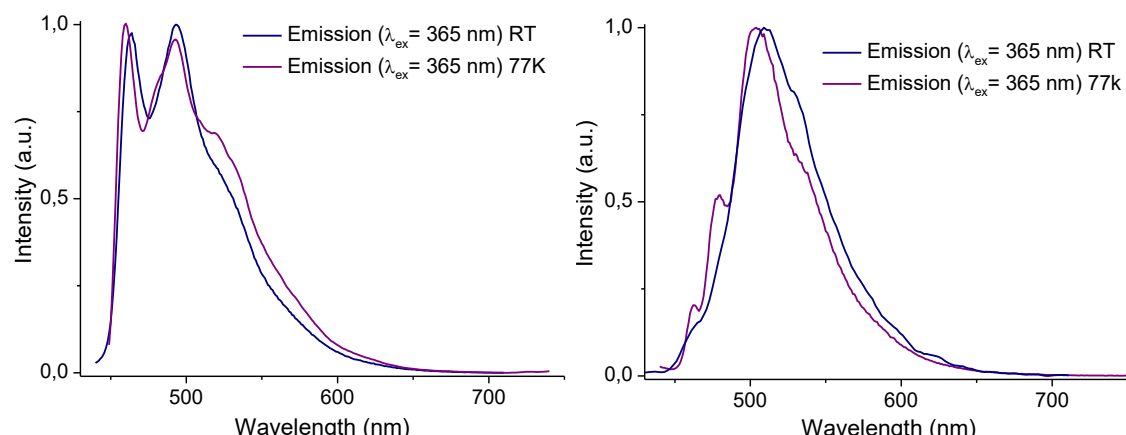


**Figure 1.20.** Emission spectra of complex **1** in THF solution ( $5 \times 10^{-4}$  M, right) and in solid state (left), at room temperature and at 77K.

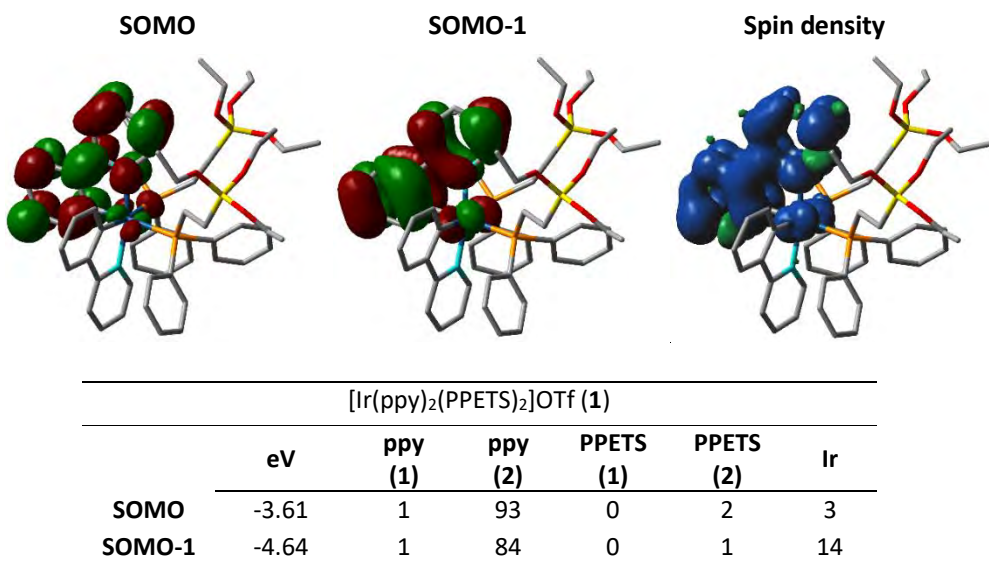


**Figure 1.21.** SOMO, SOMO-1 and Spin density of complex **1** with their composition (%) in the first triplet-state in THF.

In the solid state, a bathochromic shift with a strong *emission enhancement* is observed. As shown in figure 1.20, the solid powder features a very intense and non-structured emission band in the green region of the spectrum ( $\lambda_{\text{em}} 512 \text{ nm}$ ). In addition, both the quantum yield ( $\phi 31.2\%$  solid vs. 3.4% THF) and the lifetime ( $0.97 \mu\text{s}$  solid vs.  $0.27 \mu\text{s}$  THF) of the emission increase remarkably in relation to the solution. This behavior, that could be attributed to an increment in the rigidity of the system, which reduces the twisting and/or torsional motions of the phosphine ligands, also suggests the appearance of *aggregation enhanced induced emission* (AIEE) due to non-covalent intermolecular interactions. As previously observed in other systems,<sup>64</sup> this fact is usually reflected in red-shifted emissions.

Thus, we tentatively ascribe the emission in the solid state to the occurrence of excimer like emission due to the closeness of the molecules in this medium.

**Table 1.2.** Emission data of complex **1** in the solid state, solution (THF,  $5 \times 10^{-4} \text{ M}$ ) and blended in PMMA.

<b>Sample</b>	<b>Medium (T/K)</b>	<b><math>\lambda_{\text{em}}^{(a)}</math> / nm</b>	<b><math>\tau</math> (<math>\mu\text{s}</math>)</b>	<b><math>\phi</math> (%)</b>
<b>1</b>	Solid (298)	512	0.97	31.2
	Solid (77)	463, 480, 504 <sub>max</sub> , 530 <sub>sh</sub>	15.8 (460)	
	THF (298)	464, 494 <sub>max</sub> , 520 <sub>sh</sub>	0.27 (460)	3.4
	THF (77)	460 <sub>max</sub> , 493, 519 <sub>sh</sub>	44.0 (460)	
1% PMMA		460, 495 <sub>max</sub> , 520 <sub>sh</sub>		28.3
10% PMMA	Solid (298)	465, 500 <sub>max</sub> , 525 <sub>sh</sub>	---	29.8
50% PMMA		465, 500 <sub>max</sub> , 530 <sub>sh</sub>		36.4
70% PMMA		465, 510 <sub>max</sub> , 530 <sub>sh</sub>		38.7

(a)  $\lambda_{\text{ex}} 365 \text{ nm}$ .

Indeed, when cooling the sample at 77K, the broad feature at 504 nm appears with two weak shoulders in the high energy region ( $\lambda_{\text{em}}$  463 and 480 nm, see figure 1.20), probably associated to the presence of a small percentage of the monomer form. The excitation spectra monitored at both maxima (460 nm and 505 nm) reveal that the emission proceeds from two different excited states.

In order to evaluate the extend of the interactions in this compound, we collected the emission spectra in a polymeric matrix (poly(methylmethacrylate), PMMA) containing different concentrations of **1**. As shown in figure 1.22, both emissions at  $\lambda_{\text{max}}$  465 nm and at  $\lambda_{\text{max}}$  500-510 nm were clearly resolved, even at the lowest complex content (1%). As expected, as the amount of complex in the polymer is increased, the maximum of the low energy band slightly shifts towards the red, and the high energy peak due to the monomer almost disappears at the concentration of 70%. Similarly, a notably increment in the quantum yield is observed upon increasing the concentration (see table 1.2). All these facts strongly support the excimeric like nature of this emission.

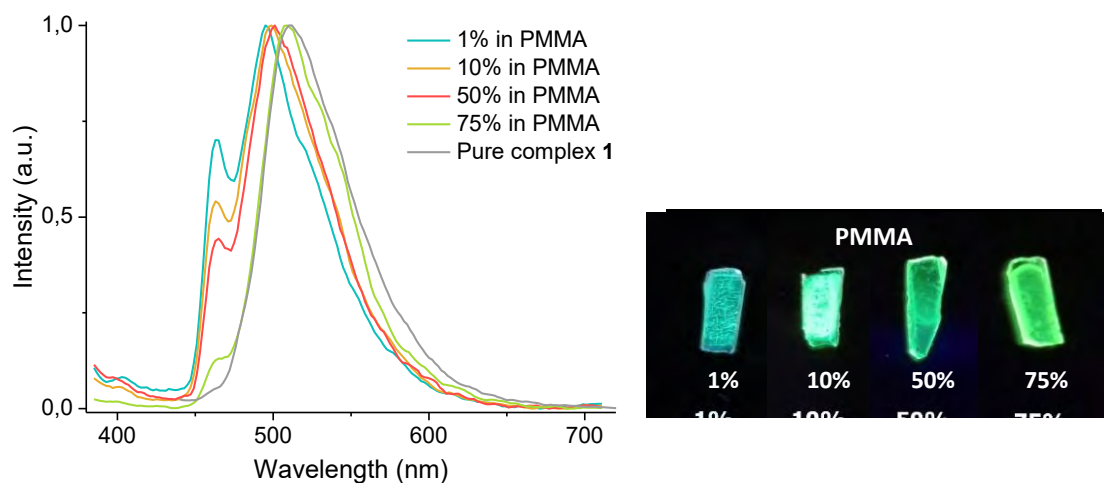


**Figure 1.22.** Normalized emission spectra of different concentrations of **1** in PMMA at room temperature.

To further support the AIEE effect in this iridium complex, we also examined the emission profiles of **1** in different THF-water mixtures in which the water concentration was gradually varied from 0 to 90%. As shown in figure 1.23, when the content of water exceeds the 75%, the intensity of the emission increases dramatically and there is an evident shift of the band to lower energies, indicating the significant AIEE effect that this iridium derivative experiments.

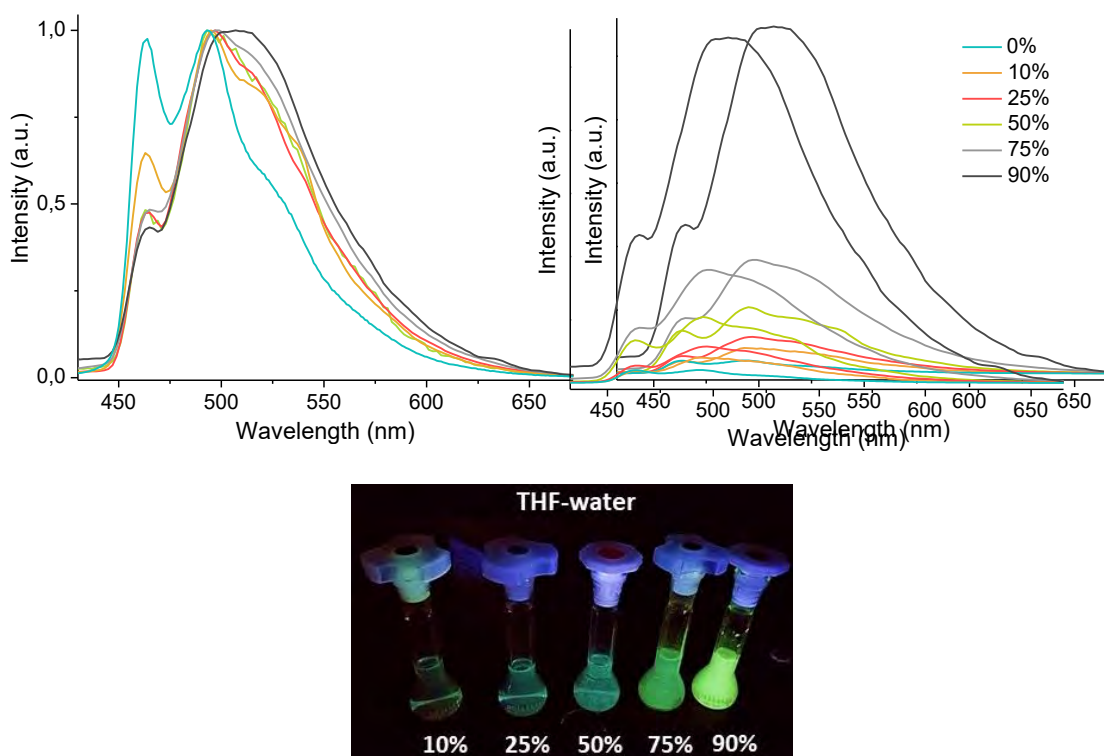


**Figure 1.23.** Normalized (left) and no-normalized (right) emission spectra of **1** in THF-water mixtures with different water concentration (0–90 vol%) (up). Photographs under UV light (bottom).

In contrast to the excellent properties of derivative **1**, the cationic platinum complex  $[\text{Pt}(\text{bzq})(\text{PPETS})_2]\text{PF}_6$  (**2**) is only weakly emissive in rigid media, in PMMA and at 77K (in solid and glass). As shown in figure 1.24, it displays a well-structured emission band with the typical vibronic interval of the bzq ligand, suggesting its contribution in the emissive excited state. With reference to other studies in Pt(II) emitters,<sup>61</sup> this emission is related to a  $^3\text{LC}/^3\text{MLCT}$  emissive state located on the Pt(bzq) subunit, with a predominant  $^3\text{LC}$  character due to the long lifetime (table 1.3) observed.

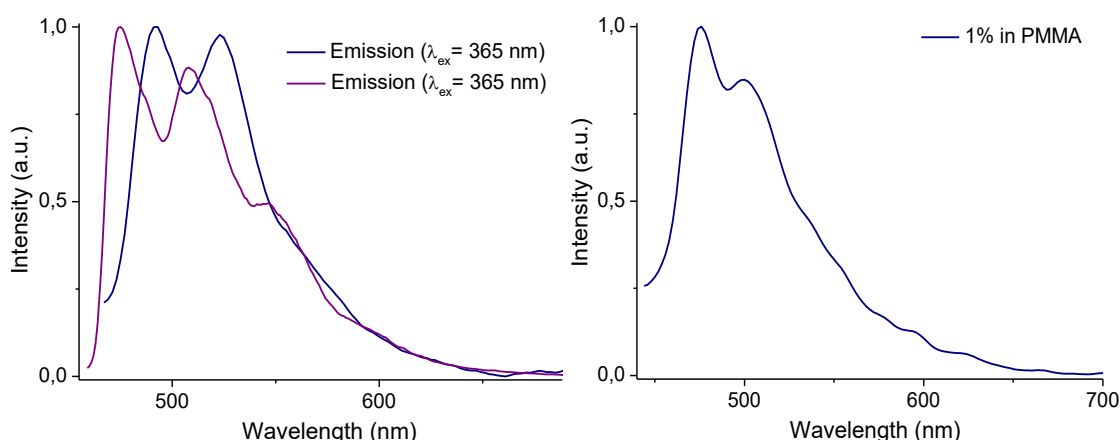


**Figure 1.24.** Emission spectra at 77K of complex **2** in solid state (in blue) and in glassy THF solution ( $5 \times 10^{-4}$  M, in purple) (left) and in PMMA at room temperature (1%, right).

In the solid state, the emission maximum is clearly shifted to lower energies ( $\lambda_{\text{max}}$  solid 490 nm vs. glassy 477 nm), a fact attributed to the presence of  $\pi\cdots\pi$  interactions between the bzq ligands or to the formation of aggregates in the solid state.

**Table 1.3.** Emission data of complexes **2** and **3** in the solid state, solution (THF,  $5 \times 10^{-4}$  M) and blended in PMMA (at different concentrations).

Sample	Medium (T/K)	$\lambda_{\text{em}}^{(a)}$ / nm	$\tau$ (μs)	$\phi$ (%)
<b>2</b> <sup>(b)</sup>	Solid (77)	493 <sub>max</sub> , 523, 552 <sub>sh</sub>	536.9 (500)	
	THF (77)	477 <sub>max</sub> , 514, 550 <sub>sh</sub>	1216 (480)	
1% PMMA	Solid (298)	475 <sub>max</sub> , 500	84.3 (500)	2.0
<b>3</b> <sup>(c)</sup>	Solid (298)	485 <sub>max</sub> , 520, 560, 610 <sub>sh</sub>	206.5	43.4
	Solid (77)	483 <sub>max</sub> , 520, 565, 610 <sub>sh</sub>	378.3	
	CH <sub>2</sub> Cl <sub>2</sub> (298)	497, 527 <sub>max</sub> , 570 <sub>sh</sub>	0.66	2.0
1% PMMA	Solid (298)	483 <sub>max</sub> , 517 <sub>max</sub> , 555	511	
				7.6
				12.2
10% PMMA	Solid (298)	485 <sub>max</sub> , 515, 560 <sub>sh</sub>	---	25.4
50% PMMA				

(a)  $\lambda_{\text{ex}}$  365 nm. (b) No emissive at room temperature. (c) No emissive in THF.

The neutral complex [Pt(bzq)(C<sub>6</sub>F<sub>5</sub>)(PPETS)] (**3**) shows very similar emission profiles in all media, with sharper vibrational features at 77K (see figure 1.25). A small hypsochromic shift was observed when compared the emissions in solid state and glassy with that in fluid solution (*ca.* 485 nm *vs.* 497 nm in CH<sub>2</sub>Cl<sub>2</sub> at 298K), a fact that might be associated to the higher rigidity of the molecules in the first two media and, probably, to the lack of remarkably intermolecular interactions.

The remarkably increase in the lifetime upon decreasing the temperature (206.5 and 0.66 μs at 298K *vs.* 378.3 and 511 μs at 77K, see table 1.3) suggests that the emission has mainly an intraligand character with some contribution of the platinum center (<sup>3</sup>LC/<sup>3</sup>MLCT). The emission quantum yield is notably enhanced in the solid state compared to fluid solution or in the PMMA matrix (*i.e.*  $\phi$  43.4% solid state *vs.* 2.0% CH<sub>2</sub>Cl<sub>2</sub>). In the same way, in this last medium the intensity of the emission is clearly enhanced when increasing the concentration (see table 1.3).

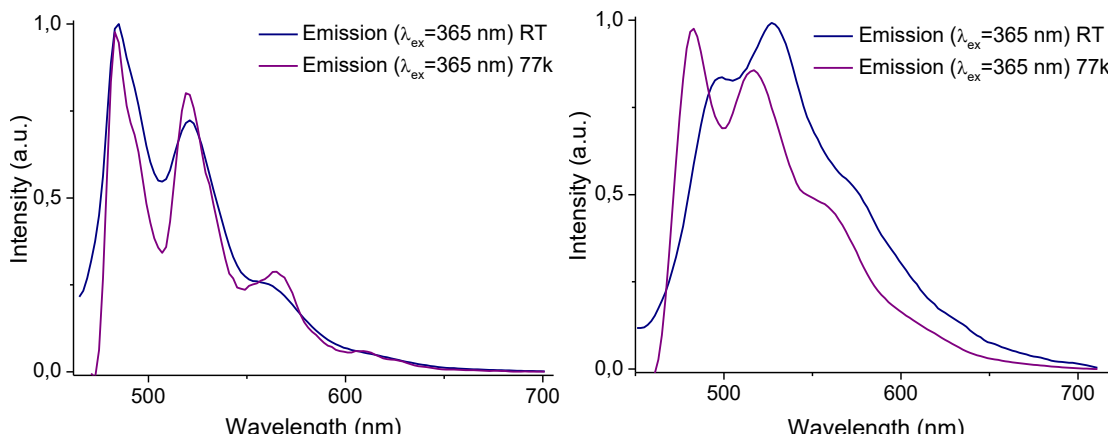


**Figure 1.25.** Emission spectra of complex **3** in solid state (left) and in THF solution ( $5 \times 10^{-4}$  M, right), at room temperature and at 77K.

### 1.1.2.2 Photophysical properties of complex **4** and formation of a gel (**4-gel**)

The absorption and emission spectra of complex  $[\text{Pt}(\text{bzq})(\text{dasipy})]\text{PF}_6$  (**4**) were collected in  $\text{CH}_2\text{Cl}_2$  solutions and in solid state, at 298K and 77K. All the data are summarized in tables 1.4-1.5 and figures 1.26-1.32.

**Table 1.4.** Absorption data in solution ( $\text{CH}_2\text{Cl}_2$ ,  $5 \times 10^{-5}$  M) and in the solid state of complex **4**.

Sample	$\lambda_{\text{abs}}/\text{nm} (\epsilon/\text{M}^{-1}\text{L}^{-1})$
$[\text{Pt}(\text{bzq})(\text{dasipy})]\text{PF}_6$ ( <b>4</b> )	257 (21.5), 280 (17.0), 290 (15.9), 313 (10.7), 384 (7.3), 460 (0.7) $\text{CH}_2\text{Cl}_2$ 254, 313, 384, 475, 565 <i>Solid</i>

As shown in figure 1.26, complex **4** exhibits in  $\text{CH}_2\text{Cl}_2$  solution intense features in the high energy region ( $\lambda < 315$  nm) assigned, according to TD-DFT theoretical calculations, to ligand centered (<sup>1</sup>LC) transitions mixed with some ligand-to-ligand and metal-to-ligand charge transfer character (<sup>1</sup>LL'CT ( $\pi(\text{bzq}) \rightarrow \pi(\text{dasipy})$ )/<sup>1</sup>ML'CT ( $d(\text{Pt}) \rightarrow \pi^*(\text{dasipy})$ )). The band observed at 384 nm, contributed from S<sub>3</sub> ( $\text{H-1} \rightarrow \text{LUMO}$ ) and S<sub>4</sub> ( $\text{HOMO} \rightarrow \text{L+1}$ ), is also related to <sup>1</sup>LC(bzq) and <sup>1</sup>LL'CT transitions. Finally, the absorption band observed at lower energies (460 nm) fits reasonably well with the lower singlet computed in  $\text{CH}_2\text{Cl}_2$  at 478 nm, associated with the HOMO to LUMO transitions. The LUMO orbital is essentially centered in the *dasipy* ligand, while the HOMO is localized in both the bzq and the platinum center (see figure 1.26). Therefore, this absorption is assigned to a charge transfer transition, having a ligand-to-ligand ( $\pi(\text{bzq}) \rightarrow \pi^*(\text{dasipy})$ ) and metal-to-ligand ( $d(\text{Pt}) \rightarrow \pi^*(\text{dasipy})$ ) character (<sup>1</sup>LL'CT/ <sup>1</sup>ML'CT, L = bzq, L' = *dasipy*).

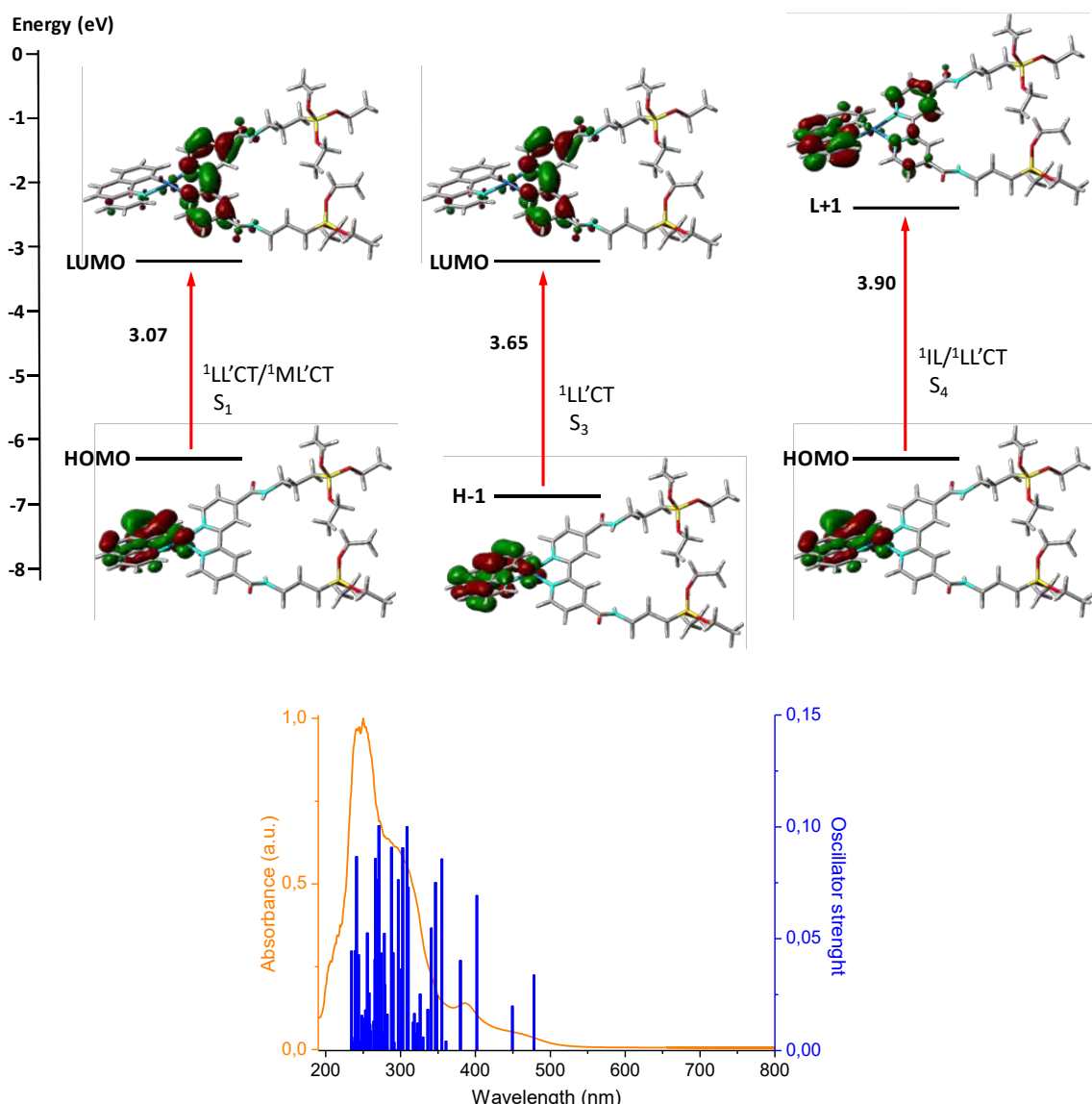


**Figure 1.26.** Calculated orbital transitions of the lower absorption bands of complex **4** (up). Absorption spectrum in  $\text{CH}_2\text{Cl}_2$  solution of complex **4** (in orange) compared to the simulated one represented in blue bars (down).

In order to evaluate the possibility of **4** to form aggregates or excimers due to its planarity, the influence of the concentration on the UV-vis absorption spectra was examined. With this aim, UV-vis spectra of **4** in  $\text{CH}_2\text{Cl}_2$  solutions were recorded in a concentration range between  $10^{-6}$  and  $10^{-3}$  M (figure 1.27, upper part), and the apparent absorbance at 470 nm vs. the concentration was then plotted (figure 1.27, lower part). As shown in this figure, at concentrations higher than  $2.5 \times 10^{-4}$  M, the absorption at 470 nm does not obey the Lambert-Beer's law, suggesting the possible formation of aggregates in the ground state by  $\pi \cdots \pi$  and/or  $\text{Pt} \cdots \text{Pt}$  interactions.<sup>65</sup>

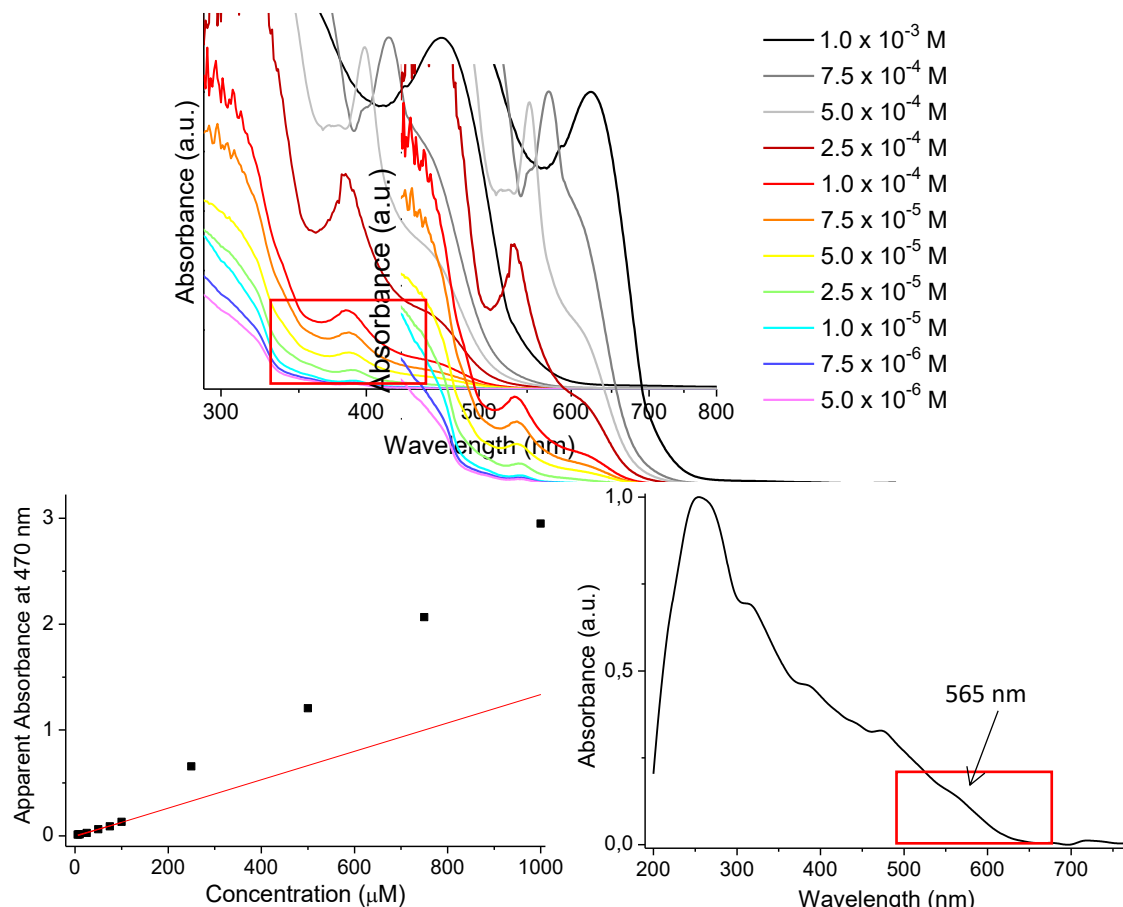


**Figure 1.27.** (Upper part) Absorption spectra of complex **4** in  $\text{CH}_2\text{Cl}_2$  solutions at different concentrations ( $1.0 \times 10^{-3}$  M to  $5.0 \times 10^{-6}$  M). (Lower part) Plot of absorbance at 470 nm vs. concentration (left). Solid DRUV spectrum of complex **4** (right).

In the solid state, the absorption profile of **4** resembles to that described in solution (see table 1.4 and figure 1.27, lower part) in the high energy region. However, the low feature is slightly shifted to the red ( $\lambda_{\text{max}}$  460 nm in  $\text{CH}_2\text{Cl}_2$  vs. 475 nm in solid state) and a new shoulder at 565 nm is resolved. This band suggests the presence of aggregates through Pt...Pt contacts in the solid state and, therefore, is attributed to a metal-metal-to-ligand charge transfer (MML'CT).

In fluid solution, the emission of the complex  $[\text{Pt}(\text{bzq})(\text{dasipy})]\text{PF}_6$  (**4**) is concentration dependent (see figure 1.28). Thus, upon excitation in the low energy absorption band (440-450 nm), a diluted solution ( $< 5 \times 10^{-5}$  M) of **4** in  $\text{CH}_2\text{Cl}_2$  displays a very weak emission in the red region. When increasing the concentration, the intensity of the band ( $\lambda_{\text{max}}$  675 nm) gradually increases and the emission shifts to lower energies in glassy solutions ( $\lambda_{\text{max}}$  705 nm at 77K, figure 1.29).

In addition, the excitation spectra (at 298, 77K) of this emission have a profile with a peak maximum at 525 nm (298 K) or 565 nm (77K) (see figure 1.29), associated to the formation of aggregates through Pt...Pt bonding interactions. Hence, according to previous assignments on

Pt…Pt stacking systems, this emission is assigned as phosphorescence from a metal-metal-to-ligand charge transfer ( ${}^3\text{MML'CT}$ ) excited state. This behavior is consistent with that found for other similar square-planar platinum(II) complexes with polypyridyl ligands (bpy, terpy, etc.).<sup>54a, 65a, 65c, 65d</sup>

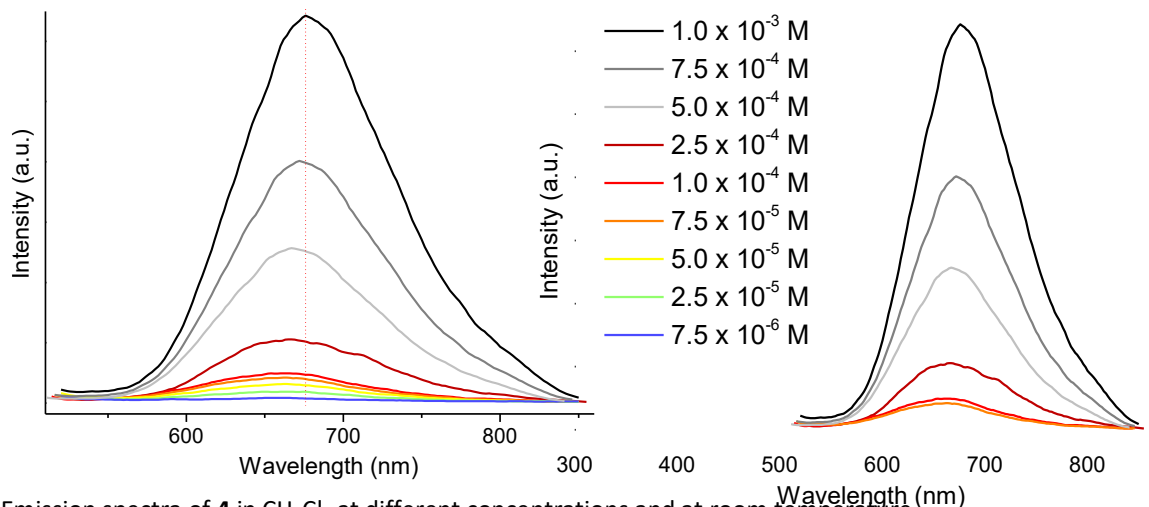


**Figure 1.28.** Emission spectra of **4** in  $\text{CH}_2\text{Cl}_2$  at different concentrations and at room temperature.

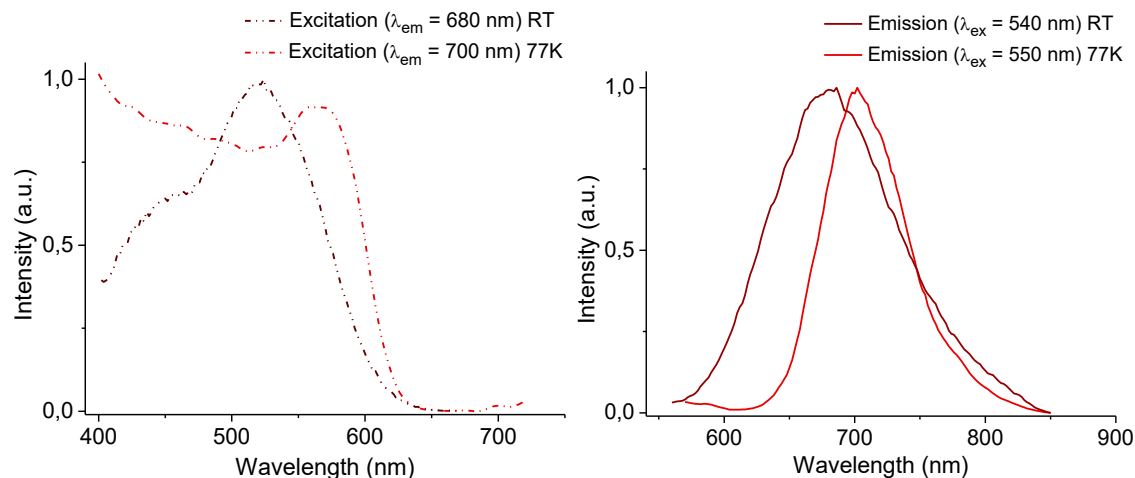


**Figure 1.29.** Excitation (left) and emission (right) spectra of **4** in  $\text{CH}_2\text{Cl}_2$  ( $5 \times 10^{-4}$  M) at room temperature and 77K.

A similar emission is observed in the solid state. At room temperature, the solid complex (**4**) features a very intense red emission ( $\lambda_{\text{max}}$  690 nm,  $\phi$  18.5 %) that slightly shifts to the red at 77K ( $\lambda_{\text{max}}$  705 nm) (see figure 1.30), being also attributed to a  ${}^3\text{MML'CT}$  excited state arising from the self-assembly of the molecules.

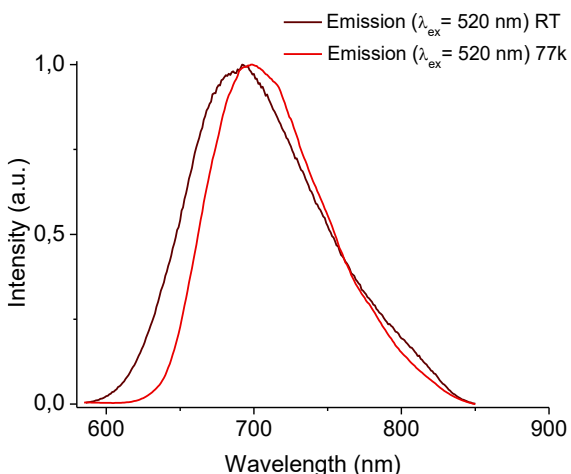


**Figure 1.30.** Emission spectra of complex **4** in the solid state, at room temperature and at 77K.

**Table 1.5.** Emission data of complex **4** (solid state and solution CH<sub>2</sub>Cl<sub>2</sub>, 5x10<sup>-4</sup> M) and the corresponding self-condensed gel (**4-gel**), at room temperature and 77K.

Sample	Medium (T/K)	λ <sub>em</sub> / nm	τ (μs) <sup>(a)</sup>	ϕ (%)
<b>4</b>	Solid (298)	690 (520)	0.13	18.5
	Solid (77)	705 (520)	11.46	
	CH <sub>2</sub> Cl <sub>2</sub> (298)	675 (540)		3.3
	CH <sub>2</sub> Cl <sub>2</sub> (77)	705 (550)		
<b>4-gel</b>	Solid (298)	680 (500)	0.52	39.9
	Solid (77)	700 (500)	---	

(a) Emission lifetimes calculated as average of a bi-exponential decay at 77K. At room temperature, calculated as mono-exponential decay.

As previously mentioned, this complex shows a remarkable tendency to self-condense through the trialkoxysilane terminal groups of the *dasipy* ligand when exposing it to fluid media under air conditions. Thus, solutions of **4** in a mixture of CH<sub>2</sub>Cl<sub>2</sub>/Et<sub>2</sub>O or MeCN/Et<sub>2</sub>O slowly forms a stable red gel (**4-gel**, see figure 1.31).

This gel exhibits comparable emission profiles to those observed for the precursor (**4**) in the solid state (λ<sub>max</sub> 680 nm at 298K vs. 700 nm at 77K, figure 1.31). In this case, the bathochromic behavior upon cooling, is slightly higher than in the complex (420 cm<sup>-1</sup> **4-gel** vs. 308 cm<sup>-1</sup> **4**). According to the previous UV-vis studies, this emission also originates from a MML'CT excited state.

This behavior suggests that the final condensed networks are probably involved in Pt···Pt and/or π···π intermolecular interactions. Therefore, we suggest that this gel is likely formed by dimers covalently bonded through the alkoxy silane units of each molecule, which stack through Pt···Pt interactions (see figure 1.32).

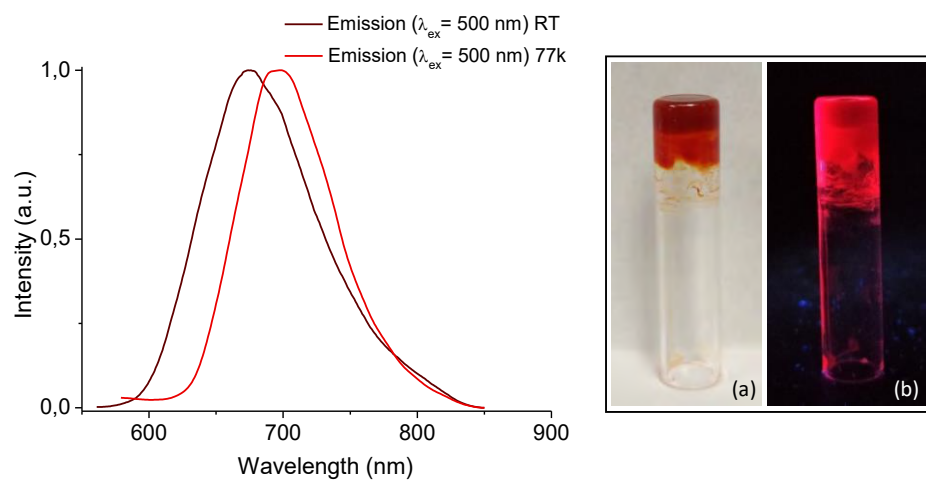


**Figure 1.31.** Emission spectra of the self-condensed gel (**4-gel**), at room temperature and at 77K (left). Photographs of the gel under visible (a) and UV (b) light irradiation (right).

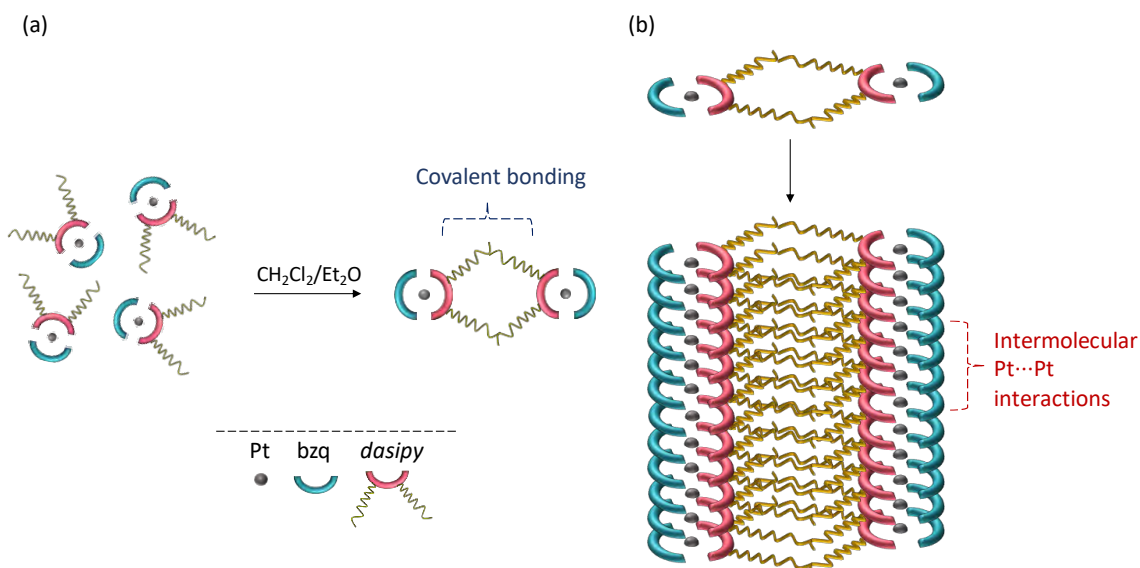


**Figure 1.32.** (a) Schematic representation of the self-condensed gel formed through covalent bonding between the trialkoxysilane terminal groups of the *dasipy* ligand. (b) Structure proposed for the assembly of the condensate moieties of the gel by intermolecular  $\text{Pt}\cdots\text{Pt}$  and  $\pi\cdots\pi$  interactions.

Finally, particularly interesting is the remarkable enhancement observed in the quantum yield of the gel, which is more than two-fold times higher than that of its precursor ( $\phi$  39.9 % **4-gel** vs. 18.5% **4**). This fact could be related to the extra rigidity imposed to the functionalized bipyridine ligand upon the total or partial condensation of the terminal  $\text{Si(OEt)}_3$  units, that reduces the non-radiative deactivation processes.

## I.2 PART II

### Synthesis of luminescent mesoporous silica-based materials

As previously exposed in the introduction, the development of luminescent silica-based materials is a very active research field.<sup>12b, 12c, 16-18</sup> The tunability of their optical properties and the facile size, shape and surface modifications make these systems versatile multi-functional platforms for different applications. Moreover, luminescent silicas can be prepared *via* different, simple and versatile methods (see the introduction of the chapter) that allow the design of materials with specific suitable properties for each application.

In the last decades, organic and inorganic compounds have been used for the preparation of these luminescent hybrids. In this sense, most of the approximations used involve *post-synthetic* methods that generally present important disadvantages, being one of the most remarkable the leaching of the incorporated chromophore. Therefore, the development of new synthetic routes that enables to reduce these problems is still a challenge.

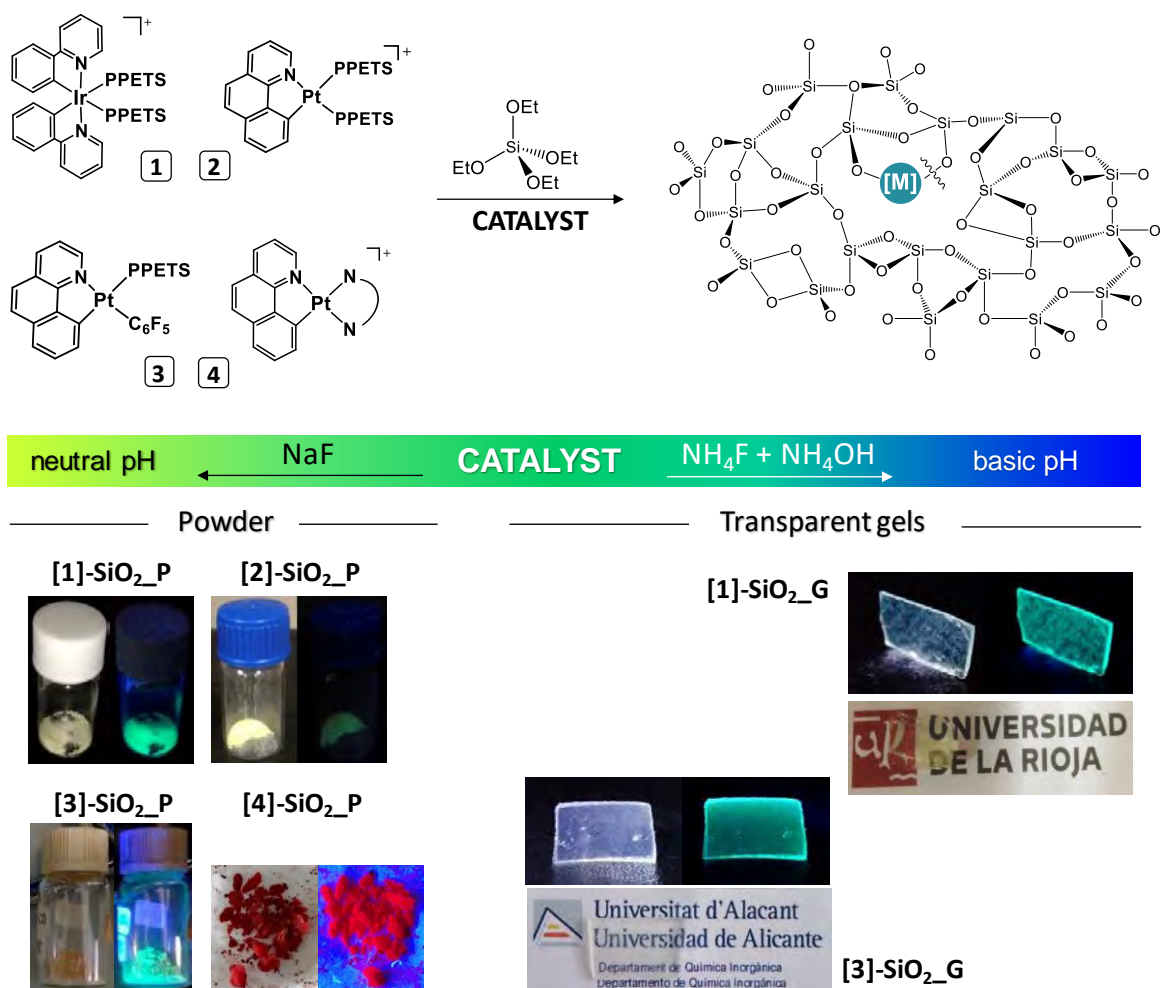
In this context, our group reported an eco-friendly one-pot strategy,<sup>35b</sup> based on the so-called Sol-Gel Coordination Chemistry, by the *in-situ* co-condensation of a properly functionalized copper acetylide phosphine complex with TEOS as the silica source. This methodology allowed to obtain a very stable and emissive material, having the chromophore well integrated into the silica framework.

Taking into account the advantages of our synthetic route, in this part of the chapter we consider of interest to explore the formation of mesoporous silica materials based on the incorporation of the new Ir<sup>III</sup> and Pt<sup>II</sup> emissive complexes (**1-4**) previously described in part I.

### I.2.1 Synthesis of hybrid organometallo-silica materials ( $\text{SiO}_2\text{-P}$ , $\text{SiO}_2\text{-G}$ )

We have designed different procedures, schematized in scheme 1.5, to prepare two series of mesoporous hybrid luminescent materials: (i) powder  $\text{SiO}_2\text{-P}$  and (ii) optically transparent  $\text{SiO}_2\text{-G}$  organometallo-silica gels.

The synthesis of both hybrid materials is based on the so-called Sol-Gel Coordination Chemistry in which the chromophores are directly co-condensated with the silica source, TEOS, through the terminal trialkoxysilane groups of the auxiliary ligands (PPETS and *dasipy*) of the metal complex precursors (**1-4**). The different synthetic details are related to reaction conditions such as pH, the catalyst and, also, the amount of chromophore added to the materials. It should be remarked that all the hybrid silicas were prepared without the concurrence of any surfactant.



**Scheme 1.5.** Schematic representation of the preparation of luminescent mesoporous hybrid organometallo-silica powders ( $[1-4]\text{-SiO}_2\text{-P}$ ) and the optically transparent gels ( $[1,3]\text{-SiO}_2\text{-G}$ ). Pictures of the as-synthesized materials illuminated with visible and UV light.

In detail, the new hybrid organometallo-silica powders (**[1-3]-SiO<sub>2</sub>-P**) were prepared under mild conditions, at room temperature and neutral pH (scheme 1.5). Each complex was firstly dissolved in THF and added to the TEOS to start the condensation process. An aqueous solution of NaF was used as catalyst to induce de hydrolysis and the precipitation of the silica material (see the experimental section). The nominal metal content of chromophore employed was kept equal to 1 wt% (organometallic complex/ TEOS  $3.3 \times 10^{-3}$  molar ratio), obtaining highly emissive hybrids (except **[2]-SiO<sub>2</sub>-P** that emits weakly) in the blue and green region.

In the case of the material based on complex **4**, the preparation was performed under argon conditions (see experimental section for more detailed information), giving rise to **[4]-SiO<sub>2</sub>-P** as a red-emitting hybrid material.

The optically transparent gels (**[1,3]-SiO<sub>2</sub>-G**, scheme 1.5) were only prepared with precursors **1** and **3**, which feature better emissive properties and stability in solution. For this purpose, following previous procedures,<sup>66</sup> the TEOS/water volume ratio was increased tenfold in comparison to the synthesis of the above materials and ethanol was used as co-solvent, instead of tetrahydrofuran. Likewise, the amount of chromophore added to these gels was also reduced tenfold (nominal metal content: 0.1 wt%, organometallic complex/TEOS *ca.*  $3.1 \times 10^{-4}$  molar ratio) with the aim of achieving its complete solution in ethanol before the addition of the silica source (TEOS). In this case, the hydrolysis and co-condensation reactions were performed at basic pH, using as catalyst a mixture of NH<sub>4</sub>F and NH<sub>4</sub>OH. After 5 minutes of stirring, the mixture was placed in a glass plate to allow the formation of a transparent gel. Multiple exchanges of the remaining fluids with acetone yielded the optically transparent wet gels shown in scheme 1.5.

All these final powders and transparent gel materials were air dried before their characterization.

## I.2.2 Characterization of the hybrid organometallo-silica materials

### I.2.2.1 Textural characterization

The porosity of the as-synthesized hybrid silica materials and the influence of the incorporation of the chromophores in the textural properties, have been examined by physisorption experiments carried out by the research group of Prof. Javier García Martínez (Molecular Nanotechnology Lab, NANOMOL, University of Alicante). For comparison purposes,

these measurements were also performed for the related complex-free silica powder (**SiO<sub>2</sub>\_P**) and transparent gel (**SiO<sub>2</sub>\_G**).

The morphology of the different silicas was evaluated by FESEM and TEM analysis. Thus, while FESEM images reveal the granular nature characteristic of silica materials prepared by the hydrolysis of TEOS (figure 1.33, a-b),<sup>67</sup> TEM studies confirm the amorphous and porous structures of the samples (figure 1.33, c-e).<sup>68</sup> Moreover, the absence of any contrast caused by metal clusters in the TEM images corroborates the fact that no agglomeration of metal particles occurred upon immobilization of the organometallic complexes in both types of hybrid materials.

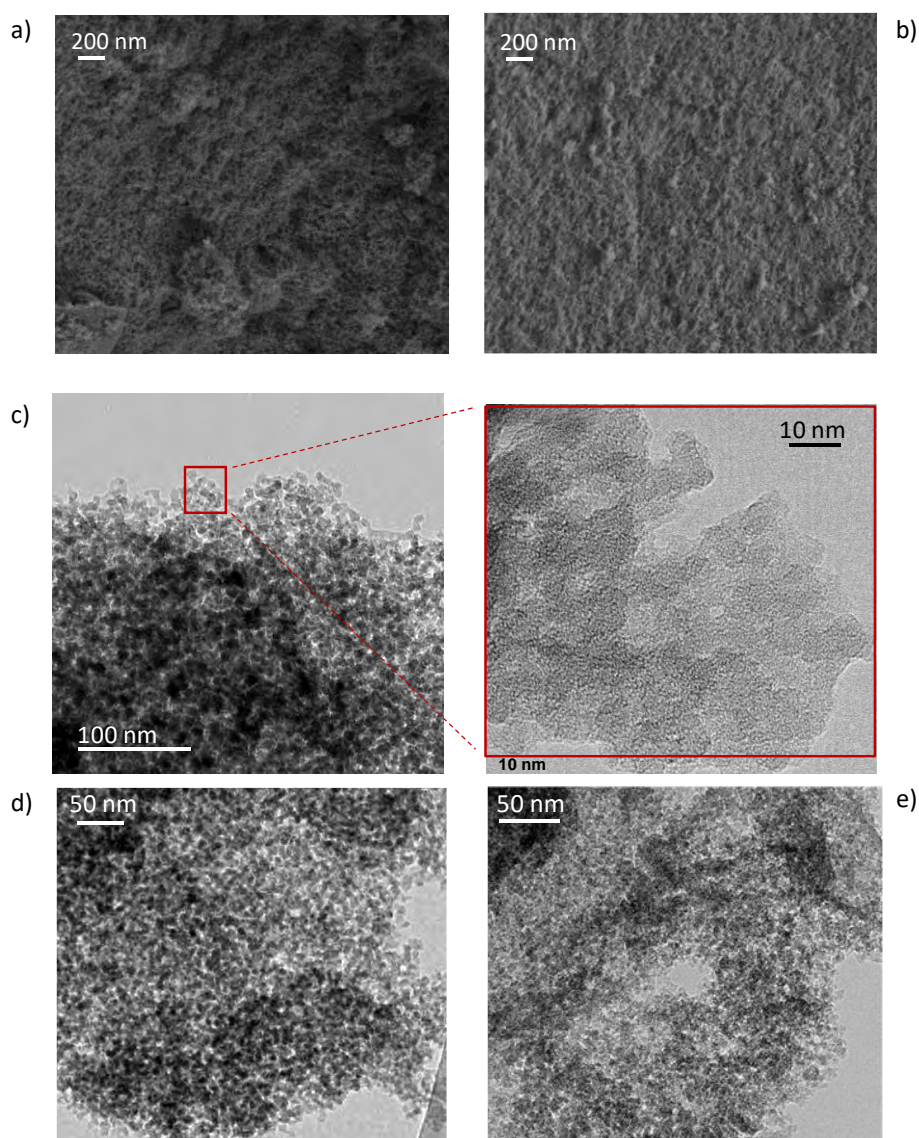


**Figure 1.33.** Representative FESEM and TEM images of the hybrid materials. FESEM images of **[2]-SiO<sub>2</sub>\_P** (a) and **[3]-SiO<sub>2</sub>\_G** (b). TEM images of **[1]-SiO<sub>2</sub>\_P** (c), **[1]-SiO<sub>2</sub>\_G** (d) and **[3]-SiO<sub>2</sub>\_G** (e).

For the physisorption studies, the samples were previously degassed during 4 hours at 373K and  $5 \times 10^5$  bars. According to the IUPAC classification,<sup>69</sup> all the samples exhibit type IV isotherms with a considerable uptake at relative pressures ( $P/P_0$ ) of about 0.5 (see figures 1.34-1.35), due to the capillary condensation of the nitrogen inside the porous of the materials. This behavior is typical of amorphous disordered mesoporous materials with complex structures, such as gels, in which the pore width exceeds a certain critical value.<sup>69</sup> Therefore, despite the absence of any surfactant in the synthetic procedure, the materials exhibit a mesoporous structure due to the aggregation of very small particles, which is known as interparticle mesoporosity. According to the pore size distribution, all the hybrids feature broad profiles (see figures 1.34-1.35, inset) with average pore sizes of *ca.* 5 nm ([1-4]-SiO<sub>2</sub>\_P) and 10 nm ([1,3]-SiO<sub>2</sub>\_G).

**Table 1.6.** Metal content and textural properties of the mesoporous hybrid silica powders ([1-4]-SiO<sub>2</sub>\_P) and gels ([1,3]-SiO<sub>2</sub>\_G). Silica gels were dried before their characterization.

Sample	M <sup>(a)</sup> (wt%)	A <sub>BET</sub> <sup>(b)</sup> (m <sup>2</sup> /g)	V <sub>p</sub> <sup>(c)</sup> (cm <sup>3</sup> /g)	d <sub>p</sub> <sup>(d)</sup> (nm)
SiO <sub>2</sub> _P	---	620	0.76	7.0
[1]-SiO <sub>2</sub> _P	0.59 (1.0)	570	0.48	5.0
[2]-SiO <sub>2</sub> _P	0.52 (1.0)	590	0.49	5.0
[3]-SiO <sub>2</sub> _P	0.74 (1.0)	605	0.71	7.0
[4]-SiO <sub>2</sub> _P	0.41 (1.0)	494	0.28	3.7
SiO <sub>2</sub> _G	---	380	0.91	10
[1]-SiO <sub>2</sub> _G	0.08 (0.1)	305	0.91	11
[3]-SiO <sub>2</sub> _G	0.05 (0.1)	285	0.81	10

(a) Metal content calculated from high resolution ICP mass spectroscopy analyses after treatment of the samples with diluted HF. Values in brackets represent the nominal metal content. (b) BET surface area estimated by multipoint BET method using the adsorption data in the relative pressure ( $P/P_0$ ) range of 0.05–0.25. (c) Pore volume. (d) Average pore diameter determined from the adsorption branch of the isotherm using the NLDFT equilibrium model.

The textural properties of [3]-SiO<sub>2</sub>\_P, based on the neutral precursor **3**, were similar to those measured for the complex-free SiO<sub>2</sub>\_P. By contrast, the porosity of the powder materials based on the cationic chromophores ([1,2,4]-SiO<sub>2</sub>\_P, having two long aliphatic chains on their structures, PPETS or *dasipy*) was slightly blocked, decreasing both the total pore volume and the average pore diameter (see table 1.6). A decrease in the inflection points of the adsorption isotherms to lower relative pressures in the three samples was also observed (figure 1.34), which directly affects to the surface area of the materials ( $A_{BET} < 600\text{ m}^2/\text{g}$ ). This is also accompanied by a decrease in the intensity of the maxima on the size distribution plot and an increase in its width (figure 1.34, inset).

This behavior suggests an increase in pore heterogeneity that, according to the literature, can be associated to the immobilization of bulky complexes or phosphine/bipyridyl ligands on the internal silica surface.<sup>37, 70</sup> The partial blocking of the porosity observed in **[1,2,4]-SiO<sub>2</sub>-P** can be tentatively related to a lower interaction between the cationic complexes and TEOS in the neutral medium in which the synthesis is performed. This is consistent with the ICP analyses that reveal lower incorporation yields for the cationic complexes (*ca.* 60% **1**, 50% **2** and 40% **4**) than for the neutral one (74% **3**).

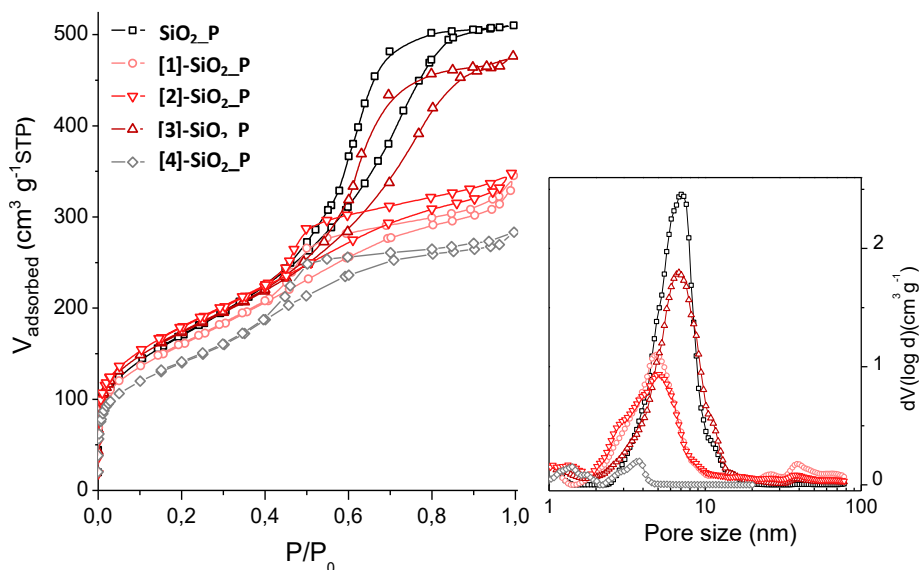


**Figure 1.34.** Nitrogen adsorption/desorption isotherms at 77K and NLDFT size distribution (inset) of the hybrid organometallo-silica powders (**[1-4]-SiO<sub>2</sub>-P**) in comparison to the related metal-free control material.

On the other hand, the silica gel materials (**[1,3]-SiO<sub>2</sub>-G**) preserved the adsorption process of the complex-free silica **SiO<sub>2</sub>-G**, maintaining the uptake at  $P/P_0 > 0.6$  (figure 1.35), which is typical of the interparticle mesoporosity in silica gels prepared in alkaline media.<sup>71</sup> In this case, no heterogeneity is expected because only minimal changes in the size distribution profiles are observed (figure 1.35, inset).

Moreover, in contrast to the powder hybrids, both the pore volume and the average pore diameter remained almost equal after the incorporation of the chromophores in the gels (see table 1.6). This fact is attributed to the open structure of these silicas and to the better dispersion and incorporation of the organometallic molecules into the silica matrix, regardless of the cationic or neutral nature of the derivatives. This is also consistent with the photophysical properties measured for these materials (see below).

Finally, ICP analysis of these hybrids gave similar incorporation yields (80% **[1]-SiO<sub>2</sub>-G** and 50% **[3]-SiO<sub>2</sub>-G**) than those observed for the powdery materials.

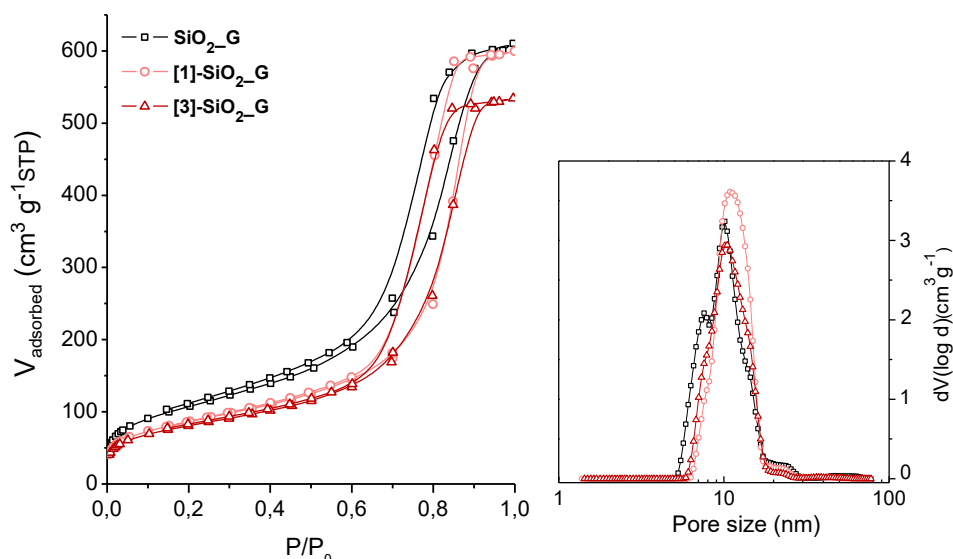


**Figure 1.35.** Nitrogen adsorption/desorption isotherms at 77K and NLDFT size distribution (inset) of the hybrid organometallo-silica transparent gels (**[1,3]-SiO<sub>2</sub>-G** air dried) in comparison to the related metal-free control material.

### 1.2.2.2 Spectroscopy characterization

The incorporation of complexes **1-4** into both types of silica frameworks, as well as the preservation of their molecular structure, were studied by FTIR and absorption and emission spectroscopies.

#### 1.2.2.2.1 Infrared spectra

As shown in figure 1.36, all the as-synthesized hybrid silica materials exhibit some of the characteristic absorption bands of their respective chromophores. Those observed in the range between 2850 and 3000 cm<sup>-1</sup> are typical of the stretching vibrations of the C-H moieties, while the absorptions at *ca.* 1400 cm<sup>-1</sup> correspond to the vibration of the aromatic rings.

In addition, all of them show the usual vibrations of the silica. Thus, the intense absorptions at *ca.* 3400 and 1630 cm<sup>-1</sup> are attributed to vibrations of the OH groups that remain on the surface of the materials after being prepared. The wide absorption band centered at 1080 cm<sup>-1</sup> is directly associated to the symmetric stretching of the Si-O-Si bonds. Other absorptions related

to this subunit are those found at 1200, 800 and 460 cm<sup>-1</sup> that are attributed to the antisymmetric and symmetric stretching and bending modes, respectively.

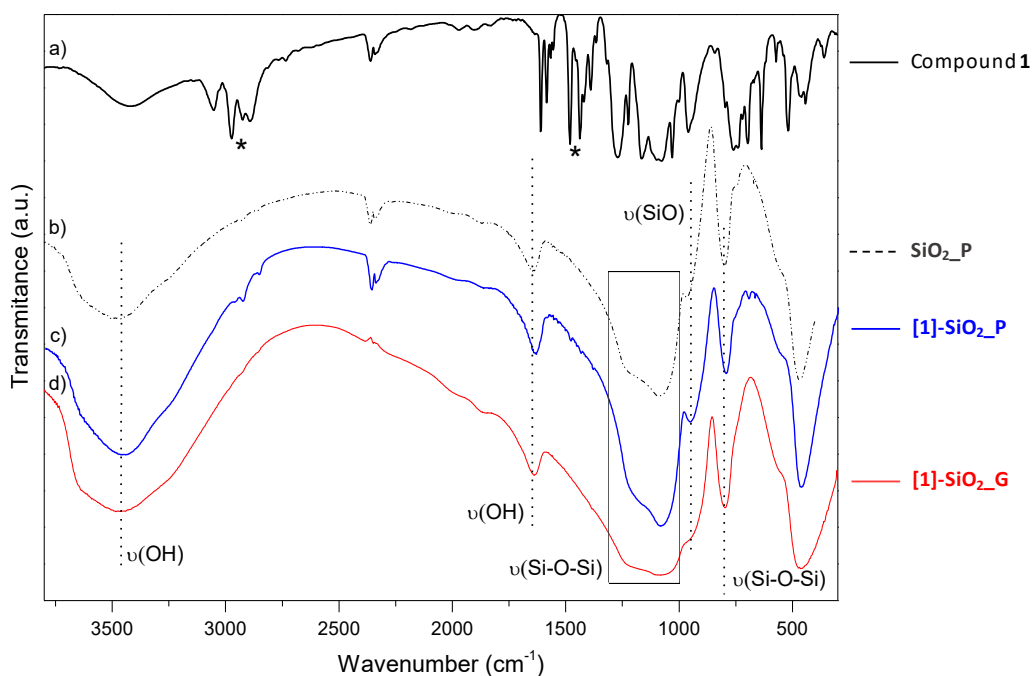


**Figure 1.36.** Representative FTIR spectra of the iridium(III) complex (**1**) in comparison to the organometallo-silicas ([**1**]-SiO<sub>2</sub>\_P, c; [**1**]-SiO<sub>2</sub>\_G, d) and the control complex-free material SiO<sub>2</sub>\_P (b). (\*) Characteristic peaks of the complexes observed in the hybrid materials.

#### I.2.2.2.2 Photophysical properties

##### i. Absorption spectra

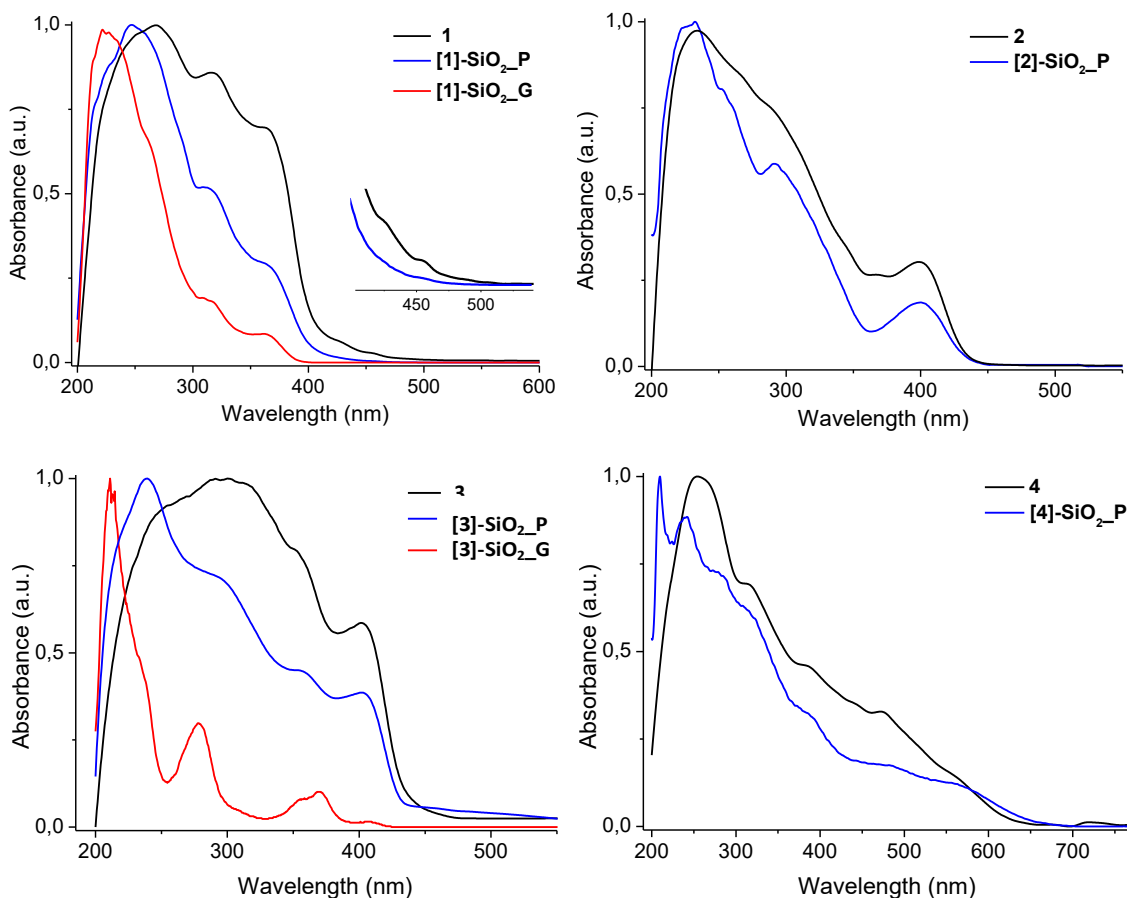
The reflectance diffuse spectra of all the silica materials are given in figure 1.37 and, for comparison purposes, those of the precursors are also included.

The two types of materials prepared from the iridium derivative ([**1**]-SiO<sub>2</sub>\_P and [**1**]-SiO<sub>2</sub>\_G) display a very similar profile to that previously described for **1** in the solid state, in the range between 220-365 nm (see figure 1.37). In addition, the weak absorptions observed in the visible region, ascribed to spin forbidden transitions, are also resolved in the powder silica (424 and 454 nm), thus supporting not only that the chromophore is well integrated but also that its molecular structure has not changed upon incorporation.

**Table 1.7.** Absorption data in the solid state (DRUV) of complexes **1-4** and their corresponding silica materials (**[1-4]-SiO<sub>2</sub>\_P** and **[1,3]-SiO<sub>2</sub>\_G**).

Sample	$\lambda_{\text{abs}}/\text{nm}$
[Ir(ppy) <sub>2</sub> (PPETS) <sub>2</sub> ]OTf ( <b>1</b> )	221, 248, 267, 321, 366, 420, 452
<b>[1]-SiO<sub>2</sub>_P</b>	224, 246, 258, 317, 365, 424, 454
<b>[1]-SiO<sub>2</sub>_G</b>	221, 234, 262, 317, 362
[Pt(bzq)(PPETS) <sub>2</sub> ]PF <sub>6</sub> ( <b>2</b> )	235, 263, 290, 400
<b>[2]-SiO<sub>2</sub>_P</b>	233, 253, 291, 400
[Pt(bzq)(C <sub>6</sub> F <sub>5</sub> )(PPETS)] ( <b>3</b> )	250, 300, 355, 390, 402
<b>[3]-SiO<sub>2</sub>_P</b>	215, 240, 290, 355, 402
<b>[3]-SiO<sub>2</sub>_G</b>	210, 235, 280, 356, 370, 407
[Pt(bzq)(dasipy)]PF <sub>6</sub> ( <b>4</b> )	254, 313, 384, 475, 565
<b>[4]-SiO<sub>2</sub>_P</b>	208, 241, 283, 314, 382, 482, 559 <sup>(a)</sup>

(a) Tail extending up to 650 nm.

**Figure 1.37.** Solid state DRUV spectra of complexes **1-4** and their related hybrid silica materials (**[1-4]-SiO<sub>2</sub>\_P** and **[1,3]-SiO<sub>2</sub>\_G**).

In the same line, the DUV spectra of the materials based on the platinum complexes (**2**, **3** and **4**) also support the presence and the incorporation of the precursors into the framework of the silica. Particularly, the absorption profile observed for the aerogel **[3]-SiO<sub>2</sub>\_G** simulates the

corresponding to **3** in THF solution, suggesting the incorporation of well separated molecules. By contrast, the corresponding powder material **[3]-SiO<sub>2</sub>\_P** displays broader bands that mimic the spectrum measured for the precursor in the solid state; a fact that is probably related to the higher complex loading in this last hybrid (1% **SiO<sub>2</sub>\_P** vs. 0.1% **SiO<sub>2</sub>\_G**).

### *ii. Emission spectra*

The emissive properties of all the hybrids are collected in figures 1.39-1.41 and in table 1.8. As illustration, photographs of the optically transparent gels, **[1,3]-SiO<sub>2</sub>\_G**, under visible and when irradiated with UV light are also shown in figure 1.38.

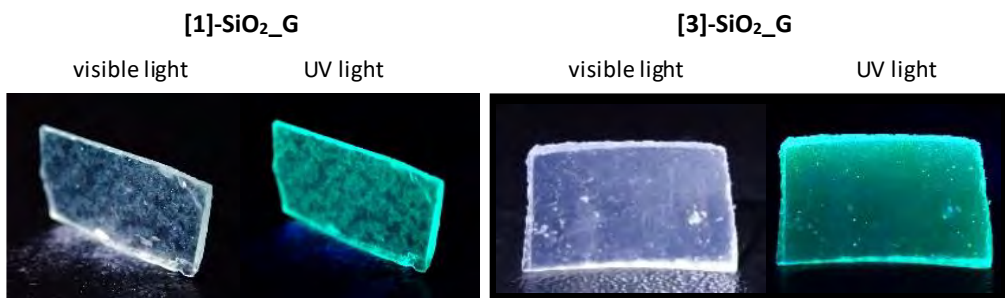


**Figure 1.38.** Photographs of the transparent gels **[1]-SiO<sub>2</sub>\_G** (left) and **[3]-SiO<sub>2</sub>\_G** (right), under visible and UV light irradiation.

All the materials display very similar profiles to those described for their corresponding organometallic precursors. As shown in figure 1.39, the aerogel **[1]-SiO<sub>2</sub>\_G** exhibits nearly the same emission to that of complex **1** in fluid solution, suggesting the incorporation of well separated molecules within the silica. Interestingly, despite the similarities in the emission profile, there is an obvious increase in the values of the lifetime (0.27  $\mu$ s **1** vs. 0.79  $\mu$ s **[1]-SiO<sub>2</sub>\_G**) and quantum yield (3.4% **1** vs. 8.5% **[1]-SiO<sub>2</sub>\_G**), which are threefold higher than in THF solution. This fact clearly supports that the rigid matrix of the silica is able to partially prevent the deactivation processes that the chromophore suffers in fluid media through the molecular distortion.

By contrast, the emission profile of **[1]-SiO<sub>2</sub>\_P** is broader and resembles to that observed for the precursor in the solid state, featuring a shoulder at the high energy region (attributed to monomers) and a broad band centered at 510 nm ascribed to some degree of AIE (see figure 1.39). This profile clearly indicates that the increase in the iridium loading contributes to enhance the intensity of the emission likely due to the aggregation of the organometallic molecules inside the framework of the silica or onto the internal surface.

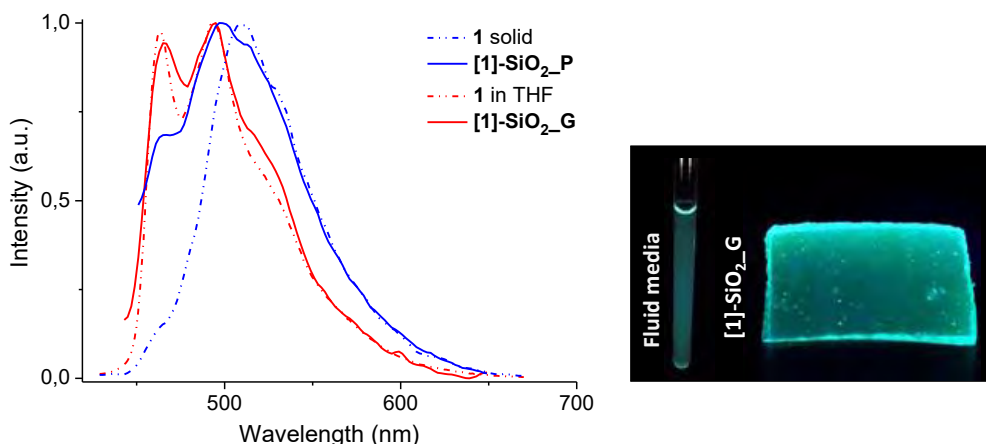


**Figure 1.39.** Emission spectra of complex **1** in solid state (dotted blue line) and THF solution (dotted red line) and of its silica materials **[1]-SiO<sub>2</sub>\_P** (blue) and **[1]-SiO<sub>2</sub>\_G** (red), at room temperature.

The mesoporous materials based on the neutral platinum(II) derivative, **[3]-SiO<sub>2</sub>\_P** and **[3]-SiO<sub>2</sub>\_G**, exhibit a similar structured profile ( $\lambda_{\text{max}}$  485 nm) to that observed for the precursor complex in the solid state (figure 1.40, right). The most significant difference found, when compared to **3**, is the notable increase in the lifetime of the transparent gel (405.7  $\mu\text{s}$  **[3]-SiO<sub>2</sub>\_G** vs. 206.5  $\mu\text{s}$  **3**), supporting that the chromophore is effectively protected by the silica matrix from luminescence quenching.

In the case of **[3]-SiO<sub>2</sub>\_P**, the lifetime is similar to that of the precursor (207.5  $\mu\text{s}$  vs. 206.5  $\mu\text{s}$  **3**), indicating that the main part of the platinum precursor is likely on the surface of the material and, therefore, less protected. Likewise, the quantum yields measured for both materials are coherent with the values observed for the complex blended in PMMA.

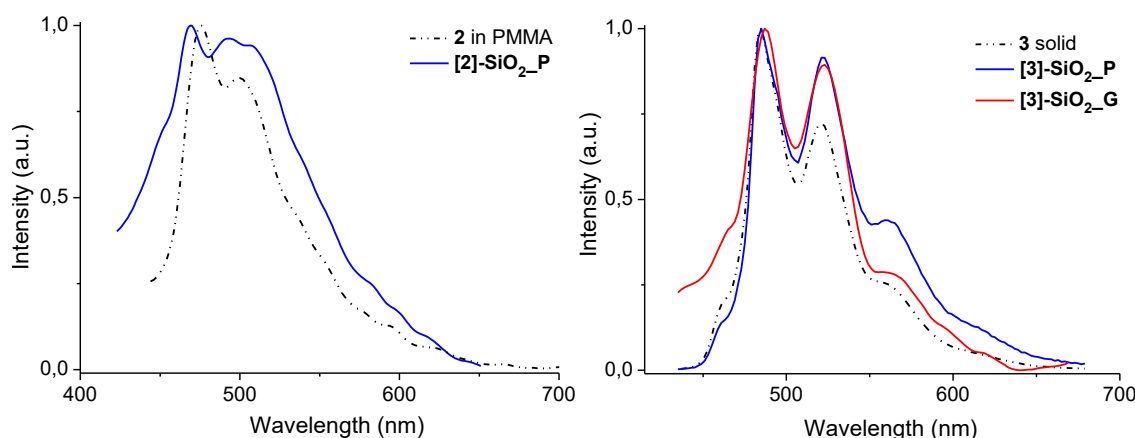


**Figure 1.40.** Emission spectra of complex **2** in PMMA (left) and **3** in the solid state (right) and their respective hybrid materials (**[2,3]-SiO<sub>2</sub>\_P** and **[3]-SiO<sub>2</sub>\_G**), at room temperature.

Interestingly, although complex **2** is not emissive at room temperature, the as-synthesized material (**[2]-SiO<sub>2</sub>-P**) shows a very weak emission band in the green region that resembles to that of **2** in PMMA (see figure 1.40). Probably, the absence of interactions between the platinum moieties in the inorganic matrix, together with the increase in the rigidity of the chromophore are the responsible of the emission of **[2]-SiO<sub>2</sub>-P** at room temperature.

**Table 1.8.** Emission data of complexes **1-4** and of their hybrid silica materials (**[1-4]-SiO<sub>2</sub>-P** and **[1,3]-SiO<sub>2</sub>-G**) in the solid state.

Sample	Medium <sup>(a)</sup>	$\lambda_{\text{em}}^{(b)}$ (nm)	$\tau$ (μs)	$\phi$ (%)
<b>1</b>	Solid	512	0.97	31.2
	THF	464, 494 <sub>max</sub> , 520 <sub>sh</sub>	0.27	3.4
<b>[1]-SiO<sub>2</sub>-P</b>	Solid	510	0.93	6.9
<b>[1]-SiO<sub>2</sub>-G<sup>(c)</sup></b>	Solid	465, 495 <sub>max</sub> , 515 <sub>sh</sub>	0.79	8.5
<b>2</b>	PMMA	475 <sub>max</sub> , 500	84.3	2.0
<b>[2]-SiO<sub>2</sub>-P</b>	Solid	469 <sub>max</sub> , 495, 505	0.35	0.5
<b>3</b>	Solid	485 <sub>max</sub> , 520, 560, 610 <sub>sh</sub>	206.5	43.4
<b>[3]-SiO<sub>2</sub>-P</b>	Solid	485 <sub>max</sub> , 520, 560, 610	207.5	13.7
<b>[3]-SiO<sub>2</sub>-G<sup>(c)</sup></b>	Solid	487 <sub>max</sub> , 523, 561, 615	405.7	8.8
<b>4</b>	Solid	690	0.13	8.5
<b>[4]-SiO<sub>2</sub>-P</b>	Solid	715	0.17	20.6

(a) Data measured at room temperature. (b)  $\lambda_{\text{ex}}$  365 nm.  $\lambda_{\text{ex}}$  520 nm **4** and  $\lambda_{\text{ex}}$  570 nm **[4]-SiO<sub>2</sub>-P**. (c) Data for air-dried **[1,3]-SiO<sub>2</sub>-G** solids. Identical data were obtained for the transparent gels.

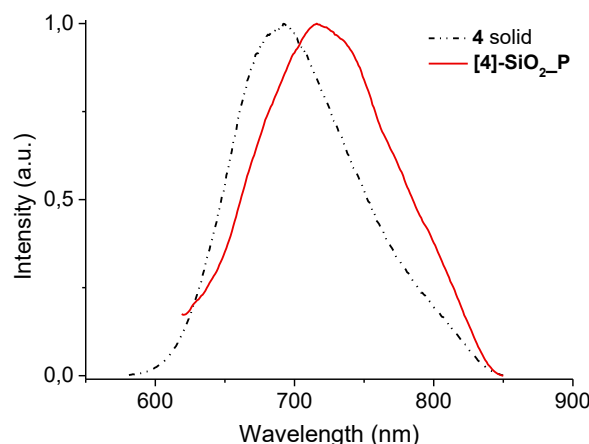


**Figure 1.41.** Emission spectra of **[4]-SiO<sub>2</sub>-P** compared with complex **4** in the solid state at room temperature.

Finally, **[4]-SiO<sub>2</sub>-P** shows a structureless emission profile comparable to that collected for its initial precursor **4** in the solid state at 298K (figure 1.41), being attributed to a  $^3\text{MML'CT}$  excited state. This suggests that the incorporated molecules are still remarkably close to interact inside the silica matrix. In addition, as observed for **4-gel**, this silica material also shows a remarkable

enhancement in the quantum yield when compared to the pure solid ( $\phi$  20.6% **[4]-SiO<sub>2</sub>\_P** vs. 8.5% **4**), which is attributed to the increase of the rigidity within the *dasipy* ligand upon condensation of the alkoxy silane groups with the TEOS.

It should be noted that both types of hybrid materials (**[1-4]-SiO<sub>2</sub>\_P** and **[1,3]-SiO<sub>2</sub>\_G**) have demonstrated to display excellent stability in suspension in the most common organic solvents, including water, and remain stable in refluxed ethanol suspensions for days without losing their emissive properties. Especially remarkable is the behavior observed for **[4]-SiO<sub>2</sub>\_P** due to the fact that its precursor (**4**) has demonstrated to display very poor stability in solution in the presence of oxygen. Hence, we have been able to stabilize the chromophore after its inclusion in the silica matrix, also enhancing its emission efficiency.



## ***Chapter II***

---

***Hybrid white-emitting organometallo-silica  
nanoparticles***

---



## Introduction

Artificial light has always been a significant contributor to both the quality and productivity of human life and, consequently, we have always consumed huge amounts of energy to produce it. Currently, lighting constitutes between the 8% and 12% of the electric power consumption in Europe and the United States. Hence, and since we are increasingly aware of the environment, the search of new and more eco-friendly white light illumination devices has become of major relevance.

In this context, solid-state lighting (SSL) devices to generate white light have become one of the leading technologies in recent years. Compared to traditional electrical filaments, arc and fluorescent lamps, solid-state lighting offers higher efficiencies, brightness, reliability and is an environmentally friendly technology due to the absence of toxic metals, such as mercury.

These SSL devices consist of a thin-film electroluminescent device based on organic or inorganic semiconductor materials, that are able to produce visible light upon an externally applied electric field.<sup>72</sup> When injecting a current across the device, the electrons can be excited and jump into the conduction band, generating the corresponding holes in the valence band (see figure 2.1). The subsequent electron-hole recombination produces an energy release that is given out as light, being the wavelength of the emitted light equivalent to the band gap of the semiconductor. So, in contrast to conventional lighting devices, in which the light is a byproduct, SSL allows a significant reduction in heat generation, as well as an enhancement in luminous efficiency. As a result, SSL light sources display superior efficiency, stability, reliability and lifetime, which makes it more energy-saving and environmental-friendly.

Traditionally, these SSL devices are divided into light-emitting diodes (LEDs), organic light-emitting diodes (OLEDs) and light-emitting electrochemical cells (LECs). LEDs<sup>72-73</sup> are small light sources made of a thin-film of inorganic semiconductors doped with elements like indium, gallium, phosphor, etc. as well as color converters. In contrast, OLEDs<sup>74</sup> and LECs<sup>75</sup> are thin-film lighting devices with a few hundred nanometers thickness, based on organic semiconductors, including small molecules, polymers or coordination complexes.

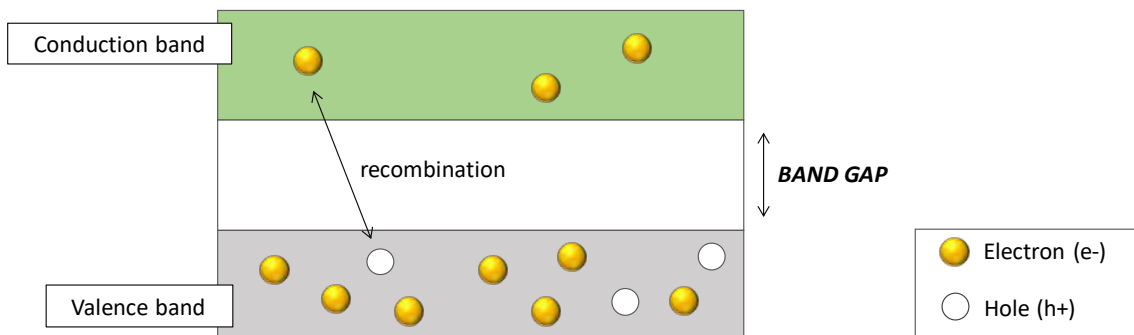


**Figure 2.1.** Schematic view of a semiconductor, showing the process that takes place.

In this context, the use of SSL devices in the form of LEDs or OLEDs for the generation of white light is revolutionizing the lighting market. They have surpassed many conventional lighting technologies in terms of energy efficiency, lifetime, versatility and color quality. Moreover, and due to their increasing cost competitiveness, they are beginning to successfully compete in a wide variety of lighting applications.

### **Design of White Light Emitting Diodes (WLEDs) devices**

Currently, there are two leading types of WLEDs devices that differ in the nature of the materials used for the emitting layers, that is, organic (WOLEDs) or inorganic (WILEDs) semiconductors.

#### i. White Organic Light Emitting Diodes (WOLEDs)

Organic light emitting diodes (OLEDs) have gained much expectative in both the industry and scientific communities due to their favorable properties such as homogeneous emission area, good color rendering, low power consumption, wide operating temperature range and substrate flexibility, among others.<sup>76</sup> Monochromatic OLEDs have already found their commercial path due to their good performance and easy fabrication.<sup>76</sup>

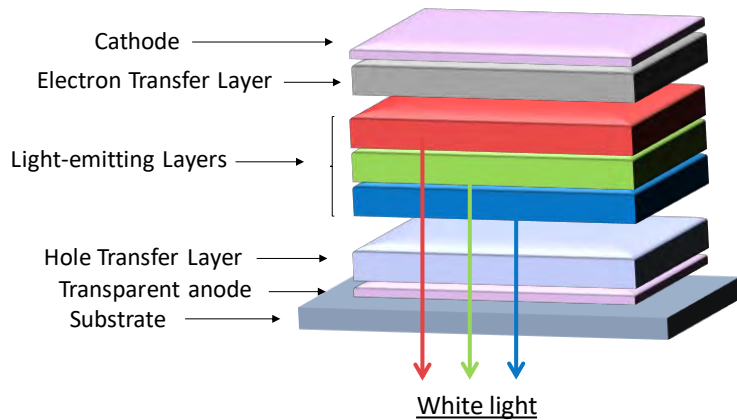


**Figure 2.2.** Schematic representation of a WOLED.

However, white OLEDs (WOLEDs) are still in a development stage. Their fabrication requires a multilayer structure based on several organic semiconductors with different emission colors, which mixture produces white light (see figure 2.2).<sup>76-77</sup> Since the pioneering work of Kido *et al.* in 1994,<sup>78</sup> various devices with luminous efficiencies of 50-60 lm/W and stabilities of thousands of hours have been reported.<sup>76</sup> Nevertheless, this is not sufficient for their large-scale manufacturing lines because other requirements need to be developed: simpler architectures to enhance both the charge transport and recombination, as well as light out-coupling efficiencies, more stable blue emitters and easy low-cost fabrication processes.<sup>77a, 79</sup>

## ii. Inorganic White Light Emitting Diodes (WILEDs)

A second approximation is related to the use of inorganic-based materials as color down-converters. These inorganic white light-emitting diodes (WILEDs) are prepared by covering a UV- or blue-diode chip with pre-coating inorganic phosphors, that are able to transform the high-energy chip emission into visible light (see figure 2.3).<sup>78, 80</sup>

As the first commercially available white LED produced by Nichia Corporation, the yellow-emitter cerium-doped yttrium aluminum garnet ( $\text{Y}_3\text{Al}_5\text{O}_{12}:\text{Ce}^{3+}$ ; YAG:Ce<sup>3+</sup>) is one of the most widely used color down-converter, among others.<sup>81</sup> These LEDs have captured the interest of the lighting market and have resulted in highly efficient devices, which match the emission efficiency of fluorescent lights. They display excellent photo- and thermal-stabilities, high photon flux saturation and photoluminescence quantum yields ( $\phi > 70\%$ ).

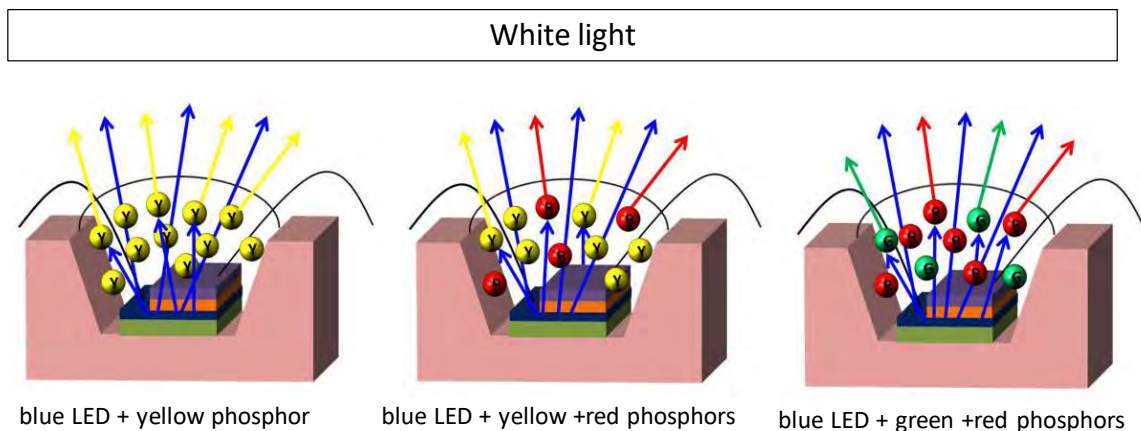


**Figure 2.3.** Different ways of generating white light with blue LED and inorganic phosphors. (Materials 2010, 3, 2172-2195)

Despite these excellent characteristics, some concerns about the future development of established phosphors need to be considered. These devices are mainly based on phosphors of rare-earth elements (cerium, europium, yttrium, etc.), which although are robust and display long lifetimes and excellent lighting performances, have potential toxicity, environmental hazardousness and high production costs. Also, the tunability of the emission color in these systems is still a challenge, which limits their LED color quality.<sup>78, 80-81, 81c, 81d</sup> This fact is the responsible that most of the WILEDs present a pronounced blue component in their emission (figure 2.4), which represents a potential health risk. The blue-light component is hazardous for the human retina of both the elderly and the children, the circadian cycle and the hormonal system, which are exquisitely sensitive to high energy wavelengths, its amount and intensity. This can cause disturbances that directly affect on the sleep-wake cycle, eating patterns, metabolism, mental alertness, hormone production, mood patterns and the immune system.<sup>82</sup> Therefore, there is a great interest in developing WILEDs that show a better white light quality, mimicking the natural sunlight, and low-toxicity fluorescent materials.

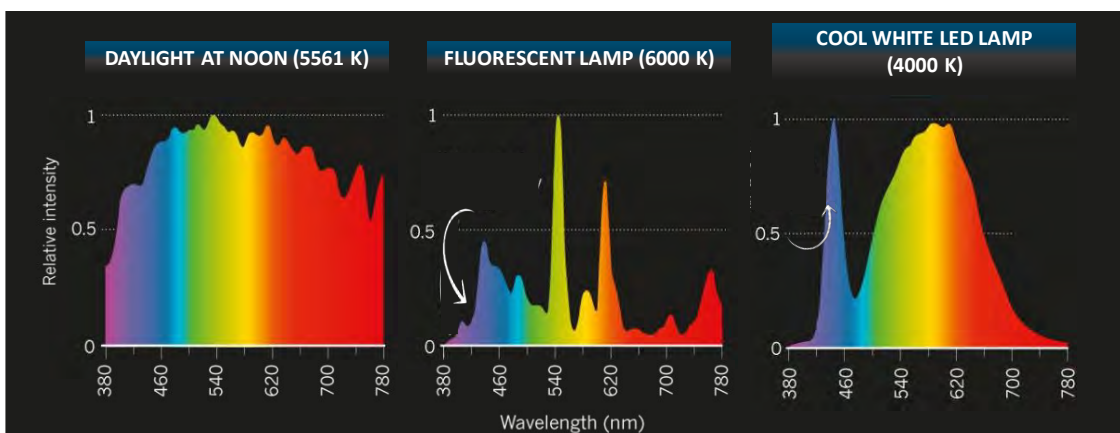


**Figure 2.4.** Comparison between the different light-source spectra.

### iii. Hybrid White Light Emitting Diodes (HWLEDs)

The aforementioned limitations in the progress of high quality lighting systems have encouraged further efforts to develop hybrid inorganic/organic WLEDs devices (HWLEDs).<sup>83</sup>

These hybrid LEDs consist of a commercially available UV- or blue-LED chip covered by an encapsulating packaging matrix, in which the organic or inorganic down-converting materials, that provide emission in the low-energy region, are immobilized (see figure 2.5).<sup>83a</sup> In this way, these HWLEDs are able to integrate not only the excellent lighting performance of inorganic LEDs, but also the easy fabrication and color tunability of the organic chromophores used in OLEDs devices.

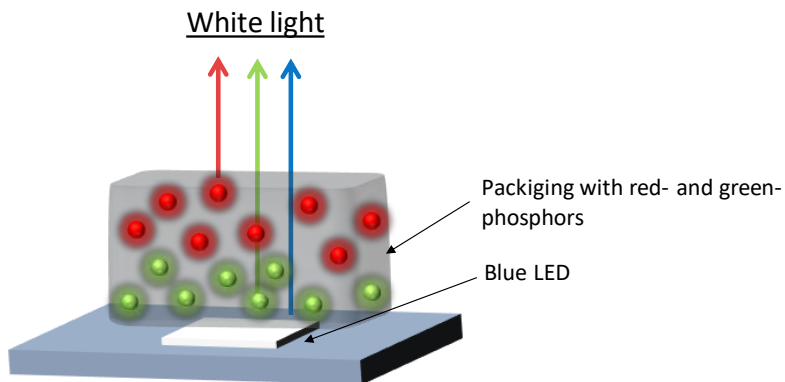


**Figure 2.5.** Schematic representation of a HWLEDs.

In recent years, different strategies to develop down-converting coatings have been established. In this context, metal organic frameworks (MOFs),<sup>84</sup> that show high-energy emissions and tunable pore sizes, have been used as the packing matrixes by embedding one or a mixture of down-converting materials inside their pores (see figure 2.6). Thus, the LED-chip can excite both the MOF and the adsorbed molecules or only the MOF that further transfers the energy to the moieties. Many authors have also claimed that this approximation is compatible with different types of molecules such as quantum dots, coordination complexes or small organic molecules. In the same line, cellulose derivatives<sup>85</sup> have also been used as matrixes to encapsulate inorganic and quantum dots, providing HWLEDs that covers the whole visible spectrum.

In both cases, white-emitting devices with good luminescence performances, such as high color rendering index (CRI) and CIE color coordinates or efficiencies, have been prepared. However, it is worth mentioning that their stabilities have not been studied in depth.

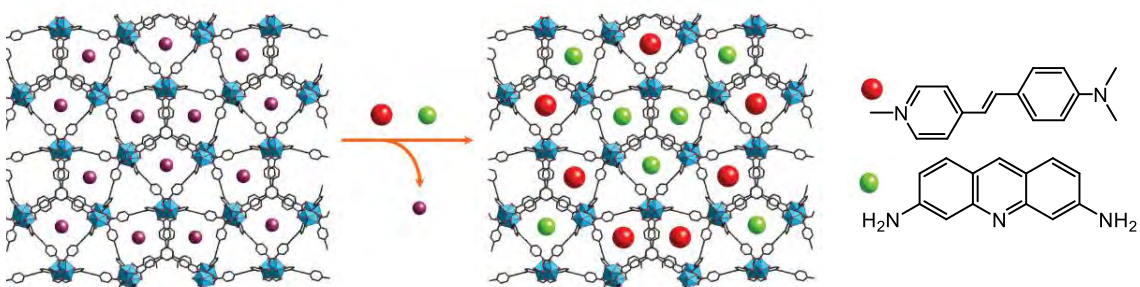


**Figure 2.6.** Example of a MOF used as a packaging matrix of two organic molecules. (Adv. Funct. Mater. 2015, 25, 4796-4802)

A more recent type of packaging involves the use of a mixture of non-cross-linked branched and linear polymers.<sup>12a, 15</sup> Their combination with luminescent molecules allows the formation of a gel that is then transformed into a rubber-like material, which is used as the coating to fabricate the hybrid LED (see figure 2.7).

Following this rubber-like encapsulation method, hybrid white LEDs are prepared by the subsequent deposition of different color rubbers on top the UV LED. Based on this approximation, proteins, quantum dots, polymers and coordination complexes have been successfully enclosed and used as down-converting materials.<sup>83a, 86</sup>

The resulting HWLEDs have shown excellent luminescent performances, such as high luminous efficiencies (above 120 lm/W) and color qualities with x/y CIE color coordinates of 0.3-0.3, color rendering index (CRI) above 80, and correlated color temperatures (CCT) between 2700K and 6500K. However, despite these appealing features, their poor stability is still a problem. The life time of the device is usually limited to a maximum of few hundred hours due to phase separation or the degradation of the down-converters when exposed to a strong blue-LED radiation intensity.<sup>83a, 86</sup>

In light of the aforementioned discussion, there are three major challenges for the preparation of high-quality and stable HWLEDs. Firstly, the development of white-emitting single-component down-converting coating is highly desirable. Basically, due to the differences in the stability and quenching of the emitters, the combination of separately matrices always ends up in loss of efficiency and quantum yields due to reabsorption, phase separation and poor color stability problems. On the other hand, it is also important to design new color down-converting coatings with better photo- and thermal-stabilities, able to support high irradiation intensities under ambient conditions. Finally, with the aim of reducing potential negative impacts on human's health, it is highly desirable the development of HWLEDs with a less blue-light

component, being essential to fabricate hybrid white LEDs with a light quality that better mimics natural sunlight.

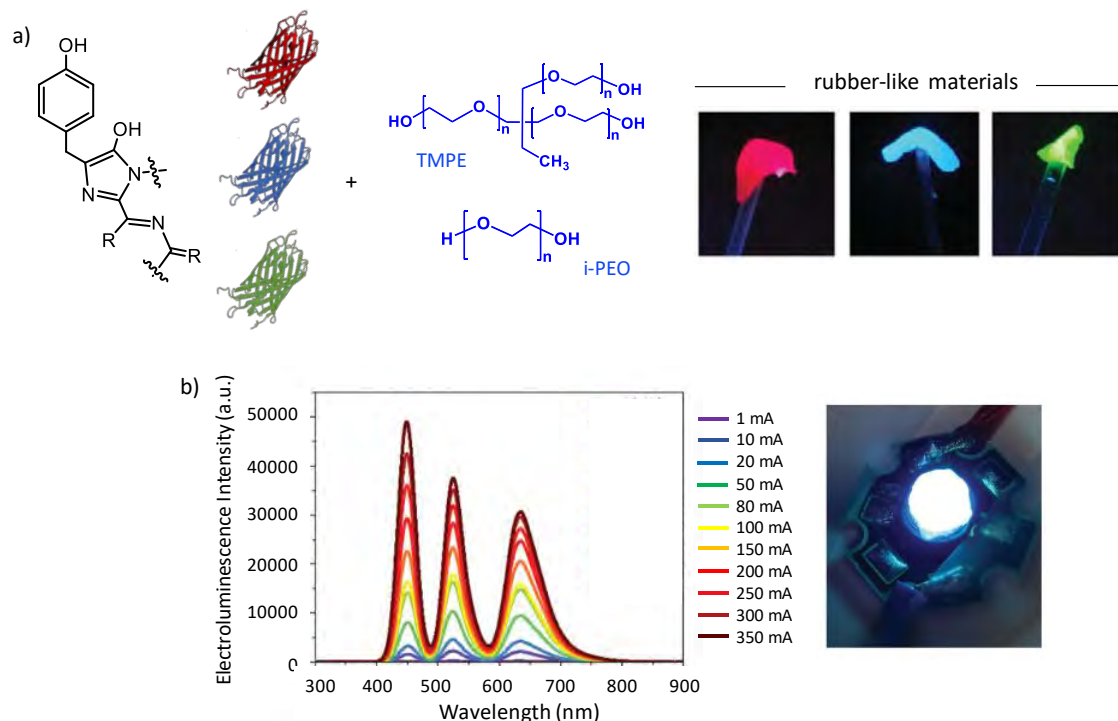


**Figure 2.7.** (a) Structure of the proteins (left) and the polymers (center) used for the preparation of the protein-based rubber-like materials and their pictures under UV light (right). (b) Electroluminescence spectra of the bio-HWLED prepared by the subsequent deposition of the blue-, green- and red-rubbers (left) and a picture of the resulting bio-HWLED (right). (Adv. Mater. 2015, 27, 5493-5498)

Tackling all challenges simultaneously, we decided to develop a white-emitting single-component system based on luminescent organometallo-silica nanoparticles. With this aim, and considering both the background in the coordination chemistry of our group<sup>87</sup> and how color down-converting materials based on organometallic complexes stand out,<sup>88</sup> we use three cyclometalated Ir<sup>III</sup> complexes, with emission wavelengths in the blue, green and red regions, to encapsulate them together into the silica matrix. The resulting hybrid will be used as a down-converting material in the fabrication of HWLEDs, following the rubber-like encapsulation approximation previously mentioned.

## **OBJECTIVES**

### **PART I: Design of blue-to-red phosphorescence cyclometalated Ir<sup>III</sup> complexes**

- In this first part, we report the synthesis, characterization and photophysical properties of two iridium(III) complexes with Si(OEt)<sub>3</sub> terminal groups in the auxiliary ligands (PPTES and *dasipy*): [Ir(dFppy)<sub>2</sub>(PPTES)<sub>2</sub>]PF<sub>6</sub> (**5 or B**) and [Ir(ppy)<sub>2</sub>(dasipy)]OTf (**6 or R**).

Both complexes, which emit in the blue and red regions, together with the green emissive compound [Ir(ppy)<sub>2</sub>(PPTES)<sub>2</sub>]OTf (**1 or G**) previously described in Chapter I, exhibit emission profiles that cover the entire visible spectrum.

We also examine the possibility of these chromophores to feature energy transfer processes, in order to use them as phosphors in the preparation of HLEDs.

### **PART II: Monochromatic- and white-emitting silica nanoparticles as down-converters for HLEDs**

- In this section, we report a novel and versatile strategy for the synthesis of monochromatic- and the first white-emitting organometallo-silica nanoparticles, using complexes **B**, **G** and **R** as precursors. An essential aspect of this synthetic approach is the formation of ultra-small organometallic dots (**ODs**) prior to the formation of the silica nanoparticles (**NPs**).

This approximation allows the separate or simultaneous (*three-in-one*) encapsulation of the iridium complexes, *via* a sol-gel process, inside the silica nanoparticles. Thus, we obtain monochromatic- (**[B,G,R]-NP**) or white-emitting (**[W]-NP**) silica nanoparticles, respectively.

- Thanks to the collaboration with Dr. Rubén D. Costa (IMDEA), this part also includes the preparation of color down-converting coatings based on both the pure complexes and the silica nanoparticles, and the use of the latter for the fabrication of a blue-, green- and red-HLEDs (**NP-HLEDs**) and a single-component HWLED (**NP-HWLED**), with exceptionally stable emissions.

Their photoluminescence properties and luminous efficiency, as well as their photo- and thermal-stabilities, under ambient conditions and extreme environments have been evaluated. The quality of the color was also examined by the measurement of parameters such as CIE color coordinates, color rendering index (CRI) and correlated color temperature (CCT).

## II.1 PART I

### Design of blue-to-red phosphorescence cyclometalated Ir<sup>III</sup> complexes

In recent years, many different types of organometallic metal complexes (*i.e.* Ru<sup>II</sup>, Cu<sup>I</sup>, Eu<sup>III</sup>, Pt<sup>II</sup> or Zn<sup>II</sup> complexes) have been used for the fabrication of emitting devices.<sup>84a, 86b, 88-89</sup> Among them, luminescent iridium(III) species stand out due to interesting properties such as intense emissions with high quantum yields, long phosphorescent lifetimes or excellent color tunability by modifying the ligands involved.<sup>50a-d</sup> In addition, these systems also exhibit high thermal- and photo-stabilities. Consequently, Ir<sup>III</sup> complexes have been widely study as potential phosphors in organic light-emitting diodes (OLEDs), exhibiting good performances.<sup>50d, 84a, 86b, 88a, 90</sup>

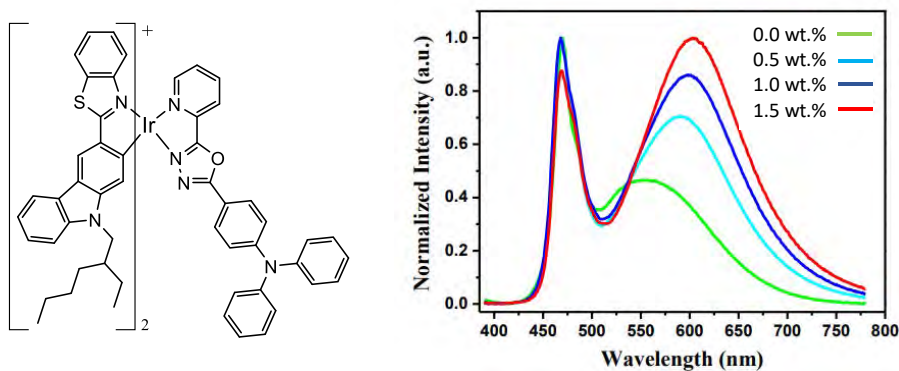


**Figure 2.8.** Structure of the red-emitting Ir(III) derivative (left). Emission spectra of the WLED (right). (New J. Chem. 2015, 39, 9535-9542)

In this area, in 2013, C.-Y. Sun and co-workers<sup>84a</sup> fabricated a white-light hybrid LED by encapsulating a yellow emissive iridium(III) complex ( $[\text{Ir}(\text{ppy})_2(\text{bpy})]\text{PF}_6$ ) into the cavities of a blue-emitting Cd-based MOF. The resulting device showed a high-quality white light with excellent luminescence performances (CIE 0.31, 0.33; CRI *ca.* 80; CCT *ca.* 5900 K and a quantum yield of 20.4%). Similarly, Z. Wang *et al.*<sup>88a</sup> reported a red-emitting Ir(III) derivative ( $[\text{Ir}(\text{ecbt})_2(\text{dpoa})]\text{PF}_6$ , see figure 2.8). They succeeded in the preparation of several devices doping the yellow inorganic emitter YAG:Ce<sup>3+</sup> with different amounts of the metal-complex, and, using

a 465 nm blue-emitting GaN chip as the excitation source. By controlling the Ir<sup>III</sup> wt%, warm-white LEDs were obtained with desirable performances.

More recently, R.D. Costa and co-workers<sup>86b</sup> also fabricated various WHLEDs using luminescent rubber-like materials based on quantum dots, polymers and coordination complexes, including two Ir(III) complexes ( $[\text{Ir}(\text{ppy})_2(\text{acac})]$  and  $[\text{Ir}(\text{ppy})_2(\text{'Bu-bpy})]\text{PF}_6$ ). The latter outperformed the others in terms of color quality (CRI > 80), luminous efficiency (> 100 lm/W) and stability (> 1000 h, extrapolated to 4000 h) under continuous operation conditions (see figure 2.9), thus demonstrating the versatility and potentiality of using these derivatives as down-converting materials.

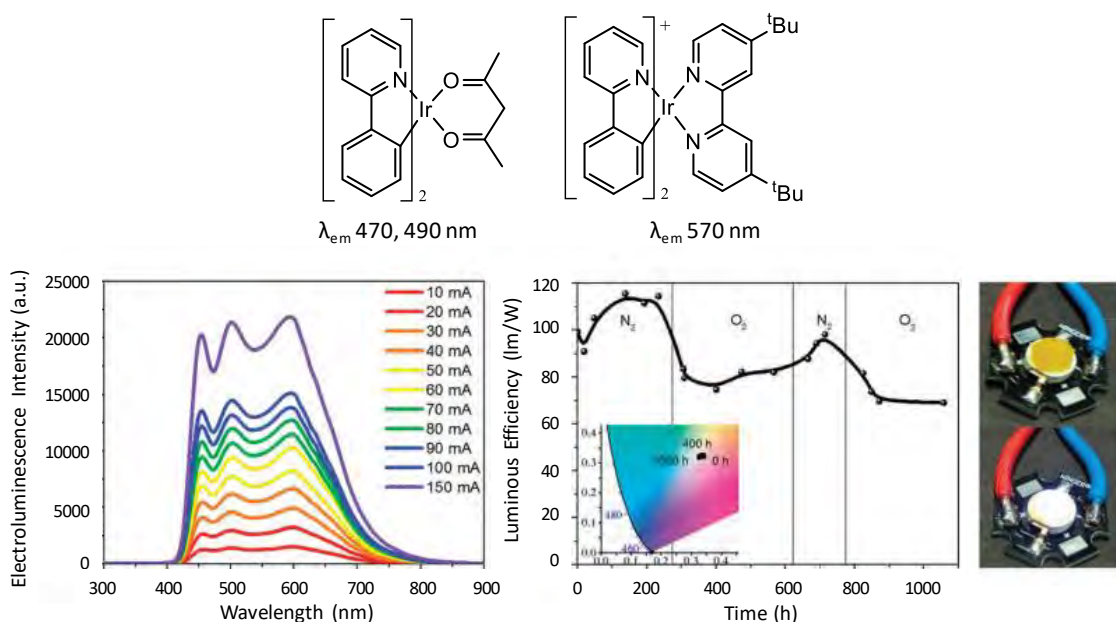


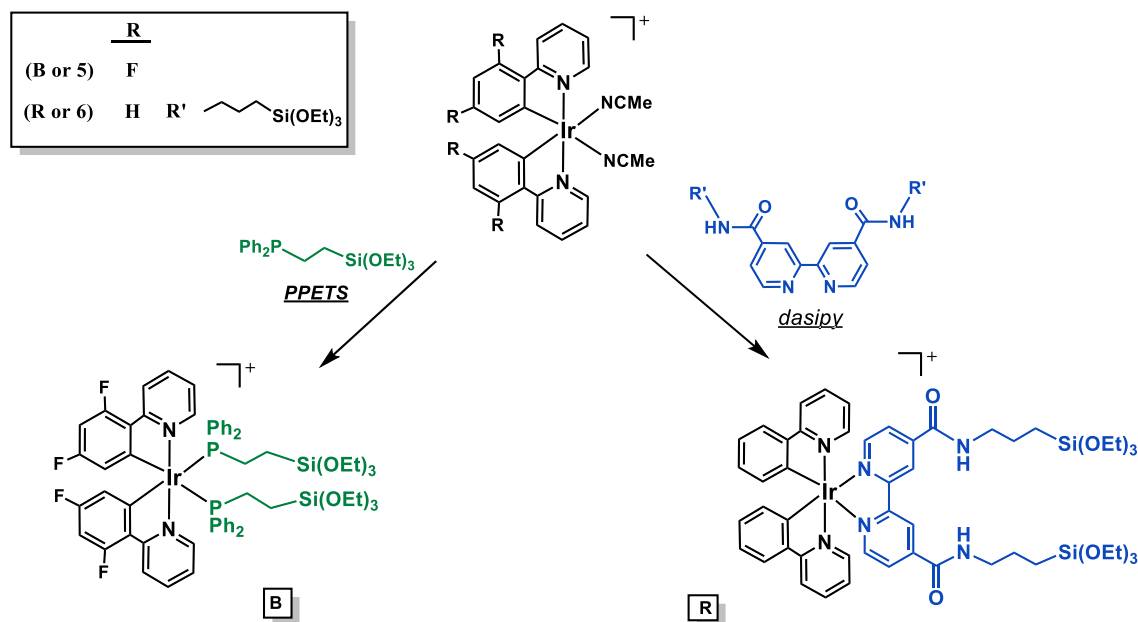
**Figure 2.9.** (Upper part) Structures of the iridium(III) complexes. (Lower part) Electroluminescence spectra of the HWLED at different applied currents (left). Luminous efficiency over time at an applied driving current of 10 mA (central) and changes of CIE coordinates (inset). Photographs of the devices (right). (Mater. Horiz. 2016, 3, 340-347)

In this context and considering the improvements that Ir<sup>III</sup> derivatives provide to the properties of the final devices, we decided to prepare new blue-, green-, and red-emitting iridium cyclometalated complexes and use them as potential phosphors for the obtaining of white light.

### II.1.1 Synthesis and characterization of the iridium(III) precursors 5-6

The iridium(III) complexes  $[\text{Ir}(\text{dFppy})_2(\text{PPETS})_2]\text{PF}_6$  (**5**) and  $[\text{Ir}(\text{ppy})_2(\text{dasipy})]\text{OTf}$  (**6**) were prepared following a similar synthesis to that previously described for the green emitter compound  $[\text{Ir}(\text{ppy})_2(\text{PPETS})_2]\text{OTf}$  (**1**) in Chapter I. To facilitate the interpretation of the results, complexes **1**, **5** and **6** will be referred as **G**, **B** and **R**, respectively.

As shown in scheme 2.1, both derivatives **B** and **R** were prepared by the reaction between the corresponding solvate precursor ( $[\text{Ir}(\text{R}_2\text{ppy})_2(\text{MeCN})_2]\text{OTf}/\text{PF}_6$ ) and the stoichiometric amount of the auxiliary ligands PPETS (**B**) and dasipy (**R**). Both reactions were performed under argon atmosphere, at room temperature and using dichloromethane as solvent. The resulting powders were obtained without further purification.



**Scheme 2.1.** Synthetic route of complexes  $[\text{Ir}(\text{dFppy})_2(\text{PPETS})_2]\text{PF}_6$  (**B**) and  $[\text{Ir}(\text{ppy})_2(\text{dasipy})]\text{OTf}$  (**R**).

As mentioned in Chapter I for the derivative containing the *dasipy* ligand ( $[\text{Pt}(\text{bzq})(\text{dasipy})]\text{PF}_6$ , **4**), complex **R** was also kept under argon atmosphere because it easily self-condenses through the  $\text{Si}(\text{OEt})_3$  groups in the presence of moisture traces.

Both Ir<sup>III</sup> derivatives were fully characterized and their structures were confirmed by a combination of elemental analyses, mass spectrometry and the usual spectroscopic means (FTIR, absorption, multinuclear NMR).

As shown in figure 2.10, the FTIR spectra of the three chromophores show the typical peaks associated to the stretching of the Si-O-C moiety of the terminal trialkoxysilyl groups, at *ca.* 1100 and 1080 cm<sup>-1</sup>. Other common features shown are those medium and intense bands observed in the high energy region attributed to the  $\nu(\text{C-H})$  of the aromatic systems ( $> 3000 \text{ cm}^{-1}$ ) and aliphatic groups ( $< 3000 \text{ cm}^{-1}$ ). Absorptions between 1600 and 1160 cm<sup>-1</sup>, related to the stretching vibrations of the aromatic rings, are also observed.

Complexes **B** and **G** also exhibit the typical peak related to the stretching of P-C of the PPETS ligand at *ca.* 1430 cm<sup>-1</sup>, while **R** shows the characteristic frequencies of N-H and C=O units of the *dasipy* group at 3315 cm<sup>-1</sup> and 1169 cm<sup>-1</sup>, respectively. The features observed at *ca.* 1410, 1030 cm<sup>-1</sup>  $\nu(\text{S-O})$  and 840 cm<sup>-1</sup>  $\nu(\text{P-F})$ , associated to the counter ions (OTf **R** and PF<sub>6</sub> **B**, respectively), are also well resolved.

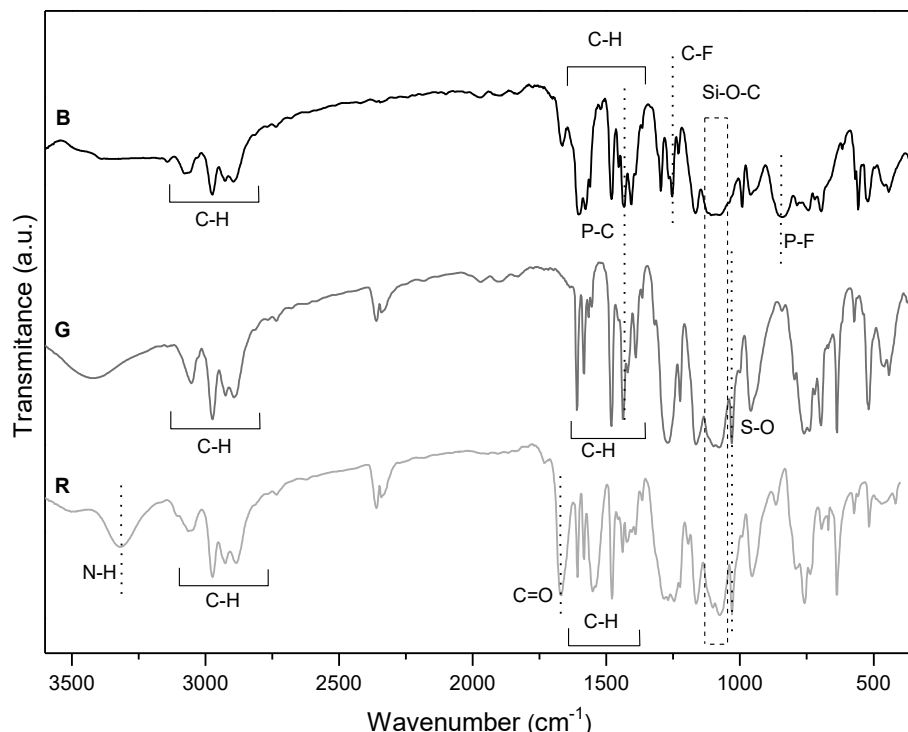


**Figure 2.10.** FTIR spectra of complexes  $[\text{Ir}(\text{dFppy})_2(\text{PPETS})_2]\text{PF}_6$  (**B**),  $[\text{Ir}(\text{ppy})_2(\text{PPETS})_2]\text{OTf}$  (**G**) and  $[\text{Ir}(\text{ppy})_2(\text{dasipy})]\text{OTf}$  (**R**).

The NMR spectra are also consistent with all the structures proposed in scheme 2.1, confirming the retention of the geometry of their respective solvate precursors.

The <sup>1</sup>H, <sup>31</sup>P{<sup>1</sup>H} and <sup>13</sup>C{<sup>1</sup>H} NMR spectra of complex **B** show signals that correspond to the presence of only one type of phosphine and cyclometalated C<sup>N</sup> ligands, confirming the mutually *trans* disposition of the pyridinic nitrogen atoms. In addition, and due to the chirality of the

iridium center, the hydrogen atoms of both their phenyl groups and their aliphatic chain are diastereotopic and, consequently, non-equivalent.

In the <sup>1</sup>H NMR spectrum of **R**, the ratios between the aromatic and aliphatic resonance peaks suggest the existence of two equivalent 2-phenylpyridines and one substituted bipyridine ligand, *dasipy*. The broad amide signal (*N-H*) shifts downfield when compared to the free ligand (8.69 ppm vs. 6.93 ppm).<sup>91</sup>

### **II.1.2 Photophysical properties of the iridium(III) complexes**

#### *i. Absorption spectra*

The absorption spectra of complexes [Ir(dFppy)<sub>2</sub>(PPETS)<sub>2</sub>]PF<sub>6</sub> (**B**) and [Ir(ppy)<sub>2</sub>(dasipy)]OTf (**R**) were performed both in tetrahydrofuran solution (5x10<sup>-5</sup> M) and in the solid state. All the data are summarized in table 2.1 and figure 2.12. The properties of derivative [Ir(ppy)<sub>2</sub>(PPETS)<sub>2</sub>]OTf (**G**) (named as **1** in Chapter I) have already been described. Nevertheless, for comparison purpose, the absorption and emission data will also be included in the discussion.

**Table 2.1.** Absorption data in solution (THF, 5x10<sup>-5</sup> M) and in the solid state of complexes **B**, **G** and **R**.

Sample	$\lambda_{\text{abs}}/\text{nm} (\epsilon/\text{M}^{-1}\text{L}^{-1})$
[Ir(dFppy) <sub>2</sub> (PPETS) <sub>2</sub> ]PF <sub>6</sub> ( <b>B</b> )	258 (44.8), 310 (18.2), 350 (6.0), 412 (0.1), 438 (0.05) <b>THF</b> 241, 279, 296, 316, 332, 350, 410, 440 <b>Solid</b>
[Ir(ppy) <sub>2</sub> (PPETS) <sub>2</sub> ]OTf ( <b>G</b> )	242 (22.1), 270 (13.8), 320 (5.5), 366 (2.1), 424 (0.3), 458 (0.02) <b>THF</b> 221, 248, 267, 321, 366, 420, 452 <b>Solid</b>
[Ir(ppy) <sub>2</sub> (dasipy)]OTf ( <b>R</b> )	255 (61.7), 270 (78.2), 285 (67.7), 323 (34.2), 360 (16.3), 384 (14.5), 467 (2.1), 490 (1.6) <b>THF</b> 223, 258, 276, 297, 320, 380, 468, 493 <b>Solid</b>

As shown in figure 2.12, both **B** and **R** iridium(III) derivatives exhibit, in solution, intense high energy absorptions ( $\lambda < 320 \text{ nm}$ ) due to spin allowed  $\pi-\pi^*$  ligand centered transitions. According to TD-DFT calculations, the feature at *ca.* 320 nm is likely of a mixed configuration and it is ascribed to <sup>1</sup>ILCT and <sup>1</sup>LL'CT (L: C<sup>N</sup>; L': PPTES, *dasipy*), with a certain <sup>1</sup>ML'CT character in the case of **R**. Similar to derivative **G**, complex **B** also displays a weak band at 350 nm that perfectly fits with the lowest energy singlet transition computed, formed by HOMO-LUMO transitions (see annex II, table A.II.3 and figure A.II.4). In this case, HOMO is mainly localized on the metal center and the phenyl groups of the cyclometalated ligands (dFppy), while the LUMO orbital is centered

on the pyridine groups (see figure 2.11). Therefore, this absorption is attributed to a  $^1\text{ILCT}/^1\text{MLCT}$  character. By contrast, the low feature at 384 nm observed for complex **R** is mainly attributed to a mixed spin allowed ligand-to-ligand ( $\text{C}^{\text{N}} \rightarrow \text{N}^{\text{N}}$ ) and metal-to ligand ( $\text{Ir} \rightarrow \text{N}^{\text{N}}$ ) charge transfer transitions.

On the other hand, and due to the strong spin-orbit coupling (SOC) associated to iridium center,<sup>50b, 50d</sup> all complexes show additional absorption bands (412, 438 nm **B**; 424, 458 nm **G**; 467, 490 nm **R**) ascribed to spin forbidden singlet-triplet transitions ( $^3\text{ILCT}/^3\text{MLCT}$  **B**, **G**;  $^3\text{LL'CT}/^3\text{ML'CT}$  **R**).

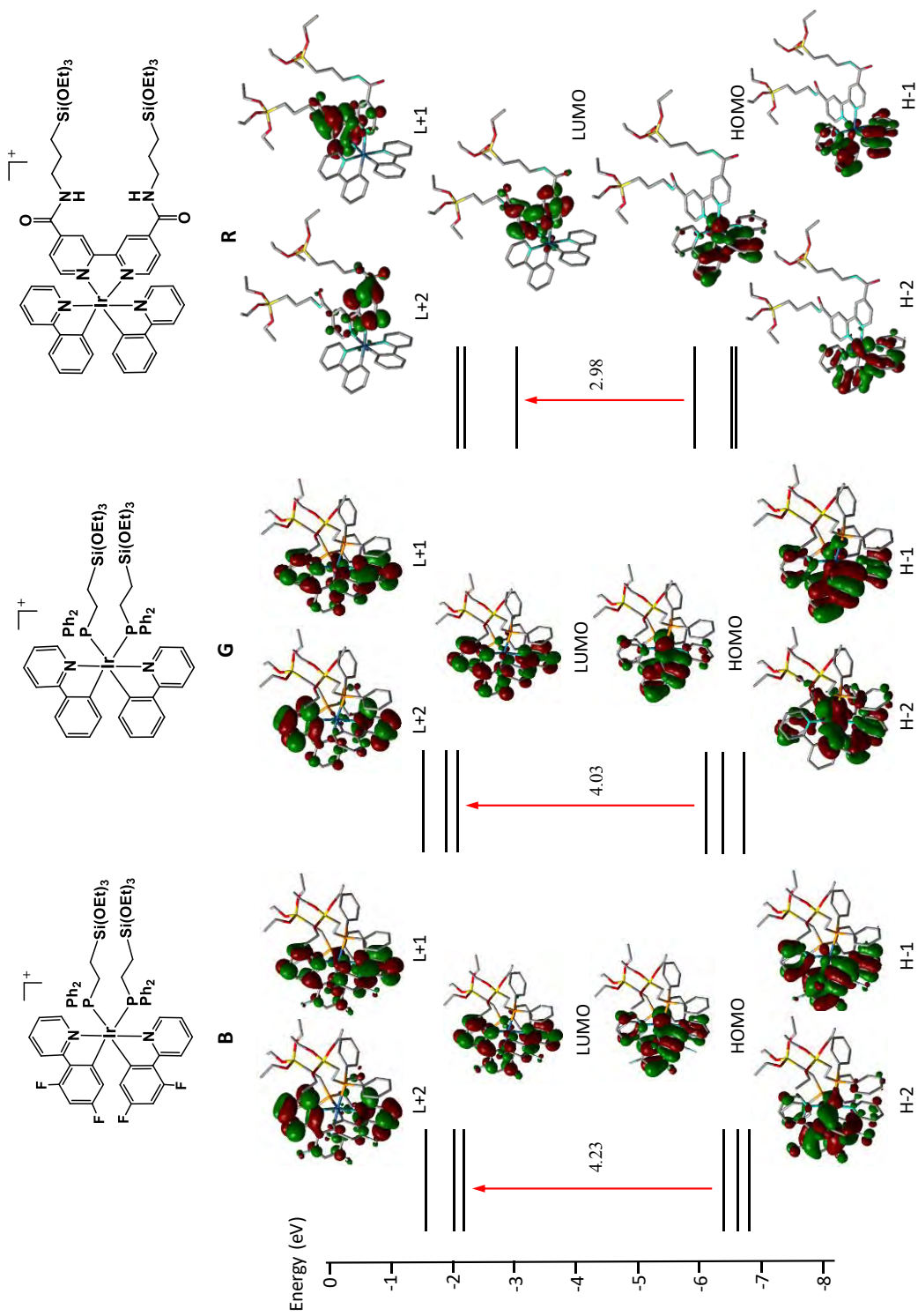


**Figure 2.11.** Selected frontier molecular orbitals for complexes B, G and R, showing the electronic gap between HOMO-LUMO orbitals (hydrogen atoms were omitted for clarity).

In the solid state, the DRUV spectra of the iridium(III) compounds display the same absorption profiles to those observed in THF solution (see figure 2.12). In addition, the weaker features that goes up to the visible region ascribed to spin forbidden transitions, are also well-resolved.

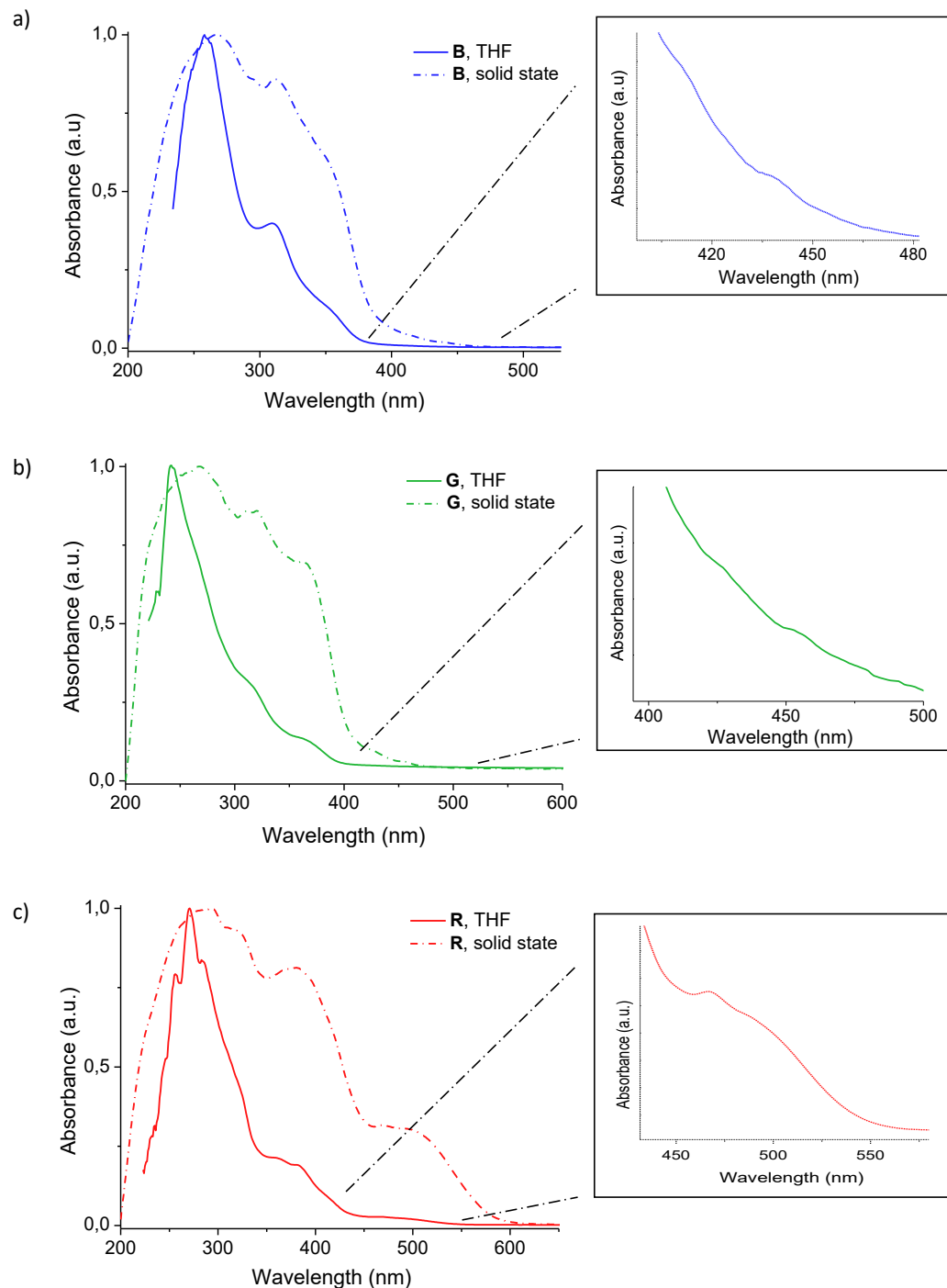


**Figure 2.12.** Normalized absorption spectra of complexes **B** (a), **G** (b) and **R** (c) in THF solution ( $5 \times 10^{-5}$  M, solid line) and in the solid state (dotted line). Inset: low energy region of the UV-Vis spectra in THF solution.

*ii. Emission spectra*

The emissive properties of the Ir<sup>III</sup> chromophores were evaluated in fluid THF solutions ( $5 \times 10^{-4}$  M) and in rigid media (solid state, glassy and in PMMA matrix), both at room temperature and at 77K. All data are summarized in table 2.2 and all the assignments are supported by theoretical calculations on model cation **B**<sup>+</sup>, **G**<sup>+</sup> and **R**<sup>+</sup>.

**Table 2.2.** Experimental and calculated emission data of complexes **B**, **G** and **R** in solid state and solution (THF,  $5 \times 10^{-4}$  M).

Sample	Medium (T/K)	$\lambda_{\text{em}}$ (nm) <sup>(a)</sup>	$\Delta E(T_1-S_0)$ (nm)	$\tau$ ( $\mu\text{s}$ ) <sup>(b)</sup>	$\phi$ (%)
<b>B</b>	Solid (298)	480	506	1.55	23.5
	Solid (77)	457, 483 <sub>max</sub> , 515 <sub>sh</sub>		28.42	
	THF (298)	450, 480 <sub>max</sub> , 510 <sub>sh</sub>	504	0.92	13.4
	THF (77)	450, 475 <sub>max</sub> , 505 <sub>sh</sub>		50.70	
<b>1% PMMA</b>		450, 477 <sub>max</sub>			36.5
<b>10% PMMA</b>	Solid (298)	458, 477 <sub>max</sub>			40.9
<b>50% PMMA</b>		462, 477 <sub>max</sub>			32.7
<b>70% PMMA</b>		477			23.5
<b>G</b>	Solid (298)	512	524	0.97	31.2
	Solid (77)	463, 480, 504 <sub>max</sub> , 530 <sub>sh</sub>		15.80	
	THF (298)	464, 494 <sub>max</sub> , 520 <sub>sh</sub>	512	0.27	3.4
	THF (77)	460 <sub>max</sub> , 493, 519 <sub>sh</sub>		44.00	
<b>R</b>	Solid (298)	620	614	0.13	13.1 <sup>(c)</sup> ; 16.5 <sup>(d)</sup>
	Solid (77)	610 <sub>max</sub> , 640 <sub>sh</sub>		1.04	
	THF (298)	610	598	0.20	28.3
	THF (77)	570 <sub>max</sub> , 600 <sub>sh</sub>		14.30	

(a)  $\lambda_{\text{ex}}$  365 nm for **B**, **G** and  $\lambda_{\text{ex}}$  420-470 nm for **R**. (b) Solid state emission lifetimes were calculated as average of a bi-exponential decay. Solution and glasses lifetimes were calculated as mono-exponential decay. (c) Quantum yield measured with  $\lambda_{\text{ex}}$  at 390 nm. (d) Quantum yield measured with  $\lambda_{\text{ex}}$  at 480 nm.

Upon excitation at 365 nm, complex **B** features, in both fluid and glassy THF solutions, long lived ( $0.92 \mu\text{s}$ , 298K;  $50.70 \mu\text{s}$ , 77K) structured emission bands ( $\lambda_{\text{em}}$  ca. 450, 480 nm, figure 2.13) ascribed to a mixed  $^3\text{ILCT}(\text{C}^{\text{N}})/^3\text{MLCT}$  ( $\text{Ir} \rightarrow \text{C}^{\text{N}}$ ) transition, which is dominated by the intraligand character. As shown in figure 2.14 (see also figure 1.21 for **G**), SOMO and SOMO-1 orbitals are mainly localized on one cyclometalated ligand with some contribution of the iridium center (ca. 11%). The calculated electronic energy from the optimized lowest  $T_1$  to  $S_0$  is similar to the experimental value (504 nm vs. 450 nm). A comparable emission profile, but slightly shifted to the red, was observed for **B** in the solid state at 77K, indicating a similar mixed  $^3\text{ILCT}(\text{C}^{\text{N}})/^3\text{MLCT}$  excited state. Notwithstanding, this profile becomes unstructured at room temperature, suggesting an increase of the  $^3\text{MLCT}$  contribution.

As previously described in Chapter I, complex **G** exhibits a very similar emissive behavior but with emission maxima slightly red shifted in relation to the difluorophenylpyridine derivative (**B**), a fact attributed to the stabilization of the HOMO orbital in this last derivative (-6.40 eV **B** vs. -6.1 eV **G**, see figure 2.11).

According to the photoluminescence quantum yields, both complexes exhibit higher values in the solid state than in THF solution. However, when compared their efficiency in this last medium, it is evident that the blue emitter complex **B** quadruples the yield of **G** (13.4% vs. 3.4%), indicating the reduced non-radiative vibrations of C-F compared to C-H bonds. However, the opposite effect was observed in the solid state. In this case (table 2.2), the quantum yield of **G** is higher than that measured for **B**, probably due to the significant AIE (Aggregation Induced Emission) effect associated to this derivative, as we commented in Chapter I.

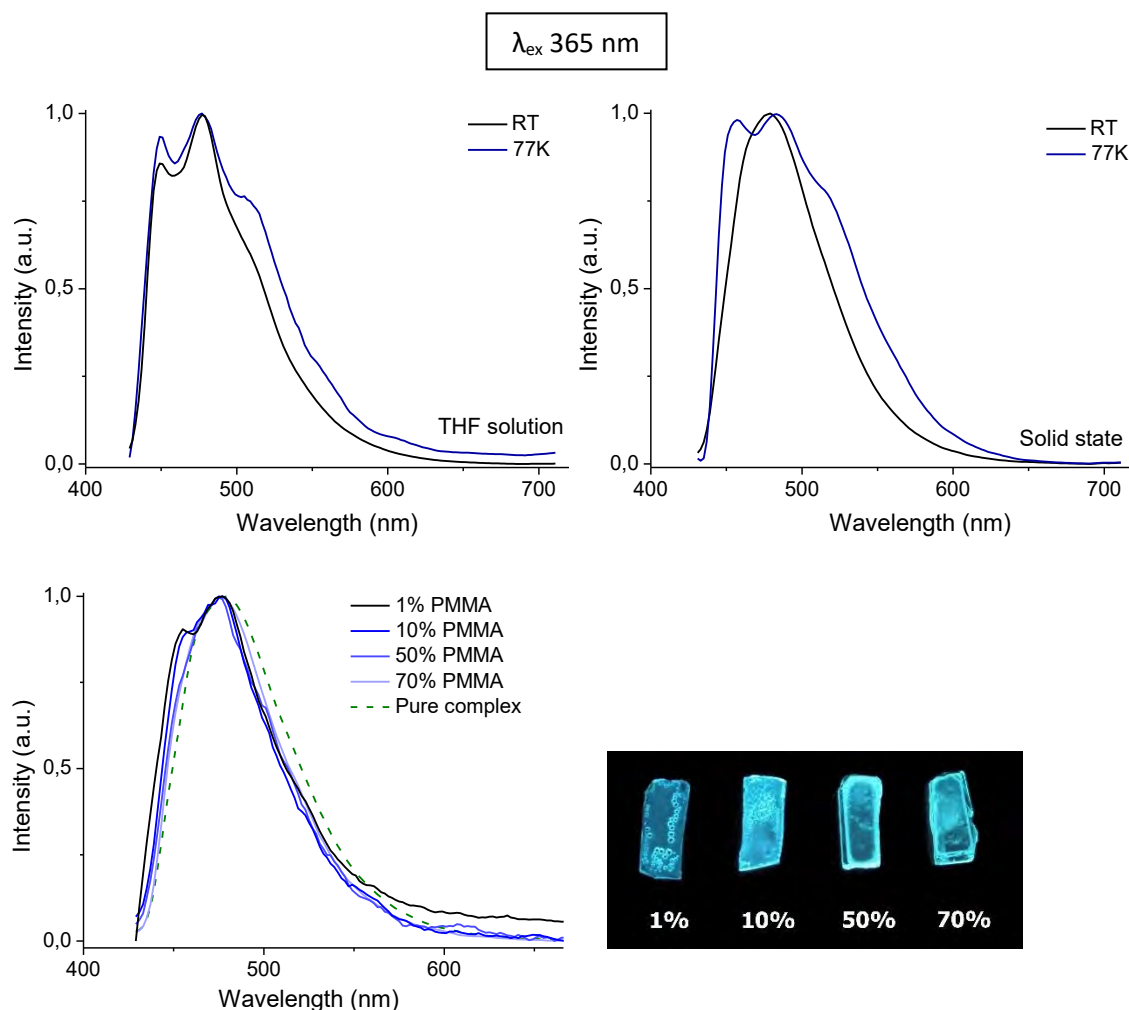


**Figure 2.13.** (Upper part) Normalized emission spectra of complex **B** in THF solution ( $5 \times 10^{-4} \text{ M}$ , left) and in the solid state (right), at room temperature (in black) and at 77K (in blue). (Lower part) Normalized emission spectra of different concentrations of complex **B** in PMMA (1%, 10%, 50% and 70%), at room temperature.

The influence of the concentration of complex **B** in PMMA was also evaluated. As illustrated in figure 2.13, at low concentrations, the emission profile monitored is similar to that seen in fluid medium, while the unstructured emission band of the solid state appears at concentrations greater than 70%. However, in contrast to **G**, no enhancement on the quantum yield was observed when increasing the concentration of **B** in the PMMA matrix, showing the highest efficiency at a concentration of 10% (table 2.2).

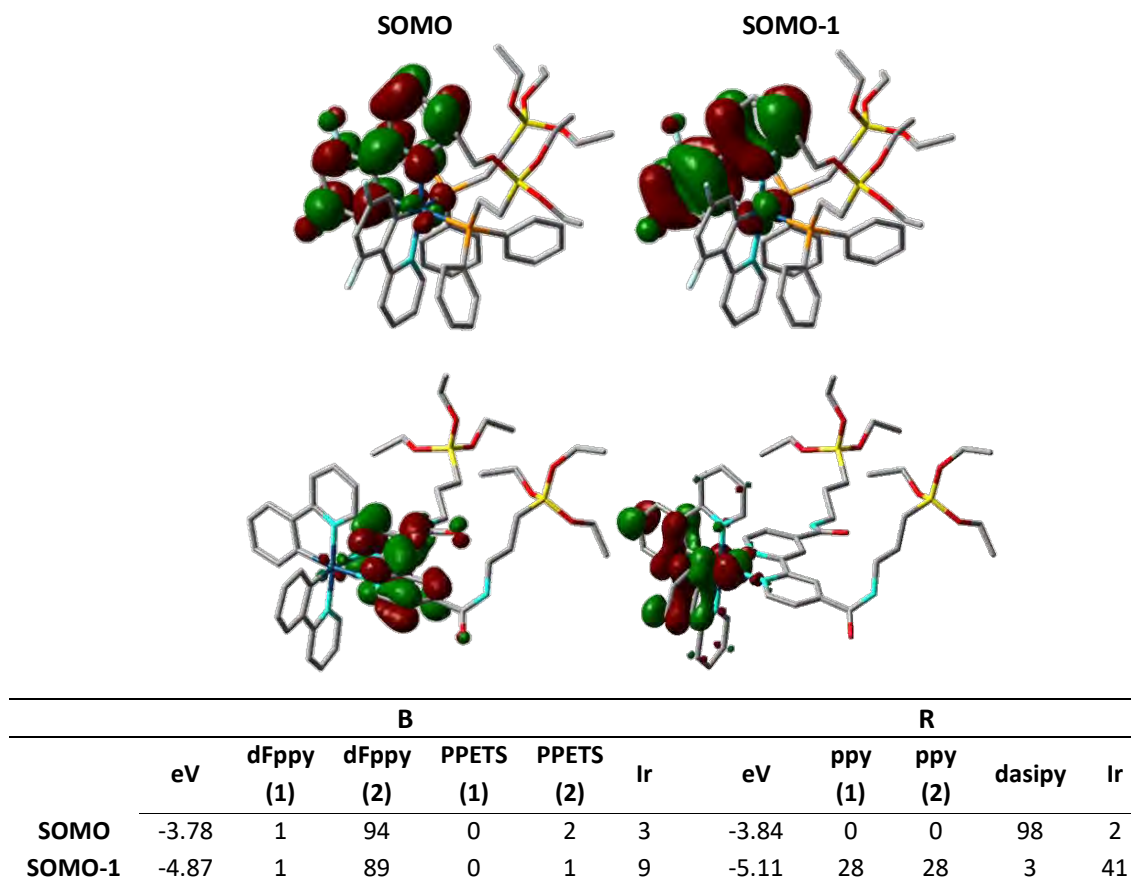


**Figure 2.14.** SOMO and SOMO-1 orbitals of complexes **B** and **R** with their composition (%) in the first triplet state in THF.

Complex  $[\text{Ir}(\text{ppy})_2(\text{dasipy})]\text{OTf}$  (**R**) exhibits broad non-structured emission bands in all media (figure 2.15). In fluid THF solution (298K), it displays a broad band at 610 nm, which is notably blue-shifted at low temperature (570 nm). As shown in figure 2.14 (see also annex II, figure A.II.3 for the spin density distribution), for this complex, the SOMO orbital is mainly located on the *dasipy* ligand (98%), whereas the SOMO-1 is contributed by the phenyl rings of both the cyclometalated ligands and the metal center. Therefore, the emission is attributed to a mixture of  ${}^3\text{ML}'\text{CT}$  ( $\text{Ir} \rightarrow \text{N}^\infty\text{N}$ )/ ${}^3\text{LL}'\text{CT}$  ( $\text{C}^\infty\text{N} \rightarrow \text{N}^\infty\text{N}$ ) with a remarkable  ${}^3\text{ML}'\text{CT}$  character (51%).

This emission is bathochromically shifted in relation to that previously reported for related complexes ( $[\text{Ir}(\text{ppy})_2(\text{bpy})]^+$ , 583 in  $\text{CH}_2\text{Cl}_2$ ; 585 in  $\text{CH}_3\text{CN}$ ),<sup>92</sup> a fact that can be attributed to the presence of the two  $\pi$ -acceptor amide groups in the target *dasipy* ligand, which decreases the energy gap in relation to the bipyridine. A similar behavior is observed for complex **R**, in the solid state, which shows a slight red-shift of the emission maximum (620 nm, 298 K; 610 nm, 77K).

In contrast to the phosphine derivatives **B** and **G**, complex **R** features higher quantum yields in solution (28.3%) than in the solid state (< 20%), likely due to the easy quenching of the emission in rigid media, through triplet-triplet annihilation.

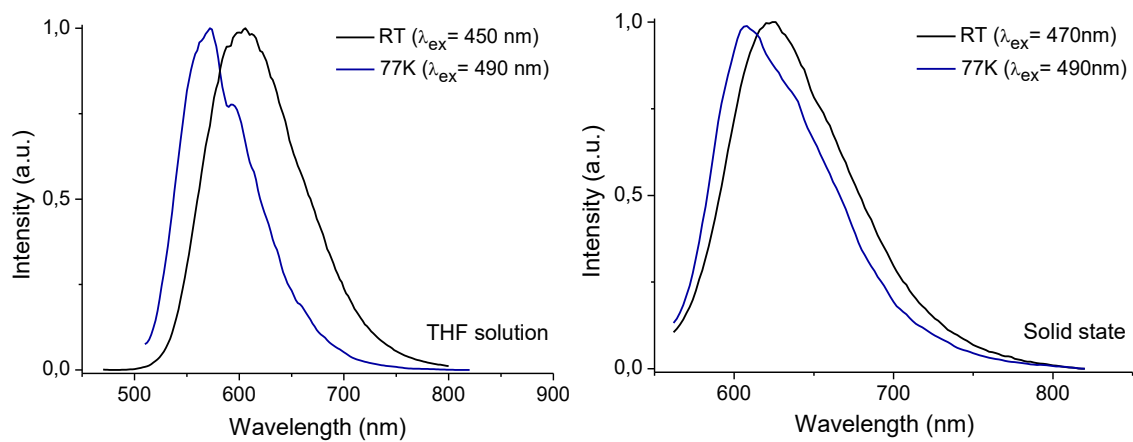


**Figure 2.15.** Normalized emission spectra of complex **R** in THF solution ( $5 \times 10^{-4} \text{ M}$ , left) and in the solid state (right), at room temperature (in black) and at 77K (in blue).

### iii. Evaluation of the possibility of energy transfer processes between the complexes

One common way to obtain a white light emission is based on the concurrence of energy transfer processes from high energy chromophores (**B** and **G**) to derivatives that emit in the low energy region (**R**). To make this possible, there must be a good overlapping between the absorption and the emission bands of the low and high energy emitters, respectively.

As shown in figure 2.16, there is a good overlap between the low energy absorption feature of **R** (450-600 nm) and the emission bands of complexes **B** and **G** (450-550 nm), indicating that complex **R** can be excited by both the blue and the green emitters, respectively, and, thus being possible energy transfer processes. Therefore, the mixture of these blue-, green- and red-emitting chromophores seems to be suitable for obtaining a white-light emission.

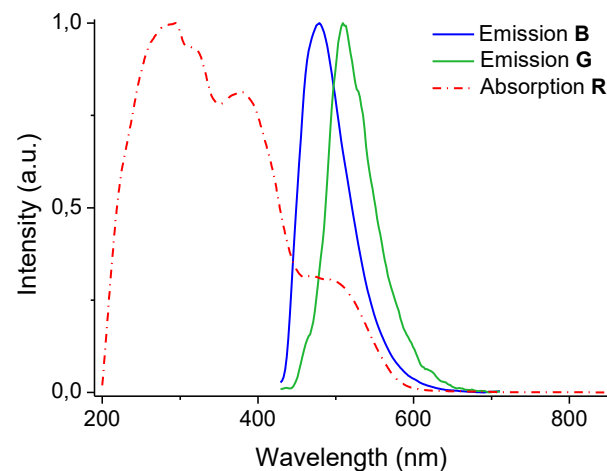


**Figure 2.16.** DRUV spectrum of complex **R** and emission spectra of complexes **B** and **G** ( $\lambda_{\text{ex}}$  365 nm) in the solid state showing the overlapping on the range 450-550 nm.



## II.2 PART II

### Monochromatic- and white-emitting silica nanoparticles as down-converters for HLEDs

As previously mentioned, one of the biggest challenges in the field of HWLEDs consists of developing white-light single-component down-converters to gain in stability and overcome problems related to phase separation, among others. Therefore, we decided to explore the possibility of establishing a new strategy for the synthesis of white emissive hybrid organometallo-silica nanoparticles.

In an effort to better integrate the active moiety in the silica matrix, we<sup>35b, 93</sup> and others<sup>32d, 32f, 35a, 88b, 94</sup> have developed the well-known Sol-Gel Coordination Chemistry, which is based on the co-condensation of an emissive organometallic complex, with alkoxysilane terminal groups, with the silica source (TEOS). Based on that, we have recently prepared a wide number of hybrid luminescent organometallo-silica materials<sup>35b, 93</sup> that have demonstrated to be not only more stable but also to have better photophysical properties than their precursors (see also Chapter I). However, although many studies have centered their attention on this synthetic technique, this methodology has only been focused on the incorporation of just a single organometallic complex,<sup>32d, 32f, 32g, 35a, 39b, 40, 88b, 94-95</sup> being unexplored the possibility of simultaneously introducing several of them.

Based on that, we have developed a new and versatile approximation to simultaneously incorporate three different iridium(III) complexes inside silica nanoparticles *via* sol-gel process, thus developing a single-component coating that will be used for the preparation of a HWLED, following the rubber-like encapsulation strategy.

## II.2.1 Synthesis of the organometallo-silica nanoparticles

The strategy developed is based on the initial formation of kinetically controlled small nanoparticles, exclusively formed by the organometallic chromophores (organometallic dots, **ODs**), which will be subjected to further sol-gel co-condensation with the TEOS to obtain the final hybrid organometallo-silica nanoparticles (**NPs**).

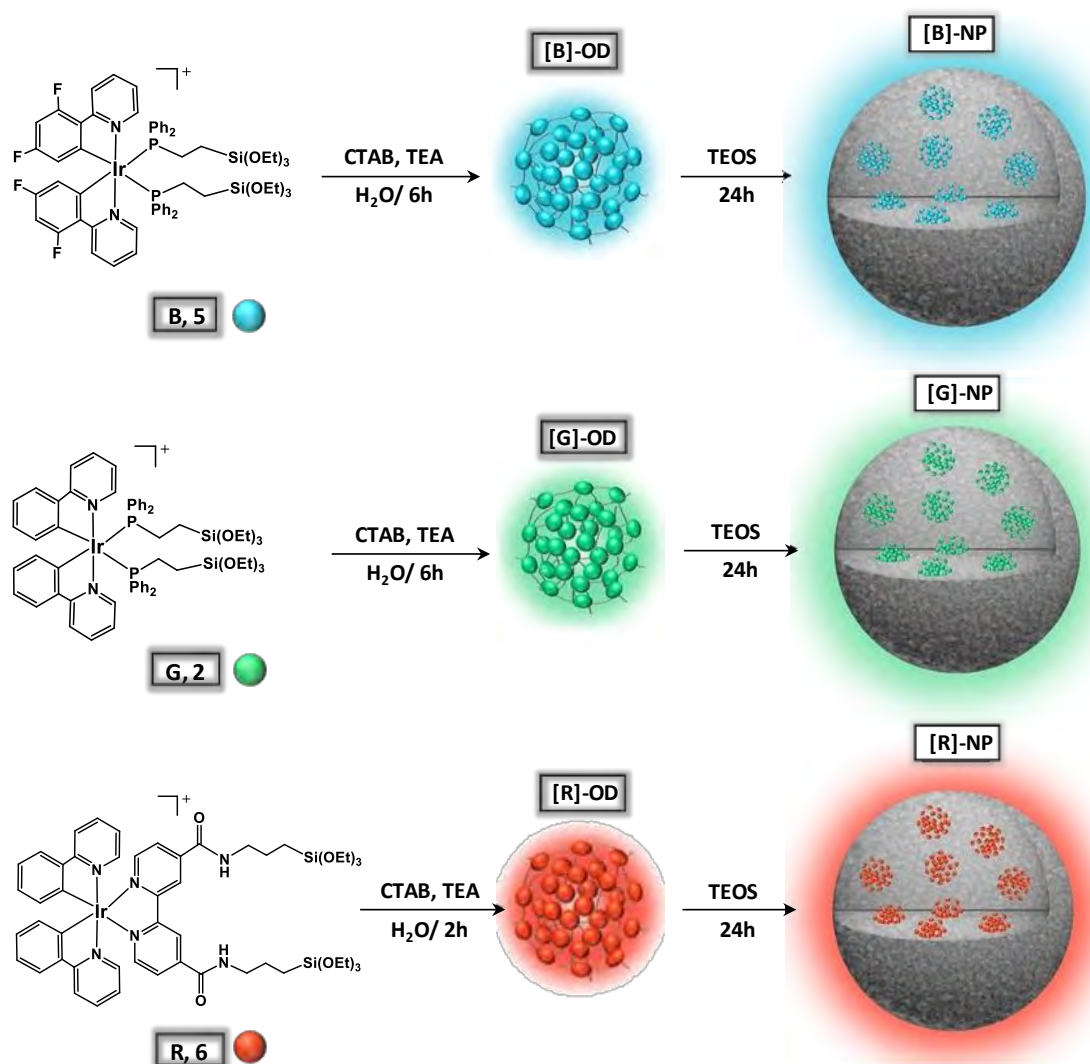
With the aim of optimising the reaction conditions, in a first step we prepared the corresponding monochromatic-emitting organometallo-silica nanoparticles (**[B,G,R]-NP**) and, then, the white-emitting material (**[W]-NP**).

### II.2.1.1 Monochromatic-emitting organometallo-silica nanoparticles (**[B,G,R]-NP**)

The synthesis was carried out following a two-step sol-gel process performed at room temperature. In detail, each iridium complex (**B**, **G** or **R**) was firstly prehydrated in an ethanolic-water mixture and in the presence of hexadecyltrimethylammonium bromide (CTAB), which allows to moderate the growth of the small particles formed, designated as organometallic dots (**[B,G,R]-OD**) (see scheme 2.2).

Taking into account that sol-gel processes are based on the condensation between alkoxy silane groups, compounds **B** and **G**, bearing the same PPETS ligand, were found to react similar and slower (6 hours) than complex **R** (2 hours), which incorporates the *dasipy* group, due to the different rates of hydrolysis of the ligands PPETS and *dasipy*. Therefore, the trialkoxysilane groups of each complex condense under mild conditions forming the small **ODs** of about 5 nm of diameter, as estimated by Transmission and Scanning Electron Microscopy (TEM and SEM, respectively, see section II.2.2). At this point, and assuming that some trialkoxysilane groups still remain on the surface of these **ODs**, TEOS was added to the reaction medium to allow further co-condensation reactions for 24 hours at room temperature, to finally yield the hybrid monochromatic-emitting organometallo-silica nanoparticles (**[B,G,R]-NP**) (scheme 2.2).

In all cases, the nominal iridium content was kept equal to 0.2 wt%.



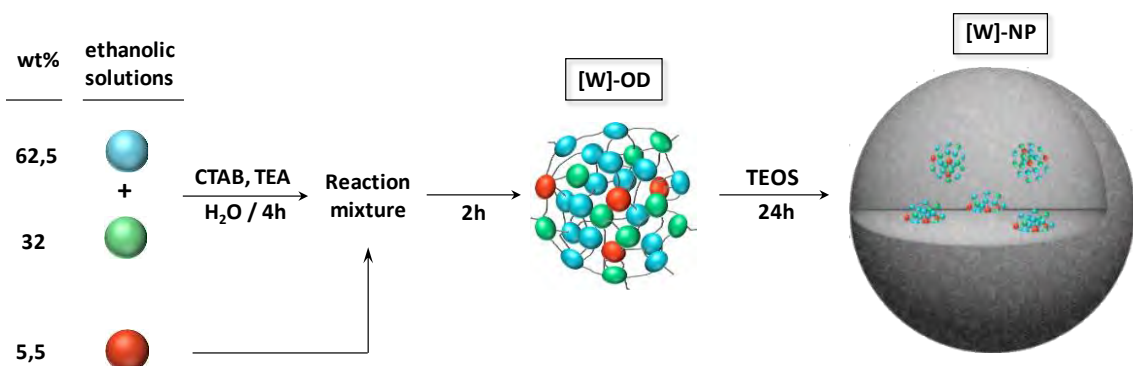
**Scheme 2.2.** Schematic representation of the synthesis of the monochromatic-emitting organometallic nanoparticles (**[B,G,R]-NP**) through the formation of their corresponding organometallic dots (**[B,G,R]-OD**).

#### II.2.1.2 White-emitting organometallo-silica nanoparticles (**[W]-NP**)

The hybrid white-emitting organometallo-silica nanoparticles, **[W]-NP**, were obtained following a similar strategy to that previously described for the monochromatic materials and, also, maintaining the total nominal metal content equal to 0.2wt%. We have denoted this approximation the *three-in-one approach*.

Considering the different rates of hydrolysis of the three derivatives, the reaction was performed under kinetic control. Thus, complexes **B** and **G** were firstly pre-hydrolyzed together (see scheme 2.3) and, after 4 hours of reaction, the derivative **R** was added to the mixture to

form the white-emitting organometallic dots (**[W]-OD**). The subsequent addition of TEOS and its reaction for 24 hours, allows the formation of the white-emitting silica nanoparticles, **[W]-NP**.



**Scheme 2.3.** Schematic representation of the synthesis of the white-emitting organometallic nanoparticles (**[W]-NP**) through the formation of their corresponding organometallic dots (**[W]-OD**).

#### Optimization of the chromophore amounts in the white-emitting silica nanoparticles

With the reaction conditions optimized, we next focused on establishing the optimal content of each chromophore in the mixture to obtain the white-emitting silica nanoparticles **[W]-NP** with an adequate white emission.

With this purpose, we first evaluated the emission profile of the nanoparticles formed by the incorporation of only complexes **B** and **R**. Thus, following the synthetic procedure above described, we synthetized different silica nanoparticles modifying the content of each derivative: mass ratio 70 **B**: 30 **R**; 80 **B**: 20 **R**; and 90 **B**: 10 **R**. As shown in figure 2.17 (left), a low content of the red-emitting complex in the mixture is required, since the increase in the concentration of **R** always causes a remarkable decrease of the blue emission.

Accordingly, we next prepared the hybrid organometallo-silica materials including the three chromophores and maintaining the relation of derivative **R** equal or lesser than 10% in mass ratio respect to the other complexes **B** and **G**. Thus, after the study of several mixtures, a warm white emission was finally achieved using the following optimized metal content of the three Ir(III) complexes: 0.125 wt% **B**, 0.064 wt% **G**, and 0.011 wt% **R**, which yields a mass ratio of 62.5 **B**: 32 **G**: 5.5 **R** (see figure 2.17, right). In this case, the total nominal metal content was also maintained equal to 0.2 wt%.

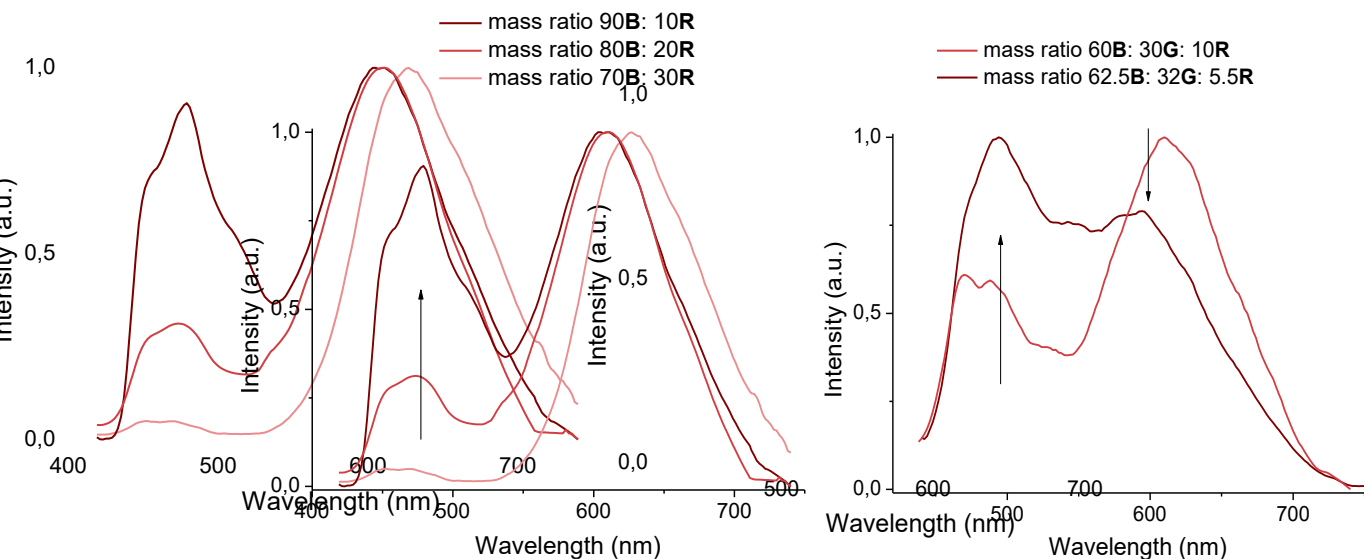


**Figure 2.17.** Emission spectra of the different optimizations for the obtaining of hybrid organometallo-silica nanoparticles with white emission. Tries with chromophores **B** and **R** (left) and with chromophores **B**, **G** and **R** (right). ( $\lambda_{\text{ex}} 390 \text{ nm}$ ).

After optimizing the mass ratio between chromophores in the mixture, we also prepared materials with higher nominal metal concentrations (0.6 wt% and 1wt%, namely **[W]-NP\_0.6** and **[W]-NP\_1**, respectively, see experimental section for more details) with the idea of improving their emission properties. Unfortunately, it was found that when increasing the final metal content on the materials, the morphology of the NPs dramatically changed. The new silicas were formed by aggregation of very small nanoparticles (figure 2.18) instead of discrete particles. In addition, these hybrids display lower quantum yields (*ca.* 18%) than those measured for both the monochromatic- and white-emitting nanoparticles with the 0.2 wt%. This fact could be related to a higher light scattering caused by the presence of greater porosity. Therefore, we decided to only focus on those materials with a nominal metal concentration of 0.2 wt%.

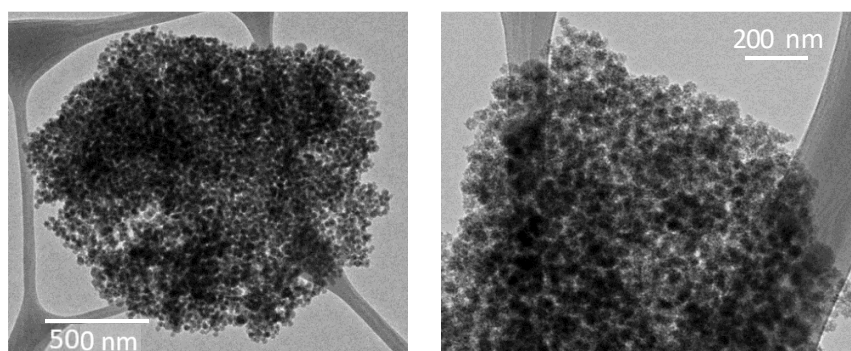


**Figure 2.18.** Representative TEM images of materials with a total nominal metal concentration of 0.6 wt% (**[W]-NP\_0.6**, left) and 1 wt% (**[W]-NP\_1**, right).

## II.2.2 Characterization of the organometallo-silica nanoparticles

### II.2.2.1 Textural characterization

The porosity of the silica materials has been examined by physisorption experiments. All the data are summarized in table 2.3 and figure 2.19. For comparison purposes, a related complex-free silica material (**NP**, see experimental section) was also examined.

As shown in figure 2.19, all samples feature type IV isotherms, typical of mesoporous materials, with an additional absorption uptake at relative pressures higher than 0.8, characteristic of the interparticle porosity. They also show mesopore volumes in the range of 0.5-0.7 cm<sup>3</sup>/g and high surface areas of *ca.* 1000 m<sup>2</sup>/g. In addition, the narrow pore size distribution observed for all the materials (2.1-2.4 nm range, see figure 2.19 and table 2.3) confirms that the mesopores are homogenous in size, thanks to the use of CTAB as surfactant during the synthetic procedure.

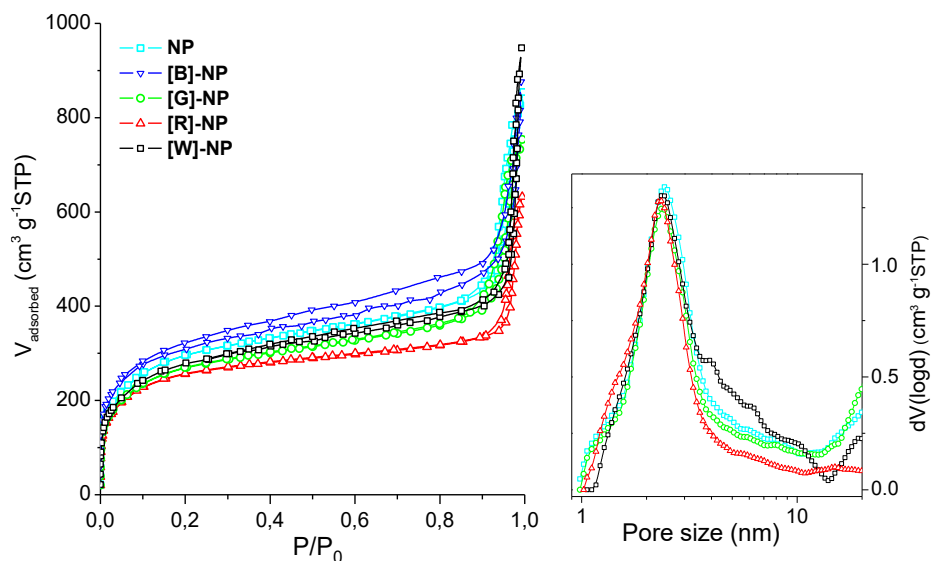


**Figure 2.19.** N<sub>2</sub> adsorption/desorption isotherms at 77K (left) and the corresponding pore size distribution calculated using the NLDFT method (right) of the monochromatic- ([B]-NP, [G]-NP and [R]-NP) and the white-emitting ([W]-NP) organometallo-silica nanoparticles in comparison with the related complex-free nanoparticles (**NP**).

In spite of the incorporation of the organometallic complexes into the silica nanoparticles ([B,G,R]-NP and [W]-NP), the values of their mesopore volume and average mesopore diameter were found very similar to those observed for the complex-free **NP** (table 2.3). This fact indicates a perfect integration of the initially formed organometallic dots (**ODs**) in the silica matrix and, it

is consistent with their photophysical properties, as shown later. In addition, ICP analyses gave incorporation rates of the chromophores between the 80 and 90% in all cases (see table 2.3).

**Table 2.3.** Metal content and textural properties of the monochromatic ([B]-NP, [G]-NP and [R]-NP) and the white emitting ([W]-NP) organometallic-silica nanoparticles in comparison with the corresponding complex-free control silica nanoparticles (NP).

Sample	Ir <sup>(a)</sup> (wt%)	A <sub>BET</sub> <sup>(b)</sup> (m <sup>2</sup> /g)	V <sub>p</sub> <sup>0.8, (c)</sup> (cm <sup>3</sup> /g)	V <sub>p</sub> <sup>0.99, (d)</sup> (cm <sup>3</sup> /g)	d <sub>p</sub> <sup>(e)</sup> (nm)
NP	---	1070	0.61	1.3	2.4
[B]-NP	0.18 (0.20)	1154	0.67	1.4	2.1
[G]-NP	0.18 (0.20)	990	0.56	1.2	2.3
[R]-NP	0.18 (0.20)	940	0.49	1.0	2.3
[W]-NP	0.16 (0.20)	1032	0.58	1.5	2.1

(a) Iridium content calculated from high resolution ICP mass spectroscopy analyses after treatment of the samples with diluted HF. Values in brackets represent the nominal metal content. (b) BET surface area estimated by multipoint BET method using the adsorption data in the relative pressure (P/P<sub>0</sub>) range of 0.05–0.25. (c) Mesopore volume directly read from the adsorption branch of the isotherm at (P/P<sub>0</sub>) = 0.8. (d) Total pore volume read directly from the adsorption branch of the isotherm at 0.99. (e) Average mesopore diameter determined from the isotherm using the NLDFT equilibrium model. Samples were centrifuged and air dried before gas adsorption measurements.

At this point, it is worth noting that reduced surface areas are highly desired to further protect the emitting chromophores but, especially, to avoid problems related to light-scattering and, so, to get better emissive properties. This problem would be overcome just reducing or removing the use of surfactant. However, this issue is directly related to our proposed synthetic approach, in which a pre-hydrolysis step under high concentrations of CTAB is the key to control the growth of the **ODs**.

Finally, TEM and FESEM images were also performed to examine the morphology of both the emitting organometallic dots (**ODs**) and silica nanoparticles (**NPs**). As observed in figure 2.20, the organometallic dots exhibit spherical shapes with average sizes of 5 nm of diameter. Therefore, according to the volume of both the organometallic dots and each iridium molecule (average diameter of 1.3 nm), these **ODs** must be formed by a maximum of 56 molecules covalently bonded through Si-O bonds. However, and taking into account that in a crystalline compact structure the occupied volume is the 74% and that our system is amorphous, we suggest that our **ODs** must be formed by less than 50 molecules.

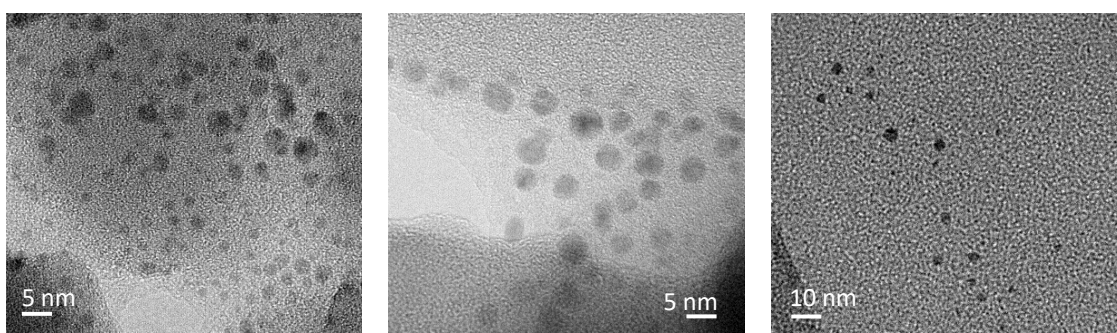


**Figure 2.20.** Some representative TEM images of the monochromatic- and white-emitting organometallic dots (**[B]-OD** (left), **[G]-NP** (middle) and **[W]-NP** (right)).

In a similar way, as shown on figures 2.21 and 2.22, both the monochromatic- (**[B]-NP**, **[G]-NP**, **[R]-NP**) and the white-emitting (**[W]-NP**) organometallo-silica materials are formed by discrete and also spherical shape nanoparticles with sizes between 50 and 70 nm of diameter. In addition, they also show the typical morphology of mesoporous nanoparticles prepared in the presence of CTAB.

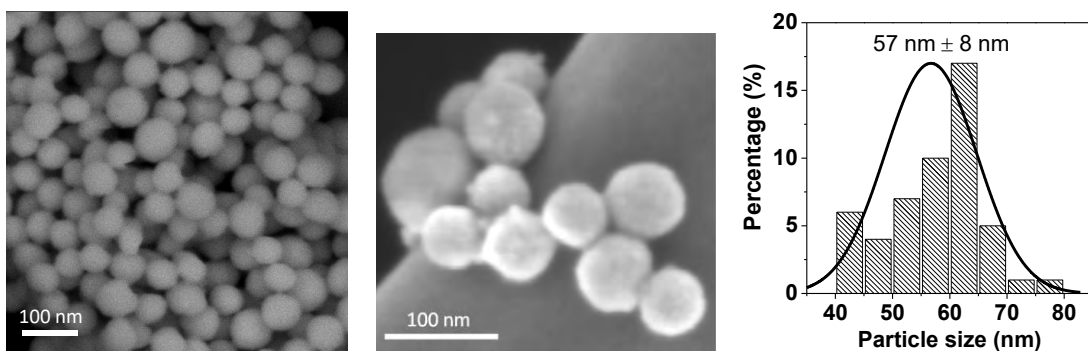


**Figure 2.21.** Representative FESEM images of the white-emitting organometallo-silica nanoparticles (**[W]-NP**, left and middle) and the corresponding histogram showing the particle size distribution (right).

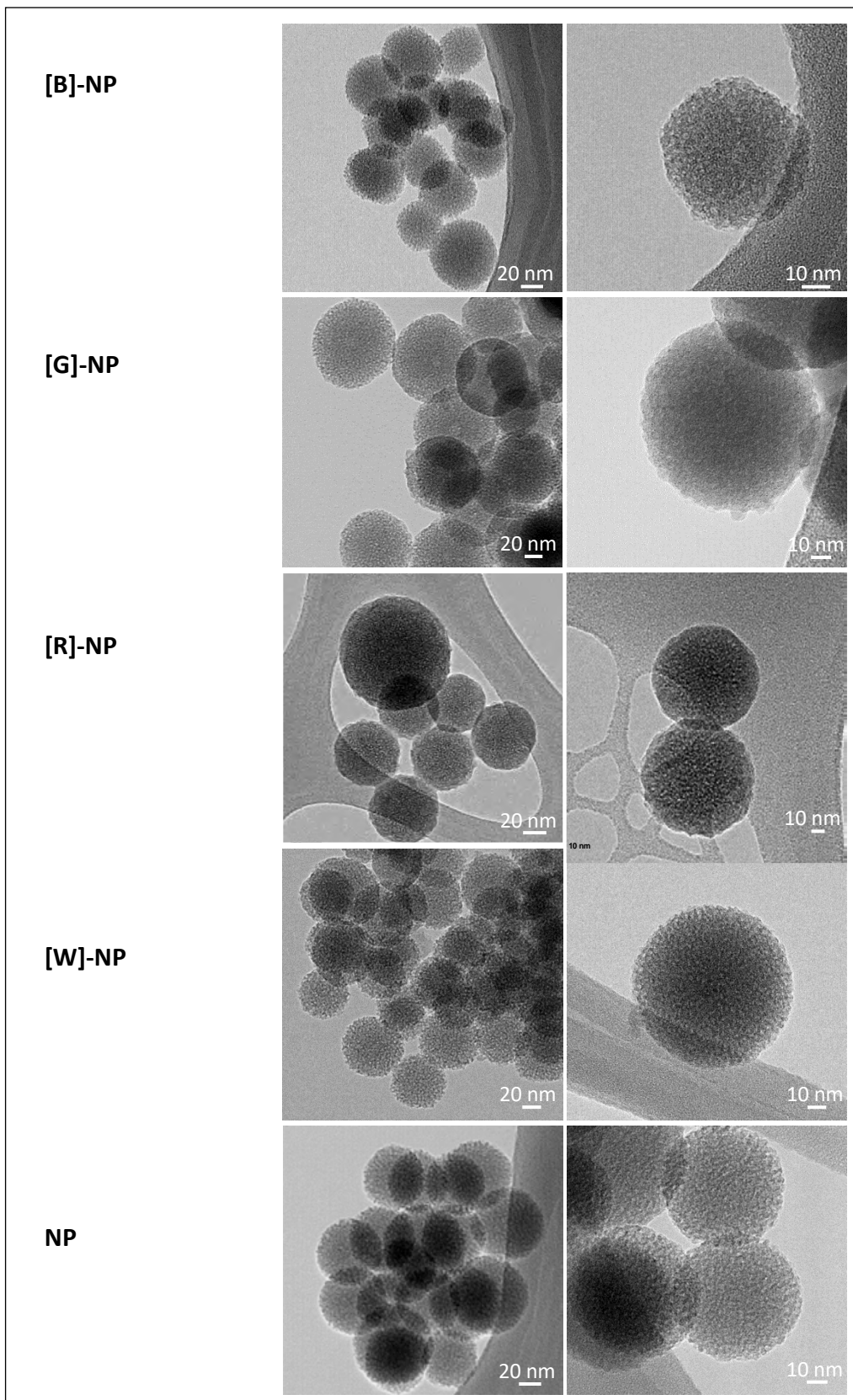


**Figure 2.22.** TEM images of the monochromatic emitting ([B]-NP, [G]-NP and [R]-NP), the white-emitting ([W]-NP) and the complex-free (NP) silica nanoparticles.

### II.2.2.2 Spectroscopy characterization

As in the previous chapter, the incorporation of the organometallic complexes (**B**, **G** and **R**) into the silica framework and the preservation of their molecular structure were evaluated by absorption, emission and FTIR spectroscopies.

#### II.2.2.2.1 Infrared spectra

Figure 2.23 shows representative FTIR spectra of the hybrid silica material based on the blue chromophore, **[B]-NP**, in comparison with the pure complex (**B**) and the control silica nanoparticles (**NP**). The spectra of **R** and **[R]-NP** are collected in annex II, figure A.II.5.

As shown in the spectra, the hybrid material (see also experimental section) exhibits weak absorption peaks between 2850-3000 cm<sup>-1</sup> and 1380-1500 cm<sup>-1</sup>, related to those found for the corresponding iridium precursor. These bands are characteristic of the stretching vibrations of methylenic and aromatic groups, respectively. The typical absorption bands assigned to the vibrations of O-H, Si-O and Si-O-Si groups are also well-resolved (see figure 2.23).

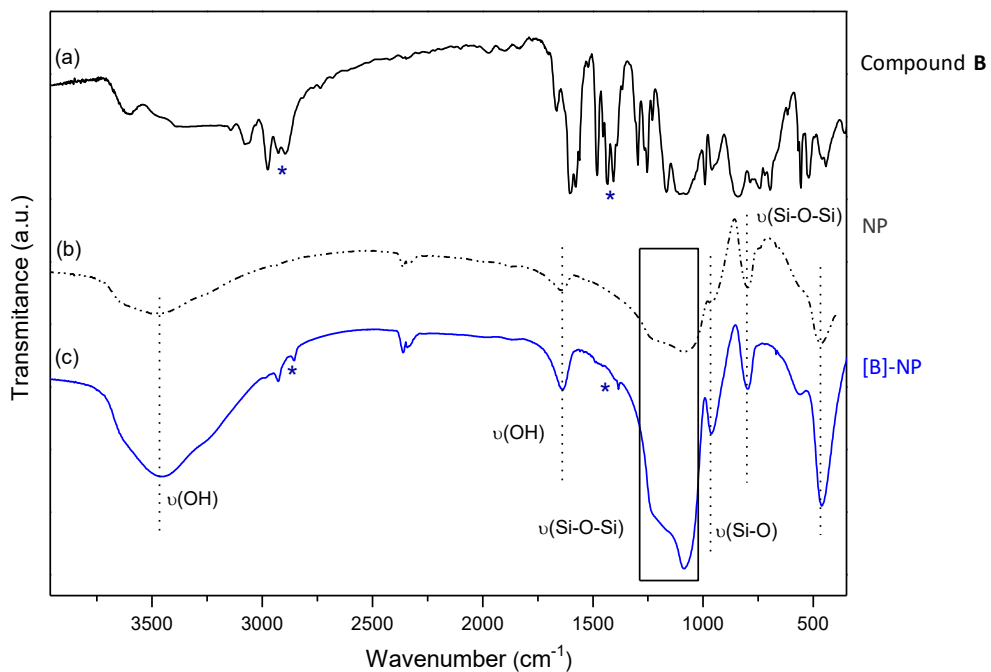


**Figure 2.23.** Representative FTIR spectra of the hybrid organometallo-silica nanoparticles **[B]-NP** (c) in comparison with the spectra of the pure complex **B** (a) and the control material (b). (\*) Characteristic absorption of the complexes observed in the hybrid material.

### *II.2.2.2.2 Photophysical properties*

The absorption and emission data of both the organometallic dots (**[B,G,R]-OD** and **[W]-OD**) and the hybrid organometallo-silica nanoparticles (**[B,G,R]-NP** and **[W]-NP**) are summarized in tables 2.4 and 2.5. Some representative figures are also collected.

#### *i. Absorption spectra*

The diffuse reflectance spectra of the monochromatic-emitting silica nanoparticles (**[B,G,R]-NP**) are very similar to those observed for the corresponding iridium precursors (**B**, **G** and **R**) in the solid state. All of them display the characteristic features between 200 and 400 nm and, in the case of **[R]-NP**, the spin forbidden absorptions at 467 and 494 nm are also resolved (see figure 2.24 and table 2.4).

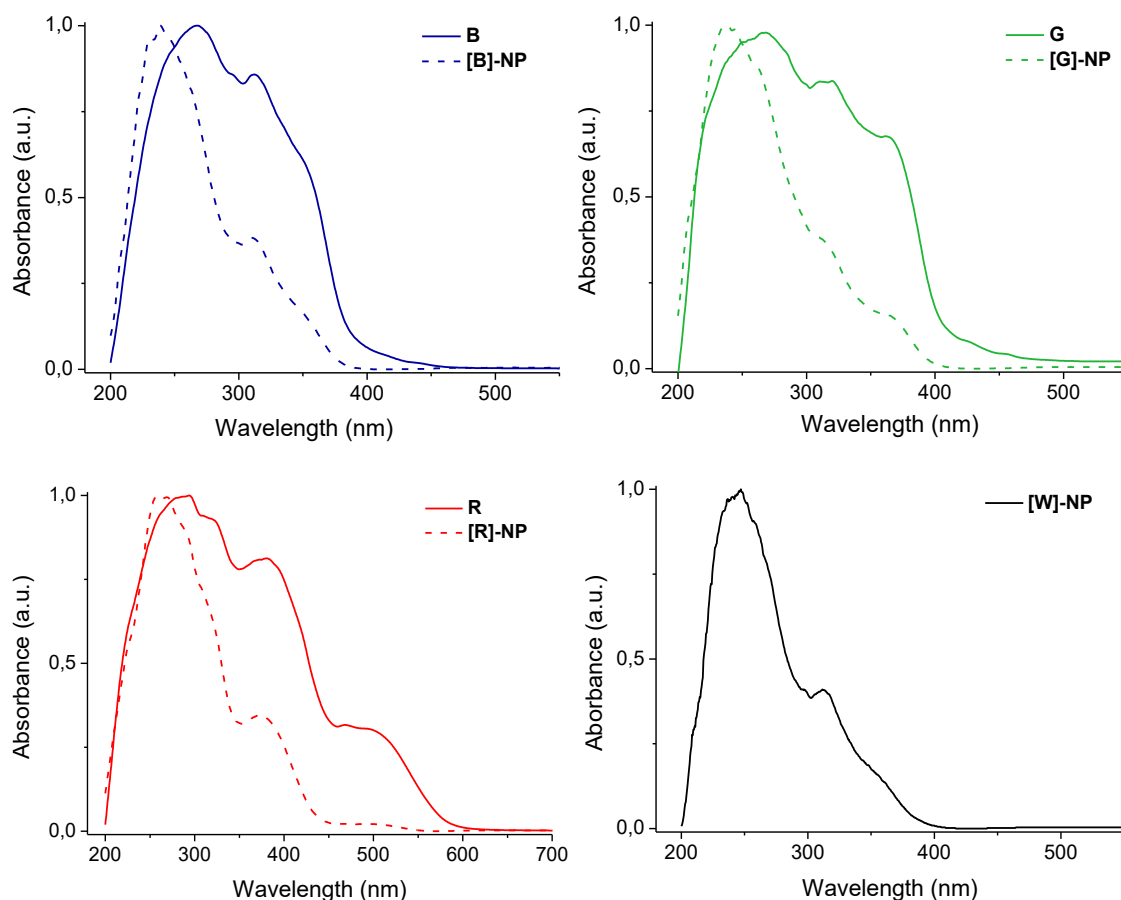


**Figure 2.24.** Comparative solid state DRUV spectra of complexes **B**, **G** and **R** and the related silica nanoparticles (**[B]-NP**, **[G]-NP** and **[R]-NP**). DRUV spectrum of the white-emitting **[W]-NP** organometallo-silica nanoparticles.

In the same way, the white-emitting material (**[W]-NP**) also shows the main absorption bands of chromophores **B** and **G** in the high energy region ( $\lambda < 360$  nm). However, and due to the little amount of complex **R** added to the mixture, no features in the low energy region are observed.

**Table 2.4.** Absorption data in the solid state (DRUV) of complexes **B**, **G** and **R** and their corresponding silica nanoparticles (**[B]-NP**, **[G]-NP**, **[R]-NP** and **[W]-NP**).

Sample	$\lambda_{\text{abs}}/\text{nm}$
[Ir(dFppy) <sub>2</sub> (PPETS) <sub>2</sub> ]PF <sub>6</sub> ( <b>B</b> )	241, 279, 296, 316, 332, 350, 410, 440
<b>[B]-NP</b>	230, 240, 260, 297, 312, 350
[Ir(ppy) <sub>2</sub> (PPETS) <sub>2</sub> ]OTf ( <b>G</b> )	221, 248, 267, 321, 366, 420, 452
<b>[G]-NP</b>	240, 264, 314, 362
[Ir(ppy) <sub>2</sub> (dasipy) <sub>2</sub> ]OTf ( <b>R</b> )	223, 258, 276, 297, 320, 380, 468, 493
<b>[R]-NP</b>	224, 238, 272, 294, 310, 372, 467, 494
<b>[W]-NP</b>	246, 258, 268, 298, 311, 358

### *ii. Emission spectra*

All the monochromatic-emitting silica nanoparticles (**[B,G,R]-NP**) exhibit very similar emission profiles to those previously observed for their respective pure complexes (**B**, **G** and **R**) in the solid state at room temperature. They feature long-lived non-structured emission bands that are also comparable to those found for the corresponding organometallic dots (**[B,G,R]-OD**) measured directly from the reaction medium (see figure 2.25 and table 2.5). This supports the fact that the mesoporous nanoparticles **NPs** are obtained by the growth of the silica around the organometallic dots **ODs**, which have been formed by the condensation of several molecules of each complex and does not experiment any relevant structural change. In this way, it makes sense to observed similar behaviors in the emission profiles of both **NPs** and **ODs** samples and the initial chromophores in the solid state.

However, although all of them exhibit comparable emission profiles, the quantum yields of both **NPs** and **ODs** are slightly smaller than those recorded for their complex precursors (table 2.5), being higher those measured for **NPs** probably due to the protection of the chromophore by the silica shell.<sup>35b, 93</sup>

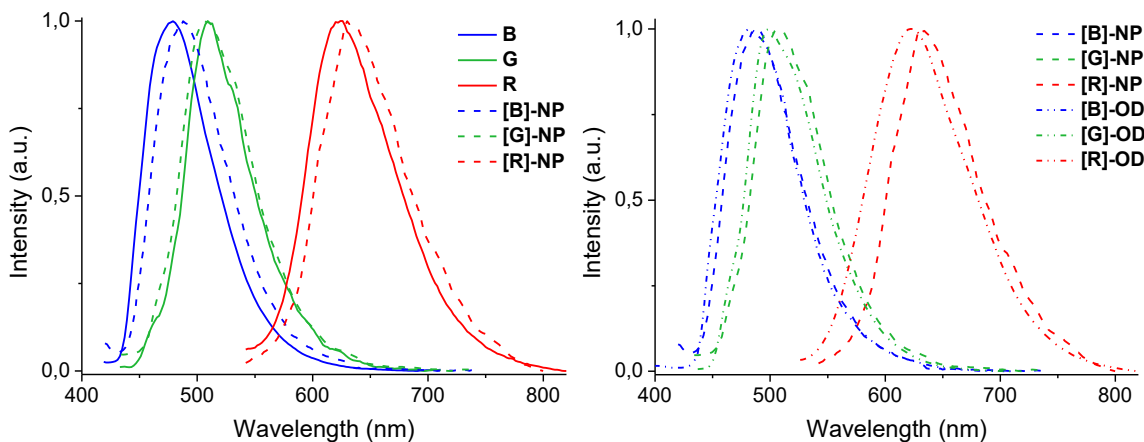


**Figure 2.25.** (Left) Emission spectra ( $\lambda_{\text{ex}} 365 \text{ nm}$  for **B** and **G**;  $\lambda_{\text{ex}} 470 \text{ nm}$  for **R**) of complexes **B**, **G**, **R** (solid line) and the related monochromatic NPs (dashed line), in solid state at room temperature. (Right) Emission spectra in suspension of the monochromatic ODs (dotted line) and in solid state of the NPs (dashed line).

**Table 2.5.** Emission data of complexes **B**, **G** and **R** in the solid state at room temperature and of their corresponding hybrid organometallo-silica nanoparticles ([**B,G,R**]-NP) and dots ([**B,G,R**]-OD).

Sample	Medium <sup>(a)</sup>	$\lambda_{\text{em}}$ (nm) <sup>(b)</sup>	$\tau$ <sup>(c)</sup> (μs)	$\phi$ (%)
<b>B</b>	Solid	480	1.55	23.5
[ <b>B</b> ]-NP	Solid	488	0.99	19.6 (365); 15.4 (390)
[ <b>B</b> ]-OD	<i>Sol</i> <sup>(d)</sup>	485	1.18	17.5 (365); 11.7 (390)
<b>G</b>	Solid	512	0.97	31.2
[ <b>G</b> ]-NP	Solid	508	0.89	15.7 (365); 13.7 (390)
[ <b>G</b> ]-OD	<i>Sol</i> <sup>(d)</sup>	500	0.75	10.0 (365); 8.5 (390)
<b>R</b>	Solid	620	0.13	13.1 (390); 16.5 (480)
[ <b>R</b> ]-NP	Solid	630	0.12	8.7 (390); 10.5 (480)
[ <b>R</b> ]-OD	<i>Sol</i> <sup>(d)</sup>	625	0.14	9.2 (390); 6.6 (480)

(a) Data recorded at room temperature (298 K). (b)  $\lambda_{\text{ex}} 365$  for samples containing chromophores **B** and **G**.  $\lambda_{\text{ex}} 470$  for samples containing chromophore **R**. (c) Emissions lifetimes calculated as average of a bi-exponential decay. (d) Measured directly from the reaction media.

In contrast, upon excitation at 390 nm, [**W**]-NP nanoparticles, which are formed by a mixture of the **B**, **G** and **R** complexes, feature a broad (width *ca.* 6250 cm<sup>-1</sup>) white emission band with maxima at 490 and 595 nm and a tail that extends up to 750 nm (figure 2.26). So, this emission covers the entire visible region and provides a high-quality white emission. In addition, they also exhibit a higher quantum yield (20.5%,  $\lambda_{\text{ex}} 390 \text{ nm}$ ) than that observed for the monochromatic-emitting materials, representing one of the highest values reported for white-emitting silica nanoparticles.<sup>96</sup>

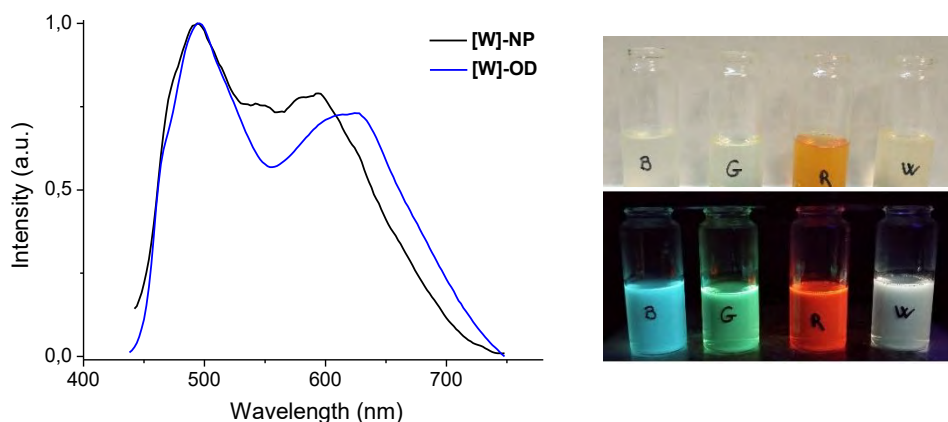


**Figure 2.26.** (Left) Emission spectra ( $\lambda_{\text{ex}} 390 \text{ nm}$ ) of the white-emitting **ODs** and **NPs** in suspension and in the solid state, respectively. (Right) Pictures of suspensions of the **ODs** in the reaction media under room and UV light.

**Table 2.6.** Emission data of the white-emitting organometallo-silica nanoparticles ([W]-NP) and dots ([W]-OD).

Sample	Medium <sup>(a)</sup>	$\lambda_{\text{em}}$ (nm) <sup>(b)</sup>	$\tau$ <sup>(c)</sup> (μs)	$\phi$ (%)
[W]-NP	Solid	490, 595 <sup>(d)</sup> (390)	0.57 (480)	
			0.64 (510)	26.7 (365); 20.5 (390)
			0.63 (595)	
[W]-OD	<i>Sol</i> <sup>(e)</sup>	490, 615 (390)	0.40 (480)	
			0.57 (510)	10.6 (365); 9.1 (390)
			0.50 (600)	

(a) Data recorded at room temperature (298 K). (b)  $\lambda_{\text{ex}} 390 \text{ nm}$ . (c) Emissions lifetimes calculated as average of a bi-exponential decay. (d) Tail extended to 750 nm. (e) Measured directly from the reaction media.

Likewise, the emission properties of the related organometallic dots, **W-[OD]**, were also measured in suspension directly from the reaction medium. As expected, they display a comparable emission profile to that observed for the **[W]-NP** nanoparticles, also exhibiting a broad white emission with maxima at 490 and 615 nm (width *ca.* 6450 cm<sup>-1</sup>, see figure 2.26). In addition, as expected, the emission bands of both samples (**[W]-OD** and **[W]-NP**) depend on the excitation wavelength ( $\lambda_{\text{ex}}$ ). As shown in figure 2.27, an enhancement on the intensity of the lowest energy band is observed when exciting at lower energies. Also, as observed in the excitation spectra (figure 2.27, up) monitored at the red low-energy maximum (580 nm, **[W]-NP** and 620 nm, **[W]-OD**), there is a peak maxima at 500 nm that overlaps with the emission of both the blue and the green chromophores. This fact, together with the good overlap previously observed between the absorption of **R** and the emissions of **B** and **G** (see figure 2.16), suggests that an energy transfer process is occurring from the high-energy emitting complexes to the red-emitting one inside the **[W]-NP**.

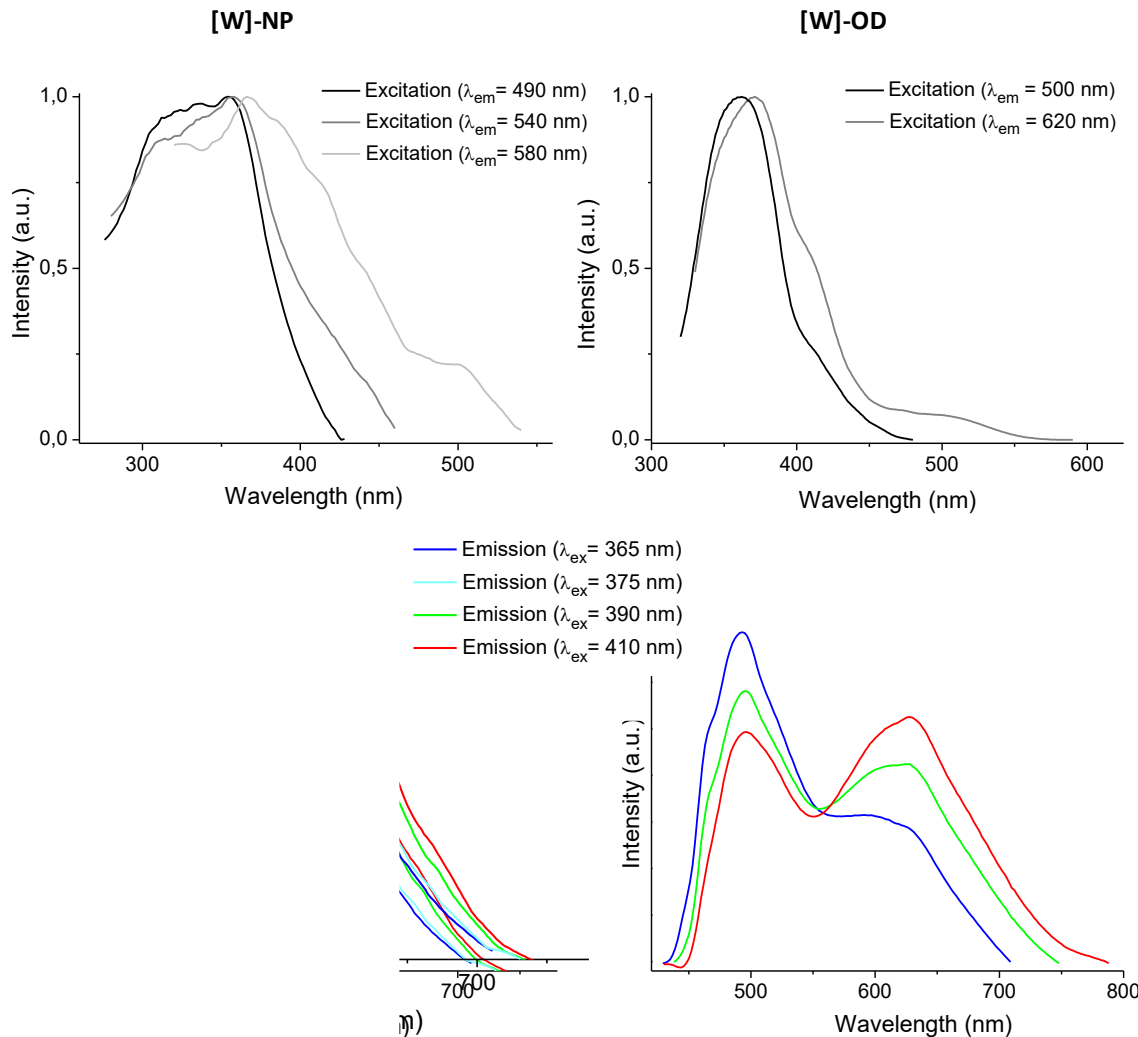


**Figure 2.27.** Excitation (up) and emission (down) spectra monitored at different emission and excitation wavelengths, respectively, of the white-emitting nanoparticles [W]-NP (left) and the organometallic dots [W]-OD (right).

Further confirmation was obtained when we compared the lifetime values ( $\tau$ ) of the [W]-NP material (monitored at 480 nm (0.57  $\mu$ s), 510 nm (0.64  $\mu$ s) and 585 nm (0.63  $\mu$ s)) with those of the monochromatic-emitting nanoparticles monitored at their respective emission maxima (0.99  $\mu$ s [B]-NP; 0.89  $\mu$ s [G]-NP; 0.12  $\mu$ s [R]-NP). This study reveals a slight decrease on the lifetime of the blue and green emitters and a clear increase on the  $\tau$  of the red one. The same behavior was also observed for the [W]-OD (monitored at 480 nm (0.40  $\mu$ s), 510 nm (0.57  $\mu$ s) and 600 nm (0.50  $\mu$ s)), when compared with the corresponding monochromatic organometallic dots (1.18  $\mu$ s [B]-OD; 0.75  $\mu$ s [G]-OD; 0.14  $\mu$ s [R]-OD). The changes observed in the excited state lifetimes point to a certain of FRET (Förster resonance energy transfer) in our system.<sup>97</sup> Nevertheless, it has also been reported a certain triplet-triplet Dexter energy transfer

contribution for other multimetallic phosphorescent systems (**Ru(II)**, **Os(II)**, **Ir(III)**),<sup>97b</sup> although chromophores are not able to get a good conjugation in the ground state.

Finally, in order to highlight the importance of the simultaneous incorporation of the three chromophores proposed by our *three-in-one* approach, we also measured the emissive response of a homologous multi-component system obtained by mixing the appropriate amounts of each monochromatic nanoparticles (**[B]-NP**, **[G]-NP** and **[R]-NP**). Thus, a homogenous solid mixture of the three monochromatic emitting NPs with the same mass ratio of chromophores as in **[W]-NP** sample was obtained. The emission spectrum of this mixture, together with that of **[W]-NP**, is displayed in figure 2.28 (left).

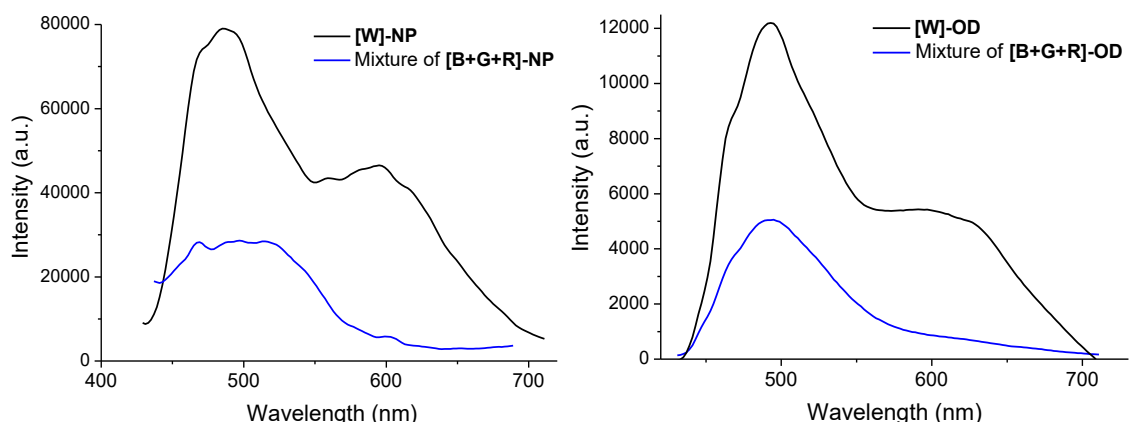


**Figure 2.28.** Emission spectra of the three-in-one white-emitting nanoparticles, **[W]-NP**, (left) and the organometallic dots, **[W]-OD**, (right) compared with a mixture of the appropriate amount of the monochromatic nanoparticles or volumes of the reaction media of the monochromatic dots, respectively, to get the same proportion of the chromophores. ( $\lambda_{\text{ex}}$  365 nm).

As shown in figure 2.28, the multi-component mixture shows not only a weaker emission band than that observed for **[W]-NP**, but also a very different profile in which the low energy maximum (*ca.* 600 nm) is lost, probably due to some degree of self-absorption. The same behavior is also observed in the mixture prepared from the organometallic dots, **[B]-OD**, **[G]-OD** and **[R]-OD**.

All these facts give more evidences about the possibility of having energy transfer from the blue and green chromophores to the red one in both **[W]-NP** and **[W]-OD** materials, and could explain the high contribution of the low energy emission in spite the small relative amount of complex **R** in **[W]-NP** or **[W]-OD** (5.5 wt%). The energy transfer is a short-range process, which cannot take place in the multi-component mixture where each chromophore is localized inside

its corresponding and distinct silica nanoparticle and, so, separated by more than 50-70 nm. By contrast, the small size of **[W]-OD** (*ca.* 5 nm) allows the concurrence of the energy transfer process between the chromophores within the nanoparticles.

### **II.2.3 Design and study of Hybrid Light Emitting Diodes (HLEDs)**

In view of the interesting results obtained, we decided to study the possibility of implementing our organometallo-silica nanoparticles in Hybrid Light Emitting Diodes (HLEDs), using them as color down-converting coatings. These studies were performed in the research group of Dr. Rubén Darío Costa (IMDEA Materiales, Madrid).

As described on the experimental section, the coatings were prepared by mixing an acetonitrile solution or suspension of each iridium complex or silica nanoparticles, respectively, with a mixture of branched (trimethylolpropane ethoxylate, TMPE) and linear polymers (poly(ethylene oxide), 1-PEO). The resulting materials display a gummy look and, are best described as rubber-like materials (see the experimental part for more details) and will be referred as **OC**-rubbers (for the iridium complexes) and **NP**-rubbers (for the emitting nanoparticles).

#### **II.2.3.1 Monochromatic-emitting HLEDs**

Following this approach, the pure complexes (**B**, **G** and **R**) and the monochromatic-emitting silica nanoparticles (**[B,G,R]-NP**) were first implemented into the polymeric coating to obtain the corresponding **OC**- and **NP**-rubbers (see figure 2.29), and their photoluminescence properties were evaluated. Figure 2.30 shows some representative spectra of the rubber materials based on samples **B** and **[B]-NP**.

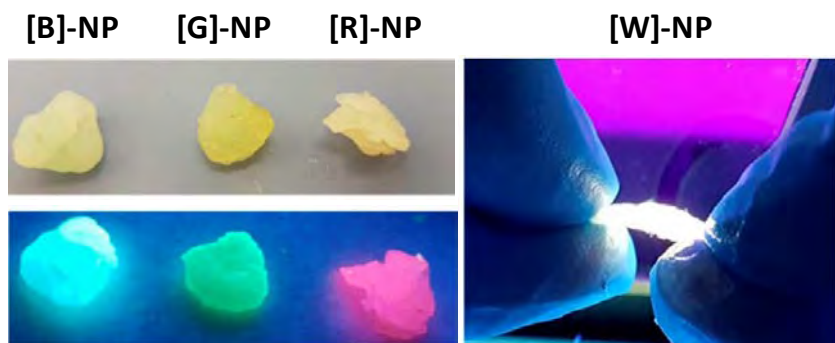


**Figure 2.29.** Picture of the rubber-like materials based on the monochromatic-emitting nanoparticles under room light (up) and UV irradiation (310 nm, 8 W) (down).

As expected, **OC**- and **NP**-rubbers show similar emission profiles to those previously observed for both the complexes (**B**, **G** and **R**) and the nanoparticles (**[B,G,R]-NP**), suggesting that the interaction between the emitting materials and the matrix is not very strong. Moreover, all

the rubbers show excellent photo- and thermal-stabilities under both ambient conditions and harsh environments, such as long-term storage, UV irradiation (310 nm, 8W), and thermal treatment up to 70°C (see figure 2.30). However, notable differences were observed when comparing the emission spectra of **OC**- and **NP**-rubber materials when stored them under extreme conditions (UV irradiation at room temperature (b) and at 70°C (c), figure 2.30). In these cases, the rubbers with the emitting nanoparticles (**NP**-rubbers) show higher photo- and thermal-stabilities than those with the coordination complexes (**OC**-rubbers), which start to degrade after few hours.

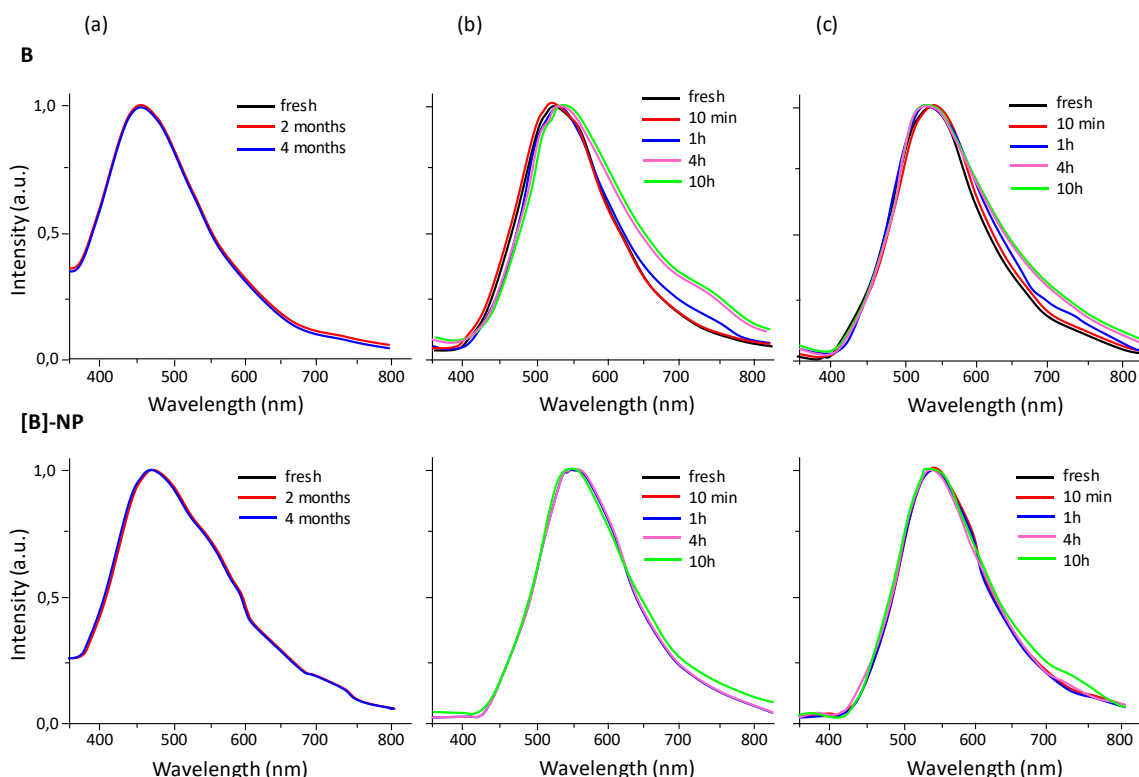


**Figure 2.30.** Changes in the emission spectra ( $\lambda_{\text{ex}} 400 \text{ nm LED}$ ) of the **OC**- (up) and **NP**-rubbers (down) based on complex **B** and the monochromatic organometallo-silica nanoparticles ([**B**]-NP), respectively, over time under ambient storage conditions (a), under UV irradiation (310 nm, 8 W) at room temperature (b), and under UV irradiation (310 nm, 8 W) at 70°C (c).

Once we evaluated the rubber-like materials, we used them as color down-converting coatings to fabricate a series of HLEDs. With this purpose, the rubbers (1 mm thick) were deposited on top of a commercial UV-LED with a 400 nm emitting chip (see the experimental section for further details). With the aim of evaluating both the color conversion efficiency and the stability of the resulting devices, they were exposed to different and constant applied currents, respectively, monitoring in both experiments the spectral changes, the luminous efficiency and the temperature of the HLEDs.

The down-conversion efficiency ( $\eta_{\text{con}}$ ) is defined as the ratio between the maxima emission of the down-converting coating and the LED employed. Therefore, the  $\eta_{\text{con}}$  of our devices was evaluated applying different currents ranging from 50 to 150 mA. As shown in figure 2.31, a linear increase was observed for both **OC**- and **NP**-HLEDs, indicating that there is no saturation, bleaching or quenching effects. In addition, **NP**-HLEDs exhibit higher conversion efficiencies than those observed for their corresponding **OC**-HLEDs, except for the green-emitting devices.

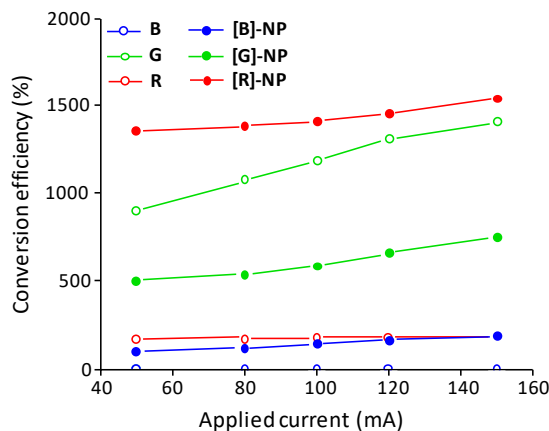


**Figure 2.31.** Conversion efficiency ( $\eta_{\text{con}}$ ) vs. applied currents for down-converting coatings prepared with **OC**- and **NP**-rubbers.

The beneficial effect of incorporating the complexes into the silica framework during the synthesis was clearly revealed by the stability tests, which were performed applying a constant current of 150 mA to the different devices. The blue and green **OC**-HLEDs feature luminous efficiencies of 0.27 and 1.65 lm/W, respectively and, also, show a quick degradation (blue **OC**-HLED) or an exponential decrease (green **OC**-HLED) in luminous efficiency within the first hour (figures 2.32 and 2.33). This low stability could be attributed to the instability of the chromophores upon time that easily degrade, probably due to the presence of monodentate phosphine ligands (PPETS). For instance, the emission intensity in the green **OC**-HLED decreases dramatically after 10 hours of measurement, and it also experiments a slightly change of the emission maximum. This last effect is more visible on the blue **OC**-HLED, in which the maximum changed from 495 to 520 nm, along with the x/y CIE color coordinates from 0.18/0.18 to 0.31/0.44 after 4 hours. By contrast, the red **OC**-HLED displays stable emission spectrum upon time (figure 2.34), probably due to the low luminous efficiency of 0.03 lm/W and to the presence of a bidentate ligand (*dasipy*), that provides additional stability.

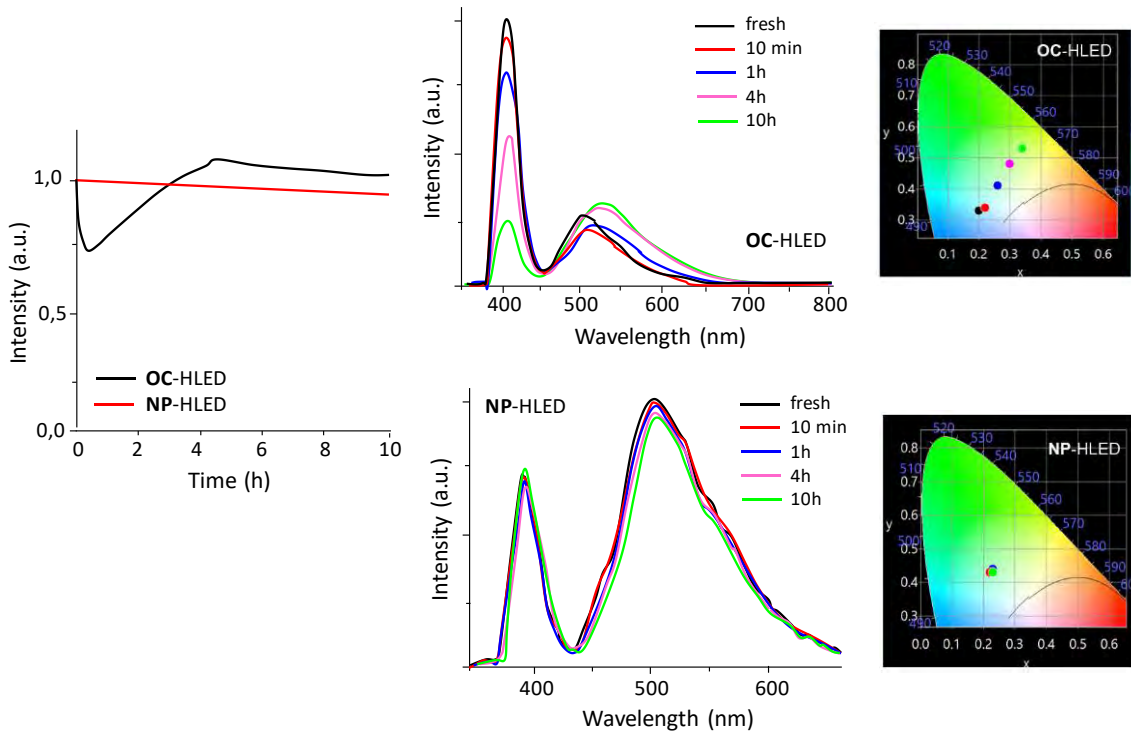


**Figure 2.32.** Changes in the intensity of the down-conversion band (left), spectrum shape (central), and x/y CIE color coordinates (right) of blue-emitting **OC-HLEDs** (top, based on **B**) and **NP-HLEDs** (bottom, based on **[B]-NP**) over time upon applying a constant current of 150 mA.

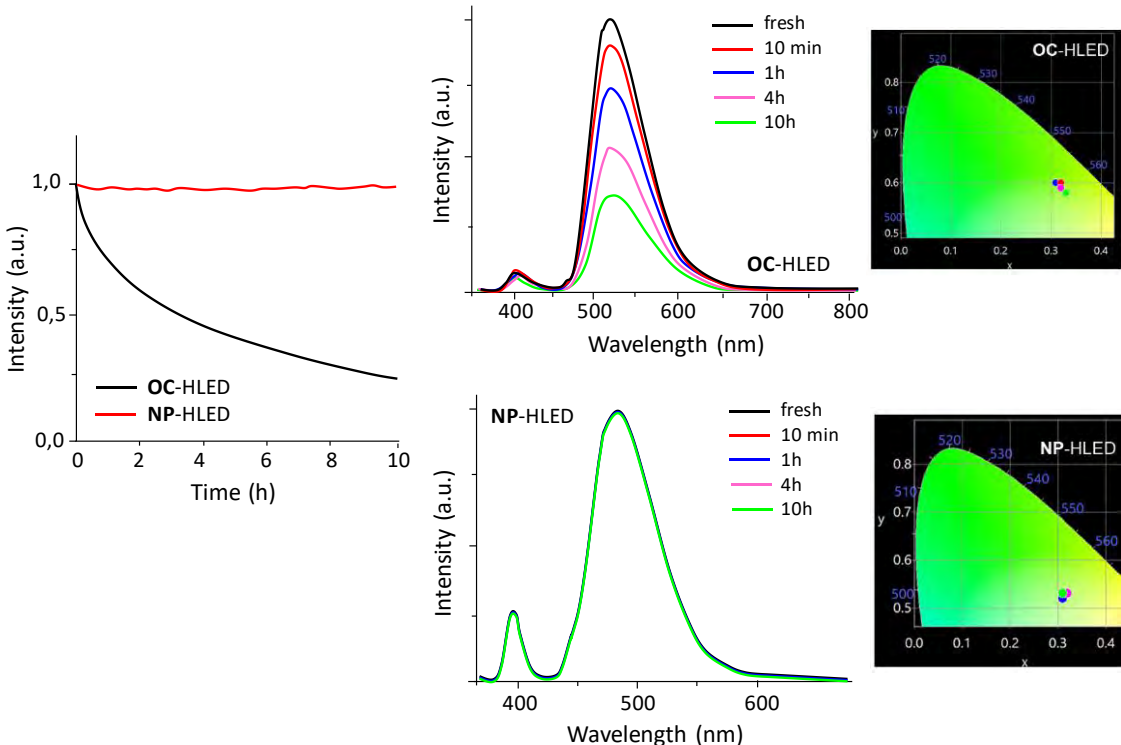


**Figure 2.33.** Changes in the intensity of the down-conversion band (left), spectrum shape (central), and x/y CIE color coordinates (right) of green-emitting **OC-HLEDs** (top, based on **G**) and **NP-HLEDs** (bottom, based on **[G]-NP**) over time upon applying a constant current of 150 mA.

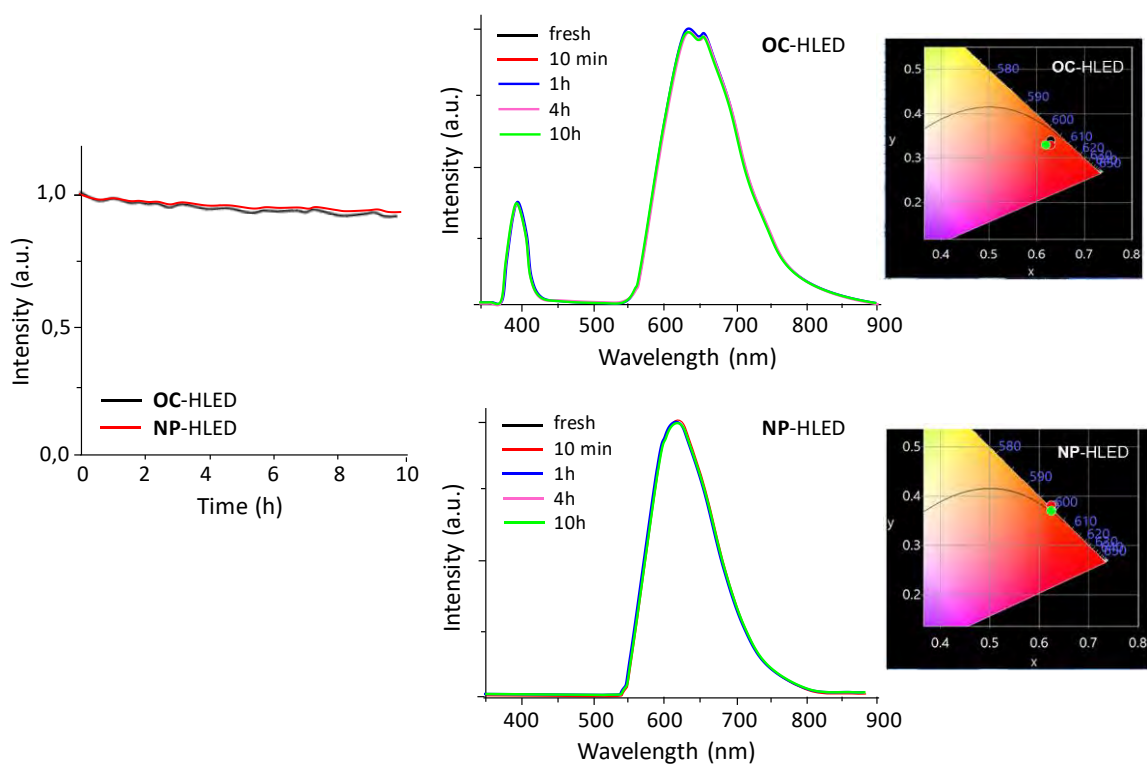


**Figure 2.34.** Changes in the intensity of the down-conversion band (Left), spectrum shape (central), and x/y CIE color coordinates (right) of red-emitting **OC-HLEDs** (top, based on R) and **NP-HLEDs** (bottom, based on [R]-NP) over time upon applying a constant current of 150 mA.

By contrast, a very different behavior was observed for the **NP-HLEDs** devices. All of them, show higher and more stable luminous efficiencies, reaching values of 1.24, 1.30 and 1.50 lm/W for the blue-, green-, and red-emitting **NP-HLEDs**, respectively (see figures 2.32-2.34). An additional fact to highlight is the stability in the temperature of the down-converting coatings that, in any case, exceed 30-32°C.

Considering all these facts, we can suggest that the main role of the silica core is the isolation of the emitters from the ambient oxygen. In addition, the constraint of the organometallic molecules into the silica matrix limits, or even avoids, non-radiative vibrations upon continuous excitations. Therefore, these experiments confirm the clear benefit of incorporating the iridium chromophores into the silica nanoparticles during their synthesis, leading to HLEDs with improved luminous efficiencies and stabilities.

### II.2.3.2 Single component white-emitting HLED

In the same line, we next fabricated a single-component **NP-HWLED** using a rubber-like material based on the white-emitting **[W]-NP** nanoparticles as the color down-converting coating (figure 2.35) and, both the photoluminescence properties and the stability were examined.

As shown in figure 2.35, **NP-HWLED** exhibits a broad emission band with a maximum at 590 nm, closely flanked by shoulders at *ca.* 500 and 620 nm, which perfectly matches with the visible part of the spectrum of the natural sunlight measured in Madrid on December (12<sup>th</sup> December 2017, 13 h). In addition, the emission in the blue region is rather moderate in our device, what would be overcoming one of the major concerns in artificial white lighting.

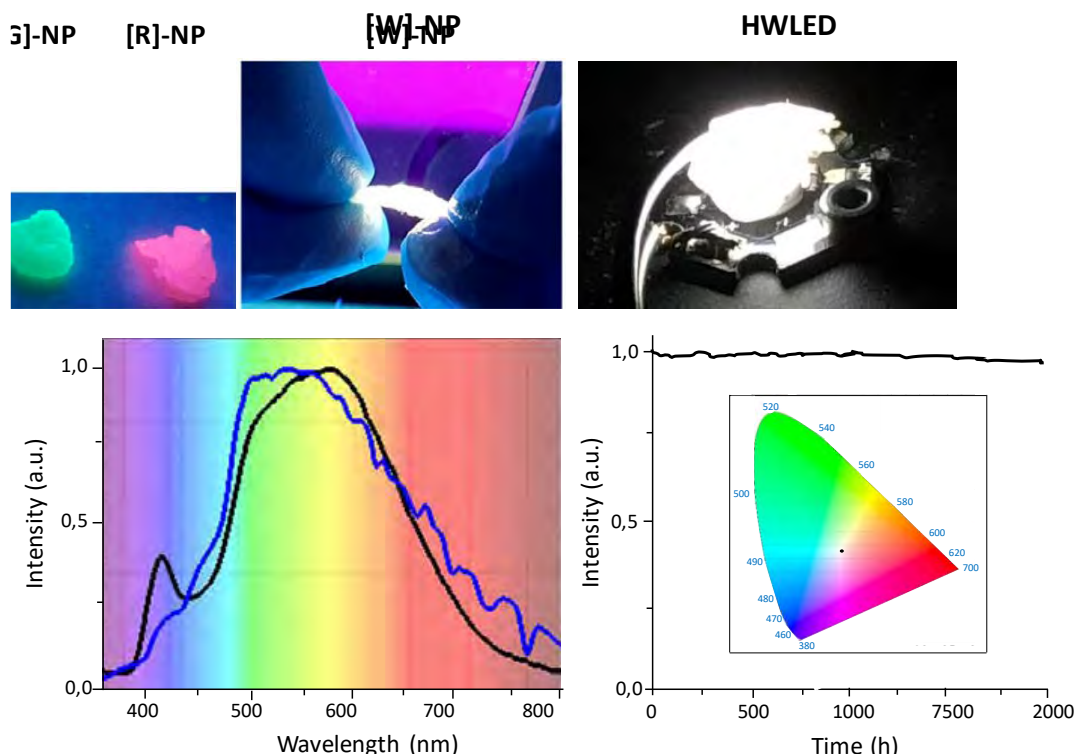


**Figure 2.35.** (Upper part, left) Picture of the rubber-like material based on the white-emitting nanoparticles under UV (310 nm, 8 W) irradiation. (Right) Picture of the HWLED under operating conditions. (Lower part, left) Electroluminescence spectrum of the single-component HWLED (in blue) compared with the visible part of the sunlight spectrum (in black). (Right) Changes of the luminous efficiency of the HWLED and the x/y CIE color coordinates (inset) over time under an applied constant current of 150 mA.

The stability was also examined by applying a constant current of 150 mA. As shown in figure 2.35, the **NP-HWLED** device exhibits remarkable stability over 2000 hours, featuring constant luminous efficiency of 2.5 lm/W, CIE color coordinates of 0.34/0.33, CRI of 85, and CCT of 5143K. These characteristics make our device one of the most stable HWLEDs reported so far.<sup>84a-c, 85b, 86b</sup>

<sup>98</sup> Moreover, this device is also able to reach values of *ca.* 10000 h of stability (based on a linear extrapolation) maintaining more than the 50% of the maxima luminance.

On the other hand, the homogeneity of the light distribution throughout the device was evaluated by examining the variation in the emission spectra at different angles (90°, 145° and 180°). As shown in figure 2.36, minimal changes were observed, suggesting a uniform spherical light distribution along the hybrid white-light emitting diode.

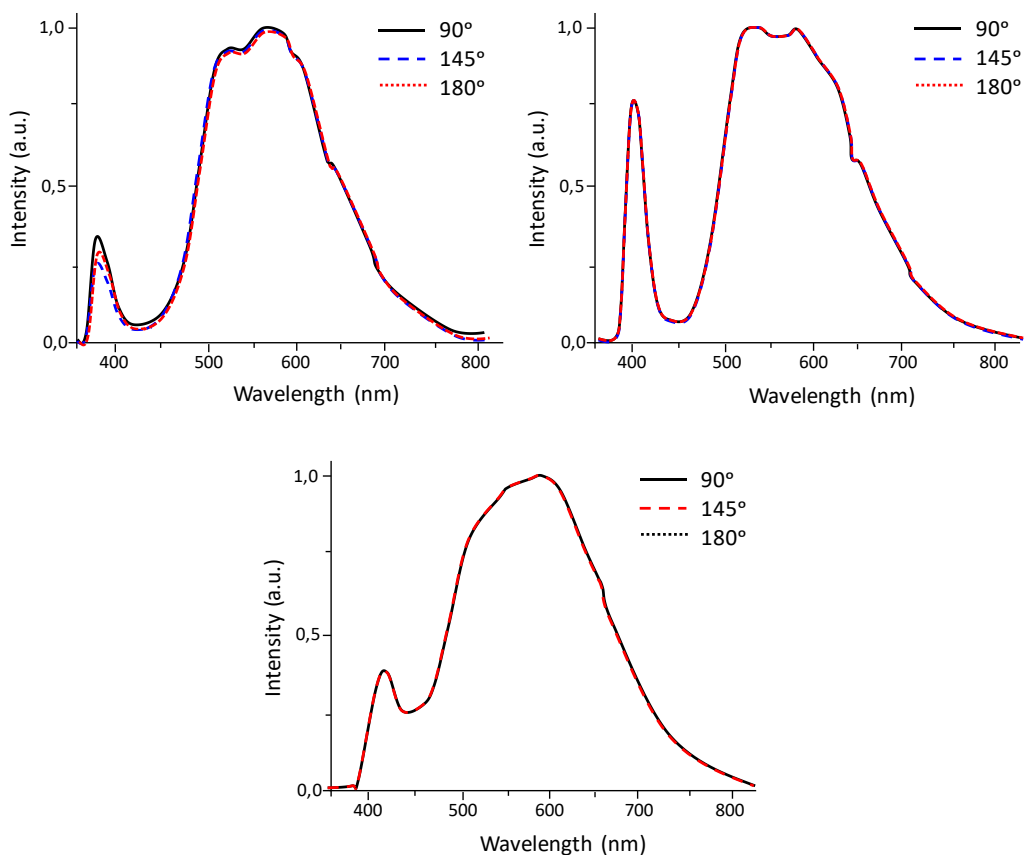


**Figure 2.36.** Electroluminescence spectra of NP-HWLED with single-component down-converting coating (based on [W]-NP) recorded at different measuring angles (top left:  $\lambda_{\text{ex}} = 375 \text{ nm}$ ; top right:  $\lambda_{\text{ex}} = 390 \text{ nm}$ ; and bottom:  $\lambda_{\text{ex}} = 410 \text{ nm}$ ).

Finally, in order to highlight the importance of using the single-component device, the corresponding HWLED with the multi-component material based on the mixture of discrete [B]-NP, [G]-NP and [R]-NP nanoparticles was also studied. As expected, for this system, there is also a lack of an efficient energy transfer between the monochromatic nanoparticles, avoiding the device to display white light due to the lack of emission in the low energy region ( $\lambda > 600 \text{ nm}$ ; see figure 2.37).

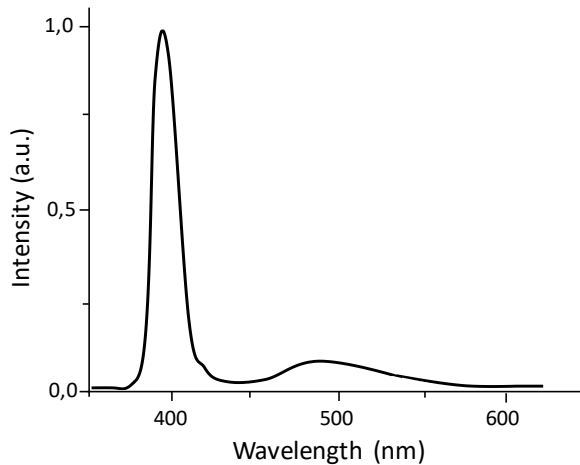


**Figure 2.37.** Electroluminescence spectra ( $\lambda_{\text{ex}} 400 \text{ nm}$ ) of NP-HWLED with multi-component NPs, based on a mixture of [B]-NP, [G]-NP and [R]-NP and maintaining the same chromophore concentration than in the single-component NPs, [W]-NP.



# **Chapter III**

---

*Nanopartículas de sílice mesoporosas como  
biomarcadores*

---



## Introducción

En las últimas décadas, el uso de materiales nanoestructurados en aplicaciones biomédicas se ha convertido en una de las tecnologías líderes para combatir diferentes tipos de enfermedades.<sup>12d, 31, 99</sup> De hecho, el desarrollo de distintos tipos de nanopartículas (NPs) que puedan ser útiles en un amplio rango de aplicaciones biomédicas nos hace pensar en la obtención de soluciones personalizadas para un buen número de problemas médicos. Por ejemplo, los puntos cuánticos semiconductores (Quantum Dots, QD) de seleniuro o sulfuro de cadmio, que pueden variar su emisión en función de su tamaño, se han convertido en biomarcadores muy populares gracias a sus anchos espectros de absorción, estrechos y variables espectros de emisión y sus altas eficiencias.<sup>100</sup> Las nanopartículas de oro coloidales, también destacadas por sus propiedades ópticas y eléctricas, se usan como agentes de contraste en tomografía computerizada (CT).<sup>101</sup> Las nanopartículas superparamagnéticas de óxido de hierro<sup>102</sup> o las estructuras moleculares metal-orgánicas (MOFs)<sup>103</sup> han sido ampliamente utilizadas como agentes de contraste en resonancia magnética y como biosensores. Además, para aumentar su especificidad sobre determinadas paredes celulares,<sup>104</sup> todos ellos se pueden funcionalizar superficialmente y, también, pueden ser usados como sistemas de administración de fármacos.<sup>105</sup>

### Nanopartículas mesoporosas de sílice (MSNs)

Entre todos estos nanomateriales, las nanopartículas mesoporosas de sílice (MSNs) se han convertido en una de las plataformas más empleadas en nanomedicina debido a sus interesantes propiedades (inercia química, transparencia óptica y estabilidad fotoquímica) y a sus estructuras

relativamente modulables (fácil síntesis, funcionalización superficial y modificación de tamaño de partícula y poro) pero, sobre todo, debido a su limitada toxicidad en medios biológicos y a su biodegradabilidad.<sup>106</sup> Así, las MSNs se han utilizado satisfactoriamente en varias aplicaciones biomédicas como marcadores biológicos,<sup>107</sup> biosensores<sup>107a, 108</sup> o agentes administradores de medicamentos.<sup>107b, 109</sup> El impacto biológico de las nanopartículas depende, fundamentalmente, de su tamaño, forma y características. Por ello, el control sobre el tamaño de partícula y poro, así como la forma y geometría de estas MSNs resulta de gran importancia.<sup>110</sup> Generalmente, el tamaño y orientación del poro están determinados por el tipo de surfactante empleado, mientras que el tamaño y la morfología de la partícula se modulan modificando la relación molar entre el precursor de sílice y el surfactante, así como controlando el pH del medio de reacción o introduciendo precursores adicionales durante el proceso de condensación.

No obstante, una de las propiedades más importantes a considerar a la hora de diseñar estos sistemas es la superficie de las nanopartículas, ya que ésta es la primera en interaccionar con el medio celular. De hecho, la naturaleza química de la superficie es la que va a determinar la interacción y el comportamiento final de las partículas. Así, debido a que las membranas celulares tienen, predominantemente, carga negativa, las superficies con cargas positivas presentan una mayor afinidad y captación celular que las cargadas negativamente. De este modo, y teniendo en cuenta el carácter aniónico de las nanopartículas de sílice nativas, se pueden obtener MSNs con cargas positivas mediante la funcionalización de la superficie con polímeros u otras moléculas biocompatibles (figura 3.1).<sup>111</sup>

En este sentido, la formación de coronas o carcasas (polietilenglicol PEG, polietilenamina, grupos orgánicos o péptidos que favorecen la incorporación celular, figura 3.1)<sup>111d</sup> alrededor de las nanopartículas permite una mejor dispersión del material en medios acuosos y una mayor biocompatibilidad, además de reducir problemas de agregación.<sup>23a</sup>

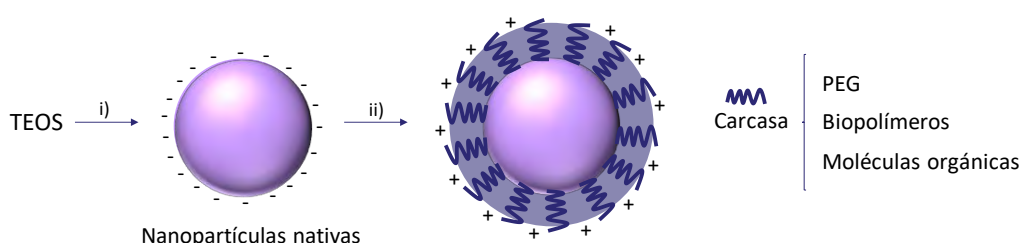


**Figura 3.1.** Formación de una nanopartícula de sílice nativa (i) y su protección con diferentes tipos de coronas (ii).

Todos estos factores influyen directamente en la captación de las nanopartículas a través de la membrana celular, proceso complicado que no siempre ocurre de la misma manera y que varía en función del tipo de célula. Así, aparte de la penetración directa que tiene lugar con partículas pequeñas, se puede decir que, en términos generales, se desarrolla a través de endocitosis (figura 3.2).<sup>104</sup> Dicho proceso se divide, a su vez, en dos grandes tipos: la fagocitosis, que principalmente tiene lugar en células especializadas en la defensa del tejido del huésped o la captación de células muertas, y la pinocitosis, que se desarrolla en muchos tipos de células. No obstante, en este capítulo no se estudiará en detalle el mecanismo de captación celular de las nanopartículas.

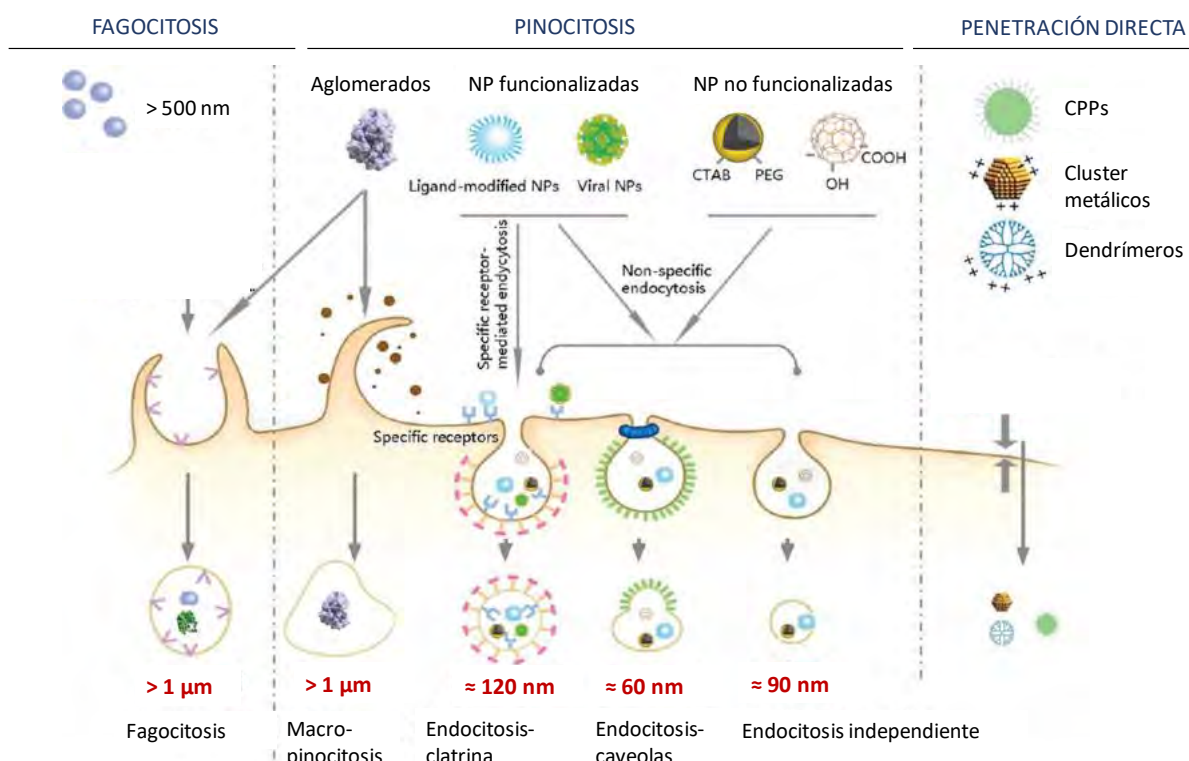


Figura 3.2. Esquema de los distintos mecanismos de captación molecular. (Biomater. Sci. 2013, 1, 896-911)

### MSNs como marcadores biológicos

Con el fin de utilizar las nanopartículas de sílice como biomarcadores resulta imprescindible functionalizarlas con cromóforos adecuados, siendo los más empleados los fluoróforos orgánicos o complejos metálicos. De esta forma, se consigue combinar las ventajas de la sílice y de las moléculas luminiscentes en una sola entidad, proporcionando una mayor foto-estabilidad al cromóforo, debido a la protección adicional que la sílice le confiere.

Por otro lado, los cromóforos empleados han de cumplir una serie de requisitos para considerarlos biomarcadores eficientes. Por norma general, han de presentar desplazamientos de Stokes significativamente grandes para evitar la auto-desactivación de la emisión, así como tiempos de vida largos para evitar interferencias con la emisión de las células,<sup>49b</sup> ya que éstas son inherentemente fluorescentes debido a la presencia de compuestos endógenos fotoactivos (flavinas, nicotinamidas o triptófano).<sup>112</sup> Por lo tanto, si la excitación y/o la emisión del fluoróforo solapa con los de estas especies autofluorescentes, o si tiene un tiempo de vida muy corto, va a ser complicado discriminar entre los dos tipos de señales. Por último, es altamente recomendable que estas moléculas muestren longitudes de onda de excitación y emisión poco energéticas, próximas al infrarrojo cercano (NIR,  $\lambda$  650-950 nm). En esta zona del espectro, la luz penetra más profundamente en los tejidos biológicos, provocando menos efectos dañinos a nivel celular. Además, al tratarse de emisiones con longitudes de onda más largas, las interferencias con la autofluorescencia del medio biológico son significativamente inferiores, lo que resulta beneficioso para los experimentos *in vivo*.<sup>113</sup>

#### *i. Funcionalización con fluoróforos orgánicos*

Estos nanomateriales fluorescentes (FSNPs) se obtienen a partir de moléculas orgánicas que, generalmente, muestran altas eficiencias de emisión en disolución pero que, en ocasiones, son poco o nada emisivas a alta concentración o cuando se agregan, debido al fenómeno conocido como desactivación de la emisión por agregación (aggregation-caused quenching, ACQ).<sup>114</sup> Este comportamiento está, sobre todo, causado por las interacciones  $\pi\cdots\pi$  entre moléculas, que hacen disminuir la intensidad de la fluorescencia suponiendo, así, un problema a la hora de diseñar nuevos sistemas FSNPs.

En este área, recientemente se ha desarrollado una nueva categoría de fluoróforos orgánicos, que se caracterizan por exhibir o incrementar la eficiencia de la fluorescencia cuando se encuentran formando agregados (emisión inducida por agregación, AIE).<sup>115</sup> Así, la acumulación de estos derivados en las nanopartículas de sílice va a permitir obtener FSNPs mucho más emisivas y, en consecuencia, más eficientes.

En la mayoría de los casos, estas FSNPs se obtienen tras la encapsulación del fluoróforo<sup>116</sup> en las nanopartículas de sílice. Así, por ejemplo, Wei y colaboradores<sup>116a</sup> introdujeron un fluoróforo orgánico con efecto AIE (10-cetil-10H-fenotiazina-3,7-(4,40-aminofenil), ATPHE) en los mesoporos de la sílice (figura 3.3, a), recubriendo las nanopartículas resultantes con una capa polimérica. Las FSNPs finales son capaces de actuar como biomarcador gracias a su

internalización efectiva en células HeLa (ver figura 3.3, b). No obstante, en este tipo de encapsulaciones, al carecer de interacciones covalentes entre ambas fases, se pueden producir pérdidas de las moléculas incorporadas por lixiviación en medios fluidos, causando una disminución en la intensidad de señal y una mayor toxicidad en el medio celular. Este problema se puede solucionar estableciendo enlaces covalentes entre los fluoróforos y la matriz de sílice,<sup>107b</sup> tal y como se comenta en el capítulo I.

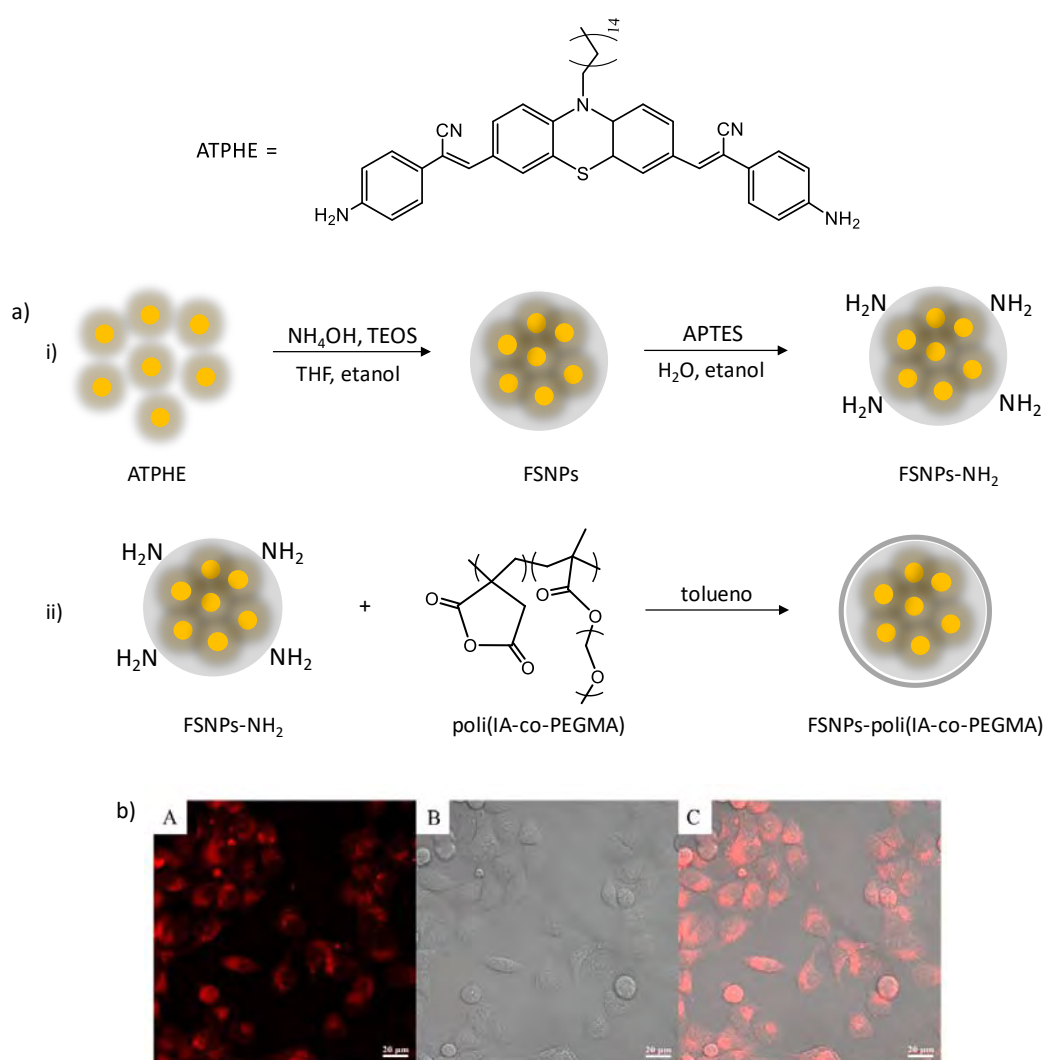


**Figura 3.3.** (a) Síntesis de FSNPs a través de la encapsulación del fluoróforo ATPHE en las nanopartículas de sílice (i), y su posterior protección con el polímero poli(IA-co-PEGMA) (ii). (b) Imágenes de fluorescencia de células HeLa incubadas con las nanopartículas. (Appl. Surf. Sci. 2017, 403, 396-402)

Sin embargo, a pesar de los avances conseguidos con este tipo de moléculas orgánicas, problemas relacionados con la desactivación de la emisión a través de otros procesos o con los tiempos de vida cortos (nanosegundos) del fluoróforo limitan, en parte, su aplicación en este campo. Por ello, es necesario diseñar otro tipo de sistemas que sean capaces de solventar o reducir alguna de estas limitaciones.

## ii. Funcionalización con complejos metálicos

El empleo de compuestos fosforescentes de metales de transición de configuración electrónica de bajo spin d<sup>6</sup> (Ru<sup>II</sup>, Re<sup>I</sup>, Ir<sup>III</sup>) o d<sup>8</sup> (Au<sup>I</sup>, Pt<sup>II</sup>),<sup>46d, 117</sup> así como algunos derivados de lantánidos (Eu<sup>III</sup>, Tb<sup>III</sup>, Yb<sup>III</sup>),<sup>118</sup> suponen una alternativa, con interesantes ventajas, al uso de fluoróforos orgánicos. Así, los derivados ciclometalados de Ir<sup>III</sup> exhiben emisiones fácilmente modulables, con altos rendimientos cuánticos y tiempos de vida largos, que permiten reducir o eliminar la interferencia con la autoflorescencia. Por otra parte, también presentan elevadas estabilidades foto- y fisicoquímicas, que permiten seguir su trazabilidad en el medio biológico. Además, el entorno de coordinación octaédrico de estas moléculas reduce los procesos de agregación frecuentes en moléculas orgánicas.<sup>43a, 50a-d</sup> Todas estas características han generado un gran interés en el ámbito de la biomedicina y, actualmente, los derivados de Ir<sup>III</sup> (ver figura 3.4) se han convertido en agentes marcadores complementarios a los fluoróforos orgánicos.<sup>44a, 44f, 117d, 119</sup>

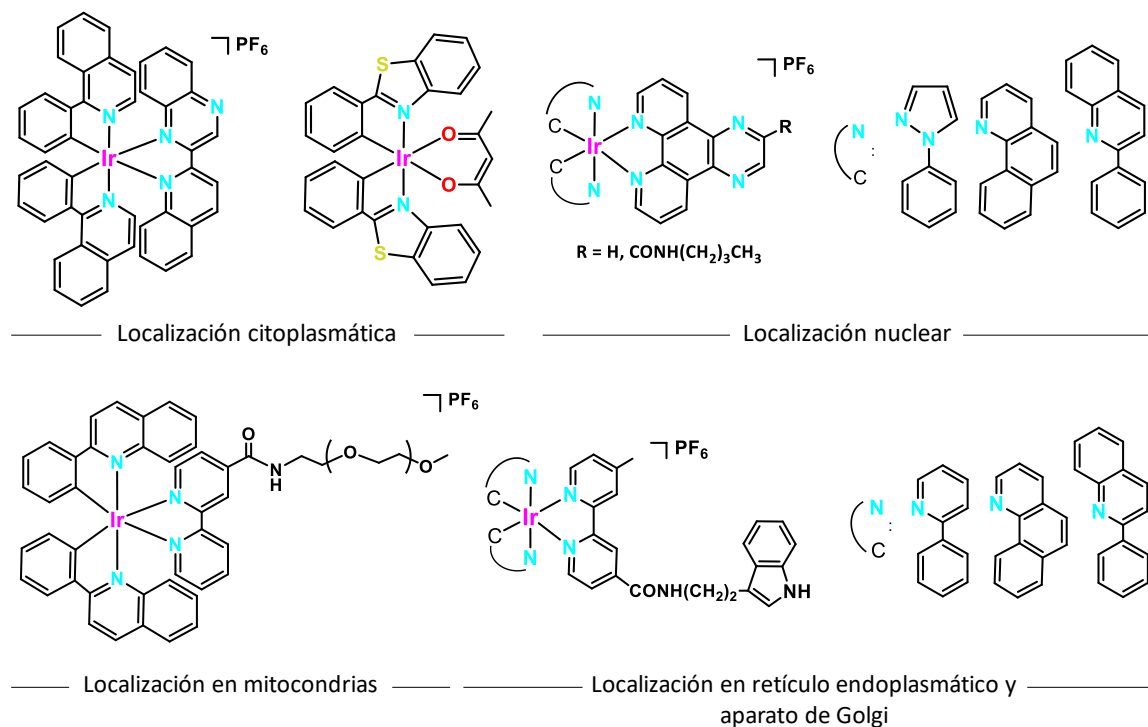


**Figura 3.4.** Ejemplos de compuestos ciclometalados de Ir<sup>III</sup> empleados como marcadores en biomedicina. (Coord. Chem. Rev. 2018, 363, 71-91)

A pesar de la versatilidad de estos derivados, existen muy pocos ejemplos en la bibliografía en los que se describa su combinación con nanopartículas de sílice para la obtención de MSNs luminiscentes y su aplicación en biomedicina.<sup>32f, 32g, 40, 120</sup> Por ejemplo, en 2015, Wei Huang y colaboradores<sup>120</sup> diseñaron unas nanopartículas de sílice basadas en dos compuestos diferentes

de Ir<sup>III</sup> (**1** y **2**, figura 3.5) para la detección de iones hipoclorito (ClO<sup>-</sup>) en células vivas a través de microscopía de fluorescencia. Así, en ausencia de los mismos, se observa únicamente la emisión azul del derivado **1** ( $\lambda_{\text{em}}$  480 nm), mientras que en presencia de ClO<sup>-</sup> las imágenes de fluorescencia muestran una intensa emisión roja ( $\lambda_{\text{em}}$  600 nm) debida a la aparición del derivado **2a** tras la reacción de **2** con dichos iones.

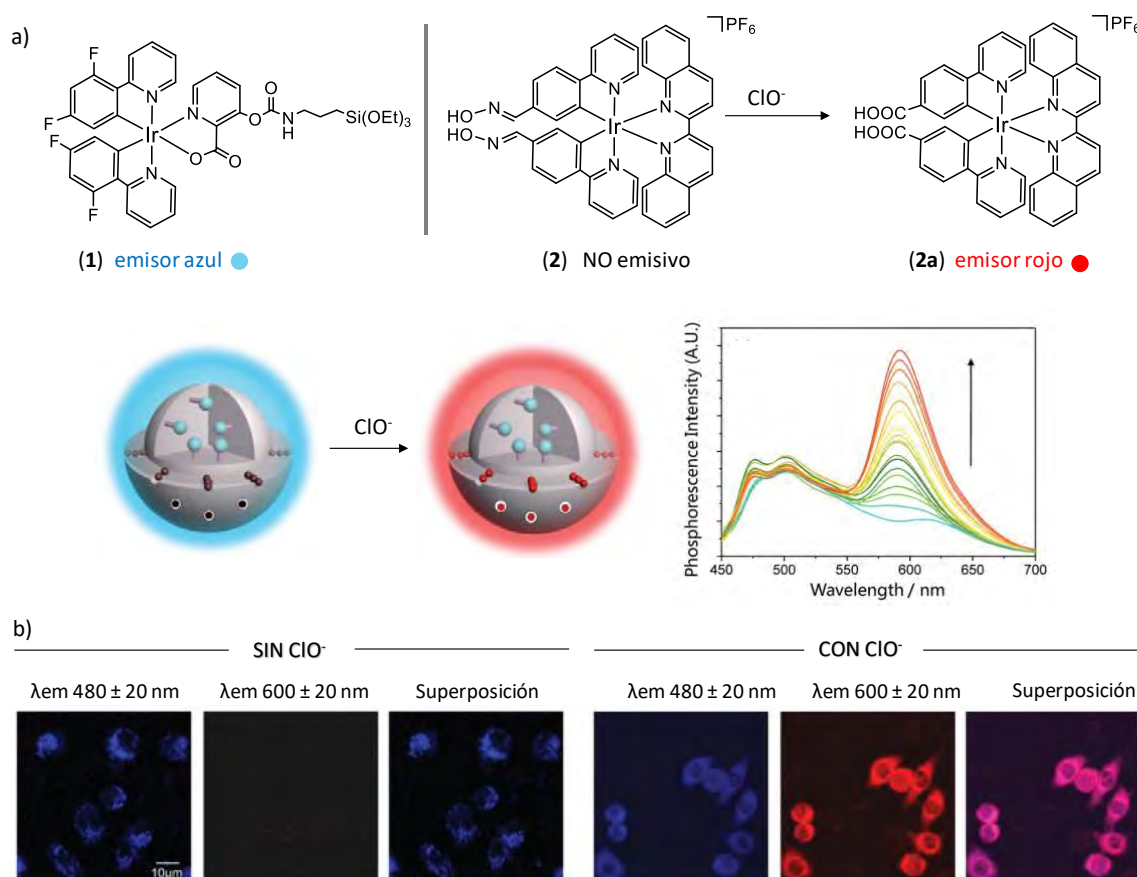


**Figura 3.5.** (a) Representación esquemática de los compuestos utilizados en la preparación de las nanopartículas (arriba) y su comportamiento emisivo en ausencia y presencia de iones ClO<sup>-</sup> exógenos (abajo). (b) Imágenes de fluorescencia de las células (RAW 264.7) tratadas con las nanopartículas en diferentes canales (azul y rojo). (Chem. Sci. 2015, 6, 301-307)

En ese mismo año, Wei Huang *et al.*<sup>40</sup> también diseñaron un sistema de nanopartículas de sílice, muy eficientes como biomarcadores, basado en la combinación de compuestos de metales de transición (Ir<sup>III</sup>) y lantánidos (Eu<sup>III</sup>) (ver figura 3.6). Así, al irradiar las nanopartículas con luz visible ( $\lambda_{\text{ex}}$  480 nm) consiguen una transferencia energética eficaz desde el derivado de iridio(III) al de europio(III), con una emisión final muy eficiente y de vida media larga en la zona de baja energía. En particular, esta última característica les convierte en prometedores candidatos como biomarcadores, ya que esto permite eliminar las interferencias con la autofluorescencia generada en el medio celular.

Sin embargo, a pesar de las ventajas que presentan la incorporación de compuestos de iridio(III) en sistemas nanoestructurados de sílice, no hemos encontrado en la bibliografía ejemplos más recientes acerca de su preparación e implicación en medios celulares.

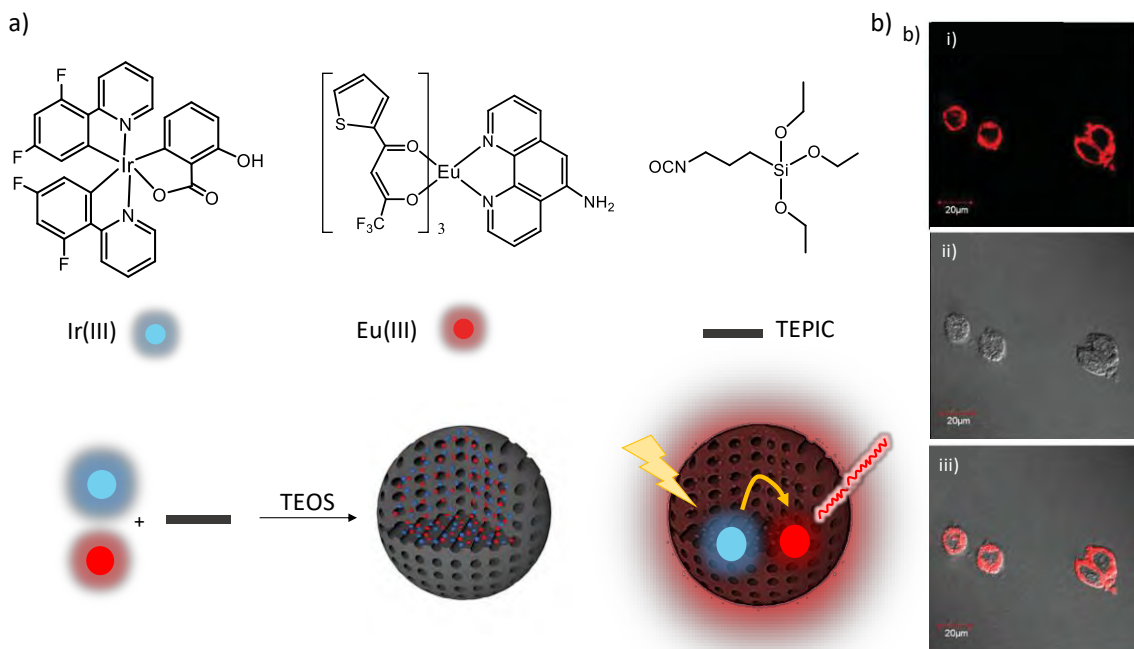


**Figura 3.6.** (a) Representación esquemática de los compuestos utilizados en la preparación de las nanopartículas (arriba) y su preparación (abajo). (b) Imágenes de fluorescencia de células HeLa tratadas con las nanopartículas ( $\lambda_{\text{ex}} 488 \text{ nm}$ ). (Adv. Optical. Mater. 2015, 3, 233-240)

### MSN como agentes transportadores de fármacos

Por otro lado, al tratarse de materiales mesoporosos, las nanopartículas de sílice cuentan con poros internos perfectamente definidos, que permiten albergar moléculas pequeñas, convirtiéndose así en interesantes candidatos como plataformas transportadoras y liberadoras de fármacos.<sup>121</sup> Uno de los métodos más empleados para incorporar estas moléculas consiste en su adsorción en los poros internos de la sílice (figura 3.7, izquierda), proceso que se puede favorecer funcionalizando la superficie de los poros con grupos ácidos o aminas para proporcionar una mayor interacción adsorbente/ adsorbato. La incorporación del fármaco se puede conseguir también estableciendo uniones covalentes entre dichas moléculas y la sílice, utilizando para ello enlaces capaces de responder a estímulos externos (figura 3.7, derecha) que permitan su posterior liberación.

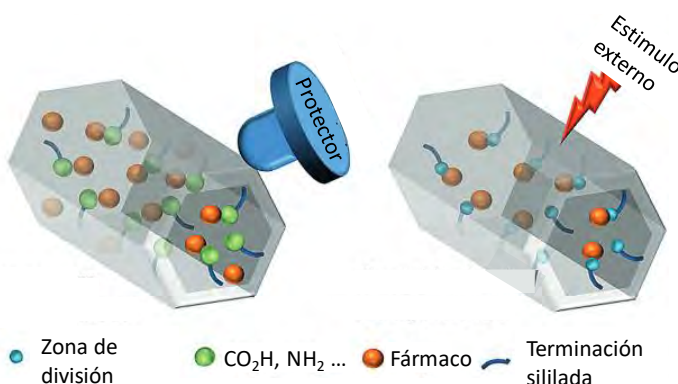


**Figura 3.7.** Estrategias para cargar los fármacos en los poros de las nanopartículas de sílice. (Chem. Eur. J. 2015, 21, 13850-13865)

Cuando las moléculas del fármaco se encuentran incorporadas por adsorción es fácil que se produzca su liberación en zonas que no son las deseadas, ya que no existen uniones covalentes entre ambas fases.<sup>122</sup> Para evitarlo, se colocan entidades que actúan como bloqueadores de poros y que son capaces de cambiar química o físicamente al ser expuestos a diferentes estímulos externos (pH, actividad enzimática, ultrasonidos, fotoirradiación).<sup>23c, 121b</sup> De esta forma, se controla la apertura y cierre de dichos poros,<sup>23c</sup> mejorando así su eficiencia terapéutica. En las figuras 3.8 y 3.9 se detalla alguna de las estrategias que pueden emplearse para tener ese control sobre la liberación del fármaco.

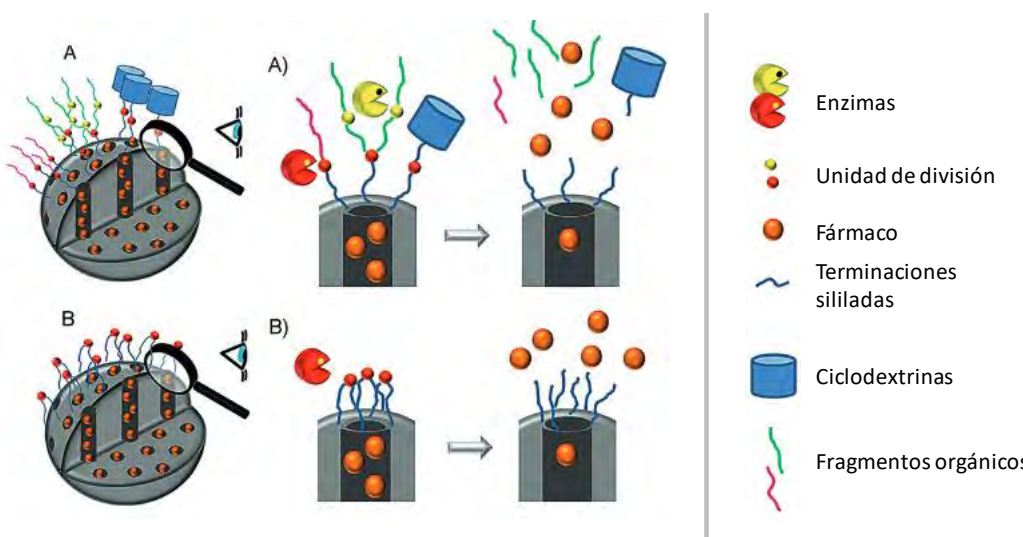


**Figura 3.8.** Diferentes tipos de transporte de fármacos en los poros de las nanopartículas (A, B) y su liberación tras la actuación de enzimas. (Chem. Eur. J. 2015, 21, 13850-13865)

La primera de ellas consiste en modificar la superficie de las nanopartículas con fragmentos que sean capaces de bloquear los poros (ciclodextrinas, cadenas con terminaciones sililadas, etc.) y liberar los fármacos únicamente tras la actuación de una enzima, generalmente hidrolasas (ver

figura 3.8).<sup>23c</sup> Para que esto sea posible, estos fragmentos han de incorporar unidades de división (funciones de tipo éster) donde puedan actuar las correspondientes enzimas.

Otra forma de controlar la liberación del fármaco consiste en funcionalizar la superficie de las nanopartículas mesoporosas con polímeros o péptidos con propiedades básicas, que sean capaces de responder a una variación en el pH. Así, como se muestra en la figura 3.9, la unión covalente del péptido poli(L-histidina) (PHis) a la superficie de la nanopartícula permite controlar la liberación de las moléculas encapsuladas en función del nivel de acidez del medio.<sup>109a</sup> Así, a pH básico, la hidrofobicidad del péptido, debida a su desprotonación, hace que sus cadenas se encuentren recogidas formando una capa protectora que bloquea la salida del fármaco. Por el contrario, a pH más ácido, su protonación permite que las cadenas adopten una disposición más abierta que favorece la liberación de las moléculas.

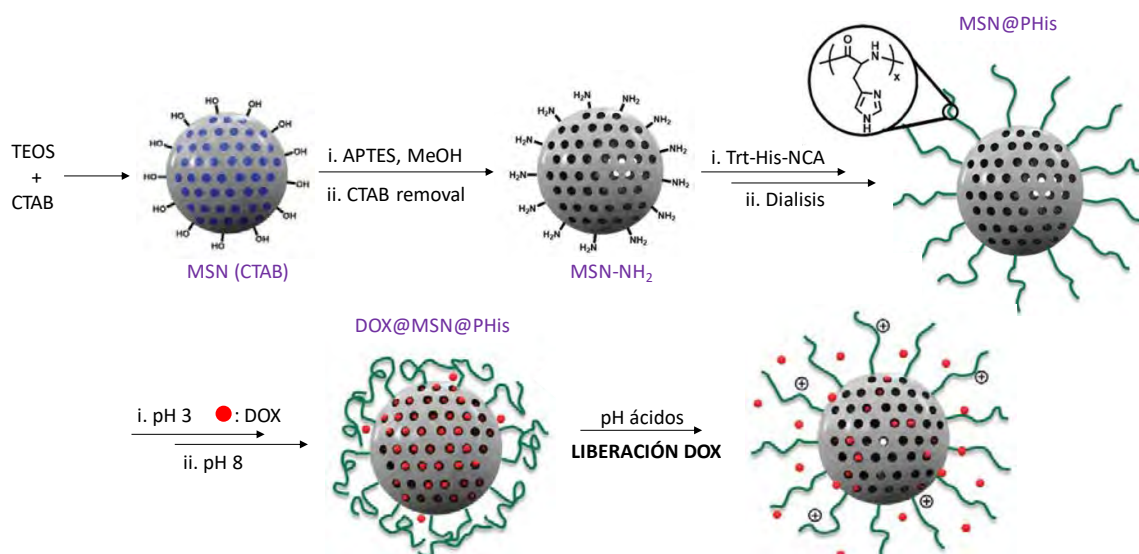


**Figura 3.9.** Ruta sintética para la preparación de unas nanopartículas funcionalizadas con el péptido PHis (MSN@PHis) y su mecanismo de liberación del fármaco doxorrubicina (DOX) en función del pH. (Polym. Chem. 2016, 7, 1475-1485).

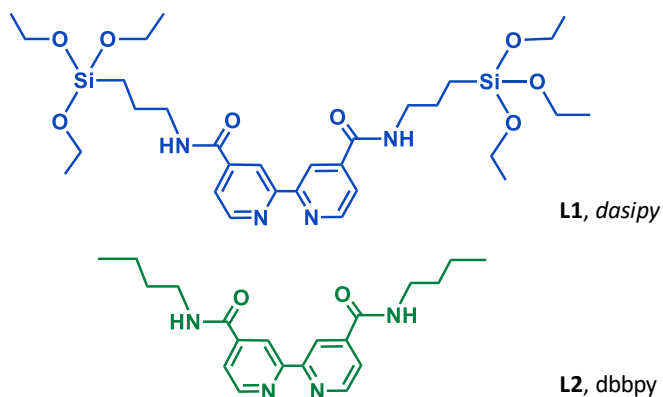
Debido al doble potencial (marcador y liberador de fármacos) de las nanopartículas de sílice, éstas pueden actuar de forma simultánea como agentes terapéuticos y de diagnóstico, convirtiéndose así en plataformas ideales en teranosis (de terapia y diagnosis),<sup>111d, 123</sup> campo que actualmente ha despertado un gran interés en el ámbito de la biomedicina.

Teniendo en cuenta todo lo anterior, así como nuestra experiencia en la síntesis de nanopartículas mesoporosas<sup>15a</sup> y de compuestos ciclometalados luminiscentes de iridio(III),<sup>15a, 93, 124</sup> decidimos diseñar sistemas nuevos y eficientes capaces de actuar, inicialmente, como

marcadores biológicos y que, posteriormente, puedan ser investigados como nanoplataformas transportadoras de fármacos.

**OBJETIVOS**

- En este capítulo se describe la síntesis, caracterización y estudio de las propiedades ópticas de dos compuestos de Ir(III):  $[\text{Ir}(\text{dFppy})_2(\text{dasipy})]\text{PF}_6$  (**7**) y  $[\text{Ir}(\text{dFppy})_2(\text{dbbpy})]\text{Cl}$  (**8**). Ambos derivados incluyen dos ligandos auxiliares diferentes basados en bipiridinas disustituidas (**L1 dasipy** y **L2 dbbpy**) (ver esquema 3.1).



**Esquema 3.1.** Vista esquemática de los ligandos empleados en la síntesis de los compuestos.

- También se describe la síntesis de nanopartículas de sílice mesoporosas (**[7]-NP<sub>OH</sub>\_IS**), las cuales se preparan de acuerdo con la Química de la Coordinación Sol-Gel, utilizando TEOS y el derivado **7** como precursores, y en presencia de CTAB como surfactante. La presencia de grupos OH en la superficie de estas nanopartículas nativas (**[7]-NP<sub>OH</sub>\_IS**) nos ha permitido modificarlas *in-situ* con dos agentes de recubrimiento, que proporcionan grupos funcionales diferentes, con el fin de modular las propiedades físico-químicas de las nanopartículas finales: dimetildietoxisilano (DMDES) y (3-aminopropil)triethoxisilano (APTES) (ver esquema 3.2). Estas moléculas cuentan con grupos alcoxilanos capaces de formar enlaces covalentes con la superficie de las nanopartículas, permitiendo así su recubrimiento y la formación de una carcasa o corona (**[7]-NP<sub>Me</sub>\_IS** y **[7]-NP<sub>APTES</sub>\_IS**) de naturaleza lipofílica e hidrofílica, respectivamente.



**DMDES:** dimetildietoxisilano

**APTES:** (3-aminopropil)triethoxisilano

**Esquema 3.2.** Vista esquemática de los agentes de funcionalización superficial.

Con fines comparativos, también se han preparado las nanopartículas de sílice con una morfología similar, pero sin la presencia del cromóforo de iridio(III) (NPs control, **NP<sub>OH</sub>**, **NP<sub>Me</sub>**, **NP<sub>APTES</sub>**). Estos materiales se han utilizado como soporte para grafted el compuesto **7** a su superficie: **[7]-NP<sub>OH</sub>\_G**, **[7]-NP<sub>Me</sub>\_G** y **[7]-NP<sub>APTES</sub>\_G**.

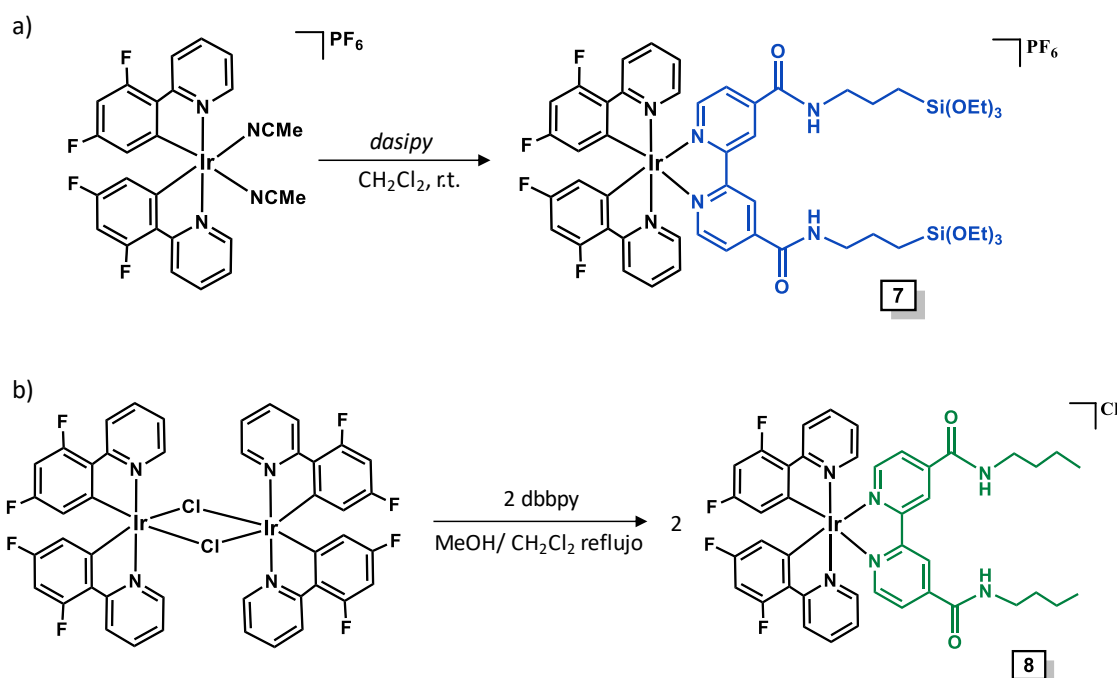
- Por último, en este capítulo también se incluye el estudio realizado acerca del uso de estas nanopartículas (**[7]-NP\_IS** y **[7]-NP\_G**) como marcadores biológicos, evaluando, en primer lugar, su citotoxicidad en dos líneas celulares tumorales diferentes, una de cáncer de cérvix (HeLa) y otra de cáncer de pulmón (A549). Posteriormente, se ha estudiado su internalización en dichas células mediante microscopía de fluorescencia y confocal. En este sentido, se establece un estudio comparativo entre los materiales **IS** y **G** con el fin de examinar la influencia de la localización del cromóforo en el comportamiento biológico de las nanopartículas.

Simultáneamente, también se estudia el comportamiento biológico del derivado **8**, utilizado como molécula modelo.

### III.1 Síntesis y caracterización de los compuestos 7-8

La reacción entre el solvato de iridio  $[\text{Ir}(\text{dFppy})_2(\text{NCMe})_2]\text{PF}_6$  y la bipiridina funcionalizada **L1** (*dasipy*) se llevó a cabo a temperatura ambiente, usando diclorometano como disolvente y una estequiométrica 1:1 (esquema 3.3, a). Tras 6 horas de reacción, se obtiene el derivado  $[\text{Ir}(\text{dFppy})_2(\text{dasipy})]\text{PF}_6$  (**7**) como un sólido de color amarillo que debe ser guardado en condiciones de atmósfera inerte dada su facilidad a auto condensar.

El compuesto homólogo conteniendo la bipiridina sustituida **L2** (*dbbpy*) y  $\text{PF}_6^-$  como contraión no se pudo preparar puro siguiendo la misma ruta sintética a partir del solvato  $[\text{Ir}(\text{dFppy})_2(\text{NCMe})_2]\text{PF}_6$  como precursor. Por ello, se decidió sintetizar el derivado análogo con  $\text{Cl}^-$  como contraión,  $[\text{Ir}(\text{dFppy})_2(\text{dbbpy})]\text{Cl}$  (**8**), siguiendo el procedimiento descrito en la bibliografía para su homólogo  $[\text{Ir}(\text{ppy})_2(\text{dbbpy})]\text{Cl}$ .<sup>91</sup> Así, la reacción entre el precursor puentes cloro  $[\text{Ir}(\text{dFppy})_2(\mu\text{-Cl})]_2$  y **L2**, en proporción 1:2, en una mezcla de metanol/diclorometano (1:2), da lugar a la obtención de  $[\text{Ir}(\text{dFppy})_2(\text{dbbpy})]\text{Cl}$  (**8**) como un sólido de color amarillo (esquema 3.3, b).



**Esquema 3.3.** Síntesis de los derivados  $[\text{Ir}(\text{dFppy})_2(\text{dasipy})]\text{PF}_6$  (**7**) (a) y  $[\text{Ir}(\text{dFppy})_2(\text{dbbpy})]\text{Cl}$  (**8**) (b).

Al igual que en casos anteriores, la caracterización de ambos derivados se llevó a cabo mediante análisis elemental, espectrometría de masas y espectroscopía FTIR, UV-visible y de RMN (ver parte experimental).

En los espectros de infrarrojo, además de las bandas correspondientes a los modos de vibración  $\nu(\text{C-H})$  de los anillos aromáticos ( $> 3000 \text{ cm}^{-1}$ ) y de las cadenas alifáticas ( $< 3000 \text{ cm}^{-1}$ ), también se muestran las correspondientes a las unidades N-H ( $3400 \text{ cm}^{-1}$ ) y C=O ( $1665 \text{ cm}^{-1}$ ) de los grupos amida de los ligandos *dasipy* y *dbbpy*. Del mismo modo, la vibración del enlace C-F aparece a  $1270 \text{ cm}^{-1}$  en ambos espectros. Por su parte, las dos bandas intensas a  $1160$  y  $1075 \text{ cm}^{-1}$  observadas en el espectro del derivado  $[\text{Ir}(\text{dFppy})_2(\text{dasipy})]\text{PF}_6$  (**7**) se corresponden con las vibraciones de los enlaces Si-O-C.

Los espectros de RMN de  $^1\text{H}$  y  $^{13}\text{C}\{^1\text{H}\}$  de ambos derivados muestran, en la relación esperada, las señales correspondientes al ligando bipiridina sustituido (*dasipy* o *dbbpy*) y la equivalencia de los ligandos ortometalados (dFppy) (ver parte experimental). Los protones CONH aparecen, como una señal ancha, a  $8.68 \text{ ppm}$  en el complejo **7**, mientras que en el derivado **8** se desplaza a campo más bajo ( $\delta 9.63$ ), probablemente debido a las interacciones con el anión cloruro ( $\text{CONH}\cdots\text{Cl}\cdots\text{HNCO}$ ), observadas por difracción de rayos X en estado sólido. Del mismo modo, los dos dobletes observados a  $\delta_F -104.71$  y  $\delta_F -107.86$  ( ${}^3J_{\text{F-F}} \approx 11.5 \text{ Hz}$ ) en los espectros de RMN de  $^{19}\text{F}\{^1\text{H}\}$  también confirman la presencia de un solo tipo de dFppy.

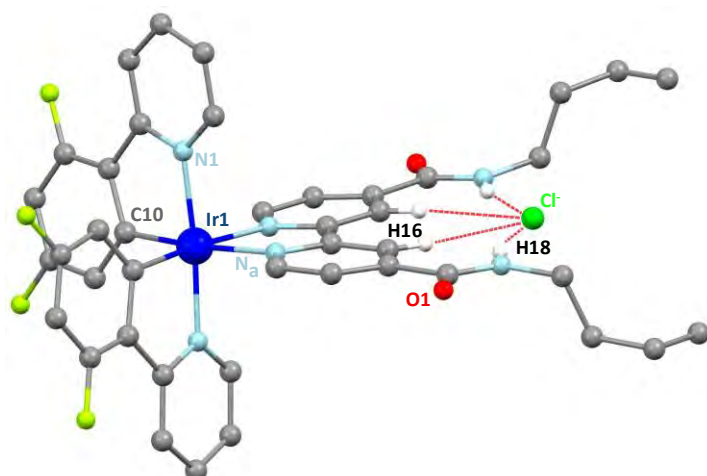


**Figura 3.10.** Estructura molecular del compuesto  $[\text{Ir}(\text{dFppy})_2(\text{dbbpy})]\text{Cl}\cdot\text{CHCl}_3$  (**8·CHCl<sub>3</sub>**). Distancias ( $\text{\AA}$ ) y ángulos ( $^\circ$ ) de enlace seleccionados: Ir(1)-N(1) 2.049(3), Ir(1)-C(10) 2.008(4), Ir(1)-N(a) 2.125 (8), Cl(1)…H(16) 2.602(5), Cl(1)…H(18) 2.458(3), N(1)-Ir(1)-C(10) 80.4(6), N(1)-Ir(1)-C(10') 95.7(3), N(1)-Ir(1)-N(1') 174.6(3), N(a)-Ir(1)-N(a') 77.2(9). Más información en el anexo III, tabla A.III.1.

La estructura del compuesto  $[\text{Ir}(\text{dFppy})_2(\text{dbbpy})]\text{Cl}$  (**8**) ha sido confirmada mediante un estudio de difracción de rayos X sobre un monocrystal amarillo, obtenido por difusión de *n*-hexano en una disolución saturada del complejo en diclorometano a temperatura ambiente. Como se observa en la figura 3.10, la estructura del catión molecular **8<sup>+</sup>** presenta el entorno octaédrico característico de los derivados de Ir<sup>III</sup>, además de la disposición mutuamente *trans* de

los átomos de nitrógeno de los ligandos 2-(2,4-difluorofenil)piridina. Las distancias y ángulos de enlace son comparables con los obtenidos mediante cálculos teóricos (ver anexo III, tabla A.III.3), y similares a los encontrados en compuestos análogos.<sup>91</sup> Debido a la presencia de grupos carboxiamida (CONH), se observan también interacciones entre el anión Cl<sup>-</sup>, que actúa como contraión, y los átomos de hidrógeno H16 y H18 de la bipiridina disustituida (Cl···H(16) 2.602(5) Å, Cl···H(18) 2.458(3) Å); hecho que podría modificar la naturaleza electrónica de los ligandos e influir en sus propiedades ópticas.

### **III.2 Propiedades fotofísicas**

#### *i. Espectros de absorción*

Como se muestra en la figura 3.11, ambos derivados, [Ir(dFppy)<sub>2</sub>(dasipy)]PF<sub>6</sub> (**7**) y [Ir(dFppy)<sub>2</sub>(dbbpy)]Cl (**8**), muestran un espectro de absorción muy similar. Así, en disolución de THF, presentan una banda intensa en la zona de alta energía ( $\lambda < 300$  nm) asociada, de acuerdo con cálculos TD-DFT, con transiciones permitidas  $\pi-\pi^*$  centradas en el ligando dFppy. La absorción que aparece en torno a 310 nm, relacionada con las transiciones S<sub>19</sub> para **7** y S<sub>20</sub> para **8**, se atribuye a una mezcla <sup>1</sup>ILCT y <sup>1</sup>LL'CT (L: dFppy, L': dasipy o dbbpy), con cierto carácter <sup>1</sup>ML'CT (ver figura 3.12). Por su parte, la banda de baja energía observada a 360 nm coincide bastante bien con las transiciones calculadas entre 380-360 nm, aproximadamente, (ver anexo III, figura A.III.6) relacionadas con transiciones HOMO → L+2, H-4 → LUMO y HOMO → L+1 (para **7**) y H-1 → LUMO, HOMO → L+1 y HOMO → L+2 (para **8**). En este caso, los orbitales HOMO, H-4 (en **7**) y HOMO, H-1 (en **8**) se encuentran centrados en los átomos de iridio (aprox. 40%) y en los anillos fenílicos de los ligandos dFppy (aprox. 60%); mientras que los orbitales LUMO, L+1, L+2 están fundamentalmente localizados en la bipiridina sustituida (96% para **7** y 75% para **8**), con cierta participación de los ligandos dFppy. Así, esta última absorción se atribuye a una mezcla de transferencia de carga de carácter ligando-ligando ( $\pi(\text{dFppy}) \rightarrow \pi^*(\text{bpy})$ ) y metal-ligando ( $d(\text{Ir}) \rightarrow \pi^*(\text{bpy})$ ) (<sup>1</sup>LL'CT/<sup>1</sup>ML'CT) con cierta contribución intraligando. Además, debido al fuerte acoplamiento spin-órbita (SOC) del centro de iridio, ambos derivados muestran absorciones débiles a muy baja energía ( $\lambda > 400$  nm) atribuidas a transiciones prohibidas singlete-triplete (<sup>3</sup>ML'CT/<sup>3</sup>LL'CT).

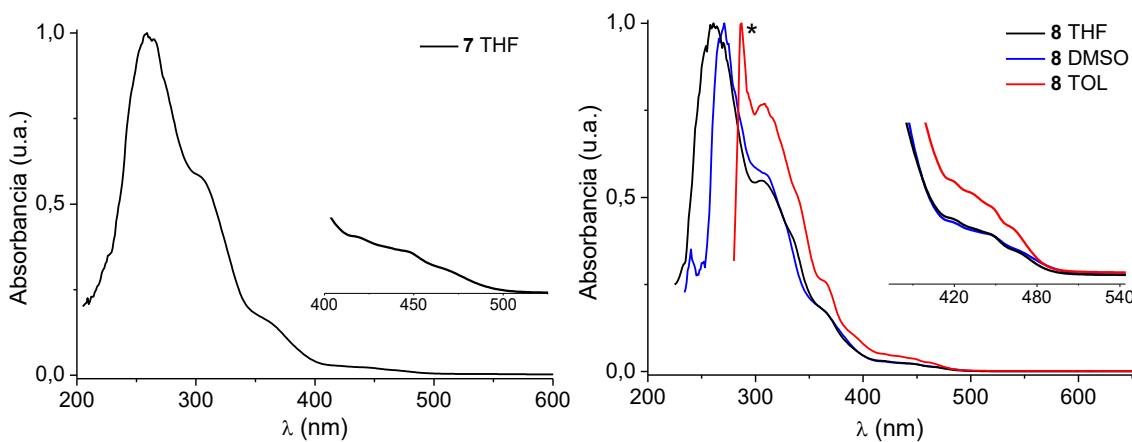


**Figura 3.11.** Espectros de absorción de los compuestos  $[\text{Ir}(\text{dFppy})_2(\text{dasipy})]\text{PF}_6$  (**7**) ( $5 \times 10^{-5}$  M, THF) (izquierda) y  $[\text{Ir}(\text{dFppy})_2(\text{dbppy})]\text{Cl}$  (**8**) ( $5 \times 10^{-5}$  M, THF, DMSO y Tolueno) (derecha). (\*) Banda correspondiente al tolueno.

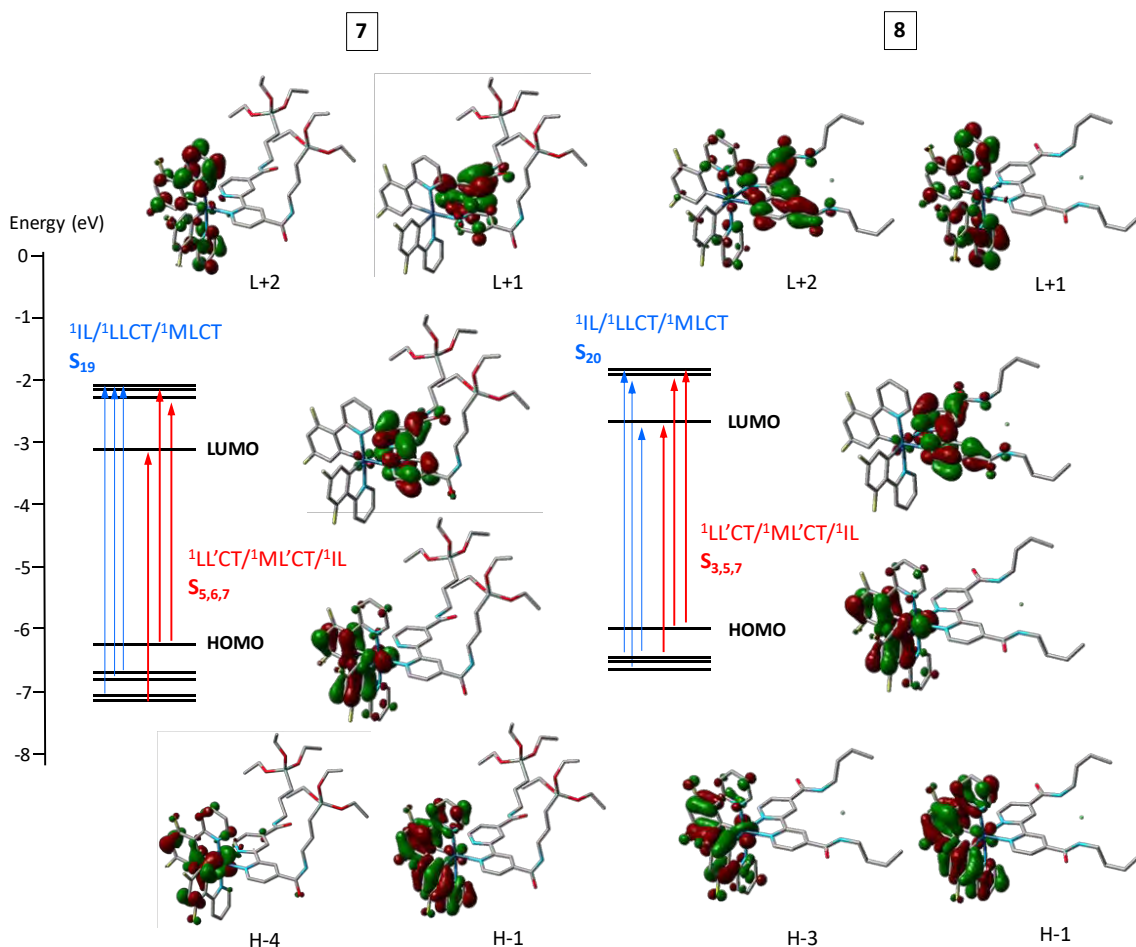


**Figura 3.12.** Orbitales moleculares y transiciones implicadas en las absorciones de los compuestos  $[\text{Ir}(\text{dFppy})_2(\text{dasipy})]\text{PF}_6$  (**7**, izquierda) y  $[\text{Ir}(\text{dFppy})_2(\text{dbppy})]\text{Cl}$  (**8**, derecha) en THF.

Los espectros UV-vis del derivado **8** se registraron en disolventes con diferentes polaridades (THF, DMSO y tolueno). Como se muestra en la figura 3.11 (derecha), no se observan cambios significativos en las bandas de absorción al modificar la polaridad del disolvente. No obstante,

como se recoge en la tabla 3.1, se observa un ligero solvatocromismo positivo al aumentar la polaridad del disolvente (363 nm en tolueno, 365 nm en THF, 368 nm en DMSO), lo que está de acuerdo con una cierta transferencia de carga en esta transición.

**Tabla 3.1.** Datos de absorción en disolución ( $5 \times 10^{-5}$  M) y en estado sólido de los compuestos  $[\text{Ir}(\text{dFppy})_2(\text{dasipy})]\text{PF}_6$  (**7**) y  $[\text{Ir}(\text{dFppy})_2(\text{dbbpy})]\text{Cl}$  (**8**).

Muestra	$\lambda_{\text{abs}}/\text{nm} (\epsilon/\text{M}^{-1}\text{L}^{-1})$
$[\text{Ir}(\text{dFppy})_2(\text{dasipy})]\text{PF}_6$ <b>(7)</b>	260 (54.04), 274h (47.89), 305 (31.59), 360 (8.77), 417 (1.05), 445 (0.78), 470 (0.43) <b>THF</b> 285, 312, 380, 420, 445, 476 <b>Solid</b>
$[\text{Ir}(\text{dFppy})_2(\text{dbbpy})]\text{Cl}$ <b>(8)</b>	287* (56.90), 308 (47.81), 363 (12.28), 419 (3.23), 432 (2.84), 446 (2.40), 463 (1.64) <b>Tol</b> 262 (67.90), 306 (29.88), 365 (9.85), 419 (1.74), 444 (1.31), 467 (0.75) <b>THF</b> 273 (62.64), 310 (33.79), 368 (9.52), 418 (1.67), 447 (1.25), 469 (0.71) <b>DMSO</b> 285, 312, 330, 365, 422, 445, 470 <b>Solid</b>

(\* ) Banda correspondiente al tolueno.

En ambos derivados, los espectros de absorción en estado sólido muestran un perfil similar a los descritos en disolución, intensificándose las absorciones de más baja energía (ver tabla 3.1 y figura 3.20 para **7** en la descripción de los materiales de base silícea).

### *ii. Espectros de emisión*

Los espectros de emisión de los dos compuestos se han estudiado en disolución y en estado sólido, a temperatura ambiente y a 77K (ver figura 3.13). Los datos se detallan en la tabla 3.2.

En disolución de THF, ambos compuestos (**7**, **8**) muestran una emisión no estructurada centrada a  $\lambda_{\text{max}}$  550 nm y 520 nm, respectivamente, que se desplaza hacia el azul a 77K ( $\lambda_{\text{max}}$  510 nm **7**, 500 nm **8**). Como se observa en la figura 3.14, en ambos derivados, el orbital SOMO se localiza en la bipiridina sustituida (*dasipy* **7** y *dbbpy* **8**), y el SOMO-1 en los ligandos dFppy y en el centro de iridio, de modo que la emisión se atribuye a un estado excitado con mezcla de transferencia de carga  $\text{Ir} \rightarrow \text{N}^{\Delta}\text{N}$  y  $\text{dFppy} \rightarrow \text{N}^{\Delta}\text{N}$  ( ${}^3\text{ML}'\text{CT}/\text{LL}'\text{CT}$ ).

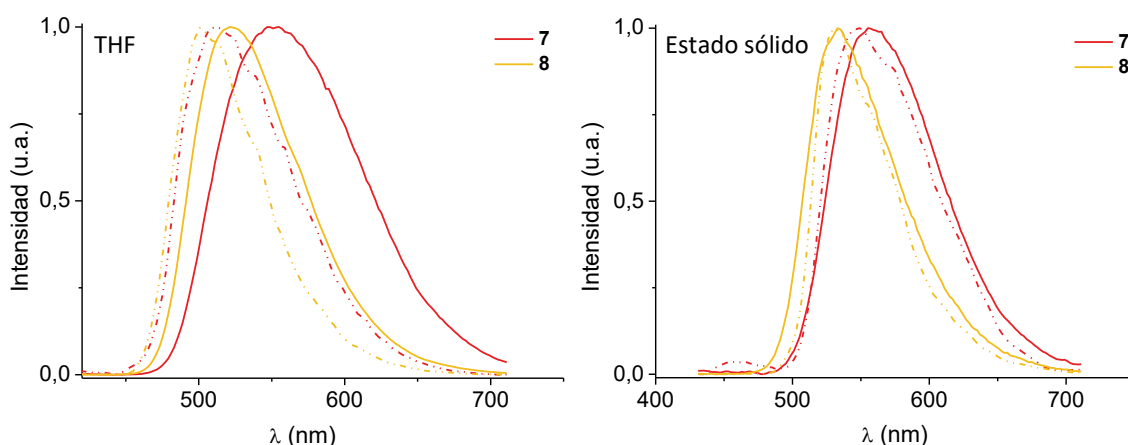


**Figura 3.13.** Espectros de emisión de **7** (rojo) y **8** (amarillo) en disolución ( $5 \times 10^{-4}$  M, THF) (izquierda) y en estado sólido (derecha) a temperatura ambiente (—) y 77K (---). ( $\lambda_{\text{ex}}$  365 nm).

El desplazamiento a energías más altas observado en el derivado **8** con respecto a **7** (ver figura 3.13 y tabla 3.2) puede atribuirse a la presencia de interacciones CONH $\cdots$ Cl entre los grupos acetamida de la bipiridina *dbbpy* y el Cl $^-$  que reducen su electronegatividad, incrementando la energía del LUMO y el salto electrónico de la transición. Del mismo modo, las emisiones calculadas (536 nm **8** vs. 575 nm **7**) también reproducen el desplazamiento hipsocrómico de **8** en relación a **7**.

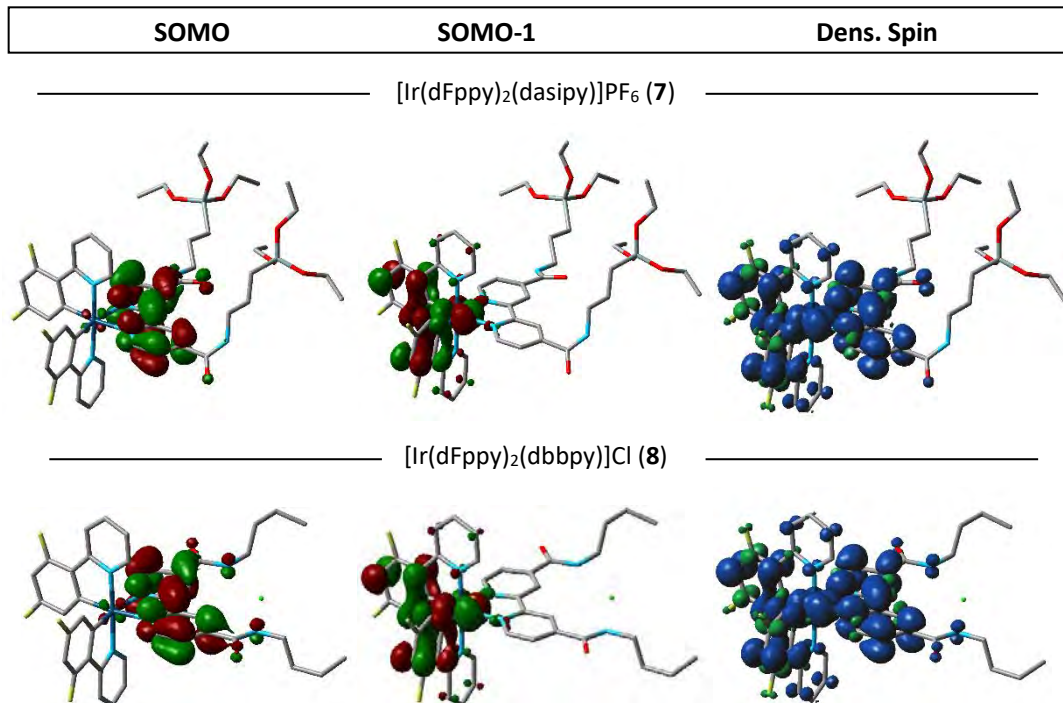


**Figura 3.14.** Orbitales SOMO, SOMO-1 y densidad de spin de los derivados [Ir(dFppy)<sub>2</sub>(dasipy)]PF<sub>6</sub> (**7**) (arriba) y [Ir(dFppy)<sub>2</sub>(dbbpy)]Cl (**8**) (abajo) en THF.

En ambos derivados, el rendimiento cuántico es considerablemente más alto en disolución (55.8% **7**, 61.6% **8**) que en estado sólido (29.4% **7**, 42.2% **8**). Este hecho puede atribuirse a la presencia de interacciones  $\pi\cdots\pi$  entre los ligandos, que favorece la desactivación de la emisión a través de la aniquilación triplete-triplete.

Las diferencias observadas en los rendimientos de los compuestos **7** y **8** están de acuerdo con los valores calculados para las constantes radiativas ( $K_r$ ) y no radiativas ( $K_{nr}$ ) (ver tabla 3.2). Así, el derivado **8**, que presenta una mayor transición electrónica, muestra mayores valores de  $K_{nr}$  que **7** y, en consecuencia, mayores rendimientos.

**Tabla 3.2.** Datos de emisión de los compuestos  $[\text{Ir}(\text{dFppy})_2(\text{dasipy})]\text{PF}_6$  (**7**) y  $[\text{Ir}(\text{dFppy})_2(\text{dbbpy})]\text{Cl}$  (**8**) en estado sólido y en disolución ( $5 \times 10^{-4}$  M), a temperatura ambiente y a 77K. Datos de las constantes radiativa ( $K_r$ ) y no radiativa ( $K_{nr}$ ) de cada derivado a temperatura ambiente.

Muestra	Medio (T/K)	$\lambda_{em}^{(a)}$ (nm)	$\Delta E(T_1-S_0)^{(b)}$ (nm)	$\tau$ ( $\mu\text{s}$ )	$\phi$ (%)	$K_r$	$K_{nr}$
$[\text{Ir}(\text{dFppy})_2(\text{dasipy})]\text{PF}_6$ ( <b>7</b> )	Solid (298)	560	---	0.35	29.4	$8.4 \times 10^5$	$2.0 \times 10^6$
	Solid (77)	550 <sub>max</sub> , 580		11.8	---		
	THF (298)	550	575	0.71	55.8	$7.9 \times 10^5$	$6.2 \times 10^5$
$[\text{Ir}(\text{dFppy})_2(\text{dbbpy})]\text{Cl}$ ( <b>8</b> )	THF (77)	510		8.10	---		
	Solid (298)	533	---	0.44	42.2	$9.6 \times 10^5$	$1.3 \times 10^6$
	Solid (77)	530, 560 <sub>sh</sub>		12.60	---		
	THF (298)	520	536	0.85	69.6	$8.1 \times 10^5$	$3.6 \times 10^5$
	THF (77)	500		10.2	---		
	Tol (298)	495	515	0.90	73.5	$8.2 \times 10^5$	$2.9 \times 10^5$
	DMSO (298)	565	557	0.81	53.2	$6.6 \times 10^5$	$5.7 \times 10^5$

(a)  $\lambda_{ex}$  365-440 nm para **7**.  $\lambda_{ex}$  365-580 nm para **8**. (b) Emisión calculada como la diferencia de energía entre la energía del triplete optimizado ( $T_1$ ) y el estado fundamental ( $S_0$ ).

Por último, también se ha examinado la influencia de la polaridad del disolvente en la emisión del compuesto **8** (figura 3.15). En contraste con la pequeña influencia observada en el espectro de absorción, en este caso, se observa un claro desplazamiento del máximo emisivo en función de la polaridad del disolvente empleado, confirmando así el notable carácter de transferencia de carga del estado excitado. Así, al aumentar la polaridad del disolvente utilizado (tolueno < THF < DMSO), la banda de emisión se desplaza hacia menores energías, pasando de 490 nm en tolueno a 565 nm en DMSO, hecho que también ha sido confirmado mediante cálculos teóricos (ver tabla 3.2 y anexo III). El marcado solvatocromismo positivo de 75 nm, aproximadamente, está de acuerdo con un estado excitado más polar que el estado fundamental. No obstante, en este derivado, la influencia de la ruptura de las asociaciones del

cación **8<sup>+</sup>** con el anión Cl<sup>-</sup> al aumentar la polaridad del disolvente puede jugar un papel importante en la energía del estado excitado. Además, las variaciones observadas en **8** en los diferentes disolventes (73.5% tol > 69.6% THF > 53.2% DMSO) estarían de acuerdo con la disminución en los valores de las constantes no radiativas (ver tabla 3.2) al aumentar la energía de la transición HOMO-LUMO.

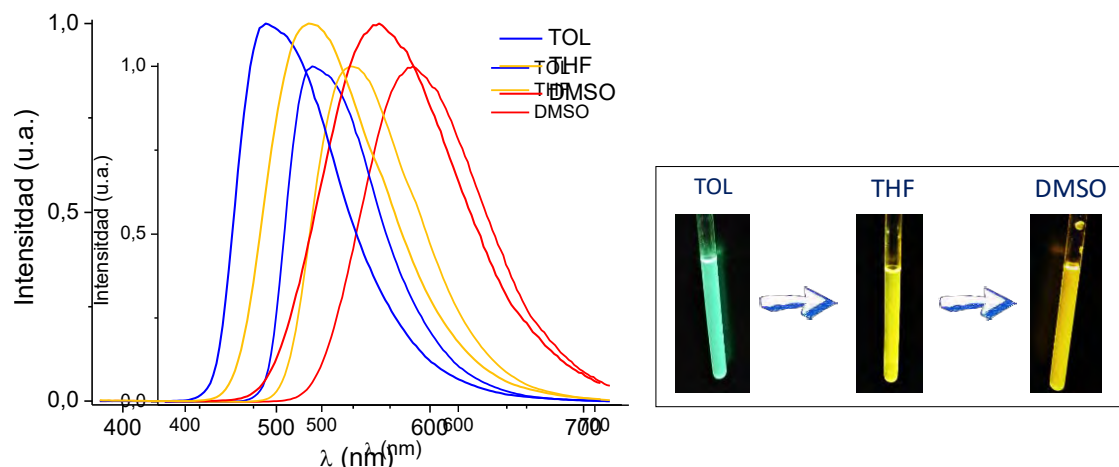


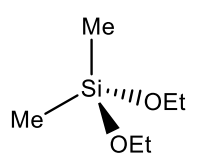
**Figura 3.15.** Espectros de emisión ( $\lambda_{\text{ex}} = 365 \text{ nm}$ ) del compuesto  $[\text{Ir}(\text{dFppy})_2(\text{dbppy})]\text{Cl}$  (**8**) en disoluciones de tolueno, THF y DMSO ( $5 \times 10^{-4} \text{ M}$ ), a temperatura ambiente (izquierda). Imágenes de la emisión de cada disolución bajo luz UV y a temperatura ambiente (derecha).

### III.3 Síntesis de nanopartículas mesoporosas de sílice (**NP<sub>OH</sub>**, **NP<sub>Me</sub>**, **NP<sub>APTES</sub>**)

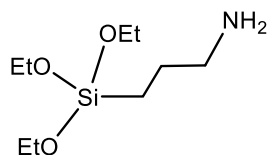
La síntesis de estas nanopartículas mesoporosas se llevó a cabo en base a la Química de la Coordinación Sol-Gel,<sup>15a, 35b, 93</sup> utilizando como precursor el derivado de iridio(III) [Ir(dFppy)<sub>2</sub>(dasipy)]PF<sub>6</sub> (**7**) y en presencia de CTAB como surfactante. En todos los casos se añadieron las cantidades de cromóforo y TEOS adecuadas para obtener nanopartículas con un contenido nominal de metal de un 0.2 wt%.

Además, y siguiendo los objetivos planteados en este capítulo, realizamos modificaciones en la superficie de las nanopartículas para evaluar su efecto al exponerlas en medios celulares. Con este fin, una primera modificación se llevó a cabo empleando una funcionalización de tipo amino, utilizando el agente de acoplamiento (3-aminopropil)triethoxsilano (APTES). Por otra parte, llevamos a cabo una segunda funcionalización, más hidrofóbica, que permitiera reducir la agregación entre partículas empleando, para ello, el dietoxidimetsiloxano (DMDES) como agente capeante (ver esquema 3.4). De este modo, dispondremos de tres tipos diferentes de nanopartículas: las no tratadas o nativas (**NP<sub>OH</sub>**) y las modificadas con DMDES (**NP<sub>Me</sub>**) o con APTES (**NP<sub>APTES</sub>**).

La modificación de las nanopartículas de sílice nativas con funcionalizaciones que contienen grupos amino permite variar su potencial zeta desde valores muy negativos, en nanopartículas no funcionalizadas (-43 ± 2 mV en EtOH, -35 ± 3 mV en agua),<sup>125</sup> a muy positivos (64 ± 3 mV en EtOH, 16 ± 2 mV en agua),<sup>125</sup> debido a la basicidad de las aminas primarias presentes en el APTES. Este cambio en la naturaleza iónica de las nanopartículas podría favorecer su interacción y afinidad con la membrana celular al reducirse las repulsiones, ya que esta última está cargada negativamente. Por el contrario, las partículas funcionalizadas con DMDES poseerán un potencial negativo relativamente similar al de las nanopartículas nativas no modificadas, tal y como sucede con otros recubrimientos hidrofóbicos.<sup>125</sup>



**DMDES:** dimetildietoxisilano



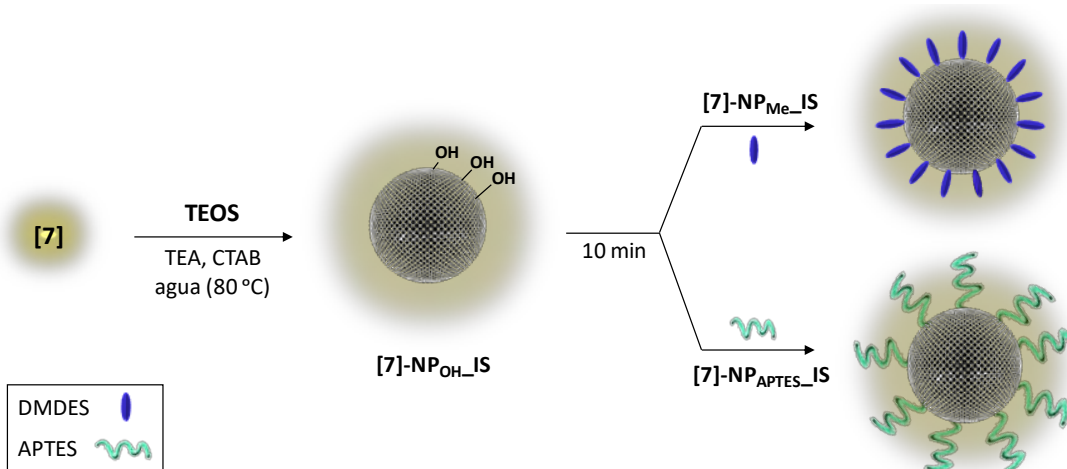
**APTES:** (3-aminopropil)triethoxsilano

**Esquema 3.4.** Vista esquemática de los agentes de capeo dietoxidimetsiloxano (DMDES) (izquierda) y (3-aminopropil)triethoxsilano (APTES) (derecha).

La síntesis de las diferentes nanopartículas se representa en el esquema 3.5. Así, la adición rápida de una disolución de **7** en 3 mL etanol y TEOS sobre una mezcla en medio básico (trietanolamina, TEA) de CTAB en agua a 80°C, permite la condensación *in-situ* de los restos alcoxisilanos del cromóforo y la fuente de sílice. De esta forma, tras dos horas de reacción a dicha temperatura, se obtienen las nanopartículas mesoporosas con el cromóforo incorporado de forma homogénea en la matriz del material (**[7]-NP<sub>OH</sub>\_IS**). Una vez obtenidas las nanopartículas, la eliminación del surfactante se consigue mediante intercambio iónico con sucesivos lavados con una disolución saturada de nitrato de amonio (ver parte experimental).

La funcionalización superficial de estas nanopartículas se llevó a cabo *in-situ* añadiendo a la mezcla anterior, tras 10 minutos de reacción, el agente de capeo correspondiente (DMDES o APTES). De este modo, una vez transcurridas las dos horas de reacción a 80°C, se obtienen los materiales **[7]-NP<sub>Me</sub>\_IS** y **[7]-NP<sub>APTES</sub>\_IS** con una corona perfectamente definido, como se confirma mediante las imágenes obtenidas por microscopía de transmisión (TEM) y de barrido (FESEM), que se comentarán más adelante.

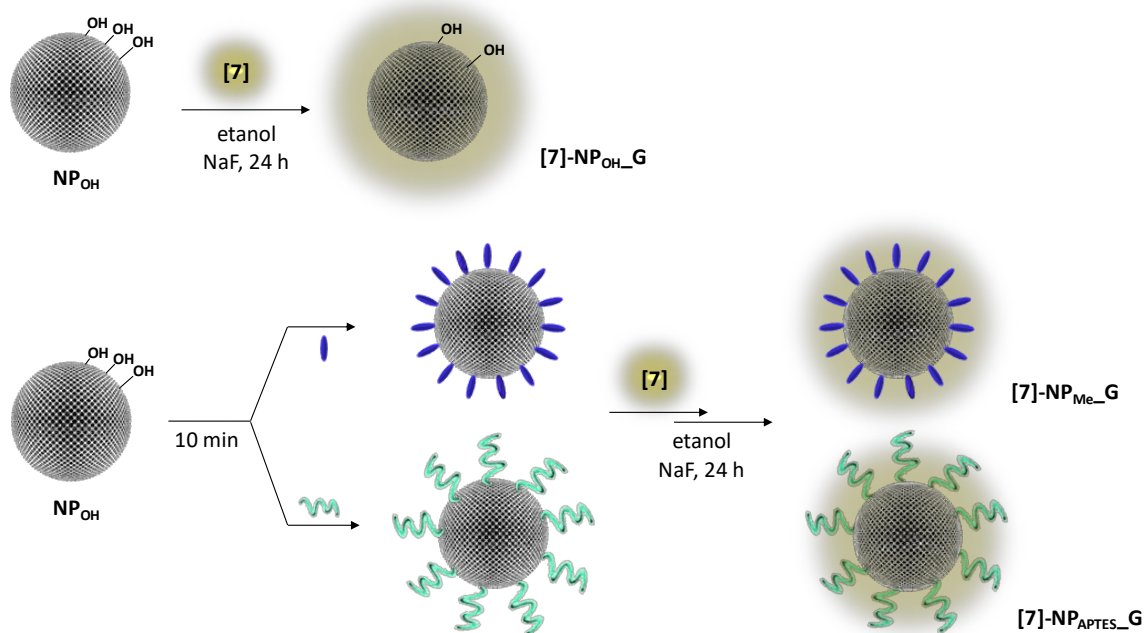
Del mismo modo, y con fines comparativos, se sintetizaron los correspondientes materiales de control (**NP<sub>OH</sub>**, **NP<sub>Me</sub>** y **NP<sub>APTES</sub>**) siguiendo la misma ruta sintética que la descrita para las nanopartículas *in-situ*, pero sin la adición del cromóforo **7**.



**Esquema 3.5.** Representación esquemática de la síntesis de los diferentes tipos de nanopartículas *in-situ*: **[7]-NP<sub>OH</sub>\_IS**, **[7]-NP<sub>Me</sub>\_IS** and **[7]-NP<sub>APTES</sub>\_IS**.

Simultáneamente, y como se comenta en la introducción del capítulo, también se prepararon los correspondientes materiales grafteados (**[7]-NP<sub>OH</sub>\_G**, **[7]-NP<sub>Me</sub>\_G** y **[7]-NP<sub>APTES</sub>\_G**), utilizando un procedimiento *post-sintético* previamente descrito en la literatura.<sup>23a-c, 23e</sup> De este modo, se podrá evaluar el efecto que tiene la localización del cromóforo (interior **IS** o superficial **G**) en la actividad biológica de las nanopartículas.

Como se recoge en el esquema 3.6, en este caso, la preparación se realiza mediante el tratamiento de una suspensión en etanol de cada uno de los materiales de control ( $\text{NP}_{\text{OH}}$ ,  $\text{NP}_{\text{Me}}$  y  $\text{NP}_{\text{APTES}}$ ) con una disolución del complejo **7** en el mismo disolvente. La agitación de la mezcla durante tres horas a temperatura ambiente nos permite obtener una distribución homogénea del cromóforo en la suspensión y su difusión a través de los poros de la sílice. Tras ello, la adición de una disolución acuosa de NaF inicia las reacciones de condensación entre el derivado **7** y los restos alcóxidos que se encuentran en la superficie de las nanopartículas de control. Así, tras 24 horas de reacción a temperatura ambiente, se obtienen los correspondientes materiales graftedeados (ver parte experimental).



**Esquema 3.6.** Representación esquemática de la síntesis de los diferentes tipos de nanopartículas graftedeadas:  $[7]\text{-NP}_{\text{OH}}\text{-G}$ ,  $[7]\text{-NP}_{\text{Me}}\text{-G}$  and  $[7]\text{-NP}_{\text{APTES}}\text{-G}$ .

### III.4 Caracterización de las nanopartículas **[7]**-NP\_IS y **[7]**-NP\_G

#### III.4.1 Caracterización textural

Al igual que para los materiales de capítulos anteriores, los experimentos de fisisorción se llevaron a cabo en la Universidad de Alicante, por el grupo de investigación del Prof. Javier García Martínez.

Los estudios de adsorción/desorción de nitrógeno a 77K confirman la naturaleza mesoporosa de todas las nanopartículas, ya que todas ellas muestran isotermas de tipo IV (figura 3.16), similares a las obtenidas para cada uno de los materiales de control. También se observa un salto adicional a presiones relativas superiores a 0.9, típico de una porosidad interparticular.

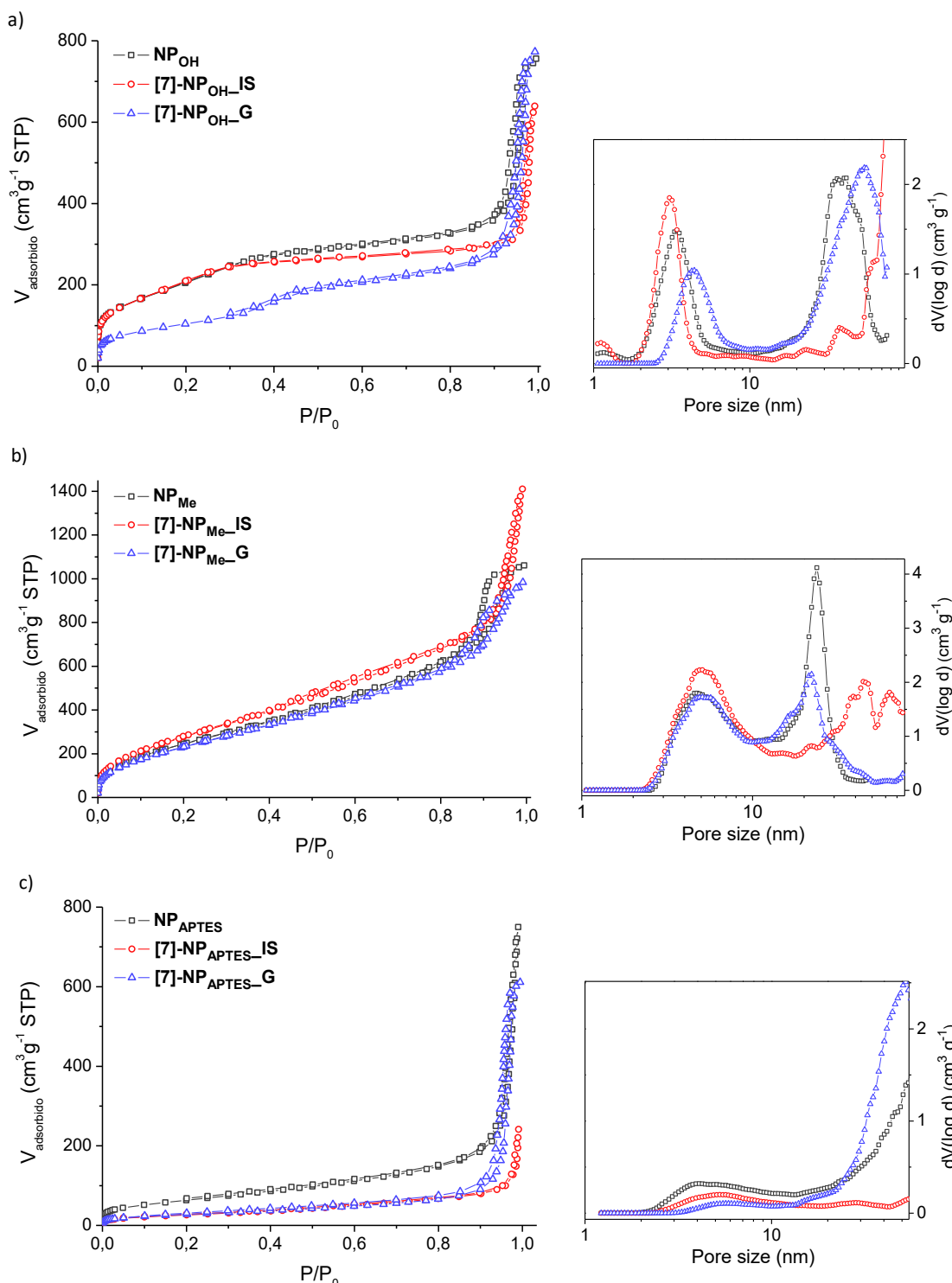


**Figura 3.16.** Isotermas de adsorción/desorción de nitrógeno a 77K y distribución de tamaño de poro de **[7]-NP<sub>OH</sub>** (a), **[7]-NP<sub>Me</sub>** (b) y **[7]-NP<sub>APTES</sub>** (c) en comparación con los materiales control **NP<sub>OH</sub>**, **NP<sub>Me</sub>** y **NP<sub>APTES</sub>**.

En cuanto al resto de parámetros texturales, los materiales híbridos (**NP\_IS** y **NP\_G**) y los de control (**NP**) muestran, en general, valores similares de volumen y diámetro promedio de poro, lo que sugiere una incorporación homogénea del compuesto en la matriz de sílice. No obstante, hay que destacar que las nanopartículas tratadas con APTES (**NP<sub>APTES</sub>**) muestran áreas superficiales considerablemente más pequeñas que el resto de los materiales ( $A_{BET}$ ,  $m^2/g$ : 230 **NP<sub>APTES</sub>**, 97 [7]-**NP<sub>APTES\_IS</sub>** y 100 [7]-**NP<sub>APTES\_G</sub>**), así como una mesoporosidad parcialmente bloqueada (ver tabla 3.3). Este hecho podría atribuirse a la presencia de las cadenas alifáticas del agente capeante, aunque, no podemos descartar una extracción incompleta del surfactante.

El contenido de iridio en cada una de las muestras se determinó mediante análisis ICP, los cuales muestran diferentes rendimientos de incorporación en función del tipo de nanopartícula. Así, [7]-**NP<sub>OH</sub>** y [7]-**NP<sub>Me</sub>** incorporan una mayor cantidad de cromóforo en los materiales grafteados que en los *in-situ* (aprox. 0.25 wt% **G** vs. 0.10 wt% **IS**), mientras que en las nanopartículas recubiertas con APTES, el material *in-situ* [7]-**NP<sub>APTES\_IS</sub>** es el que muestra un mayor rendimiento de incorporación (0.21 wt% **IS** vs. 0.11 wt% **G**). Este comportamiento podría estar relacionado con la dificultad del compuesto a unirse covalentemente a la superficie del material grafteado, debido al impedimento creado por las cadenas alifáticas del APTES.

**Tabla 3.3.** Parámetros texturales de los diferentes tipos de nanopartículas ([7]-**NP<sub>OH</sub>**, [7]-**NP<sub>Me</sub>** y [7]-**NP<sub>APTES</sub>**) en comparación con sus correspondientes materiales de control (**NP<sub>OH</sub>**, **NP<sub>Me</sub>** y **NP<sub>APTES</sub>**).

Muestra	M <sup>(a)</sup> (wt%)	A <sub>BET</sub> <sup>(b)</sup> (m <sup>2</sup> /g)	V <sub>p</sub> <sup>(c)</sup> (cm <sup>3</sup> /g)	d <sub>p</sub> <sup>(d)</sup> (nm)	V <sub>meso</sub> <sup>(e)</sup> (cm <sup>3</sup> /g)
<b>NP<sub>OH</sub></b>	---	760	1.2	3.0	0.5
[7]- <b>NP<sub>OH_IS</sub></b>	0.10 (0.2)	780	1.0	3.1	0.4
[7]- <b>NP<sub>OH_G</sub></b>	0.25 (0.2)	390	1.2	4.3	0.4
<b>NP<sub>Me</sub></b>	---	980	1.6	4.8	0.9
[7]- <b>NP<sub>Me_IS</sub></b>	0.11 (0.2)	1120	2.2	5.0	1.1
[7]- <b>NP<sub>Me_G</sub></b>	0.26 (0.2)	950	1.5	5.1	0.9
<b>NP<sub>APTES</sub></b>	---	230	1.2	4.0	0.23
[7]- <b>NP<sub>APTES_IS</sub></b>	0.21 (0.2)	97	0.4	5.2	0.1
[7]- <b>NP<sub>APTES_G</sub></b>	0.11 (0.2)	100	0.9	5.5	0.1

(a) Contenido metálico calculado mediante análisis ICP-MS después del tratamiento de las muestras con HF diluido. Los valores entre paréntesis representan el contenido nominal de metal. (b) Área superficial BET estimada mediante el método BET empleando los datos de adsorción en el rango de presiones relativas P/P<sub>0</sub> entre 0.05-0.30. (c) Volumen de poro. (d) Diámetro promedio de poro calculado a partir de la rama de adsorción de la isoterma, utilizando el modelo NLDFT. (e) Volumen de mesoporo tomado directamente de la rama de adsorción de la isoterma a P/P<sub>0</sub> = 0.8. Todas las muestras fueron desgasificadas antes de realizar las medidas de las isotermas.

La morfología de los diferentes materiales se evaluó mediante microscopía de transmisión (TEM) y de barrido (FESEM). En las figuras 3.17 y 3.18 se recogen algunas de las imágenes obtenidas para las nanopartículas **IS** (ver anexo III, figura A.III.10 para las muestras control y **NP\_G**).

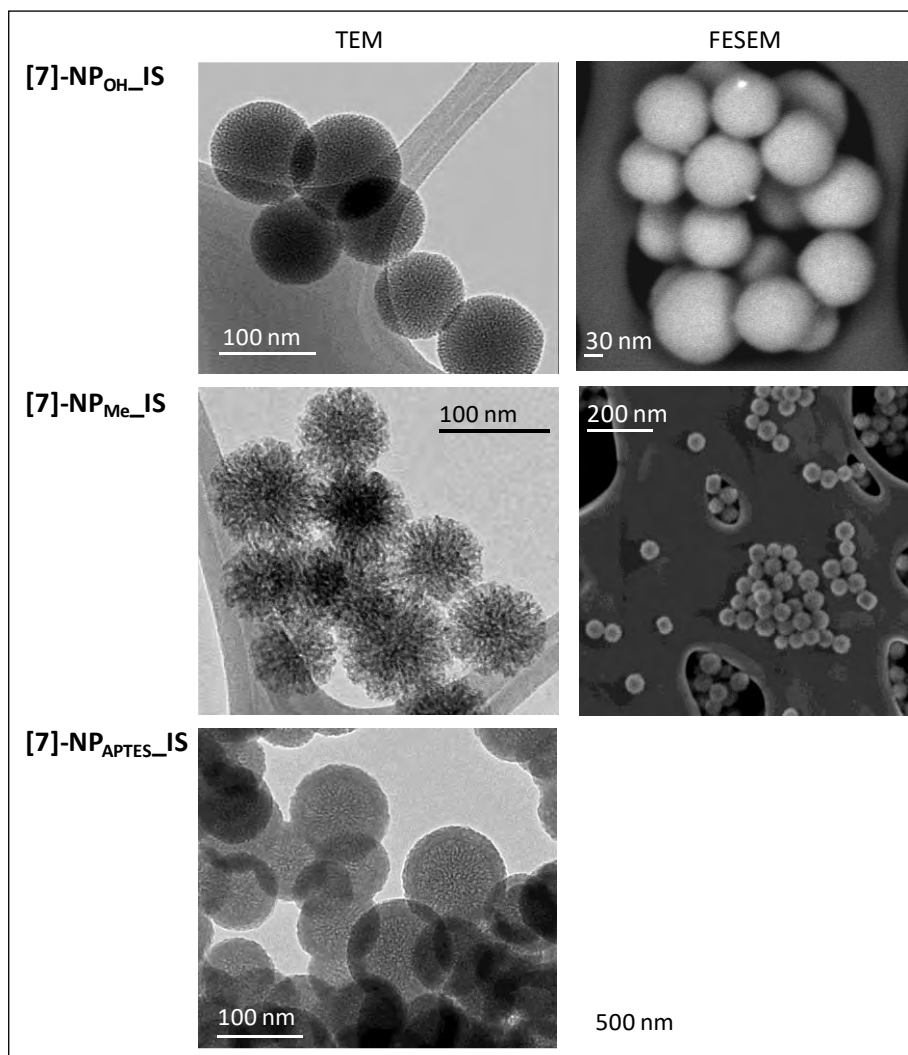


**Figura 3.17.** Imágenes TEM y FESEM representativas de las nanopartículas *in-situ*: [7]-NP<sub>OH</sub>\_IS (arriba), [7]-NP<sub>Me</sub>\_IS (medio) y [7]-NP<sub>APTES</sub>\_IS (abajo).

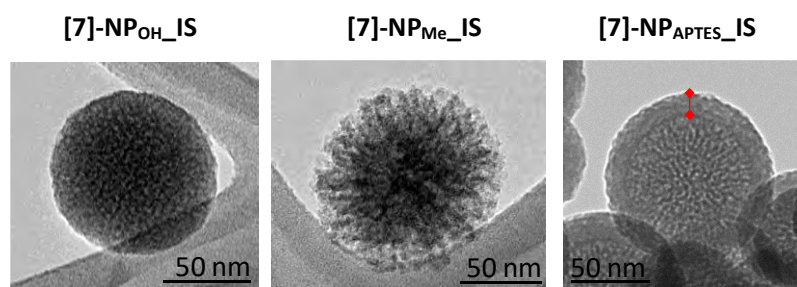


**Figura 3.18.** Imágenes TEM de nanopartículas aisladas de [7]-NP<sub>OH</sub>\_IS (izquierda), [7]-NP<sub>Me</sub>\_IS (centro) y [7]-NP<sub>APTES</sub>\_IS (derecha).

Como se observa en las imágenes, todos los materiales están formados por nanopartículas esféricas, más o menos discretas, de tamaños promedio comprendidos entre 80 y 100 nm de diámetro. Además, muestran la mesoporosidad característica que proporciona el uso de CTAB como surfactante. A pesar de las similitudes en forma y tamaño, se observa una clara diferencia en la morfología y estructura de las mismas. Así, mientras el material recubierto con DMDES (**NP<sub>Me</sub>**) muestra una forma estrellada con una mesoporosidad abierta, las nanopartículas no tratadas (**NP<sub>OH</sub>**) tienen una morfología mucho más sencilla (ver figuras 3.17 y 3.18). Además, las partículas modificadas con APTES (**NP<sub>APTES</sub>**) tienen una corona perfectamente definida de, aproximadamente, unos 10 nm de grosor que se corresponde con la cadena alifática del agente de recubrimiento (figura 3.18).

Por último, la ausencia de contrastes en las imágenes TEM, normalmente causadas por la presencia de cúmulos metálicos, corrobora que no se ha producido reducción del complejo de iridio en las condiciones de preparación.

### ***III.4.2 Caracterización espectroscópica***

Para evaluar la incorporación del compuesto  $[\text{Ir}(\text{dFppy})_2(\text{dasipy})]\text{PF}_6$  (**7**) en cada uno de los materiales, se llevó a cabo un estudio comparativo entre las nanopartículas sintetizadas y su precursor. Con este fin, se analizaron los espectros de reflectancia difusa (DRUV) de todos ellos, así como sus espectros de infrarrojo y de emisión.

#### ***III.4.2.1 Espectros de infrarrojo***

En la figura 3.19 se recogen los espectros de infrarrojo correspondientes al derivado  $[\text{Ir}(\text{dFppy})_2(\text{dasipy})]\text{PF}_6$  (**7**) y a los materiales *in-situ* sintetizados. Las nanopartículas **NP\_G** exhiben espectros muy similares (ver anexo III, figura A.III.9). Todos ellos muestran las bandas típicas asociadas a las vibraciones de los grupos Si-O y Si-O-Si. También se observan absorciones muy débiles entre 2850-3000  $\text{cm}^{-1}$  y 1400-1550  $\text{cm}^{-1}$ . Estas bandas, típicas de vibraciones de tensión de los grupos metilénicos y aromáticos, respectivamente, son debidas a la presencia del compuesto **7** de iridio.

Además, los materiales **[7]-NP<sub>Me</sub>** y **[7]-NP<sub>APTES</sub>** muestran bandas de vibración características de sus agentes de capeo. Así, los picos observados a 1265 y 850  $\text{cm}^{-1}$  en **[7]-NP<sub>Me</sub>** se corresponden

con los modos de vibración Si-CH<sub>3</sub>, mientras que la banda a 1390 cm<sup>-1</sup> en [7]-NP<sub>APTES</sub> se atribuye a la ν(N-H) del grupo amino del APTES.

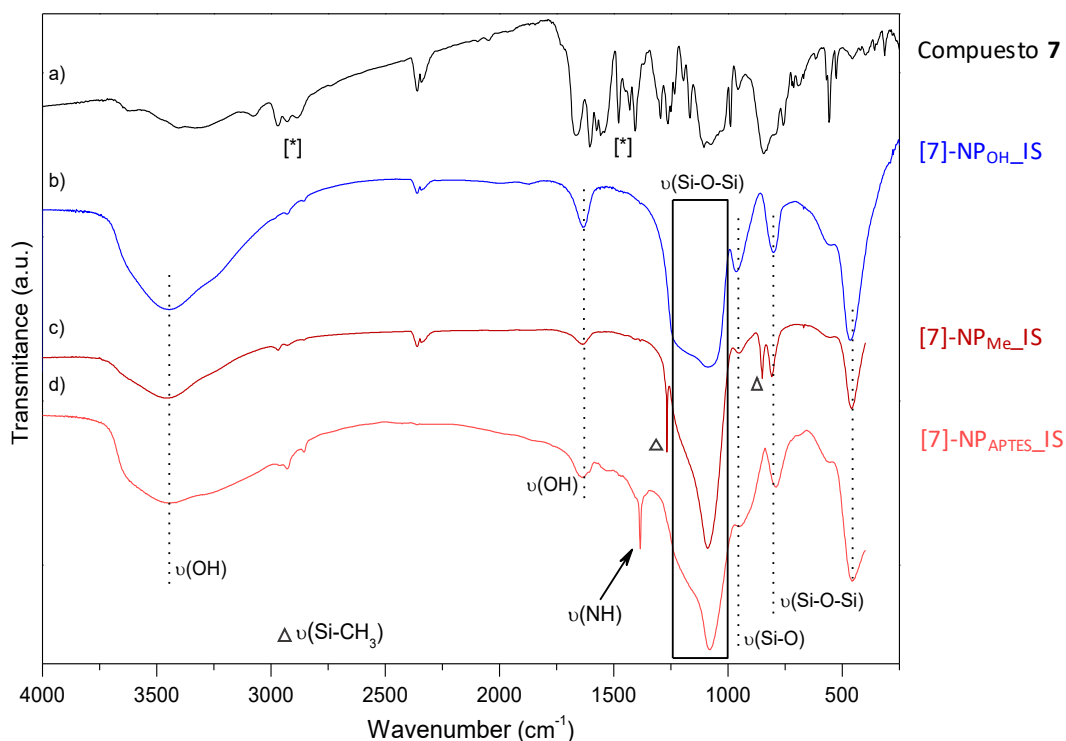


**Figure 3.19.** Espectro IR del derivado de iridio(III) 7 (a) en comparación con los correspondientes a las nanopartículas *in-situ*: [7]-NP<sub>OH</sub>\_IS (b), [7]-NP<sub>Me</sub>\_IS (c) y [7]-NP<sub>APTES</sub>\_IS (d). [\*] Absorciones características del compuesto observadas en los materiales silíceos.

### III.4.2.2 Propiedades fotofísicas

#### i. Espectros de absorción

Todas las nanopartículas muestran un perfil de absorción muy similar al descrito para el compuesto de iridio(III) [Ir(dFppy)<sub>2</sub>(dasipy)]PF<sub>6</sub> (**7**) en estado sólido, resolviéndose incluso las absorciones de baja energía ( $\lambda > 400$  nm) relacionadas con transiciones prohibidas por el spin (ver figura 3.20), lo que confirma la incorporación e integridad del cromóforo en la matriz silícea.

En las nanopartículas no tratadas ([7]-NP<sub>OH</sub>) y las capeadas con metilos ([7]-NP<sub>Me</sub>) se observa, además, una mayor absorción en los materiales grafteados que en los *in-situ*, indicando una menor incorporación de compuesto en estos últimos. Por el contrario, en los híbridos capeados con APTES, las nanopartículas [7]-NP<sub>APTES</sub>\_IS muestran una mayor absorción que, en coherencia con el mayor valor de metal determinado mediante análisis ICP, sugiere una mayor incorporación de cromóforo.

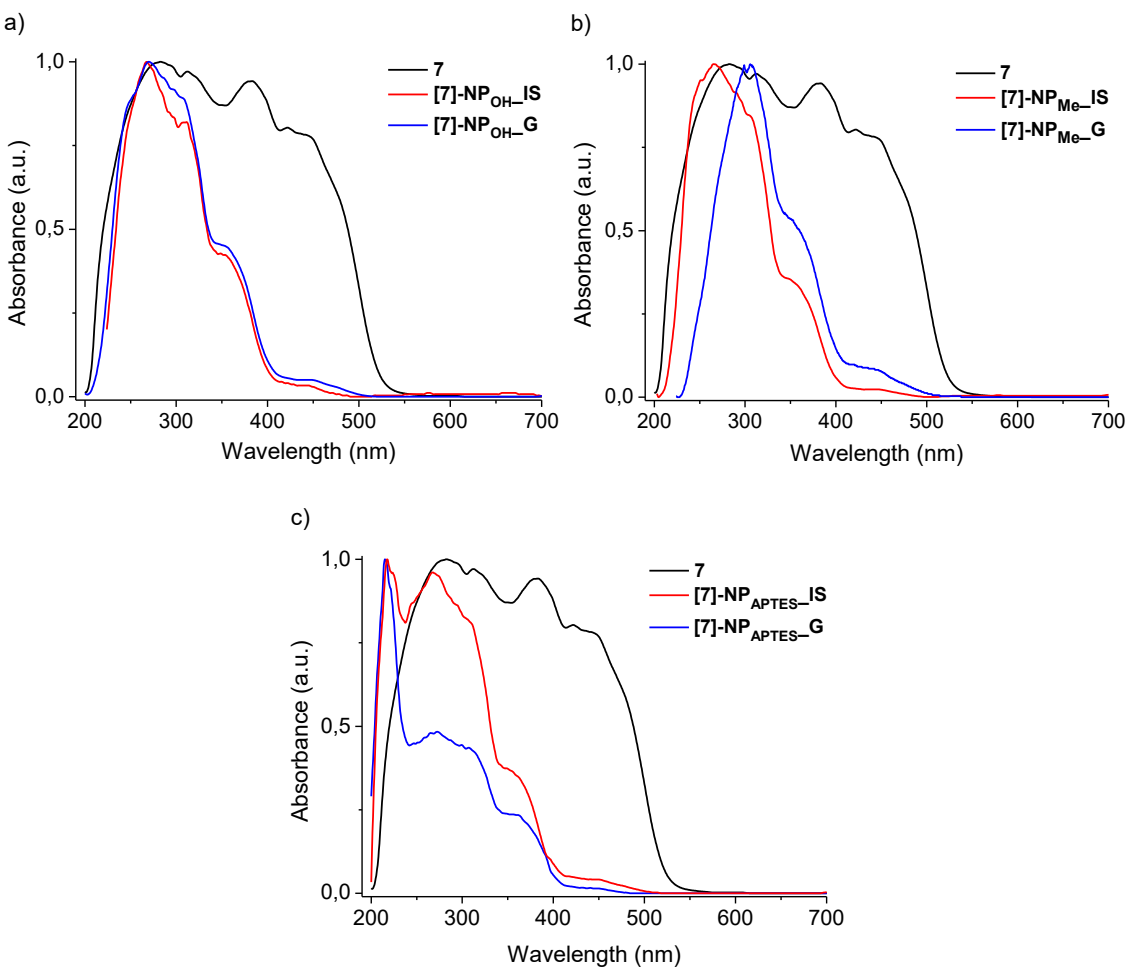


**Figura 3.20.** Espectros DRUV del compuesto  $[\text{Ir}(\text{dFppy})_2(\text{dasipy})]\text{PF}_6$  (**7**) en comparación con los materiales  $[\text{7}] \text{-NP}_{\text{OH}}$  (a),  $[\text{7}] \text{-NP}_{\text{Me}}$  (b) y  $[\text{7}] \text{-NP}_{\text{APTES}}$  (c).

#### *ii. Espectros de emisión*

Las propiedades luminiscentes de todas las nanopartículas ( $[\text{7}] \text{-NP IS}$  y  $[\text{7}] \text{-NP G}$ ) se registraron en estado sólido y, también, en suspensiones acuosas ( $5 \times 10^{-4}$  M), ya que posteriormente serán expuestas a medios celulares. Todos los datos se encuentran resumidos en la tabla 3.4 y en las figuras 3.22-3.24.

En general, las suspensiones en agua de todas las nanopartículas resultaron ser bastante estables a lo largo del tiempo, mostrando emisiones intensas bajo luz UV (figura 3.21, b). Además, tal y como cabría esperar, al tratarse de suspensiones coloidales, el efecto Tyndall se observa claramente (figura 3.21, c).

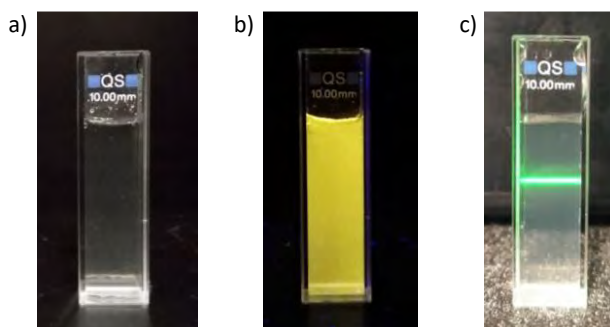


**Figura 3.21.** Imágenes de **[7]-NP<sub>OH</sub>\_IS** en suspensiones de agua ( $5 \times 10^{-4}$  M) bajo luz visible (a) y UV ( $\lambda$  365 nm) (b) e iluminada con un láser mostrando el efecto Tyndall.

Las nanopartículas *in-situ* (**[7]-NP<sub>OH</sub>\_IS**, **[7]-NP<sub>Me</sub>\_IS** y **[7]-NP<sub>APTES</sub>\_IS**) muestran, tanto en estado sólido como en suspensión, un perfil de emisión idéntico al del compuesto **[Ir(dFppy)<sub>2</sub>(dasipy)]PF<sub>6</sub>** (**7**) en disolución a temperatura ambiente. Como se observa en las figuras 3.22-3.24 (izquierda), presentan una banda de emisión no estructuradas con máximos a 550 nm, aproximadamente. Los valores obtenidos para el tiempo de vida ( $\tau$  0.70-0.80  $\mu$ s) y el rendimiento cuántico ( $\phi$  40-52 %) en estado sólido son comparables a los del precursor **7** en disolución de THF ( $\tau$  0.71  $\mu$ s,  $\phi$  56 %) (ver tabla 3.4). Este comportamiento puede atribuirse al tipo de síntesis y a la pequeña cantidad de cromóforo incorporado (0.2 wt%) que permiten que las moléculas del mismo estén homogéneamente distribuidas e incorporadas en la matriz silícea y, por tanto, relativamente separadas en el material final. De este modo, se mimetiza el comportamiento del complejo en disolución y se reduce la interacción entre las moléculas del cromóforo que, en parte, desactiva la emisión.

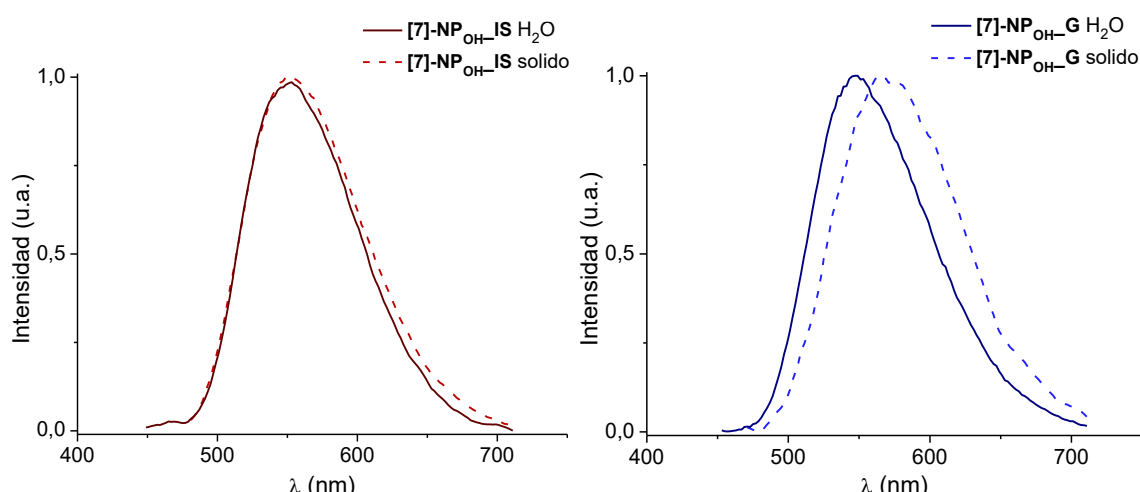


**Figura 3.22.** Espectros de emisión de los materiales **[7]-NP<sub>OH</sub>\_IS** (izquierda) y **[7]-NP<sub>OH</sub>\_G** (derecha) en estado sólido y en suspensión de agua ( $5 \times 10^{-4}$  M). ( $\lambda_{\text{ex}}$  450 nm).

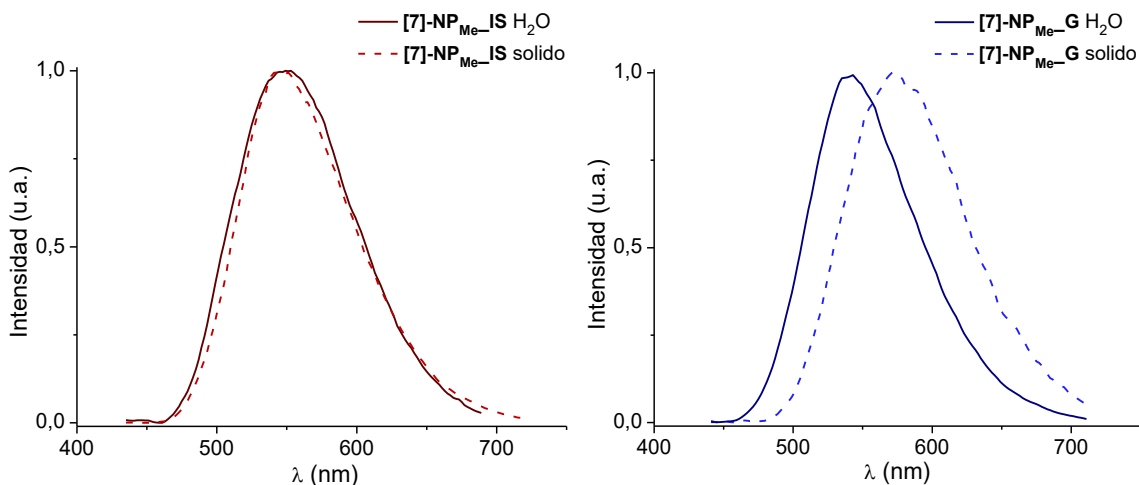


**Figura 3.23.** Espectros de emisión de los materiales [7]-NP<sub>Me</sub>\_IS (izquierda) y [7]-NP<sub>Me</sub>\_G (derecha) en estado sólido y en suspensión de agua ( $5 \times 10^{-4}$  M). ( $\lambda_{\text{ex}}$  450 nm).

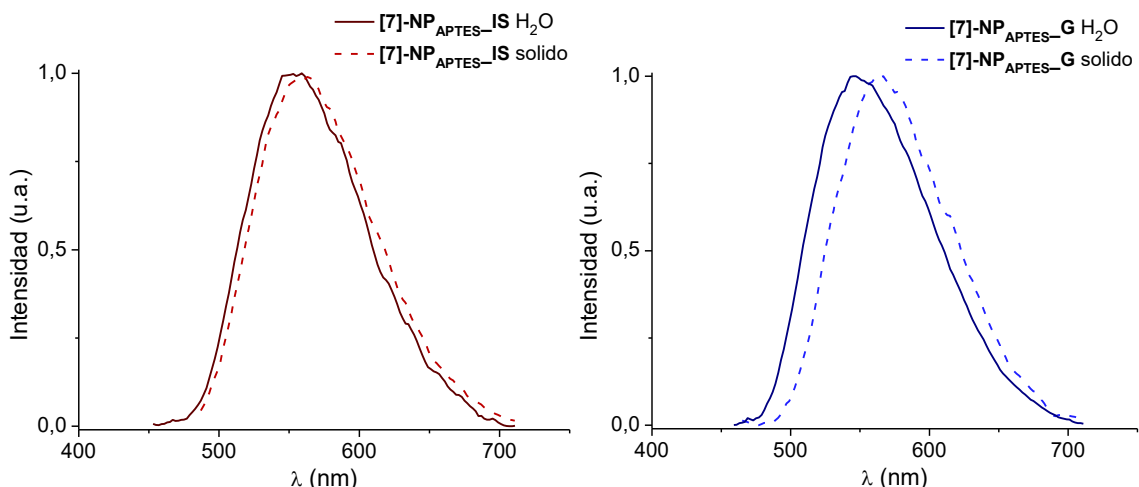


**Figura 3.24.** Espectros de emisión de los materiales [7]-NP<sub>APTES</sub>\_IS (izquierda) y [7]-NP<sub>APTES</sub>\_G (derecha) en estado sólido y en suspensión de agua ( $5 \times 10^{-4}$  M). ( $\lambda_{\text{ex}}$  450 nm).

Por el contrario, las propiedades de las nanopartículas grafteadas ([7]-NP<sub>OH</sub>\_G, [7]-NP<sub>Me</sub>\_G y [7]-NP<sub>APTES</sub>\_G) son más similares a las del complejo **7** en estado sólido, con máximos de emisión a energías más bajas (565-570 nm) y rendimientos cuánticos más pequeños (ver tabla 3.4). Este comportamiento podría estar relacionado con la localización superficial del derivado de iridio(III) y con la proximidad de las nanopartículas en estado sólido, que favorecen la agregación e interacción de las moléculas del cromóforo y, por consiguiente, su similitud con el precursor **7** en estado sólido. En coherencia con ello, el espectro de las nanopartículas grafteadas registrado en suspensión acuosa exhibe, en todos los casos, un claro desplazamiento de la banda de emisión hacia mayores energías en comparación con las muestras sólidas (aprox.,  $\lambda_{\text{max}}$  550 nm H<sub>2</sub>O vs. 570 nm sólido, ver tabla 3.4 y figuras 3.22-3.24), lo que puede atribuirse a una buena dispersión

de las nanopartículas en el agua que permite eliminar o reducir notablemente la interacción entre las moléculas del cromóforo.

**Tabla 3.4.** Datos de emisión del compuesto  $[\text{Ir}(\text{dFppy})_2(\text{dasipy})]\text{PF}_6$  (**7**) en estado sólido y disolución (THF,  $5 \times 10^{-4}$  M) y de sus nanopartículas **[7]-NP\_IS** y **[7]-NP\_G** en estado sólido y en suspensiones de agua ( $5 \times 10^{-4}$  M).

Muestra	Medio <sup>(b)</sup>	$\lambda_{\text{em}}$ (nm) <sup>(c)</sup>	$\tau$ (μs)	$\phi$ (%) <sup>(d)</sup>
<b>7</b>	Sólido	560	0.35	29.4
	THF	550	0.71	55.8
<b>[7]-NP<sub>OH</sub>_IS</b>	Sólido	552	0.69	41.2
	H <sub>2</sub> O <sup>(a)</sup>	550	---	25.8
<b>[7]-NP<sub>OH</sub>_G</b>	Sólido	570	0.52	28.4
	H <sub>2</sub> O <sup>(a)</sup>	550	---	18.5
<b>[7]-NP<sub>Me</sub>_IS</b>	Sólido	550	0.72	50.1
	H <sub>2</sub> O <sup>(a)</sup>	550	---	39.6
<b>[7]-NP<sub>Me</sub>_G</b>	Sólido	570	0.56	39.2
	H <sub>2</sub> O <sup>(a)</sup>	545	---	26.1
<b>[7]-NP<sub>APTES</sub>_IS</b>	Sólido	558	0.80	52.0
	H <sub>2</sub> O <sup>(a)</sup>	553	---	27.5
<b>[7]-NP<sub>APTES</sub>_G</b>	Sólido	565	0.64	41.4
	H <sub>2</sub> O <sup>(a)</sup>	545	---	17.3

(a) Todas las medidas se llevaron a cabo sin desoxigenar las suspensiones. (b) Medidas a temperatura ambiente. (c)  $\lambda_{\text{ex}} = 365-500$  nm. (d)  $\lambda_{\text{ex}} = 450$  nm.

Por último, también cabe destacar las ligeras modificaciones observadas en los tiempos de vida y en los rendimientos cuánticos de las nanopartículas en función de su morfología. Así, las nanopartículas nativas (**[7]-NP<sub>OH</sub>\_IS** y **[7]-NP<sub>OH</sub>\_G**) muestran, en estado sólido, unos valores de  $\tau$  y  $\phi$  inferiores a los encontrados para sus análogos capeados **[7]-NP<sub>Me</sub>** y **[7]-NP<sub>APTES</sub>** (ver tabla 3.4), lo que sugiere que la presencia de la corona externa reduce las vías de desactivación de la emisión del cromóforo. Además, las nanopartículas recubiertas con APTES (**[7]-NP<sub>APTES</sub>**  $\tau$ , 0.80 μs **IS** 0.64 μs **G**;  $\phi$ , 52% **IS** 41% **G**) exhiben unos valores superiores a los observados para los materiales funcionalizados con DMDES (**[7]-NP<sub>Me</sub>**  $\tau$ , 0.72 μs **IS** 0.56 μs **G**;  $\phi$ , 50 % **IS** 39% **G**). Este hecho podría ser debido a que el APTES proporciona un recubrimiento más denso que el formado por los grupos metilo del DMDES.

### **III.5 Propiedades biológicas**

Teniendo en cuenta las buenas propiedades mostradas por todas las nanopartículas (elevados rendimientos cuánticos, tiempos de vida largos y buenas dispersión y estabilidad en medios acuosos e iónicos), decidimos investigar su posible uso como marcadores biológicos. Estos estudios fueron llevados a cabo por los grupos de investigación de Cáncer de Pulmón y Enfermedades Respiratorias (dirigido por el Dr. José Manuel García Pichel) y Biomarcadores y Señalización Molecular (dirigido por el Dr. Ignacio Larráyoz), ambos del Centro de Investigación Biomédica de La Rioja (CIBIR, Fudación Riojasalud, Logroño).

Con fines meramente comparativos, también se evaluó el comportamiento biológico del compuesto  $[\text{Ir}(\text{dFppy})_2(\text{dbbpy})]\text{Cl}$  (**8**), el cual presenta una estructura molecular muy similar a la del cromóforo  $[\text{Ir}(\text{dFppy})_2(\text{dasipy})]\text{PF}_6$  (**7**), empleado para funcionalizar las nanopartículas.

#### ***III.5.1 Estudio de citotoxicidad***

En primer lugar, se determinó la citotoxicidad de todas las muestras (**[7]-NP** y  $[\text{Ir}(\text{dFppy})_2(\text{dbbpy})]\text{Cl}$ , **8**) en las células de cáncer de pulmón A549 (carcinoma de pulmón) y HeLa (carcinoma cervical), utilizando el ensayo MTS. Los valores de  $\text{IC}_{50}$  se determinaron tras la exposición celular a las nanopartículas o al compuesto **8** durante 24 y 1 horas, respectivamente, y utilizando como referencia los valores obtenidos para el cis-platino. Todas las gráficas empleadas para la determinación de los  $\text{IC}_{50}$  se recogen en el anexo III (figuras A.III.11- A.III.13), y los valores finales se resumen en la tabla 3.5.

**Tabla 3.5.** Valores de  $\text{IC}_{50}$  ( $\mu\text{g}/\text{mL}$ ) para cada una de las nanopartículas en células A549 y HeLa.

Muestra	A549*	HeLa*
<b>[7]-NP<sub>OH_IS</sub></b>	$166.00 \pm 23.93$	$219.30 \pm 7.64$
<b>[7]-NP<sub>OH_G</sub></b>	$184.30 \pm 32.93$	No tóxica
<b>[7]-NP<sub>Me_IS</sub></b>	No tóxica	No tóxica
<b>[7]-NP<sub>Me_G</sub></b>	No tóxica	No tóxica
<b>[7]-NP<sub>APTES_IS</sub></b>	$93.36 \pm 5.70$	$94.36 \pm 11.82$
<b>[7]-NP<sub>APTES_G</sub></b>	$74.28 \pm 11.33$	$80.23 \pm 14.29$

\* Los valores indicados representan la media de tres experimentos independientes  $\pm$  el error típico.

Como se observa en la tabla 3.5, todas las muestras de sílice mostraron valores de IC<sub>50</sub> relativamente altos, indicativos de una citotoxicidad baja, en ambas líneas celulares (ver también anexo III, figuras A.III.11 y A.III.12). Entre todas ellas, las nanopartículas **[7]-NP<sub>APTES</sub>** resultaron ser algo más tóxicas (IC<sub>50</sub>, µg/mL ≈ 90 **IS**, 80 **G**), mientras que las modificadas con grupos metilo, **[7]-NP<sub>Me</sub>**, mostraron ser atóxicas. La mayor citotoxicidad mostrada por **[7]-NP<sub>APTES</sub>** podría estar relacionada con la presencia de los grupos amino en la superficie de las nanopartículas o con la liberación de dichos grupos al medio celular. Este último fenómeno ha sido previamente observado en medios biológicos para otras partículas de sílice funcionalizadas de forma similar.<sup>125</sup> Otro hecho a resaltar es la similitud de los valores de IC<sub>50</sub> observados entre las muestras *in-situ* y graftedas, a pesar de que en estas últimas el cromóforo se encuentre en la superficie de la nanopartícula y, por tanto, más expuesto.

Por el contrario, el compuesto modelo **8** es altamente citotóxico (ver tabla 3.5, anexo III, figura A.III.13), ya que muestra unos valores de IC<sub>50</sub> entre dos y tres veces menores (3.73 ± 0.76 µM en A549, 5.53 ± 0.41 µM en HeLa) que los correspondientes al cis-platino (6.45 ± 0.47 µM en A549, 13.60 ± 0.99 µM en HeLa), bajo las mismas condiciones experimentales.<sup>126</sup> Además, este derivado es muy poco selectivo ya que presenta un índice de selectividad (SI) pequeño hacia las células tumorales (HeLa y A549) respecto a las células de pulmón no tumorales (NL-20, IC<sub>50</sub> 6.53 ± 0.20), mostrando un SI menor en células HeLa que en A549 (SI 1.75 para A549 y 1.18 para HeLa).

La alta actividad citotóxica del derivado **8** no estaría de acuerdo con el hecho de que las nanopartículas **IS** y **G** tengan valores de IC<sub>50</sub> similares, ya que las muestras graftedas **NP\_G** presentan una mayor exposición del fragmento organometálico derivado del complejo **7**, similar a **8**, por lo que se debiera esperar que fueran más citotóxicas que las **NP\_IS**. Este hecho podría sugerir que la citotoxicidad del derivado **8** podría estar relacionada con el ligando bipiridina, funcionalizado con dos grupos amiduro alifáticos. Estas cadenas se encuentran unidas covalentemente a la superficie de la nanopartícula **NP\_G**, quedando poco expuestas hacia el medio celular, lo que anularía la posible citotoxicidad del compuesto.

### III.5.2 Localización celular

Una vez establecida la baja citotoxicidad de las nanopartículas, se procedió a estudiar su posible uso como biomarcadores luminiscentes. La localización celular en células vivas se evaluó mediante microscopía de fluorescencia únicamente para las muestras **[7]-NP<sub>OH\_IS</sub>** y **[7]-NP<sub>Me\_IS</sub>**. Con este fin, las nanopartículas (50 µg/mL) se incubaron durante 24 h con los dos tipos de células

tumorales (HeLa y A549) y durante 1 hora junto con el colorante del núcleo (*Hoechst 33342*). La superposición de las diferentes imágenes obtenidas usando diferentes filtros (Nomarski, para realizar la morfología celular, y los correspondientes a la emisión del *Hoechst* y de las NPs) permite determinar la localización de las nanopartículas a nivel subcelular (ver figura 3.25).

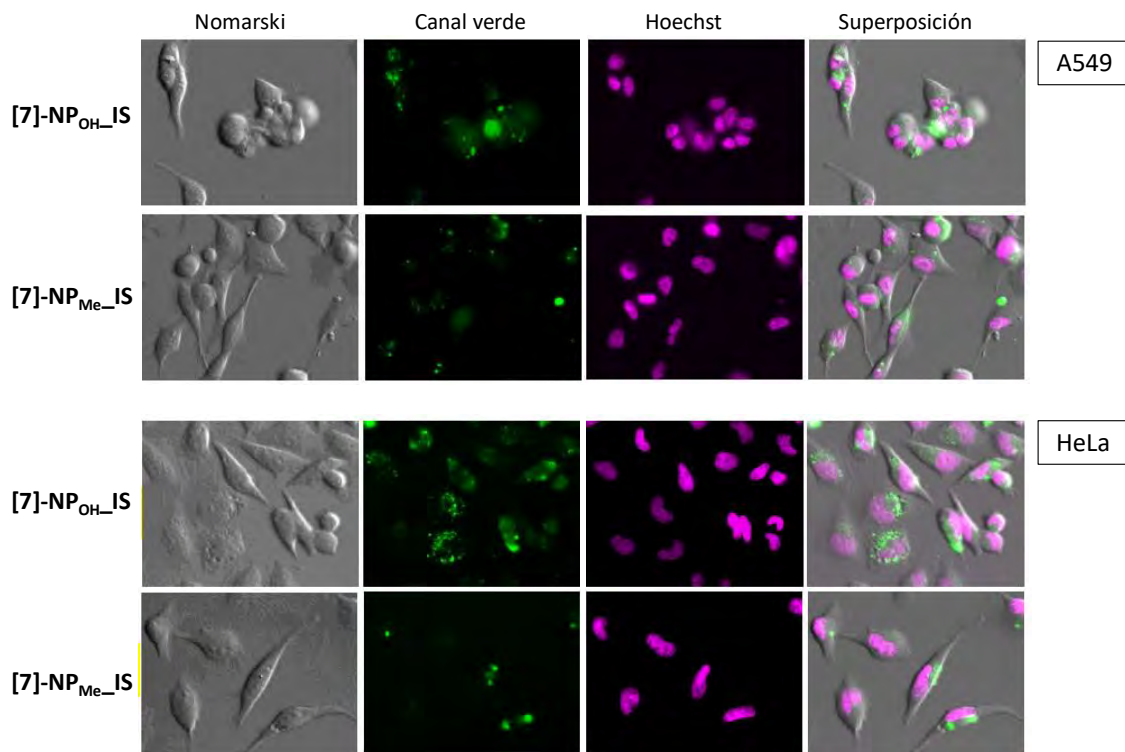


**Figura 3.25.** Imágenes de fluorescencia de células A549 y HeLa tratadas con las nanopartículas [7]-NP<sub>OH</sub>\_IS y [7]-NP<sub>Me</sub>\_IS. Las células se visualizaron por microscopía para determinar la emisión, en verde de las nanopartículas, en violeta del *Hoechst* unido al ADN, o la transmisión de luz blanca, con Nomarski.

Todas las nanopartículas muestran un comportamiento similar en ambas líneas celulares, acumulándose en las áreas perinucleares de la célula, pero sin llegar co-localizar en el núcleo, ya que las emisiones verde y violeta, correspondientes a las nanopartículas y al *Hoechst*, respectivamente, no son coincidentes en la imagen generada tras la superposición de los diferentes canales (ver figura 3.25).

No obstante, esta técnica sólo nos proporciona imágenes bidimensionales del medio celular que no nos permiten asegurar la internalización de las nanopartículas en las células, ya que éstas pueden estar simplemente depositadas en la superficie de las mismas. Por ello, con el fin de evaluar si hay o no captación celular, se llevó a cabo el estudio mediante microscopía confocal en células fijadas, tras exponer ambas líneas celulares (A549 y HeLa) a las nanopartículas (50 µg/mL) durante 24 horas.

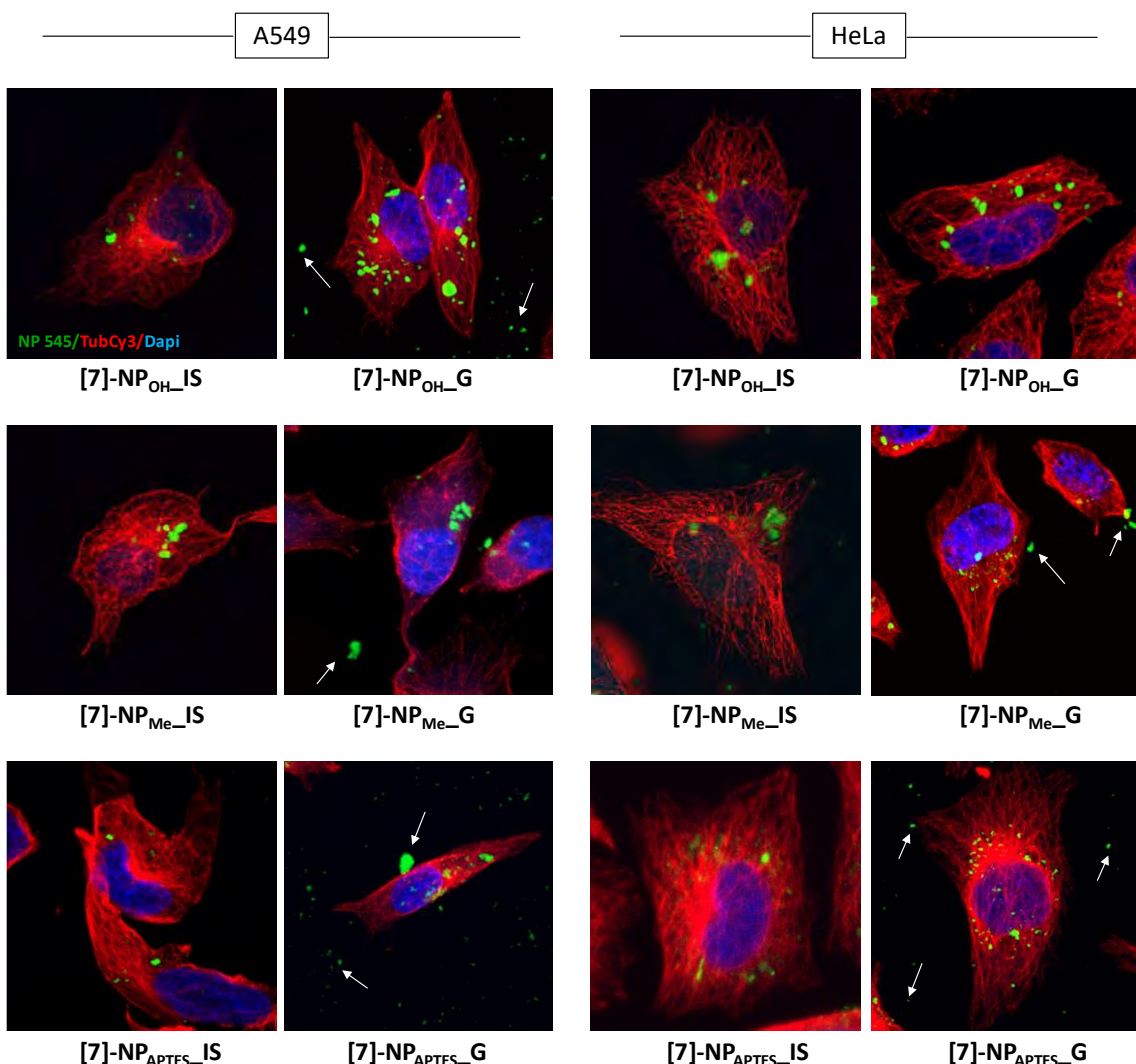


**Figura 3.26.** Imágenes de microscopía confocal en células A549 (izquierda) y HeLa (derecha) tratadas con las nanopartículas [7]-NP\_IS y [7]-NP\_G (24 h, 50 µg/mL). Las células se fijaron y se tiñeron los microtúbulos con tubulina (en rojo). Los cúmulos de nanopartículas se observan en verde; y los núcleos teñidos con DAPI en azul. Se observa una mayor agregación extracelular para las [7]-NP\_G (flechas).

En este caso, las imágenes proporcionadas por esta técnica (ver figura 3.26) nos permiten confirmar la internalización celular para todos los tipos de nanopartículas, probablemente a través de endocitosis, así como su localización citoplasmática alrededor del núcleo. Este hecho también ha sido confirmado a través del apilamiento en el eje Z de 15 imágenes planas de microscopía confocal tomadas con una separación de 0.5 µm (7 µm de anchura total) (ver figura 3.27).

A pesar de haber modificado la superficie de las nanopartículas para favorecer su afinidad con el medio celular, no hemos podido establecer ningún patrón de comportamiento en cuanto a su internalización. No obstante, las nanopartículas *in-situ* ([7]-NP\_IS) parecen mostrar una menor agregación en el exterior celular que en las muestras con el cromóforo covalentemente

unido a la superficie (**[7]-NP\_G**) (ver figura 3.26). Este hecho también parece observarse en las imágenes de las nanopartículas obtenidas por TEM (ver figura 3.17 y anexo III, figura A.III.10).

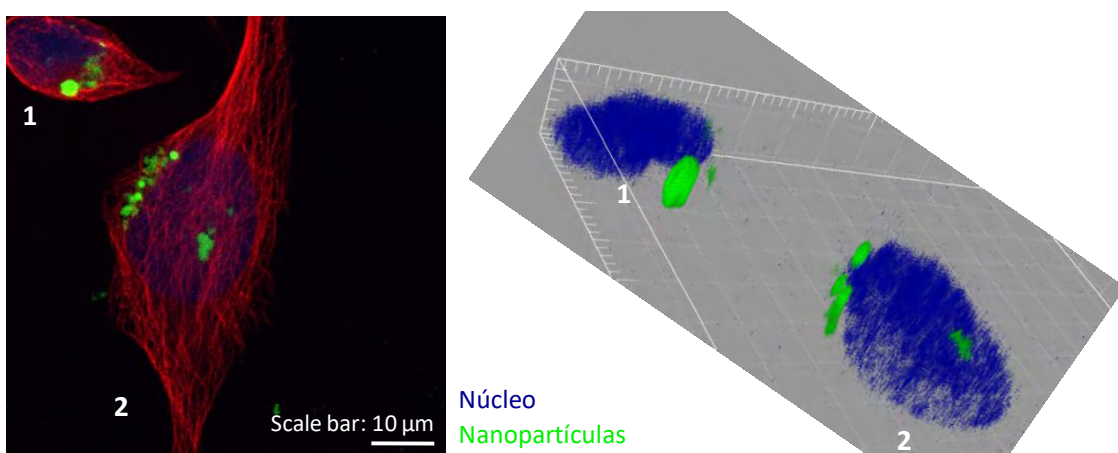


**Figura 3.27.** Imagen de microscopía confocal de dos células HeLa incubadas 24 h con **[7]-NP<sub>Me</sub>\_IS** (100 µg/mL, izquierda). Reconstrucción tridimensional del apilamiento en el eje Z de 15 imágenes planas tomadas con una separación de 0.5 µm (7 µm de anchura total, derecha).

Del mismo modo, se llevó a cabo el estudio para determinar la localización celular del compuesto de iridio(III) **8** en células vivas. Para ello, y teniendo en cuenta su elevada citotoxicidad, el tiempo de incubación en el medio celular fue únicamente de 1 hora. En este caso, además de utilizar el colorante *Hoechst* para marcar el núcleo de las células, también se utilizaron el *lysotracker* y el *mitotracker* como marcadores de lisosomas y mitocondrias, respectivamente (ver figura 3.28).

La imagen obtenida a partir de la superposición de los tres canales de emisión (figura 3.28, d) pone de manifiesto que el derivado de iridio(III) **8** se localiza en los lisosomas de la célula. A pesar de ello, el seguimiento a tiempo real de todo el proceso sugiere que la muerte celular se produce a través de la destrucción de las mitocondrias. Por ello, para evaluar si el compuesto entra también en este orgánulo citoplasmático, se repitió el ensayo en fibroblastos de pulmón de ratón (LMEFs, ver figura 3.29).

El estudio en LMEFs corrobora la localización de **8** en los lisosomas (figura 3.29, e) y excluye la posibilidad de que el compuesto **8** se localice en las mitocondrias. Tal y como se observa en la figura 3.28 (f), las emisiones verde y violeta, correspondientes a **8** y a las mitocondrias, respectivamente, se encuentran en zonas bien diferenciadas. Todo esto sugiere que, aunque el derivado de iridio parece penetrar únicamente en los lisosomas, es capaz de afectar a las mitocondrias de la célula, provocando así su muerte. No obstante, hasta el momento, no se ha podido determinar el mecanismo de actuación.

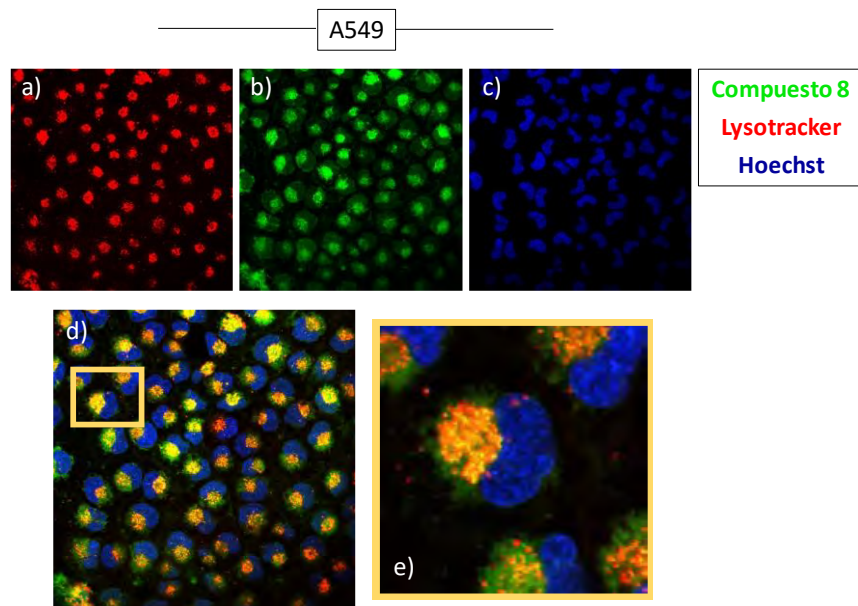


**Figura 3.28.** Imágenes de microscopía confocal obtenidas de células A549 incubadas con el compuesto de iridio(III) **8** ( $16 \mu\text{M}$ , 1h), en los diferentes canales: en rojo, la emisión correspondiente al *lysotracker* (a); en verde, la del compuesto **8** (b), y en azul, la del *Hoechst* (c). Superposición de las imágenes de los canales a, b y c (d). Magnificación del recuadro en d, mostrando color amarillo generado por superposición (co-localización) de verde (**8**) y rojo (lisosomas), pero no con azul (núcleo) (e).

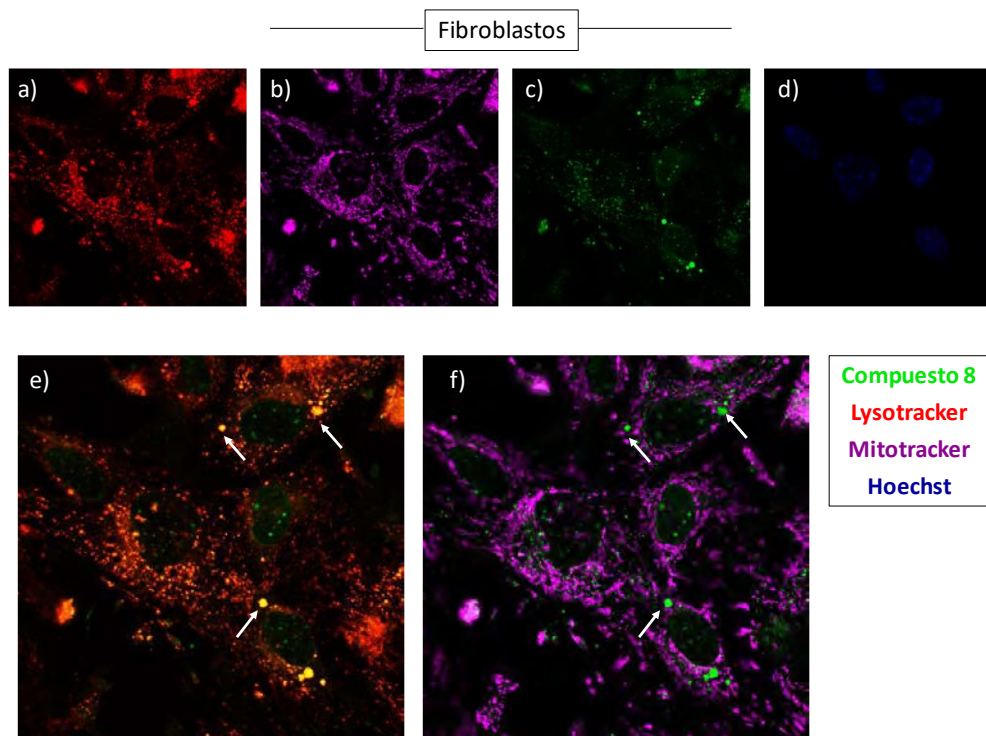


**Figura 3.29.** Imágenes de microscopía confocal obtenidas en células LMEFs (fibroblastos de pulmón) incubadas con el compuesto de iridio(III) **8** ( $16 \mu\text{M}$ , 1h), obtenidas por los diferentes canales de captura: en rojo, la emisión correspondiente al *lysotracker* (a); en violeta, la del *mitotracker* (b); en verde, la del compuesto **8** (c); y en azul, el marcador nuclear *Hoechst* (d). Imagen de superposición de a y c, mostrando color amarillo (flechas) y naranja, que indica la localización de **8** en lisosomas (e). Imagen de superposición de b y c, donde se separan los colores verde (**8**) del morado (mitocondria) (f).



## **Chapter IV**

---

***Photocatalytic activity of hybrid titania-based materials***

---



## Introduction

Photocatalytic materials are playing an important role in the development of the new and greener society required for the XXI century by opening solutions for the protection of the environment, as well as for the production of chemical energy vectors from sustainable materials and sources.<sup>127</sup> This challenge has to be answered with a low-cost solution, using abundantly available raw materials. In this context, nanostructured semiconductors have received substantial attention as building blocks for the preparation of materials able to efficiently harvest the cleanest and cheapest energy available, the solar light. The most demanding are those involved in photo-water-splitting (a renewable way to produce hydrogen using solar energy), water purification and energy generation (dye-sensitized solar cells, DSSCs).

Since the discovery of the photocatalytic activity of some metal oxide, the technology of semiconductor-based photocatalysis has progressed rapidly. However, many of these materials present important drawbacks. For example, CdSe or CdS semiconductors are not stable enough under illumination and, also, cadmium is a toxic metal; WO<sub>3</sub> and Fe<sub>2</sub>O<sub>3</sub> display low photocatalytic activity; and others show high instability in aqueous media. Therefore, titanium dioxide, TiO<sub>2</sub>, has emerged as one of the most studied and suitable candidates for this purpose, due to its excellent properties like low cost, chemical stability, biocompatibility, non-toxicity and good oxidative characteristics.<sup>3, 128</sup>

In the early 1970s, Fujishima and Honda published the water splitting process using titania as the anode of the system. This material acted as an *n-type* semiconductor, being able to generate *electron-hole* pairs under UV irradiation.<sup>129</sup> Following this idea, Frank and Bard also reported the possibility of degrading CN<sup>-</sup> molecules in water *via* the photocatalysis,<sup>130</sup> which confirmed the capability of this material to purify both water and air through ultraviolet radiation

(figure 4.1). Other important advances includes the self-cleaning capacity of  $\text{TiO}_2$  and the use of titania materials in dye sensitized solar cells (DSSCs), studied by Wang<sup>131</sup> and Grätzel,<sup>132</sup> respectively; being this last application one of the most developed.

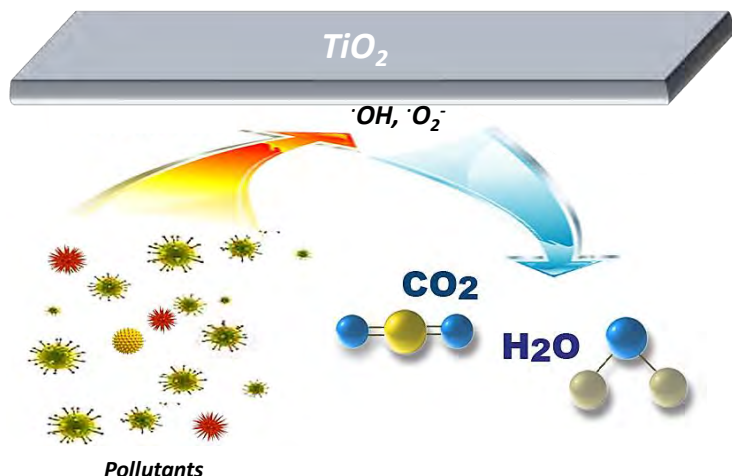


**Figure 4.1.** Photocatalytic activity of the  $\text{TiO}_2$  in water and air purification.

However, although  $\text{TiO}_2$  has been considered one of the most popular semiconductor oxides, it has been less studied in applications that requires photoactivation by natural solar light. This fact is due to some limitations: (i) The solar light is mainly formed by visible radiation (45%), while only between the 4-5% consists of UV photons. Due to its wide band gap ( $> 3 \text{ eV}$ ), the pure  $\text{TiO}_2$  can only be activated by this low percentage of photons (UV,  $\lambda \leq 400 \text{ nm}$ ) of the entire solar spectrum (figure 4.2),<sup>133</sup> which greatly limits its efficiency for solar applications. (ii) Another disadvantage when irradiating with visible light is the high electron-hole recombination range, which is directly related to the large band gap of the  $\text{TiO}_2$ . The recombination process (figure 4.2) occurs when an excited electron returns to the valence band (VB) before reacting with the adsorbed species, also causing a reduction in the overall quantum efficiency.<sup>134</sup> Thus, a shift in the optical response of the  $\text{TiO}_2$  from the UV to the visible spectrum range will mean a huge photocatalytic improvement in the energy efficiency of the material.<sup>135</sup>

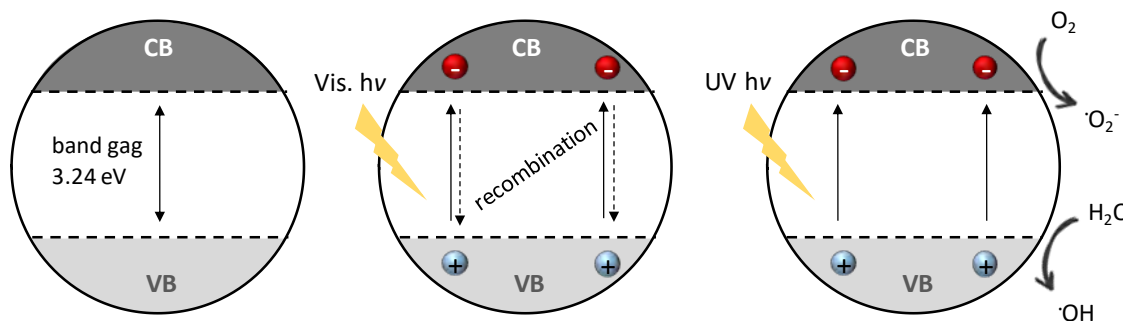


**Figure 4.2.** Schematic view of a pure titania (left), the electron-hole recombination under visible light irradiation (middle), and the oxidation and reduction processes that take place at the surface of the titania under UV light irradiation (right).

Considering all these limitations, there is a great interest in developing new titania materials with narrower band gaps, which allow the absorption in the visible or near IR range (400-900 nm). With this aim, several strategies have recently developed, being easily classified into two main groups: those related (i) to morphology modifications, in which parameters such as surface areas or porosity are adjusted, or (ii) to chemical modifications by the incorporation of additional substrates in the TiO<sub>2</sub> structure.

### **Strategies to improve the photoactivity of titania-based materials**

Traditionally, most of the strategies involved the synthesis of titanias with small crystalline size and high surface areas.<sup>136</sup> However, the efforts are now focused on reducing the band gap of the semiconductor with the aim of unlocking the poor potential of TiO<sub>2</sub> when using visible light illumination. Based on that, three are the most common studied approaches:

- Introduction of metal or non-metal ions (doping) into the regular intrinsic crystal lattice of the TiO<sub>2</sub>,<sup>137</sup> to generate impurity states in its band gap and produce dramatic changes in the electronic properties of the semiconductor (figure 4.3, a).
- Titania reduction from Ti(IV) to Ti(III) *via* hydrogenation (figure 4.3, b).<sup>133c, 138, 139</sup>
- Photosensitization *via* surface functionalization with colored organic or inorganic dyes (figure 4.3, c) that are able to inject electrons into the conduction band of the TiO<sub>2</sub> after being excited by UV or visible light.<sup>133b, 140</sup>

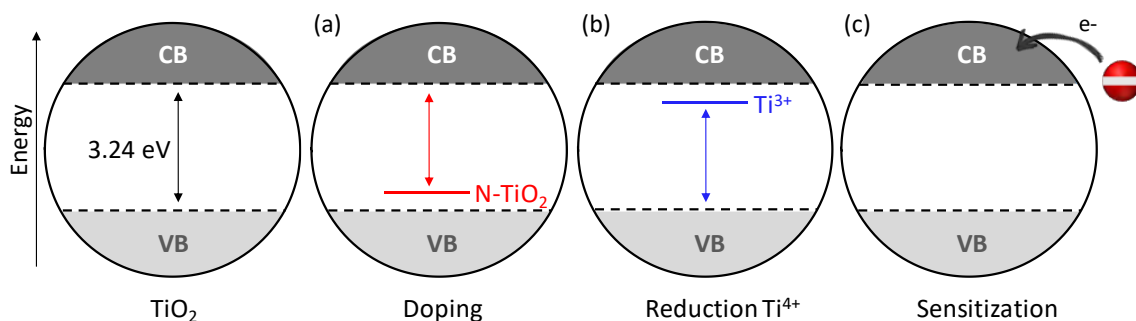


**Figure 4.3.** Different strategies of functionalizing the  $\text{TiO}_2$  for improving its photoactivity.

#### *i. Doping and titania reduction*

These two strategies allow the formation of materials with intermediate states above (doping) and under (reduction of Ti(IV)) the valence and conduction bands of the semiconductor, respectively.

In this context, the so-called *black titanias*<sup>133c, 138d, 139b, 139c</sup> have gained much attention in recent years due to their great capacity of absorbing light in a very broad range of wavelengths. However, their photocatalytic activity is strongly related to the reaction conditions, which usually include extreme temperatures.<sup>139a, 139c-e</sup> For example, Chen *et al.* reported the preparation of *black*  $\text{TiO}_2$  by its treatment with hydrogen at 20 bar and 200 °C for 5 days.<sup>133c</sup> Other methods not only include high temperature treatments but also the use of metals such as Al or Zn.<sup>141</sup> For all these reasons, these methods are difficult to implement for practical use. In addition, there is an open debate on how doping achieves enhanced  $\text{TiO}_2$  photoactivity, as well as disagreement in many of the conclusions drawn from the studies.

#### *ii. Photosensitization*

This approximation has recently become the most popular strategy for improving the photoactivity of titania materials, demonstrating to be very efficient in, for example, dye-sensitized solar cells (DSSCs).<sup>140, 142</sup>

This approach consists of incorporating different dyes able to inject electrons in the CB of the semiconductor and also to control the charge separation and recombination dynamics at the sensitizer/ $\text{TiO}_2$  interfaces.<sup>143</sup> Therefore, the interaction between the dye and the semiconductor displays an important role in the synthetic processes.

### a. Photosensitization via surface functionalization

The functionalization of these systems is usually based on *post-synthetic* procedures such as impregnation or grafting (superficial modifications of  $\text{TiO}_2$  through covalent bonding, see figure 4.4), being this last technique one of the most commonly used.<sup>139a, 139b, 144</sup>

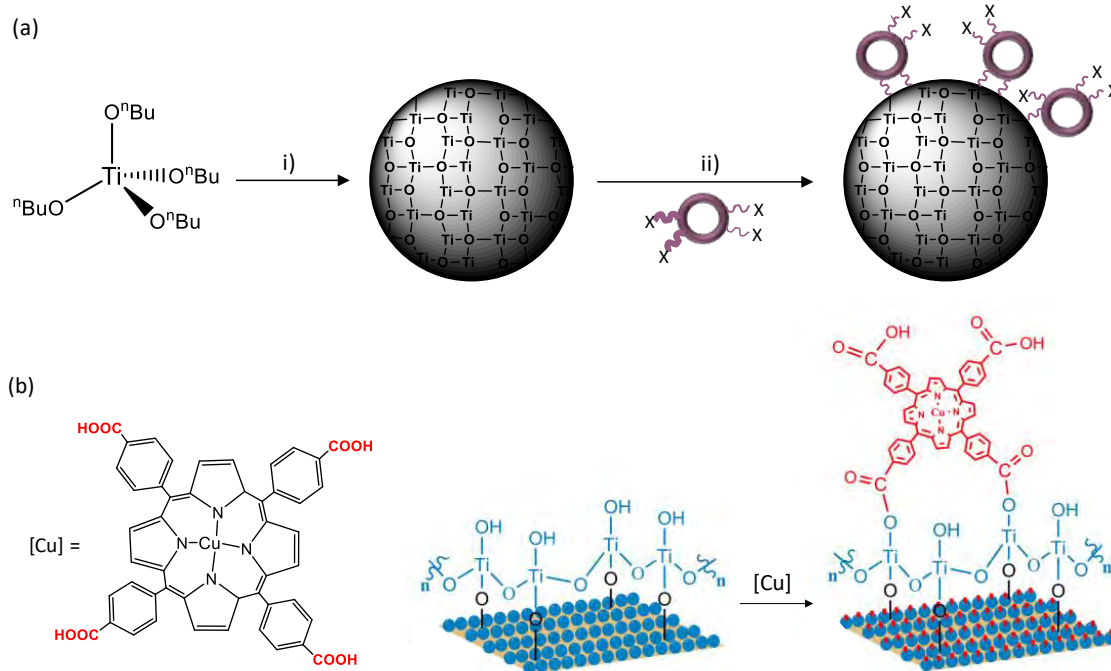


**Figure 4.4.** (a) Schematic view of the grafting process to functionalized  $\text{TiO}_2$ . (i) Synthesis of the pure  $\text{TiO}_2$ . (ii) Grafting step of the photosensitizer. (X: functionalities that will act as linkers). (b) Grafting of a Cu(II) complex on the surface of the titania material. (ACS Appl. Mater. Interfaces 2013, 5, 4753-4759)

In these cases, the dye must incorporate adequate functional groups to successfully form covalent bonds with the hydroxyl groups of the  $\text{TiO}_2$  surface. Thus, silyl (-O-Si-), amide (-NH-CO-), carboxyl (-O-CO-) or phosphonate (-O-PO<sub>2</sub>-) terminal functionalities (figure 4.5),<sup>145</sup> are widely used as linkers between both parts; being the carboxyl anchorage the most successful by now.

However, these *post-synthetic* strategies are usually accompanied by significant drawbacks in the resulting materials. Heterogeneity, bad distribution of the dye or leaching when exposing the as-synthetic material in fluid media are very common limitations in this type of preparations. These problems are closely related to the poor photostability of the charge-transfer sensitizers or to the difficulties in establishing stable interactions with the titania surface.

Nonetheless, the covalent coordination of the molecules to the  $\text{TiO}_2$  surface has proven to improve the electronic communication between the dye and the semiconductor, making the

electron injection in the CB of the  $\text{TiO}_2$  more efficient.<sup>144b</sup> This fact indicates that the properties of  $\text{TiO}_2$  materials depend not only on the inorganic semiconductor or the charge-transfer dye, but also on the interface between both phases.

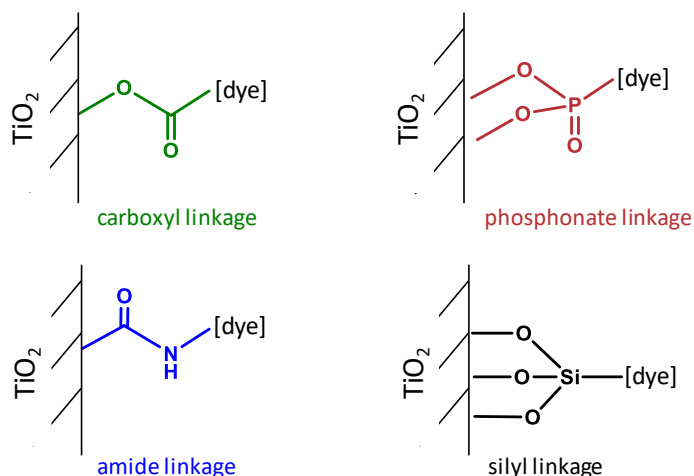


**Figure 4.5.** Schematic representation of the most common covalent anchoring groups for surface modification of  $\text{TiO}_2$ .

Following this idea, efforts in sensitization must be directed to develop more eco-friendly strategies that allow to prepare hybrid titania-based materials with dyes better integrated in the framework of the semiconductor, aiming to reduce some of the previous limitations and, therefore, to generate materials with improved efficiencies.

#### *b. Photosensitization via in-situ functionalization*

Based on the synthesis of the PMOs, we can extrapolate the Sol-Gel processes (previously described for silicas) to the preparation of hybrid titania-based materials by tuning the reaction conditions ( $\text{TiO}_2$  as precursor, reaction times, temperature, etc.) and the functionalization of the corresponding dyes (-O-Si-, -NH-CO-, -O-CO- or -O-PO<sub>2</sub>-). Following this idea, it would be possible to develop a new *in-situ* approximation, based on co-condensation reactions, that allows to obtain materials with a better integration of the dye.

In this context, Prof. Schubert prepared several titanium coordination complexes with the structure  $[\text{Ti}(\text{OR})_a(\text{BL})_b]_n$ , where BL are bidentate complexing organic ligands (see figure 4.6),<sup>146</sup> by the reaction of functionalized organic molecules (aminoalcohols,  $\beta$ -diketones,  $\beta$ -ketoesters, carboxylic and phosphonic acids) with the corresponding  $\text{Ti}(\text{OR})_4$  precursor. This pointed out the

possibility of using this type of derivatives as building blocks for the preparation of hybrid titania-based materials by the Sol-Gel procedure.

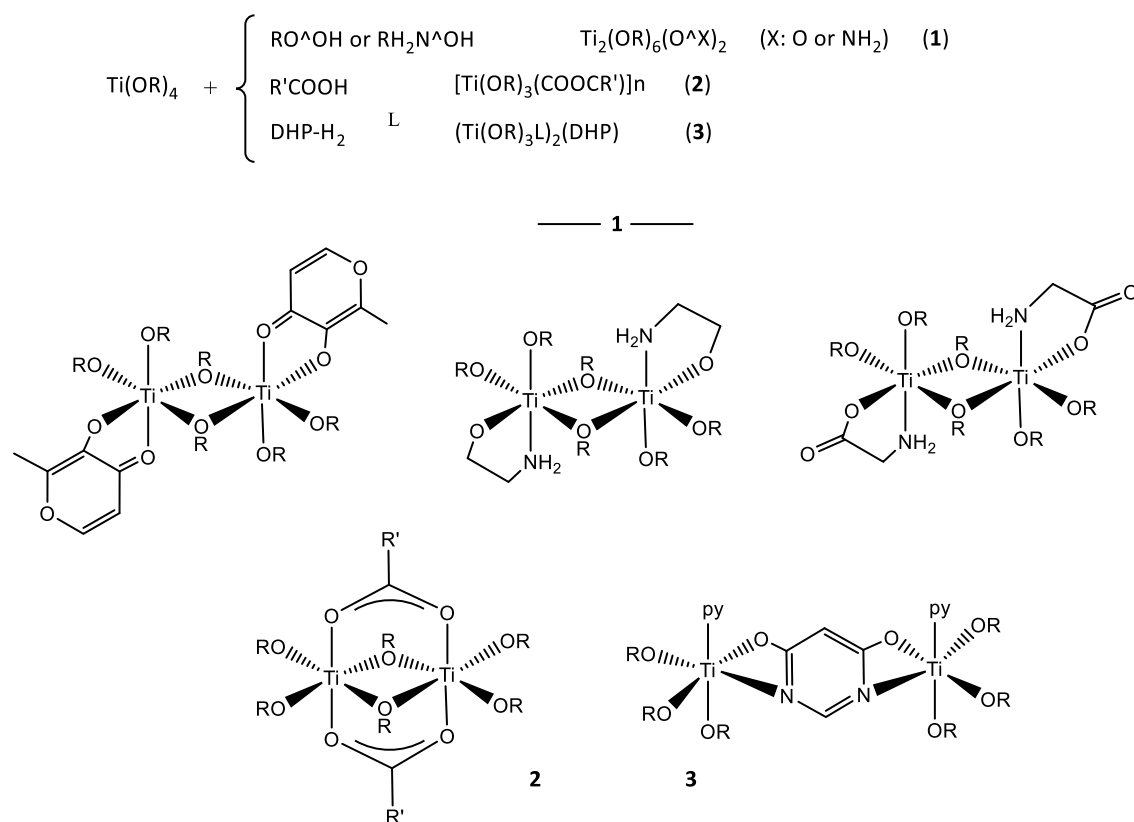


**Figure 4.6.** Schematic view of some of the titanium coordination complexes ( $[\text{Ti}(\text{OR})_a(\text{BL})_b]_n$ ) synthetized by Prof. Schubert *et al.* (J. Mater. Chem. 2005, 15, 3701-3715)

Inspired on this possibility, our group successfully adapted the *Sol-Gel Coordination Chemistry* approach (see chapter I)<sup>37</sup> to the obtaining, for the first time, of mesoporous organotitanias (see figure 4.7).<sup>147</sup> These materials contain photoactive organic molecules (4,6-dihydroxypyrimidine, DHP-H<sub>2</sub>, and p-phenylenediamine, PPD) incorporated into the framework of the semiconductor, which crystallizes adopting the anatase phase.<sup>147</sup> The one-pot co-condensation between the dyes and the titanium tetrabutoxide (TBOT, titania precursor) yielded titania-based materials with a homogeneous incorporation of the chromophore, narrower band gaps and, consequently, outstanding photocatalytic activity under visible light. In fact, a *black titania* (figure 4.7) was easily obtained when using the PPD organic compound.<sup>147</sup>

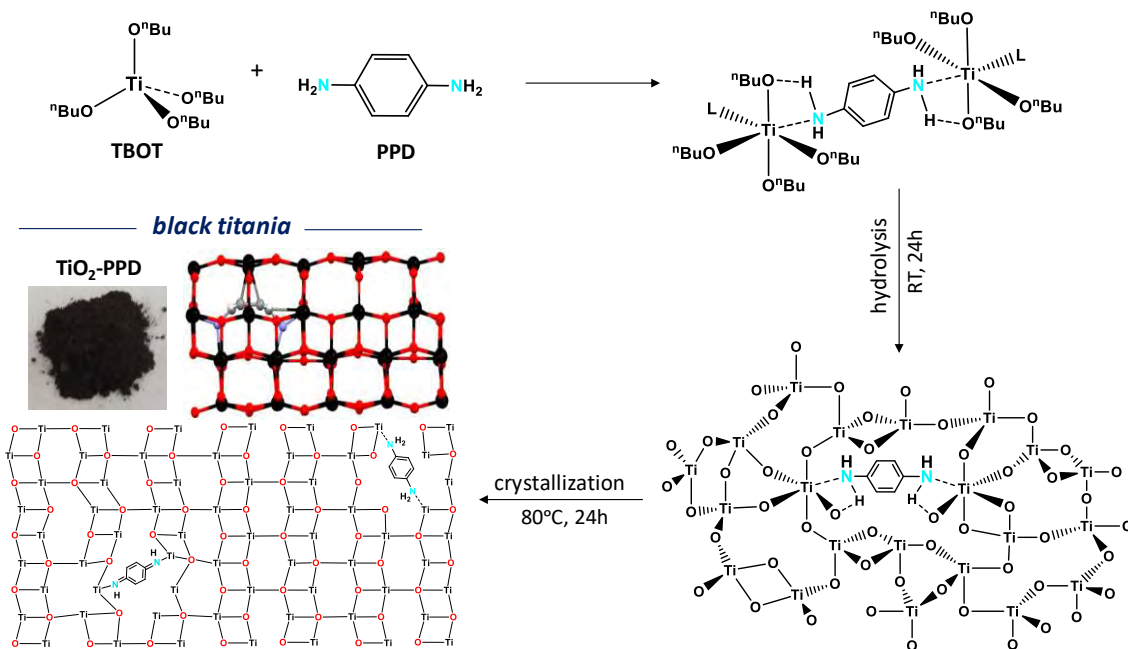


**Figure 4.7.** Synthesis of the *black titania*  $\text{TiO}_2\text{-PPD}$  prepared by the adaptation of the Sol-Gel Coordination Chemistry approach. (J. Mater. Chem. C 2014, 2, 9497-9504)

#### In-situ titania functionalization with coordination complexes

In view of the promising results obtained with the photoactive organic molecules, and, considering the charge transfer sensitizing properties of coordination complexes, we decided to explore the extension of this *in-situ* one-pot approach to the preparation of hybrid titania materials functionalized with coordination chromophores.

The new *in-situ* organometallo-titanias would be obtained by reacting coordination chromophores (bearing carboxyl, phosphonate, amino or silyl functionalities<sup>148</sup>) with the TBOT, as shown in figure 4.8. As far as we know, this synthetic approach has no precedent in the bibliography.

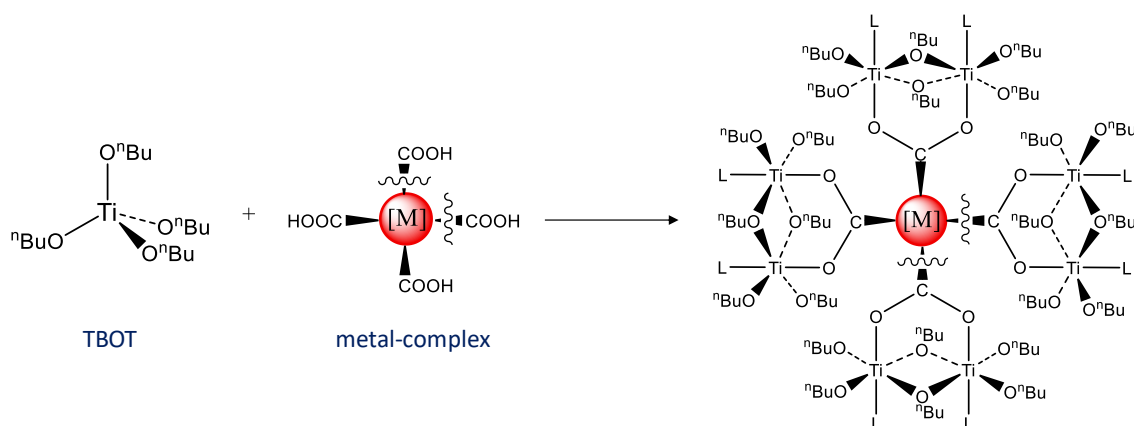


**Figure 4.8.** Schematic representation of the synthesis of hybrid metal complex-titania.

This innovative and eco-friendly approach (low reaction temperatures, neutral pH, use of water as the main solvent, etc.) will allow to obtain more stable anchorages and, consequently, more efficient titania-based photocatalysts under visible light. In addition, since both the organic and the coordination complexes are compatible with the synthetic route, a wide range of possible dyes would be incorporated into the semiconductor matrix.

### **Selection of the coordination complexes**

Nowadays, it is well known that polypyridyl Ru<sup>II</sup> complexes are efficient charge transfer sensitizers due to their great ability to inject electrons into the conduction band of the titania, after being activated by both UV and visible light.

In this topic, there are many applications of these derivatives reported in the literature. For example, Mahmoud *et al.* demonstrated the photocatalytic activity of Ru doped titania (Ru-TiO<sub>2</sub>) for the degradation of 2-chlorophenol (2-CP), reaching values of efficiency of 54% at ambient conditions.<sup>149</sup> Chen and co-workers tested the efficiency of the N3 ( $[\text{Ru}(4,4'\text{-H}_2\text{dcbpy})_2(\text{NCS})_2]$ ; 4,4'-H<sub>2</sub>dcbpy: 4,4'-dicarboxy-2,2'-bipyridine) and N719 ( $[\text{Ru}(4,4'\text{-Hdcbpy})_2(\text{NCS})_2](\text{N}^t\text{Bu}_4)_2$ ) dyes (see figure 4.9) in the removal of VOCs (Volatile Organic Compounds) from indoor pollution sources, obtaining a 95% of toluene degradation after 2 hours.<sup>150</sup>

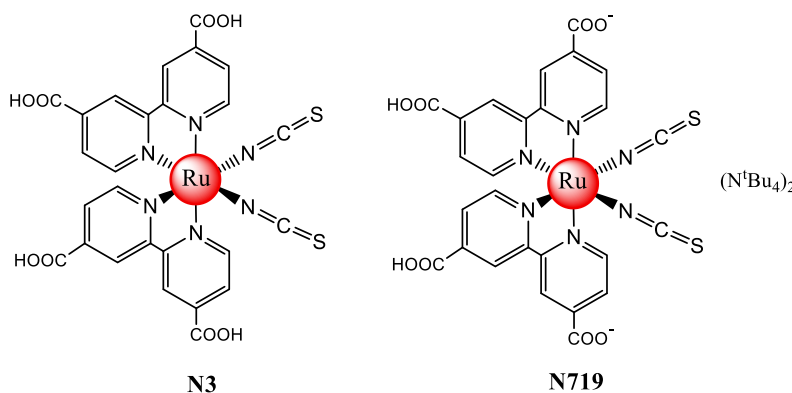


**Figure 4.9.** Schematic view of the N3 (left) and N719 (right) dyes.

Grätzel *et al.* also studied these ruthenium bipyridyl derivatives in photochemical cells, obtaining a remarkable solar-to-energy conversion yield of 10 and 11.1%, respectively for N3 and N719.<sup>132, 142a, 151</sup> Indeed, although several transition-metal complexes and many metal-free organic dyes have been studied,<sup>152</sup> the best results in terms of conversion yield and stability have been achieved with these N3 and N719 sensitizers. This behavior can be attributed to the fact

that these Ru<sup>II</sup> complexes exhibit a very intense metal-to-ligand charge transfer (MLCT) band, with molar absorptivities of *ca.* 15000 M<sup>-1</sup>cm<sup>-1</sup>, in the visible range.<sup>153</sup>

Nevertheless, the potential applications of these N3 and N719 Ru sensitizers is still limited to the poor stability of the anchorage between the charge-transfer dye and the inorganic matrix.<sup>154</sup> In addition, their long term stability is also greatly limited by the presence of the labile isothiocyanate groups that cause metal-ligand dissociation under light irradiation.<sup>155</sup> Therefore, there is a great interest in developing more stable photosensitizers. With this aim, dyes based on other transition metal complexes including platinum,<sup>156</sup> iron,<sup>157</sup> osmium,<sup>158</sup> copper,<sup>159</sup> rhenium<sup>160</sup> or iridium<sup>161</sup> have also been investigated.

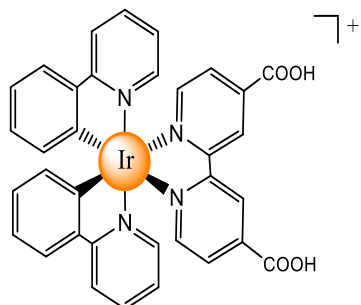


**Figure 4.10.** General structure of a heteroleptic iridium(III) complex  $[\text{Ir}(\text{C}^{\text{N}})_2(\text{N}^{\text{N}})]^+$ .

Although the efficiency of Ir-sensitizers is far from competing with that of the ruthenium dye due to the weak light absorbance in the range between 500 and 600 nm,<sup>162</sup> they display attractive photophysical properties associated to ease ligand structure changes. In particular, cyclometalated iridium(III) complexes have demonstrated to display higher thermal- and chemical- stabilities and a range of emissive states, including long live MLCT, ILCT and LLCT states, that allows the emission energy to be easily tuned.

For photoinduced electron transfer, the most attractive iridium systems are those based on heteroleptic complexes of the kind of  $[\text{Ir}(\text{C}^{\text{N}})_2(\text{N}^{\text{N}})]^+$  (see figure 4.10). In these systems, the presence of two strong ligand field increases the energy of the metal-centered (MC) states, providing the sensitizer with a high chemical stability and efficiency.<sup>163</sup> Furthermore, these iridium(III) derivatives have the potential for dual sensitization through both LLCT (ligand-to-ligand charge transfer) and MLCT (metal-to-ligand charge transfer) states,<sup>161a</sup> which could improve the efficiency of the final titania-based material. All these factors allow to consider these complexes suitable candidates to operate as photosensitizers for electron-transfer processes in the long term.

Considering all these facts, this chapter is mainly focused on the design of hybrid titania-based materials and the study of their photocatalytic activity through the degradation of Rhodamine 6G (R6G), under both UV and visible light irradiation. In this context, two are the photosensitizers used: (i) the N3 dye, due to its wide absorption band in the visible region and the excellent performance previously demonstrated, and (ii) a cyclometalated iridium complex due to their appealing properties.

**OBJECTIVES**

- We report the synthesis and characterization of a new iridium(III) complex ( $[\text{Ir}(\text{ppy})_2(3,3'\text{-H}_2\text{dcbpy})]\text{OTf}$ , **9** or **[Ir]**) and the study of its photophysical properties and those of the well-known N3 dye ( $[\text{Ru}(4,4'\text{-H}_2\text{dcpby})_2(\text{NCS})_2]$ , **10** or **[Ru]**).

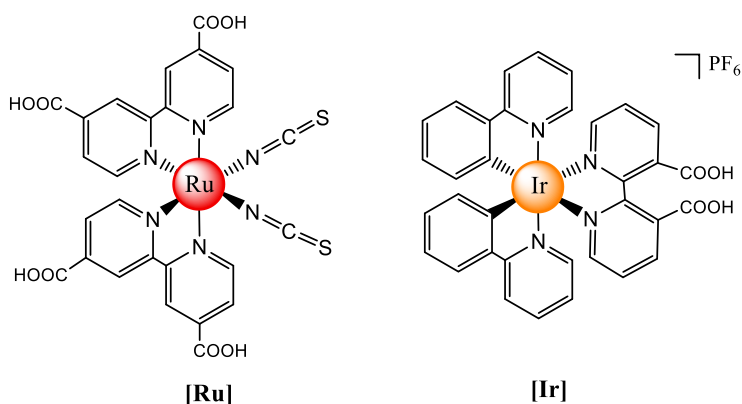


**Figure 4.11.** Schematic representation of the Ir(III) and Ru(II) complexes.

These two dyes incorporate carboxyl groups (-COOH) in the bipyridine ligand to allow the further condensation with the titania source, TBOT, and the formation of the hybrid organometallo-titania materials.

For comparison, we have also prepared the related Ir<sup>III</sup> derivative  $[\text{Ir}(\text{ppy})_2(4,4'\text{-dmbpy})]\text{PF}_6$ , where the COOH groups in the bipyridine ligand has been replaced by methyl groups.

- The corresponding titania-based materials (**[M]-TiO<sub>2</sub>\_IS**, M: Ir, Ru), are obtained following the *in-situ* approach previously reported by our group for the preparation of organotitanias, based on the Sol-Gel Coordination Chemistry.

To verify the effectiveness of our synthetic approach and to exclude the possibility of having superficial adsorption or occlusion of the dyes in the material, we also prepared the corresponding **TiO<sub>2</sub>\_IS** using as precursor complex  $[\text{Ir}(\text{ppy})_2(4,4'\text{-dmbpy})]\text{PF}_6$ .

For comparison purposes, the related grafted materials (**[M]-TiO<sub>2</sub>\_G**, M: Ir, Ru), following the usual *post-synthetic* procedure, as well as the complex-free **TiO<sub>2</sub>** are also prepared.

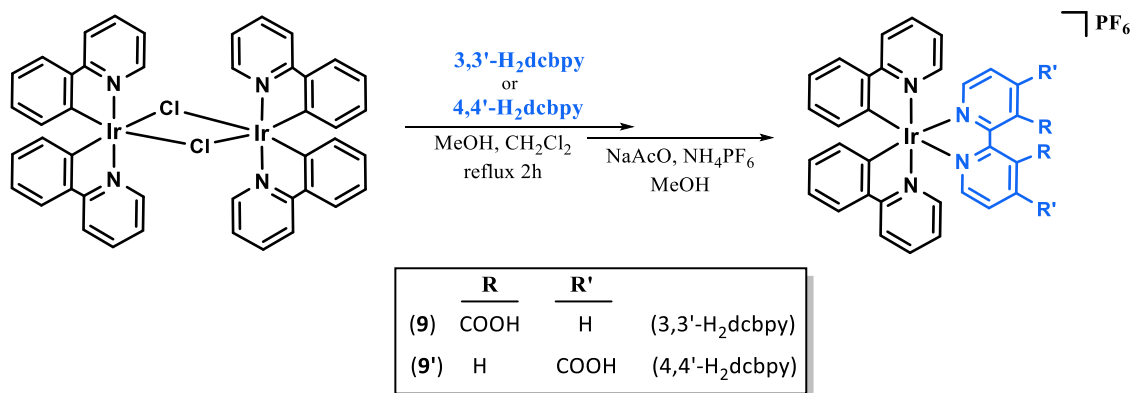
- The incorporation of the metal dyes in all titania materials has been studied by comparing their spectroscopy properties with those of their complex precursors, and, the effect of the incorporation on the band gap has been evaluated by valence band XPS spectroscopy.

- o Finally, we also evaluate the photocatalytic activity of all the as-synthetic materials. With this aim, we perform several studies based on the degradation of aqueous solutions of Rhodamine 6G (R6G,  $5 \times 10^{-5}$  M) under UV and visible light irradiation.

#### IV.1 Synthesis and characterization of metal complexes 9-10

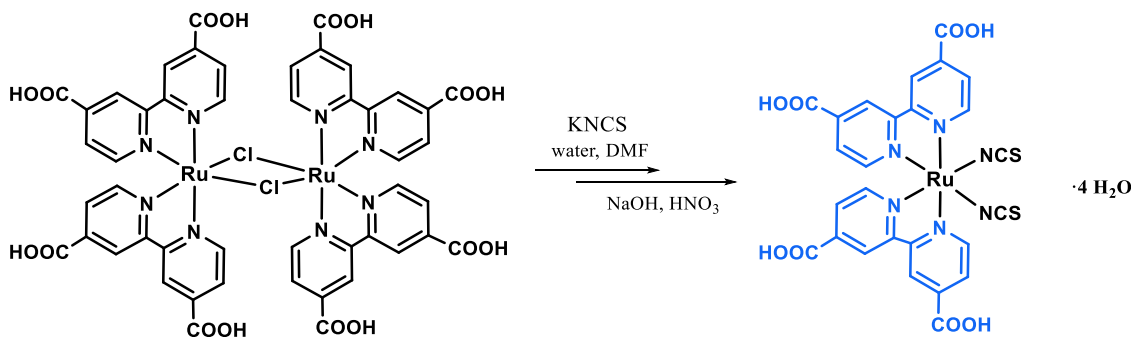
The iridium complexes were synthetized following a similar procedure to that previously reported for the 4,4'-H<sub>2</sub>dcbpy isomer.<sup>164</sup>

As shown in scheme 4.1, the stoichiometric reaction between the dichloro-bridge iridium precursor and the corresponding bipyridine ligand (3,3'-H<sub>2</sub>dcbpy: 2,2'-bipyridin-3,3'-dicarboxylic acid **9**; and 4,4'-H<sub>2</sub>dcbpy: 2,2'-bipyridin-4,4'-dicarboxylic acid **9'**) in a CH<sub>2</sub>Cl<sub>2</sub>/MeOH mixture produced an orange suspension that was neutralized with sodium acetate. The subsequent addition of a saturated methanolic solution of NH<sub>4</sub>PF<sub>6</sub> provided the pure complexes [Ir(ppy)<sub>2</sub>(3,3'-H<sub>2</sub>dcbpy)]PF<sub>6</sub> (**9**) and [Ir(ppy)<sub>2</sub>(4,4'-H<sub>2</sub>dcbpy)]PF<sub>6</sub> (**9'**) as precipitates of hexafluorophosphate salts.



**Scheme 4.1.** Synthetic route of iridium(III) complexes [Ir(ppy)<sub>2</sub>(3,3'-H<sub>2</sub>dcbpy)]PF<sub>6</sub> (**9**) and [Ir(ppy)<sub>2</sub>(4,4'-H<sub>2</sub>dcbpy)]PF<sub>6</sub> (**9'**).

On the other hand, although the ruthenium derivative ([Ru(4,4'-H<sub>2</sub>dcpby)<sub>2</sub>(NCS)<sub>2</sub>], **10**) is commercially available, it was prepared following the synthetic route described in the literature (see scheme 4.2).<sup>165</sup>



**Scheme 4.2.** Synthetic route of complex [Ru(4,4'-H<sub>2</sub>dcpby)<sub>2</sub>(NCS)<sub>2</sub>] (**10**).

All complexes were fully characterized, and their structures were confirmed by a combination of elemental analyses, mass spectrometry and usual spectroscopic means, such as infrared, absorption and multinuclear NMR.

The FTIR spectra of complexes **10** and **9** display the typical broad band of the hydroxyl groups at  $3400\text{ cm}^{-1}$ . Another characteristic band, that will allow to confirm the incorporation of the dyes in the titania material, is the  $\nu(\text{OC=O})$  stretching mode of the terminal COOH groups ( $1716\text{ cm}^{-1}$  **10**;  $1712\text{ cm}^{-1}$  **9**). The vibrations typically assigned to the bridging bidentate groups are also observed in both complexes ( $\nu_{\text{s}}(-\text{COOH})$   $1550$  **10**,  $1476$  **9**;  $\nu_{\text{as}}(-\text{COOH})$   $1383$  **10**,  $1413$  **9**), as well as peaks associated with the stretching vibrations of OC-O (ca.  $1220\text{ cm}^{-1}$ ). Ruthenium derivative (**10**) also features the corresponding vibration bands of the thiocyanate ligand ( $\nu(\text{C=N})$   $2110$  and  $1998\text{ cm}^{-1}$ ;  $\nu(\text{C=S})$   $769$  and  $750\text{ cm}^{-1}$ ), and **9** shows a weak band at  $845\text{ cm}^{-1}$  attributed to the vibration of the P-F bond of the counter ion,  $\text{PF}_6^-$ .

The  $^1\text{H}$  and  $^{13}\text{C}\{^1\text{H}\}$ NMR spectra of complex **9** (figures 4.12 and 4.13) support the structure initially proposed. The signals' assignment was carried out by using bidimensional experiments such as COSY ( $^1\text{H}$ - $^1\text{H}$  correlation), HSQC (single bond  $^1\text{H}$ - $^{13}\text{C}$  correlation), HMBC (multiple bond  $^1\text{H}$ - $^{13}\text{C}$  correlation) and TOCSY. As shown in the figures, the complex exhibits signals due to the presence of only one type of cyclometalated ligand and reveals the equivalence of both pyridine rings in the bpy group, confirming the mutually *trans* disposition of the nitrogen atoms of the phenylpyridinyl (ppy) groups.

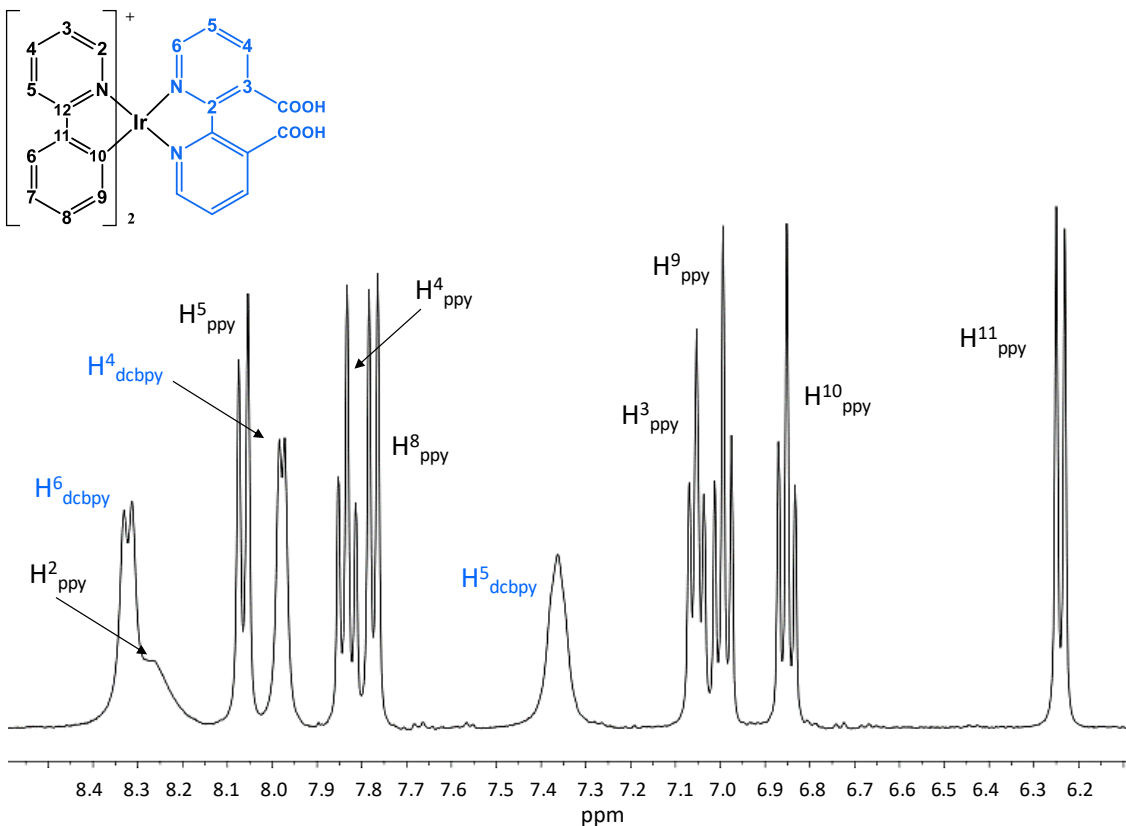


Figure 4.12.  $^1\text{H}$  NMR spectrum in  $\text{CD}_3\text{COD}$  of complex  $[\text{Ir}(\text{ppy})_2(3,3'\text{-H}_2\text{dc bpy})]\text{PF}_6$  (9).

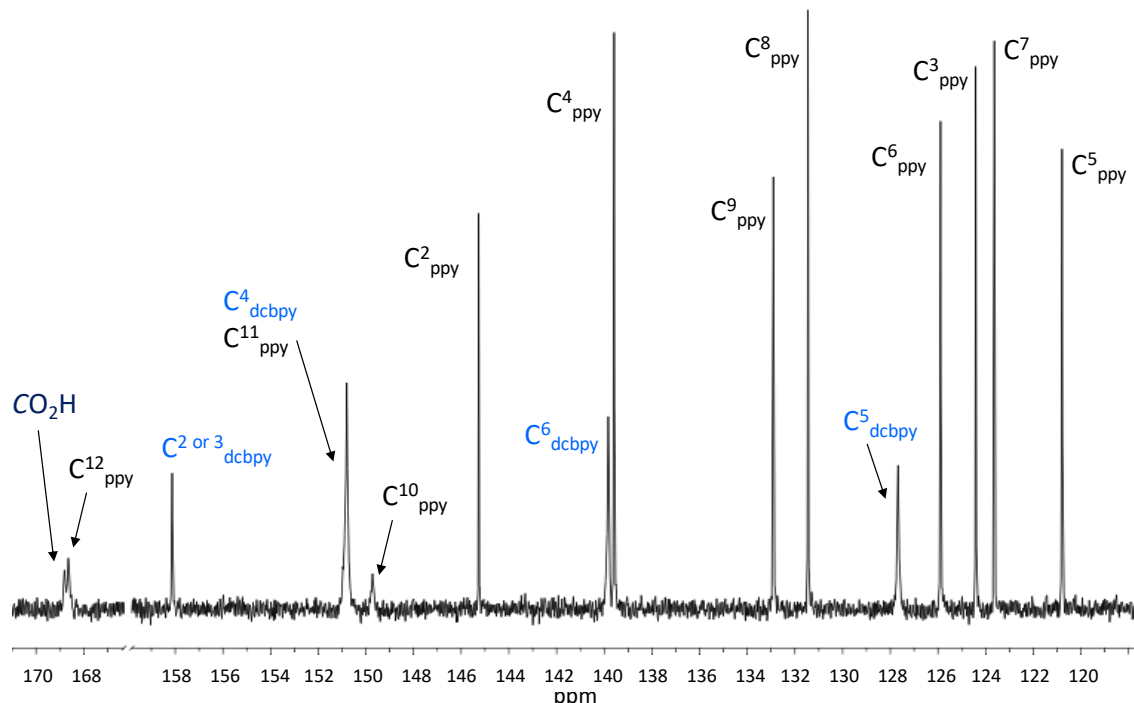
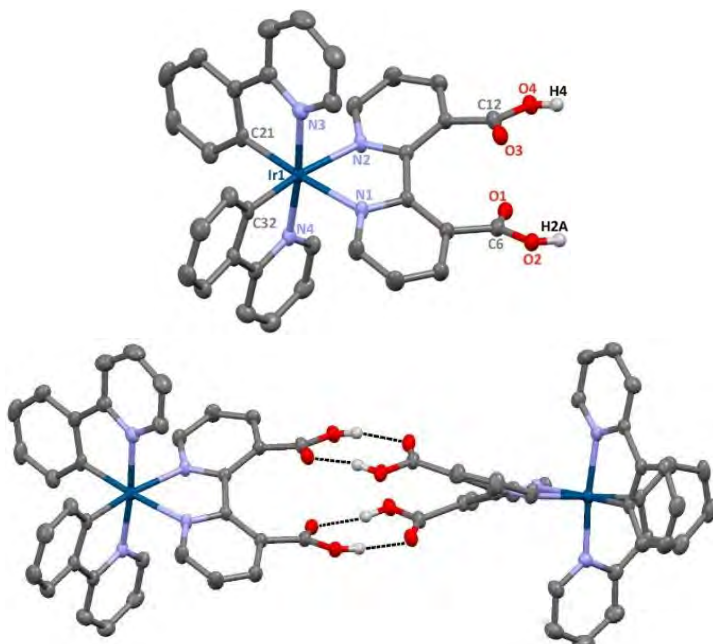


Figure 4.13.  $^{13}\text{C}\{^1\text{H}\}$  NMR spectrum in  $\text{CD}_3\text{COD}$  of complex  $[\text{Ir}(\text{ppy})_2(3,3'\text{-H}_2\text{dc bpy})]\text{PF}_6$  (9).

The molecular structure of complex **9** was also confirmed by the X-ray diffraction study performed on an orange monocrystal of the corresponding compound obtained by cooling a saturated dichloromethane solution of the derivate. As shown in figure 4.14, the molecular structure of the cation **9<sup>+</sup>** presents the expected pseudo-octahedral environment with bond distances and angles comparable to those observed for related derivatives.<sup>164, 166</sup> In addition, it behaves similarly to other compounds that incorporate the 3,3'-H<sub>2</sub>dcbpy ligand,<sup>167</sup> resolving the steric repulsion between the carboxylic acid units on the bipyridine ligand by twisting the pyridine rings to a dihedral angle of 26.53°. This distortion enables the formation of intermolecular hydrogen bonds between the carboxylic acid groups (O-H···O), giving rise to dimers with interaction distances of 2.6 Å (O···O) and 1.8 Å (H···O) and O-H···O angles of 169°.



**Figure 4.14.** (Upper part) Molecular structure of the cation complex  $[\text{Ir}(\text{ppy})_2(3,3'\text{-H}_2\text{dcbpy})]^+$  (**9<sup>+</sup>**). Most relevant bond lengths (Å): Ir-C 2.011(3), 2.015(3). Ir-N(ppy) 2.043(3), 2.048(3). Ir-N(bpy) 2.138(3), 2.155(3). (Lower part) View of the molecular dimer formed by the presence of hydrogen bonds (O-H···O) between the carboxylic acid groups. Find more data in annex IV.

## IV.2 Photophysical properties of the Ir<sup>III</sup> and Ru<sup>II</sup> complexes

### i. Absorption spectra

Complex  $[\text{Ru}(4,4'\text{-H}_2\text{dcpby})_2(\text{NCS})_2]$  (**10**) exhibits a very broad absorption spectrum in the solid state that covers the entire visible region and extends up to 800 nm (figure 4.15). The highest energy bands observed at 230 and 322 nm are assigned, according to literature,<sup>165</sup> to a

spin-allowed ligand centered transitions ( $\pi\pi^*$ ) localized on the bipyridine ligands. It also displays two more intense low energy features at 408 and 540 nm, attributed to a spin-allowed  $^1\text{MLCT}$ , and a shoulder (650 nm) that broadens to 800 nm, commonly related with a spin-forbidden metal-to-ligand charge transfer ( $^3\text{MLCT}$ ). A similar spectrum is observed in ethanolic solution (314, 398 and 538 nm, see table 4.1).<sup>165</sup>

**Table 4.1.** Absorption data in solution ( $5 \times 10^{-5}$  M) and in the solid state of complexes  $[\text{Ru}(4,4'\text{-H}_2\text{dcbpy})_2(\text{NCS})_2]$  (**10**) and  $[\text{Ir}(\text{ppy})_2(3,3'\text{-H}_2\text{dcbpy})]\text{PF}_6$  (**9**).

Sample	$\lambda_{\text{abs}}/\text{nm}$ ( $\epsilon/\text{M}^{-1}\text{L}^{-1}$ )
$[\text{Ru}(4,4'\text{-H}_2\text{dcbpy})_2(\text{NCS})_2]$ ( <b>10</b> )	314 (48.2), 398 (14.0), 538 (14.2) <b>EtOH</b> 230, 322, 408, 540, 650 <sub>sh</sub> <b>Solid</b>
	257 (28.8), 289 <sub>sh</sub> (19.9), 381 (4.2), 470 (3.0), 512 (0.4) <b>CH<sub>2</sub>Cl<sub>2</sub></b>
$[\text{Ir}(\text{ppy})_2(3,3'\text{-H}_2\text{dcbpy})]\text{PF}_6$ ( <b>9</b> )	254 (28.9), 287 <sub>sh</sub> (17.4), 381 (3.5), 401 (2.7), 470 (0.3) <b>MeOH</b> 253 (30.0), 289 <sub>sh</sub> (19.8), 381 (5.0), 403 (3.6), 475 (0.6), 514 <sub>sh</sub> (0.5) <b>MeCN</b> 290, 320, 380, 470, 510 <b>Solid</b>

The solid state DRUV spectrum of complex **9** displays, as shown in figure 4.15, two bands in the high energy region (290 and 320 nm), which are related to allowed  $\pi\pi^*$  transitions centered on bipyridine and phenylpyridine ligands. Based on previous assignments on similar derivatives,<sup>164, 166a</sup> the additional feature at 380 nm can be assigned to a mixture of metal-to-ligand and ligand-to-ligand charge transfer ( $^1\text{MLCT}/^1\text{LL'CT}$ , L: ppy; L': H<sub>2</sub>dcbpy). Finally, the weak absorption peak at 470 nm is attributed to spin-forbidden  $^3\text{MLCT}$ ,  $^3\text{LL'CT}$  and  $^3\text{LC}$  (ppy) transitions. This spectrum resembles to those observed in solution, showing minimal hypsochromic shifts in the lowest energy band when modifying the polarity of the solvents (see table 4.1 and figure 4.15).

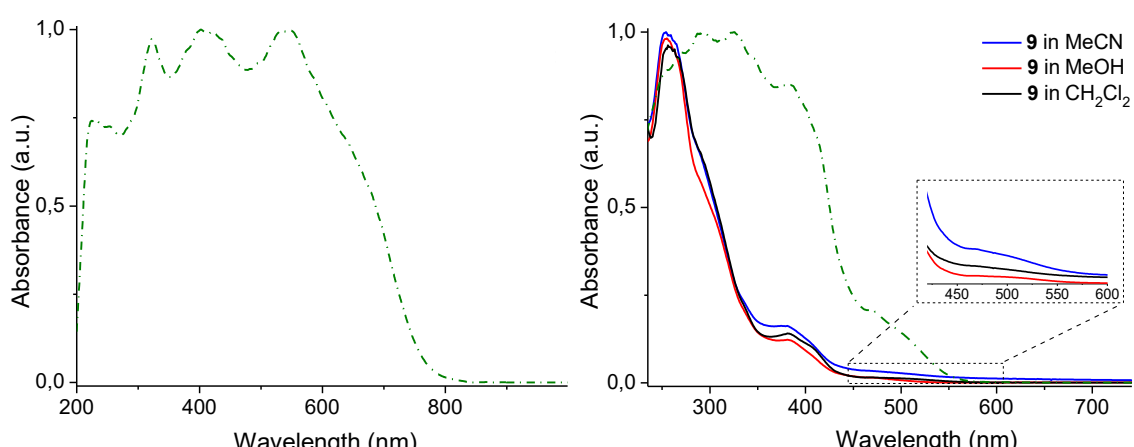


**Figure 4.15.** Absorption spectra in solution (solid line) and in the solid state (dash line) of the iridium complex **9** (right), and in the solid state of the ruthenium derivative **10** (left).

## *ii. Emission spectra*

According to the emissive properties, both derivatives show a very weak emission in both solution and solid state. As reported elsewhere,<sup>165</sup> complex **10** is only emissive in ethanolic solution where exhibits a broad emission band at 830 nm, derived from a <sup>3</sup>MLCT excited state (see table 4.2).

**Table 4.2.** Emission data of complexes  $[\text{Ru}(4,4'\text{-H}_2\text{dcbpy})_2(\text{NCS})_2]$  (**10**) and  $[\text{Ir}(\text{ppy})_2(3,3'\text{-H}_2\text{dcbpy})]\text{PF}_6$  (**9**) in solid state and in solution (EtOH, MeCN,  $5 \times 10^{-4}$  M).

Sample	Medium (T/K)	$\lambda_{\text{em}}/\text{nm}$ ( $\lambda_{\text{ex}}/\text{nm}$ )	$\tau$ ( $\mu\text{s}$ )	$\phi$ %
$[\text{Ru}(4,4'\text{-H}_2\text{dcbpy})_2(\text{NCS})_2]$ ( <b>10</b> )	EtOH (298) <sup>(a)</sup>	830 (310)	0.02	0.04
	Solid (298)	648 (400)	0.03	3.9
$[\text{Ir}(\text{ppy})_2(3,3'\text{-H}_2\text{dcbpy})]\text{PF}_6$ ( <b>9</b> )	Solid (77)	624 (400)		
	MeCN (298)	625 (425)		
	MeCN (77)	600 (450)		

(a) Data from reference <sup>133c</sup>.

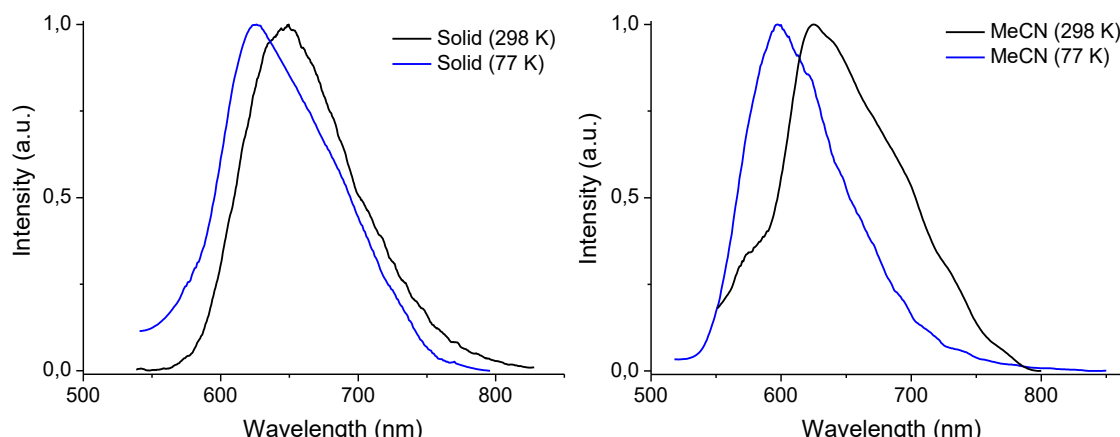


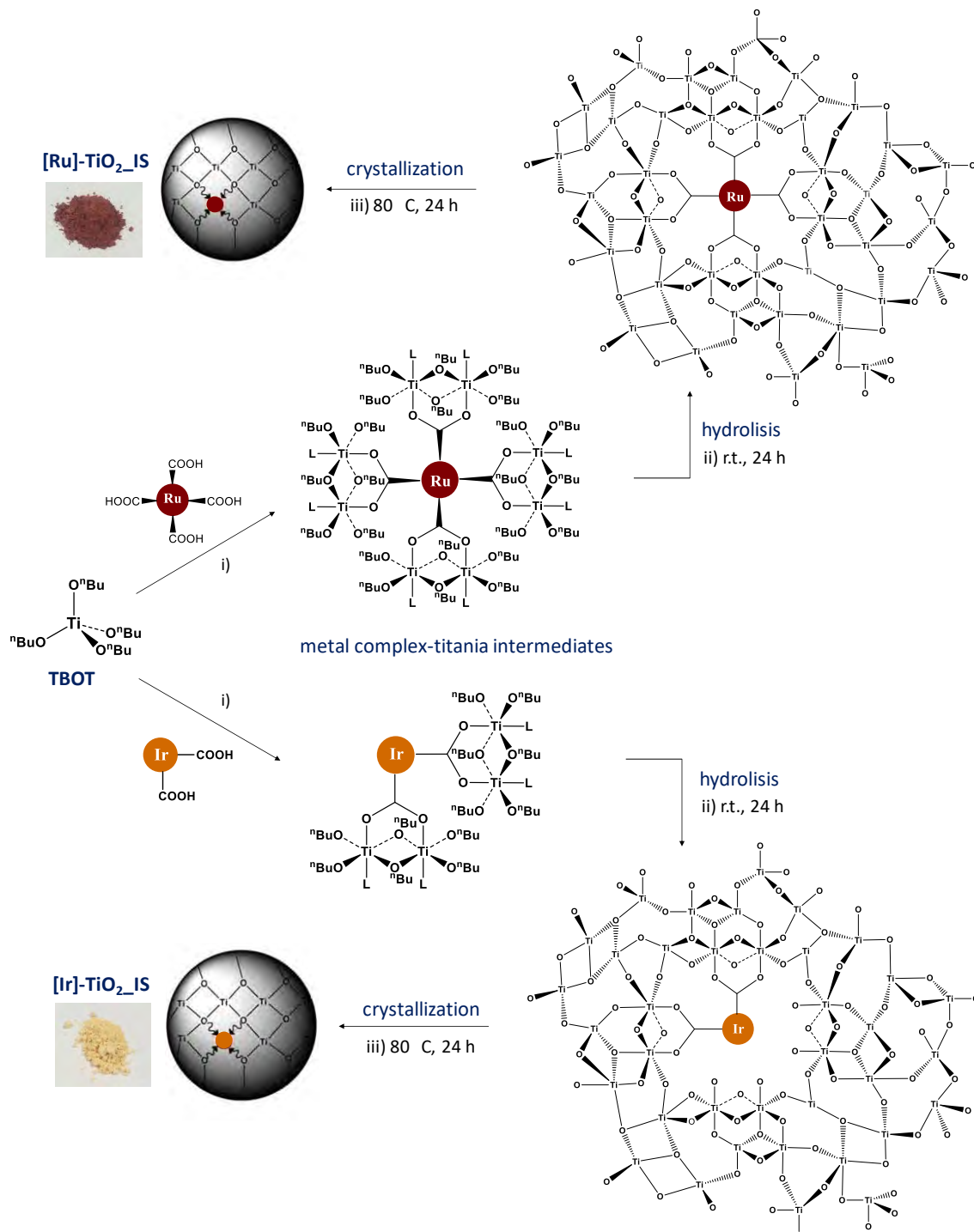
**Figure 4.16.** Emission spectra of the iridium complex  $[\text{Ir}(\text{ppy})_2(3,3'\text{-H}_2\text{dcbpy})]\text{PF}_6$  (**9**) in the solid state (left) and in acetonitrile solution (right) at both room temperature and 77K.

The iridium compound (**9**) also displays a broad non-structured emission band in all media. In the solid state at room temperature, the phosphorescence feature is centered at 648 nm, showing a low quantum yield (*ca.*  $\phi$  4%) and a short lifetime of 30 ns. As expected, the emission is notably blue-shifted when decreasing the temperature at 77K (624 nm), which is consistent with the <sup>3</sup>MLCT ( $\text{Ir} \rightarrow \text{H}_2\text{bpy}$ ) character attributed to this emission. In acetonitrile solution at 298K, complex **9** also displays an unstructured emission profile (625 nm) very similar to that observed for the corresponding isomer with the 4,4'-H<sub>2</sub>dcbpy ligand in the same solvent ( $[\text{Ir}(\text{ppy})_2(4,4'\text{-H}_2\text{dcbpy})]\text{PF}_6$ , 624 nm at 298K; 576 nm at 77K).<sup>164</sup> However, in glassy solution, the

emission of **9** experiences a bathochromic shift to lower energies in relation to  $[\text{Ir}(\text{ppy})_2(4,4'\text{-H}_2\text{dcbpy})]\text{PF}_6$  (600 nm in **9** vs. 576 nm in  $[\text{Ir}(\text{ppy})_2(4,4'\text{-H}_2\text{dcbpy})]\text{PF}_6$ )<sup>164</sup>. This fact could be tentatively attributed to the formation of dimers through hydrogen bonding in **9** (similar to those shown in figure 4.16), that enables the stabilization of the target orbital of the bipyridine ligand and, thus, causing the decrease of the energy of the emission.

### IV.3 Synthesis of hybrid titania-based materials ( $\text{TiO}_2\text{-IS}$ , $\text{TiO}_2\text{-G}$ )

Throughout this section, to facilitate the interpretation of the results, complexes  $[\text{Ir}(\text{ppy})_2(3,3'\text{-H}_2\text{dcbpy})]\text{PF}_6$  (**9**) and  $[\text{Ru}(4,4'\text{-H}_2\text{dcbpy})_2(\text{NCS})_2]$  (**10**) will be denoted as **[Ir]** and **[Ru]**, respectively, and their corresponding titania-based materials as **[Ir]- $\text{TiO}_2$**  and **[Ru]- $\text{TiO}_2$** .



**Scheme 4.3.** Synthesis of the hybrid metal complex-titania **[Ru]- $\text{TiO}_2\text{-IS}$**  and **[Ir]- $\text{TiO}_2\text{-IS}$**  materials.

The synthesis of the *in-situ* mesoporous titania-based materials (**[M]-TiO<sub>2</sub>\_IS**, M: Ru or Ir) was performed following a similar procedure to that previously reported by our group for the obtaining of organotitanias.<sup>147, 168</sup>

In detail, a mixture of each coordination dye in ethanol with 5 g of TBOT (metal complex/TBOT *ca.* 0.005 molar ratio) enables the formation of a homogenous solution of polometallic ruthenium- or iridium-titanium alkoxide intermediates, by the reaction of the carboxylic acids of the complexes and the TBOT molecules (scheme 4.3, i). According to some other reports,<sup>146a, 165</sup> these intermediates are proposed to be made of dititanium units through bidentate bridging carboxylate groups. Nevertheless, monodentate or chelating bidentate coordination to titanium centers are likely in some extent. Notwithstanding, and due to the flexibility of the medium, we consider that all these groups (four in **[Ru]** and two in **[Ir]**) should be involved in bonding. Further hydrolysis for 24 hours at room temperature allows the formation of a gel (scheme 4.3, ii), which crystallizes adopting an anatase phase after heating the suspension at 80 °C for other 24 hours (scheme 4.3, iii). After the corresponding treatment of the resulting mixture, garnet (**[Ru]-TiO<sub>2</sub>\_IS**) and pale-orange (**[Ir]-TiO<sub>2</sub>\_IS**) materials were obtained (see the experimental section for more details).

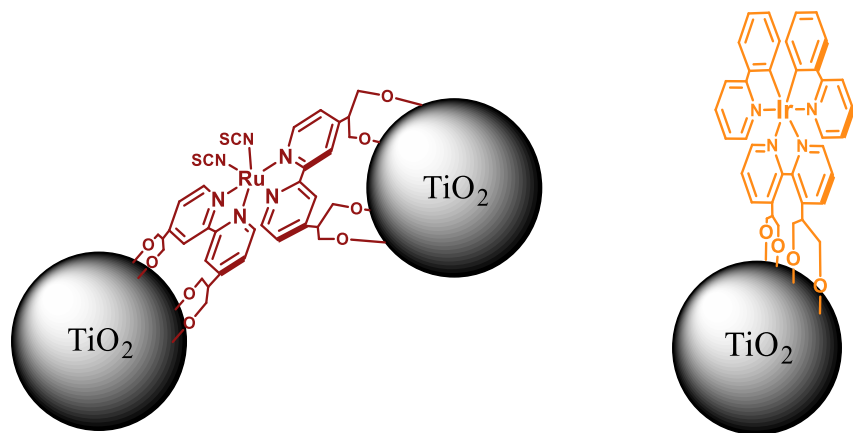


**Figure 4.17.** Ruthenium (**[Ru]**, left) and iridium (**[Ir]**, right) complexes covalently bonded to the surface of the titania by the grafting approximation (**[M]-TiO<sub>2</sub>\_G**, M: Ru, Ir).

On the other hand, following the same synthetic route but without the concurrence of any dye, a complex-free control titania (**TiO<sub>2</sub>**) was prepared for comparison purposes. In addition, as previously described in the introduction, related grafted materials (**[M]-TiO<sub>2</sub>\_G**, M: Ru and Ir, figure 4.17) were also synthetized by the superficial condensation of each dye in the aforementioned complex-free titania. Reactions to obtain the grafted materials were carried out with a similar Ti/metal molar ratio to that employed in the *in-situ* materials (see the experimental part).

Finally, in order to highlight the importance of functionalizing the dyes with carboxylate groups, we also prepared a related iridium(III) complex using a bipyridine ligand in which the -COOH have been replaced by methyl groups ( $[\text{Ir}(\text{ppy})_2(4,4'\text{-dmby})]\text{PF}_6$ , 4,4'-dmby: 4,4'-dimethyl-2,2'-bipyridine). This molecule presents very similar size to complex **[Ir]** and, so, the results are comparable.

Following the same procedure to that described for the synthesis of **[M]-TiO<sub>2</sub>\_IS** (M: Ru, Ir), we prepared the corresponding titania. However, in this case, no incorporation of the derivative to the titania material was observed and only metal-free titania was obtained. The only rational reason that could explain this fact is that the lack of covalent bonding between the coordination dye and the semiconductor crystalline network made it impossible to retain or encapsulate the molecules in the final material. This evidence excludes the possibility of having superficial adsorption or occlusion of the complexes in the anatase nanoparticles of our materials, and, supports our initial idea that the formation of covalent bonds in the system is essential to prepare *in-situ* hybrid titanias.

#### **IV.4 Characterization of the mesoporous titania-based materials**

The incorporation of the coordination complexes in the titania-based materials was studied by FTIR, XPS and absorption spectroscopies. The textural properties of all the hybrids materials were also fully studied.

##### ***IV.4.1 Textural characterization***

To study the porous nature of the titania-based materials, the physisorption experiments were performed in the research group of Prof. Javier García Martínez.

As shown in the figure 4.18, all the as-synthesized materials display type IV isotherms and textural properties very similar to those observed for the complex-free titania (table 4.3), which is indicative of the mesoporous nature of the samples. This mesoporosity does not come from any surfactant but from the spaces that are generated between the small crystallites. Both the grafted and the *in-situ* titanias show high surface areas (200-250 m<sup>2</sup>/g) and similar pore sizes, suggesting that the incorporation of the dye to the network of the semiconductor does not affect to the final textural properties of the material.

**Table 4.3.** Textural and structural parameters of both the hybrid titania-based materials (**[M]-TiO<sub>2</sub>\_IS** and **[M]-TiO<sub>2</sub>\_G**, M: Ru, Ir) and the control titania, **TiO<sub>2</sub>**.

Sample	d <sub>p</sub> <sup>(a)</sup> (nm)	V <sub>p</sub> <sup>(b)</sup> (cm <sup>3</sup> /g)	A <sub>BET</sub> <sup>(c)</sup> (m <sup>2</sup> /g)	d <sup>XRD,(d)</sup> (nm)	d <sub>101</sub> <sup>XRD,(e)</sup> (nm)	d <sub>101</sub> <sup>TEM,(f)</sup> (nm)
TiO <sub>2</sub>	5.6 (2-9)	0.29	245	6.4	0.35	0.37
[Ru]-TiO <sub>2</sub> _IS	6.0 (3-11)	0.31	200	6.4	0.35	0.38
[Ru]-TiO <sub>2</sub> _G	6.0 (3-11)	0.35	240	6.1	0.35	0.38
[Ir]-TiO <sub>2</sub> _IS	5.6 (1-9)	0.22	230	5.6	0.35	0.35
[Ir]-TiO <sub>2</sub> _G	6.0 (2-12)	0.28	220	6.5	0.35	0.38

(a) Average mesopore diameter determined from the isotherm using the NLDFT equilibrium model. (b) Mesopore volume directly read from the adsorption branch of the isotherm at (P/P<sub>0</sub>) = 0.8. (c) BET surface area estimated by multipoint BET method using the adsorption data in the relative pressure (P/P<sub>0</sub>) range of 0.05–0.25. (d) Crystalline domain size calculated from XRD. (e) Anatase spacing (d<sub>101</sub>) read from XRD. (f) Anatase spacing (d<sub>101</sub>) read from TEM images.

Samples were centrifuged and air dried before gas adsorption measurements.

On the other hand, this semiconductor can crystallize in three different phases (anatase, rutile and brookite) depending on the reaction conditions. To evaluate this, XRD studies were also performed. Thus, as shown in figure 4.18, all the materials exhibit the three main peaks that, according to the literature, correspond to the anatase phase (2θ: 25.3°, 37.8° and 48.05°).<sup>169</sup> The broad XRD peaks also indicate that the as-synthesized materials are formed by nanoparticles, with a crystalline domain size of *ca.* 6 nm. However, it is worth noting that, despite the similar molecular size of both coordination complexes (13 Å [Ru] vs. 11 Å [Ir]<sup>+</sup>), the [Ir]-TiO<sub>2</sub>\_IS sample shows the smallest value (5.6 nm). In any way, the crystalline domain size of all the materials (IS and G) is comparable to that found for the control titania (6.4 nm), suggesting that the incorporation of the organometallic derivatives does not significantly affect to the crystallinity of the TiO<sub>2</sub>.

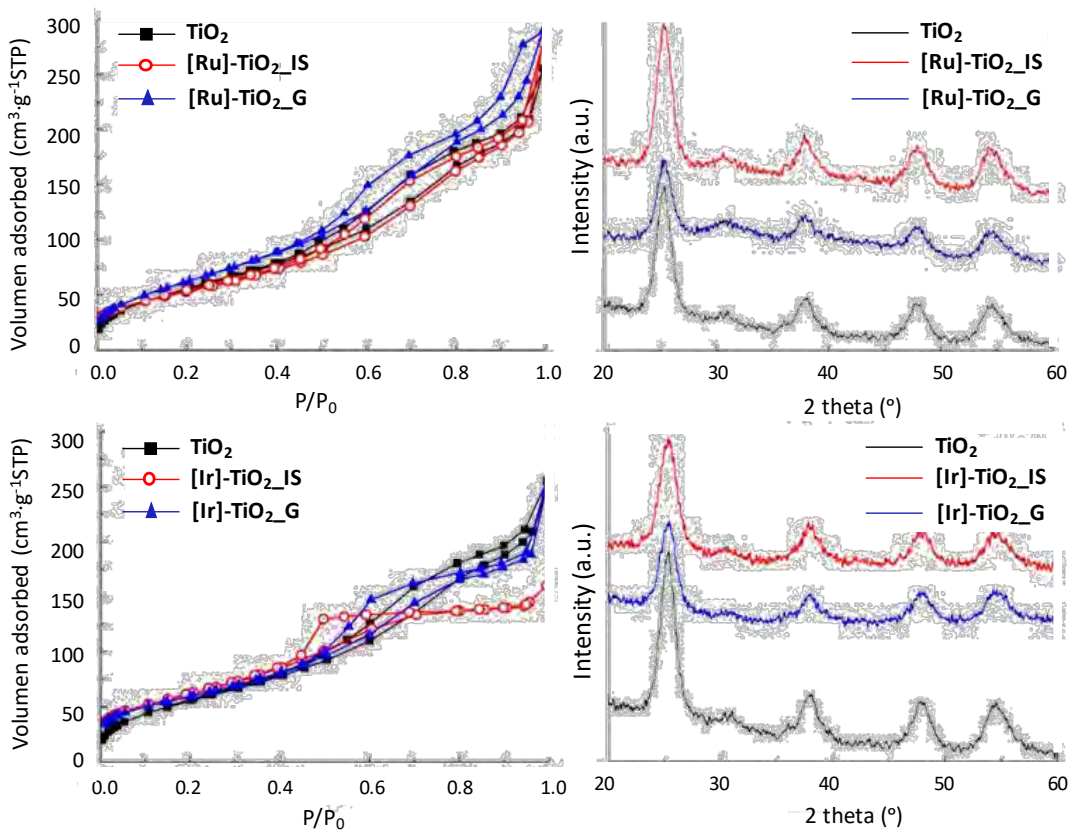


**Figure 4.18.** N<sub>2</sub> adsorption/desorption isotherms at 77k (left) and XRD patters (right) of the *in-situ* and grafted materials ([M]-TiO<sub>2</sub>\_IS and [M]-TiO<sub>2</sub>\_G, M: Ru, Ir) in comparison with the control TiO<sub>2</sub>.

Based on this XRD study, the distance between the crystalline planes (101) were determined and, despite the incorporation of the dyes, no changes were observed when compared to the control TiO<sub>2</sub> (0.35 nm). In addition, this  $d_{101}$  lattice spacing were also calculated using the Gatan software on the TEM images showing very similar values (0.35–0.38 nm, see figure 4.19).

These TEM images show that the material is formed by small particles with sizes between 7 and 9 nm of diameter and, also, confirm that there is no significant complex agglomeration in the titania nanoparticles.

Finally, the content of each complex in both types of materials was also estimated by ICP analysis. As shown in table 4.4, there is a clear difference in the incorporation yield between the *in-situ* and the grafted materials. Thus, the incorporation yield for the *in-situ* hybrids was 92 wt% and 59 wt% for [Ru] and [Ir], respectively, while the values obtained for the grafted titanias were much lower (60 wt% [Ru] and 23 wt% [Ir]). This fact indicates the effectiveness of our synthetic procedure since we are able to incorporate 1.5 and 2.5 times more chromophore *via* the *in-situ* synthesis than the grafted one. However, a lower incorporation of the iridium dye in both

materials is clearly observed, probably due to the presence of fewer carboxylate groups and its cationic nature.

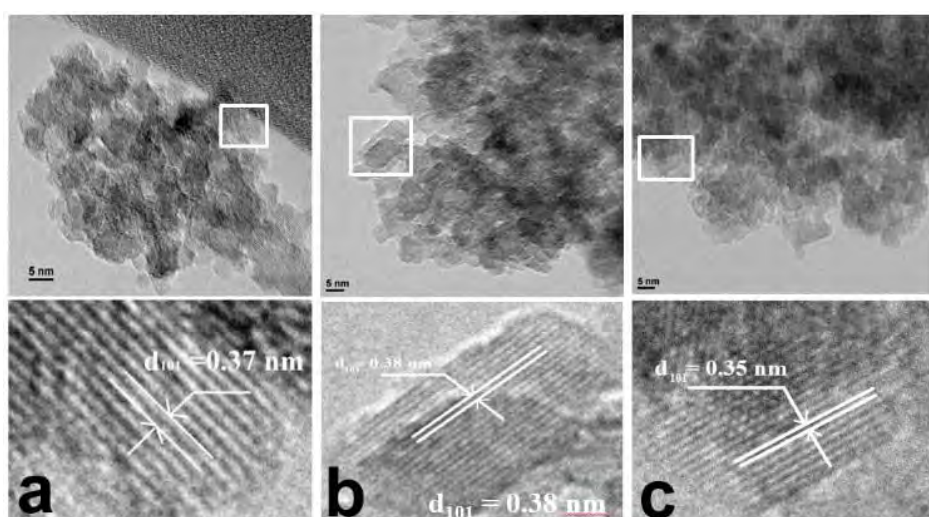


**Figure 4.19.** Representative TEM images of the control  $\text{TiO}_2$  (a),  $[\text{Ru}]\text{-TiO}_2\text{-IS}$  (b) and  $[\text{Ir}]\text{-TiO}_2\text{-IS}$  (c) materials.

**Table 4.4.** Estimated and calculated metal content in the titania-based materials.

Sample	$M^{(a)}$ (wt%)	$M^{(a)}$ (mol%)	Incorporation yield <sup>(a)</sup> (%)
$[\text{Ru}]\text{-TiO}_2\text{-IS}$	0.49 (0.53)	0.35 (0.38)	92
$[\text{Ru}]\text{-TiO}_2\text{-G}$	0.32 (0.53)	0.24 (0.38)	60
$[\text{Ir}]\text{-TiO}_2\text{-IS}$	0.87 (1.47)	0.35 (0.59)	59
$[\text{Ir}]\text{-TiO}_2\text{-G}$	0.34 (1.47)	0.14 (0.59)	23

(a) Metal content calculated by ICP-OES analysis. Values in brackets represent the theoretical values.

#### IV.4.2 Spectroscopy characterization

##### i. Absorption spectra

As shown in figure 4.20, the DRUV spectra clearly determine the presence of the corresponding derivatives in both types of titania samples ( $[\text{M}]\text{-TiO}_2\text{-IS}$  and  $[\text{M}]\text{-TiO}_2\text{-G}$ , M: Ru, Ir), due to the presence of some characteristic absorption bands of the dyes. Besides the typical intense band related to  $\text{TiO}_2$  ( $\approx 280 \text{ nm}$ ), the most significant features are those observed in the low energy region. As expected, the two bands observed for both the ruthenium and the iridium materials (**IS** and **G**) are similar to those previously recorded for the corresponding pure complexes (see table 4.5), although the features for the ruthenium titanias are slightly blue-shifted (390, 500 nm vs. 408, 540 nm, see table 4.5).

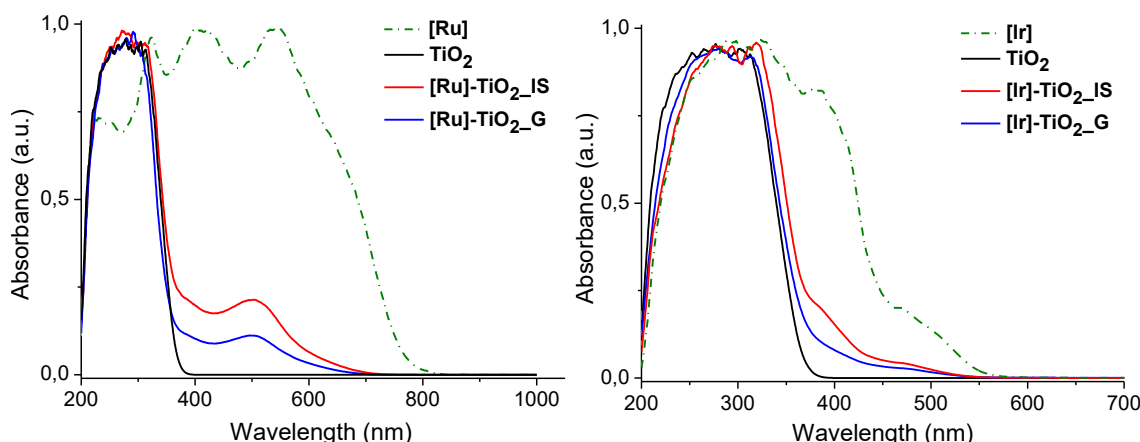


**Figure 4.20.** Solid state DRUV spectra of complexes **[Ru]** (left) and **[Ir]** (right), and those of their corresponding hybrid metal complex-titania materials compared with the control **TiO<sub>2</sub>**.

Notwithstanding, the DRUV spectra clearly suggest a higher incorporation of the coordination dye in the *in-situ* materials than in the grafted ones, a fact that has also been confirmed by ICP analyses, thus, again suggesting the effectiveness of our synthetic proposal.

**Table 4.5.** Absorption data in the solid state (DRUV) of complexes **[Ru]** and **[Ir]** and their corresponding titania-based materials (**[M]-TiO<sub>2</sub>\_IS** and **[M]-TiO<sub>2</sub>\_G**, M: Ru, Ir).

Sample	$\lambda_{\text{abs}}/\text{nm}$
<b>[Ru(4,4'-H<sub>2</sub>dcbpy)<sub>2</sub>(SCN)<sub>2</sub>] [Ru]</b>	230, 322, 408, 540, 650 <sub>sh</sub>
<b>[Ru]-TiO<sub>2</sub>_IS</b>	280, 390 <sub>sh</sub> , 500 <sup>(a)</sup>
<b>[Ru]-TiO<sub>2</sub>_G</b>	280, 390 <sub>sh</sub> , 504 <sup>(a)</sup>
<b>[Ir(ppy)<sub>2</sub>(3,3'-H<sub>2</sub>dcbpy)]PF<sub>6</sub> [Ir]</b>	290, 320, 380, 470, 510
<b>[Ir]-TiO<sub>2</sub>_IS</b>	280, 316, 380, 470 <sup>(b)</sup>
<b>[Ir]-TiO<sub>2</sub>_G</b>	280, 316, 380, 470 <sup>(b)</sup>

(a) Tail extending to 700 nm. (b) Tail extending to 540 nm.

### *ii. Infrared spectra*

The incorporation of the coordination dyes in the semiconductor materials was also confirmed by FTIR spectroscopy. As illustrated in figure 4.21, the infrared spectra of both the complexes (**[Ru]** and **[Ir]**) and the titania samples (**[M]-TiO<sub>2</sub>\_IS** and **[M]-TiO<sub>2</sub>\_G**), including the metal-free control titania (**TiO<sub>2</sub>**), are included. As expected, all the materials exhibit characteristic broad and intense features due to **TiO<sub>2</sub>** (figure 4.21). Thus, below 750 cm<sup>-1</sup>, the bands related with the asymmetric stretching of the Ti-O-Ti moiety centered at ca. 580 and 470 cm<sup>-1</sup> are observed. The broad bands at around 1620 and 3400 cm<sup>-1</sup> are also attributed to the vibration of the terminal hydroxyl groups that remain on the surface of the **TiO<sub>2</sub>**.<sup>170</sup>

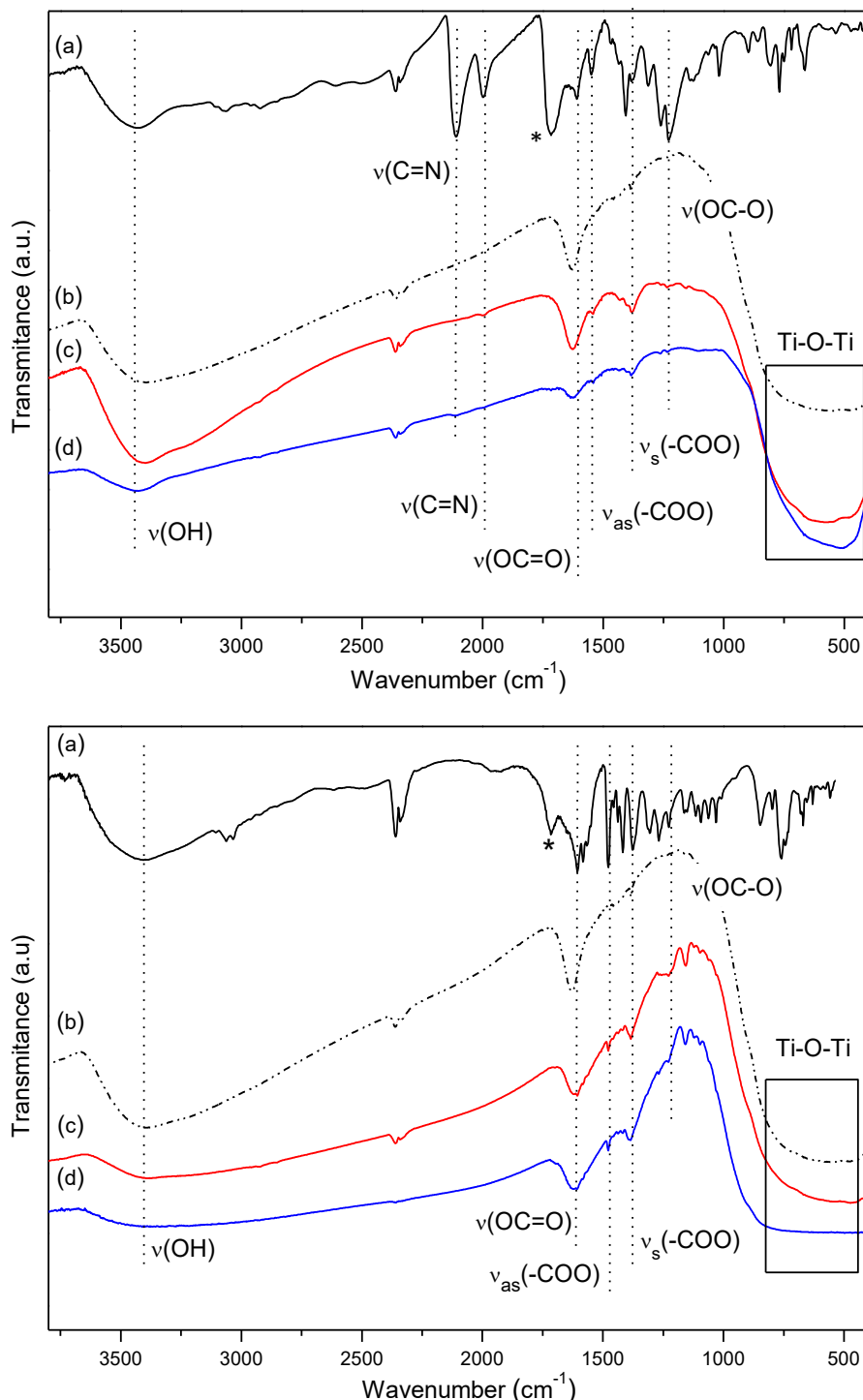


**Figure 4.21.** FTIR spectra of the ruthenium- (up) and iridium- (down) titania materials **[M]-TiO<sub>2</sub>\_IS** (c) and **[M]-TiO<sub>2</sub>\_G** (d) in comparison with the spectra of the pure complexes **[Ru]** and **[Ir]** (a) and the control titania, **TiO<sub>2</sub>** (b). (\*)  $\nu(\text{OC=O})$  of the terminal –COOH groups.

On the other hand, both metal complex-titania based materials (**IS** and **G**) also show distinctive features of the corresponding pure complexes. The disappearance of the  $\nu(\text{OC=O})$  stretching mode of the terminal COOH groups ( $1716 \text{ cm}^{-1}$  **[Ru]**;  $1712 \text{ cm}^{-1}$  **[Ir]**) supports the incorporation of the complexes through the participation of bidentate bridging carboxylate

groups.<sup>171</sup> In fact, the bands typically assigned to the stretching vibration of bridging bidentate groups ( $\nu_s(-\text{COO}) \sim 1370 \text{ cm}^{-1}$ ,  $\nu_{as}(-\text{COO}) \sim 1500 \text{ cm}^{-1}$ ) are clearly resolved. Nevertheless, the presence of monodentate carboxylate binding groups in some extension cannot be excluded as a weak peak at  $1220 \text{ cm}^{-1}$ , associated with  $\nu(\text{OC}-\text{O})$ , in the carboxylate groups, is also observed in both hybrid materials. This would be consistent with the wider binding vibration of the superficial hydroxyl groups observed for the hybrid materials when compared with the complex-free titania. Finally, very weak bands at  $1997$  and  $2113 \text{ cm}^{-1}$  related to the thiocyanate ligands in the ruthenium dye are also observed in the hybrid ruthenium samples.

### *iii. XPS analysis*

The surface of all the materials was also evaluated by XPS measurements. Representative XPS spectra of the Ti 2p and O 1s regions of the ruthenium and iridium materials (**[M]-TiO<sub>2</sub>\_IS** and **[M]-TiO<sub>2</sub>\_G**, [M]: Ru, Ir), as well as the complex-free titania are collected in figure 4.22.

The spectrum of the control **TiO<sub>2</sub>** in the Ti 2p level shows two well-defined peaks at  $458.5$  and  $464.5 \text{ eV}$ , characteristic of Ti(IV)  $2p_{3/2}$  and Ti(IV)  $2p_{1/2}$  states, respectively, where Ti displays an octahedral coordination.<sup>143c, 172</sup> On the other hand, the O 1s XPS spectra of all the materials were deconvoluted using symmetric Gaussian curves. As shown in figure 4.22, the corresponding spectrum of the control titania shows a main peak at  $529.8 \text{ eV}$ , which is attributed to the bridging oxygen between titanium centers (Ti-O-Ti).<sup>173</sup> The additional peak that appears at  $531.7 \text{ eV}$  is related to the oxygen atoms in the form of hydroxyl groups that remain on the surface of the titania (Ti-OH species).<sup>173a, 174</sup>

The *in-situ* (**[M]-TiO<sub>2</sub>\_IS**) and grafted (**[M]-TiO<sub>2</sub>\_G**) samples do not show any shift or shape changes in the Ti 2p peaks when compared to the control titania (see figure 4.22), suggesting that the incorporation of the cyclometalated complexes in the hybrid materials does not affect neither the anatase structure nor the Ti coordination. The same behavior is found on the O 1s spectra, where the peak at  $531 \text{ eV}$  is now attributed to the oxygen not only in the surface of the material but also in the carboxylic groups of the dyes.

Finally, it is should be noted that the presence of the Ru(II) and Ir(III) complexes cannot be observed by XPS likely due to the small amount incorporated (0.04 g **[Ru]** and 0.08 g **[Ir]**) and the overlapping of their characteristic binding energies with other peaks: Ru 3p with Ti 2p at *ca.*  $460 \text{ eV}$ , Ru  $3d_{3/2}$  with one of the C 1s peaks at  $287.8 \text{ eV}$ ; and Ir  $4f_{5/2}$  and Ir  $4f_{7/2}$  with Ti 3s at  $62 \text{ eV}$ .<sup>143c,</sup>

<sup>175</sup>

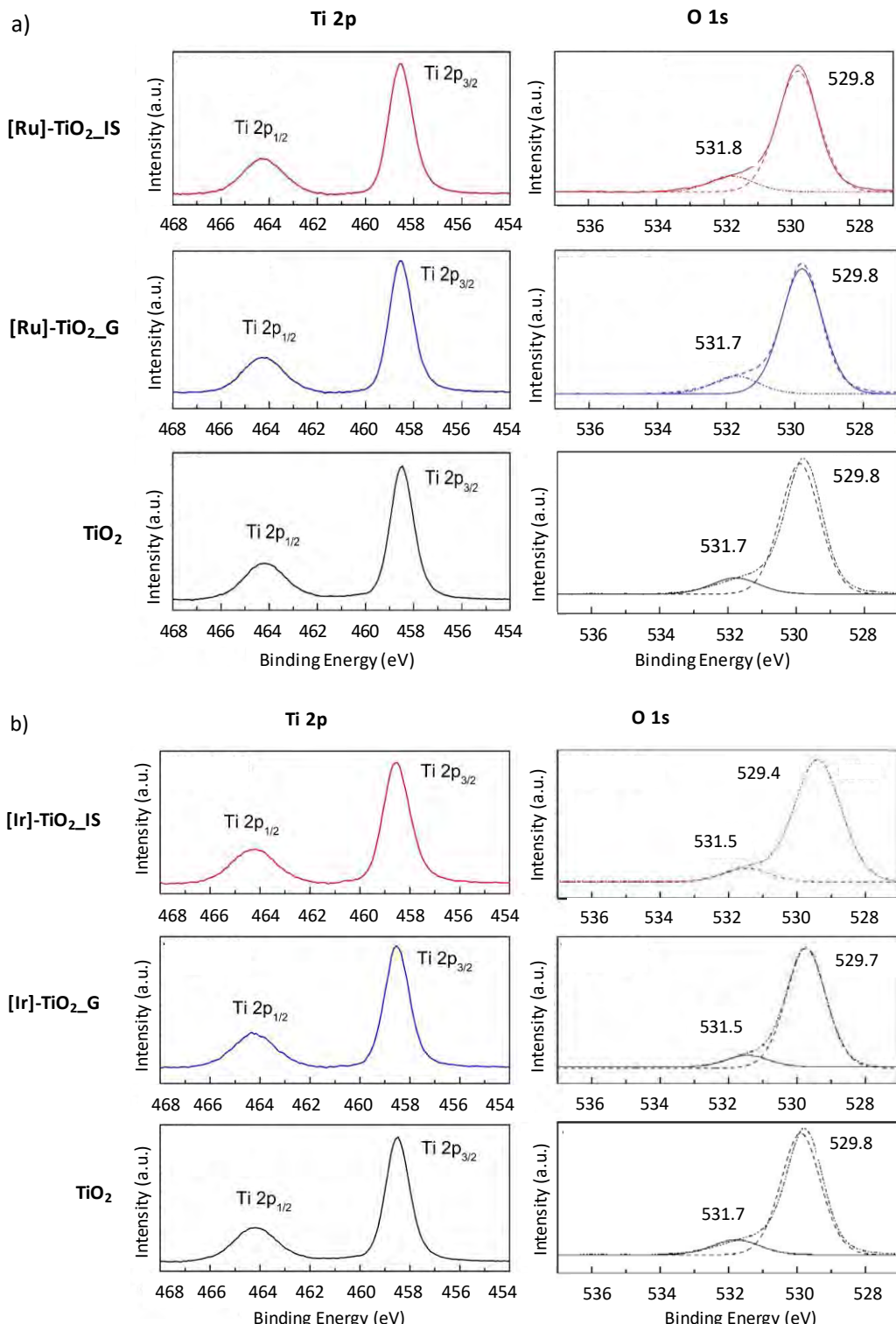


**Figure 4.22.** Representative XPS spectra in the Ti 2p and O 1s regions of **[M]-TiO<sub>2</sub>\_IS** (up) and **[M]-TiO<sub>2</sub>\_G** (middle) compared with the control **TiO<sub>2</sub>** (down) of the ruthenium- (a) and iridium- (b) titanias.

## IV.5 Photocatalytic activity of the metal-complex titania-based materials

### IV.5.1 Estimation of the band-gap energies

To determine the band gap energy of the as-synthetic materials, we transformed the DRUV spectra previously described (figure 4.20) into Tauc plots (intensity of the absorption vs. energy in electronvolts), which are commonly used to determine the optical band gaps in semiconductors. Based on these diagrams, we can simply estimate this characteristic energy just extrapolating the corresponding energy absorption band edges in the spectra (figure 4.23, dotted line). This study allows not only to calculate the band gap related to the titania network but also to confirm the presence of the coordination dyes in the semiconductor. The position of the higher energy level of the valence bands (VB), measured by XPS, and the density of states diagrams (DOS) are also shown in figure 4.24 (a and b, respectively).

The band gap of the control  $\text{TiO}_2$  was estimated to be 3.24 eV. This energy, related to the indirect transition of the anatase phase, is in agreement with other values reported in the literature.<sup>147, 176</sup> The edge of the maximum energy at about 2.28 eV is also similar to that observed for other titania samples.<sup>174a</sup>

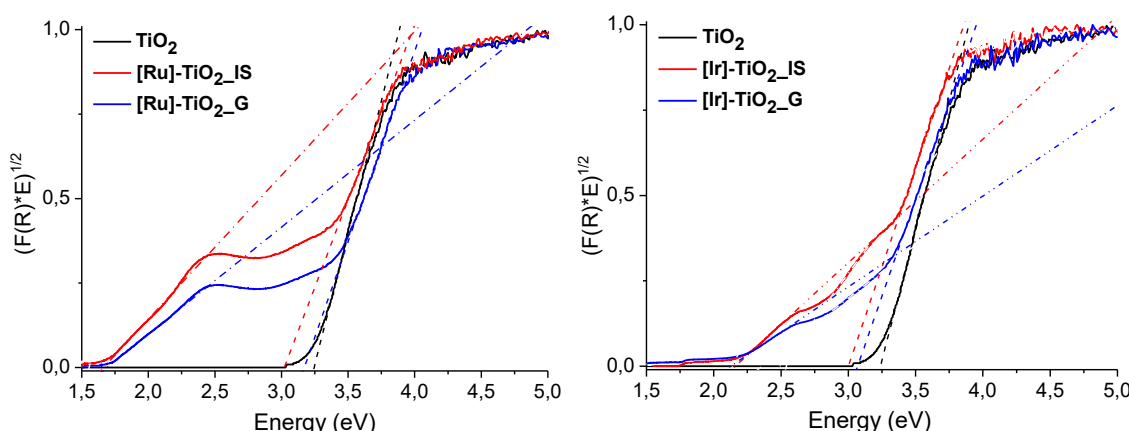


**Figure 4.23.** Tauc plots of the transformed Kubelka-Munk function vs. the energy of the light absorbed of both types of titania materials ( $[\text{M}]\text{-TiO}_2\text{-IS}$  and  $[\text{M}]\text{-TiO}_2\text{-G}$ , M: Ru, Ir) in comparison with the control  $\text{TiO}_2$ .

As shown in figure 4.23, the Tauc plots of the hybrid materials ( $[\text{M}]\text{-TiO}_2\text{-IS}$  and  $[\text{M}]\text{-TiO}_2\text{-G}$ , M: Ru, Ir) feature two different absorption band edges. The lower energy absorption band edge is directly associated to the presence of each complex in the as-synthesized materials (eV/nm 1.70/ 729, Ru; 2.15/ 590, Ir), while the higher energy one is related, as in the control  $\text{TiO}_2$ , to the primary band gap of the anatase phase. In addition, there is an evident decrease on the energy of this last band edge for the *in-situ* materials (2.82 eV  $[\text{Ru}]\text{-TiO}_2\text{-IS}$ , 3.00 eV  $[\text{Ir}]\text{-TiO}_2\text{-IS}$ ) when

compared to the control  $\text{TiO}_2$  (3.24 eV), causing a narrowing in their corresponding band gaps that now lie in the visible region (figure 4.24, b).

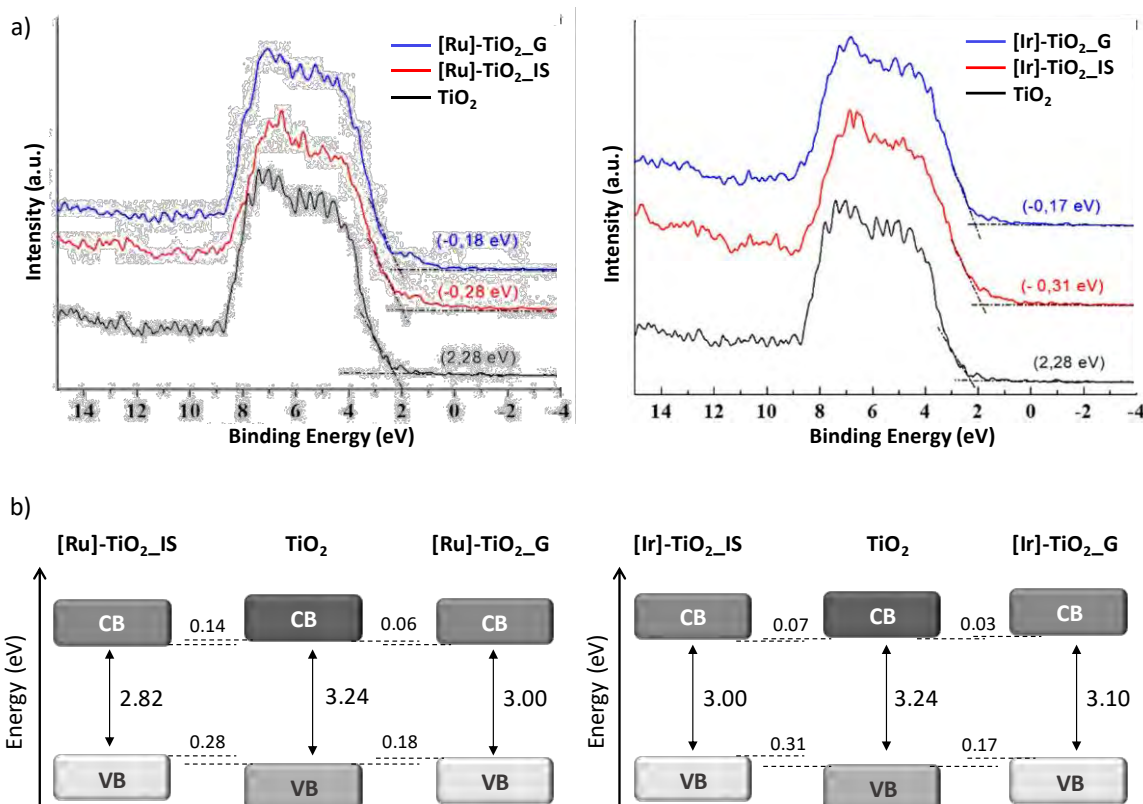


**Figure 4.24.** (a) Valence band XPS spectra, and (b) schematic view of the DOS diagrams of both types of titania materials ( $[\text{M}]\text{-TiO}_2\text{-IS}$  and  $[\text{M}]\text{-TiO}_2\text{-G}$ , M: Ru, Ir) in comparison with the control  $\text{TiO}_2$ .

When comparing the *in-situ* titanias, the decrease in the indirect band gap transition energy is less remarkable for the iridium-based material (3.00 eV, 413 nm  $[\text{Ir}]\text{-TiO}_2\text{-IS}$ ) than for the ruthenium one (2.82 eV, 440 nm  $[\text{Ru}]\text{-TiO}_2\text{-IS}$ ), which is notably red-shifted. Nevertheless, a slight increase in the highest energy level of the valence band (*ca.* 0.30 eV; figure 4.24, b) is also observed in both samples respect to the value calculated for  $\text{TiO}_2$ .

A similar behavior, although less pronounced, was observed for the grafted hybrids ( $[\text{M}]\text{-TiO}_2\text{-G}$ , M: Ru, Ir), suggesting that the incorporation of the dyes following the grafting procedure produces less impact on the band gap transition. Also, the decrease on the band gap is only about half of that observed for the **IS** materials, with an increase in the energy of the VB of *ca.* 0.17 eV.

Finally, it is worth noting that although both the *in-situ* and the grafted titanias present the same anatase structure and similar textural and spectroscopic properties, the ICP analyses and

the DRUV spectra have shown a more efficient uptake of the dyes in the [M]-TiO<sub>2</sub>\_IS samples. This fact is supposed to have a decisive role when evaluating their photocatalytic activity.

#### ***IV.5.2 Photocatalytic activity of the Ir<sup>III</sup> and Ru<sup>II</sup> titania-based materials***

The photocatalytic activity of both the *in-situ* and grafted materials was evaluated by following the degradation of aqueous solutions of Rhodamine 6G (R6G, 5x10<sup>-5</sup> M), under UV and visible light irradiation, in the presence of the as-synthesized catalysts (0.15 g/L, [M]-TiO<sub>2</sub>\_IS and [M]-TiO<sub>2</sub>\_G, M: Ru or Ir). When irradiating with UV light, a 400W medium-pressure Hg lamp located in a cooled, double-walled quartz immersion well was used. On the other hand, to perform the study under visible irradiation, a Pyrex immersion well cooled with a 2 M NaNO<sub>2</sub> solution was also used as a UV cutoff filter for wavelengths higher than 400 nm used (see the experimental part for more details).

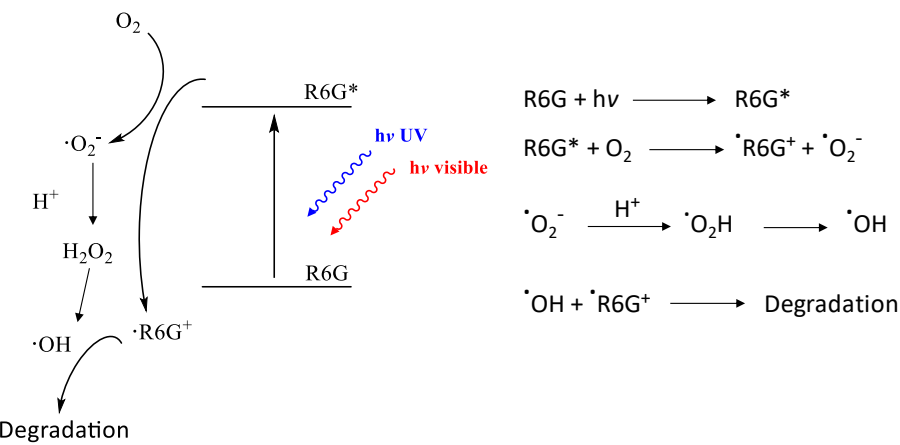
The aqueous solutions of R6G are deep orange colored, showing a bleaching when the Rhodamine has been degraded (see figure 4.25). Nevertheless, the degradation process was followed by UV/Vis spectroscopy along 180 min of irradiation, by monitoring the decreasing of the characteristic absorption peak of the Rhodamine at 525 nm (see the experimental part for more details).



**Figure 4.25.** Photographs of the different samples taken along the degradation reaction of the aqueous solution of R6G (5x10<sup>-5</sup> M) under UV radiation, under visible (left) and UV (right) light.

The degradation mechanism of these R6G molecules in aqueous solutions has been extensively studied<sup>177</sup> and, it is known that, in the absence of any titanium catalyst this dye scarcely degrades under our test conditions. Notwithstanding, the reaction mechanism in the absence of TiO<sub>2</sub> and the presence of O<sub>2</sub> includes the following processes (scheme 4.4):

The excitation of the Rhodamine molecules *via* UV or visible light generates R6G\*, increasing its redox potential. This causes an electron transfer and the formation of ·O<sub>2</sub><sup>-</sup> and ·R6G<sup>+</sup> radicals. The further reaction of the superoxide radicals with protons from the solvent produces ·OH groups, which yield the final degradation of the cationic radical ·R6G<sup>+</sup> to CO<sub>2</sub>, H<sub>2</sub>O and mineral acids.



**Scheme 4.4.** Schematic representation of the photodegradation of the Rhodamine 6G.

For comparison purpose, the catalytic activity of the related complex-free titania material (**TiO<sub>2</sub>**) was also evaluated.

#### IV.5.2.1 Study of the photocatalytic activity under UV and visible light irradiation

Figures 4.26 and 4.27 represent the level of degradation of the Rhodamine after being catalyzed with the titania-based materials during the first 3 hours, under both types of illumination.

When irradiating with UV light (figure 4.26), both hybrid materials (**IS** and **G**) are able to photodegrade R6G molecules to a great extent within the first three hours (between 70 and 100% yield), while the complex-free titania **TiO<sub>2</sub>** only yields a 50% of conversion at this time and needs more than 12 hours for the total bleaching of the solution. A similar behavior is observed under visible light (figure 4.27), although all the hybrids seem to be less efficient than under UV irradiation, at least within the experimental conditions chosen.

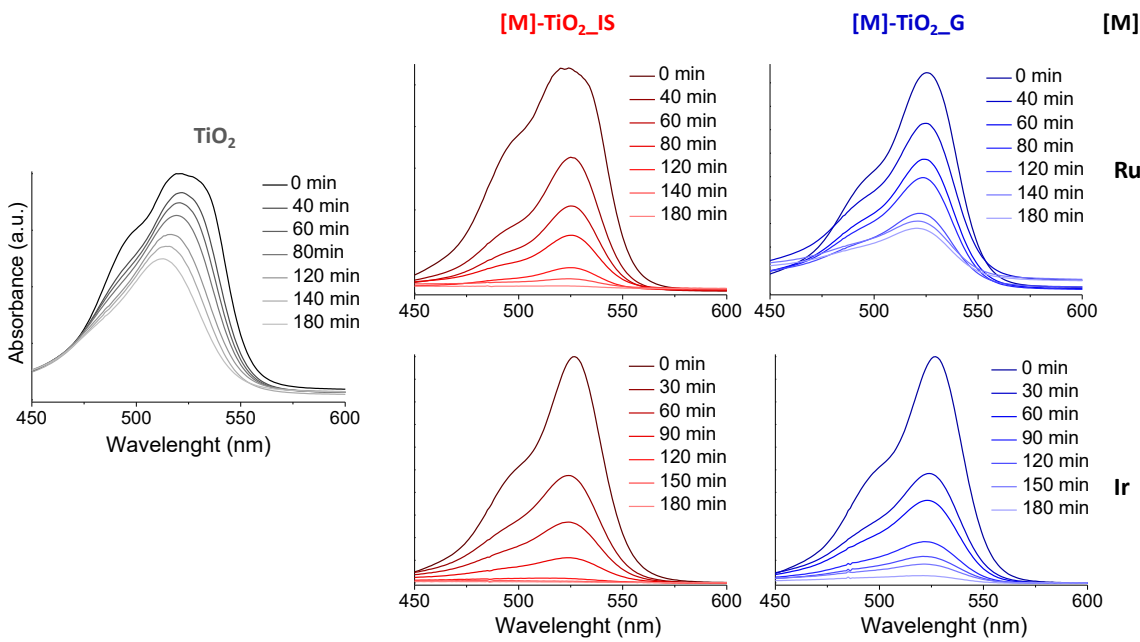


**Figure 4.26.** UV-Vis absorption spectra of the degradation reaction of an aqueous solution of R6G ( $5 \times 10^{-5}$  M) under UV light irradiation.

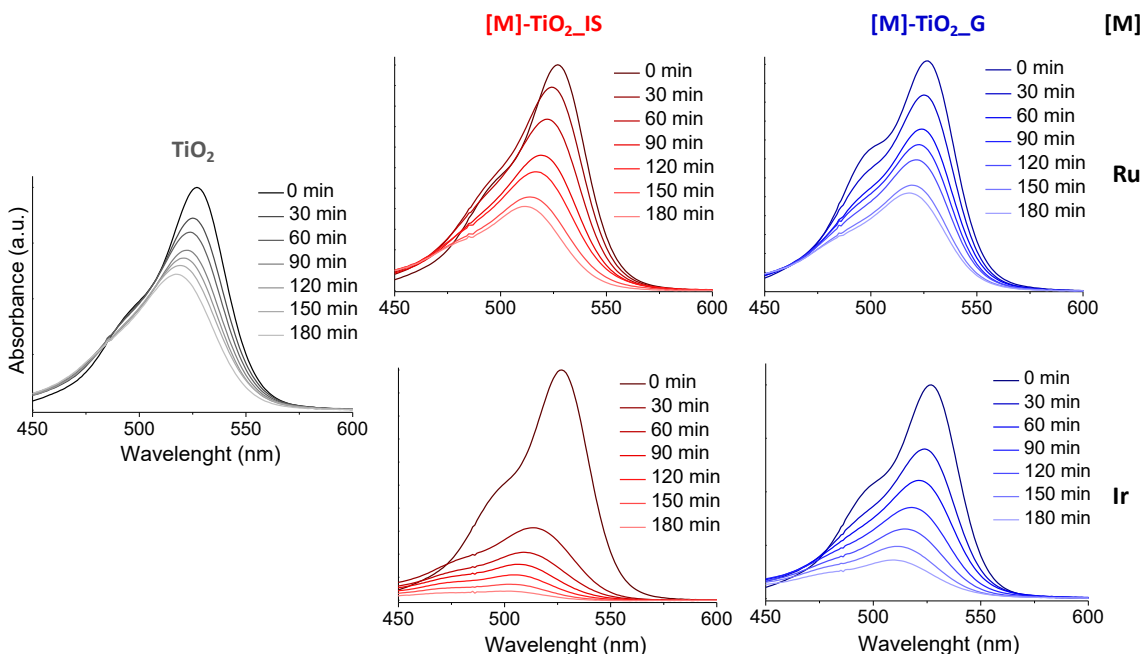


**Figure 4.27.** UV-Vis absorption spectra of the degradation reaction of an aqueous solution of R6G ( $5 \times 10^{-5}$  M) under visible light irradiation.

The same differences between the hybrid titanias (**IS** and **G**) and the control **TiO<sub>2</sub>** material were observed when determining the kinetic of the process. As shown in figure 4.28, which represents the relation between the  $\ln(C_0/C)$  and the reaction time, where  $C_0$  and  $C$  refers to the initial and successive dye concentrations, respectively, all the experimental data can be adjusted

to a linear regression, indicating that the process follows a pseudo-first order kinetic. This way, we are able to determine the kinetic constants of the degradation processes.

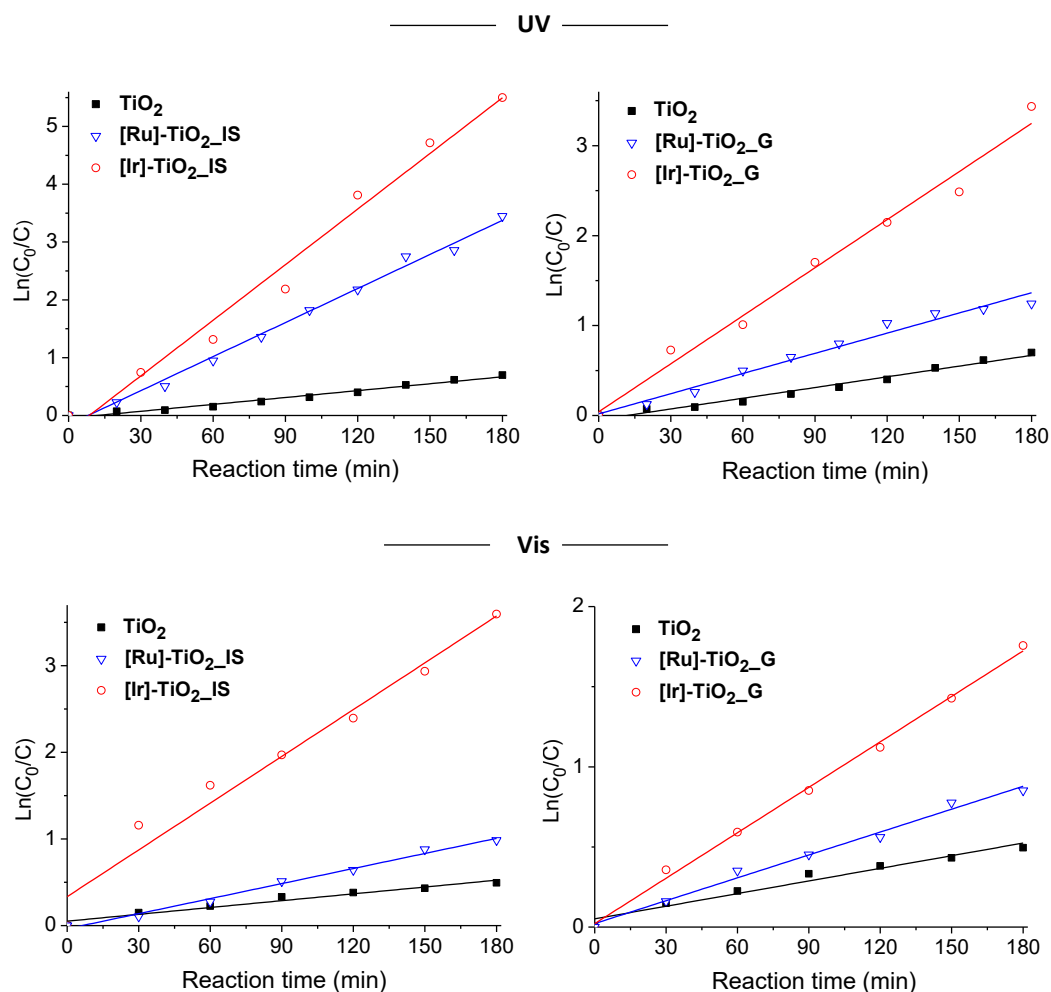


**Figure 4.28.** Representation of the pseudophotocatalytic constant ( $K'$ ) of *in-situ* (left) and grafted (right) materials compared with the control  $\text{TiO}_2$ , in the degradation of R6G under UV (up) and visible (down) light irradiation.

As detailed in table 4.6, the *in-situ* materials  $[\text{M}]\text{-TiO}_2\text{-IS}$  ( $\text{M}$ : Ru, Ir) exhibit, under both types of illumination, a clear enhancement in their photocatalytic activity when compared to both the grafted ( $k'_{\text{IS}}/k'_{\text{G}}$  (UV) 3.3 Ru, 1.8 Ir;  $k'_{\text{IS}}/k'_{\text{G}}$  (vis) 1.2 Ru, 2.0 Ir) and the complex-free titanias ( $k'_{\text{IS}}/k'_{\text{TiO}_2}$  (UV) 5.6 Ru, 9.0 Ir;  $k'_{\text{IS}}/k'_{\text{TiO}_2}$  (vis) 2.4 Ru, 7.3 Ir). This improvement in the photocatalytic performance could be attributed to the synergic combination of the band gap reduction and the higher concentration of dye in the **IS** materials with respect to the grafted ones.

In particular, the photocatalytic activity of  $[\text{Ir}]\text{-TiO}_2\text{-IS}$ , which exhibits the lowest crystalline domain size (5.6 nm), is much higher than that observed not only for the control titania  $\text{TiO}_2$

(nine- or seven-fold under UV and visible light, respectively) but also for the ruthenium material **[Ru]-TiO<sub>2</sub>\_IS** ( $18.2 \text{ min}^{-1}$  Ir vs.  $6.0 \text{ min}^{-1}$  Ru, under visible light) (see table 4.6). In this case, this behavior could be attributed to the low crystalline domain size of the material, which may reduce the recombination rate of charge carriers, a fact that has also been observed in other organotitanias previously described by our group.<sup>147</sup>

**Table 4.6.** Constant values of the photocatalytic activity under UV and visible light irradiation, regression coefficients and conversions at different times of all the titania-based materials (**[M]-TiO<sub>2</sub>\_IS** and **[M]-TiO<sub>2</sub>\_G**, M: Ru, Ir) compared with the complex-free titania, **TiO<sub>2</sub>**.

Sample	$E_g^{(a)}$ (eV)	$K' \cdot 10^3^{(b)}$ (min <sup>-1</sup> )	$R^{(c)}$	% Conversion <sup>(d)</sup>			$K'/K'_{\text{TiO}_2}^{(e)}$
				1h	2h	3h	
<b>UV</b>							
<b>TiO<sub>2</sub></b>	3.24	$3.5 \pm 1.0$ (4.4)	0.9928	14.0	33.0	50.3	---
<b>[Ru]-TiO<sub>2</sub>_IS</b>	2.82	$19.5 \pm 2.0$ (20.3)	0.9935	61.2	88.6	96.8	5.6
<b>[Ru]-TiO<sub>2</sub>_G</b>	3.00	$6.0 \pm 1.5$ (7.5)	0.9781	39.2	64.1	71.1	1.7
<b>[Ir]-TiO<sub>2</sub>_IS</b>	3.00	$31.6 \pm 1.0$ (32.1)	0.9825	73.1	97.8	99.6	9.0
<b>[Ir]-TiO<sub>2</sub>_G</b>	3.10	$17.8 \pm 0.8$ (18.0)	0.9821	63.4	88.6	96.9	5.1
<b>VIS</b>							
<b>TiO<sub>2</sub></b>	3.24	$2.5 \pm 0.7$ (2.63)	0.9640	20.2	31.7	39.0	---
<b>[Ru]-TiO<sub>2</sub>_IS</b>	2.82	$6.0 \pm 0.4$ (5.8)	0.8989	26.8	48.3	63.5	2.4
<b>[Ru]-TiO<sub>2</sub>_G</b>	3.00	$4.8 \pm 0.3$ (4.7)	0.9881	26.2	44.3	58.0	1.9
<b>[Ir]-TiO<sub>2</sub>_IS</b>	3.00	$18.2 \pm 0.2$ (18.0)	0.9697	86.2	90.9	97.3	7.3
<b>[Ir]-TiO<sub>2</sub>_G</b>	3.10	$9.3 \pm 0.7$ (9.5)	0.9973	44.7	67.4	82.7	3.7

(a) Band gap energies calculated from the Tauc plot. (b) First order reaction rate pseudophotocatalytic constant of the reaction of degradation of an aqueous solution of Rhodamine 6G ( $5 \times 10^{-5}$  M) obtained as an average of a minimum of three runs. Values in brackets indicate the  $k$  value used to determine the degree of conversion. (c) Regression coefficient for the same degradation reaction. (d) Degree of conversion (%) achieved after 1h, 2h and 3h of reaction. (e) Ratio between the average  $K'$  values of the hybrid complex-titania materials compared with the average  $K'$  value of the control **TiO<sub>2</sub>**.

The stability of the materials was also tested during seven recycling cycles under both types of illumination. As observed in figure 4.29, the **[M]-TiO<sub>2</sub>\_IS** materials (in red) revealed higher stability than the related grafted ones (in blue). After seven photodegradation cycles, all the *in-situ* titanias retain more than the 80% of their initial efficiency, being 100% in the case of **[Ru]-TiO<sub>2</sub>\_IS** under visible light irradiation. Particularly remarkable is the stability shown by the *in-situ* **[Ir]-TiO<sub>2</sub>\_IS** material under visible light, which retains the 75% of efficiency after seven cycles, while the activity of its counterpart **[Ir]-TiO<sub>2</sub>\_G** falls below the 20% only after the fourth recycling cycle (see figure 4.29).

The higher stability of the *in-situ* materials (**[M]-TiO<sub>2</sub>\_IS**, M: Ru, Ir) in relation to their grafted counterparts (**[M]-TiO<sub>2</sub>\_G**, M: Ru, Ir) can be attributed to the better integration of the dye into the anatase matrix in the **IS** titanias.

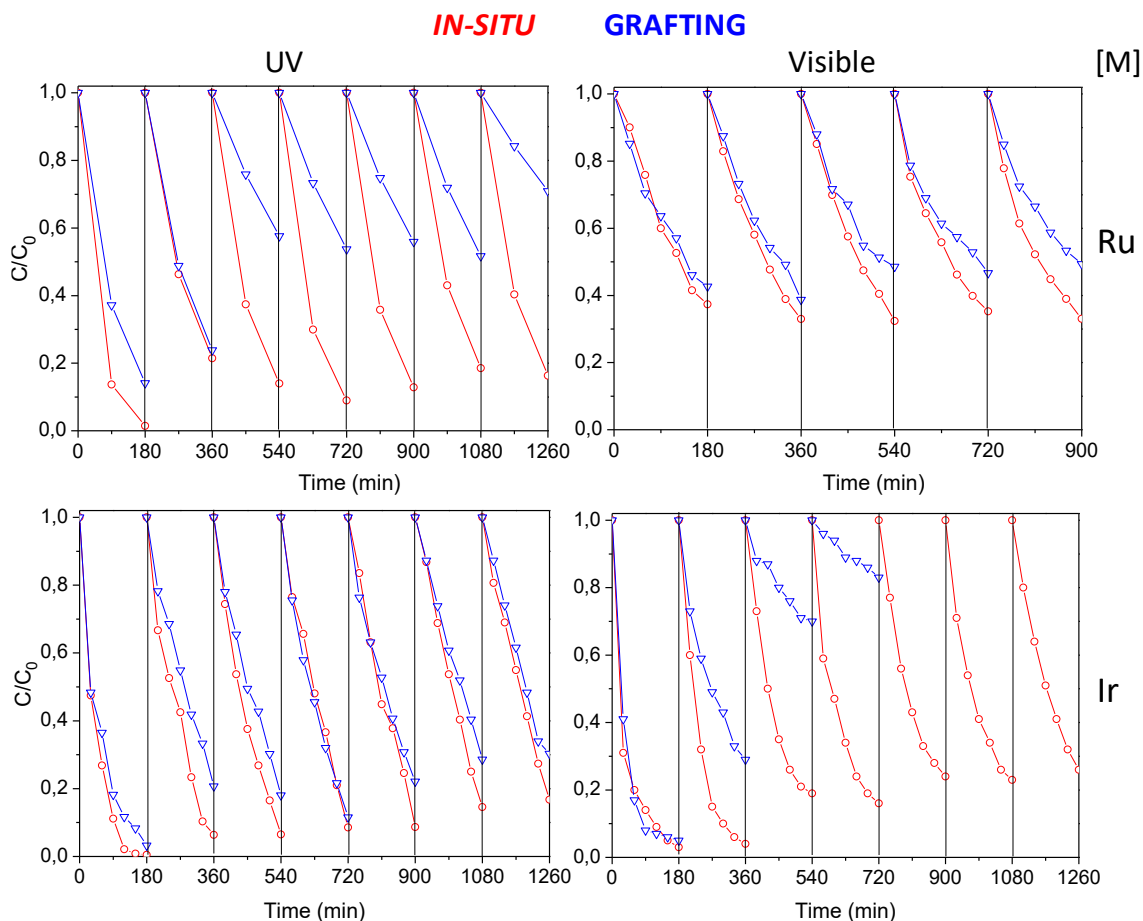


**Figure 4.29.** Recycling tests of the degradation reaction of aqueous solutions of Rhodamine 6G ( $5 \times 10^{-5}$  M) under UV (left) and visible (right) light irradiation of the ruthenium and iridium *in-situ* **[M]-TiO<sub>2</sub>\_IS** (in red) and grafted **[M]-TiO<sub>2</sub>\_G** (in blue) titania-based materials (M: Ru, up; Ir, down).

All the results reveal that our new synthetic approach leads to the preparation of materials (**[M]-TiO<sub>2</sub>\_IS**, M: Ru or Ir) with better photocatalytic performances than those obtained by traditional *post-synthetic* methods (**[M]-TiO<sub>2</sub>\_G**, M: Ru or Ir). The final **IS** titanias display narrower band gaps and higher stabilities than the grafted ones, which has enabled them to feature a better performance in the photocatalytic degradation of the Rhodamine 6G, under UV light and visible irradiation, one of our main goals. In addition, when comparing the activity of both photosensitizers, it was found that the iridium-based material (**[Ir]-TiO<sub>2</sub>\_IS**) is more efficient and, in general, more stable than the ruthenium one (**[Ru]-TiO<sub>2</sub>\_IS**). This fact could be attributed to the higher oxidation state of the iridium complexes (Ir<sup>III</sup> vs. Ru<sup>II</sup>) that leads to less-accessible

metal-centered states and, consequently, increases the chemical stability of the iridium sensitizer.

#### IV.5.2.2 The role of the carboxylic group on the sensitizer

Aiming to explore the role of the carboxylic group on the sensitizer, the photoactivity of the *in-situ* titania ( $[\text{Ir}']\text{-TiO}_2\text{-IS}$ ) obtained using the related iridium(III) complex  $[\text{Ir}(\text{ppy})_2(4,4\text{-H}_2\text{dcbpy})]\text{PF}_6$  ( $[\text{Ir}']$ ) was also examined. This dye, previously described,<sup>164</sup> allowed us to evaluate the influence of the position of the carboxylic acids on the bipyridine ligand (3,3' vs. 4,4' position). The experiments were only performed under visible irradiation.

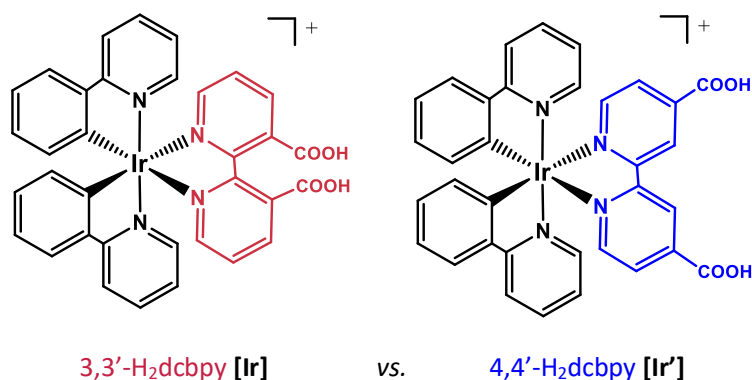


**Figure 4.30.** Schematic representation of complexes  $[\text{Ir}(\text{ppy})_2(3,3'\text{-H}_2\text{dcbpy})]\text{PF}_6$  ( $[\text{Ir}]$ ) (left) and  $[\text{Ir}(\text{ppy})_2(4,4'\text{-H}_2\text{dcbpy})]\text{PF}_6$  ( $[\text{Ir}']$ ) (right).

**Table 4.7.** Constant values of the photocatalytic activity under visible light irradiation, regression coefficients and conversions at different times of the *in-situ* titanias  $[\text{Ir}]\text{-TiO}_2\text{-IS}$  and  $[\text{Ir}']\text{-TiO}_2\text{-IS}$  compared with the complex-free  $\text{TiO}_2$ .

Sample	$E_g^{(a)}$ (eV)	$K' \cdot 10^3^{(b)}$ (min <sup>-1</sup> )	$R^{(c)}$	% Conversion <sup>(d)</sup>			$K'/K'_{\text{TiO}_2}^{(e)}$
				1h	2h	3h	
<b>VIS</b>							
$\text{TiO}_2$	3.24	$2.5 \pm 0.7$ (2.63)	0.9640	20.2	31.7	39.0	---
$[\text{Ir}]\text{-TiO}_2\text{-IS}$ 3,3'-H <sub>2</sub> dcbpy	3.00	$18.2 \pm 0.2$ (18.0)	0.9697	86.2	90.9	97.3	7.3
$[\text{Ir}']\text{-TiO}_2\text{-IS}$ 4,4'-H <sub>2</sub> dcbpy	3.00	$9.2 \pm 0.7$ (9.5)	0.9753	24.1	60.3	80.2	3.7

(a) Band gap energy calculated from the Tauc plot. (b) First order reaction rate pseudophotocatalytic constant of the reaction of degradation of an aqueous solution of Rhodamine 6G ( $5 \cdot 10^{-5}$  M) obtained as an average of a minimum of three runs. Values in brackets indicate the  $k$  value used to determine the degree of conversion. (c) Regression coefficient for the same degradation reaction. (d) Degree of conversion (%) achieved after 1h, 2h and 3h of reaction. (e) Ratio between the average  $K'$  values of the hybrid complex-titania materials compared with the average  $K'$  value of the control  $\text{TiO}_2$ .

The resulting hybrid titania (**[Ir']-TiO<sub>2</sub>\_IS**) exhibits very similar textural properties to its homologous material and, in addition, the same value for the primary band gap (3.00 eV). The results obtained on the photodegradation of the R6G, together with those of the **[Ir]-TiO<sub>2</sub>\_IS**, are included in table 4.7.

As shown in table 4.7 and figure 4.31, this new material (**[Ir']-TiO<sub>2</sub>\_IS**) is able to better photodegrade the Rhodamine 6G than the control **TiO<sub>2</sub>** ( $K'/K'_{\text{TiO}_2}$  3.7). However, its catalytic capacity is reduced by half in relation to the original titania ( $K'$  9.2 min<sup>-1</sup> **[Ir']-TiO<sub>2</sub>\_IS** vs. 18.2 min<sup>-1</sup> **[Ir]-TiO<sub>2</sub>\_IS**), and it is only able to degrade about the 80% of R6G after the 3 hours of reaction. In addition, this material (**[Ir']-TiO<sub>2</sub>\_IS**) is less stable after being recycling during 7 cycles (60% of efficiency) than **[Ir]-TiO<sub>2</sub>\_IS**, which retains more than the 75% of its initial efficiency (see figure 4.31, c).

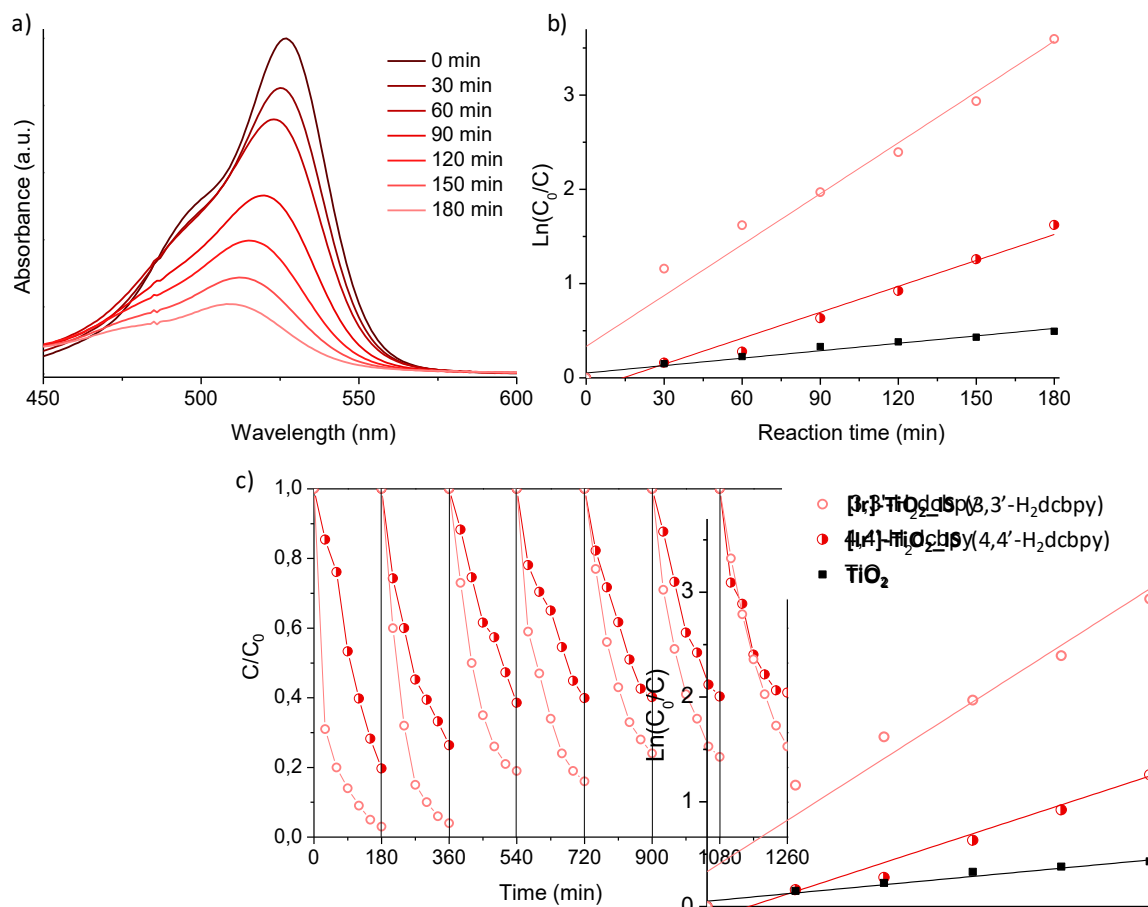


**Figure 4.31.** All data under visible irradiation. UV-Vis absorption spectra of the degradation of an aqueous solution of R6G ( $5 \times 10^{-5}$  M) by **[Ir']-TiO<sub>2</sub>\_IS** (4,4'-H<sub>2</sub>dcbpy) (a). Comparative results in the representation of the pseudophotocatalytic constant ( $K'$ ) (b) and the recycling tests (c) of the degradation reaction carried out with **[Ir]-TiO<sub>2</sub>\_IS** and **[Ir']-TiO<sub>2</sub>\_IS**.

All in all, the new *in-situ* material (**[Ir']-TiO<sub>2</sub>\_IS**) exhibits worst photocatalytic activity than its counterpart titania **[Ir]-TiO<sub>2</sub>\_IS**, suggesting that the position of the carboxylic group has an important influence on the photoactivity of the sensitizer.

#### *IV.5.3 Evaluation of the stability of the hybrid materials*

The *in-situ* materials (**[M]-TiO<sub>2</sub>\_IS**, M: Ru, Ir) have demonstrated a higher catalytic activity and stability in the reaction bulk than the grafted titanias. So, in order to confirm the higher stability, additional experiments were performed. These studies were based on the intensity loss of the characteristic absorptions (DRUV) of each dye in the titania materials (*ca.* 500 and 470 nm for **[Ru]-TiO<sub>2</sub>** and **[Ir]-TiO<sub>2</sub>**, respectively), before and after being tested.

To evaluate the stability of the dyes against leaching and chemical degradation, they were stirred in aqueous NaOH solutions ( $10^{-5}$  M) during different periods of time (figure 4.32). After this basic treatment, none of the samples are able to retain the entire amount of the initial complex. After one hour, **[Ru]-TiO<sub>2</sub>\_IS** maintains about the 75% of the initial amount of the dye, while this value falls below 50% in the grafted **[Ru]-TiO<sub>2</sub>\_G**. This difference is more remarkable in the iridium-based materials. The *in-situ* **[Ir]-TiO<sub>2</sub>\_IS** retains the 40% of the dye after one hour of reaction, while the grafted one (**[Ir]-TiO<sub>2</sub>\_G**) loses the 90% of complex only after 2 minutes of stirring. This fact clearly confirms that the dyes are better protected against the chemical media in the *in-situ* materials.

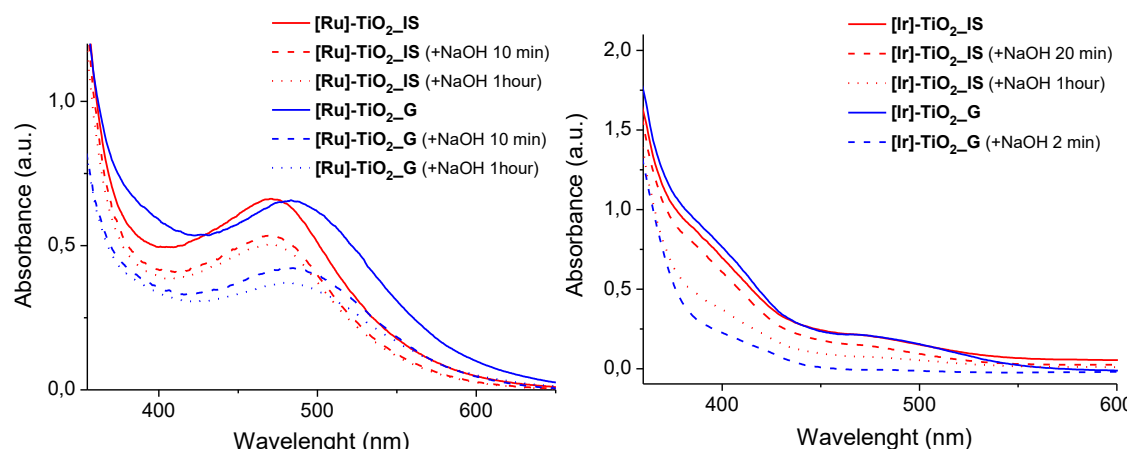


**Figure 4.32.** Selected region of the DRUV spectra of the ruthenium- (left) and iridium- (right) titania-based materials before and after being washed with an aqueous NaOH solution ( $10^{-5}$  M).

Otherwise, the results obtained in the recycling tests also pointed to an additional stability against photodegradation. To confirm this, the hybrid materials were also stirred under continuous illumination for 9 hours (equivalent to three recycling cycles), simulating the situations in which both grafted materials lost their efficiency more quickly (UV irradiation for **[Ru]-TiO<sub>2</sub>-G** and visible light for **[Ir]-TiO<sub>2</sub>-G**). Under these conditions, the **IS** materials retain *ca.* 40% of the initial amount of the coordination dye (M: Ru 35%, Ir 45%), while the amount in the grafted titanias is reduced to *ca.* 15% (M: Ru 13%, Ir 14%) (see figure 4.33).

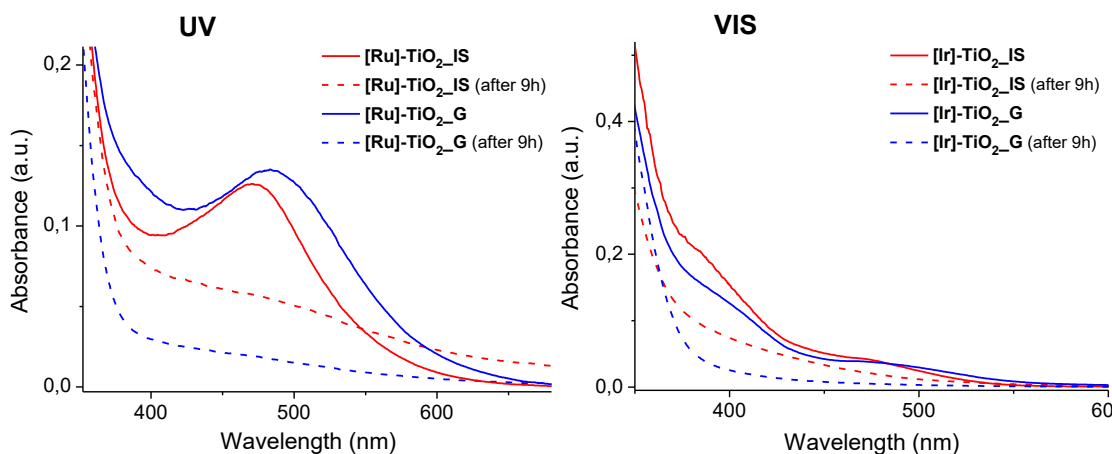


**Figure 4.33.** Selected region of the DRUV spectra of ruthenium- (left) and iridium- (right) titania-based materials before and after being irradiated under UV (left) or visible (right) light for 9 hours with stirring.

These results suggest that, compared with the standard *post-synthetic* grafting method (**[M]-TiO<sub>2</sub>-G**), the *in-situ* synthetic route leads to hybrid titanias (**[M]-TiO<sub>2</sub>-IS**) with an exceptional stability, probably due to a better integration of the coordination dyes in the matrix of the semiconductor. However, it is worth noting that in both types of materials (**IS** and **G**) there must also be surface incorporation of the dyes. During the synthesis of the *in-situ* titanias, the metal complexes are homogeneously distributed through the titania gel, likely forming covalent linkages with Ti atoms (scheme 4.3). This fact should enable their inclusion in the anatase network as defects or crystals disruptors during the last crystallization step (scheme 4.3, iii), as previously proposed by us with similar organic dyes,<sup>147</sup> making the **IS** materials more stable against bleaching and photodegradation.

#### IV.5.4 Photocatalytic mechanisms

To gain a better understanding of the mechanism that takes place in the bulk of the reaction, we also studied the role of the complex-free titania ( $\text{TiO}_2$ ) under both types of illumination (UV and visible light).

As shown in figure 4.34, UV light can easily excite the electrons of the semiconductor and form reactive hole-electron pairs (*hole way*), which gives rise to the formation of the  $\cdot\text{OH}$  radicals responsible of the degradation the R6G. However, it may seem surprising that this control  $\text{TiO}_2$  is also able to photocatalyze the degradation of the Rhodamine 6G under visible light, because wavelengths higher than 400 nm are not energetic enough to generate the reactive hole-electron pairs (band gap of 3.24 eV). Nevertheless, as observed in the energy levels in scheme 4.5, the organic molecules are able to get excited under visible irradiation due to its narrow band gap (2.30 eV) and, so, to generate both  $\cdot\text{R6G}^+$  radicals and electrons. These electrons can be easily injected into the conduction band (CB) of the titania (*dye way*), because it is placed lower in energy than the LUMO orbital of the R6G (scheme 4.5), allowing the formation of  $\cdot\text{OH}$  radicals. This way, the  $\text{TiO}_2$  would be acting only as an electron mediator between the excitation of the R6G and the formation of the  $\cdot\text{OH}$  radicals.<sup>147</sup>

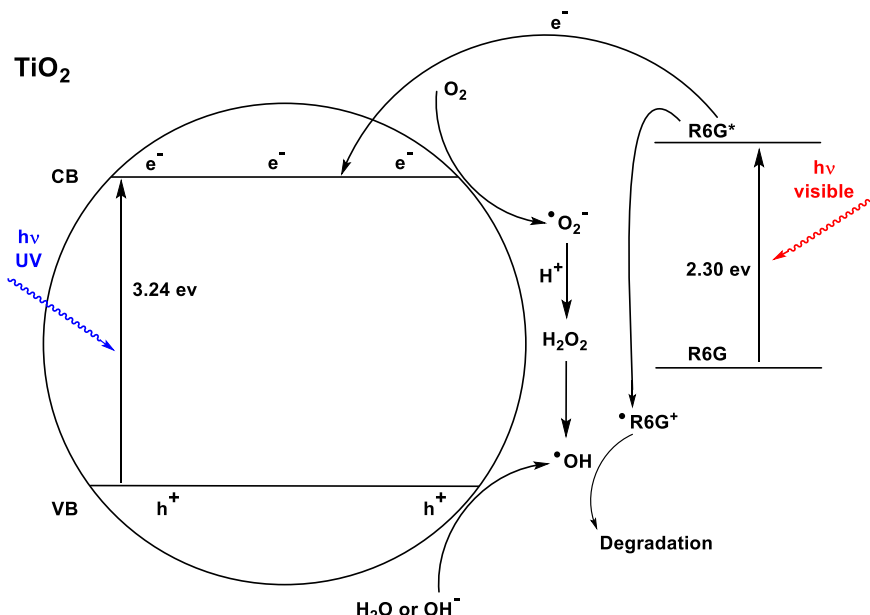
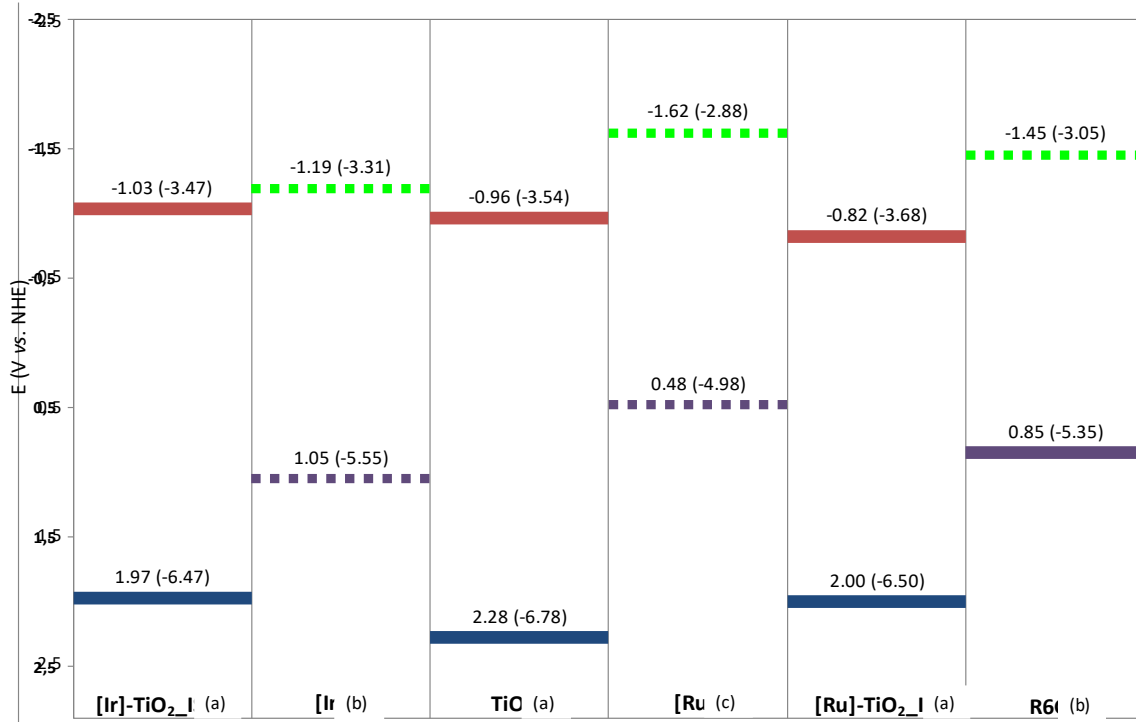


**Figure 4.34.** Schematic representation of the photo-induced charge transfers in the complex-free  $\text{TiO}_2$  system and the mechanism of the photocatalytic degradation process.



**Scheme 4.5.** Schematic representation of the energy levels of the hybrid *in-situ* **[M]-TiO<sub>2</sub>\_IS** (M: Ru, Ir) and the control **TiO<sub>2</sub>**. Maximum energy level of the valence band (in blue) and minimum energy level of the conduction band (in red). HOMO (violet) and LUMO (green) orbitals of complexes **[Ir]** and **[Ru]** and the R6G in solution. The energy levels have been determined using Valence Band XPS and absorption spectra (a), by cyclic voltammetry and absorption spectra (b) or from the literature (c).<sup>178</sup>

By contrast, in both **[M]-TiO<sub>2</sub>\_IS** (M: Ru, Ir) materials, the semiconductor is sensitized by the coordination dye that is able to absorb light between 200-500 nm, or even 600 nm for **[Ru]**. This light absorption produces the excitation of the dye, and the subsequent electron transfer from the excited state of the inorganic molecule to the conduction band of the semiconductor (*the dye way*, see figure 4.35 and scheme 4.5 for the energy levels). In addition, unlike what happened with the control titania, the *in-situ* materials exhibit reduced primary band gaps (2.82 eV **[Ru]-TiO<sub>2</sub>\_IS** and 3.00 eV **[Ir]-TiO<sub>2</sub>\_IS**) that allow them to be excited by photons from both UV and visible lights, and generate the corresponding reactive hole-electron pairs *via the hole way* mechanism (figure 4.35).

Thus, we can assume that the synergic effect of both mechanisms (*the hole way* and the *dye way*), which can be acting together even under visible light irradiation, produces an enhancement in the production of the ·OH radicals and, therefore, in the photocatalytic properties of the *in-situ* materials.

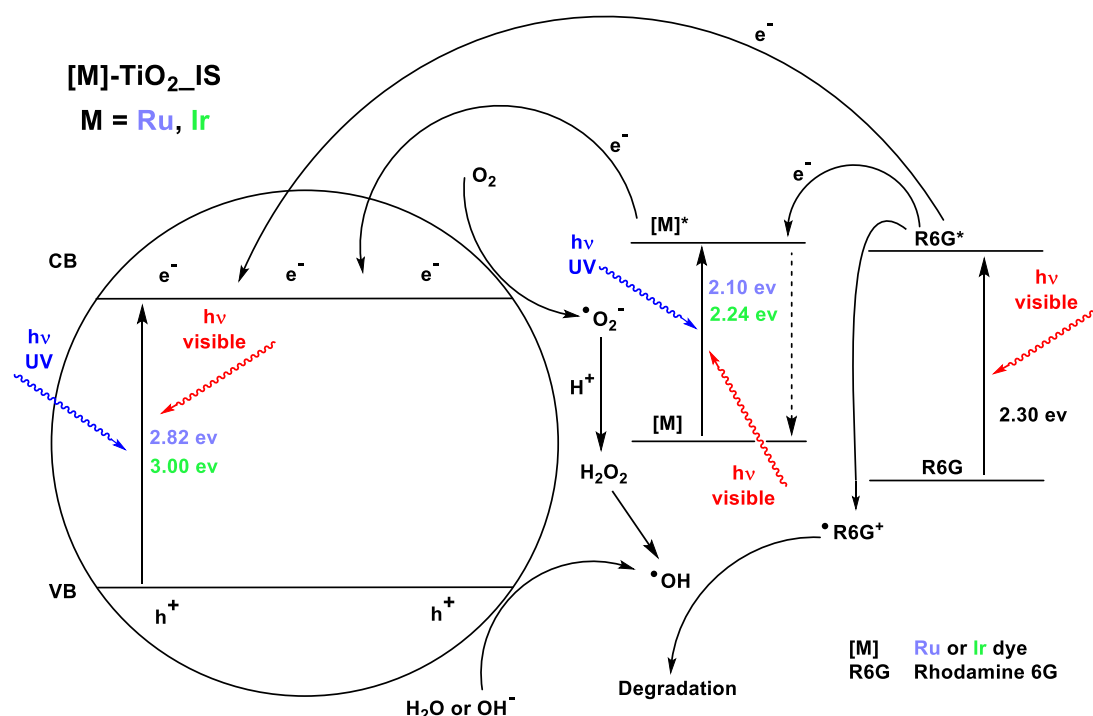


**Figure 4.35.** Schematic representation of the photo-induced charge transfers in the  $[M]\text{-TiO}_2\text{-IS}$  ( $M: \text{Ru, Ir}$ ) systems and the mechanism of the photocatalytic degradation process.

To gain a better understanding of the degree of contribution of each pathway on the total photocatalytic activity of the *in-situ* materials, we decided to test the influence of two different scavengers in the photodegradation reaction. With this aim, isopropanol ( ${}^i\text{PrOH}$ ), as a radical scavenger, and triethanolamine (TEOA), as a hole scavenger, were selected.<sup>139e</sup> These experiments were carried out under both UV and visible light irradiation.

As shown in table 4.8, the addition of both scavengers only causes moderate changes in the final conversion rates of the reaction, suggesting that, although both the *hole way* and *dye way* mechanisms should be operative, the *dye way* seems to be the dominant one even under UV illumination, and in the experimental conditions used. Nevertheless, under UV light, the reaction rate constant values for  $[\text{Ir}]\text{-TiO}_2\text{-IS}$  decrease more than half in the presence of the scavengers ( $31.6 \text{ min}^{-1}$  vs.  $16.0 \text{ min}^{-1}$   ${}^i\text{PrOH}$  and  $12.5 \text{ min}^{-1}$  TEOA), suggesting a more important contribution of the *hole way* in this case.

**Table 4.8.** First order reaction rate constant values of the photocatalytic activity and conversions at different times of  $[M]\text{-TiO}_2\text{-IS}$  ( $M$ : Ru, Ir) in the absence or presence of different scavengers (isopropanol or triethanolamine,  $5 \times 10^{-2}$  M).

Sample	UV			VIS				
	$K' \cdot 10^3$ (min <sup>-1</sup> )	% Conversion		$K' \cdot 10^3$ (min <sup>-1</sup> )	% Conversion			
		1h	2h	3h		1h	2h	3h
$[\text{Ru}]\text{-TiO}_2\text{-IS}$	19.5	61.2	88.6	96.8	6.0	26.8	48.3	63.5
$[\text{Ru}]\text{-TiO}_2\text{-IS} + i\text{PrOH}$	18.6	93.7	94.3	95.6	18.6	16.3	43.0	57.7
$[\text{Ru}]\text{-TiO}_2\text{-IS} + \text{TEOA}$	10.7	85.0	91.2	91.5	10.7	26.3	44.5	49.9
$[\text{Ir}]\text{-TiO}_2\text{-IS}$	31.6	73.1	97.8	99.6	18.2	86.2	90.9	97.3
$[\text{Ir}]\text{-TiO}_2\text{-IS} + i\text{PrOH}$	16.0	95.5	95.9	97.0	16.0	75.9	80.0	86.5
$[\text{Ir}]\text{-TiO}_2\text{-IS} + \text{TEOA}$	12.5	94.9	95.1	96.1	12.5	82.7	89.9	90.1

Finally, we have also observed that the mechanism of the degradation of the R6G must be influenced by the type of illumination as suggested by controlling its characteristic band at 525 nm. Hence, for both  $[M]\text{-TiO}_2\text{-IS}$  and  $[M]\text{-TiO}_2\text{-G}$  materials there is a notable blue shift in the absorption band of the dye when using visible light irradiation (from 525 nm to 515 nm for  $[\text{Ru}]$  and 500 nm for  $[\text{Ir}]$ , see figure 4.36, left). This behavior, also observed for the complex-free  $\text{TiO}_2$  under both types of light, has been associated with a selective N-deethylation of R6G to Rhodamine previous to the destruction of the polyaromatic systems (figure 4.37).<sup>179</sup> This fact suggests that the ·OH radicals attack the areas of the dye that are directly in contact with the surface of the titania,<sup>179-180</sup> inducing the photocatalytic degradation of the organic molecules on the surface of the catalyst.

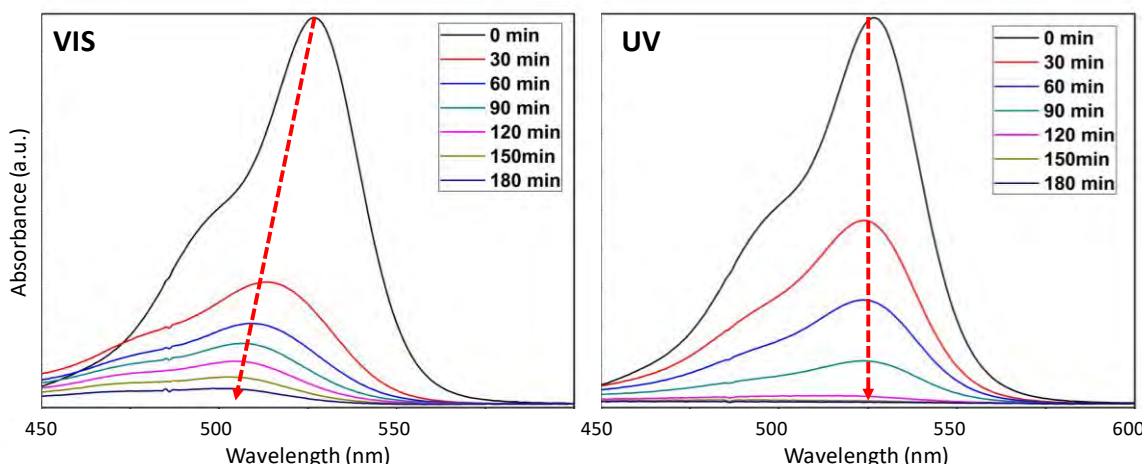


**Figure 4.36.** UV-vis absorption spectra of the degradation reaction of an aqueous solution of R6G ( $5 \times 10^{-5}$  M) under visible (left) and UV (right) irradiation using as photocatalyst  $[\text{Ir}]\text{-TiO}_2\text{-IS}$ .

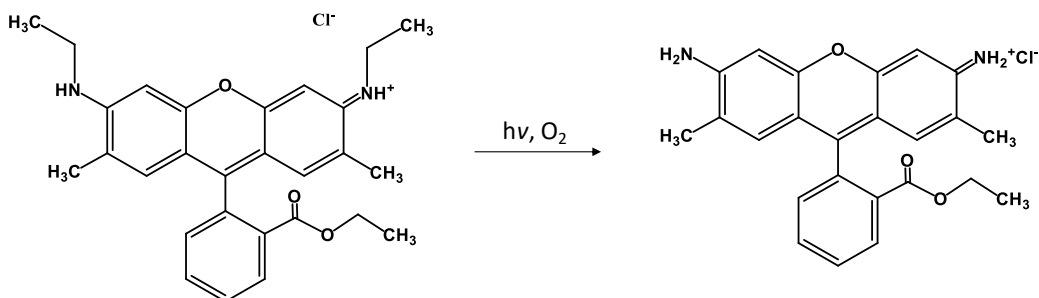


**Figure 4.37.** N-deethylation reaction of R6G to Rhodamine.

By contrast, under UV illumination no shifts of the absorption maxima are observed (figure 4.36, right), suggesting that the R6G must be degraded by the initial cleavage of the polyaromatic systems, giving rise to organic species that do not contain aromatic rings.<sup>177</sup>



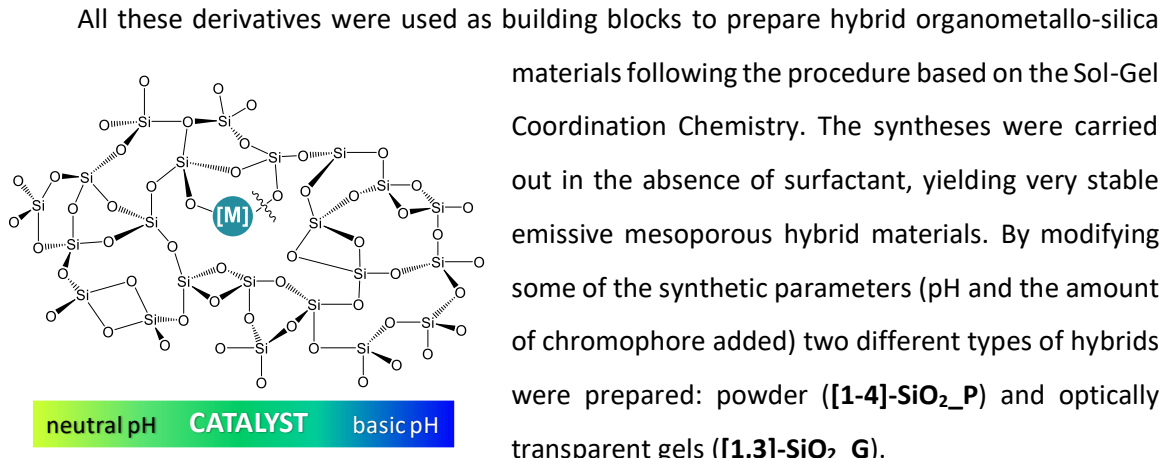
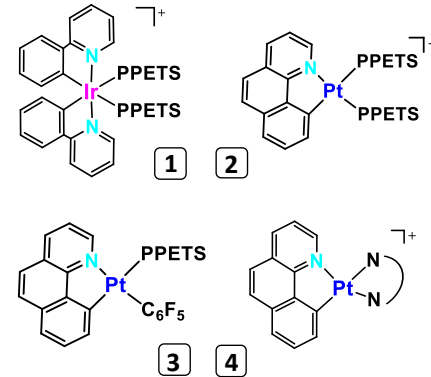
## ***Summary***





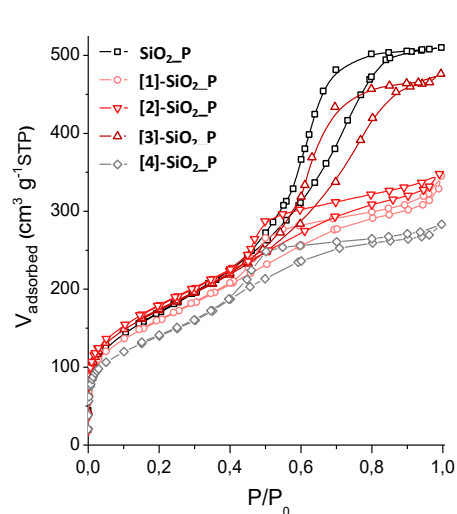
## Chapter I. Luminescent mesoporous silica materials based on Ir<sup>III</sup> and Pt<sup>II</sup> complexes

This chapter reports the synthesis and characterization of new luminescent iridium(III) and platinum(II) complexes. They incorporate trialkoxysilane terminal groups in their structures by using two different auxiliary ligands, PPETS and *dasipy*:  $[\text{Ir}(\text{ppy})_2(\text{PPETS})_2]\text{OTf}$  (**1**),  $[\text{Pt}(\text{bzq})(\text{PPETS})_2]\text{PF}_6$  (**2**),  $[\text{Pt}(\text{bzq})(\text{C}_6\text{F}_5)(\text{PPETS})]$  (**3**) and  $[\text{Pt}(\text{bzq})(\text{dasipy})]\text{PF}_6$  (**4**). Except **2**, they have shown excellent photophysical properties, covering the entire visible spectrum. Especially, complex **4** has demonstrated a great ability to self-condense and jellify (**4-gel**) when exposing to protic solvents. Both the organometallic derivative and the resulting gel show a typical red emission with a bathochromic shift at 77K, in accordance to the presence of close Pt…Pt and/or  $\pi$ … $\pi$  intermolecular interactions, also supported by concentration dependent studies performed in dichloromethane.



The analysis of the solid state properties of the as-synthesized hybrid materials (FTIR, DRUV, emissive properties, ICP) reveals a good incorporation of the organometallic derivatives into the silica network and, also, excellent textural and emissive properties. This study supports that the silica acts as a host-matrix, increasing not only the rigidity but also the separation of the metal chromophores and, thus, reducing possible aggregation quenching effects. The silica matrix also improves the stability of the complexes. Particularly interesting is the remarkable stability observed for **[4]-SiO<sub>2</sub>-P**, which has demonstrated to be very stable in aqueous media even in the

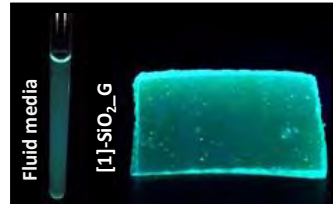
presence of oxygen, while its precursor  $[\text{Pt}(\text{bzq})(\text{dasipy})]\text{PF}_6$  (**4**) is highly sensitive to water traces and needs to be kept under argon atmosphere due to its ability to self-condense.



On the other hand, some structure-property relationships have been found. Thus, the geometry of the complex barely affects to the textural properties of the final material since similar properties were observed for the materials prepared with octahedral (**[1]-SiO<sub>2</sub>-P**) or square planar (**[2]-SiO<sub>2</sub>-P**) complexes. However, the charge of the chromophore and the auxiliary ligands notably influences on the characteristics of the final hybrid materials. Thus, the cationic precursors yield silicas (**[1,2,4]-SiO<sub>2</sub>-P**) with lower surface areas and pore

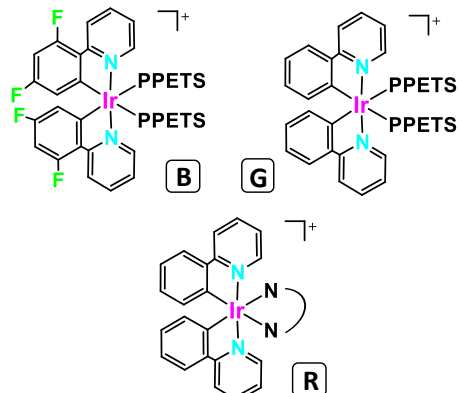
volume and diameter than those obtained with the neutral complex (**[3]-SiO<sub>2</sub>-P**). This behavior has been attributed to the low compatibility between the cationic nature of the chromophores and the neutral medium in which the synthesis is performed.

The optically transparent gels, **[1,3]-SiO<sub>2</sub>-G**, are particularly interesting since their behavior at room temperature mimic the emission properties of their corresponding precursors in solution, exhibiting a remarkable enhancement in their quantum yields (up to fourfold), which makes them ideal candidates for photoluminescence applications.

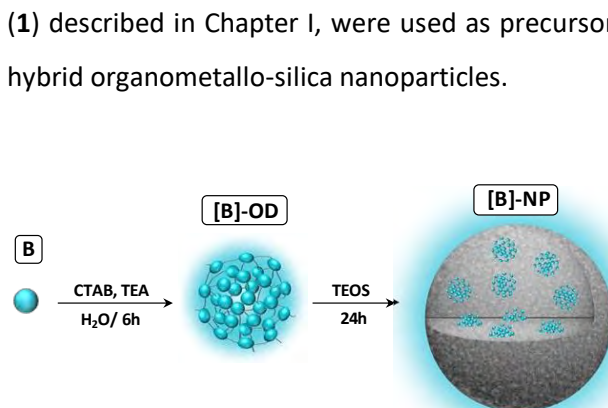


In conclusion, we have demonstrated that the Sol-Gel Coordination Chemistry can be successfully extended to different types of organometallic chromophores. In addition, the employed synthetic approach is environmentally friendly since it requires mild reaction conditions and only requires small amounts of organic solvents.

## Chapter II. Hybrid white-emitting organometallo-silica nanoparticles

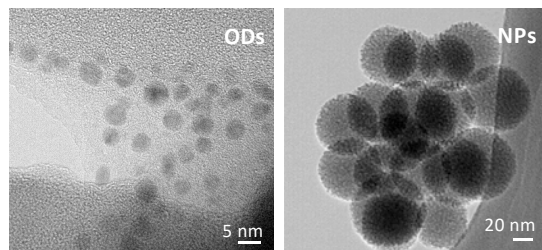


In this chapter, new blue (**B**) and red (**R**) emitting iridium(III) complexes were synthesized and fully characterized. These compounds feature ppy and dFppy, as cyclometalating groups, and *dasipy* or PPETS ligands bearing trialkoxysilane terminal groups, as auxiliary ligands. Their photophysical properties have demonstrated very efficient emissions in the blue (**B**) and red (**R**) region. Both complexes along with the green-emitting chromophore **G**,  $[\text{Ir}(\text{ppy})_2(\text{PPETS})_2]\text{OTf}$  (1) described in Chapter I, were used as precursors in the preparation of discrete luminescent hybrid organometallo-silica nanoparticles.

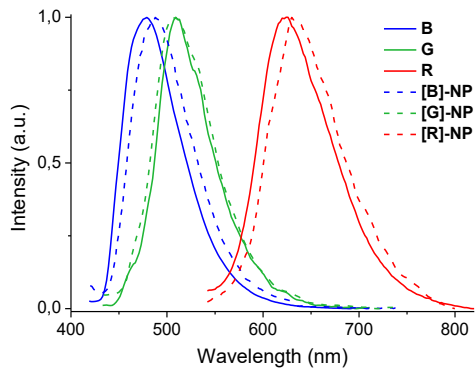
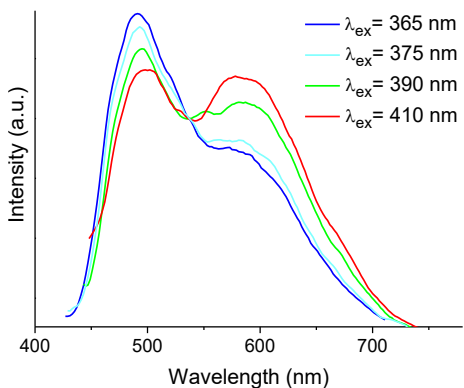


The hybrid silica nanoparticles were prepared following a new synthetic procedure based on the Sol-Gel Coordination Chemistry approach, similar to that described in Chapter I. This new approximation is based on the

kinetically controlled condensation of the alkoxy silane terminal groups of the different complexes (**B**, **G** and **R**) and, takes place with the initial formation of organometallic dots (**ODs**). The subsequent reaction between the *in-situ* generated **ODs** and TEOS yields the final emissive silica nanoparticles (**NPs**). Following this strategy, and based on the **B**, **G** and **R** chromophores, we have prepared the monochromatic-emitting organometallic dots (**[B]-OD**, **[G]-OD** and **[R]-OD**) and the corresponding silica nanoparticles (**[B]-NP**, **[G]-NP** and **[R]-NP**).



Both the **ODs** and **NPs** showed very similar emission properties to those of the pure complexes in the solid state, indicating that the **ODs** are generated without significant structural changes of their constituent chromophores. However, the monochromatic-emitting nanoparticles showed lower quantum yields than those measured for the corresponding iridium precursors in the solid state.

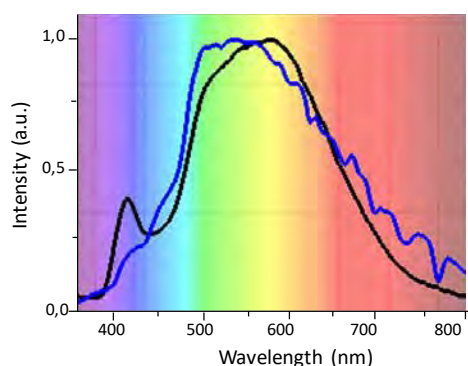
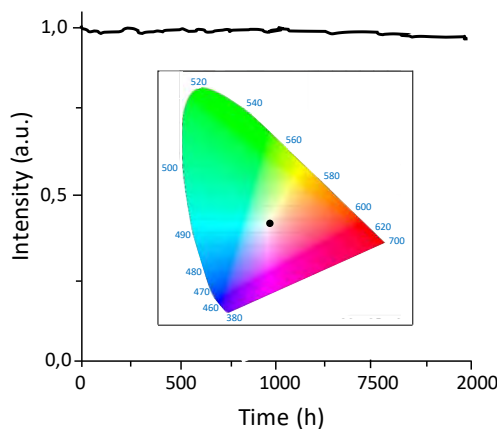


Next, we extended the synthetic procedure to prepare white-emitting silica nanoparticles **[W]-NP**, which were formed from a mixture of the complexes **B**, **G** and **R** in the appropriate mass ratio (*three-in-one*). As expected, this material displayed a bright white emission (20%) formed by two main bands that cover the visible range and proved to be excitation wavelength dependent.

The analyses of the textural properties revealed that all the nanoparticles featured type IV isotherms, typical of mesoporous materials, with high surface areas (*ca.* 1000 m<sup>2</sup>/g), mesopore volumes in the range of 0.5–0.7 cm<sup>3</sup>/g and pore size between 2.1 and 2.4 nm. TEM images of the **ODs** showed particles of 5 nm in diameter, while **NPs** were observed as mono-discrete and spherically shaped particles with sizes in the 50–70 nm range. In addition, ICP analysis revealed incorporation yields between 80 and 90%.

In a subsequent step, the three complexes and the corresponding hybrid silica nanoparticles were implemented into rubber-like down-converting coatings for the fabrication of Hybrid Light Emitting Diodes (HLEDs), and their efficiency and stability were evaluated. The rubber-like materials based on the iridium complexes (**OC-rubbers**) and the monochromatic-emitting silica nanoparticles (**NP-rubbers**) were prepared and their properties examined. Significant differences in the stability and efficiency were observed. In general, **NP-rubbers** displayed better performance, what is consistent with the idea that the silica shell-core protects the chromophores from quenching and photodegradation.

The rubber-like material based on the white-emitting silica nanoparticles was also prepared and directly implemented onto a UV-LED chip. This HWLED showed a homogenous light distribution and a remarkable stability over 2000 hours (minimal changes in luminous efficiency, 2.5 lm/W, constant x/y CIE color coordinates, 0.34/0.33, and CCT of 5143 K), becoming one of the most stable single-component HWLEDs reported so far. In addition, using a linear extrapolation, this device would maintain more than its 50% of the maxima luminance after 10000 hours operating.

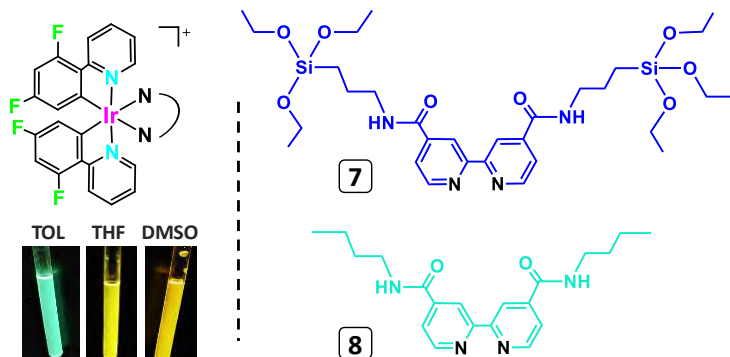


All-in-all, we were able to fabricate an eye-friendly, exceptionally efficient and highly stable HWLED. These unique features, which are usually mutually exclusive, have been achieved by using a new *three-in-one* approach to prepare white-emitting silica nanoparticles ([W]-NP). By using this NPs is possible to overcome quenching, poor color stability and phase separation issues, which are common drawbacks of organic color down-converting coatings for HWLEDs.

On the one hand, following this strategy, the molecules of the complexes, which are well incorporated within the protective silica shell, are close enough to allow energy transfer processes between them; and, on the other hand, the photostability of the chromophores is notably enhanced, thanks to the geometry constraint produced by the silica matrix.

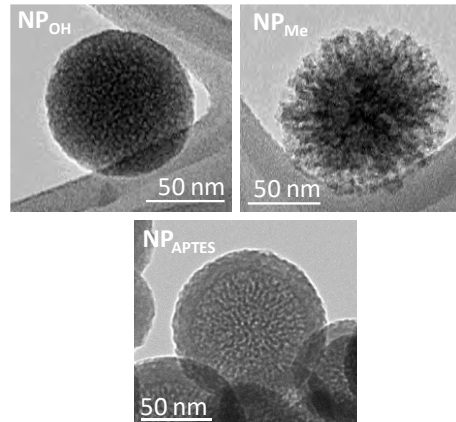
### Chapter III. Mesoporous silica nanoparticles as biomarkers

In chapter III, we describe the properties of two new Ir(III) complexes containing ancillary ligands based on functionalized bipyridines (*dasipy* L1 and *dbbpy* L2):  $[\text{Ir}(\text{dFppy})_2(\text{dasipy})]\text{PF}_6$  (7) and  $[\text{Ir}(\text{dFppy})_2(\text{dbbpy})]\text{Cl}$  (8).



The optical properties were studied, and, in particular, complex **8** featured emissive properties that depend on the polarity of the solvent, thus confirming the charge transfer character (ligand(dFppy)-to-ligand(N<sup>N</sup>N) and metal(Ir)-to-ligand(N<sup>N</sup>N)) of the excited state in both derivatives.

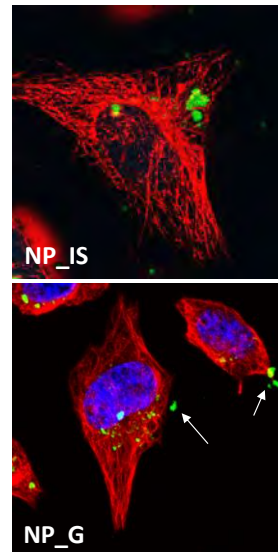
Following the Coordination Sol-Gel Chemistry approach, chromophore **7** was used as precursor for the preparation of native mesoporous silica nanoparticles (**[7]-NP<sub>OH</sub>\_IS**). Thanks to the presence of OH groups on their surface, we could modify them with two capping agents: DMDES (diethoxydimethylsilane) and APTES ((3-aminopropyl)triethoxysilane). Thus, small *in-situ* modifications in the synthetic procedure allowed us to obtain two types of nanoparticles with perfectly established shells (**[7]-NP<sub>Me</sub>\_IS** and **[7]-NP<sub>APTES</sub>\_IS**) and different physicochemical properties. For comparative purposes, the corresponding grafted nanoparticles were also prepared (**[7]-NP<sub>OH</sub>\_G**, **[7]-NP<sub>Me</sub>\_G** and **[7]-NP<sub>APTES</sub>\_G**).



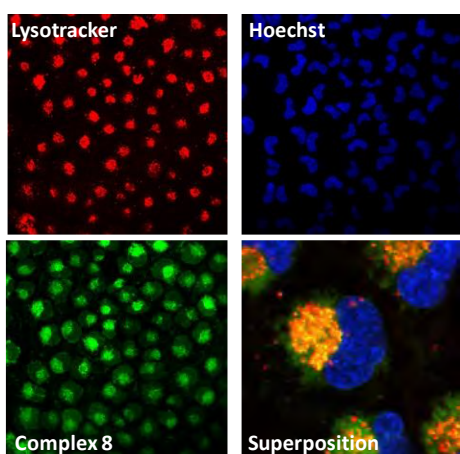
The study of the textural properties revealed the mesoporous nature of all the samples, showing high surface areas for **NP<sub>OH</sub>** (ca. 770 m<sup>2</sup>/g) and **NP<sub>Me</sub>** (ca. 1000 m<sup>2</sup>/g). However, those modified with APTES (**NP<sub>APTES</sub>**) exhibited the smallest surface areas and a partially blocked porosity (A<sub>BET</sub>, m<sup>2</sup>/g: 230 **NP<sub>APTES</sub>**, 97 **[7]-NP<sub>APTES</sub>\_IS** and 100 **[7]-NP<sub>APTES</sub>\_G**), probably due to the presence of the aliphatic chains in the capping agent APTES.

All the as-synthesized nanoparticles showed emissive properties similar to those described for **7**, including long lifetimes ( $\tau$ , 0.52-0.80  $\mu$ s) and high quantum yields ( $\phi$ , 17-52 %). In particular, *in-situ* samples (**[7]-NP\_IS**) mimic the behavior of the pure complex in THF solution, probably due to the good separation of the chromophoric molecules through the silica matrix. By contrast, the grafted nanoparticles (**[7]-NP\_G**) feature comparable emissive properties to **7** in the solid state. Accordingly, in aqueous suspensions, **[7]-NP\_G** exhibit a blue shifted emission band attributed to a good dispersion of the nanoparticles, which could reduce the interaction between the molecules of the chromophore.

Considering the excellent photophysical performance of the functionalized nanoparticles, we also studied their possible use as biomarkers. With this purpose, cytotoxicity assays against two different cell lines (HeLa, cervix carcinoma, and A549, lung carcinoma) were carried out. In accordance to the IC<sub>50</sub> assessment, all samples, especially those containing methyl groups ([7]-NP<sub>Me</sub>), did not present cytotoxicity. The intracellular localization in living cells was assessed by fluorescence and confocal microscopies, showing bright emissions in perinuclear areas. A greater particle aggregation outside the cell was observed in the grafted nanoparticles ([7]-NP\_G) than in the *in-situ* ones ([7]-NP\_IS), thus supporting one of the strengths of the new *in-situ* synthetic approach.



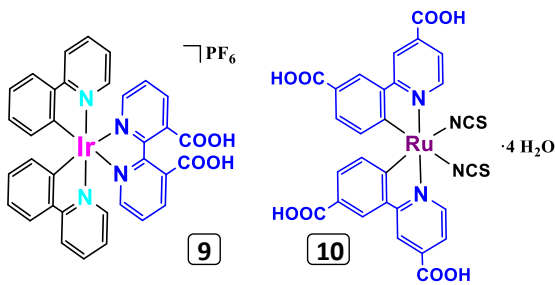
So, considering their appealing emissive properties, low toxicity and easy cell internalization, they could act as potential biomarkers. In addition, and taking into account their porous nature, they could also keep and transport different types of molecules, acting simultaneously as biolabels and drug carriers.



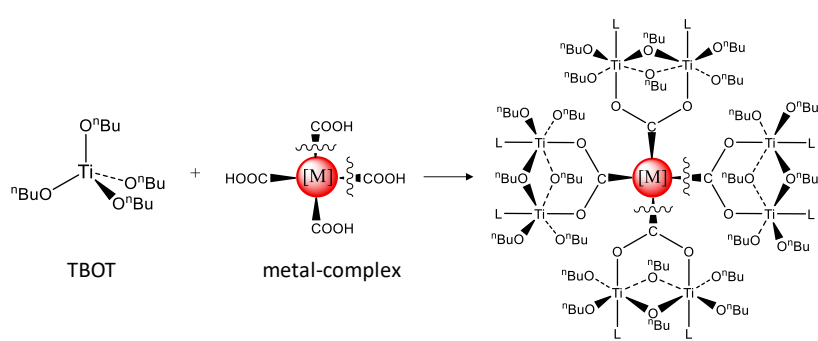
By contrast, complex **8** showed high cytotoxicity in both cell lines, showing smaller IC<sub>50</sub> values ( $3.73 \pm 0.76 \mu\text{M}$  en A549,  $5.53 \pm 0.41 \mu\text{M}$  en HeLa) than those observed for cisplatin under the same experimental conditions. Finally, confocal microscopy revealed its localization and accumulation in the lysosomes of the cell. However, cell death seems to occur through the destruction of the mitochondria, although we still have not been able to determine the mechanism of action.

#### **Chapter IV. Photocatalytic activity of hybrid titania-based materials**

A new cationic iridium(III) complex ( $[\text{Ir}(\text{ppy})_2(3,3'\text{-H}_2\text{dcbpy})]\text{PF}_6$ , **9** or **[Ir]**) has been synthetized and fully characterized. This derivative, like the neutral ruthenium compound  $[\text{Ru}(4,4'\text{-H}_2\text{dcbpy})_2(\text{NCS})_2]$  (**10** or **[Ru]**), known as N3 dye, incorporates carboxylic groups in the structures, which provide linkers to be used as sensitizers for semiconductors systems.



Therefore, we have used both derivatives as building blocks for the design of a new type of hybrid titania-based materials (**[M-TiO<sub>2</sub>\_IS]**, M: Ru, Ir). To improve the interactions of the complex with the TiO<sub>2</sub> matrix, we followed the *in-situ* one-pot strategy based on the previously

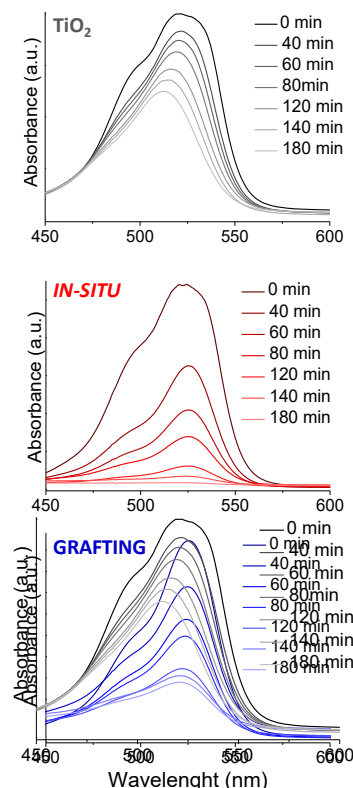
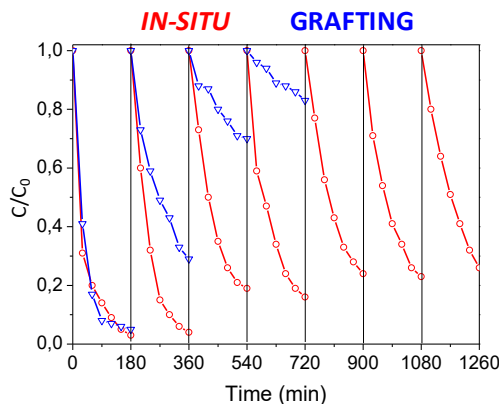


commented Sol-Gel Coordination Chemistry used for the preparation of the hybrid organometallo-titanias. It has been shown that the carboxylic groups are

the responsible for their successful covalent attachment between the complexes and the titania network. The results indicate that the *in-situ* methodology could be suitable for the incorporation of photoactive metal complexes with different properties. According to ICP analyses on related *in-situ* and grafted materials, this technique allows to incorporate higher amounts of dye than the traditional *post-synthetic* grafting method (**IS** 92% **[Ru]**, 59% **[Ir]** vs. **G** 60% **[Ru]**, 23% **[Ir]**).

This procedure allows an efficient integration of the coordination dyes in the semiconductor matrix, showing minimal changes in parameters such as crystallinity, surface area or mesopore diameter. It is also worth noting that the anatase phase found in the complex-free titania **TiO<sub>2</sub>** is maintained in all these hybrid materials.

Furthermore, this new strategy allows to reduce problems related to heterogeneity or leaching of the dye, since covalent bonding occurs not only on the surface of the semiconductor but also in its framework. This fact provides additional protection of the photosensitizer, leading to an exceptional stability against both photodegradation and leaching. Indeed, the *in-situ* materials (**[M]-TiO<sub>2</sub>\_IS**, M: Ru, Ir) have demonstrated to be more stable than the grafted ones (**[M]-TiO<sub>2</sub>\_G**, M: Ru, Ir), exhibiting better photocatalytic performance even after several recycling cycles.



The hybrid *in-situ* titanias (**[M]-TiO<sub>2</sub>\_IS**, M: Ru, Ir) present narrower primary band gap (0.42 eV and 0.18 eV) than the control **TiO<sub>2</sub>** and **[M]-TiO<sub>2</sub>\_G**, respectively. This effect is the responsible of the increase of their photocatalytic performance not only under UV light but also under visible irradiation. The activity of the **IS** materials enhanced more than 2 and 1.5 times in comparison with the complex-free and the grafted titanias, respectively. This improvement in the photocatalytic activity of **[M]-TiO<sub>2</sub>\_IS** could be associated with the synergic combination of the band gap reduction, the additional stability and the higher concentration of dye compared with the grafted materials. Furthermore, we have studied the possible photocatalytic mechanisms followed by these materials, showing the key role of the coordination dye (*dye way*) in the degradation of aqueous solutions of Rhodamine 6G (R6G).

In summary, this synthetic approach represents a new simple, environmentally friendly and standardized strategy for the rational design of highly stable photoactive titania-based materials with potential in areas such as environmental remediation or the design of solar energy conversion devices.



## ***Conclusions***





Along this PhD work, we have manifested the importance of incorporating photoactive materials into inorganic matrices, with the aim of improving their properties and expanding their potential applications. In this sense, it has been designed a synthetic route based on the Sol-Gel Coordination Chemistry with a great versatility, allowing us to obtain different types of photoactive hybrid silica- and titania-based materials. Comparative studies performed between materials prepared following the new *in-situ* approach and those obtained by *post-synthetic* strategies allowed us to show their more notable strengths.

It has been demonstrated that this technique can be easily adapted to chromophores with different structural and electronic features (octahedral or square-planar geometries, cationic or neutral derivatives, with one or several alkoxysilane groups). In addition, using a single silica source (TEOS) and just slightly modifying the reaction conditions, luminescent hybrid silica-based materials with different morphologies and textural properties have been obtained. Thus, we have prepared macroscopic nanostructured materials and discrete nanoparticles with different superficial modifications, with potential application in a wide range of topics as optically transparent gels, light emitting devices or biomarkers. Generally, the new hybrid materials display better physical properties and stabilities than those of the organometallic chromophores incorporated. This methodology is relatively flexible and has allowed us to obtain materials that mimic the photoemission of the organometallic precursor in the solid state or in solution, depending on the concentration used.

On the other hand, we have successfully adapted this synthetic strategy to the preparation of titania-based materials. This fact, unprecedented in the bibliography, allows to broaden the possibilities for the design of new and stable photoactive materials, able to be used after several catalytic cycles for the photodegradation of organic compounds. This improved stability should be attributed to the good integration of the photoactive complexes inside the anatase matrix, which provides them additional protection and stability. In addition, the resulting hybrid titanias present narrower band gaps than those observed for the complex-free control titania and for other materials obtained following *post-synthetic* approaches. All these features are the responsible of their improved photocatalytic performance, not only under UV light but also under visible irradiation.

All these features, together with the easy modulation of the reaction conditions and the extra protection provided by the inorganic matrix to the incorporated chromophores, represent an important advance in the design of photoactive systems.



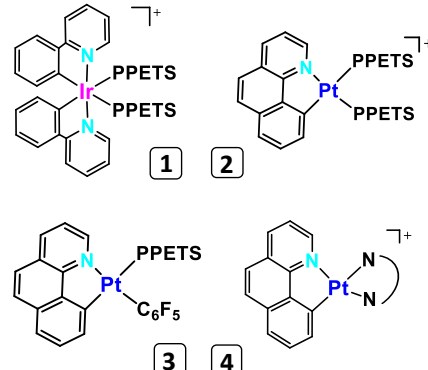
## ***Resumen***



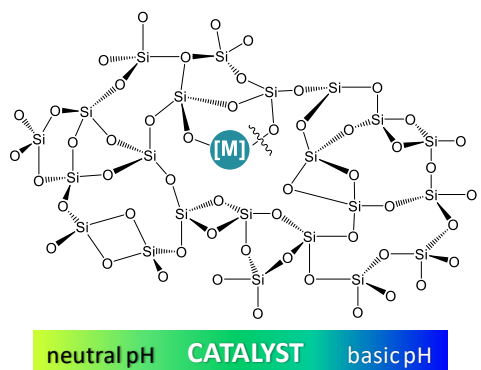


## Capítulo I. Materiales de sílice luminiscentes basados en compuestos de Ir<sup>III</sup> y Pt<sup>II</sup>

En este capítulo se describe la síntesis y caracterización de nuevos compuestos de iridio(III) y platino(II), todos ellos incorporando grupos trialcoxisisilano en dos ligandos diferentes, PPETS y dasipy:  $[\text{Ir}(\text{ppy})_2(\text{PPETS})_2]\text{OTf}$  (**1**),  $[\text{Pt}(\text{bzq})(\text{PPETS})_2]\text{PF}_6$  (**2**),  $[\text{Pt}(\text{bzq})(\text{C}_6\text{F}_5)(\text{PPETS})]$  (**3**) and  $[\text{Pt}(\text{bzq})(\text{dasipy})]\text{PF}_6$  (**4**). Excepto el derivado **2**, todos ellos muestran excelentes propiedades fotofísicas. En particular, el compuesto **4** ha mostrado una gran facilidad para auto-condensar y gelificar (**4-gel**) al exponerlo a determinados disolventes. Tanto el derivado organometálico como su gel muestran una emisión roja que experimenta un desplazamiento batocrómico a 77K, sugiriendo la presencia de interacciones intermoleculares Pt···Pt y/o  $\pi\cdots\pi$ .

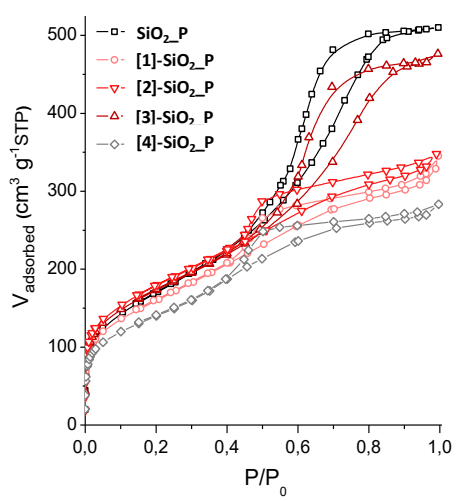


Todos estos derivados se han utilizado como precursores en la preparación de materiales híbridos mesoporosos de base silícea siguiendo, para ello, el procedimiento basado en la Química



de la Coordinación Sol-Gel, y sin la participación de ningún surfactante. Además, la modificación de algún parámetro sintético, como el pH o la cantidad de cromóforo añadido, nos ha permitido obtener dos tipos de materiales mesoporosos diferentes: en polvo sólido (**[1-4]-SiO<sub>2</sub>\_P**) y como gel ópticamente transparente (**[1,3]-SiO<sub>2</sub>\_G**).

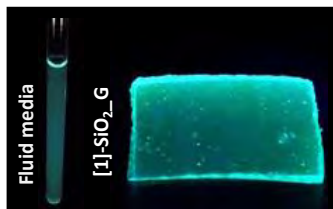
El análisis de estos materiales (FTIR, DRUV, propiedades ópticas, ICP) confirma la incorporación de los derivados organometálicos en la red de sílice, mostrando excelentes propiedades emisivas y texturales. Por otro lado, este estudio revela la capacidad protectora y la estabilidad adicional que la sílice confiere a los cromóforos que incorpora. Así, es destacable el comportamiento observado para **[4]-SiO<sub>2</sub>\_P**, que ha demostrado ser muy estable en medios acuosos, incluso en presencia de oxígeno, mientras que su precursor  $[\text{Pt}(\text{bzq})(\text{dasipy})]\text{PF}_6$  (**4**) necesita mantenerse bajo condiciones de atmósfera inerte debido a su facilidad para auto-condensar. La alta estabilidad de este material se atribuye a la protección que el compuesto de platino(II) adquiere tras su incorporación en la matriz silícea.



Basándonos en las propiedades químicas de los cromóforos precursores, se ha podido establecer un patrón sobre su incorporación. Así, se ha observado que la geometría de los compuestos apenas afecta a las propiedades texturales de las sílices, obteniéndose valores muy similares en los materiales preparados con moléculas octaédricas (**[1]-SiO<sub>2</sub>-P**) y plano-cuadradas (**[2]-SiO<sub>2</sub>-P**). Sin embargo, la naturaleza iónica (catiónica o neutra) del cromóforo y/o el tipo de ligando auxiliar empleado influyen en las características finales de los híbridos.

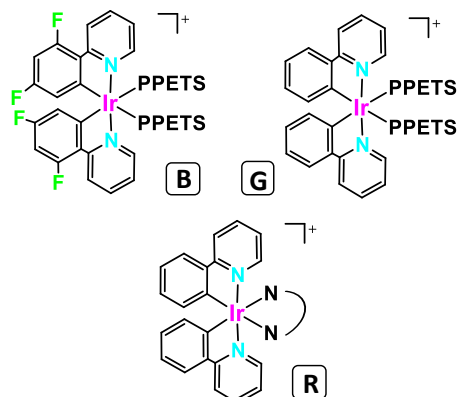
En general, los materiales pulverulentos obtenidos a partir de precursores catiónicos (**[1,2,4]-SiO<sub>2</sub>-P**) presentan áreas superficiales, volúmenes y diámetros de poro menores que los observados para las sílices preparadas con compuestos neutros (**[3]-SiO<sub>2</sub>-P**). Este hecho se ha atribuido a la baja compatibilidad entre la naturaleza catiónica de los cromóforos y el medio neutro en el que se lleva a cabo la síntesis.

Los geles ópticamente transparentes, **[1,3]-SiO<sub>2</sub>-G**, muestran un perfil de emisión idéntico al de sus precursores en disolución, pero con un notable incremento en el rendimiento cuántico (hasta cuatro veces mayor), incluso en presencia de oxígeno, lo que les convierte en buenos candidatos para aplicaciones fotoluminiscentes.



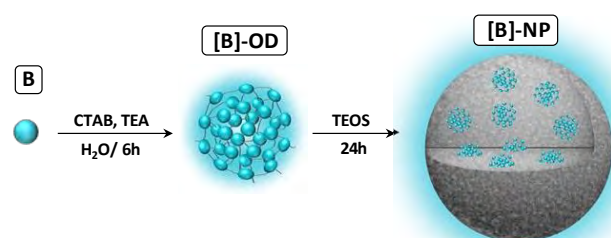
En conclusión, se ha puesto de manifiesto que la Química de la Coordinación Sol-Gel es una estrategia sintética amigable para el medioambiente, ya que requiere condiciones de reacción suaves y pequeñas cantidades de disolventes orgánicos. Además, puede extenderse fácilmente a la síntesis de materiales híbridos mesoporosos luminiscentes mediante la incorporación de cromóforos organometálicos.

## Capítulo II. Nanopartículas hibridas sílice-organometálico emisoras de luz blanca



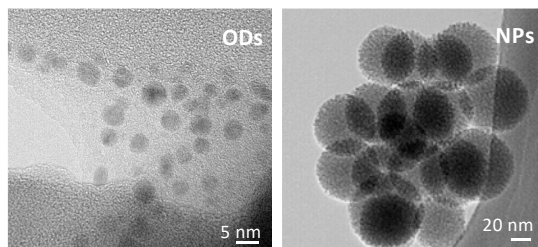
En este capítulo se aborda la preparación y caracterización de dos derivados nuevos de iridio(III), los cuales incorporan dos ligandos ciclometalados diferentes (ppy y dFppy) y uno (*dasipy*) o dos (PPETS) ligandos auxiliares con grupos trialcoxilano terminales:  $[\text{Ir}(\text{dFppy})_2(\text{PPETS})_2]\text{PF}_6$ , **B**, y  $[\text{Ir}(\text{ppy})_2(\text{dasipy})]\text{OTf}$ , **R**. Estos compuestos muestran emisiones azul y roja, respectivamente, con rendimientos cuánticos elevados, que junto con el cromóforo emisor verde **G**,

$[\text{Ir}(\text{ppy})_2(\text{PPETS})_2]\text{OTf}$  (**1**), descrito en el capítulo I, se han utilizado como precursores en la preparación de nanopartículas discretas luminiscentes de sílice.

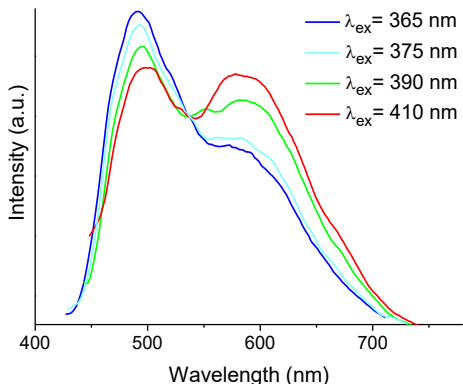
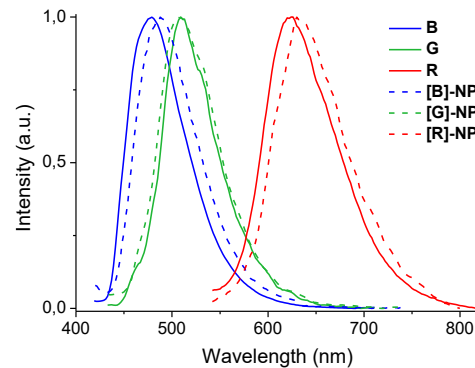


Estas nanopartículas híbridas de sílice se han preparado utilizando una nueva metodología sintética basada en la Química de la Coordinación Sol-Gel.

Esta nueva estrategia consiste en la condensación, cinéticamente controlada, de los grupos terminales alcoxilano de los compuestos (**B**, **G** y **R**), y tiene lugar con la formación inicial de unas partículas pequeñas formadas exclusivamente por moléculas de los complejos, denominadas *organometallic dots* (**ODs**). La posterior reacción de los **ODs** generados en el medio de reacción con el TEOS forma las nanopartículas híbridas de sílice luminiscentes (**NPs**). Siguiendo esta estrategia, y partiendo de los cromóforos descritos, hemos preparado los **ODs** monocromáticos ([**B**]-**OD**, [**G**]-**OD** y [**R**]-**OD**) y sus correspondientes nanopartículas de sílice ([**B**]-**NP**, [**G**]-**NP** y [**R**]-**NP**).



Las propiedades emisivas de los **ODs** y de las **NPs** mostraron propiedades emisivas muy similares a las descritas para los compuestos puros en estado sólido, indicando que los *organometallic dots* se generan sin producirse cambios significativos en la estructura inicial de los compuestos. Sin embargo, las nanopartículas mostraron rendimientos cuánticos más bajos que los medidos para cada uno de los precursores de iridio(III) en estado sólido.



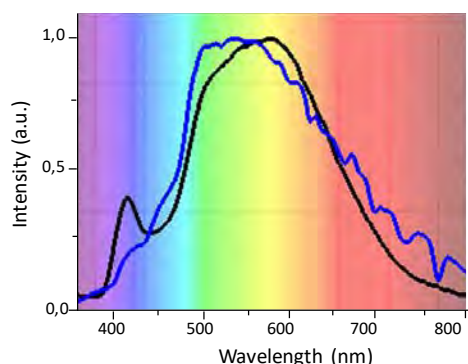
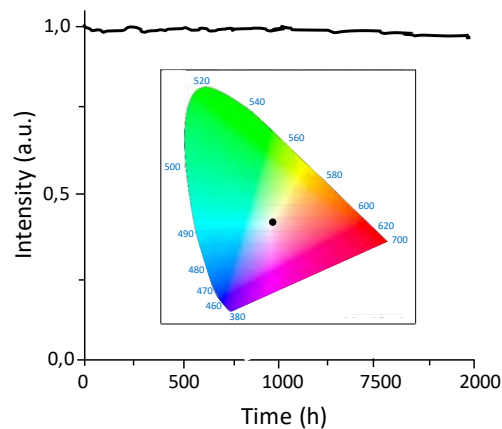
Hemos extendido esta metodología sintética con el fin de preparar nanopartículas emisoras de luz blanca **[W]-NP** a partir de una mezcla formada por los compuestos **B**, **G** y **R** en las cantidades adecuadas (*tres en uno*). Como cabría esperar, este material muestra una intensa (20%) emisión blanca debido a la presencia de un perfil emisivo con dos máximos que cubre el rango del visible, y cuya intensidad depende de la longitud de onda de excitación.

El análisis de las propiedades texturales revela que todas las nanopartículas muestran isotermas de tipo IV, características de materiales mesoporosos, con áreas superficiales elevadas ( $1000\text{ m}^2/\text{g}$ , aprox.), volúmenes de mesoporo en el rango de  $0.5\text{-}0.7\text{ cm}^3/\text{g}$  y tamaño de poro entre 2.1 and 2.4 nm. Por su parte, el estudio mediante microscopía electrónica de transmisión (TEM) nos permitió determinar el tamaño de partícula. Así, los **ODs** mostraron tamaños de unos 5 nm de diámetro, mientras que **NPs** resultaron ser partículas esféricas y discretas con tamaños comprendidos entre 50 y 70 nm. Además, el análisis por ICP de las nanopartículas ha mostrado rendimientos de incorporación de los complejos entre el 80 y 90%.

Se ha estudiado el uso de las nanopartículas en el diseño de nuevos recubrimientos elásticos fotoluminiscentes (*down-converting coatings*) y su empleo en la fabricación de diodos emisores de luz híbridos (HLEDs), evaluándose su eficiencia y estabilidad. Los recubrimientos preparados a partir de los compuestos de iridio (**OC-rubbers**) y de las nanopartículas monocromáticas (**NP-rubbers**), presentan diferencias significativas en sus comportamientos. En general, las **NP-rubbers** mostraron mejores propiedades, lo que es consistente con la idea de que la matriz

silícea protege a los cromóforos frente a la desactivación de la emisión, así como de la fotodegradación.

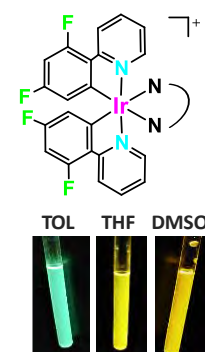
El dispositivo fabricado a partir de las nanopartículas con emisión blanca **[W]-NP** (HWLED) mostró una excelente y homogénea distribución de luz, y una estabilidad superior a las 2000 horas (sin cambios significativos en la eficiencia lumínica, 2.5 lm/W, y en el valor de CCT, 5143K, así como en el valor de las coordenadas de color x/y, 0.34/0.33), convirtiéndose en uno de los HWLDs más estables publicados hasta la fecha. Además, se ha utilizado una extrapolación lineal que predice que este dispositivo debería mantener más del 50% de su intensidad lumínica máxima tras 10000 horas de funcionamiento.



En definitiva, mediante el empleo de nanopartículas de sílice de luz blanca (**[W]-NP**) se ha fabricado un dispositivo HWLED altamente eficiente y estable, con un color de emisión blanco cálido. De esta forma, se solucionan alguno de los problemas habituales en este tipo de dispositivos como son la desactivación de la emisión, la baja estabilidad del color o la separación de fases. Así, la nueva ruta sintética (*tres en uno*) permite superar estas limitaciones mediante el uso de nanopartículas de sílice de emisión blanca (**[W]-NP**). Por un lado, las moléculas de los compuestos, que están bien incorporadas en la matriz de sílice, están lo suficientemente cerca como para que haya procesos de transferencia energética entre ellas; y, por el otro, se aumenta la fotoestabilidad de los cromóforos gracias a las restricciones geométricas producidas por la matriz inorgánica.

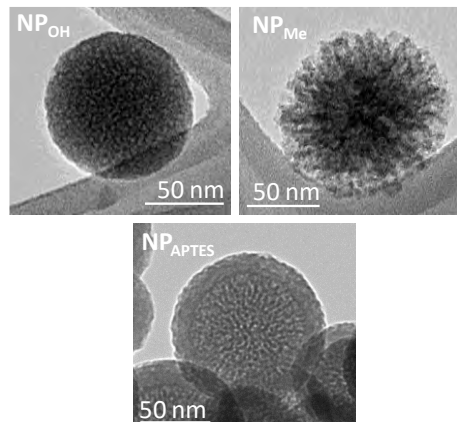
### Capítulo III. Nanopartículas de sílice mesoporosas como biomarcadores

En el capítulo III se describen las propiedades de dos compuestos nuevos de iridio(III) que incorporan dos ligandos auxiliares, basados en bipiridinas disustituidas (*dasipy*) L1 y *dbbpy* L2):  $[\text{Ir}(\text{dFppy})_2(\text{dasipy})]\text{PF}_6$  (7) y



$[\text{Ir}(\text{dFppy})_2(\text{dbbpy})]\text{Cl}$  (8). Este último derivado mostró un comportamiento emisivo dependiente de la polaridad del disolvente, confirmando así el carácter de transferencia de carga del estado excitado.

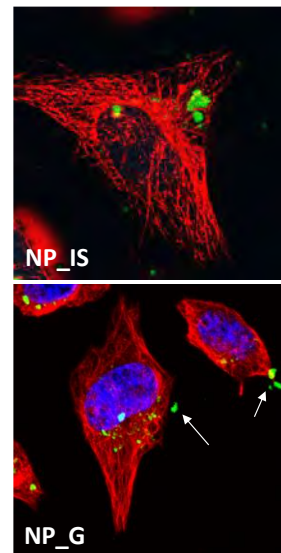
El cromóforo 7 se utilizó como precursor en la preparación de nanopartículas de sílice mesoporosas nativas ([7]-NP<sub>OH</sub>\_IS), siguiendo un método sintético basado en la Química de la Coordinación Sol-Gel. A partir de ellas, y gracias a la presencia de grupos OH en su superficie, se procedió a modificarlas con dos agentes de recubrimiento diferentes: el dimetildietoxisilano (DMDES) y el (3-aminopropil)etrioxisilano (APTES). Así, mediante pequeñas modificaciones, llevadas a cabo en el propio medio de reacción (*in-situ*), se pudieron obtener dos tipos de nanopartículas con coronas o carcasas perfectamente establecidas ([7]-NP<sub>Me</sub>\_IS y [7]-NP<sub>APTES</sub>\_IS) y con propiedades físico-químicas diferentes. Simultáneamente, y con fines comparativos, también se prepararon las nanopartículas graftedas correspondientes ([7]-NP<sub>OH</sub>\_G, [7]-NP<sub>Me</sub>\_G y [7]-NP<sub>APTES</sub>\_G).



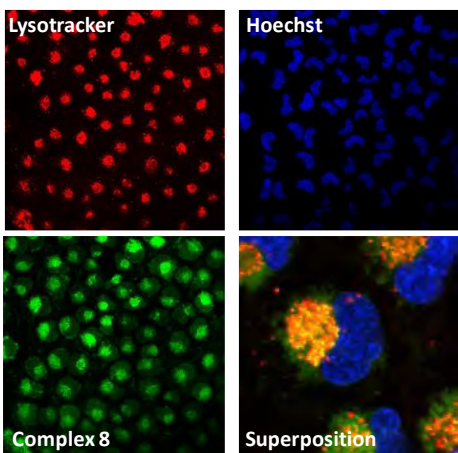
Las propiedades texturales de estas nanopartículas confirmaron su naturaleza mesoporosa; mostrando elevadas áreas superficiales en el caso de NP<sub>OH</sub> (aprox.  $770 \text{ m}^2/\text{g}$ ) y NP<sub>Me</sub> (aprox.  $1000 \text{ m}^2/\text{g}$ ). Sin embargo, las modificadas con APTES (NP<sub>APTES</sub>) mostraron los valores de áreas superficiales más pequeños y una mesoporosidad parcialmente bloqueada ( $A_{\text{BET}}$ ,  $\text{m}^2/\text{g}$ : 230  $\text{NP}_{\text{APTES}}$ , 97 [7]-NP<sub>APTES</sub>\_IS y 100 [7]-NP<sub>APTES</sub>\_G) debido, probablemente, a la presencia de las cadenas alifáticas del agente de recubrimiento (APTES).

Todas las nanopartículas sintetizadas mostraron propiedades emisivas muy similares a las descritas para el compuesto **7** puro, incluyendo tiempos de vida largos ( $\tau$ , 0.52-0.80  $\mu$ s) y rendimientos cuánticos elevados ( $\phi$ , 17-52 %). En las muestras *in-situ* ([**7**]-NP\_IS) se mimetiza el comportamiento del complejo en disolución de THF, probablemente debido a la buena dispersión del cromóforo dentro de la matriz inorgánica, lo que permite que las moléculas del mismo estén separadas. Por el contrario, las nanopartículas graftedas ([**7**]-NP\_G) mostraron un comportamiento similar al descrito para el precursor **7** en estado sólido. De acuerdo con esto, su espectro en suspensiones acuosas exhibe un desplazamiento hacia mayores energías, hecho que se atribuye a una buena dispersión de las nanopartículas en el agua, lo que podría reducir la interacción entre las moléculas del cromóforo.

Teniendo en cuenta las buenas propiedades fotofísicas mostradas por las nanopartículas, se ha examinado su posible uso como biomarcadores, evaluando, en primer lugar, su citotoxicidad frente a dos líneas celulares diferentes, HeLa (carcinoma cervical) y A549 (carcinoma de pulmón). En general, todas ellas mostraron valores de IC<sub>50</sub> considerablemente altos, destacando las muestras modificadas con grupos metilo ([**7**]-NP<sub>Me</sub>) que demostraron ser completamente atóxicas. La localización celular se determinó mediante microscopías de fluorescencia y confocal, observándose en todos los casos la acumulación de nanopartículas en áreas perinucleares. No obstante, se percibe una mayor agregación de partícula fuera de la célula en las nanopartículas graftedas ([**7**]-NP\_G) que en las *in-situ* ([**7**]-NP\_IS), destacando así uno de los puntos fuertes de los materiales preparados a partir de nuestra ruta sintética.



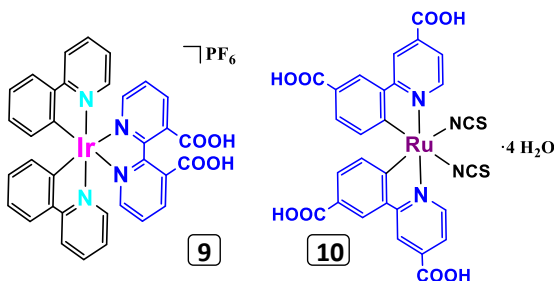
Así, gracias a sus buenas propiedades luminiscentes, baja toxicidad y fácil internalización celular podemos considerar estas nanopartículas como biomarcadores adecuados. Además, al tratarse de nanopartículas mesoporosas, serán capaces de albergar diferentes moléculas en sus poros y actuar, simultáneamente, como biomarcadores y agentes transportadores de fármacos.



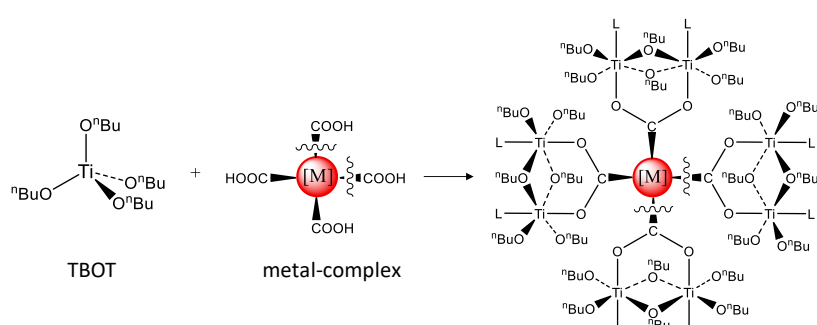
Por su parte, el compuesto **8** utilizado como modelo resultó ser muy citotóxico en ambas líneas celulares, mostrando valores de  $IC_{50}$  ( $3.73 \pm 0.76 \mu\text{M}$  en A549,  $5.53 \pm 0.41 \mu\text{M}$  en HeLa) inferiores, incluso, que los correspondientes al cis-platino. Las imágenes obtenidas a partir de microscopía confocal sugieren que este derivado se localiza y acumula en los lisosomas de la célula. No obstante, la muerte celular parece producirse a través de la destrucción de la mitocondria, aunque todavía no hemos sido capaces de determinar el mecanismo de acción.

#### Capítulo IV. Actividad fotocatalítica de materiales híbridos de base titania

En este capítulo se ha sintetizado y caracterizado un nuevo compuesto de iridio(III) ( $[\text{Ir}(\text{ppy})_2(3,3'-\text{H}_2\text{dcbpy})]\text{PF}_6$ , **9** o **[Ir]**) similar al derivado neutro  $[\text{Ru}(4,4'-\text{H}_2\text{dcbpy})_2(\text{NCS})_2]$  (**10** o **[Ru]**), conocido como N3 dye, que incorpora grupos carboxílicos en su estructura.



Ambos derivados se han utilizado como agentes captadores de energía (*dyes* o *sensitizers*) en el diseño de un nuevo tipo de materiales híbridos de base titania ( $[\text{M}-\text{TiO}_2]_\text{IS}$ , M: Ru, Ir). Para ello, hemos seguido una innovadora estrategia basada en la co-condensación *in-situ* de los compuestos de coordinación funcionalizados con TBOT. Se ha puesto de manifiesto que, durante

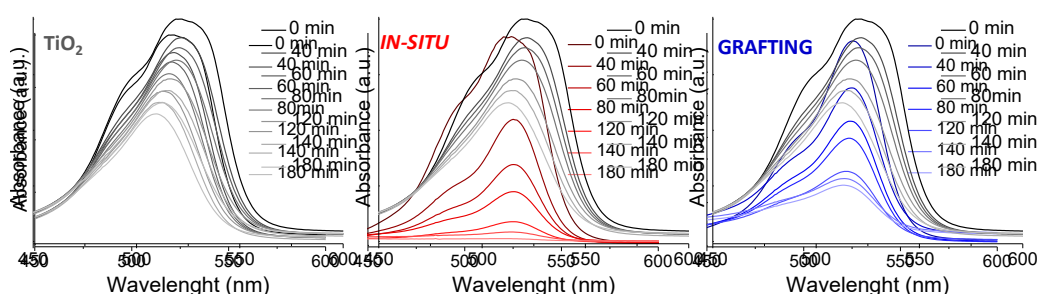
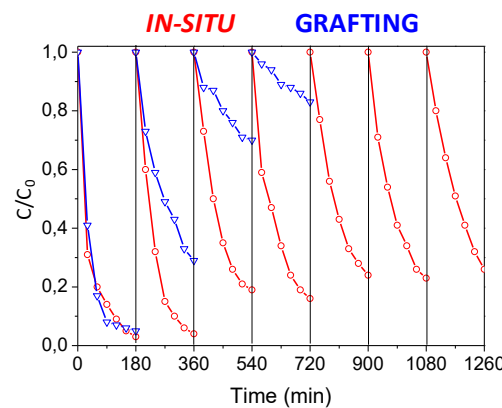


el proceso de condensación, son los grupos carboxílicos los responsables de la unión covalente de los compuestos a la matriz del semiconductor. Esta

estrategia sintética, basada en la Química de la Coordinación Sol-Gel utilizada en la preparación de las sílicas híbridas de los Capítulos I-III, nos ha permitido incorporar complejos metálicos

fotoactivos con cargas y propiedades diferentes, ampliando así el abanico de posibilidades a la hora de seleccionar los *dyes*. Además, de acuerdo con los análisis ICP, esta técnica permite incorporar cantidades mayores de *dye* que el método *post-sintético* tradicional (**IS** 92% [**Ru**], 59% [**Ir**] vs. **G** 60% [**Ru**], 23% [**Ir**]).

Este procedimiento permite integrar de manera eficiente los compuestos en la matriz de la titania sin apenas modificar parámetros como su cristalinidad, área superficial o diámetro de mesoporo, manteniendo además la fase de anatasa que se ha encontrado en el material de control **TiO<sub>2</sub>**. También se ha conseguido reducir los problemas relacionados con la heterogeneidad o la pérdida del *dye*, ya que las uniones covalentes se producen no solo en la superficie del semiconductor sino también en el interior de la matriz, lo que permite una mayor protección del *sensitizer* y, por tanto, una mayor estabilidad frente a la fotodegradación y a la lixiviación. Los materiales *in-situ* ([M]-TiO<sub>2</sub>\_IS, M: Ru, Ir) han mostrado ser más estables que los homólogos obtenidos a partir de la aproximación grafting ([M]-TiO<sub>2</sub>\_G, M: Ru, Ir). Además, esta protección adicional no afecta a la accesibilidad electrónica, ya que estas titanias todavía exhiben buenas propiedades photocatalíticas incluso tras siete ciclos catalíticos.



La incorporación de los compuestos de Ir(III) y Ru(II) modifica, también, la transición energética entre las bandas de valencia y conducción (*band gap*) del semiconductor. Así, los materiales *in-situ* ([M]-TiO<sub>2</sub>\_IS, M: Ru, Ir) presentan un *band gap* 0.42 eV y 0.18 eV más estrecho que el correspondiente a la titania de control **TiO<sub>2</sub>** y a [M]-TiO<sub>2</sub>\_G, respectivamente. Este hecho afecta positivamente a su actividad photocatalítica, no solo bajo radiación UV sino también bajo iluminación visible. Así, hemos observado un aumento de la actividad de los materiales **IS** de 2 y 1.5 veces con respecto a las titanias de control y graftedas, respectivamente. Esta mejora en las

propiedades fotocatalíticas de **[M]-TiO<sub>2</sub>-IS** puede atribuirse al efecto sinérgico entre la reducción de su *band gap* y la mayor estabilidad y concentración de *dye* incorporado en el semiconductor, en comparación con los materiales graftedos.

Por último, también estudiamos el mecanismo de actuación de estos materiales, mostrando la importancia que tiene el *dye* (*dye way*) en la fotodegradación de disoluciones de Rodamina 6G (R6G).

En conclusión, esta aproximación sintética representa una nueva estrategia, amigable con el medio ambiente, para el diseño de materiales fotoactivos altamente estables y con un gran potencial en el diseño de dispositivos de conversión de energía solar o de planes de recuperación medioambiental, por ejemplo.

## ***Conclusiones***





A lo largo de la presente memoria se ha manifestado la importancia de incorporar adecuadamente materiales fotoactivos en matrices de sólidos inorgánicos, con el fin de mejorar sus propiedades y ampliar sus aplicaciones potenciales. Se ha diseñado una ruta sintética *in-situ* basada en la Química de la Coordinación Sol-Gel con gran versatilidad, que nos ha permitido preparar diferentes tipos de materiales híbridos fotoactivos de sílice y de titania. El estudio comparativo realizado entre los materiales sintetizados mediante la nueva aproximación *in-situ* y los obtenidos a partir de estrategias *post-sintéticas*, nos ha permitido demostrar sus puntos fuertes.

Como ha quedado demostrado, esta técnica se puede adaptar a cromóforos organometálicos con características estructurales y electrónicas diferentes (geometrías octaédricas o plano-cuadradas, derivados catiónicos o neutros, con uno o varios grupos alcoxisilano). Por otra parte, introduciendo pequeñas modificaciones en las condiciones de reacción, se pueden obtener materiales híbridos luminiscentes de base silícea que presentan diferentes morfologías y propiedades texturales. Así, se han preparado desde materiales macroscópicos nanoestructurados, a nanopartículas discretas con acabados superficiales distintos, que posibilitan su uso en una gran variedad de aplicaciones como geles luminiscentes ópticamente transparentes, dispositivos emisores de luz o biomarcadores. En general, los materiales híbridos obtenidos presentan propiedades fotofísicas mejoradas, incrementando, además, la estabilidad de los cromóforos organometálicos incorporados. Esta metodología es relativamente flexible y permite obtener materiales que mimetizan el comportamiento emisivo de los cromóforos en estado sólido o en disolución, dependiendo de la concentración empleada.

Por otro lado, se ha conseguido adaptar la estrategia sintética a la preparación de materiales basados en titania. Este hecho, sin precedentes en la bibliografía, permite ampliar el abanico de posibilidades a la hora de diseñar materiales semiconductores fotoactivos altamente estables, con posibilidad de reutilización tras varios ciclos catalíticos de fotodegradación de materia orgánica. Estas características se atribuyen a la buena integración de los complejos fotoactivos en la matriz de anatasa, que les confiere una alta protección y una estabilidad excepcional. Las titanias híbridas semiconductoras resultantes presentan saltos electrónicos más pequeños que los correspondientes a la titania de control y a materiales similares obtenidos mediante técnicas *post-sintéticas*. Todo ello afecta positivamente a su actividad fotocatalítica, no solo bajo radiación UV sino también bajo luz visible.

En conjunto, creemos que todas estas características, junto con la facilidad de modular las condiciones de reacción y la protección adicional que la matriz inorgánica confiere a los

cromóforos incorporados, suponen un avance importante y un gran potencial a la hora de diseñar diferentes tipos de sistemas fotoactivos.

## ***Experimental Part***





## **Instrumental and spectroscopic techniques used in the characterization of both the compounds and the materials**

### ***I. Elemental Analysis***

Elemental analysis of C, H, N and S of all the complexes were carried out with a Carlo Erba EA1110 CHNS/O microanalyzer.

### ***II. Mass Spectrometry***

Mass spectra of the organometallic complexes were recorded on a Microflex MALDI-TOF Bruker spectrometer operating in the linear and reflector modes using dithranol as the matrix.

### ***III. Infrared Spectra***

IR spectra were obtained on a Nicolet Nexus FT-IR Spectrometer in the range between 4000  $\text{cm}^{-1}$  to 200  $\text{cm}^{-1}$ . Samples were prepared using KBr pallets or from Nujol mulls between polyethylene sheets. These last spectra will also show the characteristic absorption bands of Nujol at 2900 (s, broad), 1452 (s), 1377 (s) and 1362  $\text{cm}^{-1}$  and the polyethylene at 729 (s) and 718 (s)  $\text{cm}^{-1}$ .

### ***IV. Nuclear Magnetic Resonance (RMN)***

NMR spectra were recorded on Bruker ARX300 and ARX400 spectrometers. Chemical shifts are reported in parts per million (ppm) relative to external standards ( $\text{SiMe}_4$  for  $^1\text{H}$  and  $^{13}\text{C}\{^1\text{H}\}$ ,  $\text{CFCl}_3$  for  $^{19}\text{F}\{^1\text{H}\}$  and  $\text{H}_3\text{PO}_4$  (88%) for  $^{31}\text{P}\{^1\text{H}\}$ ) and coupling constants in hertz (Hz).  $^1\text{H}$  and  $^{13}\text{C}\{^1\text{H}\}$  spectra were assigned by means of 2D experiments ( $^1\text{H}$ - $^1\text{H}$  COSY and TOCSY; and  $^1\text{H}$ - $^{13}\text{C}$  HSQC and HMBC).

### ***V. UV-Vis Spectroscopy***

UV-Vis spectra in solution were recorded on a Hewlet Packard 8453 spectrophotometer, in the concentration range between  $10^{-4}$ - $10^{-6}$  M and using quartz cubets with 1 mm or 1 cm of optical path. Diffuse Reflectance UV-Vis (DRUV) spectra were carried out using a Shimazdu UV-3600 spectrophotometer with a Harrick Praying Mantis accessory, and recalculated following the Kubelka-Munk function (equation 1). The samples of the complexes were prepared in a mixture of KBr pallets.

$$F(R') = [1-(R')]/2(R') \quad (1)$$

, where R' is the reflectance value obtained directly from the spectrophotometer.

DRUV spectra of titania materials were also used for the estimation of their band-gaps. Band-gap calculations were based on the  $[F(R')h\nu]$  vs. photon energy ( $h\nu$ ) plot (Tauc plots).

vi. Luminescence spectroscopy, lifetimes and quantum yields.

Excitation and emission spectra were obtained in a Jobin Yvon Horiba Fluorolog 3-11 Tau-3 spectrofluorimeter. All spectra were collected both in the solid state and in solution (THF,  $\text{CH}_2\text{Cl}_2$  or  $\text{CH}_3\text{CN}$ ) at room temperature and 77K. The lifetime measurements were performed operating in the phosphorimeter mode (with a F1-1029 lifetime emission PMT assembly, using a 450 W Xe lamp) or with a Datastation HUB-B with a nanoLED controller and software DAS6. The nano-LEDs employed for lifetime measurements were of wavelength between 370 and 450 nm with pulse lengths of 0.8-1.4 ns. The lifetime data were fitted using the Jobin-Yvon software package. Quantum yields were measured using a F-3018 Integrating Sphere mounted on the Fluorolog 3-11 Tau-3 spectrofluorimeter.

vii. X-Ray Crystallography

Single-crystal X-Ray: The diffraction data were collected using graphite monochromatic  $\text{Mo-K}\alpha$  radiation with a Nonius- $\kappa$ CCD diffractometer (data processed with DENZO and SCALEPACK suite of programs)<sup>181</sup> or with a Bruker D8QUEST (PHOTON 100 CMOS) area-detector diffractometer, using the APEX3 software.<sup>182</sup> The absorption corrections were carried out by semi-empirical methods. The structures were solved by intrinsic phasing using SHELXT,<sup>183</sup> with the WinGX graphical user interface,<sup>184</sup> and refined by full-matrix least squares on  $F^2$  with SHELXL.<sup>185</sup> All non-hydrogen atoms were assigned anisotropic displacement parameters. All hydrogen atoms were constrained to idealized geometries fixing isotropic displacement parameters 1.2 times the  $U_{iso}$  value of their attached atoms, except those of methyl and OH groups, which were fixed to 1.5 times the  $U_{iso}$  value of their attached carbons. Complete crystallographic data for each of the structures are given in the annexes.

Powder X-ray diffraction (XRD): The analyses were carried out with a Bruker D8-Advance diffractometer (operating at 40 kV and 40 mA), using a  $\text{CuK}\alpha$  radiation ( $\lambda = 1.54056 \text{ \AA}$ ). The samples were scanned from  $20^\circ$  to  $60^\circ$  ( $2\theta$ ), at a scanning velocity of  $0.05 \text{ min}^{-1}$ . Domain size and

anatase spacing ( $d_{101}$ ) of the samples were calculated using the Eq. Scherrer and Eq. Bragg, respectively.

#### VIII. Theoretical Calculations

Calculation were carried out with the Gaussian 09 package<sup>186</sup> using Becke's three-parameter functional combined with Lee-Yang-Parr's correlation functional (B3LYP) in the singlet state ( $S_0$ ) and the unrestricted U-B3LYP in the triplet state ( $T_1$ ).<sup>187</sup> The basis set used was the LanL2DZ effective core potential for Ir and 6-31G(d,p) for the ligands atoms. DFT and TD-DFT calculations were carried out using the polarized continuum model approach<sup>188</sup> implemented in the Gaussian 09 software. The emission energies were calculated as the difference of the DFT-optimized  $T_1$  geometry for both states. Overlap populations between molecular fragments were calculated using the GaussSum program.<sup>189</sup>

#### IX. X-ray Photoelectron Spectroscopy (XPS)

XPS analyses were carried out in a VG-MicrotechMultilab instrument, using MgK-alpha radiation of energy 1253.6 eV and pass energy of 50 eV. The pressure during the data acquisition was  $5 \times 10^{-7}$  Pa. A careful deconvolution of the spectra was made, and the areas under the peaks were estimated by calculating the integral of each peak after subtracting a Shirley background and fitting the experimental peak to a combination of Lorentzian/Gaussian lines of 30-70 % proportions. XPS spectra were analyzed by referencing the binding energies to both the C1s line at 284.6 eV from adventitious carbon and Ti2p line at 458.5 eV.

#### X. Physical Gas Adsorption

When a gas comes into contact with a solid surface, some of the molecules of the gas will be adsorbed on the surface, as shown in figure 5.1. This phenomena is known as adsorption, being the adsorbent the solid matrix and the adsorbate the gas. Regarding this phenomena, the differences between physisorption or physical adsorption (weak gas-solid interactions) and chemisorption or chemical adsorption (covalent bonds between the adsorbate and the adsorbent) need to be considered. The study of the adsorption process allows to fully characterize the porosity of porous materials.

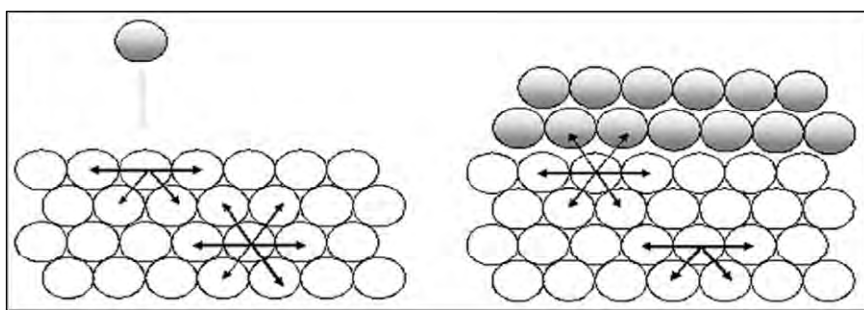


**Figure 5.1.** Schematic representation of the cohesive forces in a solid (left) and in a solid with an adsorbed gas (right).

The measurement of the amount of gas adsorbed over a range of partial pressure at constant temperature results in a graph known as adsorption isotherm. Different types of isotherms have been reported (figure 5.2) depending on the type of adsorbent and adsorbate, and the intermolecular interactions between the gas and the surface of the solid. The analysis of these curves allows to determine the porous texture of the materials. Considering the classification of the IUPAC, different materials are described regarding the size of the pore.

- Macroporous: pore diameters bigger than 50 nm.
- Mesoporous: pore diameter between 2 and 50 nm.
- Microporous: pore diameter smaller than 2 nm.

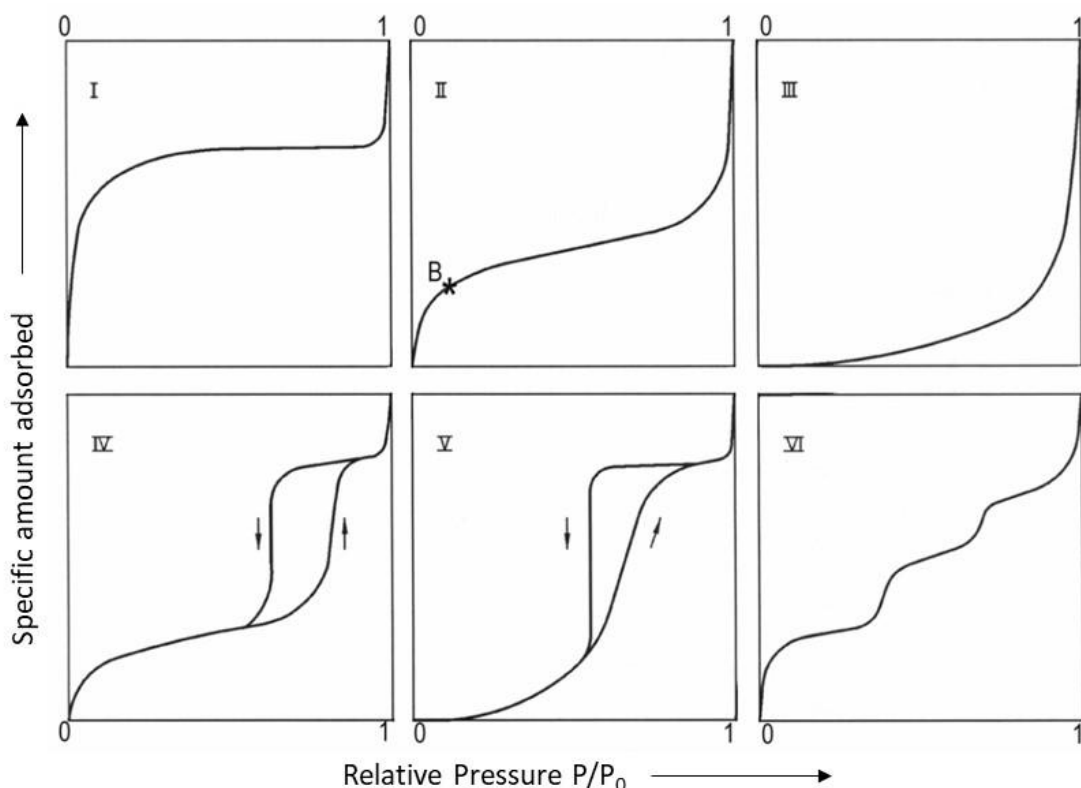


**Figure 5.2.** Schematic representation of the six types of isotherms according to the classification of the IUPAC.

The majority of the isotherms may be grouped into the six types shown in figure 5.2.

- Type I: adsorption in microporous solids that present relatively small external surfaces. The limiting uptake is due to the accessibility of the micropore volume rather than the internal surface area.
- Type II: adsorption in non-porous or macroporous adsorbent. It represents unrestricted monolayer-multilayer adsorption. Point B, the beginning of the almost linear middle section of the isotherm, is often taken to indicate the stage at which monolayer coverage is complete and multilayer adsorption about to begin.
- Type III: this isotherm is convex to the pressure axis and it does not exhibit any Point B. The interaction between the adsorbent and the adsorbate is very weak.
- Type IV: typical of mesoporous materials. The initial part of the isotherm is attributed to monolayer adsorption, since it displays the same behavior as type II. It usually features a hysteresis loop, which is associated with capillary condensation taking place in the mesopores.
- Type V: The adsorbent-adsorbate interaction is weak, but it displays a hysteresis loop associated with the condensation in the mesopores. It is a very uncommon isotherm.
- Type VI: features a stepwise multilayer adsorption. It is typical of uniform solids with pores of different sizes. The step-height now represents the monolayer capacity for each adsorbed layer, and it remains nearly constant for the first two or three adsorbed layers.

Porous texture was characterized by nitrogen adsorption/desorption measurements at 77K in an AUTOSORB-6 apparatus. The samples were previously degassed at 373 K for 8 h and  $5 \times 10^{-5}$  bars. Adsorption data were analyzed using the software QuadraWinTM (version 6.0) of Quantachrome Instruments. The BET surface area was estimated by multipoint BET method, using the adsorption data in the relative pressure ( $P/P_0$ ) range of 0.05–0.25. Pore-size distribution curves were calculated using the Barret-Joyner-Halenda (BJH) method or the DFT method (NLDFT equilibrium model, which assumes nitrogen adsorption at 77K in cylindrical silica pores for the mesopore range). The total pore volume and the mesopore volume were read directly from the adsorption branch of the isotherm at 0.8 and 0.99, respectively (the micropore volume was determined by using t-plot method to be 0).

XI. Transmission (TEM) and Field Emission Scanning (FESEM) Electron Microscopy

The morphology of the mesoporous materials was investigated by transmission electron microscopy (TEM) and field emission scanning electron microscopy (FESEM). Samples for TEM and FESEM studies were prepared by dipping a sonicated suspension of the sample in ethanol on a carbon-coated copper. Both electron diffraction experiments and TEM images were performed using a JEM-2010 microscope (JEOL, 0.14 nm of resolution), at an accelerating voltage of 200 kV. The digital analysis of the TEM micrographs was performed using DigitalMicrographTM 3.6.1. by Gatan, being the particle size estimated as an average of the size of eighty particles. SEM analyses were carried out in a field emission scanning electron microscope (FESEM) Merlin VP Compact (Zeiss, 1.6 nm of resolution at 1 kV).

XII. High Resolution Inductively Coupled Plasma Mass Spectrometry (HR-ICP-MS)

Metal contents on each hybrid materials were determined by HR-ICP-MS using a Thermo Scientific ELEMENT XR spectrometer. The samples were dissolved in a mixture of 3.5 mL HCl + 1 mL HNO<sub>3</sub> + 1 mL HF + 5 mL H<sub>3</sub>BO<sub>5</sub> (5%), digested in a microwave (260 °C, 45 bar) and filtered off (0.45 µm) prior to analysis. This treatment is able to entirely dissolve the samples.

XIII. Photocatalytic Activity of titania materials

The photocatalytic activity of the as-synthesized titania-based materials was evaluated by following the degradation of Rhodamine 6G in aqueous solution under UV and visible radiation. For a typical UV light degradation test, 200 mL of an aqueous suspension of Rhodamine 6G (R6G, 5x10<sup>-5</sup> M) with 0.15 g/L of the catalyst was stirred during 30 min in the dark, to achieve the adsorption/desorption equilibrium of the dye on the catalyst surface. Afterwards, this suspension was irradiated with UV light using a photochemical reactor system with a 400W medium-pressure Hg lamp located in a cooled, double-walled quartz, immersion well. The concentration of the dye was monitored by taking 1 mL sample of the mixture each 20 or 30 minutes for 3 hours. Every sample was centrifuged twice and the resulting solution was studied by UV-Vis spectroscopy analysis in the 700-300 nm wavelength range, using a Hewlet Packard 8453 spectrophotometer. As several intermediate species can appear during the photodegradation process, the total concentration of the Rhodamine species was estimated based on the maximum absorbance observed in the 490 to 530 nm range. For the experiments under visible light, a similar procedure was followed, also using a 400 W medium-pressure Hg lamp located in a double-walled Pyrex immersion well, but cooling with a 2M solution of NaNO<sub>2</sub>.

(UV cutoff filter  $> 400$  nm, figure 5.3). Recycling tests were performed in the same way, but recovering the titania materials collected on each 1 mL sample (a total of about 4 mg) and returning it to the reaction mixture before each new charge of Rhodamine 6G. To further investigate the mechanism of the R6G degradation process under UV or visible light using the hybrid photocatalyst **[Ru]-TiO<sub>2</sub>\_IS** and **[Ir]-TiO<sub>2</sub>\_IS**, controlled experiments have been carried out to determine the dominant active species involved in the photocatalytic reactions. The experimental procedure was similar to that described before, but using aqueous solutions of Rhodamine 6G ( $5 \times 10^{-5}$  M) with triethanolamine (TEA,  $5 \times 10^{-2}$  M) or isopropanol ( $i\text{PrOH}$ ,  $5 \times 10^{-2}$  M), which were used to scavenge photogenerated holes ( $\text{h}^+$ ) or hydroxyl radicals ( $\cdot\text{OH}$ ), respectively.

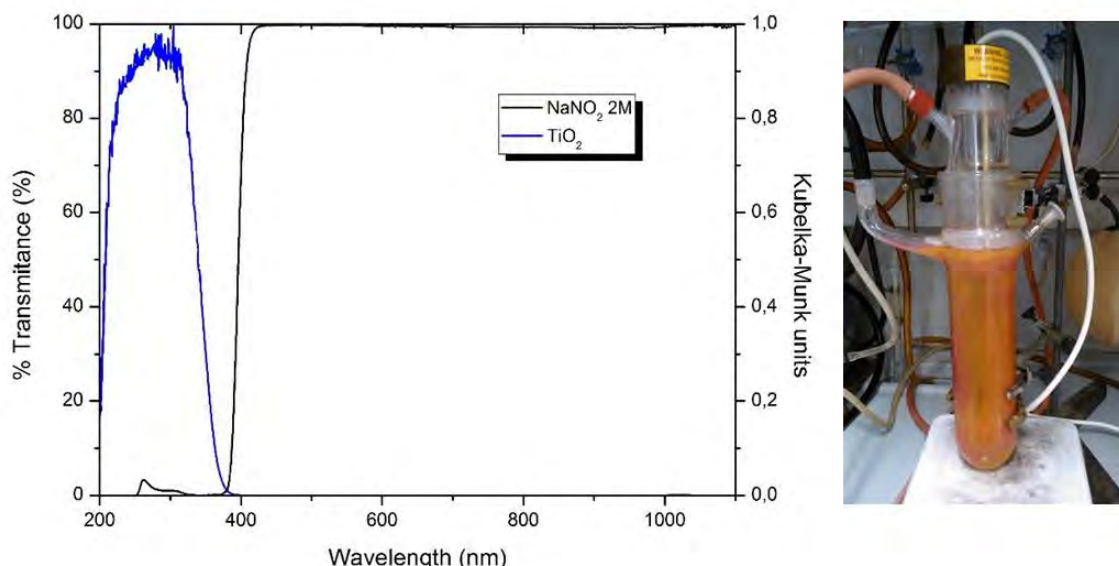


**Figure 5.3.** (Left) Solid state DRUV spectra of the complex-free control titania vs. transmittance spectrum of the 2M solution of  $\text{NaNO}_2$  used as UV cutoff filter and (right) photograph of the reactor used on the photocatalytic study.

#### xiv. Preparation of the gels and rubber-like materials

These materials were prepared by the research group of Dr. Rubén D. Costa at IMDEA Materials Institute.

To prepare the coatings, an acetonitrile solution or suspension of the corresponding complex or silica nanoparticles, respectively, was added to a 6:1 mixture of branched (trimethylolpropane ethoxylate, TMPE, 450 mol/g) and linear (poly(ethylene oxide), 1-PEO,  $5 \times 10^6$  mol/g) polymers. The optimize mixture was complex/NP: TMPE: 1-PEO, in a mass ratio of 1: 40: 6.7.

The mixture becomes a gel upon strong stirring (1500 r.p.m.) under ambient conditions overnight. The doctor-blading was performed using a rectangular stamp of a thickness of 50 µm that was placed onto the support. They can also be applied onto 3D substrates by introducing them into the gels. After that, the films were introduced into a vacuum station under 1-10 mbar for less than 1 hour. The final materials are best described as rubber-like materials, which are easily peeled off from the substrate with tweezers and can be transferred to another substrate. The thickness of these rubber-like materials can be controlled either by the thickness of the stamp or by the subsequent deposition of one layer on top of another with an excellent adhesion.

The resulting rubber materials will be referred as **OC**-rubbers, for the complex coatings, and **NP**-rubbers, for the emitting silica nanoparticles coatings.

xv. Fabrication of the HLEDs

The preparation of the Hybrid Light Emitting Diodes (HLEDs) was also performed by the group of Dr. Rubén D. Costa and is based on a two-step procedure. The gels are firstly deposited onto a commercial UV-LED with a 400 nm emitting chip (WINGER WEPUV3-S2 UV Power LED Star, Black-light, 1.2 W), wetting the whole surface. After that, the coated LED is transferred to the vacuum chamber under 1-10 mbar for less than 1 hour. This procedure is repeated to enhance the light down-conversion efficiency of the HLED. The optimized thickness of the coating is 1-1.5 mm, approximately.

The HLEDs were characterized using a Keithley 2400 as a current source, while the luminous efficiency and changes of the electroluminescence spectrum were monitored by using Avantes spectrophotometer (Avaspec-ULS2048L-USB2) in conjunction with an integrating sphere (Avasphere 30-Irrad). At the applied driving conditions, the top temperature of the LED did not significantly change from room temperature values over time.

FIGURES OF MERIT

When preparing a new lighting device, different parameters must be examined.

- The device efficiency is one of the most important criteria when assessing a new lighting technology. It describes the performance of the light source and is commonly measured in lumens per watt (lm/W).
- The light emitted by the device will be only perceived as white light by the human eye if its spectrum matches with that observed for an incandescent blackbody with a temperature

between 2500 and 6500 K. This parameter is called correlated color temperature (CCT). For instance, the CCT value of the sunlight is 5800 K.

- A different way to describe the emission color is using the CIE color coordinates (Commission Internationale de l'Eclairage) criteria.

This parameter details, using a pair of numbers, how the human eye perceives the emission color of the light source, and it is commonly plotted in the so-called CIE diagram (figure 5.4).

The CIE coordinates for a white light emission should be closed to 0.33, 0.33.

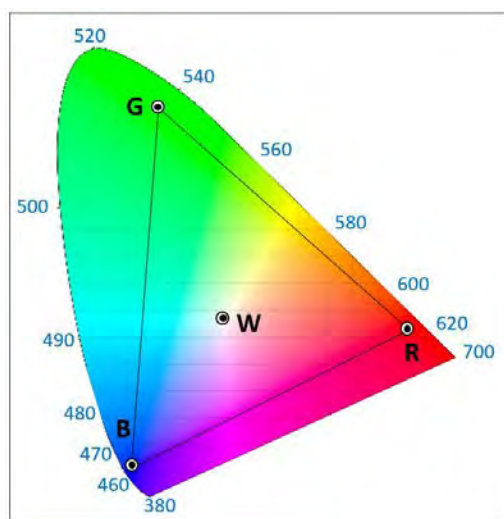


**Figure 5.4.** CIE diagram showing the coordinates of a blue (B), green (G), red (R) and white (W) light emission.

- As a source of white light, an ideal device should emit a continuous spectrum covering the entire visible range (400-800 nm). Thus, the color of any object illuminated by the source is sampled properly. This behavior is usually controlled by the so-called color rendering index (CRI), which consists of a number between 0 and 100, being its value above 80 for indoor-lighting applications. In general, 100 represent the maximum color acquired under sunlight illumination and, therefore, the greater the CRI number, the better the color reproduction and the highest the quality of the light source.

#### xvi. *Biological assays*

Cell lines and culture conditions: A549 (tumor adenocarcinomic alveolar basal epithelial cells), HeLa (tumor epitheloid cervix carcinoma cells), and NL-20 (nontumor immortalized bronchial epithelial cells) human cell lines, in addition to immortalized mouse embryonic fibroblasts (3T3) obtained from lungs (LMEFs), were cultured following the American Type

Culture Collection ([www.atcc.org](http://www.atcc.org)) recommendations and standard methods, as previously described.<sup>61c, 65b</sup> A549 and HeLa cell lines were maintained in an RPMI 1640 medium supplemented with 10% fetal bovine serum (FBS). The NL-20 cell line was grown in Ham's F-12 medium supplemented with 1.5 g/L sodium bicarbonate, 2.7 g/L glucose, 2.0 mM L-glutamine, 0.1 mM nonessential amino acids, 0.005 mg/mL insulin, 10 ng/mL epidermal growth factor, 0.001 mg/mL transferrin, 500 ng/mL hydrocortisone, and 4% FBS. LMEF cells were maintained in DMEM (Dulbecco's Modified Eagle's Medium), supplemented with 10% fetal bovine serum (FBS) and 2.0 mM L-glutamine. Penicillin (100 U/mL) and streptomycin (100 µg/mL) were added to all media. Cultures were maintained under a humidified atmosphere of 95% air/5% CO<sub>2</sub> at 37 °C and subcultured before they became confluent using a 0.25% trypsin/EDTA solution.

Cytotoxicity assay: The 3-(4,5-dimethylthiazol-2-yl)-5-(3-carboxymethoxyphenyl)-2-(4-sulfophenyl)-2H-tetrazolium (MTS) hydrolysis method (MTS-based CellTiter 96, AQueous Assay; Promega Corp., Madison, WI) was used to determine the cell viability as an indicator of A549 and HeLa cell sensitivity to the complexes as previously reported.<sup>61c</sup> Each experiment was repeated three times. The IC<sub>50</sub> (drug concentration that produced 50% inhibition of cell proliferation) was calculated by plotting the percentage of growing inhibition versus log of the drug concentration.

SI: The SI was calculated according to the following equation: SI = IC<sub>50</sub> nontumor cell (NL-20)/IC<sub>50</sub> tumor cells (A549 or HeLa), as previously reported.<sup>190</sup> Nontumor NL-20 epithelial lung cells served as the selectivity reference to match the same tissue origin of A549 lung carcinoma (epithelial origin) cells, as suggested.<sup>191</sup>

Localization in cells by fluorescence microscopy: Cytolocalization of nanoparticles [7]-NP<sub>OH</sub>\_IS and [7]-NP<sub>Me</sub>\_IS, in A549 and HeLa living cells, was performed as previously described.<sup>61c</sup> Cells were cultured over 1-cm-diameter poly(L-lysine) (Sigma-Aldrich)-coated coverslips into a 24-well plate in 0.5 mL of a supplemented culture medium per well for 72 h. Then, 0.5 mL of a medium containing 100 µg/mL of each sample was incubated during 1 day (50 µg/mL final concentration). After that, 3.2 µM of Hoechst 33342 (Sigma-Aldrich) was added, and the cells were additionally incubated at 37 °C for 1 h. The medium was removed, and the cells were washed twice with a phosphate buffer saline (PBS, pH 7.2). As a control to discard emission bleeding between light channels, incubation of the cells was also performed separately with Hoechst alone. Coverslips were removed from the plates and mounted on glass slides before being immediately examined under a fluorescence microscope (Leica DM600B).

Localization in cells by confocal Microscopy: A549 and HeLa cells were cultured over 1-cm-diameter poly(L-lysine) (SigmaAldrich)-coated coverslips into a 24-well plate in 0.5 mL of a

supplemented culture medium per well for 48 h. Then, 0.5 mL of a medium containing complex **8** or the nanoparticles was added in order to achieve 16  $\mu$ M and 50  $\mu$ g/mL, respectively. Cells were incubated with these compounds at 37 °C during 1 y 24 h, respectively, the medium was removed, and the cells were washed twice with PBS (pH 7.2) and fixed in 4% paraformaldehyde in PBS. Finally, coverslips were placed on glass slides using a ProLong Gold Antifade Reagent (Molecular Probes) containing 4',6-diamidino-2-phenylindole (DAPI; Molecular Probes) for fixed cells. For analysis in living conditions, cells (A549 and LMEFs) were grown in 35 mm dishes with 14 mm diameter glass coverslips coated with poly-D-Lysine attached at the bottom (MatTek Corp., Ashland, MA) using appropriate media. To asses subcellular localization of complex **8**, cells were incubated with new medium containing 16  $\mu$ M of complex **8** in combination with 3.2  $\mu$ M of Hoechst 33342 (nuclear/DNA stain), and/or Lysotracker®Red DND-99 (Cat. no. L7528, Molecular Probes Inc; Eugene, OR) (lysosome counterstain) or Mitotracker® Deep Red FM (Cat. No. M22426, Molecular Probes Inc) (mitochondria counterstain) during 1 h. Samples were examined and documented using a confocal microscope (Leica SP5).

### Synthesis of starting materials

All starting materials and some of the ligands were prepared following the procedures previously reported on the literature.

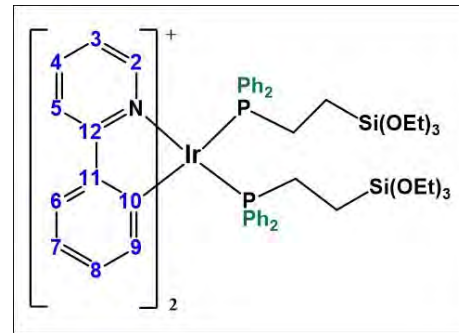
- $[\text{Ir}(\text{ppy})_2(\mu\text{-Cl})]_2^{192}$
- $[\text{Ir}(\text{ppy})_2(\text{MeCN})_2]\text{OTf}^{57}$
- $[\text{Ir}(\text{dFppy})_2(\mu\text{-Cl})]_2^{193}$
- $[\text{Ir}(\text{dFppy})_2(\text{MeCN})_2]\text{PF}_6^{194}$
- $[\text{Pt}(\text{bzq})(\text{C}_6\text{F}_5)(\text{acetone})]^{54e}$
- $[\text{Pt}(\text{bzq})(\text{MeCN})_2]\text{PF}_6^{58}$
- $4,4'[\text{CONH}(\text{CH}_2)_3\text{Si}(\text{OCH}_2\text{CH}_3)_3]_2\text{-bipyridine}^{195}$  (*dasipy*, **L1**)
- $4,4'[\text{CONH}(\text{CH}_2)_3\text{CH}_3]_2\text{-bipyridine}^{91}$  (*dbbpy*, **L2**)
- $[\text{Ir}(\text{ppy})_2(4,4'\text{-H}_2\text{dcipy})]\text{PF}_6^{164}$  (**9'**)
- $[\text{Ru}(4,4'\text{-H}_2\text{dcipy})_2(\text{SCN})_2]^{165}$  (**10**)
- $[\text{Ir}(\text{ppy})_2(4,4'\text{-dmbpy})]\text{PF}_6^{196}$

## Synthesis of new iridium(III) and platinum(II) complexes

All reactions were carried out under an atmosphere of dry argon, using standard Schlenk techniques. Solvents were obtained from a solvent purification system (M-BRAUN MB SPS-800).

### Synthesis of $[\text{Ir}(\text{ppy})_2(\text{PPETS})_2]\text{OTf}$ (**1**, **G**)

A yellow solution of 0.15 g (0.21 mmol) of the precursor  $[\text{Ir}(\text{ppy})_2(\text{MeCN})_2]\text{OTf}$  in 15 mL of anhydrous  $\text{CH}_2\text{Cl}_2$  was treated with 147  $\mu\text{L}$  (0.42 mmol) of PPETS (PPETS:  $\text{PPh}_2(\text{CH}_2)_2\text{Si}(\text{OCH}_2\text{CH}_3)_3$ ). The mixture was then stirred for 1.5 hours and the resulting solution was evaporated to dryness. Treatment of the solid residue with diethyl ether yielded complex **1** as a yellow solid (0.29 g, 55%).



In *Chapter II*, complex **1** will be referred as **G** for a better understanding.

**Elemental Analysis:** calculated for  $\text{C}_{63}\text{H}_{74}\text{F}_3\text{IrN}_2\text{O}_9\text{P}_2\text{SSi}_2$ : C, 53.95; H, 5.32; N, 2.00; S, 2.29.

Found: C, 53.87; H, 5.29; N, 2.05; S, 1.88.

**ESI (+):**  $m/z$  1253 [M]<sup>+</sup> (100%); 877 [M-PPETS]<sup>+</sup> (11%).

**IR (KBr, cm<sup>-1</sup>):**  $\nu(\text{C-H})$  3050 (s), 2970 (vs), 2924 (s), 2887 (s);  $\nu(\text{ring})$  1609 (vs), 1582 (s), 1479 (vs), 1383 (s);  $\nu(\text{P-C})$  1438 (vs);  $\nu(\text{C-H})+\nu(\text{ring})$  1270 (vs);  $\nu(\text{ring})$  1082 (vs);  $\nu(\text{Si-O-C})$  1095 (vs), 1074 (vs);  $\nu(\text{S-O})$  1418 (m), 1027 (vs).

**<sup>1</sup>H NMR (400 MHz, CDCl<sub>3</sub>, δ):** 8.64 (d,  $J_{\text{H-H}} = 5.8$ , 2H, H<sup>2</sup>); 7.74 (t,  $J_{\text{H-H}} = 7.9$ , 2H, H<sup>4</sup>); 7.61 (d,  $J_{\text{H-H}} = 8.3$ , 2H, H<sup>5</sup>); 7.46 (d,  $J_{\text{H-H}} = 8.1$ , 2H, H<sup>6</sup>); 7.41 (t,  $J_{\text{H-H}} = 8.0$ , 4H, Ph); 7.32 (t,  $J_{\text{H-H}} = 7.1$ , 2H, Ph); 7.25 (t,  $J_{\text{H-H}} = 8.1$ , 2H, Ph); 7.13 (t,  $J_{\text{H-H}} = 7.4$ , 4H, Ph); 7.04 (t,  $J_{\text{H-H}} = 7.5$ , 4H, Ph); 6.98 (t,  $J_{\text{H-H}} = 7.5$ , 2H, H<sup>7</sup>); 6.83 (t,  $J_{\text{H-H}} = 7.4$ , 2H, H<sup>3</sup>); 6.79 (t,  $J_{\text{H-H}} = 7.4$ , 2H, H<sup>8</sup>); 6.60 (t,  $J_{\text{H-H}} = 7.5$ , 4H, Ph); 5.81 (d,  $J_{\text{H-H}} = 7.8$ , 2H, H<sup>9</sup>); 3.55 (q,  $J_{\text{H-H}} = 7.0$ , 12H, OCH<sub>2</sub>CH<sub>3</sub>); 2.17 (pst,  $J_{\text{H-H}} = 12.4$ , 2H, PCH<sub>2</sub>CH<sub>2</sub>-Si); 1.86 (pst,  $J_{\text{H-H}} = 12.6$ , 2H, PCH<sub>2</sub>CH<sub>2</sub>-Si); 1.03 (t,  $J_{\text{H-H}} = 6.9$ , 18H, OCH<sub>2</sub>CH<sub>3</sub>); 0.21 (m, 2H, PCH<sub>2</sub>CH<sub>2</sub>-Si); 0.07 (m, 2H, PCH<sub>2</sub>CH<sub>2</sub>-Si).

**<sup>13</sup>C{<sup>1</sup>H} NMR (100.6 MHz, CDCl<sub>3</sub>, δ):** 167.8 (t,  ${}^1J_{\text{N-C}} = 2.7$ , C<sup>12</sup>); 154.6 (s ancho,  ${}^1J_{\text{N-C}} = 2.7$ , C<sup>2</sup>); 153.7 (AXX',  ${}^2J_{\text{P-C}} = 11.9$ , C<sup>10</sup>); 143.6 (s, C<sup>11</sup>); 138.2 (s, C<sup>4</sup>); 134.8 (t,  ${}^2J_{\text{P-C}} = 5.9$ , o-Ph); 131.8 (t,  ${}^2J_{\text{P-C}} = 3.3$ , o-Ph); 131.5 (s, C<sup>9</sup>); 131.3 (s, p-Ph); 130.5 (s, C<sup>8</sup>); 129.9 (s, p-Ph); 128.2 (t,  ${}^3J_{\text{P-C}} = 3.8$ , m-Ph); 128.0

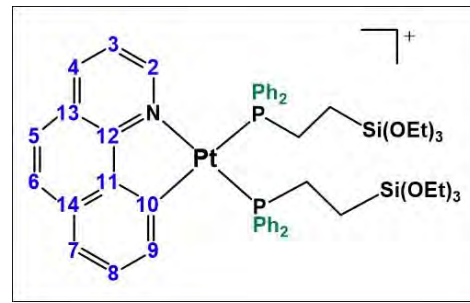
(t,  $^3J_{P-C} = 4.6$ , m-Ph); 126.6 (AXX',  $^{1+3}J_{P-C} = 33.0$ , *ipso*-C); 126.0 (AXX',  $^{1+3}J_{P-C} = 42.0$ , *ipso*-C); 125.0 (s, C<sup>6</sup>); 123.7 (s, C<sup>7</sup>); 123.1 (s, C<sup>3</sup>); 120.9 (s, C<sup>5</sup>); 58.3 (s, OCH<sub>2</sub>CH<sub>3</sub>); 19.1 (AXX',  $^{1+3}J_{P-C} = 26.0$ , PCH<sub>2</sub>CH<sub>2</sub>-Si); 18.2 (s, -OCH<sub>2</sub>CH<sub>3</sub>); 4.69 (s, PCH<sub>2</sub>CH<sub>2</sub>Si).

**$^{31}P\{^1H\}$  NMR (162.1 MHz, CDCl<sub>3</sub>,  $\delta$ ):** -6.5 (s).

**$^{19}F\{^1H\}$  NMR (376.5 MHz, CDCl<sub>3</sub>,  $\delta$ ):** -78.0 (s).

### Synthesis of $[\text{Pt}(\text{bzq})(\text{PPETS})_2]\text{PF}_6$ (2)

A red solution of 0.38 g (0.63 mmol) of  $[\text{Pt}(\text{bzq})(\text{MeCN})_2]\text{PF}_6$  in 15 mL of anhydrous  $\text{CH}_2\text{Cl}_2$  was treated with 500  $\mu\text{L}$  (1.25 mmol) of PPETS and stirred for 10 minutes. The resulting yellow solution was evaporated to dryness and the yellow solid was treated with hexane (0.59 g, 74%).



**Elemental Analysis:** calculated for  $C_{53}\text{H}_{66}\text{F}_6\text{PtNO}_6\text{P}_3\text{Si}_2$ : C, 50.07; H, 5.23; N, 1.10.

Found: C, 50.42; H, 5.17; N, 1.40.

**ESI (+):**  $m/z$  1126 [M]<sup>+</sup> (100 %).

**IR (KBr, cm<sup>-1</sup>):**  $\nu(\text{C-H})$  3050 (w), 2969 (s), 2923 (m), 2892 (m), 2848 (m); 1626 (w); 1570 (w);  $\nu(\text{ring})$  1481 (m), 1437 (s), 1408 (m); 1385 (m); 1328 (w); 1264 (w); 1168 (s);  $\nu(\text{Si-O-C})$  1095 (vs), 1074 (vs); 960 (m);  $\nu(\text{P-F})$  840 (vs);  $\nu(\text{Pt-N})$  557 (s).

**<sup>1</sup>H NMR (400 MHz, CDCl<sub>3</sub>, δ):** 8.43 (d,  $J_{\text{H-H}} = 8.0$ , 1H, H<sup>2</sup>); 8.36 (d,  $J_{\text{H-H}} = 4.6$ , 1H, H<sup>4</sup>); 7.87 (d,  $J_{\text{H-H}} = 8.6$ , 1H, H<sup>5</sup>); 7.71 (m, 1H<sup>6</sup>, 1H<sup>7</sup> or H<sup>8</sup> and 4H Ph); 7.64 (pst, 4H, Ph); 7.53 (m, 4H, Ph); 7.42 (pst, 4H, Ph); 7.33 (m broad, 1H<sup>7</sup> or H<sup>8</sup> and 4H Ph); 7.27 (m, 1H, H<sup>9</sup>); 7.17 (t,  $J_{\text{H-H}} = 6.7$ , 1H, H<sup>3</sup>); 3.48 (q,  $J_{\text{H-H}} = 7.0$ , 12H, OCH<sub>2</sub>CH<sub>3</sub>); 2.65 (m broad, 2H, PCH<sub>2</sub>CH<sub>2</sub>-Si); 1.58 (m broad, 2H, PCH<sub>2</sub>CH<sub>2</sub>-Si); 0.99 (t,  $J_{\text{H-H}} = 6.9$ , 18H, OCH<sub>2</sub>CH<sub>3</sub>); 0.87 (m broad, 2H, PCH<sub>2</sub>CH<sub>2</sub>-Si); 0.42 (psc,  $J_{\text{H-H}} = 9.1$ , 2H, PCH<sub>2</sub>CH<sub>2</sub>-Si).

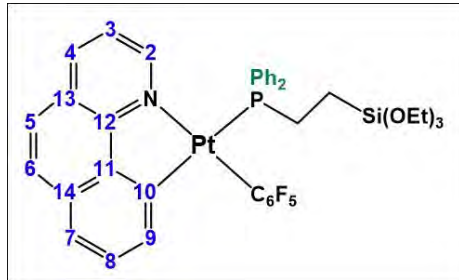
**<sup>13</sup>C{<sup>1</sup>H} NMR (100.6 MHz, CDCl<sub>3</sub>, δ):** 156.3 (s, C<sup>12</sup>); 151.4 (s, C<sup>4</sup>); 143.0 (s, tentatively assigned to C<sup>10</sup>); 140.3 (s broad, C<sup>2</sup>); 135.2 (s, C<sup>9</sup>); 134.4 (m, Ph); 133.8 (d,  $J_{\text{P-C}} = 10.2$ , Ph); 132.4 (s, tentatively assigned to C<sup>14</sup>); 132.2 (s, Ph); 130.4 (s, C<sup>5</sup>); 129.7 (d,  $J_{\text{P-C}} = 9.7$ , Ph); 129.4 (s, C<sup>7</sup> or C<sup>8</sup>); 129.0 (s broad, Ph); 128.6 (s broad, tentatively assigned to C<sup>11</sup>); 128.0 (s, C<sup>13</sup>); 125.2 (s, C<sup>7</sup> or C<sup>8</sup>); 124.3 (s, C<sup>6</sup>); 122.4 (s, C<sup>3</sup>); 58.6 (s, OCH<sub>2</sub>CH<sub>3</sub>); 26.9 (m, PCH<sub>2</sub>CH<sub>2</sub>-Si); 22.0 (m, PCH<sub>2</sub>CH<sub>2</sub>-Si); 18.3 (s, OCH<sub>2</sub>CH<sub>3</sub>); 6.9 (m, PCH<sub>2</sub>CH<sub>2</sub>-Si); 6.3 (m, PCH<sub>2</sub>CH<sub>2</sub>-Si).

**<sup>31</sup>P{<sup>1</sup>H} NMR (162.1 MHz, CDCl<sub>3</sub>, δ):** 23.6 (d,  $^2J_{\text{P-P}} = 17.5$ ,  $^1J_{\text{Pt-P}} = 1950$  Hz, P *trans* to C); 16.7 (d,  $^2J_{\text{P-P}} = 19.0$ ,  $^1J_{\text{Pt-P}} = 3950$  Hz, P *trans* to N); -144.1 (sp,  $^1J_{\text{F-P}} = 723$ ).

**<sup>19</sup>F{<sup>1</sup>H} NMR (376.5 MHz, CDCl<sub>3</sub>, δ):** -74.7 (d,  $^1J_{\text{P-F}} = 719$ ).

**Synthesis of [Pt(bzq)(C<sub>6</sub>F<sub>5</sub>)(PPETS)] (3)**

The addition of 0.22 mL (0.60 mmol) of PPETS to a solution of 0.33 g (0.54 mmol) of the precursor [Pt(bzq)(C<sub>6</sub>F<sub>5</sub>)(acetone)] in 20 mL of anhydrous CH<sub>2</sub>Cl<sub>2</sub> yielded a yellow solution, which was stirred at room temperature for 15 minutes. The mixture was then evaporated to dryness and the residue was treated with hexane, affording complex **3** as a yellow solid (0.32 g, 65%).



**Elemental Analysis (%):** calculated for C<sub>39</sub>H<sub>37</sub>F<sub>5</sub>NO<sub>3</sub>PPtSi: C, 51.09; H, 4.07; N, 1.53.

Found: C, 50.64; H, 3.99; N, 1.66.

**ESI (+):** <sup>m/z</sup> 917 [M+ H]<sup>+</sup> (100%).

**IR (KBr, cm<sup>-1</sup>):**  $\nu$ (C-H) 3042 (m), 2970 (s), 2924 (s), 2885 (s), 2848 (m);  $\nu$ (ring) 1501 (vs), 1456 (s), 1436 (s), 1402 (w), 1264 (w), 1163 (s);  $\nu$ (Si-O-C) 1100 (vs), 1078 (vs); 1061 (s); 953 (vs); 828 (s);  $\nu$ (C<sub>6</sub>F<sub>5</sub>)<sub>x-sens</sub> 800 (m).

**<sup>1</sup>H NMR (400 MHz, CDCl<sub>3</sub>, δ):** 8.34 (d,  $J_{H-H}$  = 4.9, H<sup>2</sup>); 8.22 (d,  $J_{H-H}$  = 7.8, H<sup>4</sup>); 7.87 (m, Ph, 4H); 7.78 (d,  $J_{H-H}$  = 8.0, H<sup>5</sup> or H<sup>6</sup>); 7.61 (d,  $J_{H-H}$  = 7.8, H<sup>7</sup>); 7.51 (d,  $J_{H-H}$  = 8.0, H<sup>5</sup> or H<sup>6</sup>); 7.45 (t,  $J_{H-H}$  = 7.7, H<sup>8</sup>); 7.41 (m, Ph, 6H); 7.01 (m, H<sup>3</sup>, H<sup>9</sup>); 3.68 (q,  $J_{H-H}$  = 7.0 Hz, 6H, OCH<sub>2</sub>CH<sub>3</sub>); 2.34 (m, 2H, PCH<sub>2</sub>CH<sub>2</sub>-Si); 1.14 (t,  $J_{H-H}$  = 7.0, 9H, OCH<sub>2</sub>CH<sub>3</sub>); 0.60 (m, 2H, PCH<sub>2</sub>CH<sub>2</sub>-Si).

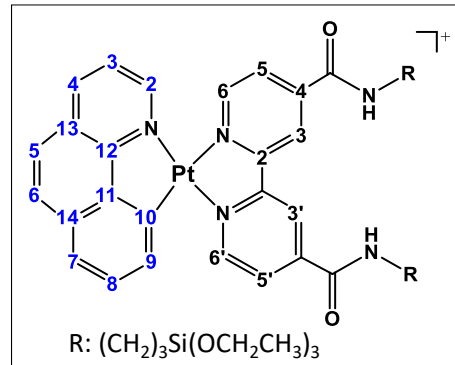
**<sup>13</sup>C{<sup>1</sup>H} NMR (100.6 MHz, CDCl<sub>3</sub>, δ):** 159.3 (s, bzq); 157.8 (s, bzq), 157.7 (d,  $^2J_{P-C}$  = 6.0, C<sup>10</sup>); 150.2 (d,  $^3J_{P-C}$  = 4.7,  $^2J_{P-C}$  = 17, C<sup>2</sup>); 147.0 (dm,  $J_{F-C}$  = 219, C<sub>6</sub>F<sub>5</sub>); 142.7 (s,  $J_{P-C}$  = 20, bzq); 137.6 (s, C<sup>4</sup>); 136.9 (dm,  $J_{F-C}$  = 253, C<sub>6</sub>F<sub>5</sub>); 134.1 (d,  $J_{P-C}$  = 4.5, bzq); 133.7 (d,  $^2J_{P-C}$  = 11.4, o-Ph); 131.6 (d,  $^2J_{P-C}$  = 40.1, ipso- Ph); 130.6 (d,  $^4J_{P-C}$  = 1.9, p-Ph); 130.1 (s, C<sup>5</sup> or C<sup>6</sup>); 128.6 (d,  $^3J_{P-C}$  = 9.5, m-Ph); 127.2 (s,  $^3J_{P-C}$  = 17, C<sup>8</sup>); 123.2 (s, C<sup>7</sup>); 122.9 (s, C<sup>5</sup> or C<sup>6</sup>); 121.2 (s,  $^3J_{P-C}$  = 22, C<sup>3</sup>); 58.5 (s, OCH<sub>2</sub>CH<sub>3</sub>); 22.0 (d,  $^1J_{P-C}$  = 22, PCH<sub>2</sub>CH<sub>2</sub>-Si); 18.1 (s, -OCH<sub>2</sub>CH<sub>3</sub>); 5.6 (d,  $^2J_{P-C}$  = 2.7, PCH<sub>2</sub>CH<sub>2</sub>Si).

**<sup>31</sup>P{<sup>1</sup>H} NMR (162.1 MHz, CDCl<sub>3</sub>, δ):** 22.15 (s,  $^1J_{P-P}$  = 1967 Hz).

**<sup>19</sup>F{<sup>1</sup>H} NMR (282.5 MHz, CDCl<sub>3</sub>, δ):** -116.4 (dd,  $^3J_{P-F}$  = 504 Hz, o-F, 2F); -163.7 (m, p-F, 1F), -164.1 (m, m-F, 2F).

### Synthesis of $[\text{Pt}(\text{bzq})(\text{dasipy})]\text{PF}_6$ (**4**)

Under extremely inert conditions, 0.14 g (0.21 mmol) of the *dasipy* ligand were added to a solution of 0.13 g (0.21 mmol) of the corresponding platinum precursor ( $[\text{Pt}(\text{bzq})(\text{MeCN})_2]\text{PF}_6$ ) in 15 mL of anhydrous  $\text{CH}_2\text{Cl}_2$ . After 10 minutes of stirring at room temperature, a clear red solution was observed. The subsequent solvent removal yielded complex **4** as a red powder, which was kept under argon atmosphere (0.24 g, 70%).



**Elemental Analysis (%):** calculated for  $\text{C}_{43}\text{H}_{58}\text{F}_6\text{PPtN}_5\text{O}_8\text{Si}_2$ : C, 44.17; H, 5.00; N, 5.99.

Found: C, 42.91; H, 4.92; N, 6.24.

**ESI (+):**  $m/z$  1024 [M]<sup>+</sup> (100%).

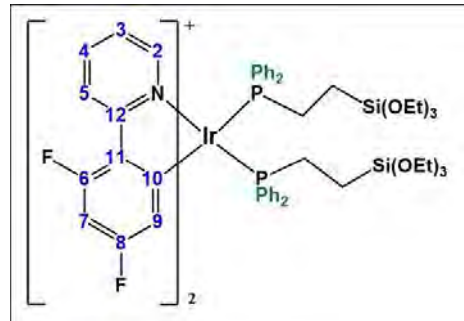
**IR (KBr, cm<sup>-1</sup>):**  $\nu(\text{N-H})$  3420 (s);  $\nu(\text{N-C})$  3272 (m);  $\nu(\text{C-H})$  3061 (s), 2961 (s), 2927 (m), 2872 (m);  $\nu(\text{ring})$  1535 (s), 1482 (m), 1454 (m), 1402 (m), 1305 (m), 1261 (m), 1200 (m);  $\nu(\text{C=O})$  1657 (s);  $\nu(\text{Si-O-C})$  1079 (s), 1040 (s);  $\nu(\text{P-F})$  833 (vs);  $\nu(\text{Pt-N})$  558 (s).

**<sup>1</sup>H NMR (400 MHz, CDCl<sub>3</sub>, δ):** 9.40 (d,  $J_{\text{H-H}} = 5.1$  Hz, 1H, H<sup>6</sup><sub>dasipy</sub>); 8.91 (d,  $J_{\text{H-H}} = 5.4$  Hz, 1H, H<sup>6'</sup><sub>dasipy</sub>); 8.79 (m, 1H, H<sup>2</sup><sub>bzq</sub>); 8.46 (m, 1H, H<sup>3'</sup><sub>dasipy</sub>); 8.39 (d,  $J_{\text{H-H}} = 7.2$  Hz, 2H, H<sup>3</sup><sub>dasipy</sub>, H<sup>4</sup><sub>bzq</sub>); 8.10 (d,  $J_{\text{H-H}} = 5.1$  Hz, 1H, H<sup>5'</sup><sub>dasipy</sub>); 7.95 (d,  $J_{\text{H-H}} = 5.6$  Hz, 1H, H<sup>5</sup><sub>dasipy</sub>); 7.82 (d,  $J_{\text{H-H}} = 8.2$  Hz, 1H, H<sup>5</sup><sub>bzq</sub>); 7.78 (d,  $J_{\text{H-H}} = 9.6$  Hz, 1H, H<sup>7</sup><sub>bzq</sub> or H<sup>9</sup><sub>bzq</sub>); 7.65 (m, 3H, H<sup>3</sup><sub>bzq</sub>, H<sup>6</sup><sub>bzq</sub>, H<sup>7</sup><sub>bzq</sub> or H<sup>9</sup><sub>bzq</sub>); 7.49 (t,  $J_{\text{H-H}} = 7.8$  Hz, 1H, H<sup>8</sup><sub>bzq</sub>); 7.33 (m broad, 1H, NH); 3.89 (m broad, 12H, OCH<sub>2</sub>CH<sub>3</sub>); 3.57 (m, 4H, CH<sub>2</sub>CH<sub>2</sub>CH<sub>2</sub>-Si); 1.90 (m, 4H, CH<sub>2</sub>CH<sub>2</sub>CH<sub>2</sub>-Si); 1.27 (m broad, 18H, OCH<sub>2</sub>CH<sub>3</sub>); 0.79 (m, 4H, CH<sub>2</sub>CH<sub>2</sub>CH<sub>2</sub>-Si).

**<sup>13</sup>C{<sup>1</sup>H} NMR (100.6 MHz, CDCl<sub>3</sub>, δ):** the poor stability of the complex in solution precludes its characterization by <sup>13</sup>C{<sup>1</sup>H} NMR.

**Synthesis of  $[\text{Ir}(\text{dFppy})_2(\text{PPETS})_2]\text{PF}_6$  (5, B)**

A yellow solution of 0.2 g (0.25 mmol) of  $[\text{Ir}(\text{dFppy})_2(\text{MeCN})_2]\text{PF}_6$  in 20 mL of  $\text{CH}_2\text{Cl}_2$  was treated with 312  $\mu\text{L}$  (0.87 mmol) of PPETS. The yellow mixture was stirred for 48h and the resulting solution was evaporated to dryness. The treatment of the residue with hexane yielded compound 5 as a pale-yellow solid (0.26 g, 71%).



In *Chapter II*, complex 5 will be referred as **B** for a better understanding.

**Elemental Analysis (%):** calculated for  $\text{C}_{62}\text{F}_{10}\text{H}_{70}\text{IrN}_2\text{O}_6\text{P}_3\text{Si}_2$ : C, 50.60; H, 4.79; N, 1.90.

Found: C, 50.64; H, 4.36; N, 1.74.

**ESI (+):**  $m/z$  1325 [ $\text{M}]^+$  (100%); 949 [ $\text{M-PPETS}]^+$  (13%).

**IR (KBr,  $\text{cm}^{-1}$ ):**  $\nu(\text{C-H})$  3069 (m), 2970 (s), 2925 (m), 2890 (m);  $\nu(\text{ring})$  1603 (vs), 1576(vs), 1480(vs);  $\nu(\text{P-C})$  1430 (vs);  $\nu(\text{ring})$  1405(vs);  $\nu(\text{C-F})$  1254 (s);  $\nu(\text{C-H})+\nu(\text{ring})$  1296(s); 1164(vs);  $\nu(\text{Si-O-C})$  1102 (vs), 1080 (vs);  $\nu(\text{P-F})$  842 (vs).

**$^1\text{H}$  NMR (400 MHz,  $\text{CDCl}_3$ ,  $\delta$ ):** 8.75 (d,  $J_{\text{H-H}} = 6.2$  Hz, 2H,  $\text{H}^2$ ); 7.94 (d,  $J_{\text{H-H}} = 8.1$  Hz, 2H,  $\text{H}^5$ ); 7.76 (t,  $J_{\text{H-H}} = 7.9$  Hz, 2H,  $\text{H}^4$ ); 7.38-7.28 (m, 8H, o-Ph); 7.14 (psc,  $J_{\text{H-H}} = 8.3$  Hz, 8H, m-Ph); 7.0 (t,  $J_{\text{H-H}} = 6.6$  Hz, 2H,  $\text{H}^3$ ); 6.70 (t,  $J_{\text{H-H}} = 8.3$  Hz, 4H, p-Ph); 6.51 (pst,  $J_{\text{H-H}} = 10.3$  Hz, 2H,  $\text{H}^7$ ); 5.20 (d,  $J_{\text{H-H}} = 9.3$  Hz, 2H,  $\text{H}^9$ ); 3.58 (c,  $J_{\text{H-H}} = 6.7$  Hz, 12H,  $\text{OCH}_2\text{CH}_3$ ); 2.11 (m, 2H,  $\text{PCH}_2\text{CH}_2\text{Si}$ ); 1.88 (m, 2H,  $\text{PCH}_2\text{CH}_2\text{Si}$ ); 1.05 (t,  $J_{\text{H-H}} = 6.9$  Hz, 18H,  $\text{OCH}_2\text{CH}_3$ ); 0.21 (m, 2H,  $\text{PCH}_2\text{CH}_2\text{Si}$ ); 0.05 (m, 2H,  $\text{PCH}_2\text{CH}_2\text{Si}$ ).

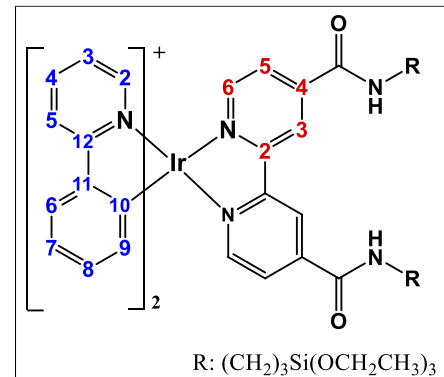
**$^{13}\text{C}\{^1\text{H}\}$  NMR (100.6 MHz,  $\text{CDCl}_3$ ,  $\delta$ ):** 164.2 (s,  $\text{C}^{12}$ ); 161.7 (s broad,  $\text{C}^8$ ); 159.9 (s broad,  $\text{C}^6$ ); 155.0 (s,  $\text{C}^2$ ); 139.2 (s,  $\text{C}^4$ ); 134.3 (t,  ${}^2J_{\text{P-C}} = 5.3$  Hz, o-Ph); 131.8 (t,  ${}^2J_{\text{P-C}} = 3.5$  Hz, o-Ph); 131.5 (s, p-Ph); 130.4 (s, p-Ph); 128.8-128.4 (m broad, m-Ph and probably ipso-C); 127.9 (s,  $\text{C}^{11}$ ); ~125 (ipso-C); 123.8 (s,  $\text{C}^5$ ); 122.5 (s,  $\text{C}^3$ ); 113.7 (d,  ${}^2J_{\text{F-C}} = 18.5$  Hz,  $\text{C}^9$ ); 100.0 (pst,  ${}^{2+2}J_{\text{F-C}} = 26.8$  Hz,  $\text{C}^7$ ); 58.4 (s,  $\text{OCH}_2\text{CH}_3$ ); 19.3 (m,  $\text{PCH}_2\text{CH}_2\text{Si}$ ); 18.3 (m,  $\text{PCH}_2\text{CH}_2\text{Si}$ ); 17.7 (s,  $\text{OCH}_2\text{CH}_3$ ); 4.6 (m,  $\text{PCH}_2\text{CH}_2\text{Si}$ ).

**$^{19}\text{F}\{^1\text{H}\}$  NMR (376.5 MHz,  $\text{CDCl}_3$ ,  $\delta$ ):** -73.2 (d,  $J_{\text{P-F}} = 712$  Hz,  $\text{PF}_6^-$ ); -104.5 (d,  $J = 9.4$  Hz,  $\text{F}^6$ ); -107.7 (d,  $J = 8.8$  Hz,  $\text{F}^8$ ).

**$^{31}\text{P}\{^1\text{H}\}$  NMR (162.1 MHz,  $\text{CDCl}_3$ ,  $\delta$ ):** -144.4 (sp,  $J_{\text{P-F}} = 712$  Hz,  $\text{PF}_6^-$ ); -8.89 (s,  $\text{PPh}_2$ ).

### Synthesis of $[\text{Ir}(\text{ppy})_2(\text{dasipy})]\text{OTf}$ (6, R)

The addition of 0.18 g (0.27 mmol) of *dasipy* to a yellow solution of 0.20 g (0.27 mmol) of  $[\text{Ir}(\text{ppy})_2(\text{CH}_3\text{CN})_2]\text{OTf}$  in 30 mL of dichloromethane gave a red solution, which was stirred for 2 hours at room temperature. The mixture was then evaporated to dryness. The final solid (6) was kept under argon atmosphere to avoid its auto-condensation through the trialkoxysilane groups (0.27 g, 77%).



In *Chapter II*, complex 6 will be referred as R for a better understanding.

**Elemental Analysis (%):** calculated for  $\text{C}_{53}\text{F}_3\text{H}_{66}\text{IrN}_6\text{O}_{11}\text{SSi}_2$ : C, 48.91; H, 5.12; N, 6.46; S, 2.46.

Found: C, 48.88; H, 4.66; N, 7.28; S, 3.94.

**ESI (+):**  $m/z$  1151 [M]<sup>+</sup> (100%).

**IR (KBr, cm<sup>-1</sup>):**  $\nu(\text{N-H})$  3315 (m);  $\nu(\text{C-H})$  3062 (m), 2974 (m), 2924 (m), 2874 (m);  $\nu(\text{C=O})$  1669 (vs);  $\nu(\text{ring})$  1608 (s), 1583 (s), 1550 (vs), 1479 (vs), 1439 (m), 1419 (m);  $\nu(\text{Si-O-C})$  1164 (vs), 1069 (vs);  $\nu(\text{S-O})$  1403 (m), 1031 (vs).

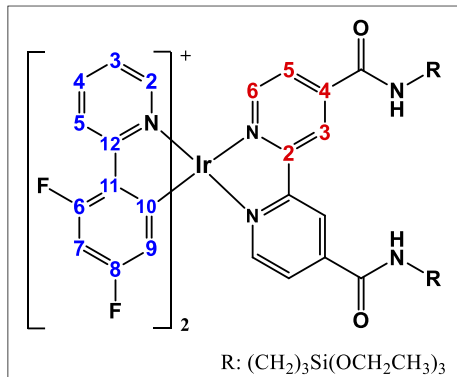
**<sup>1</sup>H NMR (400 MHz, CDCl<sub>3</sub>, δ):** 9.11 (s broad, 2H, H<sup>3</sup><sub>dasipy</sub>); 8.69 (s broad, 2H, NH); 8.04 (d,  $J_{\text{H-H}} = 5.6$  Hz, 2H, H<sup>6</sup><sub>dasipy</sub> or H<sup>5</sup><sub>dasipy</sub>); 7.94 (m, 4H, 2H<sup>2</sup>, 2H<sup>6</sup><sub>dasipy</sub> or 2H<sup>5</sup><sub>dasipy</sub>); 7.78 (t,  $J_{\text{H-H}} = 7.6$  Hz, 2H, H<sup>3</sup><sub>ppy</sub>); 7.70 (d,  $J_{\text{H-H}} = 7.7$  Hz, 2H, H<sup>6</sup><sub>ppy</sub>); 7.46 (d,  $J_{\text{H-H}} = 5.6$  Hz, 2H, H<sup>5</sup><sub>ppy</sub>); 7.07 (t,  $J_{\text{H-H}} = 7.4$  Hz, 2H, H<sup>7</sup><sub>ppy</sub>), 7.00 (t,  $J_{\text{H-H}} = 6.5$  Hz, 2H, H<sup>4</sup><sub>ppy</sub>); 6.94 (t,  $J_{\text{H-H}} = 7.3$  Hz, 2H, H<sup>8</sup><sub>ppy</sub>); 6.28 (d,  $J_{\text{H-H}} = 7.5$  Hz, 2H, H<sup>9</sup><sub>ppy</sub>); 3.81 (c,  $J_{\text{H-H}} = 7.0$  Hz, 12H, OCH<sub>2</sub>CH<sub>3</sub>); 3.47 (m, 4H, CH<sub>2</sub>CH<sub>2</sub>CH<sub>2</sub>Si); 1.79 (m, 4H, CH<sub>2</sub>CH<sub>2</sub>CH<sub>2</sub>Si); 1.21 (t,  $J_{\text{H-H}} = 7.0$  Hz, 18H, OCH<sub>2</sub>CH<sub>3</sub>); 0.70 (t,  $J_{\text{H-H}} = 8.4$  Hz, 4H, CH<sub>2</sub>CH<sub>2</sub>CH<sub>2</sub>Si).

**<sup>13</sup>C{<sup>1</sup>H} NMR (100.6 MHz, CDCl<sub>3</sub>, δ):** 167.9 (s, C<sup>12</sup><sub>ppy</sub>); 163.7 (s, CO); 156.0 (s, C<sup>4</sup><sub>dasipy</sub> or C<sup>2</sup><sub>dasipy</sub>); 151.0 (s, C<sup>6</sup><sub>dasipy</sub> or C<sup>5</sup><sub>dasipy</sub>); 149.9 (s, C<sup>10</sup><sub>ppy</sub>); 148.5 (s, C<sup>5</sup><sub>ppy</sub>); 146.0 (s, C<sup>4</sup><sub>dasipy</sub> or C<sup>2</sup><sub>dasipy</sub>); 143.4 (s, C<sup>11</sup><sub>ppy</sub>); 138.4 (s, C<sup>3</sup><sub>ppy</sub>); 131.8 (s, C<sup>9</sup><sub>ppy</sub>); 131.2 (s, C<sup>8</sup><sub>ppy</sub>); 128.0 (s, C<sup>6</sup><sub>dasipy</sub> or C<sup>5</sup><sub>dasipy</sub>); 125.1 (s, C<sup>6</sup><sub>ppy</sub>); 123.5 (s, C<sup>4</sup><sub>ppy</sub>); 123.1 (s, C<sup>7</sup><sub>ppy</sub>); 122.4 (s, C<sup>3</sup><sub>dasipy</sub>); 119.9 (s, C<sup>2</sup><sub>ppy</sub>); 58.5 (s, OCH<sub>2</sub>CH<sub>3</sub>); 43.5 (s, CH<sub>2</sub>CH<sub>2</sub>CH<sub>2</sub>Si); 22.7 (s, CH<sub>2</sub>CH<sub>2</sub>CH<sub>2</sub>Si); 18.4 (s, OCH<sub>2</sub>CH<sub>3</sub>); 8.0 (s, CH<sub>2</sub>CH<sub>2</sub>CH<sub>2</sub>Si).

**<sup>19</sup>F{<sup>1</sup>H} NMR (376.5 MHz, CDCl<sub>3</sub>, δ):** -78.0 (s).

**Synthesis of  $[\text{Ir}(\text{dFppy})_2(\text{dasipy})]\text{PF}_6$  (7)**

The addition of 0.16 g (0.25 mmol) of *dasipy* in a solution of 0.20 g (0.25 mmol) of  $[\text{Ir}(\text{dFppy})_2(\text{CH}_3\text{CN})_2]\text{PF}_6$  in 30 mL of dry  $\text{CH}_2\text{Cl}_2$  resulted on a yellow mixture that was stirred for 6 hours at room temperature. The resulting solution was evaporated to dryness and the yellow powdery solid was kept under inert conditions to avoid the condensation of the solid (0.27 g, 81%).



**Elemental Analysis (%):** calculated for  $\text{C}_{52}\text{F}_{10}\text{H}_{62}\text{IrN}_6\text{O}_8\text{PSi}_2$ : C, 47.59; H, 4.76; N, 6.40.

Best analyses found: C, 43.06; H, 4.89; N, 6.14 (fits well for **7**·2 $\text{CH}_2\text{Cl}_2$ ).

**ESI (+):**  $m/z$  1223 [M]<sup>+</sup> (100%); 1195 [M-Et + H] (23%).

**IR (KBr, cm<sup>-1</sup>):**  $\nu(\text{N-H})$  3327 (vs);  $\nu(\text{C-H})$  3270 (s), 3070 (s), 2959 (vs), 2930 (vs), 2875 (m);  $\nu(\text{C=O})$  1670 (s);  $\nu(\text{C-H ring})$  1604 (vs), 1558 (vs), 1479 (s), 1430 (s), 1405 (vs);  $\nu(\text{C-F})$  1261 (s);  $\nu(\text{Si-O-C})$  1163 (s), 1074 (vs);  $\nu(\text{P-F})$  840 (vs).

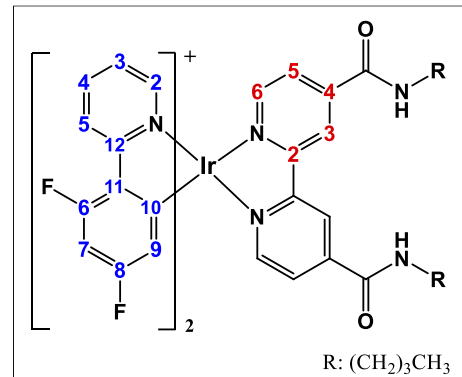
**<sup>1</sup>H NMR (400 MHz, CDCl<sub>3</sub>, δ):** 8.91 (s, 2H, H<sup>3</sup><sub>dFppy</sub>); 8.68 (s broad, NH); 8.34 (d,  $J_{\text{H-H}} = 8.7$  Hz, 2H, H<sup>2</sup><sub>dFppy</sub>); 8.05 (d,  $J_{\text{H-H}} = 5.5$  Hz, 2H, H<sup>6</sup><sub>bpy</sub> or H<sup>5</sup><sub>bpy</sub>); 7.97 (d,  $J_{\text{H-H}} = 5.3$  Hz, 2H, H<sup>6</sup><sub>bpy</sub> or H<sup>5</sup><sub>bpy</sub>); 7.83 (pst,  $J_{\text{H-H}} = 6.6$  Hz, 2H, H<sup>3</sup><sub>dFppy</sub>); 7.45 (d,  $J_{\text{H-H}} = 5.5$  Hz, 2H, H<sup>5</sup><sub>dFppy</sub>); 7.08 (pst,  $J_{\text{H-H}} = 6.2$  Hz, 2H, H<sup>4</sup><sub>dFppy</sub>); 6.60 (pst,  $^3J_{\text{F-H}} \approx 10$  Hz, 2H, H<sup>7</sup><sub>dFppy</sub>); 5.67 (dd,  $^3J_{\text{F-H}} \approx 8$  Hz,  $J_{\text{H-H}} = 2$  Hz, 2H, H<sup>9</sup><sub>dFppy</sub>); 3.82 (c,  $J_{\text{H-H}} = 7.3$  Hz, 12H, O-CH<sub>2</sub>CH<sub>3</sub>); 3.52 (m, 4H, CH<sub>2</sub>-CH<sub>2</sub>-CH<sub>2</sub>-Si); 1.81 (m, 4H, CH<sub>2</sub>CH<sub>2</sub>CH<sub>2</sub>-Si); 1.20 (t,  $J_{\text{H-H}} = 7.0$  Hz, 18H O-CH<sub>2</sub>CH<sub>3</sub>); 0.72 (m, 4H, CH<sub>2</sub>CH<sub>2</sub>CH<sub>2</sub>-Si).

**<sup>13</sup>C{<sup>1</sup>H} NMR (100.6 MHz, CDCl<sub>3</sub>, δ):** 165.5 (s, C<sup>10</sup><sub>dFppy</sub>); 164.3 (s, C<sup>12</sup><sub>dFppy</sub>); 164.1 (d,  $J_{\text{F-C}} = 230$  Hz, C<sup>8</sup><sub>dFppy</sub>); 163.5 (s, CO); 161.5 (d,  $J_{\text{F-C}} = 233$  Hz, C<sup>6</sup><sub>dFppy</sub>); 155.8 (s, C<sup>4</sup><sub>bpy</sub> or C<sup>2</sup><sub>bpy</sub>); 150.8 (s, C<sup>6</sup><sub>bpy</sub> or C<sup>5</sup><sub>bpy</sub>); 148.6 (s, C<sup>5</sup><sub>dFppy</sub>); 146.5 (s, C<sup>4</sup><sub>bpy</sub> or C<sup>2</sup><sub>bpy</sub>); 139.6 (s, C<sup>3</sup><sub>dFppy</sub>); 128.1 (s, C<sup>6</sup><sub>bpy</sub> or C<sup>5</sup><sub>bpy</sub>); 127.5 (s broad, C<sup>11</sup><sub>dFppy</sub>); 124.0 (m, C<sup>2</sup><sub>dFppy</sub> or C<sup>4</sup><sub>dFppy</sub>); 122.6 (s, C<sup>3</sup><sub>bpy</sub>); 114.2 (d,  $J_{\text{C-F}} \approx 18$  Hz, C<sup>9</sup><sub>dFppy</sub>); 99.9 (pst,  $J_{\text{C-F}} \approx 27$  Hz, C<sup>7</sup><sub>dFppy</sub>); 58.6 (s, O-CH<sub>2</sub>CH<sub>3</sub>); 43.5 (s, CH<sub>2</sub>CH<sub>2</sub>CH<sub>2</sub>-Si); 22.8 (s, CH<sub>2</sub>CH<sub>2</sub>CH<sub>2</sub>-Si); 18.4 (s, O-CH<sub>2</sub>CH<sub>3</sub>); 7.9 (s, CH<sub>2</sub>CH<sub>2</sub>CH<sub>2</sub>-Si).

**<sup>19</sup>F{<sup>1</sup>H} NMR (376.5 MHz, CDCl<sub>3</sub>, δ):** -71.40 (d,  $J_{\text{F-P}} = 712$ ); -104.73 (d,  $J_{\text{F-F}} = 11.3$  Hz, 2F, F<sup>6</sup>); -107.91 (d,  $J_{\text{F-F}} = 11.2$  Hz, 2F, F<sup>8</sup>).

### Synthesis of $[\text{Ir}(\text{dFppy})_2(\text{dbbpy})]\text{Cl}$ (8)

This compound was synthesized in a similar way to that previously described for  $[\text{Ir}(\text{ppy})_2(\text{dbbpy})]\text{Cl}$ .<sup>91</sup> 0.25 g (0.21 mmol) of  $[\text{Ir}(\text{dFppy})_2(\mu\text{-Cl})]_2$  and 0.18 g (0.49 mmol) of *dbbpy* (**L2**) in a mixture of methanol and dichloromethane (1:2 v/v) were refluxed overnight under argon conditions. After cooling, the solution was concentrated and then precipitated with diethyl ether to finally yield a yellow solid (0.27 g, 70%).



**Elemental Analysis (%):** calculated for  $\text{C}_{42}\text{H}_{38}\text{ClF}_4\text{IrN}_6\text{O}_2$ : C, 52.41; H, 3.98; N, 8.73.

Best analyses found: C, 50.73; H, 4.29; N, 8.82 (fits well with **8**·0.5  $\text{CH}_2\text{Cl}_2$ ).

**ESI (+):**  $m/z$  927 [ $\text{M}]^+$  (100%).

**IR (KBr,  $\text{cm}^{-1}$ ):**  $\nu(\text{N-H})$  3427 (m);  $\nu(\text{C-H})$  3297 (m), 3240 (m), 3060 (m), 2956 (m), 2920 (m), 2863 (m);  $\nu(\text{C=O})$  1660 (s);  $\nu(\text{C-H ring})$  1603 (vs), 1570 (s), 1553 (s), 1473 (s), 1426 (m), 1403 (s);  $\nu(\text{C-F})$  1286 (m).

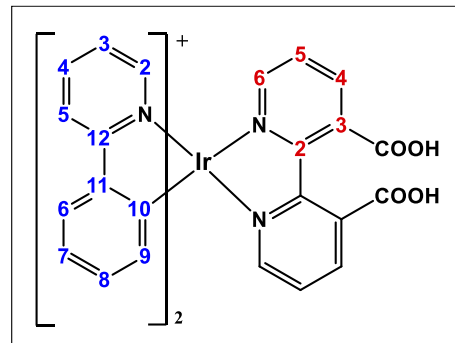
**$^1\text{H}$  NMR (400 MHz,  $\text{CDCl}_3$ ,  $\delta$ ):** 10.66 (s, 2H,  $\text{H}^3_{\text{bpy}}$ ); 9.63 (s broad, NH); 8.35 (d,  $J_{\text{H-H}} = 8.5$  Hz, 2H,  $\text{H}^2_{\text{dFppy}}$ ); 8.18 (d,  $J_{\text{H-H}} = 5.7$  Hz, 2H,  $\text{H}^6_{\text{bpy}}$  or  $\text{H}^5_{\text{bpy}}$ ); 8.00 (d,  $J_{\text{H-H}} = 5.7$  Hz, 2H,  $\text{H}^6_{\text{dFppy}}$  or  $\text{H}^5_{\text{dFppy}}$ ); 7.85 (t,  $J_{\text{H-H}} = 8.1$  Hz, 2H,  $\text{H}^3_{\text{dFppy}}$ ); 7.40 (d,  $J_{\text{H-H}} = 5.9$  Hz, 2H,  $\text{H}^5_{\text{dFppy}}$ ); 7.03 (t,  $J_{\text{H-H}} = 6.8$  Hz, 2H,  $\text{H}^4_{\text{dFppy}}$ ); 6.60 (pst,  $^3J_{\text{F-H}} = 10.7$  Hz, 2H,  $\text{H}^7_{\text{dFppy}}$ ); 5.69 (dd,  $^3J_{\text{F-H}} = 8.2$  Hz,  $J_{\text{H-H}} = 2.3$  Hz, 2H,  $\text{H}^9_{\text{dFppy}}$ ); 3.56 (c,  $J_{\text{H-H}} = 7.0$  Hz, 4H,  $\text{CH}_2\text{CH}_2\text{CH}_2\text{H}_3$ ); 1.77 (q,  $J_{\text{H-H}} = 7.5$  Hz, 4H,  $\text{CH}_2\text{-CH}_2\text{-CH}_2\text{-CH}_3$ ); 1.43 (sx,  $J_{\text{H-H}} = 7.5$  Hz, 4H,  $\text{CH}_2\text{CH}_2\text{CH}_2\text{CH}_3$ ); 0.94 (t,  $J_{\text{H-H}} = 7.3$  Hz, 6H,  $\text{CH}_2\text{CH}_2\text{CH}_2\text{CH}_3$ ).

**$^{13}\text{C}\{^1\text{H}\}$  NMR (100.6 MHz,  $\text{CDCl}_3$ ,  $\delta$ ):** 164.6 (s,  $\text{C}^{12}_{\text{dFppy}}$ ); 161.8 (s, CO); 161.6 (dd,  $J_{\text{F-C}} = 232$  Hz,  $^3J_{\text{F-C}} = 13$  Hz,  $\text{C}^6_{\text{dFppy}}$  or  $\text{C}^8_{\text{dFppy}}$ ); 156.4 (s,  $\text{C}^4_{\text{bpy}}$  or  $\text{C}^2_{\text{bpy}}$ ); 153.2 (m,  $\text{C}^{10}_{\text{dFppy}}$  or  $\text{C}^{11}_{\text{dFppy}}$ ); 150.4 (s,  $\text{C}^6_{\text{bpy}}$  or  $\text{C}^5_{\text{bpy}}$ ); 148.3 (s,  $\text{C}^5_{\text{dFppy}}$ ); 145.2 (s,  $\text{C}^4_{\text{bpy}}$  or  $\text{C}^2_{\text{bpy}}$ ); 139.0 (s,  $\text{C}^3_{\text{dFppy}}$ ); 128.1 (s,  $\text{C}^6_{\text{bpy}}$  or  $\text{C}^5_{\text{bpy}}$ ); 127.6 (d,  $J_{\text{F-C}} = 280$  Hz,  $\text{C}^6_{\text{dFppy}}$  or  $\text{C}^8_{\text{dFppy}}$ ); 127.5 ( $\text{C}^{10}_{\text{dFppy}}$  or  $\text{C}^{11}_{\text{dFppy}}$ ); 124.3 (s,  $\text{C}^2_{\text{dFppy}}$  or  $\text{C}^3_{\text{bpy}}$ ); 124.1 (s,  $\text{C}^2_{\text{dFppy}}$  or  $\text{C}^3_{\text{bpy}}$ ); 123.7 (s,  $\text{C}^4_{\text{dFppy}}$ ); 114.2 (d,  $^2J_{\text{F-C}} \approx 20$  Hz,  $\text{C}^9_{\text{dFppy}}$ ); 99.8 (pst,  $^2J_{\text{F-C}} \approx 28$  Hz,  $\text{C}^7_{\text{dFppy}}$ ); 40.7 (s,  $\text{CH}_2\text{CH}_2\text{CH}_2\text{CH}_3$ ); 31.5 (s,  $\text{CH}_2\text{CH}_2\text{CH}_2\text{CH}_3$ ); 20.5 (s,  $\text{CH}_2\text{CH}_2\text{CH}_2\text{CH}_3$ ); 14.0 (s,  $\text{CH}_2\text{CH}_2\text{CH}_2\text{CH}_3$ ).

**$^{19}\text{F}\{^1\text{H}\}$  NMR (376.5 MHz,  $\text{CDCl}_3$ ,  $\delta$ ):** -104.71 (d,  $J_{\text{F-F}} = 11.4$  Hz, 2F,  $\text{F}^6$ ); -107.86 (d,  $J_{\text{F-F}} = 11.5$  Hz, 2F,  $\text{F}^8$ ).

**Synthesis of  $[\text{Ir}(\text{ppy})_2(3,3'\text{-H}_2\text{dcbpy})]\text{PF}_6$  (**9**, [Ir])**

This compound was synthesized in a similar way to that previously described for the 4,4'-H<sub>2</sub>dcbpy isomer.<sup>164</sup> A yellow solution of 0.25 g (0.23 mmol) of  $[\text{Ir}(\text{ppy})_2(\mu\text{-Cl})]_2$  in 20 mL of CH<sub>2</sub>Cl<sub>2</sub> was treated with a solution of 0.12 g (0.47 mmol) of 2,2'-bipyridin-3,3'-dicarboxylic acid (3,3'-H<sub>2</sub>dcbpy) in 20 mL of MeOH. The mixture was refluxed for 2 hours. 5 mL of a saturated solution of NaAcO in MeOH were added to the above solution and the mixture was again refluxed during 1 hour. Finally, 5 mL of a saturated solution of NH<sub>4</sub>PF<sub>6</sub> in MeOH were added to the final mixture, stirring it for further 30 minutes. The resulting solution was evaporated to dryness and the residue was treated with 20 mL of HCl 1M, and stirred during 10 minutes at room temperature. The orange solid formed was filtered and washed with water (2 x 10 mL) and extracted with MeOH. 5 mL of a saturated solution of NH<sub>4</sub>PF<sub>6</sub> in MeOH were added and the mixture was stirred for 30 minutes and evaporated to dryness. The residue was extracted with CH<sub>2</sub>Cl<sub>2</sub> and the resulting solution was evaporated to dryness to give compound **9** as an orange solid (0.19 g, 59%).



This derivative will be referred as **[Ir]** in *Chapter IV*.

**Elemental Analysis (%):** calculated for C<sub>34</sub>H<sub>24</sub>F<sub>6</sub>IrN<sub>4</sub>O<sub>4</sub>P: C, 45.90; H, 2.72; N, 6.30.

Found: C, 46.30; H, 3.13; N, 5.96.

**ESI(+):** 754.14 ([M-PF<sub>6</sub>]<sup>+</sup>, 100%).

**IR (KBr, cm<sup>-1</sup>):**  $\nu$ (O-H) 3400 (s broad);  $\nu$ (C-H) 3103 (s), 3060 (s), 3031 (s), 2960 (m), 2920 (m); 2850 (m);  $\nu$ (C=O) 1712 (s); 1612 (vs); 1476 (s); 1413 (s); 1303 (s);  $\nu$ (OC-O) 1219 (s);  $\nu$ (P-F) 845(s).

**<sup>1</sup>H NMR (400 MHz, CD<sub>3</sub>COD, δ):** 8.32 (d,  $J_{\text{H-H}} = 7.1$  Hz, 2H, H<sup>6</sup><sub>dcbpy</sub>); 8.26 (broad, 2H, H<sup>2</sup><sub>ppy</sub>); 8.06 (d,  $J_{\text{H-H}} = 8.1$  Hz, 2H, H<sup>5</sup><sub>ppy</sub>); 7.98 (d,  $J_{\text{H-H}} = 4.6$  Hz, 2H, H<sup>4</sup><sub>dcbpy</sub>); 7.83 (t,  $J_{\text{H-H}} = 7.8$  Hz, 2H, H<sup>4</sup><sub>ppy</sub>); 7.77 (d,  $J_{\text{H-H}} = 7.7$  Hz, 2H, H<sup>8</sup><sub>ppy</sub>); 7.36 (s broad, 2H, H<sup>5</sup><sub>dcbpy</sub>); 7.05 (t,  $J_{\text{H-H}} = 6.5$  Hz, 2H, H<sup>3</sup><sub>ppy</sub>); 6.99 (t,  $J_{\text{H-H}} = 7.5$  Hz, 2H, H<sup>9</sup><sub>ppy</sub>); 6.85 (t,  $J_{\text{H-H}} = 7.4$  Hz, 2H, H<sup>10</sup><sub>ppy</sub>), 6.24 (d,  $J_{\text{H-H}} = 7.5$  Hz, 2H, H<sup>11</sup><sub>ppy</sub>).

**<sup>13</sup>C{<sup>1</sup>H} NMR (100.6 MHz, CD<sub>3</sub>OD, δ):** 168.8 (s, CO<sub>2</sub>H); 168.6 (s, C<sup>12</sup><sub>ppy</sub>); 158.1 (s, C<sup>2</sup><sub>dcbpy</sub> or C<sup>3</sup><sub>dcbpy</sub>); 150.8 (s, C<sup>4</sup><sub>dcbpy</sub> and C<sup>11</sup><sub>ppy</sub>); 149.8 (s, C<sup>10</sup><sub>ppy</sub>); 145.3 (s, C<sup>2</sup><sub>ppy</sub>); 139.8 (s, C<sup>6</sup><sub>dcbpy</sub>); 139.6 (s, C<sup>4</sup><sub>ppy</sub>);

132.9 (s, C<sup>9</sup> <sub>p</sub>ppy); 131.5 (s, C<sup>8</sup> <sub>p</sub>py); 127.7 (s, C<sup>5</sup> <sub>dcb</sub>py); 125.9 (s, C<sup>6</sup> <sub>p</sub>py); 124.4 (s, C<sup>3</sup> <sub>p</sub>py); 123.6 (s, C<sup>7</sup> <sub>p</sub>py); 120.8 (s, C<sup>5</sup> <sub>p</sub>py).

**<sup>19</sup>F{<sup>1</sup>H} NMR (376.5 MHz, CD<sub>3</sub>COD, δ):** -74.8 (d, <sup>1</sup>J<sub>F-P</sub> = 710 Hz).

**<sup>31</sup>P{<sup>1</sup>H} NMR (162.1 MHz, CD<sub>3</sub>COD, δ):** -144.5 (d, <sup>1</sup>J<sub>F-P</sub> = 710 Hz).

## Synthesis of silica- and titania-based materials

Synthesis of mesoporous luminescent hybrid organometallo-silica materials: [1]-SiO<sub>2</sub>\_P, [2]-SiO<sub>2</sub>\_P, [3]-SiO<sub>2</sub>\_P, [4]-SiO<sub>2</sub>\_P

The hybrid silica-based materials were prepared according to our previous procedure,<sup>35b</sup> but without the concurrence of any surfactant. Their synthesis were carried out through the co-condensation of the corresponding organometallic complex (**1**, **2** or **3**) and the silica source, TEOS.

A solution of each derivative (0.04 g, 0.03 mmol **1**; 0.04 g, 0.03 mmol **2**; 0.03 g, 0.03 mmol **3**) in 3 mL of THF was added to 1.9 g (9.12 mmol) of TEOS and stirred during 1 hour. Then, 30 mL of water were added to the mixture and stirred for one additional hour. The later addition of 1.4 mL of a 0.05 M NaF solution induced the precipitation of the silica. The resulting mixture was reacted at room temperature during 24 hours, under vigorous magnetic stirring. The resulting pale-yellow solids were filtered, washed with water, ethanol and acetone and dried overnight.

On the other hand, the synthesis of **[4]-SiO<sub>2</sub>\_P** was slightly modified due to the poor stability that this chromophore (**4**) has demonstrated in solution under air conditions. Hence, complex **4** was prepared *in-situ*, in the same reaction medium as the hybrid material. 19 mg (0.03 mmol) of [Pt(bzq)(MeCN)<sub>2</sub>]PF<sub>6</sub> and 17 mg (0.03 mmol) of *dasipy* were reacted in 3 mL of anhydrous THF during 10 minutes. Then, 1.9 g (9.12 mmol) of TEOS were added and the resulting mixture was stirred for 1 hour. The subsequent synthetic treatment was the same to that above describe for the analogous materials.

In all cases, the molar ratio of the synthesis gel is 1.0 TEOS: 182 H<sub>2</sub>O: 4 THF: 7.7x10<sup>-3</sup> F<sup>-</sup>.

The nominal metal concentration in these silica gels was kept equal to 1wt%.

→ **[1]-SiO<sub>2</sub>\_P** (0.33 g, 56%)

**IR (KBr, cm<sup>-1</sup>):** v(O-H) 3450 (s broad), 1633 (m); v(C-H) 2961 (w), 2923 (w), 2848 (w); v(ring) 1483 (w), 1435 (w), 1382 (w); v(Si-O-Si) 1220, 1080 (s broad), 800 (m), 460 (s); v(Si-O) 940 (s).

**DRUV (KBr):**  $\lambda_{\text{max/nm}}$  224, 246, 258, 317, 365, 424, 454.

→ [2]-SiO<sub>2</sub>-P (0.50 g, 87%)

**IR (KBr, cm<sup>-1</sup>):** ν(O-H) 3450 (s broad), 1633 (m); ν(C-H) 2960 (w), 2920 (w), 2855; ν(ring) 1484 (w), 1453 (w), 1435 (w); ν(Si-O-Si) 1220, 1080 (s broad), 800 (m), 460 (s); ν(Si-O) 940 (m).

**DRAV (KBr):** λ<sub>max/nm</sub> 233, 253, 291, 400.

→ [3]-SiO<sub>2</sub>-P (0.51 g, 87%)

**IR (KBr, cm<sup>-1</sup>):** ν(O-H) 3450 (s broad), 1633 (m); ν(C-H) 2924 (w), 2850 (w); ν(ring) 1501 (w), 1460 (w), 1401 (m), 1384 (m); ν(Si-O-Si) 1220, 1080 (s broad), 800 (m), 460 (s); ν(Si-O) 940 (w).

**DRAV (KBr):** λ<sub>max/nm</sub> 215, 240, 290, 355, 402.

→ [4]-SiO<sub>2</sub>-P (0.36 g, 63%)

**IR (KBr, cm<sup>-1</sup>):** ν(O-H) 3472 (s broad), 1640 (m); ν(C-H) 2920 (w), 2850 (w); ν(C=O) 1657 (vw); ν(ring) 1535 (w); ν(Si-O-Si) 1220, 1080 (s broad), 800 (m), 460 (s); ν(Si-O) 950 (m).

**DRAV (KBr):** λ<sub>max/nm</sub> 208, 241, 283, 314, 382, 482, 559.

Synthesis of mesoporous complex-free silica powder: SiO<sub>2</sub>\_P

The control complex-free silica powder was obtained following the same procedure described for [1-4]-SiO<sub>2</sub>\_P hybrid silica materials, but without adding the coordination complexes (0.43 g, 78%).

The molar ratio of the synthesis gel is also 1.0 TEOS: 182 H<sub>2</sub>O: 4 THF: 7.7x10<sup>-3</sup> F<sup>-</sup>.

**IR (KBr, cm<sup>-1</sup>):** v(O-H) 3450 (s broad), 1633 (m); v(Si-O-Si) 1220, 1080 (s broad), 800 (m), 460 (s); v(Si-O) 940 (s).

Synthesis of mesoporous luminescent hybrid organometallo-silica gels: [1]-SiO<sub>2</sub>\_G, [3]-SiO<sub>2</sub>\_G

Optically transparent hybrid organometallo-silica gels were prepared following a modification of a previously reported method.<sup>66</sup> In this case, ammonium fluoride (NH<sub>4</sub>F) and ammonium hydroxide (NH<sub>4</sub>OH) were used as nucleophilic catalysts for the condensation of the silica network. No surfactant was used.

In a typical synthesis, the desired complex (10.8 mg, 7.7x10<sup>-3</sup> mmol **1**; 6 mg, 6.6x10<sup>-3</sup> mmol **3**) was previously dissolved in 4 mL of absolute ethanol and then added to 5 mL (22.4 mmol) of TEOS. After 10 minutes of stirring, the mixture was treated with 11 mL of a solution (water/ ethanol, 2.4: 1) containing 0.37 mL of ammonium fluoride 0.5 M and 0.083 mL of ammonium hydroxide 30%. The resulting mixture was reacted at room temperature, under vigorous stirring for 5 minutes, until the beginning of the hydrolysis and placed in a glass plate to allow the formation of a transparent thin film that will correspond to the silica gel. The fluids that remains on the pores of the gel were exchanged multiple times with acetone. **[1]-SiO<sub>2</sub>\_G** and **[3]-SiO<sub>2</sub>\_G** were obtained as optically transparent silica films.

The molar ratio of the synthesis gel is 1.0 TEOS: 19 H<sub>2</sub>O: 5.5 EtOH: 8.3x10<sup>-3</sup> F<sup>-</sup>: 0.06 NH<sub>4</sub>OH.

The nominal metal concentration in these silica gels was kept equal to 0.1wt%.

→ **[1]-SiO<sub>2</sub>\_G**

**IR (KBr, cm<sup>-1</sup>):** v(O-H) 3450 (s broad), 1633 (S); v(C-H) 2920 (w), 2850 (w); v(ring) 1382 (w); v(Si-O-Si) 1230 (s), 1080 (s broad), 800 (m), 460 (s); v(Si-O) 940 (s).

**DRUV (KBr):**  $\lambda_{\text{max/nm}}$  221, 234, 262, 317, 362.

→ **[3]-SiO<sub>2</sub>\_G**

**IR (KBr, cm<sup>-1</sup>):** v(O-H) 3450 (s broad), 1633 (m); v(C-H) 2980 (w), 2928 (w); v(Si-O-Si) 1250-1030 (s broad), 800 (s), 460 (s); v(Si-O) 940 (w).

**DRUV (KBr):**  $\lambda_{\text{max/nm}}$  210, 235, 280, 356, 370, 407.

Synthesis of mesoporous complex-free silica gel SiO<sub>2</sub>\_G

The control complex-free silica transparent gel was obtained following the same procedure to that described for [1,3]-SiO<sub>2</sub>\_G, but without the addition of the coordination complexes.

The molar ratio of the synthesis gel is also 1.0 TEOS: 19 H<sub>2</sub>O: 5.5 EtOH: 8.3x10<sup>-3</sup> F<sup>-</sup>: 0.06 NH<sub>4</sub>OH.

**IR (KBr, cm<sup>-1</sup>):**  $\nu$ (O-H) 3450 (s broad), 1633 (s);  $\nu$ (Si-O-Si) 1230 (s), 1080 (s broad), 800 (m), 460 (s);  $\nu$ (Si-O) 940 (s).

**Synthesis of mesoporous luminescent organometallo-silica nanoparticles: [B]-NP, [G]-NP, [R]-NP**

The synthesis of the monochromatic silica nanoparticles were carried out following a modification of the Sol-Gel Coordination Chemistry approach. The strategy is based on the initial formation of kinetically controlled small nanoparticles, exclusively formed by the organometallic chromophores (organometallic dots, **ODs**), which are then subjected to co-condensation with the TEOS.

A solution of the corresponding complexes (8 mg, 0.006 mmol **B**; 8 mg, 0.006 mmol **G** or 7 mg, 0.006 mmol **R**) in 3 mL of absolute ethanol was added dropwise to an initial solution of 0.20 g (0.55 mmol) of CTAB and 31.4 µL (0.24 mmol) of triethanolamine (TEA) in 13.3 mL (0.74 mmol) of distilled water. The mixture was kept under magnetic stirring for 6 (for **B** and **G**) or 2 (**R**) hours to form the corresponding monochromatic emitting organometallic dots (**[B]-OD**, **[G]-OD**, **[R]-OD**). After the addition of the 2 mL (9.12 mmol) of TEOS in 1 mL of absolute ethanol, the mixture was reacted during 24 hours at room temperature. The resulting suspension was centrifuged (20000 r.p.m. 20 minutes) and washed thoroughly with ethanol to finally obtain the materials as pale yellow (**[B]-NP**, **[G]-NP**) and orange (**[R]-NP**) powders. The surfactant was removed by ionic exchange with an ethanolic solution of ammonium nitrate (10 mg/mL).

The molar ratio of the synthesis gel is the following: 1.0 TEOS: 0.06 CTAB: 0.026 TEA: 80 H<sub>2</sub>O.

The nominal iridium metal concentration was kept equal to 0.2 wt%.

→ **[B]-NP** (0.41 g, 73%)

**IR (KBr, cm<sup>-1</sup>):** v(O-H) 3475 (s broad), 1640 (m); v(C-H) 2980 (vw), 2925 (w), 2854 (w); v(ring) 1487 (w), 1401(w), 1380(w); v(Si-O-Si) 1220, 1080 (vs broad), 800 (m), 460 (s); v(Si-O) 950 (m).

**DRUV (KBr):**  $\lambda_{\text{max/nm}}$  230, 240, 260, 297, 312, 350.

→ **[G]-NP** (0.38 g, 69%)

**IR (KBr, cm<sup>-1</sup>):** v(O-H) 3450 (s broad), 1633 (m); v(C-H) 2980 (vw), 2924 (m), 2851 (m); v(ring) 1490 (w), 1478(w), 1457(w), 1383(w); v(Si-O-Si) 1220, 1080 (s broad), 800 (m), 460 (s); v(Si-O) 940 (s).

**DRUV (KBr):**  $\lambda_{\text{max/nm}}$  240, 264, 314, 362.

→ [R]-NP (0.38 g, 69%)

**IR (KBr, cm<sup>-1</sup>):** ν(O-H) 3450 (s broad), 1630 (m); ν(C-H) 2925 (m), 2855 (m); ν(ring) 1560 (vw), 1540(vw), 1475(vw); ν(Si-O-Si) 1220, 1080 (vs broad), 800 (m), 460 (s); ν(Si-O) 950 (m).

**DRUV (KBr):** λ<sub>max/ nm</sub> 224, 238, 272, 294, 310, 372, 467, 494.

Synthesis of white emissive mesoporous organometallo-silica nanoparticles: [W]-NP

[W]-NP nanoparticles were prepared following a similar approach to that described for the monochromatic [B,G,R]-NP materials. A combination of complexes **B** and **G** (5.25 mg, 0.004 mmol **B** and 2.25 mg, 0.002 mmol **G**) in 2 mL of absolute ethanol was added dropwise to the starting mixture of CTAB and TEA in distilled water. The resulting mixture was stirred for 4 hours at room temperature. Then, a solution of complex **R** (0.4 mg, 0.0003 mmol) in 1 mL of EtOH was added dropwise and stirred for 2 additional hours to allow the formation of the white emitting organometallic dots [W]-OD. The subsequent treatment was the same to that previously described for the synthesis of the monochromatic [B,G,R]-NP nanoparticles (0.30 g, 54%). [W]-NP were obtained as a white solid powder.

The total nominal iridium metal content was also 0.2 wt% (0.125 wt% **B**, 0.064 wt% **G** and 0.011 wt% **R**), and the molar ratio of the synthesis gel is the same than that for [B,G,R]-NP.

**IR (KBr, cm<sup>-1</sup>):**  $\nu(\text{O-H})$  3465 (s broad), 1638 (w);  $\nu(\text{C-H})$  2956(w), 2925 (m), 2854 (m);  $\nu(\text{ring})$  1559 (w), 1540 (w), 1506(w), 1489(w), 1456(w);  $\nu(\text{Si-O-Si})$  1220, 1084 (vs broad), 800 (m), 460 (m);  $\nu(\text{Si-O})$  950 (s).

**DRUV (KBr):**  $\lambda_{\text{max/nm}}$  246, 258, 268, 298, 311, 358.

The same approach was followed to prepare materials with a higher total nominal metal concentration: 0.6 wt% (0.375 wt% **B**, 0.192 wt% **G** and 0.033 wt% **R**; [W]-NP\_0.6) and 1 wt% (0.625 wt% **B**, 0.320 wt% **G** and 0.055 wt% **R**; [W]-NP\_1). We tried the same molar ratio of the synthesis gels and also more diluted media (for instance 1.0 TEOS: 0.18 CTAB: 0.078 TEA: 237.6 H<sub>2</sub>O): [W]-NP\_0.6 (0.36 g, 63%) and [W]-NP\_1 (0.41 g, 73%).

In all cases, the materials were formed by aggregation of nanoparticles and not by discrete nanoparticles, showing lesser phosphorescence quantum yields (*ca.* 18%) than those observed for both [B,G,R]-NP and [W]-NP.

**Synthesis of mesoporous complex-free silica nanoparticles: control NP**

The control complex-free nanoparticles were obtained following the same procedure to that described for the monochromatic materials **[B,G,R]-NP**, but without adding the coordination complexes (0.48 g, 87 %).

The molar ratio of the synthesis gel is the following: 1.0 TEOS: 0.06 CTAB: 0.026 TGA: 80 H<sub>2</sub>O.

**IR (KBr, cm<sup>-1</sup>):** v(O-H) 3475 (m broad), 1640 (w); v(Si-O-Si) 1220, 1080 (s broad), 800 (w), 460 (m); v(Si-O) 950 (w).

Synthesis of *in-situ* mesoporous organometallo-silica nanoparticles: [7]-NP<sub>OH</sub>\_IS, [7]-NP<sub>Me</sub>\_IS, [7]-NP<sub>APTES</sub>\_IS

The synthesis of the *in-situ* hybrid materials was carried out accomplishing the co-condensation of the silica precursor (TEOS) with the iridium complex **7**. In all the cases, the nominal metal concentration was 0.2 wt% (without considering the addition of DMDES or APTES) and the molar ratio of the synthesis gel was the following: 1.00 TEOS: 0.0598 CTAB: 0.026 TEA: 80.0 H<sub>2</sub>O (0.135 DMDES or 0.023 APTES, when appropriate).

→ [7]-NP<sub>Me</sub>\_IS

In a typical synthesis, 0.20 g (0.55 mmol) of CTAB (hexadecyltrimethylammonium bromide) was added to a mixture of 13.1 mL of distilled water and 31.4 μL (0.24 mmol) of triethanolamine (TEA). The resulting suspension was heated up to 80 °C for 1 hour. Simultaneously, a solution of complex **7** (7.9 mg, 5.78 mmol) in 3 mL of absolute ethanol and 1.9 g (9.12 mmol) of TEOS was stirred at room temperature. This last solution was added to that containing the surfactant at 80°C. After 10 minutes of reaction, 0.21 mL of diethoxydimethylsilane (DMDES, 1.22 mmol) were added and stirred for another 2 hours. The mixture was cooled to room temperature and the particles were recovered by centrifugation (20 min at 20000 r.p.m.) and washed thoroughly with distilled water and ethanol. Finally, the surfactant was removed by ionic exchange with a saturated ammonium nitrate solution. [7]-NP<sub>Me</sub>\_IS was obtained as pale-yellow powder. (0.36 g, 82%).

**IR (KBr, cm<sup>-1</sup>):** v(O-H) 3475 (m broad), 1640 (w); v(C-H) 2968 (vw), 2928 (vw), 2852 (vw); v(ring) 1552 (vw), 1452 (vw), 1452 (vw), 1405 (vw); v(Si-CH<sub>3</sub>) 1267 (w), 850 (w); v(Si-O-Si) 1220, 1080 (s broad), 800 (w), 460 (m); v(Si-O) 950 (w).

**DRUV (KBr):**  $\lambda_{\text{max/nm}}$  265, 284, 310, 350, 420, 445.

→ [7]-NP<sub>OH</sub>\_IS

The synthesis was performed following the same procedure to that described for [7]-NP<sub>Me</sub>\_IS, but without the concurrence of the capping agent (DMDES). The particles were obtained as pale-yellow powder. (0.39 g, 90%).

**IR (KBr, cm<sup>-1</sup>):** v(O-H) 3475 (m broad), 1640 (w); v(C-H) 2927 (vw), 2854 (vw); v(Si-O-Si) 1220, 1080 (s broad), 800 (w), 460 (m); v(Si-O) 950 (w).

**DRUV (KBr):**  $\lambda_{\text{max/nm}}$  305, 350, 418, 445.

→ [7]-NP<sub>APTES\_IS</sub>

The same synthetic pathway was followed for the obtaining of these nanoparticles, but in this case, the capping agent used was (3-aminopropyl)triethoxysilane (APTES). Thus, after the 10 minutes of stirring at 80°C, 48 µL (0.205 mmol) of APTES were added to the mixture. The resulting suspension was reacted over 1 hour at 80 °C and the nanoparticles were collected by centrifugation. (0.20 g, 36%).

**IR (KBr, cm<sup>-1</sup>):** v(O-H) 3440 (m broad), 1640 (w); v(N-H) 3285 (m broad), 1390 (w); v(C-H) 2966 (vw), 2927 (vw), 2856 (vw); v(ring) 1536 (vw), 1475; v(Si-O-Si) 1220, 1080 (s broad), 800 (w), 460 (m); v(Si-O) 950 (w).

**DRUV (KBr):**  $\lambda_{\text{max/nm}}$  215, 270, 308, 357, 418, 450.

Synthesis of mesoporous complex-free silica nanoparticles: control NP: **NP<sub>OH</sub>, NP<sub>Me</sub>, NP<sub>APTES</sub>**

Complex-free mesoporous silica nanoparticles were prepared following the same procedure previously described for each *in-situ* materials, but without adding the metal complex.

→ **NP<sub>OH</sub>** (0.41 g, 76%)

Molar ratio of the synthesis gel 1.00 TEOS: 0.0598 CTAB: 0.026 TEA: 80.0 H<sub>2</sub>O.

**IR (KBr, cm<sup>-1</sup>):** v(O-H) 3475 (m broad), 1640 (w); v(Si-O-Si) 1220, 1080 (s broad), 800 (w), 460 (m); v(Si-O) 950 (w).

→ **NP<sub>Me</sub>** (0.31 g, 68%)

Molar ratio of the synthesis gel 1.00 TEOS: 0.0598 CTAB: 0.026 TEA: 80.0 H<sub>2</sub>O: 0.135 DMDES.

**IR (KBr, cm<sup>-1</sup>):** v(O-H) 3475 (m broad), 1640 (w); v(Si-CH<sub>3</sub>) 1267 (w), 850 (w); v(Si-O-Si) 1220, 1080 (s broad), 800 (w), 460 (m); v(Si-O) 950 (w).

→ **NP<sub>APTES</sub>** (0.47 g, 81%)

Molar ratio of the synthesis gel 1.00 TEOS: 0.0598 CTAB: 0.026 TEA: 80.0 H<sub>2</sub>O: 0.023 APTES.

**IR (KBr, cm<sup>-1</sup>):** v(O-H) 3440 (m broad), 1640 (w); v(N-H) 3285 (m broad), 1390 (w); v(Si-O-Si) 1220, 1080 (s broad), 800 (w), 460 (m); v(Si-O) 950 (w).

Synthesis of grafted mesoporous organometallo silica nanoparticles: [7]-NP<sub>OH</sub>\_G, [7]-NP<sub>Me</sub>\_G, [7]-NP<sub>APTES</sub>\_G

The synthesis of the grafted materials was carried out maintaining the same nominal molar ratio as in the hybrid *in-situ* silica nanoparticles. In a typical synthesis, 0.40 g (6.67 mmol) of the corresponding complex-free silica nanoparticles (**NP<sub>OH</sub>**, **NP<sub>Me</sub>** and **NP<sub>APTES</sub>**) were suspended in 30 mL of ethanol. A solution of 5.8 mg (4.2 mmol) of complex **7** in 3 mL of ethanol was added dropwise and the mixture was stirred during 3 hours until a homogeneous distribution was provided. Subsequently, 1 mL of an aqueous solution 0.05M of NaF was added and the resulting mixture was kept under magnetic stirring for 24 hours. The yellow solids were centrifuged and washed thoroughly with ethanol.

The nominal metal concentration in these silica nanoparticles was kept equal to 0.2 wt%.

→ [7]-NP<sub>OH</sub>\_G (0.31 g, 77%)

**IR (KBr, cm<sup>-1</sup>):** v(O-H) 3450 (m broad), 1640 (w); v(C-H) 2929 (vw), 2858 (vw); v(ring) 1554 (vw), 1479 (vw); v(Si-O-Si) 1220, 1090 (s broad), 800 (w), 460 (m); v(Si-O) 950 (m).

**DRUV (KBr):**  $\lambda_{\text{max/nm}}$  266, 290, 305, 348, 419, 448.

→ [7]-NP<sub>Me</sub>\_G (0.36 g, 87%)

**IR (KBr, cm<sup>-1</sup>):** v(O-H) 3450 (m broad), 1640 (w); v(C-H) 2969 (vw), 2029 (vw), 2854 (vw); v(ring) 1554 (vw), 1454 (vw), 1406 (vw); v(Si-CH<sub>3</sub>) 1264 (w), 845 (w); v(Si-O-Si) 1220 (m), 1090 (vs broad), 800 (w), 460 (m); v(Si-O) 950 (w).

**DRUV (KBr):**  $\lambda_{\text{max/nm}}$  270, 288, 307, 350, 422, 447, 476.

→ [7]-NP<sub>APTES</sub>\_G (0.34g, 85%)

**IR (KBr, cm<sup>-1</sup>):** v(O-H) 3430 (m broad), 1640 (w); v(N-H) 3280 (m broad), 1390 (w); v(C-H) 2962 (vw), 2025 (vw), 2854 (vw); v(ring) 1533 (vw), 1467 (vw); v(Si-O-Si) 1220, 1080 (s broad), 800 (w), 460 (m); v(Si-O) 950 (w).

**DRUV (KBr):**  $\lambda_{\text{max/nm}}$  215, 267, 290, 307, 351, 419, 448.

Synthesis of *in-situ* hybrid mesoporous metal complex-titania: [Ru]-TiO<sub>2</sub>\_IS, [Ir]-TiO<sub>2</sub>\_IS

Mesoporous titania materials were prepared according to the procedure previously reported<sup>147</sup> but without the concurrence of any surfactant. The synthesis of the hybrid titania-based materials was carried out accomplishing the co-condensation of the titania precursor (TBOT) with each complex ([Ru(4,4'-H<sub>2</sub>dcbpy)<sub>2</sub>(SCN)<sub>2</sub>] **[Ru]** or [Ir(ppy)<sub>2</sub>(3,3'-H<sub>2</sub>dcbpy)]PF<sub>6</sub> **[Ir]**).

Therefore, a solution of the corresponding derivatives (0.04 g, 0.06 mmol **[Ru]**; 0.08 g, 0.09 mmol **[Ir]**) in 2 mL of absolute ethanol was added to 5 g (14.7 mmol) of tetrabutyl orthotitanate (TBOT). The mixture was stirred during 30 minutes and then dissolved in 35 mL of absolute ethanol. Then, 123.5 g (6.86 mol) of water were added drop-wise to finally cause the precipitation of the material. The mixture was reacted at room temperature for 24 hours under vigorous magnetic stirring, and heated up at 80 °C for another 24 hours. The resulting pale garnet (**[Ru]-TiO<sub>2</sub>\_IS**) and beige (**[Ir]-TiO<sub>2</sub>\_IS**) solids were filtered, washed with water and acetone and dried in an oven at 100 °C during 8 hours.

→ **[Ru]-TiO<sub>2</sub>\_IS** (0.97 g, 80%)

Molar ratio of the synthesis gel: 1.0 TBOT: 4x10<sup>-3</sup> complex: 41.3 EtOH: 467 H<sub>2</sub>O.

**IR (KBr, cm<sup>-1</sup>):** v(O-H) 3400 (vs broad), 3065 (m), 3027 (m); v(C-H) 2965 (w), 2925 (w), 2854 (w), 2831 (w); v(C=N) 2113 (w), 1997 (s); δ(O-H) 1620 (vs); ν<sub>as</sub>(-COO) 1539 (m), 1429 (w), 1404(w); ν<sub>s</sub>(-COO) 1366 (m), 1234 (w); v(Ti-O) 573 (vs broad), 474 (vs broad).

**DRUV (KBr):** λ<sub>max/nm</sub> 280, 390<sub>sh</sub>, 500 (extending to 700 nm).

→ **[Ir]-TiO<sub>2</sub>\_IS** (1.20 g, 97%)

Molar ratio of the synthesis gel: 1.0 TBOT: 6x10<sup>-3</sup> complex: 41.3 EtOH: 467 H<sub>2</sub>O.

**IR (KBr, cm<sup>-1</sup>):** v(O-H) 3400 (vs broad), v(C-H) 2960 (w), 2921 (w), 2851 (w); δ(O-H) 1620 (vs); ν<sub>as</sub>(-COO) 1477 (m), 1436 (w), 1417(w); ν<sub>s</sub>(-COO) 1381 (m), 1219 (w), 1156 (m); v(Ti-O) 593 (vs broad), 470 (vs broad).

**DRUV (KBr):** λ<sub>max/nm</sub> 280, 316, 380, 470 (extending to 540 nm).

Synthesis of mesoporous complex-free titania: TiO<sub>2</sub>

Complex-free titania was prepared following the same procedure to that described for the *in-situ* material, but without adding the metal complex (1.06 g, 90%).

The molar ratio of the synthesis gel was 1.0 TBOT: 41.3 EtOH: 467 H<sub>2</sub>O.

**IR (KBr, cm<sup>-1</sup>):**  $\nu(\text{O-H})$  3400 (vs broad), 3065 (m), 3027 (m);  $\delta(\text{O-H})$  1620 (vs);  $\nu(\text{Ti-O})$  573 (vs broad), 474 (vs broad).

**DRUV (KBr):**  $\lambda_{\text{max/nm}}$  290 (broad).

Synthesis of grafted mesoporous metal complex-titania: [Ru]-TiO<sub>2</sub>\_G, [Ir]-TiO<sub>2</sub>\_G

In a typical synthesis, 1.17 g (14.65 mmol) of the as-synthesized complex-free control titania were added to a solution of the corresponding complex (0.04 g, 0.06 mmol [Ru]; 0.08 g, 0.09 mmol [Ir]) in 35 mL of EtOH. The mixture was stirred during 30 min until a homogeneous distribution was provided. Then, the mixture was refluxed overnight to allow the condensation between the carboxylic acids of the organometallic compounds and the superficial OH groups of the material. The resulting solid was filtered, washed with ethanol and acetone, and dried in an oven at 100°C during 8 h. [Ru]-TiO<sub>2</sub>\_G and [Ir]-TiO<sub>2</sub>\_G were obtained as purple and beige solids, respectively. The syntheses were carried out maintaining a similar Ti/metal complex molar ratio than those obtained for the *in-situ* materials.

→ [Ru]-TiO<sub>2</sub>\_G (0.95g, 78%)

Molar ratio: 1.0 TiO<sub>2</sub>: 4x10<sup>-3</sup> [Ru].

**IR (KBr, cm<sup>-1</sup>):** v(O-H) 3420 (vs broad); v(C-H) 2963 (w), 2924 (w), 2851 (w); v(C=N) 2114 (w), 1997 (w); δ(O-H) 1620 (s); v<sub>as</sub>(-COO) 1540 (m), 1433 (w), 1405 (w); v<sub>s</sub>(-COO) 1366 (m), 1263 (w), 1233 (w); v(Ti-O) 570 (vs broad), 480 (vs broad).

**DRUV (KBr):**  $\lambda_{\text{max/nm}}$  280, 390<sub>sh</sub>, 504 (extending to 700 nm).

→ [Ir]-TiO<sub>2</sub>\_G (0.85 g, 69%)

Molar ratio: 1.0 TiO<sub>2</sub>: 6x10<sup>-3</sup> [Ir].

**IR (KBr, cm<sup>-1</sup>):** v(O-H) 3412 (vs broad), v(C-H) 2924 (w), 2848 (w); δ(O-H) 1620 (vs); v<sub>as</sub>(-COO) 1478 (m), 1436 (w), 1418(w); v<sub>s</sub>(-COO) 1384 (m), 1220 (w), 1154 (m); v(Ti-O) 593 (vs broad), 470 (vs broad).

**DRUV (KBr):**  $\lambda_{\text{max/nm}}$  280, 316, 380, 470 (extending to 540 nm).



## ***Bibliography***





1. Ozin, G. A.; Arsenault, A., *Nanochemistry: a chemical approach to nanomaterials*. Royal Society of Chemistry: 2015.
2. (a) Xing, M.; Qiu, B.; Du, M.; Zhu, Q.; Wang, L.; Zhang, J., Spatially separated CdS shells exposed with reduction surfaces for enhancing photocatalytic hydrogen evolution. *Adv. Funct. Mater.* **2017**, *27*, 1702624; (b) Mishra, M.; Chun, D.-M.,  $\alpha$ -Fe<sub>2</sub>O<sub>3</sub> as a photocatalytic material: A review. *Appl. Catal., A* **2015**, *498*, 126-141; (c) Kuo, C.-H.; Mosa, I. M.; Poyraz, A. S.; Biswas, S.; El-Sawy, A. M.; Song, W.; Luo, Z.; Chen, S.-Y.; Rusling, J. F.; He, J., Robust mesoporous manganese oxide catalysts for water oxidation. *ACS Catal.* **2015**, *5*, 1693-1699; (d) Gnanasekaran, L.; Hemamalini, R.; Saravanan, R.; Ravichandran, K.; Gracia, F.; Agarwal, S.; Gupta, V. K., Synthesis and characterization of metal oxides (CeO<sub>2</sub>, CuO, NiO, Mn<sub>3</sub>O<sub>4</sub>, SnO<sub>2</sub> and ZnO) nanoparticles as photo catalysts for degradation of textile dyes. *J. Photochem. Photobiol., B* **2017**, *173*, 43-49; (e) Rong, F.; Zhao, J.; Chen, Z.; Xu, Y.; Zhao, Y.; Yang, Q.; Li, C., Highly active water oxidation on nanostructured biomimetic calcium manganese oxide catalysts. *J. Mater. Chem. A* **2016**, *4*, 6585-6594; (f) Dorraj, M.; Alizadeh, M.; Sairi, N. A.; Basirun, W. J.; Goh, B. T.; Woi, P. M.; Alias, Y., Enhanced visible light photocatalytic activity of copper-doped titanium oxide-zinc oxide heterojunction for methyl orange degradation. *Appl. Surf. Sci.* **2017**, *414*, 251-261; (g) Zhao, X.; Huang, L., Iridium, carbon and nitrogen multiple-doped TiO<sub>2</sub> Nanoparticles with enhanced photocatalytic activity. *Ceram. Int.* **2017**, *43*, 3975-3980; (h) Ouyang, W.; Munoz-Batista, M. J.; Kubacka, A.; Luque, R.; Fernández-García, M., Enhancing photocatalytic performance of TiO<sub>2</sub> in H<sub>2</sub> evolution via Ru co-catalyst deposition. *Appl. Catal., B* **2018**, *238*, 434-443.
3. (a) Shen, S.; Chen, J.; Wang, M.; Sheng, X.; Chen, X.; Feng, X.; Mao, S. S., Titanium dioxide nanostructures for photoelectrochemical applications. *Prog. Mater. Sci.* **2018**, *98*, 299-385; (b) Chen, X.; Selloni, A., Introduction: Titanium Dioxide (TiO<sub>2</sub>) Nanomaterials. *Chem. Rev.* **2014**, *114*, 9281-9282; (c) Kamat, P. V., TiO<sub>2</sub> Nanostructures: Recent Physical Chemistry Advances. *J. Phys. Chem. C* **2012**, *116*, 11849-11851; (d) Teoh, W. Y.; Scott, J. A.; Amal, R., Progress in heterogeneous photocatalysis: from classical radical chemistry to engineering nanomaterials and solar reactors. *J. Phys. Chem. Lett.* **2012**, *3*, 629-639.
4. (a) Rao, C. e. N. e. R.; Sood, A. e. K.; Subrahmanyam, K. e. S.; Govindaraj, A., Graphene: the new two-dimensional nanomaterial. *Angew. Chem. Int. Ed.* **2009**, *48*, 7752-7777; (b) Pumera, M., Graphene-based nanomaterials and their electrochemistry. *Chem. Soc. Rev.* **2010**, *39*, 4146-4157; (c) Zhu, Y.; Murali, S.; Cai, W.; Li, X.; Suk, J. W.; Potts, J. R.; Ruoff, R. S., Graphene and graphene oxide: synthesis, properties, and applications. *Adv. Mater.* **2010**, *22*, 3906-3924.
5. Julkapli, N. M.; Bagheri, S., Graphene supported heterogeneous catalysts: An overview. *Int. J. Hydrogen Energy* **2015**, *40*, 948-979.
6. (a) Tian, Y.; Liu, Y.; Wang, W.-p.; Zhang, X.; Peng, W., CuO nanoparticles on sulfur-doped graphene for nonenzymatic glucose sensing. *Electrochim. Acta* **2015**, *156*, 244-251; (b) Fan, Y.; Lu, H.-T.; Liu, J.-H.; Yang, C.-P.; Jing, Q.-S.; Zhang, Y.-X.; Yang, X.-K.; Huang, K.-J., Hydrothermal preparation and electrochemical sensing properties of TiO<sub>2</sub>-graphene nanocomposite. *Colloids Surf. B* **2011**, *83*, 78-82; (c) Kannan, P.; Maiyalagan, T.; Sahoo, N. G.; Opallo, M., Nitrogen doped graphene nanosheet supported platinum nanoparticles as high performance electrochemical homocysteine biosensors. *J. Mater. Chem. B* **2013**, *1*, 4655-4666; (d) Hossain, M.; Park, J. Y., Amperometric Glucose Biosensor Based on Pt-Pd Nanoparticles Supported by Reduced Graphene Oxide and Integrated with Glucose Oxidase. *Electroanalysis* **2014**, *26*, 940-951.
7. (a) Wang, Z.; Liu, C.-J., Preparation and application of iron oxide/graphene based composites for electrochemical energy storage and energy conversion devices: Current status and perspective. *Nano Energy* **2015**, *11*, 277-293; (b) Giri, S.; Ghosh, D.; Das, C. K., Growth of vertically aligned tunable polyaniline on graphene/ZrO<sub>2</sub> nanocomposites for supercapacitor energy-storage application. *Adv. Funct. Mater.* **2014**, *24*, 1312-1324.
8. Zhang, N.; Yang, M.-Q.; Liu, S.; Sun, Y.; Xu, Y.-J., Waltzing with the versatile platform of graphene to synthesize composite photocatalysts. *Chem. Rev.* **2015**, *115*, 10307-10377.

9. (a) Pocklanova, R.; Rathi, A. K.; Gawande, M. B.; Datta, K. K. R.; Ranc, V.; Cepe, K.; Petr, M.; Varma, R. S.; Kvitek, L.; Zboril, R., Gold nanoparticle-decorated graphene oxide: synthesis and application in oxidation reactions under benign conditions. *J. Mol. Catal. A: Chem.* **2016**, *424*, 121-127; (b) Kabir, S.; Serov, A.; Artyushkova, K.; Atanassov, P., Design of novel graphene materials as a support for palladium nanoparticles: highly active catalysts towards ethanol electrooxidation. *Electrochim. Acta* **2016**, *203*, 144-153; (c) Li, X.; Hao, Z.; Zhang, F.; Li, H., Reduced graphene oxide-immobilized tris (bipyridine) ruthenium (II) complex for efficient visible-light-driven reductive dehalogenation reaction. *ACS Appl. Mater. Interfaces* **2016**, *8*, 12141-12148.
10. Falcaro, P.; Ricco, R.; Yazdi, A.; Imaz, I.; Furukawa, S.; MasPOCH, D.; Ameloot, R.; Evans, J. D.; Doonan, C. J., Application of metal and metal oxide nanoparticles@MOFs. *Coord. Chem. Rev.* **2016**, *307*, 237-254.
11. Yu, J.; Mu, C.; Yan, B.; Qin, X.; Shen, C.; Xue, H.; Pang, H., Nanoparticle/MOF composites: preparations and applications. *Mater. Horiz.* **2017**, *4*, 557-569.
12. (a) Montalti, M.; Prodi, L.; Rampazzo, E.; Zaccheroni, N., Dye-doped silica nanoparticles as luminescent organized systems for nanomedicine. *Chem. Soc. Rev.* **2014**, *43*, 4243-4268; (b) Feng, Y.; Panwar, N.; Tng, D.; Tjin, S.; Wang, K.; Yong, K.-T., The application of mesoporous silica nanoparticle family in cancer theranostics. *Coord. Chem. Rev.* **2016**, *319*, 86-109; (c) Takeda, H.; Ohashi, M.; Goto, Y.; Ohsuna, T.; Tani, T.; Inagaki, S., A Versatile Solid Photosensitizer: Periodic Mesoporous Organosilicas with Ruthenium Tris(bipyridine) Complexes Embedded in the Pore Walls. *Adv. Func. Mater.* **2016**, *26*, 5068-5077; (d) Wolfbeis, O. S., An overview of nanoparticles commonly used in fluorescent bioimaging. *Chem. Soc. Rev.* **2015**, *44*, 4743-4768; (e) Mukhametshina, A. R.; Fedorenko, S. V.; Zueva, I. V.; Petrov, K. A.; Masson, P.; Nizameev, I. R.; Mustafina, A. R.; Sinyashin, O. G., Luminescent silica nanoparticles for sensing acetylcholinesterase-catalyzed hydrolysis of acetylcholine. *Biosens. Bioelectron.* **2015**, *77*, 871-878.
13. (a) Huang, W.; Zhang, Y.; Li, D., Adsorptive removal of phosphate from water using mesoporous materials: A review. *J. Environ. Manage.* **2017**, *193*, 470-482; (b) Da'na, E., Adsorption of heavy metals on functionalized-mesoporous silica: A review. *Microporous Mesoporous Mater.* **2017**, *247*, 145-157; (c) Nasreen, S.; Urooj, A.; Rafique, U.; Ehrman, S., Functionalized mesoporous silica: Absorbents for water purification. *Desalin. Water Treat.* **2016**, *57*, 29352-29362; (d) Gargiulo, N.; Verlotta, A.; Peluso, A.; Aprea, P.; Caputo, D., Modeling the performances of a CO<sub>2</sub> adsorbent based on polyethylenimine-functionalized macro-/mesoporous silica monoliths. *Microporous Mesoporous Mater.* **2015**, *215*, 1-7; (e) Liao, Q.; Zeng, L.; Li, L.; Guo, F.; Wu, L.; Le, S., Synthesis of functionalized mesoporous silica and its application for Cu (II) removal. *Desalin. Water Treat.* **2015**, *56*, 2154-2159; (f) Bhagiyalakshmi, M.; Yun, L. J.; Anuradha, R.; Jang, H. T., Synthesis of chloropropylamine grafted mesoporous MCM-41, MCM-48 and SBA-15 from rice husk ash: their application to CO<sub>2</sub> chemisorption. *J. Porous Mater.* **2010**, *17*, 475-484.
14. (a) Pal, N.; Bhaumik, A., Mesoporous materials: versatile supports in heterogeneous catalysis for liquid phase catalytic transformations. *RSC Adv.* **2015**, *5*, 24363-24391; (b) Oschatz, M.; Lamme, W. S.; Xie, J.; Dugulan, A. I.; de Jong, K. P., Ordered Mesoporous Materials as Supports for Stable Iron Catalysts in the Fischer-Tropsch Synthesis of Lower Olefins. *ChemCatChem* **2016**, *8*, 2846-2852.
15. (a) Ezquerro, C.; Fresta, E.; Serrano, E.; Lalinde, E.; García-Martínez, J.; Berenguer, J. R.; Costa, R. D., White-emitting organometallo-silica nanoparticles for sun-like light-emitting diodes. *Mater. Horiz.* **2019**, *6*, 130-136; (b) Mori, K.; Yamashita, H., Metal Complexes Supported on Solid Matrices for Visible-Light-Driven Molecular Transformations. *Chem. Eur. J.* **2016**, *22*, 11122-11137; (c) Parola, S.; Julián-López, B.; Carlos, L. D.; Sanchez, C., Optical Properties of Hybrid Organic-Inorganic Materials and their Applications. *Adv. Funct. Mater.* **2016**, *26*, 6506-6544; (d) Wang, M.-S.; Guo, G.-C., Inorganic-organic hybrid white light phosphors. *Chem. Commun.* **2016**,

- 52, 13194-13204; (e) Chateau, D.; Chaput, F.; Lopes, C.; Lindgren, M.; Brännlund, C.; Öhgren, J.; Djourelov, N.; Nedelec, P.; Desroches, C.; Eliasson, B.; Kindahl, T.; Lerouge, F.; Andraud, C.; Parola, S., Silica hybrid sol-gel materials with unusually high concentration of Pt-organic molecular guests: studies of luminescence and nonlinear absorption of light. *ACS Appl. Mater. interfaces* **2012**, *4*, 2369-2377; (f) Carlos, L. D.; Ferreira, R. A. S.; de Zea Bermudez, V.; Julian-Lopez, B.; Escribano, P., Progress on lanthanide-based organic-inorganic hybrid phosphors. *Chem. Soc. Rev.* **2011**, *40*, 536-549; (g) Brühwiler, D.; Calzaferri, G.; Torres, T.; Ramm, J.; Gartmann, N.; Dieu, L.-Q.; López-Duarte, I.; Martínez-Díaz, V. M., Nanochannels for supramolecular organization of luminescent guests. *J. Mater. Chem.* **2009**, *19*, 8040.
16. (a) Amonette, J. E.; Matyáš, J., Functionalized silica aerogels for gas-phase purification, sensing, and catalysis: A review. *Microporous Mesoporous Mater.* **2017**, *250*, 100-119; (b) Suárez, P. L.; García-Cortés, M.; Fernández-Argüelles, M. T.; Encinar, J. R.; Valledor, M.; Ferrero, F. J.; Campo, J. C.; Costa-Fernández, J. M., Functionalized phosphorescent nanoparticles in (bio)chemical sensing and imaging – A review. *Anal. Chim. Acta* **2019**, *1046*, 16-31; (c) Ge, X.; Sun, L.; Ma, B.; Jin, D.; Dong, L.; Shi, L.; Li, N.; Chen, H.; Huang, W., Simultaneous realization of  $Hg^{2+}$  sensing, magnetic resonance imaging and upconversion luminescence in vitro and in vivo bioimaging based on hollow mesoporous silica coated UCNPs and ruthenium complex. *Nanoscale* **2015**, *7*, 13877-13887.
17. (a) Rampazzo, E.; Prodi, L.; Petrizza, L.; Zaccheroni, N., Luminescent silica nanoparticles featuring collective processes for optical imaging. In *Light-Responsive Nanostructured Systems for Applications in Nanomedicine*, Springer: 2016; pp 1-28; (b) Yang, Y.; Yu, C., Advances in silica based nanoparticles for targeted cancer therapy. *Nanomed. Nanotechnol. Biol. Med.* **2016**, *12*, 317-332.
18. del Rosal, B.; Jia, B.; Jaque, D., Beyond Phototherapy: Recent Advances in Multifunctional Fluorescent Nanoparticles for Light-Triggered Tumor Theranostics. *Adv. Funct. Mater.* **2018**, *28*, 1803733.
19. Liu, J.-L.; Yan, B., Lanthanide-centered organic–inorganic hybrids through a functionalized aza-crown ether bridge: coordination bonding assembly, microstructure and multicolor luminescence. *Dalton Trans.* **2011**, *40*, 1961-1968.
20. I.U.P.A.C., Compendium of Chemical Terminology (the "GoldBook"), 2<sup>a</sup> ed., Compiled by McNaught, A.D. and Wilkinson, A. *Blackwell Scientific Publications, Oxford* **1997**.
21. de AA Soler-Illia, G. J.; Crepaldi, E. L.; Grosso, D.; Sanchez, C., Block copolymer-templated mesoporous oxides. *Curr. Opin. Colloid Interf. Sci.* **2003**, *8*, 109-126.
22. (a) Sanz-Pérez, E.; Arencibia, A.; Calleja, G.; Sanz, R., Tuning the textural properties of HMS mesoporous silica. Functionalization towards  $CO_2$  adsorption. *Microporous Mesoporous Mater.* **2018**, *260*, 235-244; (b) Niu, M.; Yang, H.; Zhang, X.; Wang, Y.; Tang, A., Amine-impregnated mesoporous silica nanotube as an emerging nanocomposite for  $CO_2$  capture. *ACS Appl. Mater. Interfaces* **2016**, *8*, 17312-17320; (c) Singh, B.; Polshettiwar, V., Design of  $CO_2$  sorbents using functionalized fibrous nanosilica (KCC-1): insights into the effect of the silica morphology (KCC-1 vs. MCM-41). *J. Mater. Chem. A* **2016**, *4*, 7005-7019; (d) Seo, Y.; Kim, K.; Jung, Y.; Ryoo, R., Synthesis of mesoporous carbons using silica templates impregnated with mineral acids. *Microporous Mesoporous Mater.* **2015**, *207*, 156-162; (e) Meth, S.; Goeppert, A.; Prakash, G. S.; Olah, G. A., Silica nanoparticles as supports for regenerable  $CO_2$  sorbents. *Energy & Fuels* **2012**, *26*, 3082-3090; (f) Madden, D.; Curtin, T.; Hanrahan, J. P.; Tobin, J.,  $CO_2$  sorption performance by aminosilane functionalized spheres prepared via co-condensation and post-synthesis methods. *AIChE J.* **2016**, *62*, 2825-2832.
23. (a) Xu, Z.; Ma, X.; Gao, Y.-E.; Hou, M.; Xue, P.; Li, C. M.; Kang, Y., Multifunctional silica nanoparticles as a promising theranostic platform for biomedical applications. *Mater. Chem. Front.* **2017**, *1*, 1257-1272; (b) Sharma, R.; Sharma, S.; Dutta, S.; Zboril, R.; Gawande, M. B., Silica-nanosphere-based organic–inorganic hybrid nanomaterials: synthesis, functionalization and applications in catalysis. *Green Chemistry* **2015**, *17*, 3207-3230; (c) Giret, S.; Wong Chi Man, M.;

- Carcel, C., Mesoporous-Silica-Functionalized Nanoparticles for Drug Delivery. *Chem. Eur. J.* **2015**, *21*, 13850-13865; (d) Sanz, R.; Calleja, G.; Arencibia, A.; Sanz-Perez, E. S., CO<sub>2</sub> capture with pore-expanded MCM-41 silica modified with amino groups by double functionalization. *Microporous Mesoporous Mater.* **2015**, *209*, 165-171; (e) Sanz, R.; Calleja, G.; Arencibia, A.; Sanz-Pérez, E. S., Development of high efficiency adsorbents for CO<sub>2</sub> capture based on a double-functionalization method of grafting and impregnation. *J. Mater. Chem. A* **2013**, *1*, 1956-1962.
24. (a) Abboud, M.; Bel-Hadj-Tahar, R.; Fakhri, N.; Sayari, A., Synthesis of ferrocenylazobenzene-functionalized MCM-41 via direct co-condensation method. *Microporous Mesoporous Mater.* **2018**, *265*, 179-184; (b) Feinle, A.; Leichtfried, F.; Straßer, S.; Hüsing, N., Carboxylic acid-functionalized porous silica particles by a co-condensation approach. *J. Sol-Gel Sci. Technol.* **2017**, *81*, 138-146; (c) Li, Y.; Xiong, W.; Wang, C.; Song, B.; Zhang, G., Synthesis of hexagonal mesoporous silicates functionalized with amino groups in the pore channels by a co-condensation approach. *RSC Adv.* **2016**, *6*, 53991-54000; (d) Han, Y. R.; Park, J.-W.; Kim, H.; Ji, H.; Lim, S. H.; Jun, C.-H., A one-step co-condensation method for the synthesis of well-defined functionalized mesoporous SBA-15 using trimethylsilanes as organosilane sources. *Chem. Commun.* **2015**, *51*, 17084-17087.
25. Yu, Q.; Zhang, K.; Liang, H.; Zhao, Q.; Yang, T.; Liu, S.; Zhang, C.; Shi, Z.; Xu, W.; Huang, W., Dual-Emissive NanoHybrid for Ratiometric Luminescence and Lifetime Imaging of Intracellular Hydrogen Sulfide. *ACS Appl. Mater. Interfaces* **2015**, *7*, 5462-5470.
26. (a) Hoffmann, F.; Cornelius, M.; Morell, J.; Fröba, M., Silica-based mesoporous organic-inorganic hybrid materials. *Angew. Chem. Int. Ed.* **2006**, *45*, 3216-3251; (b) Mutin, P. H.; Guerrero, G.; Vioux, A., Hybrid materials from organophosphorus coupling molecules. *J. Mater. Chem.* **2005**, *15*, 3761-3768.
27. (a) Asefa, T.; MacLachlan, M. J.; Coombs, N.; Ozin, G. A., Periodic mesoporous organosilicas with organic groups inside the channel walls. *Nature* **1999**, *402*, 867; (b) Inagaki, S.; Guan, S.; Fukushima, Y.; Ohsuna, T.; Terasaki, O., Novel mesoporous materials with a uniform distribution of organic groups and inorganic oxide in their frameworks. *J. Am. Chem. Soc.* **1999**, *121*, 9611-9614; (c) Melde, B. J.; Holland, B. T.; Blanford, C. F.; Stein, A., Mesoporous sieves with unified hybrid inorganic/organic frameworks. *Chem. Mater.* **1999**, *11*, 3302-3308.
28. (a) Birault, A.; Molina, E.; Toquer, G.; Lacroix-Desmazes, P.; Marcotte, N.; Carcel, C.; Katouli, M.; Bartlett, J. R.; Gerardin, C.; Wong Chi Man, M., Large-Pore Periodic Mesoporous Organosilicas as Advanced Bactericide Platforms. *ACS Appl. Bio Mater.* **2018**, *1*, 1787-1792; (b) Teng, Z.; Wang, C.; Tang, Y.; Li, W.; Bao, L.; Zhang, X.; Su, X.; Zhang, F.; Zhang, J.; Wang, S., Deformable Hollow Periodic Mesoporous Organosilica Nanocapsules for Significantly Improved Cellular Uptake. *J. Am. Chem. Soc.* **2018**, *140*, 1385-1393; (c) Liu, W.; Ma, N.; Li, S.; Zhang, X.; Huo, W.; Xu, J.; Meng, X.; Yang, J., A one-step method for pore expansion and enlargement of hollow cavity of hollow periodic mesoporous organosilica spheres. *J. Mater. Sci.* **2017**, *52*, 2868-2878; (d) Karimi, B.; Mansouri, F.; Khorasani, M., Recent progress in design and application of functional ordered/periodic mesoporous silicas (OMSS) and organosilicas (PMOS) as catalyst support in carbon-carbon coupling reactions. *Curr. Org. Chem.* **2016**, *20*, 349-380; (e) Wahab, M. A.; Beltramini, J. N., Recent advances in hybrid periodic mesostructured organosilica materials: opportunities from fundamental to biomedical applications. *RSC Adv.* **2015**, *5*, 79129-79151.
29. Gao, M.; Han, S.; Hu, Y.; Zhang, L., Enhanced Fluorescence in Tetraylnitrilomethylidyne-Hexaphenyl Derivative-Functionalized Periodic Mesoporous Organosilicas for Sensitive Detection of Copper(II). *J. Phys. Chem. C* **2016**, *120*, 9299-9307.
30. (a) Mizoshita, N.; Tani, T.; Inagaki, S., Syntheses, properties and applications of periodic mesoporous organosilicas prepared from bridged organosilane precursors. *Chem. Soc. Rev.* **2011**, *40*, 789-800; (b) Van Der Voort, P.; Esquivel, D.; De Canck, E.; Goethals, F.; Van Driessche, I.; Romero-Salguero, F. J., Periodic mesoporous organosilicas: from simple to complex bridges; a comprehensive overview of functions, morphologies and applications. *Chem. Soc. Rev.* **2013**, *42*, 3913-3955; (c) Ha, C.-S.; Park, S. S., Synthetic Routes and New Precursors for the Preparation of

- PMOs. In *Periodic Mesoporous Organosilicas*, Springer: Singapore, 2019; pp 87-100; (d) Ha, C.-S.; Park, S. S., *Periodic Mesoporous Organosilicas: Preparation, Properties and Applications*. Springer: 2018; Vol. 281; (e) Croissant, J. G.; Picard, S.; Aggad, D.; Klausen, M.; Jimenez, C. M.; Maynadier, M.; Mongin, O.; Clermont, G.; Genin, E.; Cattoën, X., Fluorescent periodic mesoporous organosilica nanoparticles dual-functionalized via click chemistry for two-photon photodynamic therapy in cells. *J. Mater. Chem. B* **2016**, *4*, 5567-5574.
31. Croissant, J. G.; Cattoën, X.; Man, M. W. C.; Durand, J.-O.; Khashab, N. M., Syntheses and applications of periodic mesoporous organosilica nanoparticles. *Nanoscale* **2015**, *7*, 20318-20334.
32. (a) Fadieiev, Y. M.; Smola, S. S.; Malinka, E. V.; Rusakova, N. V., Study of association of Eu(III)  $\beta$ -diketonato-1,10-phenanthroline complexes in silica-based hybrid materials. *J. Lumin.* **2017**, *183*, 121-128; (b) Feng, J.; Zhang, H., Hybrid materials based on lanthanide organic complexes: a review. *Chem. Soc. Rev.* **2013**, *42*, 387-410; (c) Vilvamani, N.; Gupta, R. D.; Awasthi, S. K., Ru(II)-polypyridyl complex-grafted silica nanohybrids: versatile hybrid materials for Raman spectroscopy and photocatalysis. *RSC Adv.* **2015**, *5*, 13451-13461; (d) Zanarini, S.; Rampazzo, E.; Ciana, L.; Marcaccio, M.; Marzocchi, E.; Montalti, M.; Paolucci, F.; Prodi, L., Ru(bpy)<sub>3</sub> covalently doped silica nanoparticles as multicenter tunable structures for electrochemiluminescence amplification. *J. Am. Chem. Soc.* **2009**, *131*, 2260-2267; (e) Aiello, D.; Talarico, A.; Teocoli, F.; Szerb, E. I.; Aiello, I.; Testa, F.; Ghedini, M., Self-incorporation of a luminescent neutral iridium(III) complex in different mesoporous micelle-templated silicas. *New J. Chem.* **2011**, *35* (1), 141-148; (f) Liu, S.; Zhang, J.; Shen, D.; Liang, H.; Liu, X.; Zhao, Q.; Huang, W., Reaction-based phosphorescent nanosensor for ratiometric and time-resolved luminescence imaging of fluoride in live cells. *Chem. Commun.* **2015**, *51*, 12839-12842; (g) Sun, H.; Zhang, J.; Zhang, K. Y.; Liu, S.; Liang, H.; Lv, W.; Qiao, W.; Liu, X.; Yang, T.; Zhao, Q.; Huang, W., Development of Two-Channel Phosphorescent Core–Shell Nanoprobe for Ratiometric and Time-Resolved Luminescence Imaging of Intracellular Oxygen Levels. *Part. Part. Syst. Charac.* **2015**, *32*, 48-53; (h) de Barros e Silva Botelho, M.; Fernandez-Hernandez, J. M.; de Queiroz, T. B.; Eckert, H.; De Cola, L.; de Camargo, A. S. S., Iridium(III)-surfactant complex immobilized in mesoporous silica *via* templated synthesis: a new route to optical materials. *J. Mater. Chem.* **2011**, *21*, 8829-8834.
33. (a) Huo, C.; Zhang, H.; Zhang, H.; Yang, B.; Zhang, P.; Wang, Y., Synthesis and assembly with mesoporous silica MCM-48 of platinum(II) porphyrin complexes bearing carbazyl groups: spectroscopic and oxygen sensing properties. *Inorg. Chem.* **2006**, *45*, 4735-4742; (b) Carlos, L. D.; Ferreira, R. A. S.; de Bermudez, V.; Ribeiro, S. J. L., Lanthanide-Containing Light-Emitting Organic–Inorganic Hybrids: A Bet on the Future. *Adv. Mater.* **2009**, *21*, 509-534; (c) Pasha, S. S.; Fageria, L.; Climent, C.; Rath, N. P.; Alemany, P.; Chowdhury, R.; Roy, A.; Laskar, I. R., Evaluation of novel platinum(II) based AIE compound-encapsulated mesoporous silica nanoparticles for cancer theranostic application. *Dalton Trans.* **2018**, *47*, 4613-4624; (d) Pasha, S.; Alam, P.; Sarmah, A.; Roy, R.; Laskar, I., Encapsulation of multi-stimuli AIE active platinum(II) complex: a facile and dry approach for luminescent mesoporous silica. *RSC Adv.* **2016**, *6*, 87791-87795; (e) Sarmiento, J. T.; Suárez-Pantiga, S.; Olmos, A.; Varea, T.; Asensio, G., Silica-Immobilized NHC-Gold(I) Complexes: Versatile Catalysts for the Functionalization of Alkynes under Batch and Continuous Flow Conditions. *ACS Catalysis* **2017**, *7*, 7146-7155.
34. (a) Lin, X.-X.; Li, Z.-H.; Huang, X.-Y.; Jiang, Y.; Wei, Q.-H.; Chen, G.-N., Pt<sub>2</sub>Ag acetyllide-doped silica nanoparticles: enabling luminescence of Pt<sub>2</sub>Ag complexes in water and sensors for highly sensitive detection of cyanide anions. *Dalton Trans.* **2014**, *43*, 8861-8867; (b) Titos-Padilla, S.; Colacio, E.; Pope, S. J.; Delgado, J. J.; Melgosa, M.; Herrera, J. M., Photophysical properties of [Ir(tpy)<sub>2</sub>]<sup>3+</sup>-doped silica nanoparticles and synthesis of a colour-tunable material based on an Ir(core)–Eu(shell) derivative. *J. Mater. Chem. C* **2013**, *1*, 3808-3815.
35. (a) Lewis, D. J.; Dore, V.; Rogers, N. J.; Mole, T. K.; Nash, G. B.; Angelis, P.; Pikramenou, Z., Silica Nanoparticles for Micro-Particle Imaging Velocimetry: Fluorosurfactant Improves Nanoparticle Stability and Brightness of Immobilized Iridium(III) Complexes. *Langmuir* **2013**, *29*,

- 14701-14708; (b) Rico, M.; Sepulveda, A. E.; Ruiz, S.; Serrano, E.; Berenguer, J. R.; Lalinde, E.; Garcia-Martinez, J., A stable luminescent hybrid mesoporous copper complex-silica. *Chem. Commun.* **2012**, *48*, 8883-8885; (c) Perruchas, S.; Desboeufs, N.; Maron, S.; Goff, X. F.; Fargues, A.; Garcia, A.; Gacoin, T.; Boilot, J.-P., Siloxanol-functionalized copper iodide cluster as a thermochromic luminescent building block. *Inorg. Chem.* **2012**, *51*, 794-798.
36. (a) Corriu, R. J. P.; Mehdi, A.; Reyé, C.; Thieuleux, C., Mesoporous hybrid materials containing two transition metal ions, one in the framework, the other in the channel pores. *Chem. Commun.* **2003**, (13), 1564-1565; (b) Corma, A.; Das, D.; García, H.; Leyva, A., A periodic mesoporous organosilica containing a carbapalladacycle complex as heterogeneous catalyst for Suzuki cross-coupling. *J. Catal.* **2005**, *229*, 322-331; (c) Dufaud, V.; Beauchesne, F.; Bonneviot, L., Organometallic Chemistry Inside the Pore Walls of Mesostructured Silica Materials. *Angew. Chem. Int. Ed.* **2005**, *44*, 3475-3477; (d) Yang, X.; Zhu, F.; Huang, J.; Zhang, F.; Li, H., Phenyl@Rh(I)-Bridged Periodic Mesoporous Organometalsilica with High Catalytic Efficiency in Water-Medium Organic Reactions. *Chem. Mater.* **2009**, *21*, 4925-4933; (e) Huang, J.; Zhu, F.; He, W.; Zhang, F.; Wang, W.; Li, H., Periodic mesoporous organometallic silicas with unary or binary organometals inside the channel walls as active and reusable catalysts in aqueous organic reactions. *J. Am. Chem. Soc.* **2010**, *132*, 1492-1493; (f) Huang, J.; Zhang, F.; Li, H., Organometal-bridged PMOs as efficiency and reusable bifunctional catalysts in one-pot cascade reactions. *Appl. Catal., A* **2012**, *431*-432, 95-103.
37. Serrano, E.; Linares, N.; Garcia-Martinez, J.; Berenguer, J. R., SolGel Coordination Chemistry: Building Catalysts from the Bottom-Up. *ChemCatChem* **2013**, *5*, 844-860.
38. (a) Linares, N.; Sepulveda, A. E.; Pacheco, M. C.; Berenguer, J. R.; Lalinde, E.; Najera, C.; Garcia-Martinez, J., Synthesis of mesoporous metal complex-silica materials and their use as solvent-free catalysts. *New J. Chem.* **2011**, *35*, 225-234; (b) Linares, N.; Sepúlveda, A. E.; Berenguer, J. R.; Lalinde, E.; Garcia-Martinez, J., Mesoporous organosilicas with Pd(II) complexes in their framework. *Microporous Mesoporous Mater.* **2012**, *158*, 300-308; (c) Linares, N.; Serrano, E.; Carrillo, A. I.; Garcia-Martinez, J., Metal-complex ionosilicas: Cationic mesoporous silica with Ni(II) and Cu(II) complexes in their framework. *Mater. Lett.* **2013**, *95*, 93-96.
39. (a) Armelao, L.; Bottaro, G.; Quici, S.; Cavazzini, M.; Raffo, M.; Barigelli, F.; Accorsi, G., Photophysical properties and tunable colour changes of silica single layers doped with lanthanide (III) complexes. *Chem. Commun.* **2007**, 2911-2913; (b) Valenti, G.; Rampazzo, E.; Bonacchi, S.; Petrizza, L.; Marcaccio, M.; Montalti, M.; Prodi, L.; Paolucci, F., Variable doping induces mechanism swapping in electrogenerated chemiluminescence of Ru(bpy)<sub>3</sub><sup>2+</sup> core-shell silica nanoparticles. *J. Am. Chem. Soc.* **2016**, *138*, 15935-15942.
40. Zhao, Q.; Liu, Y.; Cao, Y.; Lv, W.; Yu, Q.; Liu, S.; Liu, X.; Shi, M.; Huang, W., Rational Design of Nanoparticles with Efficient Lanthanide Luminescence Sensitized by Iridium(III) Complex for Time-Gated Luminescence Bioimaging. *Adv. Opt. Mater.* **2015**, *3*, 233-240.
41. (a) Fujita, K. i.; Furukawa, S.; Morishima, N.; Shimizu, M.; Yamaguchi, R., N-Alkylation of Aqueous Ammonia with Alcohols Leading to Primary Amines Catalyzed by Water-Soluble N-Heterocyclic Carbene Complexes of Iridium. *ChemCatChem* **2018**, *10*, 1993-1997; (b) Wan, K. Y.; Roelfes, F.; Lough, A. J.; Hahn, F. E.; Morris, R. H., Iridium and Rhodium Complexes Containing Enantiopure Primary Amine-Tethered N-Heterocyclic Carbenes: Synthesis, Characterization, Reactivity, and Catalytic Asymmetric Hydrogenation of Ketones. *Organometallics* **2018**, *37*, 491-504; (c) Tehfe, M. A.; Lepeltier, M.; Dumur, F.; Gigmes, D.; Fouassier, J. P.; Lalevée, J., Structural Effects in the Iridium Complex Series: Photoredox Catalysis and Photoinitiation of Polymerization Reactions under Visible Lights. *Macromol. Chem. Phys.* **2017**, *218*, 1700192; (d) Suna, Y.; Himeda, Y.; Fujita, E.; Muckerman, J. T.; Ertem, M. Z., Iridium Complexes with Proton-Responsive Azole-Type Ligands as Effective Catalysts for CO<sub>2</sub> Hydrogenation. *ChemSusChem* **2017**, *10*, 4535-4543.
42. Zhang, Q.-C.; Xiao, H.; Zhang, X.; Xu, L.-J.; Chen, Z.-N., Luminescent oligonuclear metal complexes and the use in organic light-emitting diodes. *Coord. Chem. Rev.* **2019**, *378*, 121-133.

43. (a) Ma, D.-L.; Lin, S.; Wang, W.; Yang, C.; Leung, C.-H., Luminescent chemosensors by using cyclometalated iridium(III) complexes and their applications. *Chem. Sci.* **2017**, *8*, 878-889; (b) Chi, Y.; Chang, T.-K.; Ganesan, P.; Rajakannu, P., Emissive bis-tridentate Ir(III) metal complexes: Tactics, photophysics and applications. *Coord. Chem. Rev.* **2017**, *346*, 91-100.
44. (a) Caporale, C.; Massi, M., Cyclometalated iridium (III) complexes for life science. *Coord. Chem. Rev.* **2018**, *363*, 71-91; (b) Chen, Y.; Rees, T. W.; Ji, L.; Chao, H., Mitochondrial dynamics tracking with iridium(III) complexes. *Curr. Opin. Chem. Biol.* **2018**, *43*, 51-57; (c) Daniels, R. E.; McKenzie, L. K.; Shewring, J. R.; Weinstein, J. A.; Kozhevnikov, V. N.; Bryant, H. E., Pyridazine-bridged cationic diiridium complexes as potential dual-mode bioimaging probes. *RSC Adv.* **2018**, *8*, 9670-9676; (d) Liu, J.-B.; Yang, C.; Ko, C.-N.; Vellaisamy, K.; Yang, B.; Lee, M.-Y.; Leung, C.-H.; Ma, D.-L., A long lifetime iridium(III) complex as a sensitive luminescent probe for bisulfite detection in living zebrafish. *Sens. Actuators, B* **2017**, *243*, 971-976; (e) Solomatina, A. I.; Su, S.-H.; Lukina, M. M.; Dudenkova, V. V.; Shcheslavskiy, V. I.; Wu, C.-H.; Chelushkin, P. S.; Chou, P.-T.; Koshevoy, I. O.; Tunik, S. P., Water-soluble cyclometalated platinum(II) and iridium(III) complexes: synthesis, tuning of the photophysical properties, and in vitro and in vivo phosphorescence lifetime imaging. *RSC Adv.* **2018**, *8*, 17224-17236; (f) Zamora, A.; Vigueras, G.; Rodríguez, V.; Santana, M. D.; Ruiz, J., Cyclometalated iridium(III) luminescent complexes in therapy and phototherapy. *Coord. Chem. Rev.* **2018**, *360*, 34-76.
45. (a) Lu, G.-Z.; Tu, Z.-L.; Liu, L.; Zheng, Y.-X.; Zhao, Y., Two platinum(II) complexes with a 4-phenyl-4 H-1, 2, 4-triazole derivative as an ancillary ligand for efficient green OLEDs. *Dalton Trans.* **2019**, *48*, 1892-1899; (b) Fleetham, T.; Li, G.; Li, J., Phosphorescent Pt(II) and Pd(II) Complexes for Efficient, High-Color-Quality, and Stable OLEDs. *Adv. Mater.* **2017**, *29*, 1601861; (c) Strassner, T., Phosphorescent Platinum(II) Complexes with C<sup>4</sup>C<sup>5</sup> Cyclometalated NHC Ligands. *Acc. Chem. Res.* **2016**, *49*, 2680-2689.
46. (a) Pasha, S. S.; Das, P.; Rath, N. P.; Bandyopadhyay, D.; Jana, N. R.; Laskar, I. R., Water soluble luminescent cyclometalated platinum(II) complex—A suitable probe for bio-imaging applications. *Inorg. Chem. Commun.* **2016**, *67*, 107-111; (b) Wu, J.; Li, Y.; Tan, C.; Wang, X.; Zhang, Y.; Song, J.; Qu, J.; Wong, W.-Y., Aggregation-induced near-infrared emitting platinum(II) terpyridyl complex: cellular characterisation and lysosome-specific localisation. *Chem. Commun.* **2018**, *54*, 11144-11147; (c) Li, K.; Tong, G.; Wan, Q.; Cheng, G.; Tong, W.-Y.; Ang, W.-H.; Kwong, W.-L.; Che, C.-M., Highly phosphorescent platinum(II) emitters: photophysics, materials and biological applications. *Chem. Sci.* **2016**, *7*, 1653-1673; (d) Mauro, M.; Aliprandi, A.; Septiadi, D.; Kehr, N. S.; De Cola, L., When self-assembly meets biology: luminescent platinum complexes for imaging applications. *Chem. Soc. Rev.* **2014**, *43*, 4144-4166.
47. (a) Zhang, J.; Zhou, L.; Al-Attar, H. A.; Shao, K.; Wang, L.; Zhu, D.; Su, Z.; Bryce, M. R.; Monkman, A. P., Efficient Light-Emitting Electrochemical Cells (LECs) Based on Ionic Iridium(III) Complexes with 1, 3, 4-Oxadiazole Ligands. *Adv. Funct. Mater.* **2013**, *23*, 4667-4677; (b) Kessler, F.; Costa, R. D.; Di Censo, D.; Scopelliti, R.; Ortí, E.; Bolink, H. J.; Meier, S.; Sarfert, W.; Grätzel, M.; Nazeeruddin, M. K., Near-UV to red-emitting charged bis-cyclometallated iridium(III) complexes for light-emitting electrochemical cells. *Dalton Trans.* **2012**, *41*, 180-191.
48. (a) Choi, W. J.; Choi, S.; Ohkubo, K.; Fukuzumi, S.; Cho, E. J.; You, Y., Mechanisms and applications of cyclometalated Pt(II) complexes in photoredox catalytic trifluoromethylation. *Chem. Sci.* **2015**, *6*, 1454-1464; (b) Lin, S.; Kitamoto, K.; Ozawa, H.; Sakai, K., Improved photocatalytic hydrogen evolution driven by chloro(terpyridine)platinum(II) derivatives tethered to a single pendant viologen acceptor. *Dalton Trans.* **2016**, *45*, 10643-10654; (c) Zhong, J.-J.; Yang, C.; Chang, X.-Y.; Zou, C.; Lu, W.; Che, C.-M., Platinum(II) photo-catalysis for highly selective difluoroalkylation reactions. *Chem. Commun.* **2017**, *53*, 8948-8951.
49. (a) Baggaley, E.; Weinstein, J. A.; Williams, J. A. G., Lighting the way to see inside the live cell with luminescent transition metal complexes. *Coord. Chem. Rev.* **2012**, *256*, 1762-1785; (b) Ma, D. L.; He, H. Z.; Leung, K. H.; Chan, D. S. H.; Leung, C. H., Bioactive luminescent transition-metal complexes for biomedical applications. *Angew. Chem. Int. Ed.* **2013**, *52*, 7666-7682; (c)

- Ruggi, A.; van Leeuwen, F. W. B.; Velders, A. H., Interaction of dioxygen with the electronic excited state of Ir(III) and Ru(II) complexes: Principles and biomedical applications. *Coord. Chem. Rev.* **2011**, 255, 2542-2554; (d) Lincoln, R.; Kohler, L.; Monro, S.; Yin, H.; Stephenson, M.; Zong, R.; Chouai, A.; Dorsey, C.; Hennigar, R.; Thummel, R. P.; McFarland, S. A., Exploitation of Long-Lived <sup>3</sup>IL Excited States for Metal–Organic Photodynamic Therapy: Verification in a Metastatic Melanoma Model. *J. Am. Chem. Soc.* **2013**, 135, 17161-17175.
50. (a) Im, Y.; Byun, S. Y.; Kim, J. H.; Lee, D. R.; Oh, C. S.; Yook, K. S.; Lee, J. Y., Recent Progress in High-Efficiency Blue-Light-Emitting Materials for Organic Light-Emitting Diodes. *Adv. Func. Mater.* **2017**, 27, 1603007; (b) Henwood, A. F.; Zysman-Colman, E., Lessons learned in tuning the optoelectronic properties of phosphorescent iridium(III) complexes. *Chem. Commun.* **2017**, 53, 807-826; (c) Henwood, A. F.; Zysman-Colman, E., Luminescent Iridium Complexes Used in Light-Emitting Electrochemical Cells (LEECs). *Top. Curr. Chem.* **2016**, 374, 1-41; (d) Ma, D.; Tsuboi, T.; Qiu, Y.; Duan, L., Recent progress in ionic iridium(III) complexes for organic electronic devices. *Adv. Mater.* **2017**, 29, 1603253; (e) Reddy, M. L. P.; Bejoymohandas, K. S., Evolution of 2, 3'-bipyridine class of cyclometalating ligands as efficient phosphorescent iridium(III) emitters for applications in organic light emitting diodes. *J. Photochem. Photobiol., C* **2016**, 29, 29-47.
51. Chou, P.-T.; Chi, Y.; Chung, M.-W.; Lin, C.-C., Harvesting luminescence via harnessing the photophysical properties of transition metal complexes. *Coord. Chem. Rev.* **2011**, 255, 2653-2665.
52. (a) Yersin, H.; Rausch, A. F.; Czerwieniec, R.; Hofbeck, T.; Fischer, T., The triplet state of organo-transition metal compounds. Triplet harvesting and singlet harvesting for efficient OLEDs. *Coord. Chem. Rev.* **2011**, 255, 2622-2652; (b) Rausch, A. F.; Homeier, H. H.; Yersin, H., Organometallic Pt(II) and Ir(III) triplet emitters for OLED applications and the role of spin-orbit coupling: A study based on high-resolution optical spectroscopy. In *Photophysics of Organometallics*, Springer: Berlin, Heidelberg, **2010**; pp 193-235; (c) Xu, H.; Chen, R.; Sun, Q.; Lai, W.; Su, Q.; Huang, W.; Liu, X., Recent progress in metal–organic complexes for optoelectronic applications. *Chem. Soc. Rev.* **2014**, 43, 3259-3302.
53. (a) Yoshida, M.; Kato, M., Regulation of metal–metal interactions and chromic phenomena of multi-decker platinum complexes having π-systems. *Coord. Chem. Rev.* **2018**, 355, 101-115; (b) Yam, V. W.-W.; Au, V. K.-M.; Leung, S. Y.-L., Light-Emitting Self-Assembled Materials Based on d<sup>8</sup> and d<sup>10</sup> Transition Metal Complexes. *Chem. Rev.* **2015**, 115, 7589-7728; (c) Alessandro, A.; Damiano, G.; Matteo, M.; Luisa, D. C., *Chem. Lett.* **2015**, 44, 1152-1169; (d) Gray, H. B.; Záliš, S.; Vlček, A., Electronic structures and photophysics of d<sup>8</sup>-d<sup>8</sup> complexes. *Coord. Chem. Rev.* **2017**, 345, 297-317; (e) Atoini, Y.; Prasetyanto, E. A.; Chen, P.; Silvestrini, S.; Harrowfield, J.; De Cola, L., Luminescence of Amphiphilic Pt<sup>II</sup> Complexes Controlled by Confinement. *Chem. Eur. J.* **2018**, 24, 12054-12060.
54. (a) Carrara, S.; Aliprandi, A.; Hogan, C. F.; De Cola, L., Aggregation-induced electrochemiluminescence of platinum(II) complexes. *J. Am. Chem. Soc.* **2017**, 139, 14605-14610; (b) Alessandro, A.; Damiano, G.; Matteo, M.; Luisa, D. C., Recent Advances in Phosphorescent Pt(II) Complexes Featuring Metallophilic Interactions: Properties and Applications. *Chem. Lett.* **2015**, 44, 1152-1169; (c) Tang, M.-C.; Chan, A. K.-W.; Chan, M.-Y.; Yam, V. W.-W., Platinum and Gold Complexes for OLEDs. *Top. Curr. Chem.* **2016**, 374, 67-110; (d) Yam, V.; Au, V.; Leung, S., Light-Emitting Self-Assembled Materials Based on d<sup>8</sup> and d<sup>10</sup> Transition Metal Complexes. *Chem. Rev.* **2015**, 115, 7598-7728; (e) Berenguer, J. R.; Lalinde, E.; Moreno, T. M.; Sánchez, S.; Torroba, J., Facile Metalation of Hbzq by [cis-Pt(C<sub>6</sub>F<sub>5</sub>)<sub>2</sub>(thf)<sub>2</sub>]: A Route to a Pentafluorophenyl Benzoquinolate Solvate Complex That Easily Coordinates Terminal Alkynes. Spectroscopic and Optical Properties. *Inorg. Chem.* **2012**, 51, 11665-11679; (f) Díez, Á.; Lalinde, E.; Moreno, M. T., Heteropolynuclear cycloplatinated complexes: Structural and photophysical properties. *Coord. Chem. Rev.* **2011**, 255, 2426-2447.
55. (a) Wenger, O. S., Vapochromism in Organometallic and Coordination Complexes: Chemical Sensors for Volatile Organic Compounds. *Chem. Rev.* **2013**, 113, 3686-3733; (b)

- McConnell, A. J.; Wood, C. S.; Neelakandan, P. P.; Nitschke, J. R., Stimuli-Responsive Metal-Ligand Assemblies. *Chem. Rev.* **2015**, *115*, 7729-7793; (c) Sagara, Y.; Yamane, S.; Mitani, M.; Weder, C.; Kato, T., Mechanoresponsive luminescent molecular assemblies: an emerging class of materials. *Adv. Mat.* **2016**, *28*, 1073-1095; (d) Xue, P.; Ding, J.; Wang, P.; Lu, R., Recent progress in the mechanochromism of phosphorescent organic molecules and metal complexes. *J. Mat. Chem. C* **2016**, *4*, 6688-6706.
56. (a) Kobayashi, A.; Kato, M., Vapochromic Platinum(II) Complexes: Crystal Engineering toward Intelligent Sensing Devices. *Eur. J. Inorg. Chem.* **2014**, *2014*, 4469-4483; (b) Zhang, X.; Li, B.; Chen, Z.-H.; Chen, Z.-N., Luminescence vapochromism in solid materials based on metal complexes for detection of volatile organic compounds (VOCs). *J. Mater. Chem.* **2012**, *22*, 11427-11441.
57. Schmid, B.; Garces, F. O.; Watts, R. J., Synthesis and characterizations of cyclometalated iridium(III) solvento complexes. *Inorg. Chem.* **1994**, *33*, 9-14.
58. Forniés, J.; Fuertes, S.; López, J. A.; Martín, A.; Sicilia, V., New Water Soluble and Luminescent Platinum(II) Compounds, Vapochromic Behavior of  $[K(H_2O)][Pt(bzq)(CN)_2]$ , New Examples of the Influence of the Counterion on the Photophysical Properties of  $d^8$  Square-Planar Complexes. *Inorg. Chem.* **2008**, *47*, 7166-7176.
59. Nakamoto, K., *Infrared and Raman Spectra of Inorganic and Coordination Compounds. Part B Applications in Coordination, Organometallic, and Bioinorganic Chemistry*. 6<sup>th</sup> ed.; John Wiley & Sons Inc.: New Jersey, **2009**.
60. Laflamme, P.; Beaudoin, A.; Chapaton, T.; Spino, C.; Soldera, A., Simulated infrared spectra of triflic acid during proton dissociation. *J. Comput. Chem.* **2012**, *33*, 1190-1196.
61. (a) Díez, A.; Forniés, J.; García, A.; Lalinde, E.; Moreno, M. T., Synthesis, Structural Characterization, and Photophysical Properties of Palladium and Platinum(II) Complexes Containing 7,8-Benzoquinolinate and Various Phosphine Ligands. *Inorg. Chem.* **2005**, *44*, 2443-2453; (b) Haghghi, M. G.; Nabavizadeh, S. M.; Rashidi, M.; Kubicki, M., Selectivity in metal-carbon bond protonolysis in p-tolyl-(or methyl)-cycloplatinated(II) complexes: kinetics and mechanism of the uncatalyzed isomerization of the resulting Pt(II) products. *Dalton Trans.* **2013**, *42*, 13369-13380; (c) Berenguer, J. R.; Pichel, J. G.; Giménez, N.; Lalinde, E.; Moreno, M. T.; Pineiro-Hermida, S., Luminescent pentafluorophenyl-cycloplatinated complexes: synthesis, characterization, photophysics, cytotoxicity and cellular imaging. *Dalton Trans.* **2015**, *44*, 18839-18855; (d) Martín, A.; Belío, Ú.; Fuertes, S.; Sicilia, V., Luminescent Pt–Ag Clusters Based on Neutral Benzoquinolate Cyclometalated Platinum Complexes. *Eur. J. Inorg. Chem.* **2013**, *2013*, 2231-2247.
62. Giménez, N.; Lara, R.; Moreno, M. T.; Lalinde, E., Facile Approaches to Phosphorescent Bis(cyclometalated) Pentafluorophenyl Pt<sup>IV</sup> Complexes: Photophysics and Computational Studies. *Chem Eur. J.* **2017**, *23*, 5758-5771.
63. Chin, C.; Eum, M. S.; yi Kim, S.; Kim, C.; Kang, S., Blue-Light-Emitting Complexes: Cationic (2-Phenylpyridinato)iridium(III) Complexes with Strong-Field Ancillary Ligands. *Eur. J. Inorg. Chem.* **2007**, *2007*, 372-375.
64. (a) Ravotto, L.; Ceroni, P., Aggregation induced phosphorescence of metal complexes: from principles to applications. *Coord. Chem. Rev.* **2017**, *346*, 62-76; (b) Mei, J.; Hong, Y.; Lam, J. W. Y.; Qin, A.; Tang, Y.; Tang, B., Aggregation-Induced Emission: The Whole Is More Brilliant than the Parts. *Adv. Mater.* **2014**, *26*, 5429-5479; (c) Maji, S.; Alam, P.; Kumar, G.; Biswas, S.; Sarkar, P.; Das, B.; Rehman, I.; Das, B.; Jana, N.; Laskar, I.; Acharya, S., Induced Aggregation of AIE-Active Mono-Cyclometalated Ir(III) Complex into Supramolecular Branched Wires for Light-Emitting Diodes. *Small* **2017**, *1603780*; (d) Wu, Y.; Sun, H.-Z.; Cao, H.-T.; Li, H.-B.; Shan, G.-G.; Duan, Y.-A.; Geng, Y.; Su, Z.-M.; Liao, Y., Stepwise modulation of the electron-donating strength of ancillary ligands: understanding the AIE mechanism of cationic iridium(III) complexes. *Chem. Commun.* **2014**, *50*, 10986-10989; (e) Shan, G.-G.; Li, H.-B.; Qin, J.-S.; Zhu, D.-X.; Liao, Y.; Su, Z.-M., Piezochromic luminescent (PCL) behavior and aggregation-induced emission (AIE) property of a new cationic iridium(III) complex. *Dalton Trans.* **2012**, *41*, 9590-9593.

65. (a) Chan, M. H.-Y.; Ng, M.; Leung, S. Y.-L.; Lam, W. H.; Yam, V. W.-W., Synthesis of luminescent Platinum (II) 2,6-bis(N-dodecylbenzimidazol-2'-yl) pyridine foldamers and their supramolecular assembly and metallogel formation. *J. Am. Chem. Soc.* **2017**, *139*, 8639-8645; (b) Lalinde, E.; Lara, R.; López, I. P.; Moreno, M. T.; Alfaro-Arnedo, E.; Pichel, J. G.; Piñeiro-Hermida, S., Benzothiazole-Based Cycloplatinated Chromophores: Synthetic, Optical, and Biological Studies. *Chem. Eur. J.* **2018**, *24*, 2440-2456; (c) Au-Yeung, H.-L.; Tam, A. Y.-Y.; Leung, S. Y.-L.; Yam, V. W.-W., Supramolecular assembly of platinum-containing polyhedral oligomeric silsesquioxanes: an interplay of intermolecular interactions and a correlation between structural modifications and morphological transformations. *Chem. Sci.* **2017**, *8*, 2267-2276; (d) Cheng, H.-K.; Yeung, M. C.-L.; Yam, V. W.-W., Molecular Engineering of Platinum(II) Terpyridine Complexes with Tetraphenylethylene-Modified Alkynyl Ligands: Supramolecular Assembly via Pt...Pt and/or π-π Stacking Interactions and the Formation of Various Superstructures. *ACS Appl. Mater. Interfaces* **2017**, *9*, 36220-36228.
66. Grau, A.; Baeza, A.; Serrano, E.; Garcia-Martinez, J.; Najera, C., Mesoporous Metal Complex-Silica Aerogels for Environmentally Friendly Amination of Allylic Alcohols. *ChemCatChem* **2015**, *7*, 87-93.
67. (a) Huo, J.; Fang, L.; Lei, Y.; Zeng, G.; Zeng, H., Facile preparation of yttrium and aluminum co-doped ZnO via a sol-gel route for photocatalytic hydrogen production. *J. Mater. Chem. A* **2014**, *2*, 11040-11044; (b) Qin, J.; Zeng, H., Photocatalysts fabricated by depositing plasmonic Ag nanoparticles on carbon quantum dots/graphitic carbon nitride for broad spectrum photocatalytic hydrogen generation. *Appl. Catal., B* **2017**, *209*, 161-173.
68. Qin, J.; Huo, J.; Zhang, P.; Zeng, J.; Wang, T.; Zeng, H., Improving the photocatalytic hydrogen production of Ag/gC<sub>3</sub>N<sub>4</sub> nanocomposites by dye-sensitization under visible light irradiation. *Nanoscale* **2016**, *8*, 2249-2259.
69. Thommes, M.; Kaneko, K.; Neimark, A. V.; Olivier, J. P.; Rodriguez-Reinoso, F.; Rouquerol, J.; Sing, K. S. W., Physisorption of gases, with special reference to the evaluation of surface area and pore size distribution (IUPAC Technical Report). *Pure Appl. Chemistry* **2015**, *87*, 1051-1069.
70. Nunes, C. D.; Valente, A. A.; Pillinger, M.; Fernandes, A. C.; Romao, C. C.; Rocha, J.; Goncalves, I. S., MCM-41 functionalized with bipyridyl groups and its use as a support for oxomolybdenum(VI) catalysts. *J. Mater. Chem.* **2002**, *12*, 1735-1742.
71. (a) Mrowiec-Białoń, J.; Pajak, L.; Jarzębski, A. B.; Lachowski, A. I.; Malinowski, J. J., Morphology of Silica Aerogels Obtained from the Process Catalyzed by NH<sub>4</sub>F and NH<sub>4</sub>OH. *Langmuir* **1997**, *13*, 6310-6314; (b) Casas, L.; Roig, A.; Rodríguez, E.; Molins, E.; Tejada, J.; Sort, J., Silica aerogel-iron oxide nanocomposites: structural and magnetic properties. *J. Non-Cryst. Solids* **2001**, *285*, 37-43; (c) Venkateswara Rao, A.; Bhagat, S. D.; Hirashima, H.; Pajonk, G. M., Synthesis of flexible silica aerogels using methyltrimethoxysilane (MTMS) precursor. *J. Colloid Interface Sci.* **2006**, *300*, 279-285; (d) Soleimani Dorcheh, A.; Abbasi, M. H., Silica aerogel; synthesis, properties and characterization. *J. Mater. Process. Technol.* **2008**, *199*, 10-26; (e) Musgo, J.; Echeverría, J. C.; Estella, J.; Laguna, M.; Garrido, J. J., Ammonia-catalyzed silica xerogels: Simultaneous effects of pH, synthesis temperature, and ethanol:TEOS and water:TEOS molar ratios on textural and structural properties. *Microporous Mesoporous Mater.* **2009**, *118*, 280-287; (f) Echeverría, J. C.; Faustini, M.; Garrido, J. J., Effects of the porous texture and surface chemistry of silica xerogels on the sensitivity of fiber-optic sensors toward VOCs. *Sens. Actuators, B* **2016**, *222*, 1166-1174.
72. Humphreys, C. J., Solid-state lighting. *MRS Bull.* **2008**, *33*, 459-470.
73. Ye, S.; Xiao, F.; Pan, Y.; Ma, Y.; Zhang, Q., Phosphors in phosphor-converted white light-emitting diodes: Recent advances in materials, techniques and properties. *Mater. Sci. Eng., R* **2010**, *71*, 1-34.
74. Gaspar, D. J.; Polikarpov, E., *OLED fundamentals: materials, devices, and processing of organic light-emitting diodes*. CRC press: 2015.

75. Costa, R. D., Light-Emitting Electrochemical Cells. *Light-Emitting Electrochemical Cells*, ISBN 978-3-319-58612-0. Springer International Publishing AG, 2017 2017.
76. Zhao, D.; Qin, Z.; Huang, J.; Yu, J., Progress on material, structure and function for tandem organic light-emitting diodes. *Org. Electron.* **2017**, *51*, 220-242.
77. (a) Chen, J.; Zhao, F.; Ma, D., Hybrid white OLEDs with fluorophors and phosphors. *Mater. Today* **2014**, *17*, 175-183; (b) Gather, M. C.; Könen, A.; Meerholz, K., White organic light-emitting diodes. *Adv. Mater.* **2011**, *23*, 233-248.
78. Kido, J.; Hongawa, K.; Okuyama, K.; Nagai, K., White light-emitting organic electroluminescent devices using the poly (N-vinylcarbazole) emitter layer doped with three fluorescent dyes. *Appl. Phys. Lett.* **1994**, *64*, 815-817.
79. (a) Kamtekar, K. T.; Monkman, A. P.; Bryce, M. R., Recent Advances in White Organic Light-Emitting Materials and Devices (WOLEDs). *Adv. Mater.* **2010**, *22*, 572-582; (b) Zhao, F.; Ma, D., Approaches to high performance white organic light-emitting diodes for general lighting. *Mater. Chem. Front.* **2017**, *1*, 1933-1950.
80. Cho, J.; Park, J. H.; Kim, J. K.; Schubert, E. F., White light-emitting diodes: History, progress, and future. *Laser Photon. Rev.* **2017**, *11*, 1600147.
81. (a) Dai, P.-P.; Li, C.; Zhang, X.-T.; Xu, J.; Chen, X.; Wang, X.-L.; Jia, Y.; Wang, X.; Liu, Y.-C., A single Eu<sup>2+</sup>-activated high-color-rendering oxychloride white-light phosphor for white-light-emitting diodes. *Light Sci. Appl.* **2016**, *5*, e16024; (b) Chen, L.; Lin, C.-C.; Yeh, C.-W.; Liu, R.-S., Light converting inorganic phosphors for white light-emitting diodes. *Mater.* **2010**, *3*, 2172-2195; (c) Cheng, W.; Rechberger, F.; Niederberger, M., Three-dimensional assembly of yttrium oxide nanosheets into luminescent aerogel monoliths with outstanding adsorption properties. *ACS Nano* **2016**, *10*, 2467-2475; (d) Tolhurst, T. M.; Schmiechen, S.; Pust, P.; Schmidt, P. J.; Schnick, W.; Moewes, A., Electronic structure, bandgap, and thermal quenching of Sr [Mg<sub>3</sub>SiN<sub>4</sub>]:Eu<sup>2+</sup> in comparison to Sr [LiAl<sub>3</sub>N<sub>4</sub>]:Eu<sup>2+</sup>. *Adv. Opt. Mater.* **2016**, *4*, 584-591.
82. (a) ([https://energy.gov/sites/prod/files/2016/06/f32/ssl\\_rd-plan\\_%20jun2016\\_0.pdf](https://energy.gov/sites/prod/files/2016/06/f32/ssl_rd-plan_%20jun2016_0.pdf)). U.S. Department of Energy ; (b) Denneman, J., Voice of the Lighting Industry in Europe Opens Exciting Opportunities for the European Lighting Industry. **2016**; (c) Shang, Y.-M.; Wang, G.-S.; Sliney, D.; Yang, C.-H.; Lee, L.-L., White Light-Emitting Diodes (LEDs) at Domestic Lighting Levels and Retinal Injury in a Rat Model. *Environ. Health Perspect.* **2014**, *122*, 269-276; (d) Eckle, T., Editorial: Health Impact and Management of a Disrupted Circadian Rhythm and Sleep in Critical Illnesses. *Curr. Pharm. Des.* **2015**, *21*, 3428-3430; (e) Krigel, A.; Berdugo, M.; Picard, E.; Levy-Boukris, R.; Jaadane, I.; Jonet, L.; Dernigoghossian, M.; Andrieu-Soler, C.; Torriglia, A.; Behar-Cohen, F., Light-induced retinal damage using different light sources, protocols and rat strains reveals LED phototoxicity. *Neuroscience* **2016**, *339*, 296-307.
83. (a) Niklaus, L.; Tansaz, S.; Dakhlil, H.; Weber, K. T.; Pröschel, M.; Lang, M.; Kostrzewa, M.; Coto, P. B.; Detsch, R.; Sonnewald, U., Micropatterned Down-Converting Coating for White Bio-Hybrid Light-Emitting Diodes. *Adv. Funct. Mater.* **2017**, *27*, 1601792; (b) Fresta, E.; Fernández-Luna, V.; Coto, P. B.; Costa, R. D., Merging Biology and Solid-State Lighting: Recent Advances in Light-Emitting Diodes Based on Biological Materials. *Adv. Funct. Mater.* **2018**, *28*, 1707011; (c) Fernández-Luna, V.; Coto, P. B.; Costa, R. D., When Fluorescent Proteins Meet White Light-Emitting Diodes. *Angew. Chem. Int. Ed.* **2018**, *57*, 8826-8836; (d) Schlotter, P.; Schmidt, R.; Schneider, J., Luminescence conversion of blue light emitting diodes. *Appl. Phys. A* **1997**, *64*, 417-418.
84. (a) Sun, C.-Y.; Wang, X.-L.; Zhang, X.; Qin, C.; Li, P.; Su, Z.-M.; Zhu, D.-X.; Shan, G.-G.; Shao, K.-Z.; Wu, H., Efficient and tunable white-light emission of metal-organic frameworks by iridium-complex encapsulation. *Nat. Commun.* **2013**, *4*, 2717; (b) Cui, Y.; Song, T.; Yu, J.; Yang, Y.; Wang, Z.; Qian, G., Dye Encapsulated Metal-Organic Framework for Warm-White LED with High Color-Rendering Index. *Adv. Funct. Mater.* **2015**, *25*, 4796-4802; (c) Gong, Q.; Hu, Z.; Deibert, B. J.; Emge, T. J.; Teat, S. J.; Banerjee, D.; Mussman, B.; Rudd, N. D.; Li, J., Solution processable MOF yellow phosphor with exceptionally high quantum efficiency. *J. Am. Chem. Soc.* **2014**, *136*, 16724-

- 16727; (d) Lu, Y.; Yan, B., Lanthanide organic–inorganic hybrids based on functionalized metal–organic frameworks (MOFs) for a near-UV white LED. *Chem. Commun.* **2014**, *50*, 15443-15446.
85. (a) Zhou, D.; Zou, H.; Liu, M.; Zhang, K.; Sheng, Y.; Cui, J.; Zhang, H.; Yang, B., Surface Ligand Dynamics-Guided Preparation of Quantum Dots–Cellulose Composites for Light-Emitting Diodes. *ACS Appl. Mater. Interfaces* **2015**, *7*, 15830-15839; (b) Tetsuka, H.; Nagoya, A.; Asahi, R., Highly luminescent flexible amino-functionalized graphene quantum dots@ cellulose nanofiber-clay hybrids for white-light emitting diodes. *J. Mater. Chem. C* **2015**, *3*, 3536-3541.
86. (a) Weber, M. D.; Niklaus, L.; Pröschel, M.; Coto, P. B.; Sonnewald, U.; Costa, R. D., Bioinspired Hybrid White Light-Emitting Diodes. *Adv. Mater.* **2015**, *27*, 5493-5498; (b) Niklaus, L.; Dakhlil, H.; Kostrzewa, M.; Coto, P. B.; Sonnewald, U.; Wierschem, A.; Costa, R. D., Easy and versatile coating approach for long-living white hybrid light-emitting diodes. *Mater. Horiz.* **2016**, *3*, 340-347.
87. Berenguer, J. R.; Lalinde, E.; Moreno, M. T., Luminescent cyclometalated-pentafluorophenyl Pt<sup>II</sup>, Pt<sup>IV</sup> and heteropolynuclear complexes. *Coord. Chem. Rev.* **2018**, *366*, 69-90.
88. (a) Meng, G.; Chen, Z.; Tang, H.; Liu, Y.; Wei, L.; Wang, Z., Application of a novel cationic iridium(III) complex as a red phosphor in warm white light-emitting diodes. *New J. Chem.* **2015**, *39*, 9535-9542; (b) Kim, O.-H.; Ha, S.-W.; Kim, J. I.; Lee, J.-K., Excellent photostability of phosphorescent nanoparticles and their application as a color converter in light emitting diodes. *ACS Nano* **2010**, *4*, 3397-3405; (c) Costa, R. D.; Ortí, E.; Bolink, H. J.; Monti, F.; Accorsi, G.; Armaroli, N., Luminescent ionic transition-metal complexes for light-emitting electrochemical cells. *Angew. Chem. Int. Ed.* **2012**, *51*, 8178-8211.
89. Yao, E. P.; Yang, Z.; Meng, L.; Sun, P.; Dong, S.; Yang, Y.; Yang, Y., High-Brightness Blue and White LEDs based on Inorganic Perovskite Nanocrystals and their Composites. *Adv. Mater.* **2017**, *29*, 1606859.
90. Yang, H.; Meng, G.; Zhou, Y.; Tang, H.; Zhao, J.; Wang, Z., The photoluminescent properties of new cationic iridium(III) complexes using different anions and their applications in white light-emitting diodes. *Materials* **2015**, *8*, 6105-6116.
91. Sahin, C.; Goren, A.; Demir, S.; Cavus, M. S., New amide based iridium(III) complexes: synthesis, characterization, photoluminescence and DFT/TD-DFT studies. *New J. Chem.* **2018**, *42*, 2979-2988.
92. (a) Tinker, L. L.; McDaniel, N. D.; Curtin, P. N.; Smith, C. K.; Ireland, M. J.; Bernhard, S., Visible light induced catalytic water reduction without an electron relay. *Chem. Eur. J.* **2007**, *13*, 8726-8732; (b) Costa, R. D.; Ortí, E.; Bolink, H. J.; Gruber, S.; Schaffner, S.; Neuburger, M.; Housecroft, C. E.; Constable, E. C., Archetype Cationic Iridium Complexes and Their Use in Solid-State Light-Emitting Electrochemical Cells. *Adv. Funct. Mater.* **2009**, *19*, 3456-3463.
93. Ezquerro, C.; Sepúlveda, A.; Grau-Atienza, A.; Serrano, E.; Lalinde, E.; Berenguer, J. R.; Garcia-Martinez, J., Organometallic phosphors as building blocks in sol-gel chemistry: luminescent organometallo-silica materials. *J. Mater. Chem. C* **2017**, *5*, 9721-9732.
94. Bonacchi, S.; Genovese, D.; Juris, R.; Montalti, M.; Prodi, L.; Rampazzo, E.; Zaccheroni, N., Luminescent silica nanoparticles: extending the frontiers of brightness. *Angew. Chem. Int. Ed.* **2011**, *50*, 4056-4066.
95. Donato, L.; Atoini, Y.; Prasetyanto, E. A.; Chen, P.; Rosticher, C.; Bizzarri, C.; Rissanen, K.; De Cola, L., Selective Encapsulation and Enhancement of the Emission Properties of a Luminescent Cu(I) Complex in Mesoporous Silica. *Helv. Chim. Acta* **2018**, *101*, e1700273.
96. (a) Di, X.; Shen, L.; Jiang, J.; He, M.; Cheng, Y.; Zhou, L.; Liang, X.; Xiang, W., Efficient white LEDs with bright green-emitting CsPbBr<sub>3</sub> perovskite nanocrystal in mesoporous silica nanoparticles. *J. Alloy. Comp.* **2017**, *729*, 526-532; (b) Qu, Y.; Feng, L.; Liu, B.; Tong, C.; Lü, C., A facile strategy for synthesis of nearly white light emitting mesoporous silica nanoparticles. *Colloids Surf. A* **2014**, *441*, 565-571; (c) Gai, F.; Zhou, T.; Zhang, L.; Li, X.; Hou, W.; Yang, X.; Li, Y.; Zhao, X.; Xu, D.; Liu, Y., Silica cross-linked nanoparticles encapsulating fluorescent conjugated

- dyes for energy transfer-based white light emission and porphyrin sensing. *Nanoscale* **2012**, *4*, 6041-6049; (d) Luwang, M. N.; Ningthoujam, R. S.; Srivastava, S. K.; Vatsa, R. K., Preparation of white light emitting  $\text{YVO}_4:\text{Ln}^{3+}$  and silica-coated  $\text{YVO}_4:\text{Ln}^{3+}$ ( $\text{Ln}^{3+} = \text{Eu}^{3+}, \text{Dy}^{3+}, \text{Tm}^{3+}$ ) nanoparticles by CTAB/n-butanol/hexane/water microemulsion route: energy transfer and site symmetry studies. *J. Mater. Chem.* **2011**, *21*, 5326-5337; (e) Malinge, J.; Allain, C.; Brosseau, A.; Audebert, P., White fluorescence from core-shell silica nanoparticles. *Angew. Chem. Int. Ed.* **2012**, *124*, 8662-8665; (f) Liu, C.; Zhao, Z.; Zhang, R.; Yang, L.; Wang, Z.; Yang, J.; Jiang, H.; Han, M.-Y.; Liu, B.; Zhang, Z., Strong infrared laser ablation produces white-light-emitting materials via the formation of silicon and carbon dots in silica nanoparticles. *J. Phys. Chem. C* **2015**, *119*, 8266-8272; (g) Melucci, M.; Zambianchi, M.; Barbarella, G.; Manet, I.; Montalti, M.; Bonacchi, S.; Rampazzo, E.; Rambaldi, D. C.; Zattoni, A.; Reschiglian, P., Facile tuning from blue to white emission in silica nanoparticles doped with oligothiophene fluorophores. *J. Mater. Chem.* **2010**, *20*, 9903-9909.
97. (a) Pritchard, V. E.; Rota Martir, D.; Zysman-Colman, E.; Hardie, M. J., Multimetallic and Mixed Environment Iridium(III) Complexes: A Modular Approach to Luminescence Tuning Using a Host Platform. *Chem. Eur. J.* **2017**, *23*, 8839-8849; (b) Muñoz-Rodríguez, R.; Buñuel, E.; Fuentes, N.; Williams, J. G.; Cárdenas, D. J., A heterotrimetallic Ir(III), Au(III) and Pt(II) complex incorporating cyclometallating bi-and tridentate ligands: simultaneous emission from different luminescent metal centres leads to broad-band light emission. *Dalton Trans.* **2015**, *44*, 8394-8405.
98. (a) Findlay, N. J.; Bruckbauer, J.; Inigo, A. R.; Breig, B.; Arumugam, S.; Wallis, D. J.; Martin, R. W.; Skabara, P. J., An Organic Down-Converting Material for White-Light Emission from Hybrid LEDs. *Adv. Mater.* **2014**, *26*, 7290-7294; (b) Zhou, D.; Zou, H.; Liu, M.; Zhang, K.; Sheng, Y.; Cui, J.; Zhang, H.; Yang, B., Surface Ligand Dynamics-Guided Preparation of Quantum Dots–Cellulose Composites for Light-Emitting Diodes. *ACS App. Mater. Interfaces* **2015**, *7*, 15830-15839.
99. (a) Barreto, J. A.; O’Malley, W.; Kubeil, M.; Graham, B.; Stephan, H.; Spiccia, L., Nanomaterials: applications in cancer imaging and therapy. *Adv. Mater.* **2011**, *23*, H18-H40; (b) Yucai, W.; Suk, S. M.; S., L. N.; Hsing-Wen, S.; Younan, X., Stimuli-Responsive Materials for Controlled Release of Theranostic Agents. *Adv. Funct. Mater.* **2014**, *24*, 4206-4220; (c) Mukherjee, S.; Patra, C. R., Therapeutic application of anti-angiogenic nanomaterials in cancers. *Nanoscale* **2016**, *8*, 12444-12470.
100. Kilina, S. V.; Tamukong, P. K.; Kilin, D. S., Surface Chemistry of Semiconducting Quantum Dots: Theoretical Perspectives. *Acc. Chem. Res.* **2016**, *49*, 2127-2135.
101. (a) Chen, W.; Zhang, S.; Yu, Y.; Zhang, H.; He, Q., Structural-Engineering Rationales of Gold Nanoparticles for Cancer Theranostics. *Adv. Mater.* **2016**, *28*, 8567-8585; (b) Kim, H.; Chung, K.; Lee, S.; Kim, D. H.; Lee, H., Near-infrared light-responsive nanomaterials for cancer theranostics. *Wiley Interdiscip. Rev. Nanomed. Nanobiotechnol.* **2016**, *8*, 23-45.
102. (a) Hachani, R.; Lowdell, M.; Birchall, M.; Hervault, A.; Mertz, D.; Begin-Colin, S.; Thanh, N. T. K., Polyol synthesis, functionalisation, and biocompatibility studies of superparamagnetic iron oxide nanoparticles as potential MRI contrast agents. *Nanoscale* **2016**, *8*, 3278-3287; (b) Huang, Y.; Mao, K.; Zhang, B.; Zhao, Y., Superparamagnetic iron oxide nanoparticles conjugated with folic acid for dual target-specific drug delivery and MRI in cancer theranostics. *Mater. Sci. Eng. C* **2017**, *70*, 763-771.
103. (a) Li, B.; Wen, H. M.; Cui, Y.; Zhou, W.; Qian, G.; Chen, B., Emerging multifunctional metal-organic framework materials. *Adv. Mater.* **2016**, *28*, 8819-8860; (b) Cai, W.; Chu, C. C.; Liu, G.; Wang, Y. X. J., Metal-organic framework-based nanomedicine platforms for drug delivery and molecular imaging. *Small* **2015**, *11* (37), 4806-4822; (c) Zhao, H.-X.; Zou, Q.; Sun, S.-K.; Yu, C.; Zhang, X.; Li, R.-J.; Fu, Y.-Y., Theranostic metal-organic framework core-shell composites for magnetic resonance imaging and drug delivery. *Chem. Sci.* **2016**, *7*, 5294-5301.

104. Behzadi, S.; Serpooshan, V.; Tao, W.; Hamaly, M. A.; Alkawareek, M. Y.; Dreden, E. C.; Brown, D.; Alkilany, A. M.; Farokhzad, O. C.; Mahmoudi, M., Cellular uptake of nanoparticles: journey inside the cell. *Chem. Soc. Rev.* **2017**, *46*, 4218-4244.
105. Wani, W. A.; Prashar, S.; Shreaz, S.; Gómez-Ruiz, S., Nanostructured materials functionalized with metal complexes: in search of alternatives for administering anticancer metallodrugs. *Coord. Chem. Rev.* **2016**, *312*, 67-98.
106. Croissant, J. G.; Fatieiev, Y.; Khashab, N. M., Degradability and clearance of silicon, organosilica, silsesquioxane, silica mixed oxide, and mesoporous silica nanoparticles. *Adv. Mater.* **2017**, *29*, 1604634.
107. (a) Liu, C.; Yu, H.; Li, Q.; Zhu, C.; Xia, Y., Brighter, More Stable, and Less Toxic: A Host-Guest Interaction-Aided Strategy for Fabricating Fluorescent Silica Nanoparticles and Applying Them in Bioimaging and Biosensing at the Cellular Level. *ACS Appl. Mater. Interfaces* **2018**, *10*, 16291-16298; (b) Yan, L.; Zhang, Y.; Xu, B.; Tian, W., Fluorescent nanoparticles based on AIE fluorogens for bioimaging. *Nanoscale* **2016**, *8*, 2471-2487; (c) Du, X.; Li, X.; Xiong, L.; Zhang, X.; Kleitz, F.; Qiao, S. Z., Mesoporous silica nanoparticles with organo-bridged silsesquioxane framework as innovative platforms for bioimaging and therapeutic agent delivery. *Biomaterials* **2016**, *91*, 90-127; (d) Xie, M.; Shi, H.; Ma, K.; Shen, H.; Li, B.; Shen, S.; Wang, X.; Jin, Y., Hybrid nanoparticles for drug delivery and bioimaging: mesoporous silica nanoparticles functionalized with carboxyl groups and a near-infrared fluorescent dye. *J. Colloid Interface Sci.* **2013**, *395*, 306-314; (e) Jafari, S.; Derakhshankhah, H.; Alaei, L.; Fattahi, A.; Varnamkhasti, B. S.; Saboury, A. A., Mesoporous silica nanoparticles for therapeutic/diagnostic applications. *Biomed. Pharmacother.* **2019**, *109*, 1100-1111.
108. (a) Korzeniowska, B.; Nooney, R.; Wencel, D.; McDonagh, C., Silica nanoparticles for cell imaging and intracellular sensing. *Nanotechnology* **2013**, *24*, 442002; (b) Slowing, I. I.; Trewyn, B. G.; Giri, S.; Lin, V. Y., Mesoporous silica nanoparticles for drug delivery and biosensing applications. *Adv. Funct. Mater.* **2007**, *17*, 1225-1236.
109. (a) Bilalis, P.; Tziveleka, L.-A.; Varlas, S.; Iatrou, H., pH-Sensitive nanogates based on poly (L-histidine) for controlled drug release from mesoporous silica nanoparticles. *Polym. Chem.* **2016**, *7*, 1475-1485; (b) Bouchoucha, M.; Cote, M.-F.; C.-Gaudreault, R.; Fortin, M.-A.; Kleitz, F., Size-controlled functionalized mesoporous silica nanoparticles for tunable drug release and enhanced anti-tumoral activity. *Chem. Mater.* **2016**, *28*, 4243-4258.
110. Tang, F.; Li, L.; Chen, D., Mesoporous silica nanoparticles: synthesis, biocompatibility and drug delivery. *Adv. Mater.* **2012**, *24*, 1504-1534.
111. (a) Bao, G.-M.; Wang, L.; Yuan, H.-Q.; Wang, X.-Y.; Mei, T.-X.; Qu, M.-R., Taste masking of a drug by pH-responsive coordination polymer-coated mesoporous silica nanoparticles. *RSC Advances* **2016**, *6*, 109453-109459; (b) Niedermayer, S.; Weiss, V.; Herrmann, A.; Schmidt, A.; Datz, S.; Müller, K.; Wagner, E.; Bein, T.; Bräuchle, C., Multifunctional polymer-capped mesoporous silica nanoparticles for pH-responsive targeted drug delivery. *Nanoscale* **2015**, *7*, 7953-7964; (c) Bouchoucha, M.; C.-Gaudreault, R.; Fortin, M. A.; Kleitz, F., Mesoporous silica nanoparticles: selective surface functionalization for optimal relaxometric and drug loading performances. *Adv. Funct. Mater.* **2014**, *24*, 5911-5923; (d) Singh, R. K.; Patel, K. D.; Leong, K. W.; Kim, H.-W., Progress in Nanotheranostics Based on Mesoporous Silica Nanomaterial Platforms. *ACS Appl. Mater. Interfaces* **2017**, *9*, 10309-10337.
112. (a) Quinn, K. P.; Sridharan, G. V.; Hayden, R. S.; Kaplan, D. L.; Lee, K.; Georgakoudi, I., Quantitative metabolic imaging using endogenous fluorescence to detect stem cell differentiation. *Sci. Rep.* **2013**, *3*, 3432; (b) Shuttleworth, C. W., Use of NAD(P)H and flavoprotein autofluorescence transients to probe neuron and astrocyte responses to synaptic activation. *Neurochem. Int.* **2010**, *56*, 379-386; (c) Ghisaidoobe, A. B. T.; Chung, S. J., Intrinsic Tryptophan Fluorescence in the Detection and Analysis of Proteins: A Focus on Förster Resonance Energy Transfer Techniques. *Int. J. Mol. Sci.* **2014**, *15*, 22518-22538; (d) Tayeh, N.; Rungassamy, T.;

- Albani, J. R., Fluorescence spectral resolution of tryptophan residues in bovine and human serum albumins. *J. Pharm. Biomed. Anal.* **2009**, *50*, 107-116.
113. (a) Reineck, P.; Gibson, B. C., Near-Infrared Fluorescent Nanomaterials for Bioimaging and Sensing. *Adv. Opt. Mater.* **2017**, *5*, 1600446; (b) Guo, Z.; Park, S.; Yoon, J.; Shin, I., Recent progress in the development of near-infrared fluorescent probes for bioimaging applications. *Chem. Soc. Rev.* **2014**, *43*, 16-29.
114. (a) Liu, M.; Ji, J.; Zhang, X.; Zhang, X.; Yang, B.; Deng, F.; Li, Z.; Wang, K.; Yang, Y.; Wei, Y., Self-polymerization of dopamine and polyethyleneimine: novel fluorescent organic nanoprobes for biological imaging applications. *J. Mater. Chem. B* **2015**, *3*, 3476-3482; (b) Zhang, X.; Wang, S.; Xu, L.; Feng, L.; Ji, Y.; Tao, L.; Li, S.; Wei, Y., Biocompatible polydopamine fluorescent organic nanoparticles: facile preparation and cell imaging. *Nanoscale* **2012**, *4*, 5581-5584.
115. (a) Hong, Y.; Lam, J. W.; Tang, B. Z., Aggregation-induced emission. *Chem. Soc. Rev.* **2011**, *40*, 5361-5388; (b) Kwok, R. T.; Leung, C. W.; Lam, J. W.; Tang, B. Z., Biosensing by luminogens with aggregation-induced emission characteristics. *Chem. Soc. Rev.* **2015**, *44*, 4228-4238.
116. (a) Mao, L.; Liu, M.; Xu, D.; Wan, Q.; Huang, Q.; Jiang, R.; Shi, Y.; Deng, F.; Zhang, X.; Wei, Y., Synthesis, surface modification and biological imaging of aggregation-induced emission (AIE) dye doped silica nanoparticles. *Appl. Surf. Sci.* **2017**, *403*, 396-402; (b) Zhang, X.; Zhang, X.; Wang, S.; Liu, M.; Zhang, Y.; Tao, L.; Wei, Y., Facile incorporation of aggregation-induced emission materials into mesoporous silica nanoparticles for intracellular imaging and cancer therapy. *ACS Appl. Mater. Interfaces* **2013**, *5*, 1943-1947; (c) Wang, X.; Song, P.; Peng, L.; Tong, A.; Xiang, Y., Aggregation-induced emission luminogen-embedded silica nanoparticles containing DNA aptamers for targeted cell imaging. *ACS Appl. Mater. Interfaces* **2015**, *8*, 609-616.
117. (a) Wedlock, L. E.; Berners-Price, S. J., Recent advances in mapping the sub-cellular distribution of metal-based anticancer drugs. *Aust. J. Chem.* **2011**, *64*, 692-704; (b) Coogan, M. P.; Fernández-Moreira, V., Progress with, and prospects for, metal complexes in cell imaging. *Chem. Commun.* **2014**, *50*, 384-399; (c) Liu, H.-W.; Zhang, K. Y.; Law, W. H.-T.; Lo, K. K.-W., Cyclometalated iridium(III) bipyridine complexes functionalized with an N-methylamino-oxy group as novel phosphorescent labeling reagents for reducing sugars. *Organometallics* **2010**, *29*, 3474-3476; (d) Lo, K. K.-W., Luminescent Rhenium(I) and Iridium(III) Polypyridine Complexes as Biological Probes, Imaging Reagents, and Photocytotoxic Agents. *Acc. Chem. Res.* **2015**, *48*, 2985-2995.
118. (a) Sim, N.; Parker, D., Critical design issues in the targeted molecular imaging of cell surface receptors. *Chem. Soc. Rev.* **2015**, *44*, 2122-2134; (b) Wang, X.; Chang, H.; Xie, J.; Zhao, B.; Liu, B.; Xu, S.; Pei, W.; Ren, N.; Huang, L.; Huang, W., Recent developments in lanthanide-based luminescent probes. *Coord. Chem. Rev.* **2014**, *273-274*, 201-212.
119. (a) Liu, Y.; Zhang, P.; Fang, X.; Wu, G.; Chen, S.; Zhang, Z.; Chao, H.; Tan, W.; Xu, L., Near-infrared emitting iridium(III) complexes for mitochondrial imaging in living cells. *Dalton Trans.* **2017**, *46*, 4777-4785; (b) Lo, K. K.-W.; Zhang, K. Y., Iridium(III) complexes as therapeutic and bioimaging reagents for cellular applications. *RSC Adv.* **2012**, *2*, 12069-12083.
120. Zhang, K. Y.; Zhang, J.; Liu, Y.; Liu, S.; Zhang, P.; Zhao, Q.; Tang, Y.; Huang, W., Core-shell structured phosphorescent nanoparticles for detection of exogenous and endogenous hypochlorite in live cells via ratiometric imaging and photoluminescence lifetime imaging microscopy. *Chem. Sci.* **2015**, *6*, 301-307.
121. (a) Li, X.; Xie, C.; Xia, H.; Wang, Z., pH and ultrasound dual-responsive polydopamine-coated mesoporous silica nanoparticles for controlled drug delivery. *Langmuir* **2018**, *34*, 9974-9981; (b) Zhu, J.; Niu, Y.; Li, Y.; Gong, Y.; Shi, H.; Huo, Q.; Liu, Y.; Xu, Q., Stimuli-responsive delivery vehicles based on mesoporous silica nanoparticles: recent advances and challenges. *J. Mater. Chem. B* **2017**, *5*, 1339-1352; (c) Liu, J.; Luo, Z.; Zhang, J.; Luo, T.; Zhou, J.; Zhao, X.; Cai, K., Hollow mesoporous silica nanoparticles facilitated drug delivery via cascade pH stimuli in tumor microenvironment for tumor therapy. *Biomaterials* **2016**, *83*, 51-65; (d) Wang, Y.; Zhao, Q.; Han,

- N.; Bai, L.; Li, J.; Liu, J.; Che, E.; Hu, L.; Zhang, Q.; Jiang, T., Mesoporous silica nanoparticles in drug delivery and biomedical applications. *Nanomed. Nanotechnol. Biol. Med.* **2015**, *11*, 313-327.
122. Argyo, C.; Weiss, V.; Bräuchle, C.; Bein, T., Multifunctional mesoporous silica nanoparticles as a universal platform for drug delivery. *Chem. Mater.* **2013**, *26*, 435-451.
123. Perez, R. A.; Singh, R. K.; Kim, T.-H.; Kim, H.-W., Silica-based multifunctional nanodelivery systems toward regenerative medicine. *Mater. Horiz.* **2017**, *4*, 772-799.
124. Fernández-Cestau, J.; Giménez, N.; Lalinde, E.; Montaño, P.; Moreno, M. T.; Sánchez, S., Synthesis, Characterization, and Properties of Doubly Alkynyl Bridging Dinuclear Cyclometalated Iridium(III) Complexes. *Organometallics* **2015**, *34* (9), 1766-1778.
125. Graf, C.; Gao, Q.; Schütz, I.; Noufele, C. N.; Ruan, W.; Posselt, U.; Korotianskiy, E.; Nordmeyer, D.; Rancan, F.; Hadam, S.; Vogt, A.; Lademann, J.; Haucke, V.; Rühl, E., Surface Functionalization of Silica Nanoparticles Supports Colloidal Stability in Physiological Media and Facilitates Internalization in Cells. *Langmuir* **2012**, *28*, 7598-7613.
126. Millán, G.; Giménez, N.; Lara, R.; Berenguer, J. s. R.; Moreno, M. T.; Lalinde, E.; Alfaro-Arnedo, E.; López, I. a. P.; Piñeiro-Hermida, S.; Pichel, J. G., Luminescent Cycloplatinated Complexes with Biologically Relevant Phosphine Ligands: Optical and Cytotoxic Properties. *Inorg. Chem.* **2019**, *58*, 1657-1673.
127. (a) Ravelli, D.; Dondi, D.; Fagnoni, M.; Albini, A., Photocatalysis. A multi-faceted concept for green chemistry. *Chem. Soc. Rev.* **2009**, *38*, 1999-2011; (b) Colmenares, J. C.; Luque, R., Heterogeneous photocatalytic nanomaterials: prospects and challenges in selective transformations of biomass-derived compounds. *Chem. Soc. Rev.* **2014**, *43*, 765-778; (c) Kubacka, A.; Fernandez-Garcia, M.; Colon, G., Advanced nanoarchitectures for solar photocatalytic applications. *Chem. Rev.* **2011**, *112*, 1555-1614; (d) Liu, S.; Han, C.; Tang, Z.-R.; Xu, Y.-J., Heterostructured semiconductor nanowire arrays for artificial photosynthesis. *Mater. Horizons* **2016**, *3*, 270-282; (e) Yuan, L.; Han, C.; Yang, M.-Q.; Xu, Y.-J., Photocatalytic water splitting for solar hydrogen generation: fundamentals and recent advancements. *Int. Rev. Phys. Chem.* **2016**, *35*, 1-36; (f) Colmenares, J. C.; Colmenares Quintero, R. F.; Pieta, I. S., Catalytic Dry Reforming for Biomass-Based Fuels Processing: Progress and Future Perspectives. *Energy Technol.* **2016**, *4*, 881-890.
128. Chen, X.; Mao, S. S., Titanium dioxide nanomaterials: synthesis, properties, modifications, and applications. *Chem. Rev.* **2007**, *107*, 2891-2959.
129. Fujishima, A.; Honda, K., Electrochemical photolysis of water at a semiconductor electrode. *Nature* **1972**, *238*, 37-38.
130. (a) Frank, S. N.; Bard, A. J., Heterogeneous photocatalytic oxidation of cyanide and sulfite in aqueous solutions at semiconductor powders. *J. Phys. Chem.* **1977**, *81*, 1484-1488; (b) Frank, S. N.; Bard, A. J., Heterogeneous photocatalytic oxidation of cyanide ion in aqueous solutions at titanium dioxide powder. *J. Am. Chem. Soc.* **1977**, *99*, 303-304.
131. Wang, R.; Hashimoto, K.; Fujishima, A.; Chikuni, M.; Kojima, E.; Kitamura, A.; Shimohigoshi, M.; Watanabe, T., Light-induced amphiphilic surfaces. *Nature* **1997**, *388*, 431.
132. O'Regan, B., B. O'Regan and M. Grätzel, Nature (London) **353**, 737 (1991). *Nature* **1991**, *353*, 737.
133. (a) Min, S.; Wang, F.; Han, Y., An investigation on synthesis and photocatalytic activity of polyaniline sensitized nanocrystalline TiO<sub>2</sub> composites. *J. Mater. Sci.* **2007**, *42*, 9966-9972; (b) Lu, J.; Zhang, P.; Li, A.; Su, F.; Wang, T.; Liu, Y.; Gong, J., Mesoporous anatase TiO<sub>2</sub> nanocups with plasmonic metal decoration for highly active visible-light photocatalysis. *Chem. Commun.* **2013**, *49*, 5817-5819; (c) Chen, X.; Liu, L.; Peter, Y. Y.; Mao, S. S., Increasing solar absorption for photocatalysis with black hydrogenated titanium dioxide nanocrystals. *Science* **2011**, *331*, 746.
134. Zhong, M.; Shi, J.; Zhang, W.; Han, H.; Li, C., Charge recombination reduction in dye-sensitized solar cells by depositing ultrapure TiO<sub>2</sub> nanoparticles on "inert" BaTiO<sub>3</sub> films. *Mater. Sci. Eng. B* **2011**, *176*, 1115-1122.

135. Liu, Y.; Chen, X.; Li, J.; Burda, C., Photocatalytic degradation of azo dyes by nitrogen-doped TiO<sub>2</sub> nanocatalysts. *Chemosphere* **2005**, *61*, 11-18.
136. (a) Bacsa, R.; Kiwi, J., Effect of rutile phase on the photocatalytic properties of nanocrystalline titania during the degradation of p-coumaric acid. *Appl. Catal., B* **1998**, *16*, 19-29; (b) Sun, J.; Gao, L.; Zhang, Q., Synthesizing and comparing the photocatalytic properties of high surface area rutile and anatase titania nanoparticles. *J. Am. Ceram. Soc.* **2003**, *86*, 1677-1682.
137. (a) Asahi, R.; Morikawa, T.; Ohwaki, T.; Aoki, K.; Taga, Y., Visible-light photocatalysis in nitrogen-doped titanium oxides. *Science* **2001**, *293*, 269-271; (b) Khan, S. U.; Al-Shahry, M.; Ingler, W. B., Efficient photochemical water splitting by a chemically modified n-TiO<sub>2</sub>. *Science* **2002**, *297*, 2243-2245; (c) Chen, X.; Burda, C., The electronic origin of the visible-light absorption properties of C-, N-and S-doped TiO<sub>2</sub> nanomaterials. *J. Am. Chem. Soc.* **2008**, *130*, 5018-5019; (d) Park, J. H.; Kim, S.; Bard, A. J., Novel carbon-doped TiO<sub>2</sub> nanotube arrays with high aspect ratios for efficient solar water splitting. *Nano Lett.* **2006**, *6*, 24-28; (e) Hoffmann, M. R.; Martin, S. T.; Choi, W.; Bahnemann, D. W., Environmental applications of semiconductor photocatalysis. *Chem. Rev.* **1995**, *95*, 69-96; (f) Hu, Y. H., A highly efficient photocatalyst—hydrogenated black TiO<sub>2</sub> for the photocatalytic splitting of water. *Angew. Chem. Int. Ed.* **2012**, *51*, 12410-12412.
138. (a) Wang, G.; Wang, H.; Ling, Y.; Tang, Y.; Yang, X.; Fitzmorris, R. C.; Wang, C.; Zhang, J. Z.; Li, Y., Hydrogen-treated TiO<sub>2</sub> nanowire arrays for photoelectrochemical water splitting. *Nano Lett.* **2011**, *11*, 3026-3033; (b) Zheng, Z.; Huang, B.; Lu, J.; Wang, Z.; Qin, X.; Zhang, X.; Dai, Y.; Whangbo, M.-H., Hydrogenated titania: synergy of surface modification and morphology improvement for enhanced photocatalytic activity. *Chem. Commun.* **2012**, *48*, 5733-5735; (c) Wang, Z.; Yang, C.; Lin, T.; Yin, H.; Chen, P.; Wan, D.; Xu, F.; Huang, F.; Lin, J.; Xie, X., H-doped black titania with very high solar absorption and excellent photocatalysis enhanced by localized surface plasmon resonance. *Adv. Funct. Mater.* **2013**, *23*, 5444-5450; (d) Wang, Z.; Yang, C.; Lin, T.; Yin, H.; Chen, P.; Wan, D.; Xu, F.; Huang, F.; Lin, J.; Xie, X., Visible-light photocatalytic, solar thermal and photoelectrochemical properties of aluminium-reduced black titania. *Energy Environ. Sci.* **2013**, *6*, 3007-3014.
139. (a) Devi, L. G.; Kavitha, R., A review on non metal ion doped titania for the photocatalytic degradation of organic pollutants under UV/solar light: role of photogenerated charge carrier dynamics in enhancing the activity. *Appl. Catal. B: Environ.* **2013**, *140*, 559-587; (b) Zhang, H.; Zhao, Y.; Chen, S.; Yu, B.; Xu, J.; Xu, H.; Hao, L.; Liu, Z., Ti<sup>3+</sup> self-doped TiO<sub>x</sub>@anatase core-shell structure with enhanced visible light photocatalytic activity. *J. Mater. Chem. A* **2013**, *1*, 6138-6144; (c) Majumder, S.; Paramanik, D.; Solanki, V.; Bag, B.; Varma, S., Bandgap tailoring of rutile TiO<sub>2</sub> (110) via surface patterning with electron cyclotron resonance sputtering. *Appl. Phys. Lett.* **2011**, *98*, 053105; (d) Zhou, W.; Fu, H., Mesoporous TiO<sub>2</sub>: preparation, doping, and as a composite for photocatalysis. *Chem. Cat. Chem.* **2013**, *5*, 885-894; (e) Yu, J.; Li, Q.; Liu, S.; Jaroniec, M., Ionic-liquid-assisted synthesis of uniform fluorinated B/C-codoped TiO<sub>2</sub> nanocrystals and their enhanced visible-light photocatalytic activity. *Chem. Eur. J.* **2013**, *19*, 2433-2441.
140. (a) Nazeeruddin, M. K.; Grätzel, M., Transition metal complexes for photovoltaic and light emitting applications. *Struct. Bond.* **2007**, *123*, 113-175; (b) Wu, Y.; Zhu, W.-H.; Zakeeruddin, S. M.; Grätzel, M., Insight into D-A-π-A Structured Sensitizers: A Promising Route to Highly Efficient and Stable Dye-Sensitized Solar Cells. *ACS Appl. Mater. Interfaces* **2015**, *7*, 9307-9318.
141. Zheng, Z.; Huang, B.; Meng, X.; Wang, J.; Wang, S.; Lou, Z.; Wang, Z.; Qin, X.; Zhang, X.; Dai, Y., Metallic zinc-assisted synthesis of Ti<sup>3+</sup> self-doped TiO<sub>2</sub> with tunable phase composition and visible-light photocatalytic activity. *Chem. Commun.* **2013**, *49*, 868-870.
142. (a) Mishra, A.; Fischer, M. K.; Bäuerle, P., Metal-free organic dyes for dye-sensitized solar cells: From structure: Property relationships to design rules. *Angew. Chem. Int. Ed.* **2009**, *48*, 2474-2499; (b) Wu, S.-J.; Chen, C.-Y.; Chen, J.-G.; Li, J.-Y.; Tung, Y.-L.; Ho, K.-C.; Wu, C.-G., An efficient light-harvesting ruthenium dye for solar cell application. *Dyes Pigm.* **2010**, *84*, 95-101;

- (c) Heo, J. H.; Im, S. H.; Noh, J. H.; Mandal, T. N.; Lim, C.-S.; Chang, J. A.; Lee, Y. H.; Kim, H.-j.; Sarkar, A.; Nazeeruddin, M. K., Efficient inorganic–organic hybrid heterojunction solar cells containing perovskite compound and polymeric hole conductors. *Nat. Photonics* **2013**, *7*, 486.
143. (a) Sahin, C.; Dittrich, T.; Varlikli, C.; Icli, S.; Lux-Steiner, M. C., Role of side groups in pyridine and bipyridine ruthenium dye complexes for modulated surface photovoltaic in nanoporous TiO<sub>2</sub>. *Sol. Energy Mater. Sol. Cells* **2010**, *94*, 686-690; (b) Hirata, N.; Lagref, J. J.; Palomares, E. J.; Durrant, J. R.; Nazeeruddin, M. K.; Grätzel, M.; Di Censo, D., Supramolecular control of charge-transfer dynamics on dye-sensitized nanocrystalline TiO<sub>2</sub> films. *Chem. Eur. J.* **2004**, *10*, 595-602; (c) Singh, J.; Gusain, A.; Saxena, V.; Chauhan, A.; Veerender, P.; Koiry, S.; Jha, P.; Jain, A.; Aswal, D.; Gupta, S., XPS, UV-vis, FTIR, and EXAFS studies to investigate the binding mechanism of N719 dye onto oxalic acid treated TiO<sub>2</sub> and its implication on photovoltaic properties. *J. Phys. Chem. C* **2013**, *117*, 21096-21104.
144. (a) Afzal, S.; Daoud, W. A.; Langford, S. J., Photostable self-cleaning cotton by a copper (II) porphyrin/TiO<sub>2</sub> visible-light photocatalytic system. *ACS App. Mater. Interfaces* **2013**, *5*, 4753-4759; (b) Hagfeldt, A.; Grätzel, M., Molecular photovoltaics. *Acc. Chem. Res.* **2000**, *33*, 269-277.
145. Kalyanasundaram, K.; Grätzel, M., Applications of functionalized transition metal complexes in photonic and optoelectronic devices. *Coord. Chem. Rev.* **1998**, *177*, 347-414.
146. (a) Schubert, U., Chemical modification of titanium alkoxides for sol-gel processing. *J. Mater. Chem.* **2005**, *15*, 3701-3715; (b) Liu, P.; Li, H.; Wang, Y.; Liu, B.; Zhang, W.; Wang, Y.; Yan, W.; Zhang, H.; Schubert, U., Europium complexes immobilization on titania via chemical modification of titanium alkoxide. *J. Mater. Chem.* **2008**, *18*, 735-737; (c) Maurer, C.; Pittenauer, E.; Du, V. A.; Allmaier, G.; Schubert, U., Cyclic bis ( $\beta$ -diketonate)-and bis ( $\beta$ -ketoesterate)-bridged titanium and zirconium alkoxide derivatives. *Dalton Trans.* **2012**, *41*, 2346-2353.
147. Rico-Santacruz, M.; Sepúlveda, Á. E.; Serrano, E.; Lalinde, E.; Berenguer, J. R.; García-Martínez, J., Organotitanias: a versatile approach for band gap reduction in titania based materials. *J. Mater. Chem. C* **2014**, *2*, 9497-9504.
148. Fung, A. K.; Chiu, B. K.; Lam, M. H., Surface modification of TiO<sub>2</sub> by a ruthenium(II) polypyridyl complex via silyl-linkage for the sensitized photocatalytic degradation of carbon tetrachloride by visible irradiation. *Water Res.* **2003**, *37*, 1939-1947.
149. Elsalamony, R. A.; Mahmoud, S. A., Preparation of nanostructured ruthenium doped titania for the photocatalytic degradation of 2-chlorophenol under visible light. *Arabian J. Chem.* **2017**, *10*, 194-205.
150. Lee, C.-H.; Shie, J.-L.; Tsai, C.-Y.; Yang, Y.-T.; Chang, C.-Y., Photocatalytic decomposition of indoor air pollution using dye-sensitized TiO<sub>2</sub> induced by anthocyanin and Ru complexes. *J. Clean Energy Tech.* **2013**, *1*, 115-119.
151. (a) Stergiopoulos, T.; Karakostas, S.; Falaras, P., Comparative studies of substituted ruthenium(II)-pyrazoyl-pyridine complexes with classical N3 photosensitizer: the influence of NCS dye ligands on the efficiency of solid-state nanocrystalline solar cells. *J. Photochem. Photobiol. A* **2004**, *163*, 331-340; (b) Nazeeruddin, M. K.; Kay, A.; Rodicio, I.; Humphry-Baker, R.; Müller, E.; Liska, P.; Vlachopoulos, N.; Grätzel, M., Conversion of light to electricity by cis-X<sub>2</sub>bis (2,2'-bipyridyl-4,4'-dicarboxylate)ruthenium(II) charge-transfer sensitizers (X= Cl<sup>-</sup>, Br<sup>-</sup>, I<sup>-</sup>, CN<sup>-</sup>, and SCN<sup>-</sup>) on nanocrystalline titanium dioxide electrodes. *J. Am. Chem. Soc.* **1993**, *115*, 6382-6390; (c) Grätzel, M., M. Grätzel. *Nature* **2001**, *414*, 338-344.
152. (a) Hagberg, D. P.; Yum, J.-H.; Lee, H.; De Angelis, F.; Marinado, T.; Karlsson, K. M.; Humphry-Baker, R.; Sun, L.; Hagfeldt, A.; Grätzel, M., Molecular engineering of organic sensitizers for dye-sensitized solar cell applications. *J. Am. Chem. Soc.* **2008**, *130*, 6259-6266; (b) Kim, C.; Choi, H.; Kim, S.; Baik, C.; Song, K.; Kang, M.-S.; Kang, S. O.; Ko, J., Molecular engineering of organic sensitizers containing p-phenylene vinylene unit for dye-sensitized solar cells. *J. Org. Chem.* **2008**, *73*, 7072-7079; (c) Wong, W.-Y.; Wang, X.-Z.; He, Z.; Chan, K.-K.; Djurišić, A. B.; Cheung, K.-Y.; Yip, C.-T.; Ng, A. M.-C.; Xi, Y. Y.; Mak, C. S., Tuning the absorption, charge transport properties, and solar cell efficiency with the number of thiényl rings in platinum-containing poly

- (aryleneethynylene) s. *J. Am. Chem. Soc.* **2007**, *129*, 14372-14380; (d) Hara, K.; Sato, T.; Katoh, R.; Furube, A.; Ohga, Y.; Shinpo, A.; Suga, S.; Sayama, K.; Sugihara, H.; Arakawa, H., Molecular design of coumarin dyes for efficient dye-sensitized solar cells. *J. Phys. Chem. B* **2003**, *107*, 597-606; (e) Bessho, T.; Constable, E. C.; Graetzel, M.; Redondo, A. H.; Housecroft, C. E.; Kyberg, W.; Nazeeruddin, M. K.; Neuburger, M.; Schaffner, S., An element of surprise—efficient copper-functionalized dye-sensitized solar cells. *Chem. Commun.* **2008**, (32), 3717-3719; (f) Nazeeruddin, M. K.; Baranoff, E.; Grätzel, M., Dye-sensitized solar cells: a brief overview. *Solar Energy* **2011**, *85*, 1172-1178.
153. Bignozzi, C.; Argazzi, R.; Boaretto, R.; Busatto, E.; Carli, S.; Ronconi, F.; Caramori, S., The role of transition metal complexes in dye sensitized solar devices. *Coord. Chem. Rev.* **2013**, *257*, 1472-1492.
154. (a) Kruth, A.; Peglow, S.; Rockstroh, N.; Junge, H.; Brüser, V.; Weltmann, K.-D., Enhancement of photocatalytic activity of dye sensitised anatase layers by application of a plasma-polymerized allylamine encapsulation. *J. Photochem. Photobiol., A* **2014**, *290*, 31-37; (b) Youssef, Z.; Colombeau, L.; Yesmurzayeva, N.; Baros, F.; Vanderesse, R.; Hamieh, T.; Toufaily, J.; Frochot, C.; Roques-Carmes, T., Dye-sensitized nanoparticles for heterogeneous photocatalysis: Cases studies with TiO<sub>2</sub>, ZnO, fullerene and graphene for water purification. *Dyes Pigm.* **2018**, *159*, 49-71.
155. Bessho, T.; Yoneda, E.; Yum, J.-H.; Guglielmi, M.; Tavernelli, I.; Imai, H.; Rothlisberger, U.; Nazeeruddin, M. K.; Grätzel, M., New paradigm in molecular engineering of sensitizers for solar cell applications. *J. Am. Chem. Soc.* **2009**, *131*, 5930-5934.
156. Siu, C. H.; Lee, L. T. L.; Yiu, S. C.; Ho, P. Y.; Zhou, P.; Ho, C. L.; Chen, T.; Liu, J.; Han, K.; Wong, W. Y., Synthesis and Characterization of Phenothiazine-Based Platinum(II)-Acetylide Photosensitizers for Efficient Dye-Sensitized Solar Cells. *Chem. Eur. J.* **2016**, *22*, 3750-3757.
157. Balraju, P.; Kumar, M.; Roy, M.; Sharma, G., Dye sensitized solar cells (DSSCs) based on modified iron phthalocyanine nanostructured TiO<sub>2</sub> electrode and PEDOT: PSS counter electrode. *Synth. Met.* **2009**, *159*, 1325-1331.
158. Chi, Y.; Wu, K. L.; Wei, T. C., Ruthenium and Osmium Complexes That Bear Functional Azolate Chelates for Dye-Sensitized Solar Cells. *Chem. Asian J.* **2015**, *10*, 1098-1115.
159. Freitag, M.; Giordano, F.; Yang, W.; Pazoki, M.; Hao, Y.; Zietz, B.; Grätzel, M.; Hagfeldt, A.; Boschloo, G., Copper Phenanthroline as a Fast and High-Performance Redox Mediator for Dye-Sensitized Solar Cells. *J. Phys. Chem. C* **2016**, *120*, 9595-9603.
160. Veronese, L.; Procopio, E. Q.; De Rossi, F.; Brown, T. M.; Mercandelli, P.; Mussini, P.; D'Alfonso, G.; Panigati, M., New dinuclear hydrido-carbonyl rhenium complexes designed as photosensitizers in dye-sensitized solar cells. *New J. Chem.* **2016**, *40*, 2910-2919.
161. (a) Wang, D.; Dong, H.; Wu, Y.; Yu, Y.; Zhou, G.; Li, L.; Wu, Z.; Gao, M.; Wang, G., Effect of diphenylamine substituent on charge-transfer absorption features of the iridium complexes and application in dye-sensitized solar cell. *J. Org. Chem.* **2015**, *775*, 55-59; (b) Hierlinger, C.; Flint, H. V.; Cordes, D. B.; Slawin, A. M.; Gibson, E. A.; Jacquemin, D.; Guerchais, V.; Zysman-Colman, E., A panchromatic, near infrared Ir(III) emitter bearing a tripodal C<sup>N</sup>C ligand as a dye for dye-sensitized solar cells. *Polyhedron* **2018**, *140*, 109-115.
162. Baranoff, E.; Yum, J. H.; Jung, I.; Vulcano, R.; Grätzel, M.; Nazeeruddin, M. K., Cyclometallated Iridium Complexes as Sensitizers for Dye-Sensitized Solar Cells. *Chem. Asian J.* **2010**, *5*, 496-499.
163. (a) Yuan, Y.-J.; Zhang, J.-Y.; Yu, Z.-T.; Feng, J.-Y.; Luo, W.-J.; Ye, J.-H.; Zou, Z.-G., Impact of ligand modification on hydrogen photogeneration and light-harvesting applications using cyclometalated iridium complexes. *Inorg. Chem.* **2012**, *51*, 4123-4133; (b) Wenger, O. S., Long-range electron transfer in artificial systems with d6 and d8 metal photosensitizers. *Coord. Chem. Rev.* **2009**, *253*, 1439-1457.
164. Waern, J. B.; Desmarests, C.; Chamoreau, L.-M.; Amouri, H.; Barbieri, A.; Sabatini, C.; Ventura, B.; Barigelli, F., Luminescent Cyclometalated Rh<sup>II</sup>, Ir<sup>II</sup>, and (DIP)<sub>2</sub>Ru<sup>II</sup> complexes with

- carboxylated bipyridyl ligands: synthesis, X-ray molecular structure, and photophysical properties. *Inorg. Chem.* **2008**, *47*, 3340-3348.
165. Nazeeruddin, M. K.; Zakeeruddin, S.; Humphry-Baker, R.; Jirousek, M.; Liska, P.; Vlachopoulos, N.; Shklover, V.; Fischer, C.-H.; Grätzel, M., Acid–Base equilibria of (2,2'-Bipyridyl-4,4'-dicarboxylic acid)ruthenium(II) complexes and the effect of protonation on charge-transfer sensitization of nanocrystalline titania. *Inorg. Chem.* **1999**, *38*, 6298-6305.
166. (a) Jiang, W.; Gao, Y.; Sun, Y.; Ding, F.; Xu, Y.; Bian, Z.; Li, F.; Bian, J.; Huang, C., Zwitterionic iridium complexes: synthesis, luminescent properties, and their application in cell imaging. *Inorg. Chem.* **2010**, *49*, 3252-3260; (b) Qin, L.; Yang, H.; Qin, C.; Xiang, Z.; Zhang, M.; Ding, L.; Yi, T.; Yang, S., Guest induced morphological transformation from nanospheres to nanowires by hydrogen bond self-assembly. *Dalton Trans.* **2013**, *42*, 4790-4794.
167. (a) Perkovic, M. W., Allosteric manipulation of photoexcited state relaxation in (bpy)<sub>2</sub>Ru<sup>II</sup>(binicotinic acid). *Inorg. Chem.* **2000**, *39*, 4962-4968; (b) Bratsos, I.; Jedner, S.; Bergamo, A.; Sava, G.; Gianferrara, T.; Zangrandi, E.; Alessio, E., Half-sandwich Ru<sup>II</sup> [9]aneS<sub>3</sub> complexes structurally similar to antitumor-active organometallic piano-stool compounds: Preparation, structural characterization and in vitro cytotoxic activity. *J. Inorg. Biochem.* **2008**, *102*, 1120-1133.
168. Rico-Santacruz, M.; Sepulveda, A. E.; Serrano, E.; Berenguer, J. R.; Lalinde, E.; Garcia-Martinez, J., Spain Patent Number ES2539624 **2015**, No. sol. 201300536, 2013.
169. Wang, Y.; Jiang, Z.-H.; Yang, F.-J., Preparation and photocatalytic activity of mesoporous TiO<sub>2</sub> derived from hydrolysis condensation with TX-100 as template. *Mater. Sci. Eng. B* **2006**, *128*, 229-233.
170. Zhu, J.; Yang, D.; Geng, J.; Chen, D.; Jiang, Z., Synthesis and characterization of bamboo-like CdS/TiO<sub>2</sub> nanotubes composites with enhanced visible-light photocatalytic activity. *J. Nanopart. Res.* **2008**, *10*, 729-736.
171. (a) Paoprasert, P.; Laaser, J. E.; Xiong, W.; Franking, R. A.; Hamers, R. J.; Zanni, M. T.; Schmidt, J.; Gopalan, P., Bridge-dependent interfacial electron transfer from rhenium–bipyridine complexes to TiO<sub>2</sub> nanocrystalline thin films. *J. Phys. Chem. C* **2010**, *114*, 9898-9907; (b) Nazeeruddin, M. K.; Humphry-Baker, R.; Liska, P.; Grätzel, M., Investigation of sensitizer adsorption and the influence of protons on current and voltage of a dye-sensitized nanocrystalline TiO<sub>2</sub> solar cell. *J. Phys. Chem. B* **2003**, *107*, 8981-8987.
172. Zhao, D.; Chen, C.; Wang, Y.; Ji, H.; Ma, W.; Zang, L.; Zhao, J., Surface modification of TiO<sub>2</sub> by phosphate: effect on photocatalytic activity and mechanism implication. *J. Phys. Chem. C* **2008**, *112*, 5993-6001.
173. (a) Bocquet, A., AE Bocquet, T. Mizokawa, K. Morikawa, A. Fujimori, SR Barman, K. Maiti, DD Sarma, Y. Tokura, and M. Onoda, *Phys. Rev. B* **53**, 1161 (1996). *Phys. Rev. B* **1996**, *53*, 1161; (b) Simmons, G. W.; Beard, B. C., Characterization of acid-base properties of the hydrated oxides on iron and titanium metal surfaces. *J. Phys. Chem.* **1987**, *91*, 1143-1148; (c) Oku, M.; Matsuta, H.; Wagatsuma, K.; Waseda, Y.; Kohiki, S., Removal of inelastic scattering part from Ti2p XPS spectrum of TiO<sub>2</sub> by deconvolution method using O1s as response function. *J. Electron. Spectrosc. Relat. Phenom.* **1999**, *105*, 211-218; (d) Stefanov, P.; Shipochka, M.; Stefchev, P.; Raicheva, Z.; Lazarova, V.; Spassov, L. In *XPS characterization of TiO<sub>2</sub> layers deposited on quartz plates*, *J. Phys. Conf. Ser.*, IOP Publishing: 2008; p 012039.
174. (a) Chen, X.; Liu, L.; Peter, Y. Y.; Mao, S. S., Increasing solar absorption for photocatalysis with black hydrogenated titanium dioxide nanocrystals. *Science* **2011**, *1200448*; (b) McCafferty, E.; Wightman, J., Determination of the concentration of surface hydroxyl groups on metal oxide films by a quantitative XPS method. *Surf. Interface Anal.* **1998**, *26*, 549-564.
175. (a) Patrocínio, A. O. T.; Paniago, E. B.; Paniago, R. M.; Iha, N. Y. M., XPS characterization of sensitized n-TiO<sub>2</sub> thin films for dye-sensitized solar cell applications. *Appl. Surf. Sci.* **2008**, *254*, 1874-1879; (b) Balaraju, M.; Rekha, V.; Devi, B. P.; Prasad, R.; Prasad, P. S.; Lingaiah, N., Surface and structural properties of titania-supported Ru catalysts for hydrogenolysis of glycerol. *Appl.*

- Catal. A: Gen.* **2010**, *384*, 107-114; (c) Reyes, P.; Aguirre, M.; Melián-Cabrera, I.; Granados, M. L.; Fierro, J., Interfacial properties of an Ir/TiO<sub>2</sub> system and their relevance in crotonaldehyde hydrogenation. *J. Catal.* **2002**, *208*, 229-237; (d) Rojas, H.; Borda, G.; Reyes, P.; Martínez, J.; Valencia, J.; Fierro, J., Citral hydrogenation over Ir/TiO<sub>2</sub> and Ir/TiO<sub>2</sub>/SiO<sub>2</sub> catalysts. *Catal. Today* **2008**, *133*, 699-705.
176. Thapa, R.; Maiti, S.; Rana, T.; Maiti, U.; Chattopadhyay, K., Anatase TiO<sub>2</sub> nanoparticles synthesis via simple hydrothermal route: Degradation of Orange II, Methyl Orange and Rhodamine B. *J. Mol. Catal. A: Chem.* **2012**, *363*, 223-229.
177. Wilhelm, P.; Stephan, D., Photodegradation of rhodamine B in aqueous solution via SiO<sub>2</sub>@TiO<sub>2</sub> nano-spheres. *J. Photochem. Photobio. A: Chem.* **2007**, *185*, 19-25.
178. Jose, R.; Kumar, A.; Thavasi, V.; Ramakrishna, S., Conversion efficiency versus sensitizer for electrospun TiO<sub>2</sub> nanorod electrodes in dye-sensitized solar cells. *Nanotechnology* **2008**, *19*, 424004.
179. Wu, T.; Liu, G.; Zhao, J.; Hidaka, H.; Serpone, N., Photoassisted degradation of dye pollutants. V. Self-photosensitized oxidative transformation of rhodamine B under visible light irradiation in aqueous TiO<sub>2</sub> dispersions. *J. Phys. Chem. B* **1998**, *102*, 5845-5851.
180. Chen, F.; Zhao, J.; Hidaka, H., Highly selective deethylation of rhodamine B: Adsorption and photooxidation pathways of the dye on the TiO<sub>2</sub>/SiO<sub>2</sub> composite photocatalyst. *Int. J. Photoenergy* **2003**, *5*, 209-217.
181. Otwinowski, Z.; Minor, W., In *Methods Enzymol.*, Carter, C. V., Jr.; Sweet, R. M., Eds. Academic Press: New York, 1997; Vol. 276A, p 307.
182. Bruker (2016). APEX3 (v2016, Saint (V8.37A) and SADABS (2016/2), Bruker AXS Inc., Madison, Wisconsin, USA.
183. Sheldrick, G., SHELXT - Integrated space-group and crystal-structure determination. *Acta Crystallogr. Sect. A* **2015**, *71*, 3-8.
184. Farrugia, L. J., WinGX program features. *J. Appl. Crystallogr.* **1999**, *32*, 837-838.
185. Blessing, R. H., *Acta Crystallogr. Sect. A* **1995**, *51*, 33-38.
186. Frisch, M. J.; Trucks, G. W.; Schlegel, H. B.; Scuseria, G. E.; Robb, M. A.; Cheeseman, J. R.; Scalmani, G.; Barone, V.; Mennucci, B.; Petersson, G. A.; Nakatsuji, H.; Caricato, M.; Li, X.; Hratchian, H. P.; Izmaylov, A. F.; Bloino, J.; Zheng, G.; Sonnenberg, J. L.; Hada, M.; Ehara, M.; Toyota, K.; Fukuda, R.; Hasegawa, J.; Ishida, M.; Nakajima, T.; Honda, Y.; Kitao, O.; Nakai, H.; Vreven, T.; Montgomery, J. A.; Peralta, J. E.; Ogliaro, F.; Bearpark, M.; Heyd, J. J.; Brothers, E.; Kudin, K. N.; Staroverov, V. N.; Kobayashi, R.; Normand, J.; Raghavachari, K.; Rendell, A.; Burant, J. C.; Iyengar, S. S.; Tomasi, J.; Cossi, M.; Rega, N.; Millam, J. M.; Klene, M.; Knox, J. E.; Cross, J. B.; Bakken, V.; Adamo, C.; Jaramillo, J.; Gomperts, R.; Stratmann, R. E.; Yazyev, O.; Austin, A. J.; Cammi, R.; Pomelli, C.; Ochterski, J. W.; Martin, R. L.; Morokuma, K.; Zakrzewski, V. G.; Voth, G. A.; Salvador, P.; Dannenberg, J. J.; Dapprich, S.; Daniels, A. D.; Farkas; Foresman, J. B.; Ortiz, J. V.; Cioslowski, J.; Fox, D. J., *Gaussian 09, Revision B.01*. Gaussian, Inc., Wallingford CT, , 2010.
187. (a) Lee, C.; Yang, W.; Parr, R. G., Development of the Colle-Salvetti correlation-energy formula into a functional of the electron density. *Phys. Rev. B* **1988**, *37*, 785-789; (b) Becke, A. D., Density-functional exchange-energy approximation with correct asymptotic behavior. *Phys. Rev. A* **1988**, *38*, 3098-3100; (c) Becke, A. D., Density-functional thermochemistry. III. The role of exact exchange. *J. Chem. Phys.* **1993**, *98*, 5648-5652.
188. Barone, V.; Cossi, M., Quantum calculation of molecular energies and energy gradients in solution by a conductor solvent model. *J. Phys. Chem. A* **1998**, *102*, 1995-2001.
189. O'Boyle, N. M.; Tenderholt, A. L.; Langner, K. M., cclib: A library for package-independent computational chemistry algorithms. *J. Comput. Chem.* **2008**, *29*, 839-845.
190. (a) Badisa, R. B.; Darling-Reed, S. F.; Joseph, P.; Cooperwood, J. S.; Latinwo, L. M.; Goodman, C. B., Selective cytotoxic activities of two novel synthetic drugs on human breast carcinoma MCF-7 cells. *Anticancer Res.* **2009**, *29*, 2993-2996; (b) Peña-Morán, O.; Villarreal, M.; Álvarez-Berber, L.; Meneses-Acosta, A.; Rodríguez-López, V., Cytotoxicity, post-treatment

- recovery, and selectivity analysis of naturally occurring podophyllotoxins from *Bursera fagaroides* var. *fagaroides* on breast cancer cell lines. *Molecules* **2016**, *21*, 1013.
191. López-Lázaro, M., Two preclinical tests to evaluate anticancer activity and to help validate drug candidates for clinical trials. *Oncoscience* **2015**, *2*, 91.
192. Mauro, M.; De Paoli, G.; Otter, M.; Donghi, D.; D'Alfonso, G.; De Cola, L., Aggregation induced colour change for phosphorescent iridium(III) complex-based anionic surfactants. *Dalton Trans.* **2011**, *40*, 12106-12116.
193. Lafolet, F.; Welter, S.; Popović, Z.; De Cola, L., Iridium complexes containing p-phenylene units. The influence of the conjugation on the excited state properties. *J. Mater. Chem.* **2005**, *15*, 2820-2828.
194. Zhou, Y.; Li, W.; Liu, Y.; Zhou, M., Acid-Induced Degradation and Ancillary Ligand Replacement of Biscyclometalated Iridium(III) Complexes. *ChemPlusChem* **2013**, *78*, 413-418.
195. Greenway, G. M.; Greenwood, A.; Watts, P.; Wiles, C., Solid-supported chemiluminescence and electrogenerated chemiluminescence based on a tris(2,2-bipyridyl)ruthenium(II) derivative. *Chem. Commun.* **2006**, 85-87.
196. Zanoni, K. P. S.; Sanematsu, M. S.; Iha, N. Y. M., Photophysical characterization of  $[\text{Ir}(\text{ppy})_2(\text{dmb})][\text{PF}_6]$  towards application in light-emitting electrochemical cells (LECs). *Inorg. Chem. Commun.* **2014**, *43*, 162-164.
197. Ly, K. T.; Chen-Cheng, R.-W.; Lin, H.-W.; Shiau, Y.-J.; Liu, S.-H.; Chou, P.-T.; Tsao, C.-S.; Huang, Y.-C.; Chi, Y., Near-infrared organic light-emitting diodes with very high external quantum efficiency and radiance. *Nat. Photonics* **2017**, *11*, 63-68.

## ***Annexes***





Annex Chapter I**Table A.I.1.** Selected bond lengths ( $\text{\AA}$ ) and angles ( $^\circ$ ) for complex  $[\text{Pt}(\text{bzq})(\text{C}_6\text{F}_5)(\text{PPETS})]$  (3).

Pt(1)-N(1)	2.105(3)	Pt(1)-P(1)	2.3248(8)
Pt(1)-C(10)	2.051(3)	Pt(1)-C(15)	1.998(3)
N(1)-Pt(1)-C(10)	80.3(1)	N(1)-Pt(1)-P(1)	99.21(8)
C(10)-Pt(1)-C(15)	90.0(1)	C(15)-Pt(1)-P(1)	90.49(8)
C(15)-Pt(1)-N(1)	170.2(1)	C(10)-Pt(1)-P(1)	178.01(9)

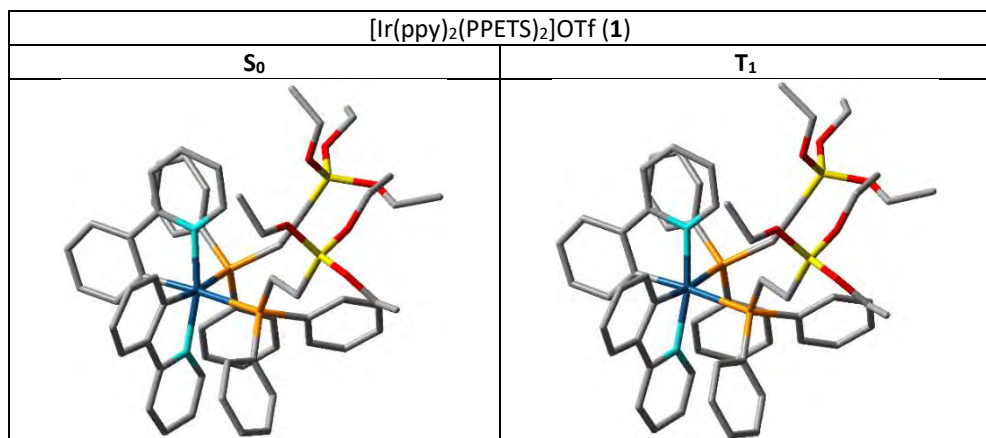
**Table A.I.2.** Crystallographic data for complex  $[\text{Pt}(\text{bzq})(\text{C}_6\text{F}_5)(\text{PPETS})]$  (3).

Empirical formula	$\text{C}_{39}\text{H}_{37}\text{F}_5\text{NO}_3\text{PPtSi}$
$F_w$	916.84
T (K)	173(1) K
Crystal system, space group	Triclinic, $P-1$
a( $\text{\AA}$ )	12.2141(5)
b( $\text{\AA}$ )	12.5271(4)
c( $\text{\AA}$ )	12.7251(5)
$\alpha$ (deg)	75.765(3)
$\beta$ (deg)	84.072(2)
$\gamma$ (deg)	71.946(3)
Volume ( $\text{\AA}^3$ )	1793.6(1)
Z	2
$D_{\text{calcd}}$ ( $\text{Mg/m}^3$ )	1.698
Absorption coefficient ( $\text{mm}^{-1}$ )	4.055
F(000)	908
$\theta$ range for data collection (deg)	3.305 to 27.471
No of data // restraints // params	7719 // 0 // 478
Goodness-of-fit on $F^2$ <sup>(a)</sup>	1.089
Final R indexes [ $ I  > 2\sigma( I )$ ] <sup>(a)</sup>	$R_1 = 0.0296, wR_2 = 0.0812$
R indexes (all data) <sup>(a)</sup>	$R_1 = 0.0306, wR_2 = 0.0821$
Largest diff peak and hole ( $e \cdot \text{\AA}^{-3}$ )	1.129 and -1.881

(a)  $R_1 = \sum (|F_o| - |F_c|) / \sum |F_o|$ ;  $wR_2 = [\sum w(F_o^2 - F_c^2)^2 / \sum wF_o^2]^{1/2}$ ; goodness of fit =  $\{\sum [w(F_o^2 - F_c^2)^2] / (N_{\text{obs}} - N_{\text{param}})\}^{1/2}$ ;  $w = [\sigma^2(F_o) + (g_1 P)^2 + g_2 P]^{-1}$ ;  $P = [\max(F_o^2; 0 + 2F_c^2)]/3$ .

**Table A.I.3.** DFT optimized geometries for ground and triplet states of  $[\text{Ir}(\text{ppy})_2(\text{PPETS})_2]\text{OTf}$  (**1**) in THF.

	<b>S<sub>0</sub></b>	<b>T<sub>1</sub></b>
Ir(1)-N(1)	2.108	2.112
Ir(1)-N(1')	2.109	2.072
Ir(1)-C(10)	2.053	2.046
Ir(1)-C(10')	2.050	2.031
Ir(1)-P(1)	2.587	2.596
Ir(1)-P(1')	2.588	2.614
N(1)-Ir(1)-N(1')	167.32	168.28
N(1)-Ir(1)-C(10)	79.03	79.09
N(1')-Ir(1)-C(10')	79.18	80.49
N(1)-Ir(1)-C(10')	91.86	91.69
N(1')-Ir(1)-C(10)	91.07	91.49
P(1)-Ir(1)-P(1')	100.38	100.08
P(1)-Ir(1)-N(1)	85.99	85.61
P(1)-Ir(1)-C(10)	87.61	87.58
P(1)-Ir(1)-N(1')	101.63	101.09
P(1)-Ir(1)-C(10')	171.91	172.74
P(1')-Ir(1)-N(1)	104.03	104.10
P(1')-Ir(1)-C(10)	171.57	171.85
P(1')-Ir(1)-N(1')	84.74	84.35
P(1')-Ir(1)-C(10')	87.70	87.12

**Figure A.I.1.** Optimized structures of S<sub>0</sub> and T<sub>1</sub> states of  $[\text{Ir}(\text{ppy})_2(\text{PPETS})_2]\text{OTf}$  (**1**) in THF.

**Table A.I.4.** Composition (%) of frontier molecular orbitals in the ground and in the first triplet states of  $[\text{Ir}(\text{ppy})_2(\text{PPETS})_2]\text{OTf}$  (**1**) in THF.

	eV	ppy(1)	ppy(2)	PPETS(1)	PPETS(2)	Ir
LUMO+5	-1.13	7	2	31	55	6
LUMO+4	-1.25	6	4	57	28	5
LUMO+3	-1.40	43	45	2	9	1
LUMO+2	-1.53	42	49	2	5	1
LUMO+1	-1.89	56	37	1	1	4
LUMO	<b>-2.07</b>	<b>38</b>	<b>57</b>	<b>2</b>	<b>2</b>	<b>2</b>
HOMO	<b>-6.10</b>	<b>28</b>	<b>33</b>	<b>1</b>	<b>1</b>	<b>36</b>
HOMO-1	-6.38	45	40	4	4	6
HOMO-2	-6.71	53	2	8	30	8
HOMO-3	-6.72	20	44	7	19	10
HOMO-4	-6.75	3	42	38	6	11
HOMO-5	-6.96	13	23	14	5	44

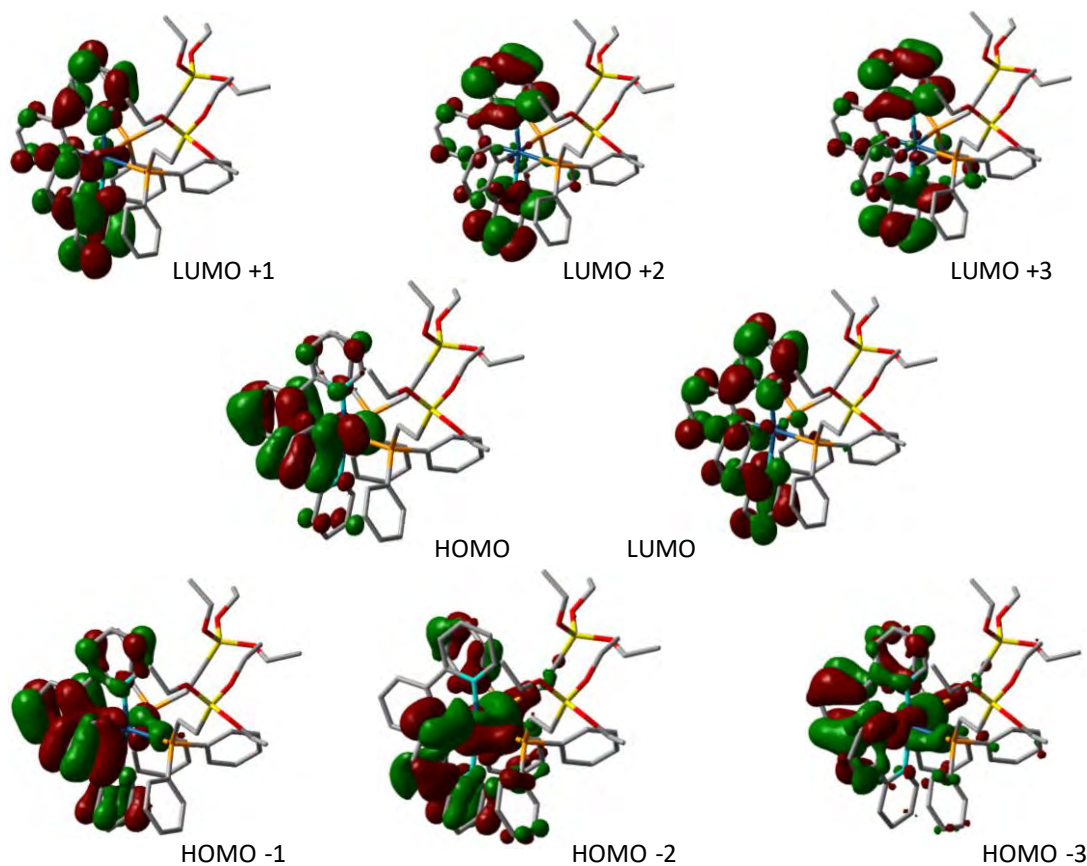


**Figure A.I.2.** Selected frontier Molecular Orbitals for complex  $[\text{Ir}(\text{ppy})_2(\text{PPETS})_2]\text{OTf}$  (**1**).

**Table A.I.6.** Selected vertical excitation energies singlets ( $S_0$ ) and first triplets computed by TDDFT/SCRF (THF) with the orbitals involved for complex **1**.

State	$\lambda_{\text{ex}}(\text{calc})$ (nm)	f	Transition (% Contribution)	Main character
T <sub>1</sub>	439.14	-	H-1→L+1 (15%), HOMO→LUMO (48%)	MLCT/IL
T <sub>2</sub>	434.54	-	H-1→LUMO (30%), HOMO→L+1 (30%)	MLCT/IL
S <sub>1</sub>	375.51	0.0427	HOMO→LUMO (97%)	MLCT/IL
S <sub>2</sub>	357.69	0.0014	HOMO→L+1 (97%)	MLCT/IL
S <sub>4</sub>	325.28	0.0311	H-1→L+1 (89%)	IL
S <sub>5</sub>	317.34	0.0253	HOMO→L+2 (90%)	MLCT/IL
S <sub>6</sub>	310.22	0.0361	H-5→LUMO (18%), H-3→LUMO (49%), H-2→LUMO (20%)	IL
S <sub>8</sub>	307.64	0.0178	H-4→LUMO (29%), HOMO→L+3 (52%)	LL'CT/MLCT
S <sub>9</sub>	304.19	0.0817	H-7→LUMO (10%), H-4→LUMO (37%), H-2→LUMO (35%)	LL'CT/IL
S <sub>10</sub>	300.36	0.0245	H-7→LUMO (32%), H-5→LUMO (15%), H-2→L+1 (12%)	LL'CT/IL
S <sub>26</sub>	270.83	0.0563	H-1→L+4 (62%)	LL'CT

**Table A.I.7.** DFT optimized geometry for ground state of  $[\text{Pt}(\text{bzq})(\text{dasipy})]\text{PF}_6$  (**4**) in  $\text{CH}_2\text{Cl}_2$ . No optimization was achieved for the state  $T_1$ .

<b>S<sub>0</sub></b>	
Pt(1)-N(1)	2.077
Pt(1)-C(10)	2.027
Pt(1)-N(2)	2.211
Pt(1)-N(2')	2.065
N(1)-Pt(1)-C(10)	80.62
N(1)-Pt(1)-N(2)	104.16
N(1)-Pt(1)-N(2')	168.40
N(2)-Pt(1)-N(2')	77.23
N(2)-Pt(1)-C(10)	163.11
N(2')-Pt(1)-C(10)	101.41

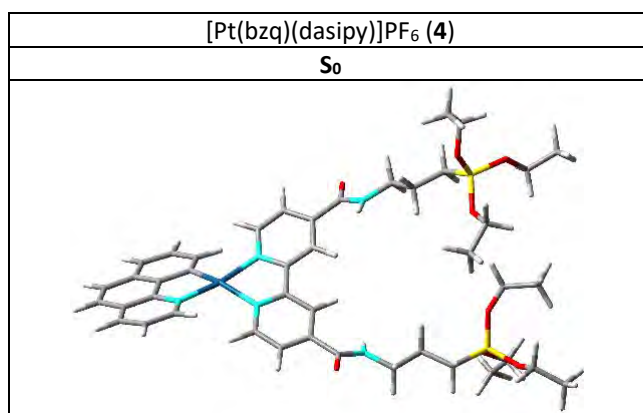


**Figure A.I.3.** Optimized structures of  $S_0$  state of  $[\text{Pt}(\text{bzq})(\text{dasipy})]\text{PF}_6$  (**4**) in  $\text{CH}_2\text{Cl}_2$ . No optimization was achieved for the state  $T_1$ .

**Table A.I.8.** Composition (%) of frontier molecular orbitals in the ground and in the first triplet states of  $[\text{Pt}(\text{bzq})(\text{dasipy})]\text{PF}_6$  (**4**) in  $\text{CH}_2\text{Cl}_2$ .

	eV	bzq	dasipy	Pt
LUMO+5	-1.24	34	17	50
LUMO+4	-1.71	92	3	5
LUMO+3	-2.18	16	83	2
LUMO+2	-2.29	13	85	2
LUMO+1	-2.38	65	33	2
<b>LUMO</b>	<b>-3.21</b>	<b>6</b>	<b>89</b>	<b>4</b>
<b>HOMO</b>	<b>-6.28</b>	<b>78</b>	<b>3</b>	<b>19</b>
HOMO-1	-6.86	81	2	17
HOMO-2	-6.98	7	4	89
HOMO-3	-7.34	30	36	34
HOMO-4	-7.39	8	72	20
HOMO-5	-7.42	42	24	35

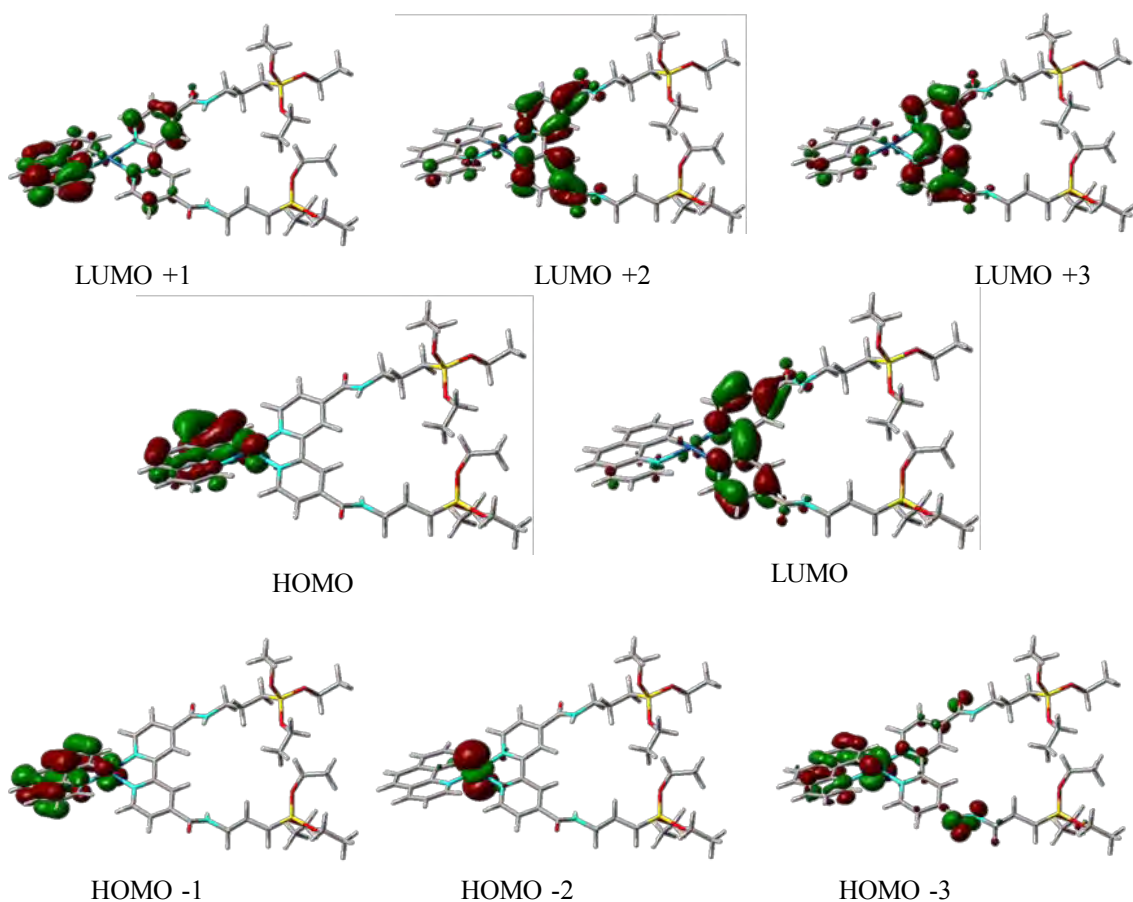


**Figure A.I.4.** Selected frontier Molecular Orbitals for complex  $[[\text{Pt}(\text{bzq})(\text{dasipy})]\text{PF}_6]$  (**4**).

**Table A.I.9.** Selected vertical excitation energies singlets ( $S_0$ ) and first triplets computed by TDDFT/SCRF ( $\text{CH}_2\text{Cl}_2$ ) with the orbitals involved for complex **4**.

State	$\lambda_{\text{ex}}(\text{calc})(\text{nm})$	f	Transition (% Contribution)	Main character
T <sub>1</sub>	502.3	---	HOMO $\rightarrow$ LUMO (90%)	ML'CT/LL'CT
T <sub>2</sub>	468.5	---	H-1 $\rightarrow$ LUMO (13%), H-1 $\rightarrow$ L+1 (20%), HOMO $\rightarrow$ L+1 (18%), HOMO $\rightarrow$ L+4 (18%)	ML'CT/LL'CT
S <sub>1</sub>	478.2	0.0338	HOMO $\rightarrow$ LUMO (96%)	ML'CT/LL'CT
S <sub>2</sub>	449.3	0.0199	H-2 $\rightarrow$ LUMO (96%)	ML'CT
S <sub>3</sub>	401.9	0.0693	H-1 $\rightarrow$ LUMO (87%)	LL'CT
S <sub>4</sub>	380.0	0.0403	HOMO $\rightarrow$ L+1 (83%)	IL/LL'CT
S <sub>17</sub>	310.3	0.0730	H-2 $\rightarrow$ L+3 (19%), H-1 $\rightarrow$ L+1 (13%), H-1 $\rightarrow$ L+2 (17%)	IL
S <sub>18</sub>	308.6	0.1001	H-1 $\rightarrow$ L+3 (31%), HOMO $\rightarrow$ L+4 (28%)	IL
S <sub>19</sub>	302.8	0.0907	H-1 $\rightarrow$ L+4 (31%)	IL
S <sub>24</sub>	296.9	0.0764	H-1 $\rightarrow$ L+1 (39%)	IL
S <sub>27</sub>	287.8	0.0908	H-1 $\rightarrow$ L+1 (34%), H-1 $\rightarrow$ L+4 (18%)	IL

**Annex Chapter II****Table A.II.1.** DFT optimized geometries for ground and triplet states of complexes  $[\text{Ir}(\text{dFppy})_2(\text{PPETS})_2]\text{PF}_6$  (**B**) and  $[\text{Ir}(\text{ppy})_2(\text{dasipy})]\text{OTf}$  (**R**) in THF.

$[\text{Ir}(\text{dFppy})_2(\text{PPETS})_2]\text{PF}_6$ ( <b>B</b> )		$[\text{Ir}(\text{ppy})_2(\text{dasipy})]\text{OTf}$ ( <b>R</b> )			
<b>S<sub>0</sub></b>	<b>T<sub>1</sub></b>	<b>S<sub>0</sub></b>	<b>T<sub>1</sub></b>		
Ir(1)-N(1)	2.108	2.117	Ir(1)-N(1)	2.085	2.083
Ir(1)-N(1')	2.107	2.072	Ir(1)-N(1')	2.082	2.083
Ir(1)-C(10)	2.049	2.046	Ir(1)-C(10)	2.024	1.999
Ir(1)-C(10')	2.046	2.031	Ir(1)-C(10')	2.034	1.997
Ir(1)-P(1)	2.587	2.596	Ir(1)-N(a)	2.208	2.201
Ir(1)-P(1')	2.584	2.614	Ir(1)-N(a')	2.207	2.193
N(1)-Ir(1)-N(1')	167.26	168.28	N(1)-Ir(1)-N(1')	173.60	176.39
N(1)-Ir(1)-C(10)	79.03	79.09	N(1)-Ir(1)-C(10)	80.05	80.85
N(1')-Ir(1)-C(10')	79.15	80.49	N(1')-Ir(1)-C(10')	80.05	80.82
N(1)-Ir(1)-C(10')	91.92	91.69	N(a)-Ir(1)-N(a')	95.50	96.79
N(1')-Ir(1)-C(10)	90.98	91.49	N(1)-Ir(1)-C(10')	95.24	96.66
P(1)-Ir(1)-P(1')	100.10	100.08	N(1')-Ir(1)-C(10)	74.79	75.01
P(1)-Ir(1)-N(1)	85.56	85.61	N(a)-Ir(1)-N(1)	88.09	87.41
P(1)-Ir(1)-C(10)	87.72	87.58	N(a)-Ir(1)-C(10)	97.98	94.62
P(1)-Ir(1)-N(1')	102.07	101.09	N(a)-Ir(1)-N(1')	96.90	95.42
P(1)-Ir(1)-C(10')	172.13	172.74	N(a)-Ir(1)-C(10')	172.24	169.18
P(1')-Ir(1)-N(1)	104.16	104.10	N(a')-Ir(1)-N(1)	96.75	95.06
P(1')-Ir(1)-C(10)	171.71	171.85	N(a')-Ir(1)-C(10)	172.26	169.09
P(1')-Ir(1)-N(1')	84.72	84.35	N(a')-Ir(1)-N(1')	88.45	87.85
P(1')-Ir(1)-C(10')	87.75	87.12	N(a')-Ir(1)-C(10')	97.91	94.63

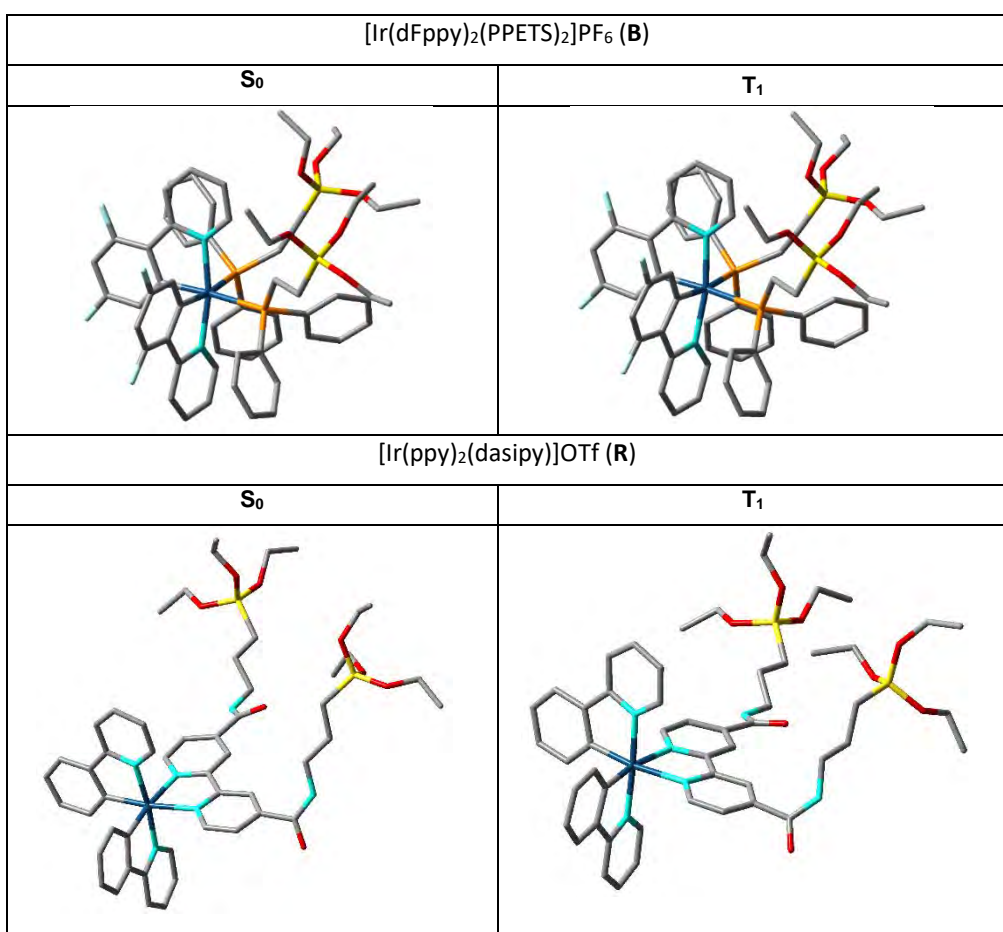


**Figure A.II.1.** Optimized structures of  $S_0$  and  $T_1$  states of complexes  $[\text{Ir}(\text{dFppy})_2(\text{PPETS})_2]\text{PF}_6$  (**B**) and  $[\text{Ir}(\text{ppy})_2(\text{dasipy})]\text{OTf}$  (**R**) in THF. in THF.

**Table A.II.2.** Composition (%) of frontier molecular orbitals in the ground and in the first triplet states of complexes  $[\text{Ir}(\text{dFppy})_2(\text{PPETS})_2]\text{PF}_6$  (**B**) and  $[\text{Ir}(\text{ppy})_2(\text{dasipy})]\text{OTf}$  (**R**) in THF. in THF.

	B						R				
	eV	dFppy (1)	dFppy (2)	PPETS (1)	PPETS (2)	Ir	eV	ppy (1)	ppy (2)	dasipy	Ir
LUMO+5	-1.22	9	3	28	52	8	-1.42	35	58	5	2
LUMO+4	-1.34	10	6	55	23	6	-1.92	55	38	4	4
LUMO+3	-1.45	41	44	2	10	1	-2.01	38	57	1	4
LUMO+2	-1.57	40	50	2	6	1	-2.07	3	2	94	1
LUMO+1	-2.02	57	36	1	1	4	-2.18	1	2	96	1
LUMO	<b>-2.17</b>	<b>36</b>	<b>58</b>	<b>2</b>	<b>2</b>	<b>2</b>	<b>-3.00</b>	<b>0</b>	<b>0</b>	<b>96</b>	<b>3</b>
HOMO	<b>-6.40</b>	<b>31</b>	<b>33</b>	<b>1</b>	<b>2</b>	<b>33</b>	<b>-5.89</b>	<b>31</b>	<b>30</b>	<b>2</b>	<b>38</b>
HOMO-1	-6.60	48	42	3	2	5	-6.52	47	45	1	7
HOMO-2	-6.80	41	43	4	1	10	-6.68	31	30	3	35
HOMO-3	-6.83	20	22	12	40	5	-6.80	26	30	7	37
HOMO-4	-6.91	8	15	45	22	10	-6.87	31	24	4	40
HOMO-5	-7.13	24	24	17	30	6	-6.97	30	38	5	28

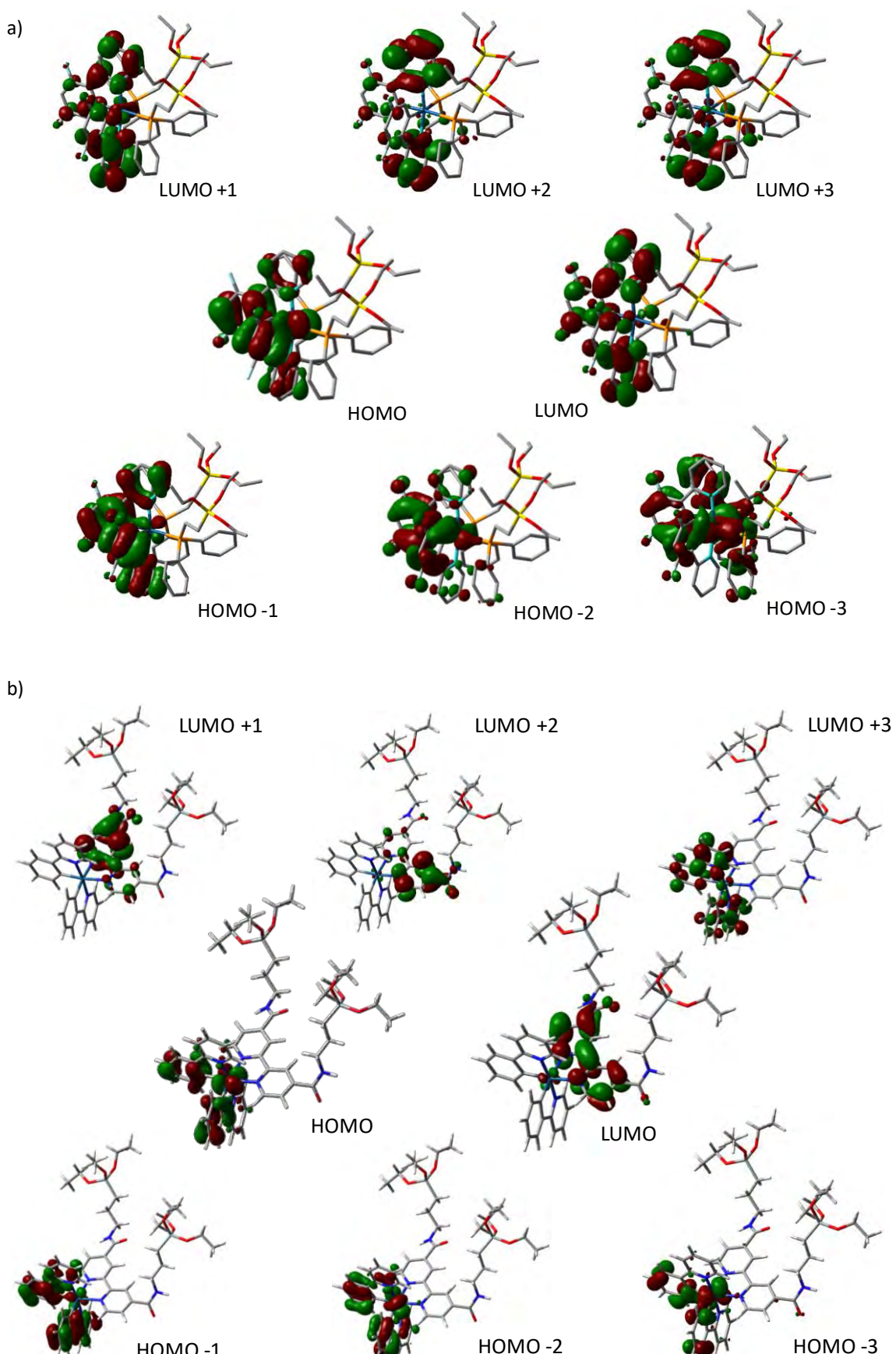


**Figure A.II.2.** Selected frontier Molecular Orbitals for complexes  $[\text{Ir}(\text{dFppy})_2(\text{PPETS})_2]\text{PF}_6$  (B, a) and  $[\text{Ir}(\text{ppy})_2(\text{dasipy})]\text{OTf}$  (R, b) in THF.

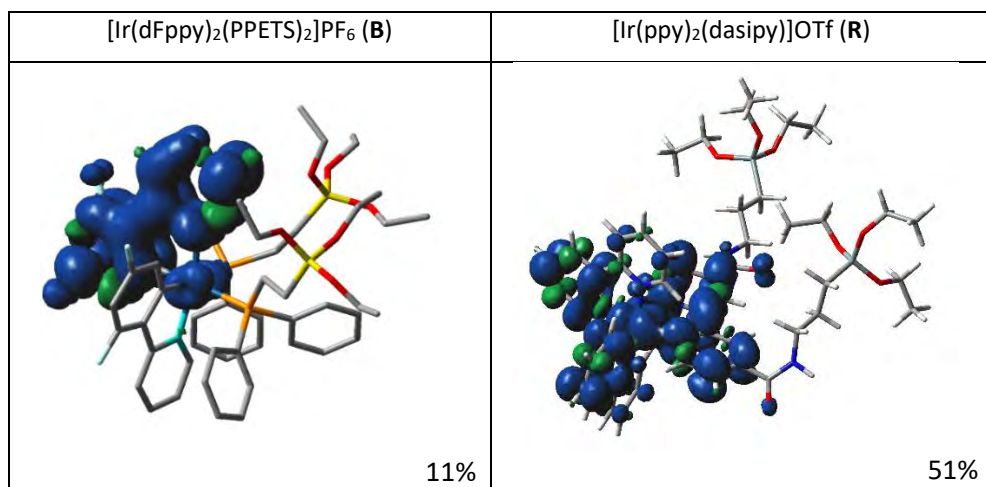


**Figure A.II.3.** Spin-density distributions calculated for the emitting excited state ( $T_1$ ) of complexes  $[\text{Ir}(\text{dFppy})_2(\text{PPETS})_2]\text{PF}_6$  (**B**) and  $[\text{Ir}(\text{ppy})_2(\text{dasipy})]\text{OTf}$  (**R**).

**Table A.II.3.** Selected vertical excitation energies singlets ( $S_0$ ) and first triplets computed by TDDFT/SCRF (THF) with the orbitals involved for complexes  $[\text{Ir}(\text{dFppy})_2(\text{PPETS})_2]\text{PF}_6$  (**B**) and  $[\text{Ir}(\text{ppy})_2(\text{dasipy})]\text{OTf}$  (**R**).

State	$\lambda_{\text{ex}}(\text{calc})(\text{nm})$	f	Transition (% Contribution)	Main character
			<b>B</b>	<b>R</b>
$T_1$	423.9	---	H-1 $\rightarrow$ L+1 (17%), HOMO $\rightarrow$ LUMO (38%)	MLCT/IL
$T_2$	421.4	---	H-1 $\rightarrow$ LUMO (29%), H-1 $\rightarrow$ L+1 (11%), HOMO $\rightarrow$ L+1 (26%)	MLCT/IL
$T_3$	356.4	---	H-2 $\rightarrow$ LUMO (23%), HOMO $\rightarrow$ LUMO (37%)	MLCT/IL
$S_1$	354.6	0.042	HOMO $\rightarrow$ LUMO (95%)	MLCT/IL
$S_2$	340.8	0.0034	HOMO $\rightarrow$ L+1 (94%)	MLCT/IL
$S_3$	323.3	0.0098	H-1 $\rightarrow$ LUMO (88%)	IL
$S_4$	314.9	0.042	H-1 $\rightarrow$ L+1 (85%)	IL
$S_5$	308.4	0.0539	H-2 $\rightarrow$ LUMO (86%)	IL
$S_6$	306.1	0.0679	H-3 $\rightarrow$ LUMO (87%)	L'LCT/IL
$S_7$	301.2	0.0502	H-4 $\rightarrow$ LUMO (90%)	L'LCT
$S_{35}$	259.2	0.0683	H-3 $\rightarrow$ L+3 (43%), HOMO $\rightarrow$ L+6 (15%)	L'LCT/IL
<hr/>				
$T_1$	498.55	---	HOMO $\rightarrow$ LUMO (98%)	ML'CT/LL'CT
$T_2$	450.01	---	H-1 $\rightarrow$ L+4 (15%), HOMO $\rightarrow$ L+3 (63%)	MLCT/IL
$S_1$	492.98	0.0004	HOMO $\rightarrow$ LUMO (99%)	ML'CT/LL'CT
$S_2$	419.27	0.0023	H-4 $\rightarrow$ LUMO (25%), H-2 $\rightarrow$ LUMO (71%)	ML'CT/LL'CT
$S_3$	415.33	0.0287	H-1 $\rightarrow$ LUMO (93%)	LL'CT/ML'CT
$S_5$	396.57	0.0591	HOMO $\rightarrow$ L+3 (96%)	IL/MLCT
$S_6$	388.98	0.0757	H-3 $\rightarrow$ LUMO (67%), HOMO $\rightarrow$ L+2 (12%)	ML'CT/LL'CT
$S_8$	377.12	0.0211	H-4 $\rightarrow$ LUMO (11%), H-3 $\rightarrow$ LUMO (11%), HOMO $\rightarrow$ L+2 (12%), HOMO $\rightarrow$ L+4 (58%)	ML'CT/LL'CT /IL/MLCT
$S_{10}$	360.74	0.0198	H-5 $\rightarrow$ LUMO (88%), H-3 $\rightarrow$ LUMO (10%)	ML'CT/LL'CT
$S_{16}$	320.35	0.0355	H-2 $\rightarrow$ L+1 (19%), H-2 $\rightarrow$ L+3 (12%), H-1 $\rightarrow$ L+3 (35%)	IL/ML'CT/LL'CT
$S_{38}$	285.52	0.2311	H-3 $\rightarrow$ L+3 (14%), H-2 $\rightarrow$ L+3 (13%), H-4 $\rightarrow$ L+4 (10%)	IL/MLCT
$S_{51}$	266.37	0.3573	H-2 $\rightarrow$ L+5 (10%), H-1 $\rightarrow$ L+6 (46%), HOMO $\rightarrow$ L+8 (20%)	IL/MLCT
$S_{60}$	257.83	0.2280	H-3 $\rightarrow$ L+6 (25%), HOMO $\rightarrow$ L+8 (37%)	IL/MLCT

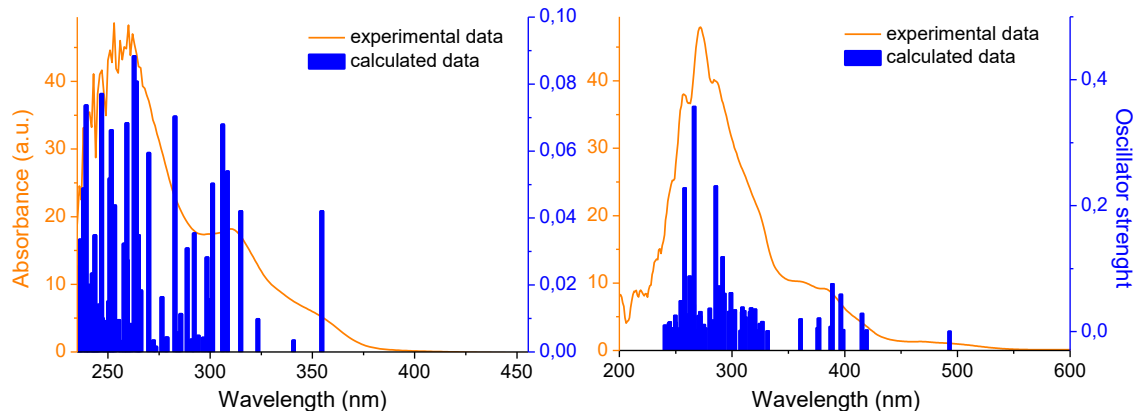


**Figure A.II.4.** Calculated stick absorption spectra of complexes  $[\text{Ir}(\text{dFppy})_2(\text{PPETS})_2]\text{PF}_6$  (B, left) and  $[\text{Ir}(\text{ppy})_2(\text{dasipy})]\text{OTf}$  (R, right) in THF compared with the experimental ones.

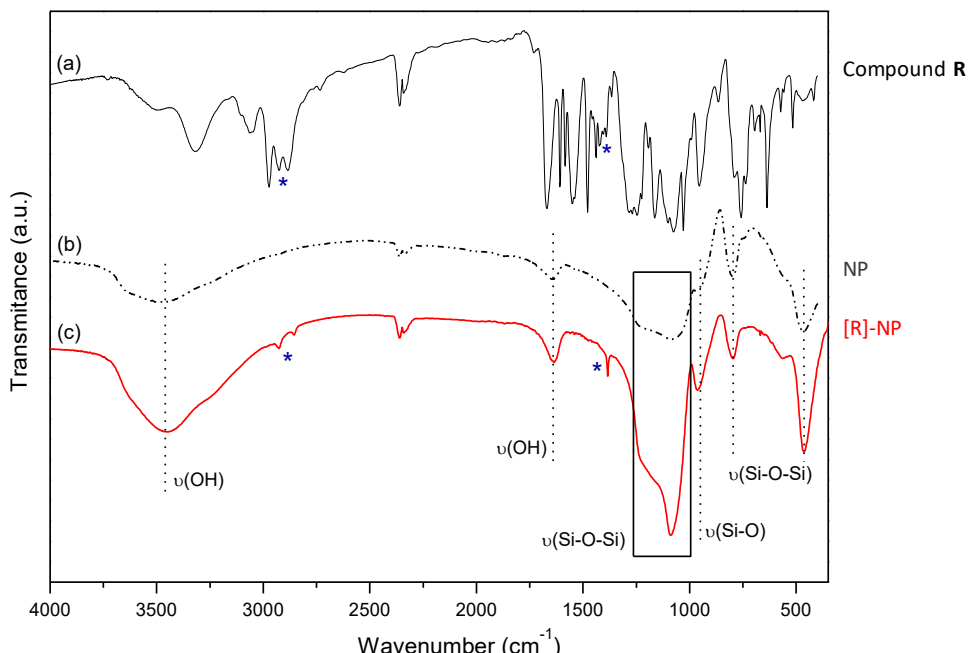


**Figure A.II.5.** FTIR spectra of the hybrid organometallo-silica nanoparticles  $[\text{R}]\text{-NP}$  (c) in comparison with the spectra of the pure complex R (a) and the control material (b). (\*) Characteristic absorption of the complexes observed in the hybrid material.

**Anexo Capítulo III****Tabla A.III.1.** Distancias de enlace ( $\text{\AA}$ ) y ángulos ( $^{\circ}$ ) para el compuesto  $[\text{Ir}(\text{dFppy})_2(\text{dbbpy})]\text{Cl}\cdot\text{CHCl}_3$  (**8·CHCl<sub>3</sub>**).

Ir(1)-N(1)	2.049(3)	Ir(1)-N(1')	2.049(3)
Ir(1)-C(10)	2.008(4)	Ir(1)-C(10')	2.008(4)
Ir(1)-N(a)	2.125(8)	Ir(1)-N(a')	2.125(8)
Cl(1)…H(16)	2.602(5)	Cl(1)…H(16')	2.602(5)
Cl(1)…H(18)	2.458(3)	Cl(1)…H(18')	2.458(3)
N(1)-Ir(1)-C(10)	80.4(6)	N(1')-Ir(1)-C(10')	80.4(6)
N(1)-Ir(1)-N(1')	174.6(3)	N(1)-Ir(1)-C(10')	95.7(3)
N(1')-Ir(1)-C(10)	95.7(3)	N(a)-Ir(1)-N(a')	77.2(9)
N(a)-Ir(1)-N(1)	88.0(2)	N(a')-Ir(1)-N(1')	88.0(2)
N(a)-Ir(1)-N(1')	96.1(9)	N(a')-Ir(1)-N(1)	96.1(9)

**Tabla A.III.2.** Datos cristalográficos para el compuesto  $[\text{Ir}(\text{dFppy})_2(\text{dbbpy})]\text{Cl}\cdot\text{CHCl}_3$  (**8·CHCl<sub>3</sub>**).

Empirical formula	C <sub>44</sub> H <sub>40</sub> Cl <sub>7</sub> F <sub>4</sub> IrN <sub>6</sub> O <sub>2</sub>
F <sub>w</sub>	1201.17
T (K)	135(1) K
Crystal system, space group	Monoclinic
a( $\text{\AA}$ )	17.941(3)
b( $\text{\AA}$ )	28.409(5)
c( $\text{\AA}$ )	11.205(2)
$\alpha$ (deg)	90
$\beta$ (deg)	110.153(6)
$\gamma$ (deg)	90
Volume ( $\text{\AA}^3$ )	5361.5(17)
Z	4
D <sub>calcd</sub> (Mg/m <sup>3</sup> )	1.488
Absorption coefficient (mm <sup>-1</sup> )	2.892
F(000)	2376
$\theta$ range for data collection (deg)	2.868 to 28.281
No of data // restraints // params	6646 // 2 // 299
Goodness-of-fit on F <sup>2(a)</sup>	1.041
Final R indexes [I>2σ(I)] <sup>(a)</sup>	R <sub>1</sub> = 0.0235, wR <sub>2</sub> = 0.0572
R indexes (all data) <sup>(a)</sup>	R <sub>1</sub> = 0.0273, wR <sub>2</sub> = 0.0584
Largest diff peak and hole (e· $\text{\AA}^{-3}$ )	0.947 and -0.586

(a)  $R_1 = \sum(|F_o| - |F_c|)/\sum|F_o|$ ;  $wR_2 = [\sum w(F_o^2 - F_c^2)^2 / \sum wF_o^2]^{1/2}$ ; goodness of fit =  $\{\sum[w(F_o^2 - F_c^2)^2] / (N_{\text{obs}} - N_{\text{param}})\}^{1/2}$ ;  $w = [\sigma^2(F_o) + (g_1P)^2 + g_2P]^{-1}$ ;  $P = [\max(F_o^2; 0) + 2F_c^2]/3$ .

**Tabla A.III.3.** Geometrías optimizadas por DFT para los estados fundamental y triplete de los compuestos  $[\text{Ir}(\text{dFppy})_2(\text{dasipy})]\text{PF}_6$  (**7**) y  $[\text{Ir}(\text{dFppy})_2(\text{dbbpy})]\text{Cl}$  (**8**) en THF.

$[\text{Ir}(\text{dFppy})_2(\text{dasipy})]\text{PF}_6$ ( <b>7</b> )			$[\text{Ir}(\text{dFppy})_2(\text{dbbpy})]\text{Cl}$ ( <b>8</b> )		
	$S_0$	$T_1$		$S_0$	$T_1$
Ir(1)-N(1)	2.081	2.080	Ir(1)-N(1)	2.080	2.079
Ir(1)-N(1')	2.082	2.080	Ir(1)-N(1')	2.080	2.079
Ir(1)-C(10)	2.021	2.000	Ir(1)-C(10)	2.022	2.002
Ir(1)-C(10')	2.022	1.999	Ir(1)-C(10')	2.022	2.002
Ir(1)-N(a)	2.204	2.191	Ir(1)-N(a)	2.199	2.180
Ir(1)-N(a')	2.202	2.182	Ir(1)-N(a')	2.199	2.180
N(1)-Ir(1)-N(1')	173.60	176.20	N(1)-Ir(1)-N(1')	173.80	176.54
N(1)-Ir(1)-C(10)	80.09	80.96	N(1)-Ir(1)-C(10)	80.09	80.85
N(1')-Ir(1)-C(10')	80.06	80.90	N(1')-Ir(1)-C(10')	80.09	80.84
N(1)-Ir(1)-C(10')	95.37	96.53	N(1)-Ir(1)-C(10')	95.47	96.80
N(1')-Ir(1)-C(10)	95.30	96.46	N(1')-Ir(1)-C(10)	95.47	96.80
N(a)-Ir(1)-N(a')	75.02	75.39	N(a)-Ir(1)-N(a')	75.39	75.68
N(a)-Ir(1)-N(1)	88.15	86.93	N(a)-Ir(1)-N(1)	87.97	87.10
N(a)-Ir(1)-C(10)	98.00	94.38	N(a)-Ir(1)-C(10)	97.63	94.53
N(a)-Ir(1)-N(1')	96.93	96.07	N(a)-Ir(1)-N(1')	96.95	95.64
N(a)-Ir(1)-C(10')	172.39	170.10	N(a)-Ir(1)-C(10')	172.58	169.83
N(a')-Ir(1)-N(1)	97.27	95.49	N(a')-Ir(1)-N(1)	96.95	95.62
N(a')-Ir(1)-C(10)	172.68	169.39	N(a')-Ir(1)-C(10)	172.58	169.81
N(a')-Ir(1)-N(1')	87.85	87.55	N(a')-Ir(1)-N(1')	87.97	87.13
N(a')-Ir(1)-C(10')	97.80	95.01	N(a')-Ir(1)-C(10')	97.63	94.55
			Cl(1)…H(16)	2.503	2.587
			Cl(1)…H(18)	2.336	2.362
			Cl(1)…H(16')	2.503	2.590
			Cl(1)…H(18')	2.336	2.362

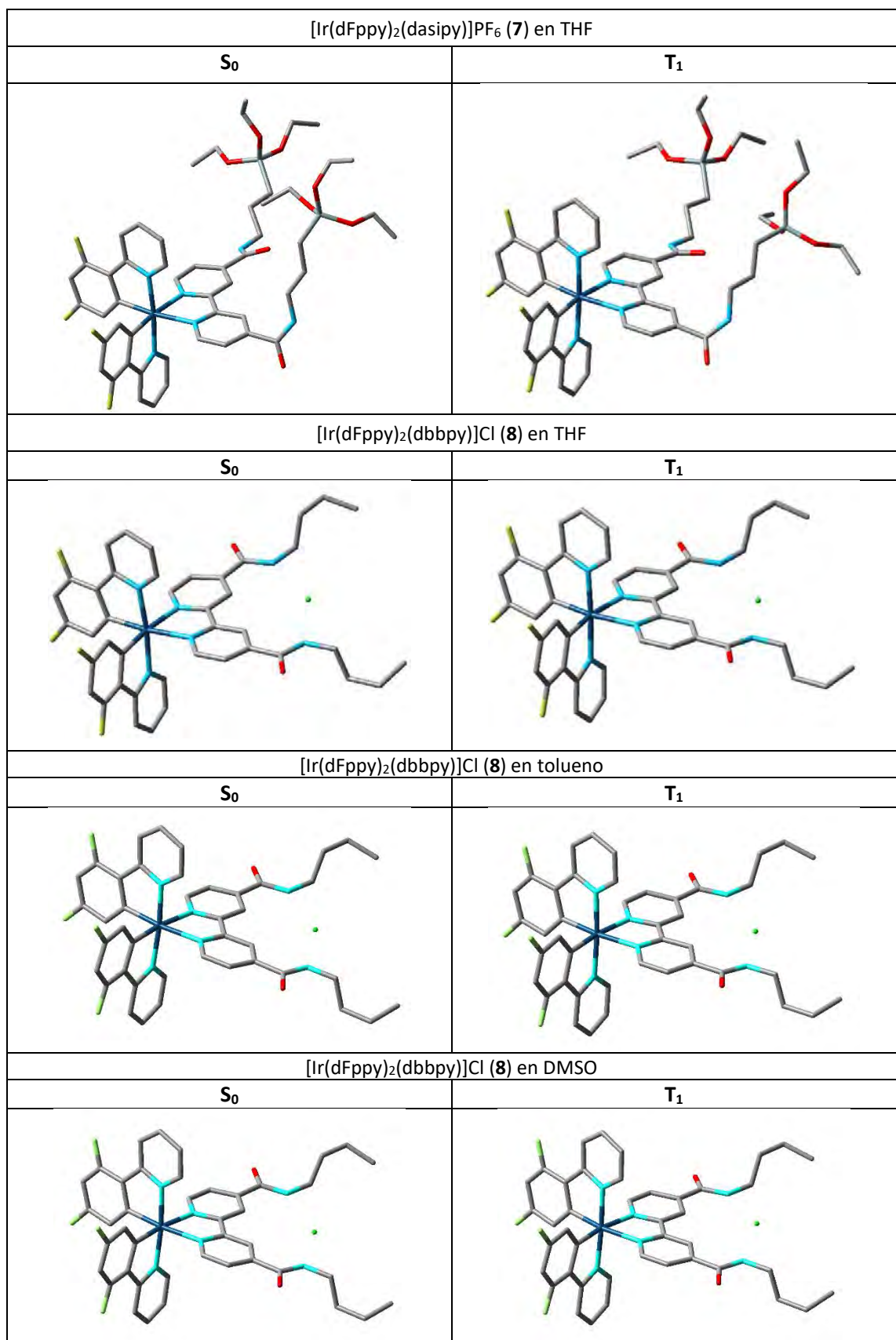


**Figura A.III.1.** Estructuras optimizadas de los estados  $S_0$  y  $T_1$  para el compuesto  $[\text{Ir}(\text{dFppy})_2(\text{dasipy})]\text{PF}_6$  (**7**) en THF y  $[\text{Ir}(\text{dFppy})_2(\text{dbbpy})]\text{Cl}$  (**8**) en THF, tolueno y DMSO.

**Tabla A.III.4.** Composición (%) de los orbitales frontera en el estado fundamental y en el primer estado triplete para los compuestos  $[\text{Ir}(\text{dFppy})_2(\text{dasipy})]\text{PF}_6$  (**7**) en THF y  $[\text{Ir}(\text{dFppy})_2(\text{dbbpy})]\text{Cl}$  (**8**) en THF, tolueno y DMSO.

	$[\text{Ir}(\text{dFppy})_2(\text{dasipy})]\text{PF}_6$ ( <b>7</b> ) en THF					$[\text{Ir}(\text{dFppy})_2(\text{dbbpy})]\text{Cl}$ ( <b>8</b> ) en THF				
	eV	dFppy (1)	dFppy (2)	dasipy	Ir	eV	dFppy (1)	dFppy (2)	dbbpy-Cl	Ir
LUMO+5	-1.47	25	68	5	2	-1.21	45	45	9	2
LUMO+4	-2.04	41	26	31	2	-1.76	4	4	90	1
LUMO+3	-2.09	26	6	65	3	-1.79	36	36	25	2
LUMO+2	-2.14	29	64	3	4	-1.86	11	11	75	2
LUMO+1	-2.27	1	2	96	1	-1.89	47	47	1	4
LUMO	<b>-3.09</b>	<b>0</b>	<b>0</b>	<b>96</b>	<b>3</b>	<b>-2.65</b>	<b>0</b>	<b>0</b>	<b>96</b>	<b>3</b>
HOMO	<b>-6.24</b>	<b>32</b>	<b>30</b>	<b>2</b>	<b>36</b>	<b>-5.98</b>	<b>30</b>	<b>30</b>	<b>2</b>	<b>38</b>
HOMO-1	-6.68	52	41	1	6	-6.45	46	46	1	8
HOMO-2	-6.79	39	49	1	11	-6.52	0	0	100	0
HOMO-3	-7.06	17	11	10	61	-6.55	42	42	2	15
HOMO-4	-7.09	24	28	8	41	-6.62	0	0	99	1
HOMO-5	-7.17	32	37	7	25	-6.70	0	0	99	1

	$[\text{Ir}(\text{dFppy})_2(\text{dbbpy})]\text{Cl}$ ( <b>8</b> ) en tolueno					$[\text{Ir}(\text{dFppy})_2(\text{dbbpy})]\text{Cl}$ ( <b>8</b> ) en DMSO				
	eV	dFppy (1)	dFppy (2)	dbbpy-Cl	Ir	eV	dFppy (1)	dFppy (2)	dbbpy-Cl	Ir
LUMO+5	-1.36	41	41	16	2	-1.14	46	45	7	2
LUMO+4	-1.78	8	8	83	1	-1.73	45	45	6	3
LUMO+3	-1.82	2	2	96	0	-1.74	3	3	92	1
LUMO+2	-1.97	46	46	4	4	-1.82	47	48	1	4
LUMO+1	-2.05	47	47	1	4	-1.85	3	2	94	1
LUMO	<b>-2.68</b>	<b>0</b>	<b>0</b>	<b>96</b>	<b>3</b>	<b>-2.63</b>	<b>0</b>	<b>0</b>	<b>96</b>	<b>3</b>
HOMO	<b>-6.10</b>	<b>30</b>	<b>30</b>	<b>3</b>	<b>38</b>	<b>-5.93</b>	<b>30</b>	<b>30</b>	<b>2</b>	<b>38</b>
HOMO-1	-6.14	0	0	100	0	-6.39	46	46	1	7
HOMO-2	-6.25	0	0	99	0	-6.50	42	41	1	16
HOMO-3	-6.38	0	0	100	0	-6.71	2	3	85	10
HOMO-4	-6.57	44	44	4	9	-6.71	16	16	9	59
HOMO-5	-6.63	3	3	91	2	-6.75	14	14	29	42

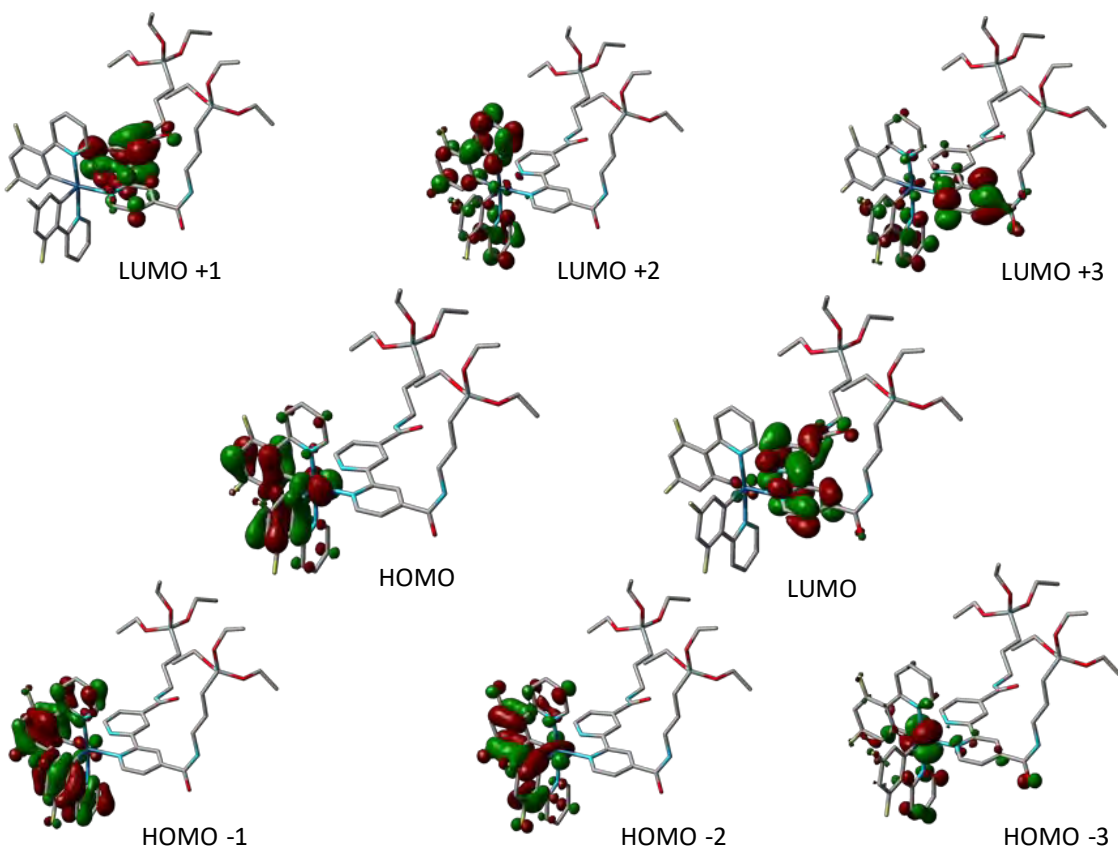


**Figura A.III.2.** Orbitales Moleculares Frontera del compuesto  $[\text{Ir}(\text{dFppy})_2(\text{dasipy})]\text{PF}_6$  (**7**) en THF.

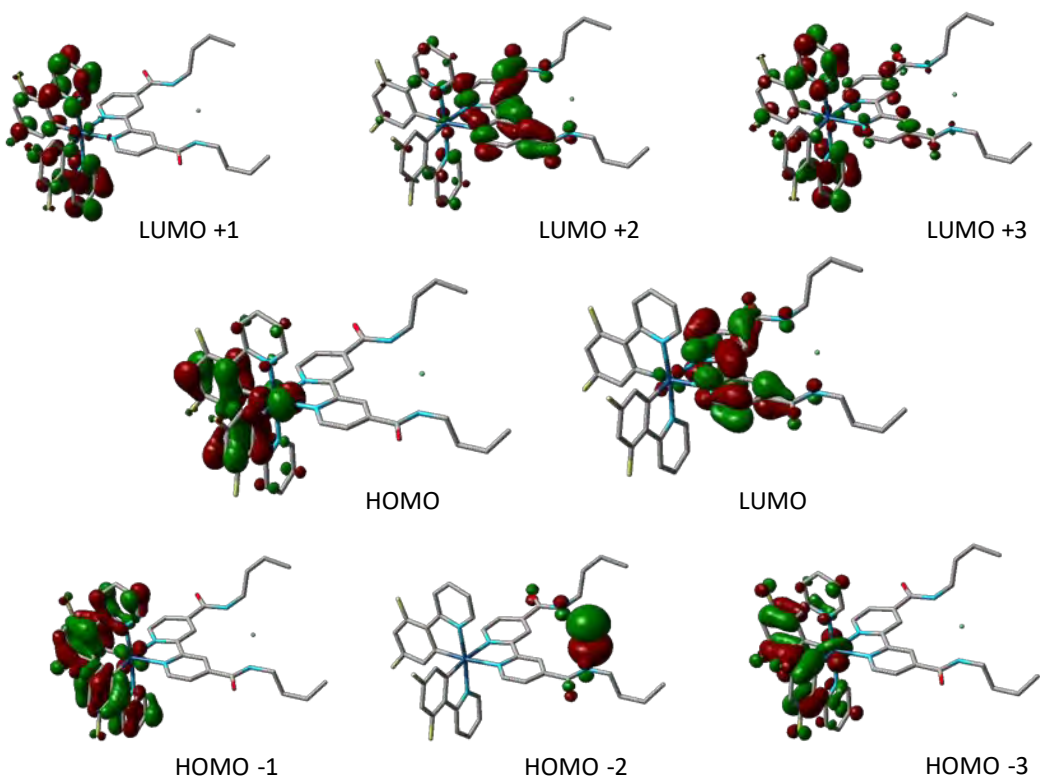


**Figura A.III.3.** Orbitales Moleculares Frontera del compuesto  $[\text{Ir}(\text{dFppy})_2(\text{dbppy})]\text{Cl}$  (**8**) en THF.

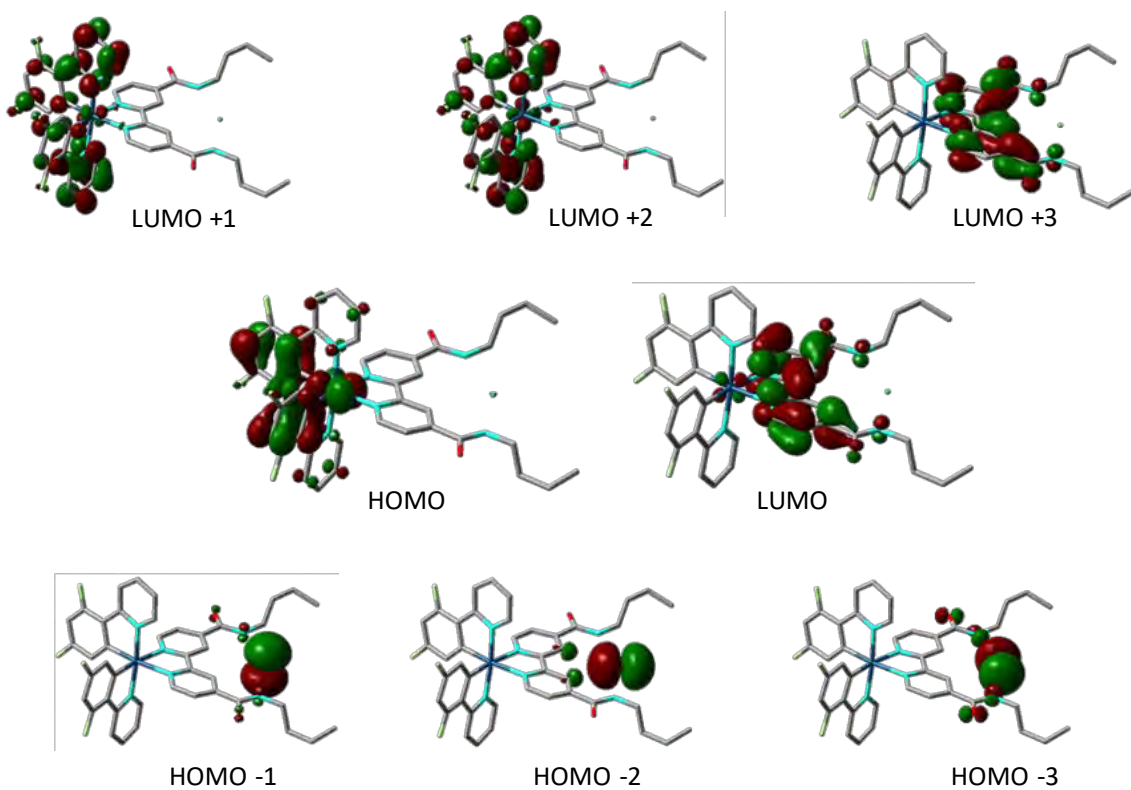


**Figura A.III.4.** Orbitales Moleculares Frontera del compuesto  $[\text{Ir}(\text{dFppy})_2(\text{dbppy})]\text{Cl}$  (**8**) en tolueno.

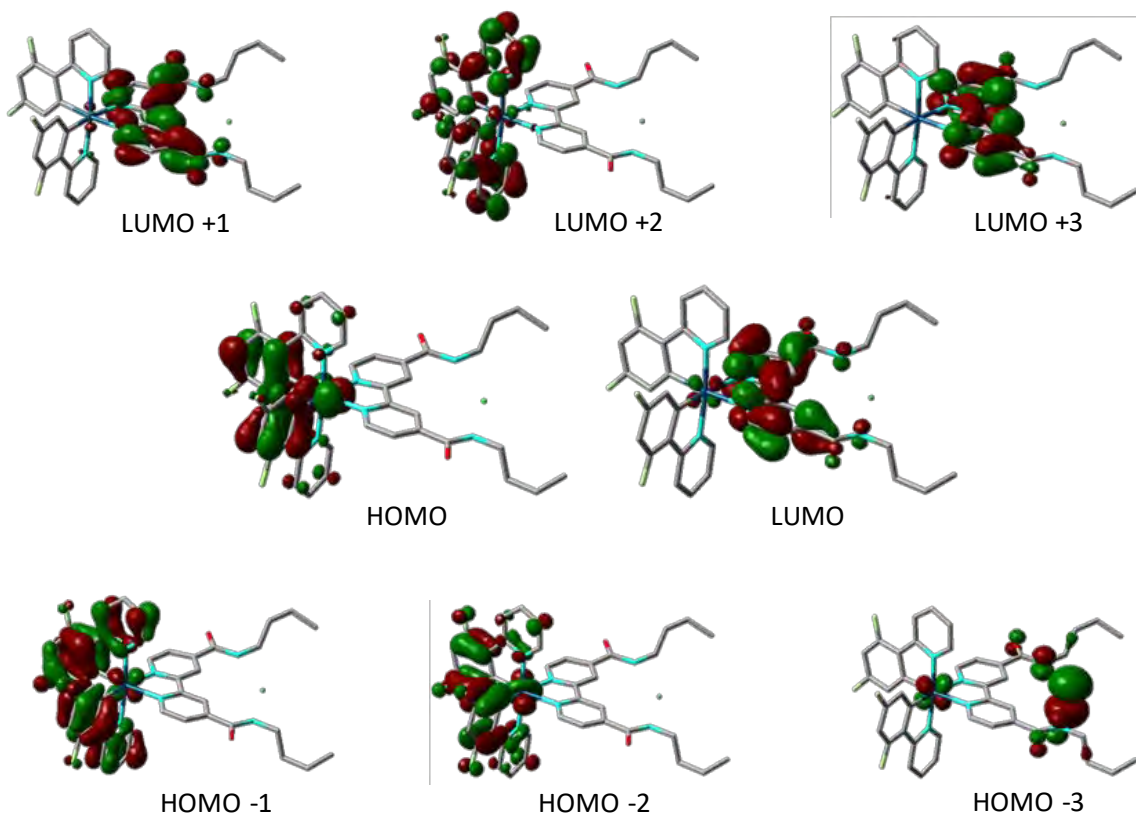


**Figura A.III.5.** Orbitales Moleculares Frontera del compuesto  $[\text{Ir}(\text{dFppy})_2(\text{dbppy})]\text{Cl}$  (**8**) en DMSO.

**Tabla A.III.5.** Selección de energías de los singletes ( $S_0$ ) y de los primeros tripletes ( $T_1$ ) calculadas por TDDFT/SCRF con los orbitales implicados para los compuestos **7** y **8**.

Estado	$\lambda_{ex}(\text{nm})$	f	Transiciones principales (% Contribución)	Carácter principal
[Ir(dFppy) <sub>2</sub> (dasipy)]PF <sub>6</sub> ( <b>7</b> ) en THF				
T <sub>1</sub>	505.70	---	HOMO→LUMO (97%)	ML'CT/LL'CT
T <sub>2</sub>	432.66	---	H-3→LUMO (43%), H-2→LUMO (11%)	ML'CT/LL'CT
T <sub>3</sub>	428.80	---	H-2→L+2 (11%), H-1→L+4 (15%), HOMO→L+2 (47%)	LL'CT/ML'CT/IL
T <sub>5</sub>	421.86	---	H-4→LUMO (22%), H-1→LUMO (42%)	LL'CT/ML'CT
S <sub>1</sub>	499.49	0.0005	HOMO→LUMO (99%)	ML'CT/LL'CT
S <sub>2</sub>	404.92	0.0213	H-1→LUMO (95%)	ML'CT/LL'CT
S <sub>5</sub>	371.12	0.0542	HOMO→L+2 (94%)	ML'CT/LL'CT
S <sub>6</sub>	369.41	0.0824	H-4→LUMO (58%)	ML'CT/LL'CT
S <sub>7</sub>	366.83	0.0301	HOMO→L+1 (70%)	ML'CT/LL'CT
S <sub>19</sub>	307.81	0.0770	H-2→L+2 (16%), H-1→L+3 (43%), H-3→L+3 (28%)	LL'CT/IL/ML'CT
S <sub>38</sub>	280.83	0.2825	H-5→L+2 (15%), H-1→L+2 (13%)	IL
S <sub>52</sub>	262.23	0.1920	H-2→L+5 (37%), HOMO→L+8 (28%)	IL
[Ir(dFppy) <sub>2</sub> (dbbpy)]Cl ( <b>8</b> ) en THF				
T <sub>1</sub>	472.34	---	HOMO→LUMO (95%)	ML'CT/LL'CT
T <sub>2</sub>	438.92	---	H-3→L+1 (11%), H-1→L+3 (17%), HOMO→L+1 (50%)	ML'CT/LL'CT/
T <sub>5</sub>	414.92	---	H-3→LUMO (45%), H-1→LUMO (37%)	ML'CT/LL'CT
S <sub>1</sub>	466.14	0.0004	HOMO→LUMO (99%)	ML'CT/LL'CT
S <sub>3</sub>	380.38	0.0469	H-1→LUMO (95%)	ML'CT/LL'CT
S <sub>5</sub>	372.39	0.0562	HOMO→L+1 (96%)	ML'CT/LL'CT
S <sub>7</sub>	361.55	0.0321	HOMO→L+2 (89%)	ML'CT/LL'CT
S <sub>20</sub>	308.61	0.0908	H-3→L+1 (20%), H-1→L+2 (37%), H-1→LUMO (23%)	IL / LL'CT/ML'CT
S <sub>22</sub>	303.78	0.0570	H-1→L+3 (15%), H-3→L+2 (16%), H-3→L+3 (35%)	IL / LL'CT/ML'CT
S <sub>52</sub>	273.32	0.2169	H-1→L+5 (26%), H-3→L+1 (24%), H-8→L+1 (30%)	IL
S <sub>66</sub>	262.56	0.1657	H-6→L+5 (17%), H-3→L+5 (58%)	IL
[Ir(dFppy) <sub>2</sub> (dbbpy)]Cl ( <b>8</b> ) en tolueno				
T <sub>1</sub>	457.17	---	HOMO→LUMO (94%)	ML'CT/LL'CT
T <sub>2</sub>	433.84	---	H-4→LUMO (93%)	ML'CT/LL'CT
T <sub>4</sub>	427.10	---	H-4→L+1 (32%), HOMO→L+2 (39%)	IL/MLCT
S <sub>1</sub>	451.11	0.0005	HOMO→LUMO (99%)	ML'CT/LL'CT
S <sub>5</sub>	377.17	0.0565	HOMO→L+1 (96%)	MLCT/ILCT
S <sub>7</sub>	370.51	0.0717	H-4→LUMO (86%)	ML'CT/LL'CT
S <sub>9</sub>	361.60	0.0278	H-4→L+3 (80%)	ML'CT/LL'CT
S <sub>30</sub>	311.28	0.1003	H-6→L+1 (16%), H-4→L+2 (65%)	IL
[Ir(dFppy) <sub>2</sub> (dbbpy)]Cl ( <b>8</b> ) en DMSO				
T <sub>1</sub>	477.98	---	HOMO→LUMO (96%)	ML'CT/LL'CT
T <sub>2</sub>	428.12	---	H-4→LUMO (24%), HOMO→L+2 (15%)	ML'CT/LL'CT
T <sub>4</sub>	423.60	---	H-1→L+2 (34%), HOMO→L+2 (35%)	ML'CT/LL'CT/IL
S <sub>1</sub>	471.67	0.0004	HOMO→LUMO (99%)	ML'CT/LL'CT
S <sub>3</sub>	384.29	0.0414	H-1→LUMO (94%)	ML'CT/LL'CT
S <sub>4</sub>	370.17	0.0577	HOMO→L+1 (96%)	ML'CT/LL'CT
S <sub>20</sub>	308.54	0.0966	H-2→L+2 (19%), H-1→L+1 (53%)	IL / LL'CT/ML'CT
S <sub>60</sub>	261.50	0.2445	H-2→L+5 (58%)	IL

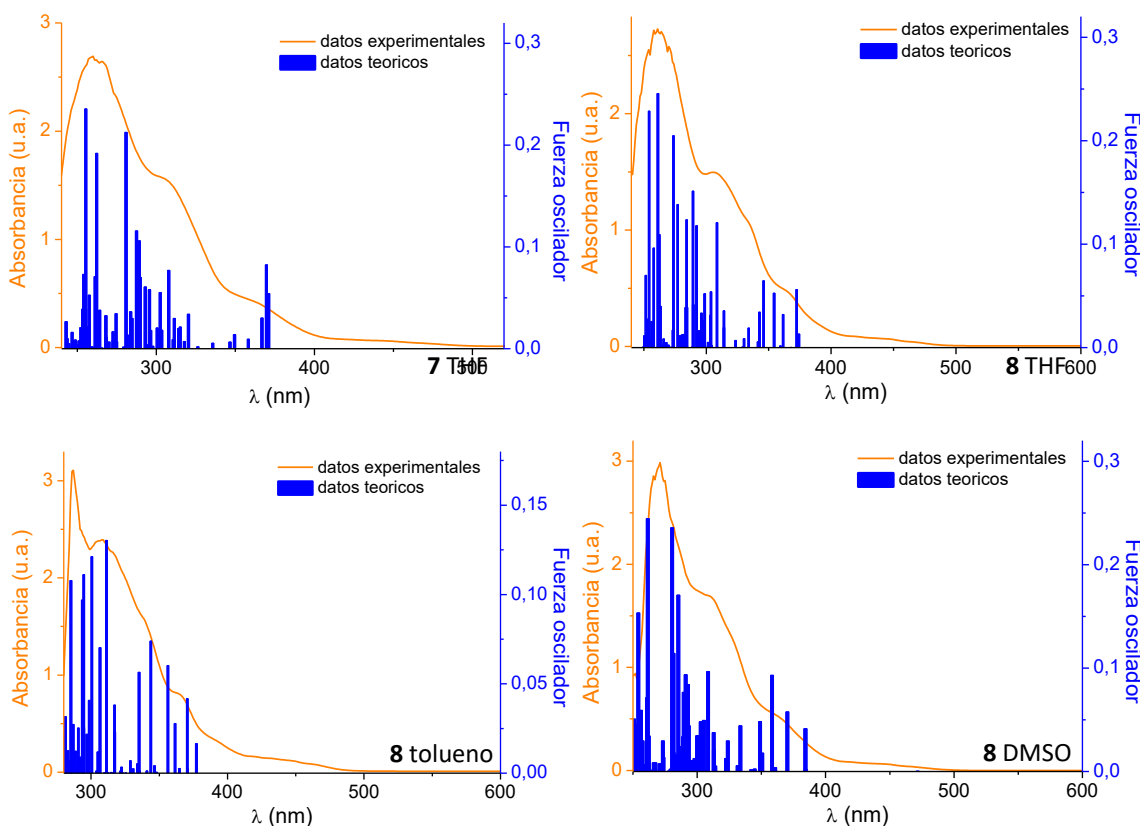


**Figura A.III.6.** Espectros de absorción calculados (en barras) para los compuestos  $[\text{Ir}(\text{dFppy})_2(\text{dasipy})]\text{PF}_6$  (**7**, izquierda) y  $[\text{Ir}(\text{dFppy})_2(\text{dbbpy})]\text{Cl}$  (**8**, derecha) en THF en comparación con los experimentales.

**Tabla A.III.6.** Composición (%) de los orbitales moleculares frontera en el primer estado triplete para los compuestos  $[\text{Ir}(\text{dFppy})_2(\text{dasipy})]\text{PF}_6$  (**7**) en THF y  $[\text{Ir}(\text{dFppy})_2(\text{dbbpy})]\text{Cl}$  (**8**) en THF, tolueno y DMSO.

	$[\text{Ir}(\text{dFppy})_2(\text{dasipy})]\text{PF}_6$ ( <b>7</b> )					$[\text{Ir}(\text{dFppy})_2(\text{dbbpy})]\text{Cl}$ ( <b>8</b> ) en THF				
	eV	dFppy (1)	dFppy (2)	dasipy	Ir	eV	dFppy (1)	dFppy (2)	dbbpy- Cl	Ir
SOMO	-3.96	0	0	98	2	-3.27	0	0	97	3
SOMO-1	-5.49	28	28	3	41	-5.31	28	27	3	41

	$[\text{Ir}(\text{dFppy})_2(\text{dbbpy})]\text{Cl}$ ( <b>8</b> ) en tolueno					$[\text{Ir}(\text{dFppy})_2(\text{dbbpy})]\text{Cl}$ ( <b>8</b> ) en DMSO				
	eV	dFppy (1)	dFppy (2)	dbbpy- Cl	Ir	eV	dFppy (1)	dFppy (2)	dbbpy- Cl	Ir
SOMO	-3.16	0	0	97	2	-3.53	0	0	97	2
SOMO-1	-5.53	19	19	22	40	-5.12	27	27	3	42

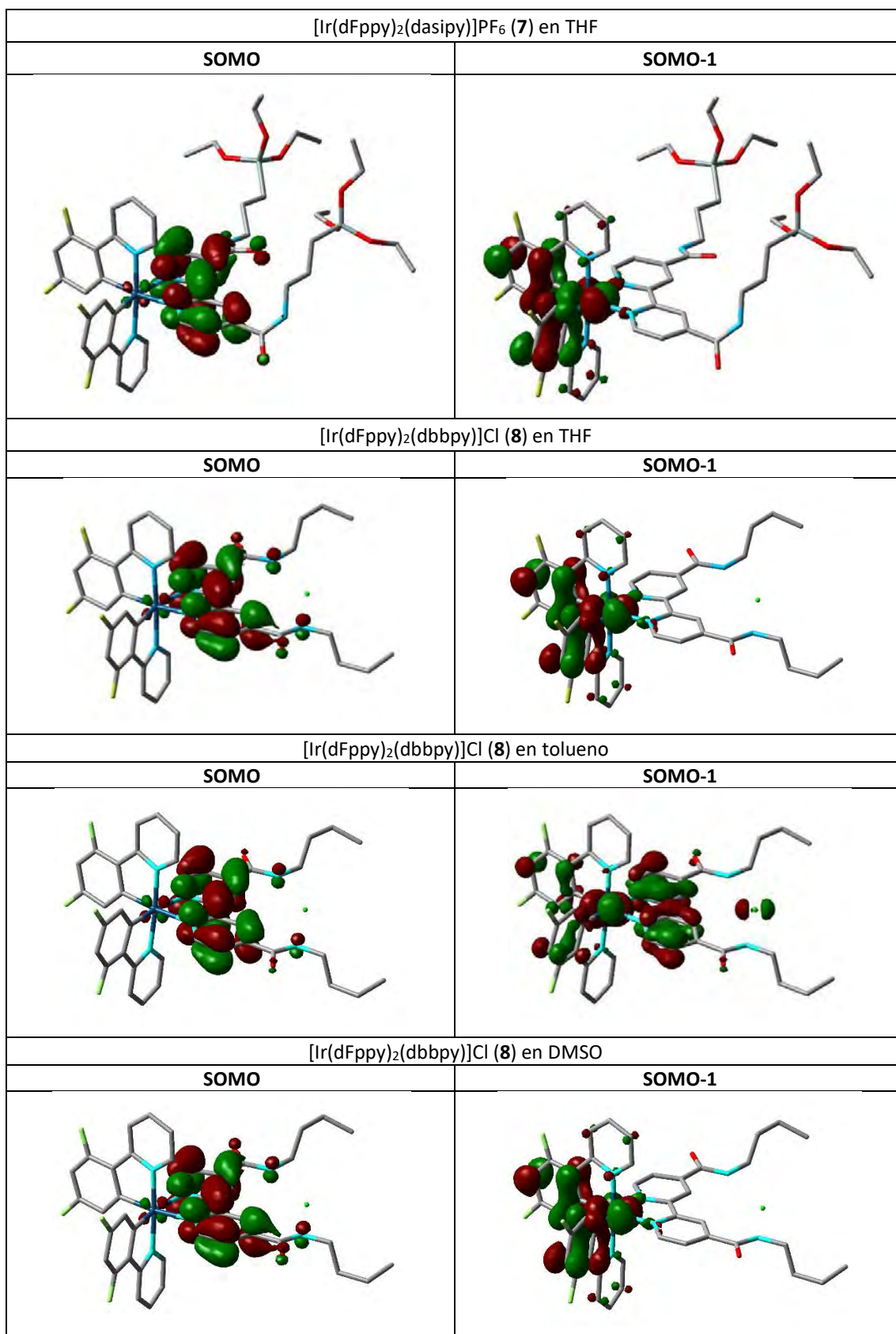


**Figura A.III.7.** Orbitales SOMO and SOMO-1 de los compuestos  $[Ir(dFppy)_2(dasipy)]PF_6$  (**7**) en THF y  $[Ir(dFppy)_2(dbbpy)]Cl$  (**8**) en THF, tolueno y DMSO.

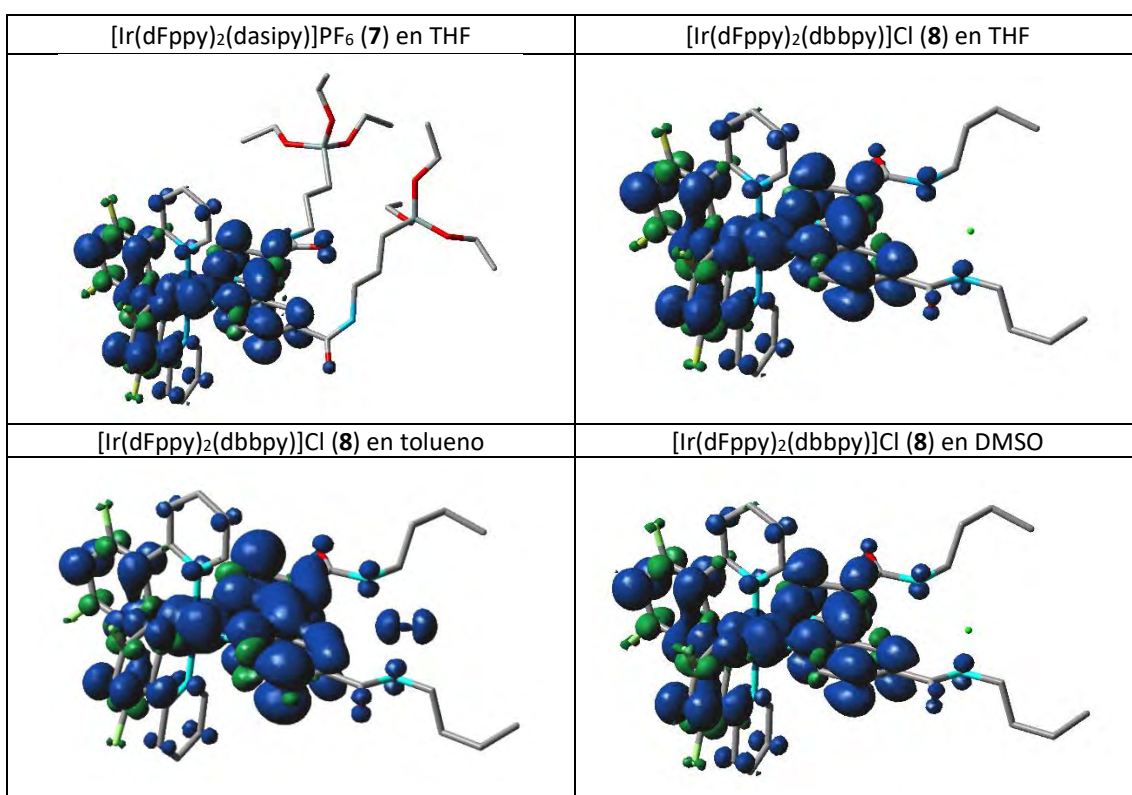


**Figura A.III.8.** Distribución de densidad de spin del estado excitado de emisión para los compuestos [Ir(dFppy)<sub>2</sub>(dasipy)]PF<sub>6</sub> (**7**) en THF y [Ir(dFppy)<sub>2</sub>(dbbpy)]Cl (**8**) en THF, tolueno y DMSO.

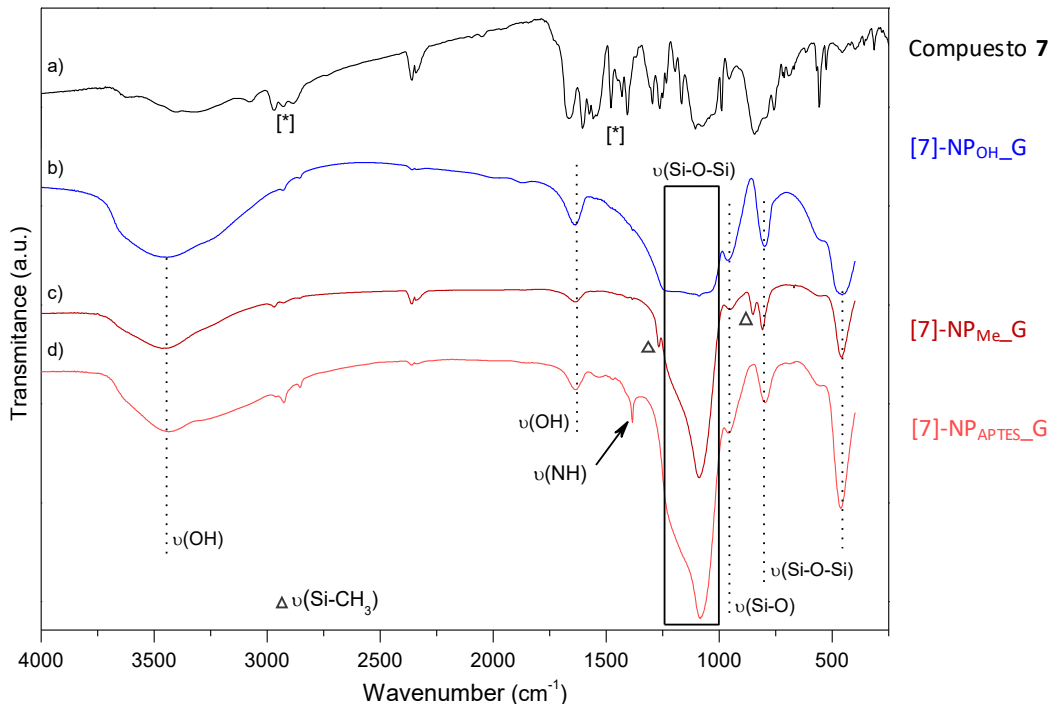


**Figura A.III.9.** Espectros IR del derivado de iridio(III) (a) en comparación con los correspondientes a las nanopartículas grafteadas: [7]-NP<sub>OH</sub>\_G (b), [7]-NP<sub>Me</sub>\_G (c) y [7]-NP<sub>APTES</sub>\_G (d). [\*] Absorciones características del compuesto observadas en los materiales silíceos.

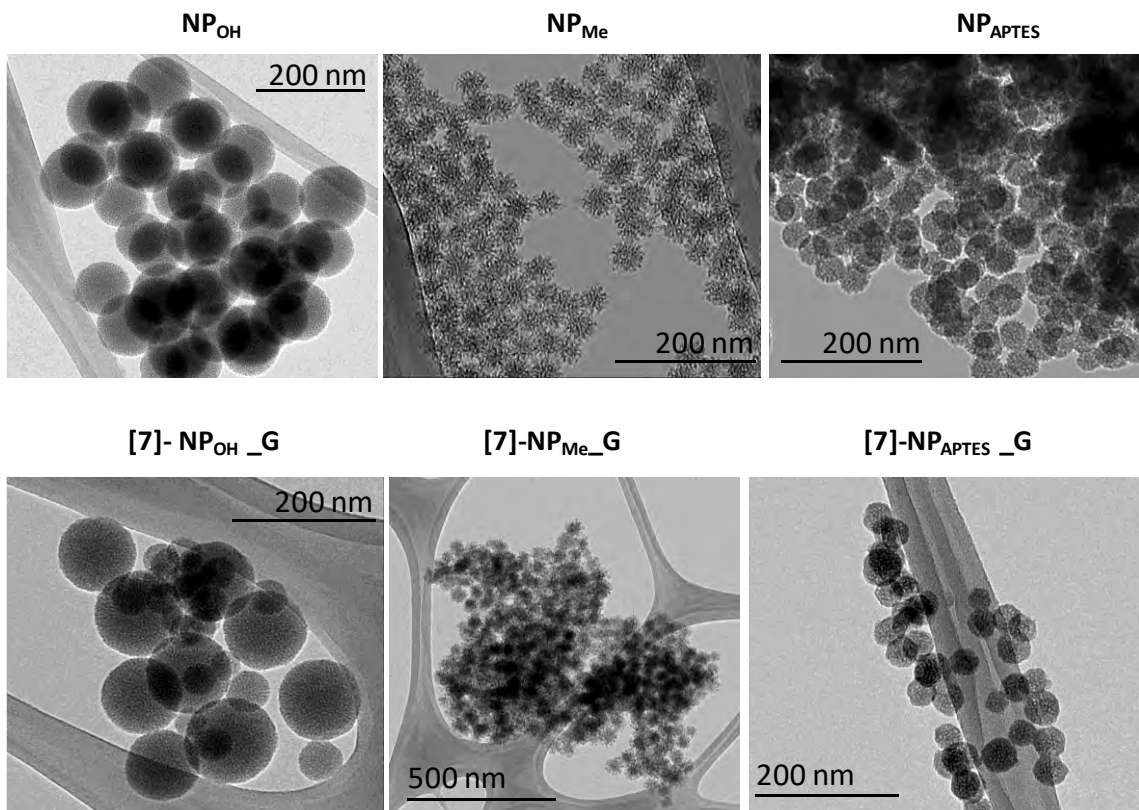


**Figura A.III.10.** Imágenes TEM representativas de las nanopartículas control (NP, arriba) y de las grafteadas ([7]-NP\_G, abajo).

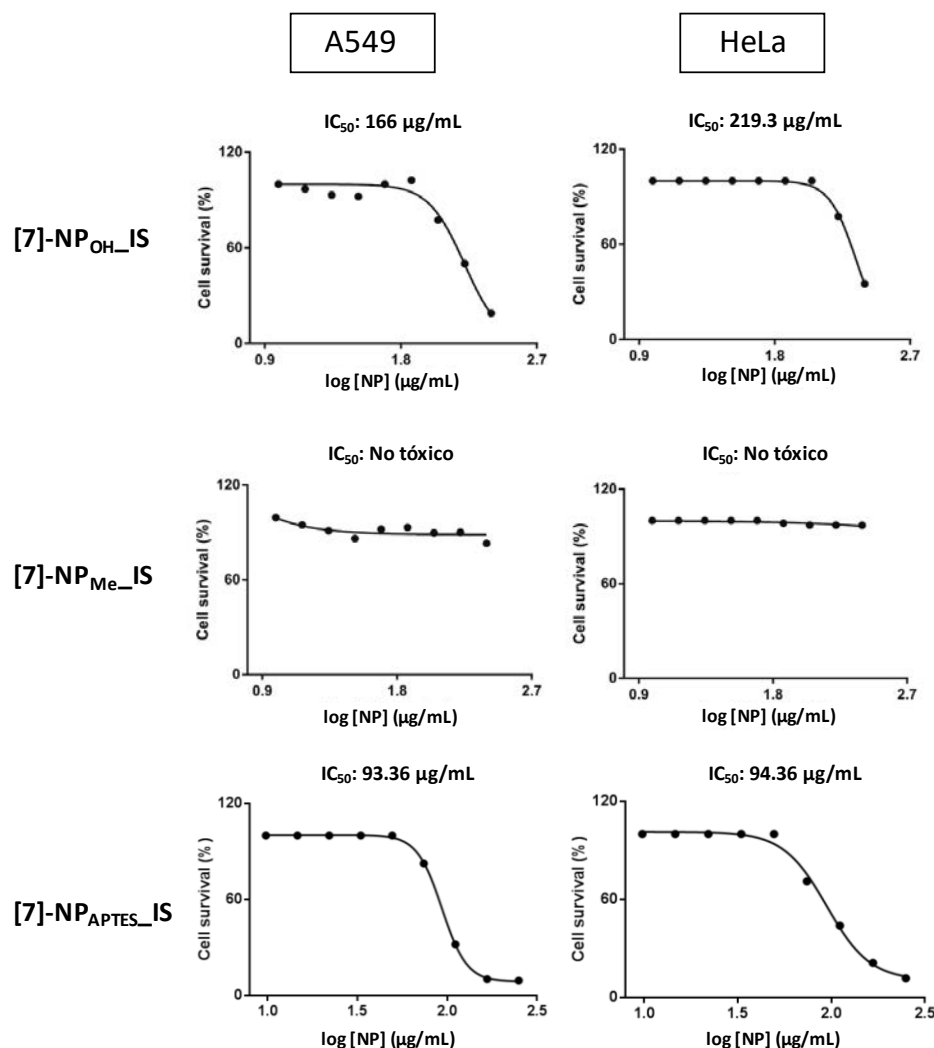


**Figura A.III.11.** Curvas de dosis-respuesta para la determinación de los valores de citotoxicidad de IC<sub>50</sub> de las nanopartículas *in-situ* [7]-NP\_IS en líneas celulares A549 y HeLa. Los valores de IC<sub>50</sub> se corresponden a la dosis necesaria para inhibir el crecimiento del 50% de las células.

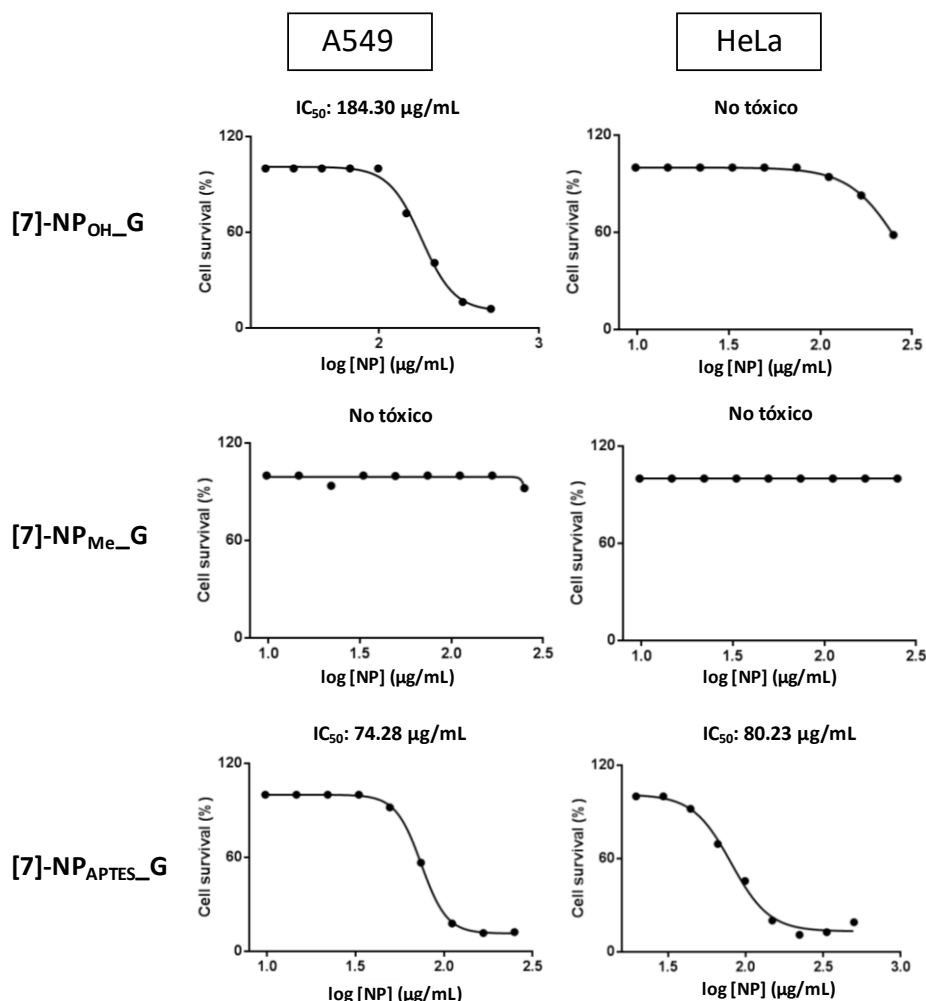


**Figura A.III.12.** Curvas de dosis-respuesta para la determinación de los valores de citotoxicidad de IC<sub>50</sub> de las nanopartículas grafteadas [7]-NP\_G en líneas celulares A549 y HeLa. Los valores de IC<sub>50</sub> se corresponden a la dosis necesaria para inhibir el crecimiento del 50% de las células.

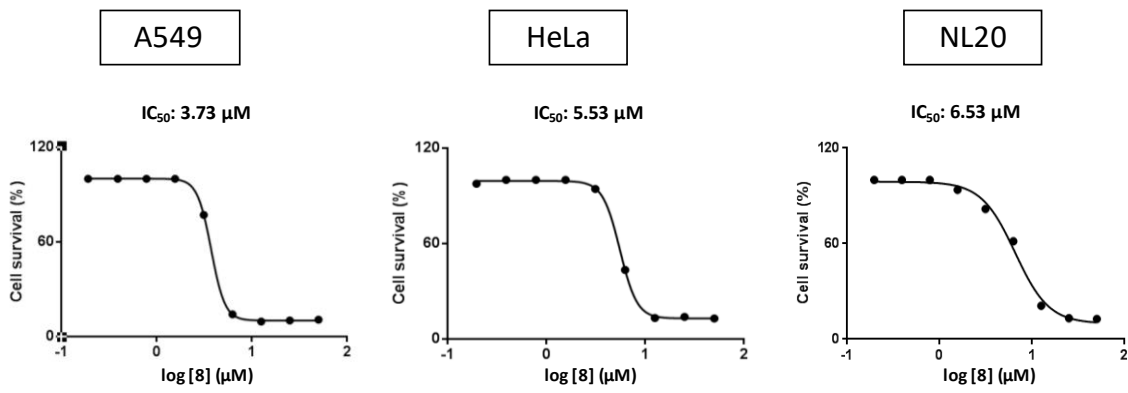


**Figura A.III.13.** Curvas de dosis-respuesta para la determinación de los valores de citotoxicidad de IC<sub>50</sub> del compuesto [Ir(dFppy)<sub>2</sub>(dbbpy)]Cl (8) en líneas celulares A549, HeLa y NL20. Los valores de IC<sub>50</sub> se corresponden a la dosis necesaria para inhibir el crecimiento del 50% de las células.

***Research at the Laboratoire de  
Chimie et des Biomatériaux  
Supramoléculaires***

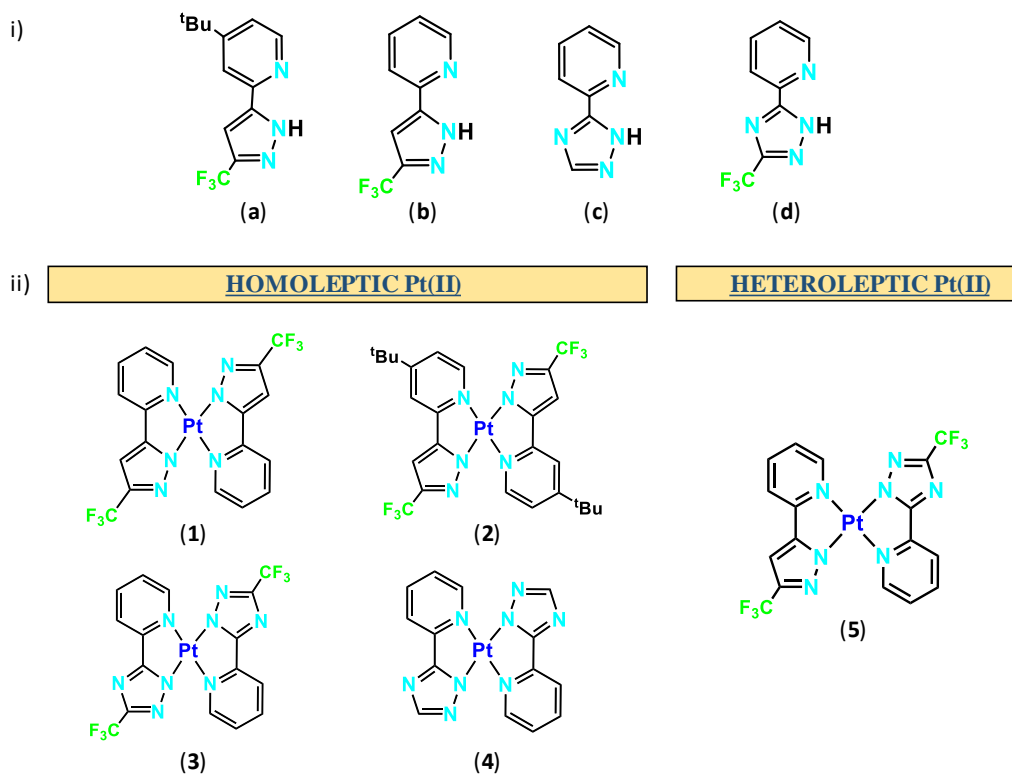




During my third year of pre-doctoral work I spent a four months research stay at the Laboratoire de Chimie et des Biomatériaux Supramoléculaires, headed by Prof. Luisa de Cola (Institut de Science et d'Ingénierie Supramoléculaires in Strasbourg, France). The main goal of the stay was strongly related with my pre-doctoral work. It was mainly focused on the design of discrete silica nanoparticles functionalized with platinum(II) complexes that emit in the low energy region (red or NIR), and their possible use as biomarkers.

Here, I present a summary of the research done during the stay.

In a first step, I prepared the pyrazole and tryazole ligands listed in scheme A.V.1 (i) and used them for the synthesis of five homo- and heteroleptic platinum(II) compounds (PtL<sub>2</sub> and PtLL', respectively). All of them were fully characterized by the usual spectroscopic means (IR, UV-vis absorption and multinuclear NMR), elemental analysis and mass spectrometry. All of them featured good emissive properties in the solid state, showing efficient emissions in the range between 560-700 nm ( $\phi$  20-63%).



**Scheme A.V.1.** Pyrazole and tryazole ligands (i) used in the synthesis of different homo- and heteroleptic platinum(II) complexes (ii).

Among them, the one emitting in the lowest energy region (**1**,  $\lambda_{\text{em}}$  655 nm solid state, r.t.) was used to prepare new stable luminescent silica nanoparticles. In this case, the functionalization was carried out according to *post-synthetic* approaches. Thus, we first

synthesized the complex-free silica nanoparticles (see figure A.V.1, a) by reacting tetramethylorthosilicate (TMOS), which acts as the silica source, in basic medium and in the presence of CTAB. The resulting material showed a mesoporous nature, determined by the type IV isotherms, with particle sizes of *ca.* 500 nm and pore diameters of 3.0 nm. The functionalized material (**[1]-SNP**) was prepared by subliming the platinum(II) complex **1**, under high vacuum at 250 °C, on the surface and into the mesopores of the silica nanoparticles (see figure A.V.1, b). The subsequent purification of the particles by several washings with THF yielded the final material (figure A.V.1, c).

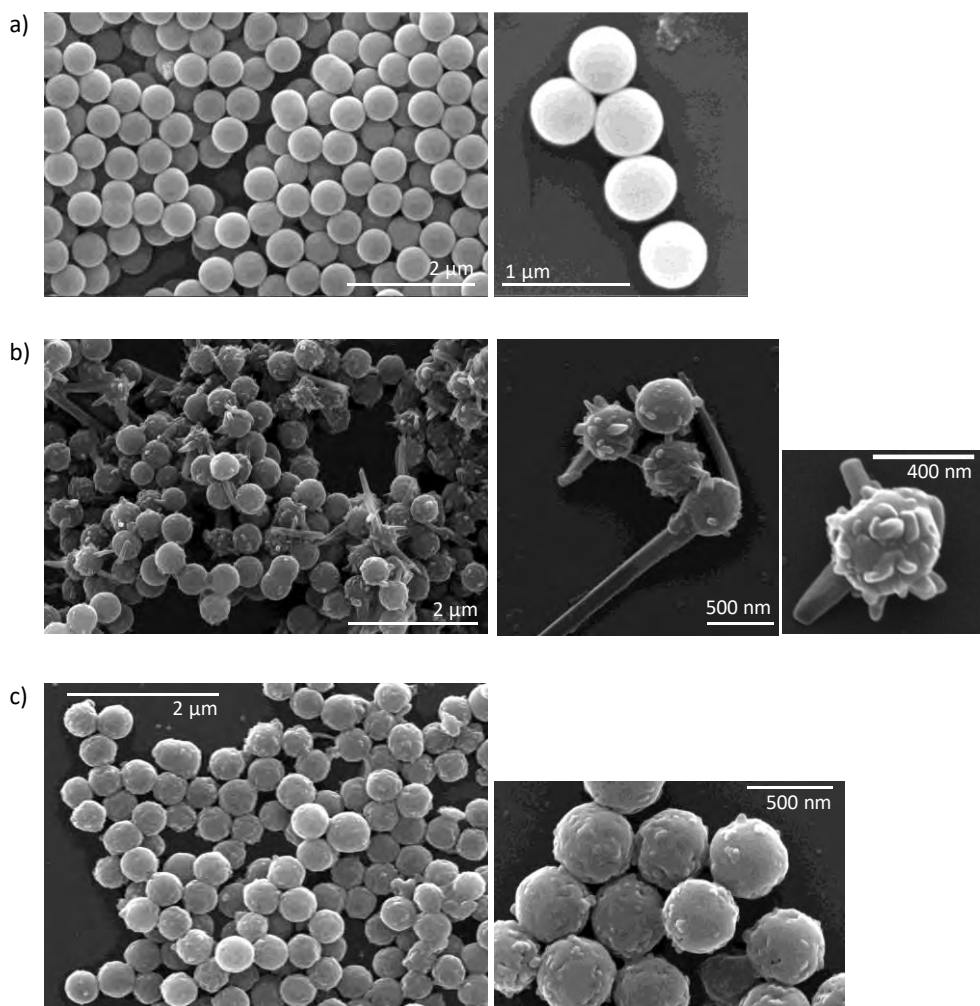


**Figure A.V.1.** SEM images of complex-free silica nanoparticles (a) and of the functionalized material (**[1]-SNP**) obtained after the sublimation process at 250 °C, before (b) and after (c) the washing step.

The textural properties (SEM, SAXS, N<sub>2</sub> adsorption/desorption, XPS) of the resulting hybrid were evaluated. Studies based on XPS or EDX spectroscopy, among others, revealed the presence of the platinum complex into the silica nanoparticles. As an example, EDX spectrum is presented in figure A.V.2. As shown, apart from the silicon and oxygen peaks, the ones corresponding to

platinum and fluorine atoms were also clearly observed. Meanwhile, XPS data allowed to determine the loading of the complex in the silica material (*ca.* 35%).

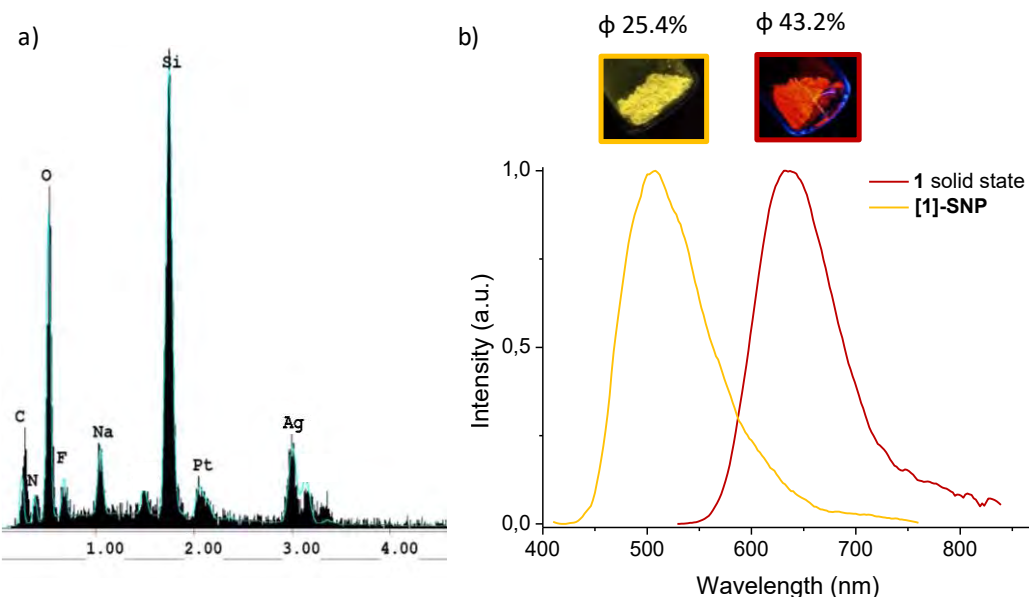


**Figure A.V.2.** EDX spectrum of the sublimed silica nanoparticles (a). Emission spectra of the pure complex in the solid state (in red) compared to the silica nanoparticles (in yellow) (b).

Finally, the photophysical properties of both the complexes and the nanoparticles were also studied. Focusing on complex **1**, this derivative is non-emissive in solution at room temperature, but exhibits an intense non-structured emission band at 655 nm ( $\phi$  43.2%). As observed for similar red-emitter Pt(II) complexes,<sup>197</sup> which exhibit solid-state aggregation and high PLQY values, this feature is ascribed to a  $^3\text{MMLCT}$  character favored by the presence of Pt···Pt and/or  $\pi\cdots\pi$  interactions. The functionalized nanoparticles **[1]-SNP** display a broad emission band at higher energies (500 nm, figure A.V.2). This blue-shifted feature seems to point towards the presence of weaker intermolecular interactions between the Pt(II) molecules sublimed inside the silica mesopores, which could preclude their optimal stacking. Nonetheless, the emission quantum yield of **[1]-SNP** is still remarkably high.

At this moment, all these data are being prepared to be sent for publishing.





